



ABSTRACTS ORAL

icavs.org



Vienna, AUSTRIA

July 12-17, 2015

Platinum Sponsors



Gold Sponsors



SUN	MON	TUE	WED	THU	FRI
08:45-9:00	Opening of ICAVS 8 - HS1 HS1 and video broadcast to HS5	HS1 and video broadcast to HS5	HS1 and video broadcast to HS5	HS1 and video broadcast to HS5	HS1 and video broadcast to HS5
09:00-10:10	Rainer Hillenbrand Mikhail Belkin	Zhenchao Dong Nathalie Picqué	Shigeki Yamamoto Klaus Gerwert	Sebastian Schlücker Rudolf Kessler	Tahel Tahara Martin Zanni
10:10-10:40	Coffee Break	Coffee Break	Coffee Break	Coffee Break	Coffee Break
10:40-12:00	HS5: Material Science 1 HS6: Biomedical Applications 1 HS8: Portable Raman Systems	HS5: Appl. in Life Sciences 1 HS6: Nanomat. 2 HS8: QCL Source Development	HS5: Biomedical Applications 4 HS6: Material Science 5 HS8: PAT 1	HS5: SERS 2 HS6: Appl. in Life Sciences 3 HS8: PAT / imPACTs	HS1: Julia Davies Kathleen Gough Gottfried Strasser Notburga Gierlinger
12:00-13:30	Lunch Time	Lunch Time	Lunch Time / What's hot session HS1	Lunch Time	ICAVS 9 and Closing of ICAVS 8
13:30-14:50	IR Imaging Material Science 2 Biomedical Applications 2 Environ. and Planetary Sci.	Surface Science Material Science 4 Comp. Spectr. 1 Gas Sensing	Excursions	Plasmonics Material Science 6 Time-resolved Spectroscopy PAT 2	
14:50-15:15	Coffee Break	Coffee Break		Coffee Break	
15:15-16:20	Nearfield IR Imaging Nanomat. 1 Biomedical Applications 3 Raman Systems	TERS SERS 1 Appl. in Life Sciences 2 QCL Spectrosc. & Imaging	Heuriger	SERS 3 Comput. Spectr. 2 Biomedical Applications 5 Advances in IR Detectors	
16:20-18:00	Poster Session A Microscopy & Imaging, Nearfield Vib. Spec., Biomedical Applications, Fine Arts, Safety Applications, Nanomaterials, Geoscience 1, Portable Raman Systems, Material Science 1	Poster Session B MIR Laser Spectroscopy 1, TERS, plasmonics, SERS, SEIRA, Time-Resolved Spectroscopy 1, Life Sciences, Instrumentation (NIR, MIR, THz)		Poster Session C VOA, PAT, Time-resolved Spectroscopy 2, Non-linear techniques, Material Science 2, Surface Science, MIR Laser Spectroscopy 2, Geoscience 2, Computational Spectroscopy 2	
Evening Program	Bruker Welcome Mixer	Shimadzu Young Scientist Event		Conference Dinner	

| ----- Workshops (12:00- 18:00) ----- |



Infrared nanoscopy and nano-FTIR spectroscopy by elastic light scattering from a scanning probe tip

Rainer Hillenbrand^{1,2}

¹CIC nanoGUNE and UPV/EHU, 20018 Donostia-San Sebastián, Spain

²IKERBASQUE, Basque Foundation for Science, 48011 Bilbao, Spain

Keywords: infrared near-field microscopy, infrared nano-spectroscopy, nano-FTIR

With the development of scattering-type scanning near-field optical microscopy (s-SNOM)¹, the analytical power of visible, infrared and THz imaging has been brought to the nanometer scale. The spatial resolution of about 10 - 20 nm opens a new era for modern nano-analytical applications such as chemical identification, free-carrier profiling and plasmonic vector near-field mapping.

s-SNOM is based on elastic light scattering from atomic force microscope

tips. Acting as optical antennas, the tips convert the illuminating light into strongly concentrated near fields at the tip apex (nanofocus) (Figure 1), which provides a means for localized excitation of molecule vibrations, plasmons or phonons in the sample surface. Recording the tip-scattered light as a function of sample position subsequently yields nanoscale resolved optical images, beating the diffraction limit in the infrared spectral range by more than two orders of magnitude.

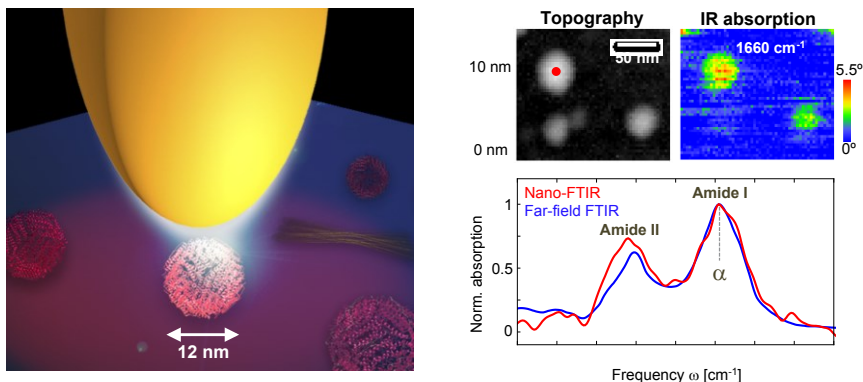


Figure 1. Infrared nanoimaging of a single protein complex (ferritin, 5000 C=O bonds, 1 attogram mass). Left: Illustration of the infrared illuminated tip of a near-field microscope on top of a ferritin complex. Right: Topography and infrared absorption image of three nanoparticles reveals that only two of them are protein complexes. The nano-FTIR spectrum (red) was taken on the complex marked by the red dot in the topography image.

Using broadband IR illumination and Fourier-transform spectroscopy of the tip-scattered light^{2,3}, IR spectra with 20 nm spatial resolution can be acquired (nano-FTIR). Near-field images and near-field absorption spectra of molecular vibrations in mid-infrared fingerprint region allow for chemical mapping, identification of polymer³ and protein⁴ nanostructures, and for quantitative measurement of the complex-valued local dielectric function⁵, among others.

¹ F. Keilmann, R. Hillenbrand, *Phil. Trans. R. Soc. Lond. A* 362, 787 (2004)

² F. Huth, et al., *Nature Mater.* 10, 352 (2011)

³ F. Huth, et al., *Nano Lett.* 12, 3973 (2012)

⁴ I. Amenabar et al., *Nat. Commun.* 4:2890 doi: 10.1038/ncomms3890 (2013)

⁵ A. Govyadinov, et al., *J. Phys. Chem. Lett.* 4, 1526 (2013)



Infrared vibrational nanospectroscopy via molecular expansion force detection

Feng Lu, Mingzhou Jin and Mikhail A. Belkin

Department of Electrical and Computer Engineering
The University of Texas at Austin, Austin, TX 78758, USA

Keywords: Infrared spectroscopy, nanoscale, opto-mechanical

Mid-infrared (mid-IR) vibrational absorption spectroscopy is a universal method to identify chemicals by their molecular absorption fingerprints. There is a growing demand for high precision characterization of materials and biological agents with nanometer spatial resolution and with a sensitivity of only a few molecules.

We report a technique for very sensitive mid-IR nanospectroscopy based on observing a deflection of an atomic force microscope (AFM) cantilever due to mechanical forces exerted by molecules photoexcited with laser pulses on the AFM tip. Spectra are obtained by recording the cantilever deflection amplitude as a function of excitation laser wavelength. Using sample photoexpansion to perform nanoscale molecular spectroscopy was originally suggested by A. Dazzi *et al.*¹. However, to produce detectable cantilever deflection, the original method required high-power laser pulses to induce sample heating by 10-50 degrees and sample thickness of at least ~100 nm. We have dramatically improved the sensitivity of photoexpansion microscopy to work with samples as thin as one molecular monolayer with better than 30 nm spatial resolution². This was achieved sending low-power laser pulses at a repetition frequency that is tuned in resonance with the mechanical vibrational frequency of the AFM cantilever and by employing tip-enhancement of the optical field below a sharp gold-coated AFM tip.

The experimental setup is presented in Fig. 1. Mid-IR laser pulse train from quantum cascade laser (QCL) is focused onto the molecules below a sharp AFM tip. Upon illumination, the molecules absorb radiation energy, rapidly expand and push the tip, which causes periodic displacement of the AFM probe. With the laser trigger as reference signal, we are able to record the AFM cantilever vibration amplitude using a lock-in amplifier. By plotting the lock-in output as a function of QCL emission wavelength, we obtain the molecular expansion force spectrum, which is a proxy for molecular infrared absorption spectrum.

When we tune the QCL repetition frequency to match the cantilever mechanical resonant frequency, the cantilever vibration amplitude is amplified by its Q factor, which can be as high as 5,000 in air. The signal can be increased further using tip-enhancement by employing

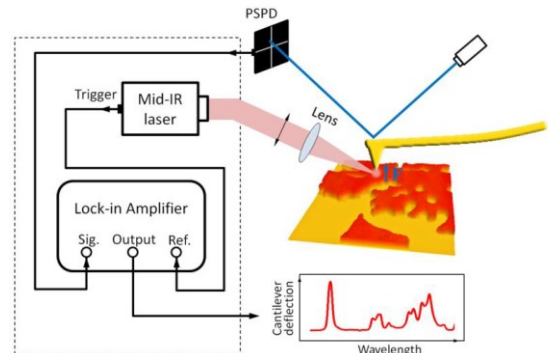


Figure 1. Experimental setup.

sharp gold-coated AFM tips and placing samples on metal substrates. The electromagnetic field intensity under the tip is increased by a factor of 4×10^5 , and is spatially localized to a ~ 10 nm-radius region. The combined mechanical and tip enhancement directly translates into very high sensitivity and spatial resolution of our method.

Nanoscale photoexpansion spectra of two self-assembled monolayers (SAMs) on flat gold substrate are shown in Figs. 2(a) and 2(b). The SAM thicknesses are 1.3 nm and 0.5 nm for hydroxyl-terminated hexa (ethylene glycol) thiol (EG6-OH) and 4-nitrothiophenol (NTP), respectively. The photoexpansion spectra (blue circles) match well with the reference macroscopic spectra (red line). To demonstrate high spatial resolution, we used a sample with monolayer islands of poly ethylene glycol thiol (PEG) and took spectra around 1342 cm^{-1} absorption peak of PEG at a series of points, separated by 30 nm steps, along the line scan show in the topographic image

in Fig. (c) The results are shown in Fig. 2(d). Absorption peak is seen clearly on top of PEG islands while on the bare gold substrate, the spectra are flat. Chemical mapping shown in Fig. 2(e) is performed by fixing the laser wavenumber at the absorption peak and scanning with cantilever deflection signal.

To sum up, non-destructive mid-IR photoexpansion spectroscopy and imaging technique with monolayer sensitivity and better than 30 nm spatial resolution is demonstrated. We estimate that approximately 300 molecules contribute to cantilever deflection in our current experiments and spectra of as few as 30 molecules would be detectable. Future work towards extensions of this method to operation in aqueous environment will also be discussed.

The authors acknowledge the financial support from the Welch Foundation (grant No. F-1705) and the U.S. Department of Energy STTR program.

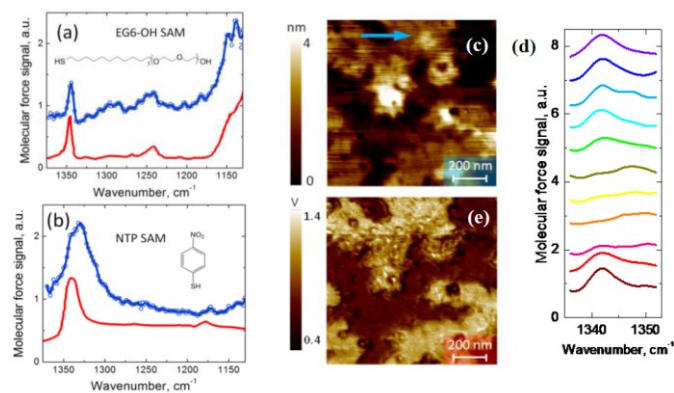


Figure 2. Nanoscale photoexpansion spectra (blue circles) compared to macroscopic infrared absorption-reflection spectra (red line) of (a) EG6-OH and (b) NTP. (c) AFM topography of PEG islands on gold. (d) Photoexpansion spectra taken along the blue arrow in (c) with 30 nm steps. (e) Chemical mapping of the area shown in (c).

¹ Dazzi, A., Prazeres, R., Glotin, F. & Ortega, J. M. (2005), “Local infrared microspectroscopy with subwavelength spatial resolution with an atomic force microscope tip used as a photothermal sensor”, *Optics Letters* 30, 2388–2390

² Lu, F., Jin, M & Belkin (2014), “Tip-enhanced infrared nanospectroscopy via molecular expansion force detection”, *Nature Photonics* 8, 307-312

Absorption Spectroscopy and Imaging from the Visible through Mid-IR with 20 nm Resolution Using AFM Probes

Andrea Centrone¹

¹Center for Nanoscale Science and Technology, National Institute of Standard and Technology,
Gaithersburg, MD 20899, United States

Keywords: PTIR, nanoscale IR spectroscopy, nanoscale visible spectroscopy, near-field.

Correlated nanoscale composition and optical property maps are important to engineer nanomaterials in applications ranging from photovoltaics to sensing and therapeutics. Light in the visible and near-IR probes electronic transitions in materials, providing information related to the band gap and defects. Light in mid-IR probes vibrational transitions and provides information on chemical composition. However, light diffraction limits the lateral resolution of conventional micro-spectroscopic techniques to approximately half the wavelength of light, which is insufficient for characterizing materials at the nanoscale (especially in the mid-IR). Additionally, the wavelength-dependent resolution impedes direct comparison of spectral maps from different spectral ranges.

Photo Thermal Induced Resonance (PTIR)^{1,2} is a novel technique that circumvents light diffraction by employing an AFM tip as a local detector to measure light absorption with a wavelength-independent resolution. The function of the passive AFM tip is to locally transduce the thermal expansion of the sample induced by light absorption into large cantilever oscillations. Our PTIR setup combines an AFM microscope with three lasers providing

wavelength-tunability from 500 nm to 16000 nm continuously.³ Local absorption spectra (electronic or vibrational) and maps are obtained recording the amplitude of the tip deflection as a function of wavelength and position, respectively.

In the first part of the talk I will briefly discuss the PTIR working principles, its lateral resolution and its sensitivity. Results show that the PTIR signal intensity is proportional to the local absorbed energy suggesting applicability of this technique for quantitative chemical analysis at nanoscale, at least for thin (< 1000 nm) samples.² Additionally, a wavelength-independent resolution of 20 nm is demonstrated across the whole spectral range.³

In the second part of the talk I will apply the PTIR technique to characterize different nanomaterials and show how the local information gathered can provide insightful information and possibly help to engineer nanomaterials for greatest efficacy. Examples will include recent work from my lab to characterize: i) plasmonic near-field hot spots and plasmonic modes,^{4,5,6} ii) chemically heterogeneous domains in Metal-Organic Frameworks crystals⁷ and iii) the in-situ degradation of multi-crystalline tri-halide perovskites.⁸

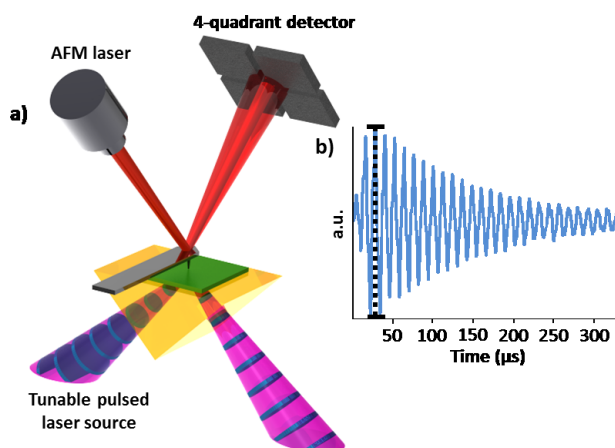


Figure 1. (a) Illustration of the PTIR measurement: if the sample absorbs the laser pulses (blue discs in purple cones) it rapidly expands deflecting the AFM cantilever which is monitored by a four-quadrant detector. (b) The maximum peak to peak deflection during the cantilever ring down is proportional to the absorbed energy.

¹ Dazzi A., Prazeres R., Glotin E., Ortega J. M. 2005. *Optics Letters*, 30, 2388-2390.

² Lahiri B., Holland G., Centrone A. (2013). *Small*, 9, 439-445.

³ Katzenmeyer A. M. Holland G., Kjoller K., Centrone A. (2015). *Analytical Chemistry*, DOI: 10.1021/ac504672t

⁴ Lahiri B., Holland G., Aksyuk V., Centrone A. (2013), *Nano Letters*, 13, 3218-3224.

⁵ Katzenmeyer A. M., Chae J., Kasica R., Holland G., Lahiri B., Centrone A. (2014), *Advanced Optical Materials*, 2, 718-722.

⁶ Aksyuk V., Lahiri B., Holland G., Centrone A., (2015), *Nanoscale*, 7, 3634-3644.

⁷ Katzenmeyer A. M., Canivet J., Holland G., Farrusseng D., Centrone A., (2014). *Angewandte Chemie International Edition* 53: 2852-2856.

⁸ Dong R., Fang Y., Chae J., Dai J., Xiao Z., Dong Q., Yuan Y., Centrone A., Zeng X. C., Huang J., (2015) *Advanced Materials*, DOI: 10.1002/adma.201405116.

Recovery of Permittivity and Depth from Near-Field Data as a Step toward Infrared Nanotomography

A.A. Govyadinov¹, S. Mastel¹, F. Golmar², A. Chuvillin^{1,3}, P.S. Carney⁴, and R. Hillenbrand^{1,3,5}

¹CIC nanoGUNE, Donostia-San Sebastian, Spain

²I.N.T.I.-CONICET and ECyT-UNSAM, San Martin, Argentina

³IKERBASQUE, Basque Foundation for Science, Bilbao, Spain

⁴ECE Dept. and Beckman Institute, U. of Illinois at Urbana-Champaign, Urbana, USA

⁵EHU/UPV, Donostia-San Sebastian, Spain

Keywords: chemical imaging, nano-FTIR, nanotomography, near-field microscopy, thin films

Scattering-type scanning near-field optical microscopy (s-SNOM) is a powerful optical technique for nondestructive spectroscopic imaging with deep subwavelength resolution¹. In s-SNOM, images are recorded by scanning a sharp illuminated probe along the sample surface and detecting the backscattering. This scattering depends on the near-field interaction between the probe and the sample, thus revealing the dielectric properties of the sample in the image contrast. While s-SNOM has demonstrated the ability of quantitative analysis of such images for samples with structure varying in two dimensions², the elucidation of sample structure in all three dimensions (3D) has proved elusive.

The main obstacle to inferring the 3D sample structure from s-SNOM images is the complicated nature of near-field interaction that intermixes (couples) the dielectric properties of sample constituents/features with their distance to the tip. Thus the same image contrast could result from the variation of the dielectric permittivity of the feature or its depth below the sample surface, i.e. from the sample geometry. The lack of simple image interpretation method resulted in s-SNOM

being traditionally regarded as a technique for surface studies.

In this work we break the traditional view at s-SNOM and open the door to the third dimension for near-field techniques by introducing and providing the first experimental demonstration of a method for performing a rapid recovery of the thickness and permittivity of simple 3D objects, such as thin films and polymer nanostructures³. This is accomplished by taking advantage of the near-field data recorded at multiple harmonics of the oscillation frequency of near-field probe as depicted in Figure 1. A complete set of such harmonics serves as a proxy for an approach curve that measures the near-field interaction as a function of tip-sample distance. Thus multiple harmonics of the demodulated signal encode information about the volumetric composition of the sample.

To recover this volumetric information, we developed a novel nonlinear model that describes the near-field interaction of the s-SNOM tip with a film deposited on a substrate. The key advantage of our model is that it allows for an analytic inversion of the associated scattering problem with respect to the sample permittivity, parameterized by a single depth/thickness variable. The correct film thickness is then obtained by enforcing

the consistency of the results derived from different harmonics of the scattered signal. Mathematically, this formulates a simple one-dimensional minimization problem that decouples the dielectric properties from the sample geometry, thus allowing for the unique interpretation of near-field images. In conjunction with the simplicity of obtaining the necessary data (the signal harmonics are routinely recorded as a part of the background suppression in s-SNOM) our technique presents a humble, practical method of recovering the subsurface sample structure from near-field measurements.

Our work enables the quantitative nondestructive nanoscale-resolved optical studies of thin films, coatings and functionalization layers, as well as the structural analysis of multiphase materials and other samples in which the topography does not correlate with the chemical or optical properties. It opens new frontiers for chemometrics, materials and bio sciences and represents a major step towards the further goal of the near-field nanotomography.

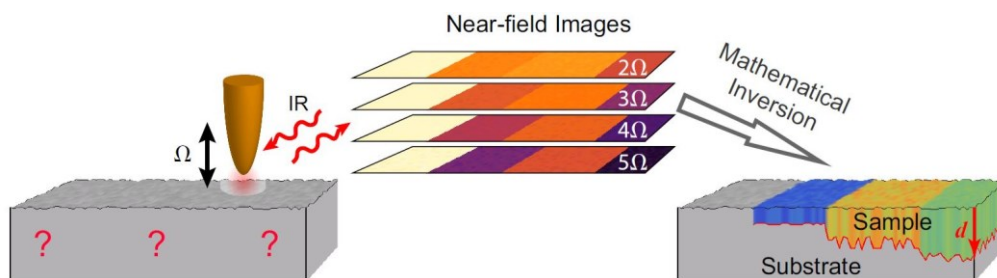


Figure 1. Schematics of the s-SNOM experiment and the conceptual representation of the reconstruction procedure that yields the sample structure. The field scattered by an oscillating AFM tip is detected interferometrically and demodulated at higher harmonics of the tip oscillation frequency. By scanning the sample surface, a set of near-field images (or spectra) is recorded. A mathematical inversion procedure is then applied at each pixel to recover the sample structure, i.e., thickness (represented by red curve) and dielectric permittivity/absorption (represented by fill color) of the sample layer.

¹ T. Taubner, R. Hillenbrand, and F. Keilmann, *Appl. Phys. Lett.* 85, 5064 (2004).

² A. Govyadinov, I. Amenabar, F. Huth et al, *J. Phys. Chem. Lett.* 4, 1562 (2013).

³ A. Govyadinov, S. Mastel, F. Golmar et al, *ACS Nano*, 8 (7) (2014).

Committing SINS: broadband synchrotron infrared nano-spectroscopy

Hans A. Bechtel¹, Eric A. Muller², Rob L. Olmon², Michael C. Martin¹, Markus B. Raschke²

¹Advanced Light Source, Lawrence Berkeley National Laboratory, Berkeley, California 94720, United States

²Department of Physics, Department of Chemistry, and JILA, University of Colorado, Boulder, Colorado 80309, United States

Keywords: near-field, *s*-SNOM, chemical imaging

The availability of suitable infrared sources has limited scattering-type-scanning near-field optical microscopy (*s*-SNOM) from reaching its full potential for nano-spectroscopic applications. Continuous wave (CW) tunable infrared lasers offer the highest spectral irradiance, but their narrow tuning range typically spans only 1 vibrational mode. Broadband femtosecond-pulsed IR lasers, which trade both spectral irradiance and total power for increased spectral bandwidth, enable the investigation of one or multiple vibrational modes without tuning^{1,2}, but the bandwidth of the broadest IR laser sources yet implemented for *s*-SNOM is only a fraction of the range provided by a thermal source. The low spectral irradiance and the lack of spatial coherence of thermal sources, however, severely limits *s*-SNOM signal levels. Synchrotron IR radiation, in contrast, is spectrally broad, bright, and spatially coherent, with a spectral irradiance 1000 times higher than a thermal source and a spectral bandwidth over 10 times that of the broadest laser sources, typically limited only by the beamsplitter/detector combination (Fig. 1).

By combining *s*-SNOM with synchrotron infrared radiation, synchrotron infrared nano-spectroscopy (SINS) enables molecular and phonon vibrational spectroscopic imaging, with rapid spectral acquisition, spanning the mid- and far-

infrared regions (330-5000 cm^{-1}) with nanoscale spatial resolution. This highly powerful combination provides access to a qualitatively new form of nano-chemometric analysis with the investigation of nanoscale, mesoscale, and surface phenomena that were previously impossible to study with IR techniques. We have installed a SINS end-station at Beamline 5.4 at the Advanced Light Source (ALS) at Lawrence Berkeley National Laboratory³, making the *s*-SNOM technique widely available to non-experts, such that it can be broadly applied to biological, surface chemistry, materials, or environmental science problems.

We demonstrate the performance of SINS on a variety of hard and soft-matter systems, including correlated and 2D materials, antennas, semiconductors, nanoparticles, biominerals, protein nanostructures, and extraterrestrial dust. Figure 2 highlights a biomineral application, showing AFM topography and SINS spectra of the transition region between two calcium carbonate polymorphs (calcite and aragonite) in a polished blue mussel (*M. edulis*) shell. SINS spectra show spectral shifts in two different vibrational modes of the two polymorphs measured simultaneously in distinct spectral ranges. A linescan across the transition region demonstrates a sharp transition (<100 nm) between calcite and aragonite, as determined by the spectral shifts.

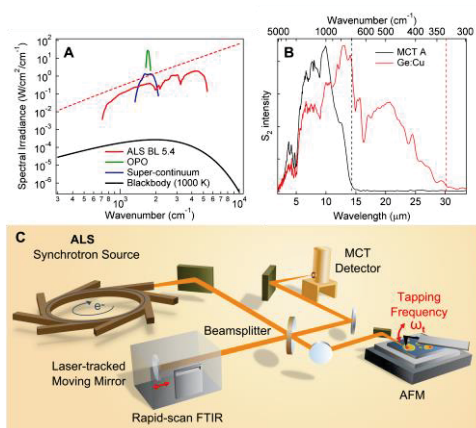


Figure 1. (A) Spectral irradiance and bandwidth achievable in a single acquisition for *s*-SNOM-implemented broadband IR sources: IR synchrotron light from Advanced Light Source (ALS) Beamline 5.4 (calculated, red-dashed; MCT detector-limited, red-solid), an OPO laser source (green) [1], a super-continuum laser source (blue) [2], and a 1000 K blackbody source (black). (B) 2nd harmonic signal on gold with KBr / MCT A (black) and Si / Ge:Cu (red) beamsplitter/detector combinations. (C) Optical layout of the SINS experiment.

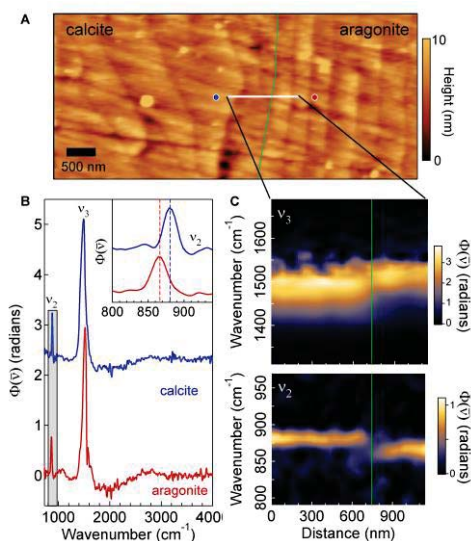


Figure 2. (A) Topography of *M. edulis* shell in the transition region between calcite and aragonite CaCO₃ polymorphs, denoted by green line. (B) SINS phase spectra of calcite (blue) and aragonite (red) acquired at the location of the blue and red circles in (A). Inset: zoom in of v₂ mode (gray box). (C) Spatio-spectral SINS line scan phase plot across the interface region between calcite (left) and aragonite (right) in an *M. edulis* shell.

¹ Xu XG, Rang M, Craig IM, Raschke MB (2012), *J. Phys. Chem. Lett.* 3 (13), 1836–184.1

² Huth F., Govyadinov A., Amarie S., Nuansing W., Keilmann K., Hillenbrand R. (2012), *Nano Letters* 12 (8), 3973–3978.

³ Bechtel HA, Muller EA, Olmon RL, Martin MC, Rashcke MB (2014), *Proceedings of the National Academy of Sciences*, 111 (20), 7191–7196.

**Nanoscale chemical identification by
infrared near-field spectroscopy (nano-FTIR)**

Stefan Mastel¹, Alexander A. Govyadinov¹, Thales V. A. G. de Oliveira¹, Iban Amenabar¹, and Rainer Hillenbrand^{2,3}

¹CIC nanoGUNE, 20018 Donostia-San Sebastian, Spain

²CIC nanoGUNE and EHU/UPV, 20018 Donostia-San Sebastian, Spain

³IKERBASQUE, Basque Foundation for Science, 48011 Bilbao, Spain

Keywords: nano-FTIR, vibrational spectroscopy, chemical identification.

Fourier transform infrared (FTIR) spectroscopy is a versatile and established technique for chemical characterization. Its resolution, however, is limited by diffraction to about half the wavelength of the mid-IR radiation (about several μm). This limitation can be overcome by scattering-type scanning near-field optical microscopy (s-SNOM). In s-SNOM, light is scattered at a metalized atomic force microscope (AFM) tip scanning in close proximity to a sample. The tip acts as an antenna, concentrating incoming radiation in a nanofocus at the tip apex, which interacts in the near field with the sample. The tip-scattered light contains optical information about the sample, such as dielectric function¹ or absorption². Because the nanofocus is of the size of the tip radius, the resolution is determined essentially by the apex diameter (about 10-20 nm), beating common far-field FTIR techniques by about three orders of magnitude.

In s-SNOM, spectroscopy is enabled by broadband illumination of the tip and detection of the scattered light with a Fourier transform (FT) spectrometer. This technique has been named nano-FTIR. In contrast to conventional FT, the nano-FTIR spectrometer is used in an asymmetric configuration, i.e. the tip/sample is located in one of the interferometer arms. This enables the measurement of amplitude and

phase of the scattered field, respectively its real and imaginary part.

Here we discuss the physical interpretation of these different quantities, and how they compare to standard far-field FTIR spectra. To that end, we study the spectral behavior of infrared near-field phase and absorption (see Figure 1 (a) and (b)) of thin polymer films, both quantities signifying the presence of a molecular resonance.

Supported by a comprehensive theoretical analysis, our results show that the near-field phase spectra only weakly depend on the film thickness and can be used for an approximate comparison with grazing incidence FTIR (GI-FTIR) spectra (compare Figure 1 (a) and (c)). In contrast, the near-field absorption spectra can be compared more precisely with far-field spectra: for ultrathin organic films they match well GI-FTIR spectra, while for thick films a good agreement with standard transmission FTIR spectra is found. This can be seen by comparing the respective curves in Figure 1 (b) and (c).

With our study we establish a solid basis for the interpretation of infrared near-field spectra³ and provide guidelines for their straightforward comparison to standard FTIR spectra, thus enabling infrared characterization and chemical identification of organic samples on the nanometer scale.

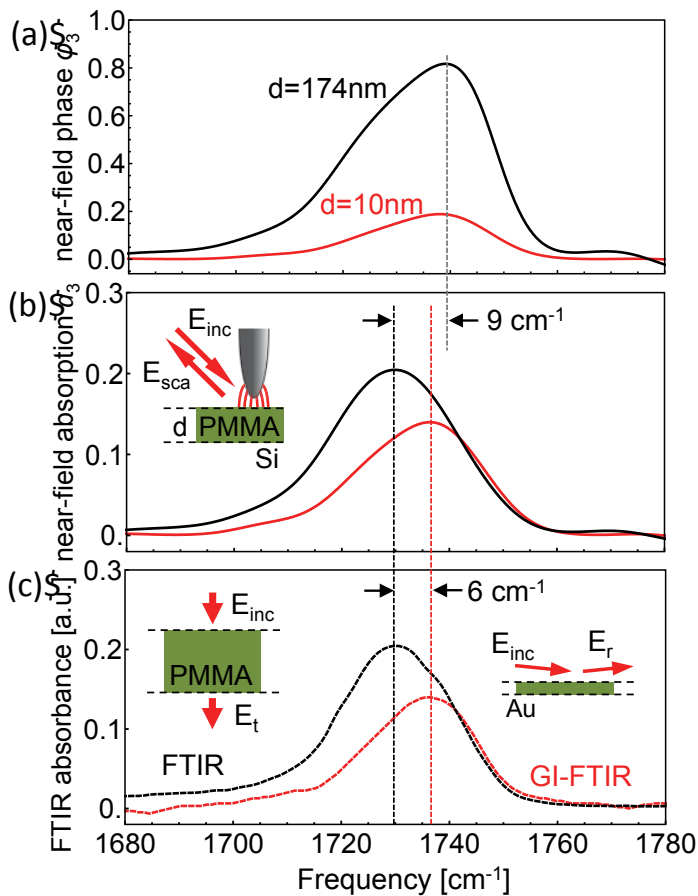


Figure 1. Nano-FTIR near-field spectra (a) Near-field phase and (b) near-field absorption spectra of Poly(methyl methacrylate) (PMMA) around the C=O molecular resonance at about 1735 cm^{-1} . (c) Far-field transmission and grazing incidence (GI) FTIR spectra of PMMA.

¹Govyadinov A. A., Mastel S., Golmar F., Chuvilin A., Carney P. S., Hillenbrand R. (2014), *ACS Nano* **8** (7), 6911-6921

²Huth F., Govyadinov A. A., Amarie S., Nuansing W., Keilmann F., Hillenbrand R. (2012), *Nano Letters* **12** (8), 3973-3978

³Mastel S., Govyadinov A. A., de Oliveira V. A. G. T., Amenabar I., Hillenbrand R. (2015), *Applied Physics Letters* **106** (023113)

Developments in Mid-Infrared Nanoscopy Instrumentation

Georg Ramer, Anna Balkbekova, Andreas Schwaighofer and Bernhard Lendl

Institute for Chemical Technology and Analytics, TU Wien, Getreidemarkt 9 UPA, 1060,
Vienna, Austria

Keywords: near-field, infrared, imaging, nanoscopy

Resonance enhanced atomic force microscopy infrared nanoscopy (RE-AFMIR) is an analytical technique that allows non-destructive chemical analysis of solid-state samples at better than 50 nm spatial resolution.¹ This technique has been applied to a range of problems spanning from biology, medicine and pharmaceuticals to polymer- and material science, synthetic chemistry and plasmonics. In each of these fields the technique has been shown to provide important information that is not easily accessible with other methods. Our own research is focused on the extension and improvement of the RE-AFMIR method itself. In our self built setup consisting of a Daylight Solutions external cavity – quantum cascade laser (EC-QCL) and a Keysight 5400 AFM we have recently demonstrated a method for time-resolved analysis using RE-AFMIR, whereby a repeating or non-repeating spectral change – such as the switch between two secondary structures of a polypeptide film – can be followed at the spatial resolution provided by RE-AFMIR and a speed of one spectrum every 1.5 seconds².

One of the main challenges in RE-AFMIR is keeping the repetition rate of the

excitation laser at the contact resonance frequency of the cantilever. Since this frequency depends on parameters of the cantilever (force constant, vibration mode, setpoint) as well as of the sample (Young's modulus, surface properties) imaging across different materials leads to shifts in the contact resonance. To the operator these shifts are only visible as changes in the signal amplitude. For tracking resonance frequencies in scanning probe microscopy several techniques such as phase-locked loops (PLL), dual-frequency excitation³ and probing of the amplitude around the resonance⁴ have been proposed.

While these published methods can serve as guide for the selection of a resonance tracking technique they were usually developed for sine-wave excitation which can not always be easily translated to the pulse-train excitation provided by lasers used in RE-AFMIR. For direct comparison of different methods regarding their capability to accurately track the contact resonance in a RE-AFMIR system a flexible controller has been designed that allows to implement different tracking methods on the same sample position. We are thus able to experimentally select the most suitable resonance tracking method.

1. A. Dazzi, C.B. Prater, Q. Hu, D.B. Chase, J.F. Rabolt, C. Marcott. "AFM-IR: Combining Atomic Force Microscopy and Infrared Spectroscopy for Nanoscale Chemical Characterization." *Appl. Spectrosc.* 2012. 66(12): 1366-1384.
2. G. Ramer, A. Balbekova, A. Schwaighofer, B. Lendl. "Article A Method for Time-Resolved Monitoring of Solid State Biological Films using Photothermal Infrared Nanoscopy on the Example of Poly-L-Lysine." 2015.
3. B.J. Rodriguez, C. Callahan, S. V Kalinin, R. Proksch. "Dual-frequency resonance-tracking atomic force microscopy." *Nanotechnology.* 2007. 18(47): 475504. 10.1088/0957-4484/18/47/475504.
4. A.B. Kos, J.P. Killgore, D.C. Hurley. "SPRITE: a modern approach to scanning probe contact resonance imaging." *Meas. Sci. Technol.* 2014. 25(2): 025405. 10.1088/0957-0233/25/2/025405.



Infrared Spectroscopy in 3D and at Nano Scales

Michael C. Martin¹, Hans A. Bechtel¹, Dilworth Y. Parkinson¹, Michael J. Nasse², Carol J. Hirschmugl³, Eric A. Muller^{4,5}, Robert L. Olmon^{4,5} and Markus B. Raschke^{4,5}

¹Advanced Light Source, Lawrence Berkeley National Laboratory, Berkeley, CA USA

²Laboratory for Applications of Synchrotron Radiation, Karlsruhe Institute of Technology, Karlsruhe, Germany

³Physics Department, University of Wisconsin–Milwaukee, Milwaukee, Wisconsin, USA

⁴Departments of Physics and Chemistry, University of Colorado, Boulder, CO 80309

⁵JILA, University of Colorado and National Institute of Standards and Technology, Boulder, CO 80309

Keywords: FTIR Tomography, 3D, s-SNOM, SINS, synchrotron, nanoscopy

Synchrotron infrared beamlines use the diffraction-limited beam properties to enable a variety of cutting edge science at the micron length scale in both reflection and transmission. It has enabled a wide variety users to perform science across numerous fields. In this talk, I will explore how can we go further?

I will describe two new techniques we have recently developed and demonstrated. First, 3D FTIR tomography [1] provides spectrally rich, label-free, nondestructive visualizations of distinctive chemical compositions throughout intact biological or materials samples. The technique has combined Fourier Transform Infrared (FTIR) spectroscopy with computed tomography (CT) to create a non-destructive 3D imaging technique that provides molecular-level chemical information of unprecedented detail on biological and other specimens with no need to stain or alter the specimen. We are installing a new IR imaging and tomography endstation at beamline 2.4 of the Advanced Light Source (ALS). I will describe how the technique works and present application examples spanning a variety of scientific disciplines.

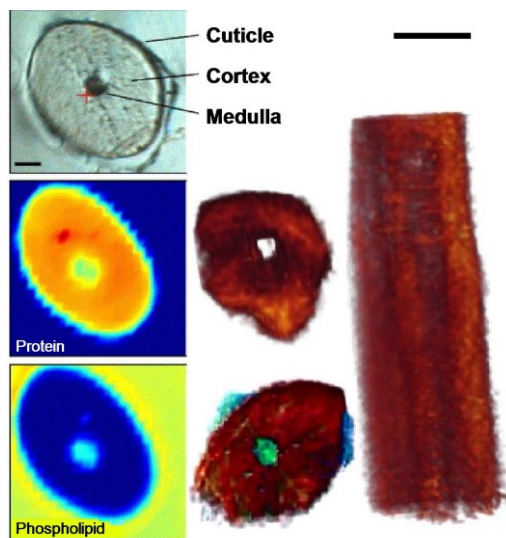


Figure 1. Spectro-microtomographic images of a human hair show absorptions of protein (red) and phospholipid (blue-green). Center, the medulla is observed to have little protein. Bottom, the medulla has higher concentrations of phospholipids.

Second, by combining scattering-scanning near-field optical microscopy (s-SNOM) with mid-infrared synchrotron radiation, Synchrotron Infrared Nano-Spectroscopy (SINS) enables molecular and phonon vibrational spectroscopic imaging,

with rapid spectral acquisition, spanning the full mid-infrared ($500\text{-}5000\text{ cm}^{-1}$) region with nanoscale spatial resolution [2]. This highly powerful combination provides access to a qualitatively new form of nano-chemometric analysis with the investigation of nanoscale, mesoscale, and surface phenomena that were previously impossible to study with IR techniques. We have installed a SINS end-station at Beamline 5.4 at the ALS at Lawrence Berkeley National Laboratory, making the s-SNOM technique widely available to non-experts, such that it can be broadly applied to biological, surface chemistry, materials, or environmental science problems. We demonstrate the performance of synchrotron infrared nano-spectroscopy (SINS) on semiconductor, biomineral and protein nanostructures, providing vibrational chemical imaging with sub-zeptomole sensitivity.

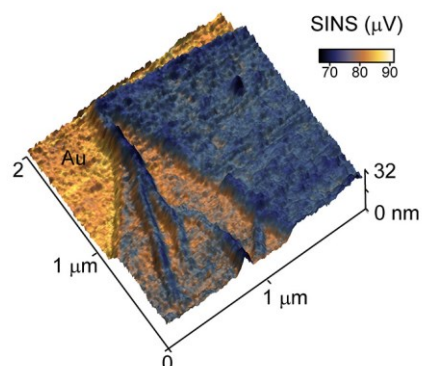


Figure 2. This peptoid nanosheet, produced by Gloria Olivier and Ron Zuckerman at Berkeley Lab, is less than 8 nanometers thick at points. SINS makes it possible to acquire spectroscopic images of these ultra-thin nanosheets for the first time.

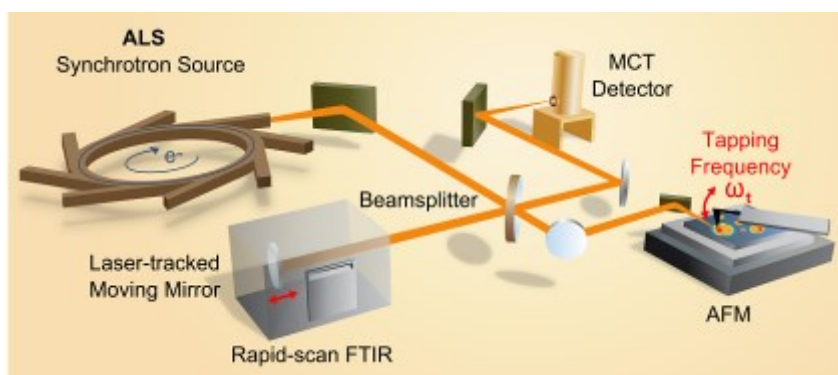


Figure 3. Experimental setup for SINS that includes the synchrotron light source, an atomic force microscope, a rapid-scan Fourier transform infrared spectrometer, a beamsplitter, mirrors and a detector.

- ¹ Michael C. Martin, Charlotte Dabat-Blondeau, Miriam Unger, Julia Sedlmair, Dilworth Y. Parkinson, Hans A. Bechtel, Barbara Illman, Jonathan M. Castro, Marco Keiluweit, David Buschke, Brenda Ogle, Michael J. Nasse, Carol J. Hirschmugl, *Nature Methods*, **10**, 861-864 (2013).
- ² Hans A. Bechtel, Eric A. Muller, Robert L. Olmon, Michael C. Martin, Markus B. Raschke, *Proceedings of the National Academy of Sciences*, **111**(20), 7191-7196 (2014).

Three-Dimensional Mid-Infrared Tomographic Imaging of Endogenous and Exogenous Molecules in Intact Cells with Subcellular Resolution

Luca Quaroni¹, Martin Obst², Marcus Nowak², Fabio Zobi³

¹ University of Fribourg, Department of Chemistry, CH-1700 Fribourg, & Functional Genomics Center Zurich, CH-8057 Zurich, Switzerland

² University of Tübingen, Department of Geosciences, D-72074 & D-72076 Tübingen, Germany

³ University of Fribourg, Department of Chemistry, CH-1700 Fribourg, Switzerland

Keywords: Infrared Imaging, Tomography, Single Cell, CORM.

Chemical imaging of cells and tissues relies on the use of spectroscopic techniques sensitive to sample composition in an optical configuration suitable for spectromicroscopy and spectroscopic imaging. Among vibrational spectroscopy techniques, absorption of middle infrared (mid-IR) radiation has been particularly successful in providing a detailed description of molecular composition. When used in a microscopy configuration, it is receiving considerable attention as a technique to study biochemistry in cells and tissue, both fixed and living, including the uptake and distribution of exogenous compounds.^[1] Despite the wealth of information in a 2D IR image, this format is intrinsically limited in its ability to associate specific compositional information to subcellular structures because of the difficulty in separating the contribution to the image arising from the complex topography of cellular samples. Also, the possibility to extract quantitative information from IR absorption spectra relies on the knowledge of the light path through the cellular structure under investigation, which is generally not available from 2D images.

We have addressed these challenges by developing a method to collect three-dimensional IR tomographic images of cellular samples. The general viability of a

mid-IR tomography experiment has been proposed by Martin et al.^[2] using a specialized synchrotron IR beamline at the Synchrotron Radiation Center (SRC) in Wisconsin. We now show that the chemical imaging capability of mid-IR tomography can be fully implemented with a benchtop microscope and a conventional light source so as to achieve spatial resolution of subcellular structures. We use *Allium cepa* cells as a sample for proof-of-concept measurements to identify the 3D spatial distribution of molecular species, both endogenous and exogenous (Figure 1).^[3]

The introduction of a protocol for 3D tomographic imaging in the mid-IR region provides a tool to greatly expand the capabilities of mid-IR microscopy in cellular physiology. The possibility of performing high-quality mid-IR tomography on a conventional IR microscope is anticipated to have major implications on the availability and thus on the versatility of the technique. Benchtop IR microscopes can be easily set-up in any cell biology laboratory. We expect that the introduction of cellular IR tomography will be one of the breakthroughs that will revolutionize IR imaging of biological systems. *Allium cepa* cells were selected because their inherent lack of mobility and rigidity reduced the risk of sample movement during the

measurement. Nonetheless the applicability of the technique is general and not limited to vegetable cells. The same protocols described in this work can be used for

benchtop tomographic imaging of any samples accessible by an IR transmission measurement.

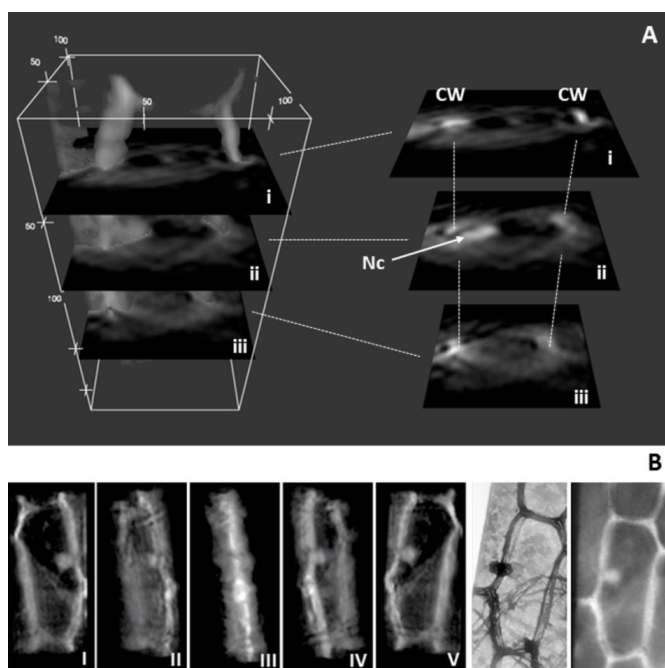


Figure 1. 3D computed tomography reconstruction of the distribution of the A1 stretching band of the exogenous metal complex ReAA in an *Allium cepa* cell. A: Reconstructed volume rendering with digital slicing at selected locations. Stacked slices to the right correspond to volume positions to the left. CW = cell wall; Nc = nucleus. Vertical dotted lines connect locations of highest A1 area intensity on CW. B: Volume rendering visualized as a function of vertical axis rotation. From left to right 45° rotation steps starting at I = 0° to VII = 180° rotation. The rotation series is accompanied by a laser scanning transmission image at 488 nm illustrating a projection of the detailed structure of the cell and one of the 2D IR maps of the A1 band used for reconstruction.

¹ L. Quaroni, T. Zlateva, *Analyst* **2011**, *136*, 3219-3232.

² M. C. Martin, C. Dabat-Blondeau, M. Unger, J. Sedlmair, D. Y. Parkinson, H. A. Bechtel, B. Illman, J. M. Castro, M. Keiluweit, D. Buschke, B. Ogle, M. J. Nasse, C. J. Hirschmugl, *Nat Methods* **2013**, *10*, 861-864.

³ Quaroni L, Obst M, Nowak P, Zobi F. Three-Dimensional Mid-Infrared Tomographic Imaging of Endogenous and Exogenous Molecules in a Single Intact Cell with Subcellular Resolution. *Angewandte Chemie* 2015, *54*, 1, pages 318–322.

Material contrasts of layered Phase Change Materials in infrared s-SNOM

Martin Lewin¹, Benedikt Hauer¹, Manuel Bornhöfft², Lena Jung¹, Ann-Katrin U. Michel¹, Joachim Mayer² and Thomas Taubner¹

¹Institute of Physics (IA), RWTH Aachen University, 52056, Aachen, Germany

²Gemeinschaftslabor für Elektronenmikroskopie, RWTH Aachen University, 52074, Aachen, Germany

Keywords: s-SNOM, phase change material, subsurface, near-field, material contrast.

Phase Change Materials (PCM) show at least two stable states in the solid phase with significantly different physical properties. They can be switched reversibly by optical or electronical means, which enables their use for storage and logical applications [1,2,3]. Commonly, the structural change of the phase change material from a short-range order to a long-range order can be imaged with atomic resolution using Transmission Electron Microscopy (TEM) [4,5]. However, functional properties, as the electrical and optical properties, cannot be derived from the TEM images. Here spectroscopic measurements have to be applied to gain information about the optical bandgap, contributions from free charge carriers or the prevailing bonding mechanism [6]. On the other hand the spatial resolution of conventional far-field measurements is usually limited by the diffraction limit to approximately half of the applied wavelength.

In contrast, scattering-type scanning near-field optical microscopy (s-SNOM) can yield information about the optical properties of the sample with sub-wavelength spatial resolution (approx. 25 nm) [7,8]. In principle, even a measurement of the local dielectric function and its contributions from molecular vibrations, phonons and free charges is possible [9, 10, 11]. Although s-SNOM uses

a sharp illuminated tip, it is not limited to surface analyses, but can also retrieve subsurface information [12]. This characteristic is crucial as most PCM devices are covered with an additional protective capping layer. We demonstrate that it is possible to distinguish amorphous and crystalline regions of $\text{Ag}_4\text{In}_3\text{Sb}_{67}\text{Te}_{26}$ (AIST) even below 100 nm of $\text{ZnS}:\text{SiO}_2$ capping layer based on the different characteristic dielectric functions in the infrared spectral range. Furthermore we investigate on the influence of the layered structure on the fundamental material contrast of AIST.

Firstly, the material contrasts of a bare 30 nm thick layer of AIST with and without capping layer are analysed. The results are compared to theoretical calculations based on an extension of the Finite-Dipole Model [13] to layered structures [14]. Secondly, correlative TEM and s-SNOM analyses are performed of a sandwiched amorphous layer with crystalline spots. The correlation proofs that even below 100 nm of $\text{ZnS}:\text{SiO}_2$ capping layer the change of the dielectric function, which accompanies the phase change, can be detected (See Figure 1). The material contrasts are found to change on the TEM sample when the Si substrate is etched away. Subsequently, the high observed material contrasts on the TEM membrane is explained by theoretical calculations taking into account the layered structure of the sample.

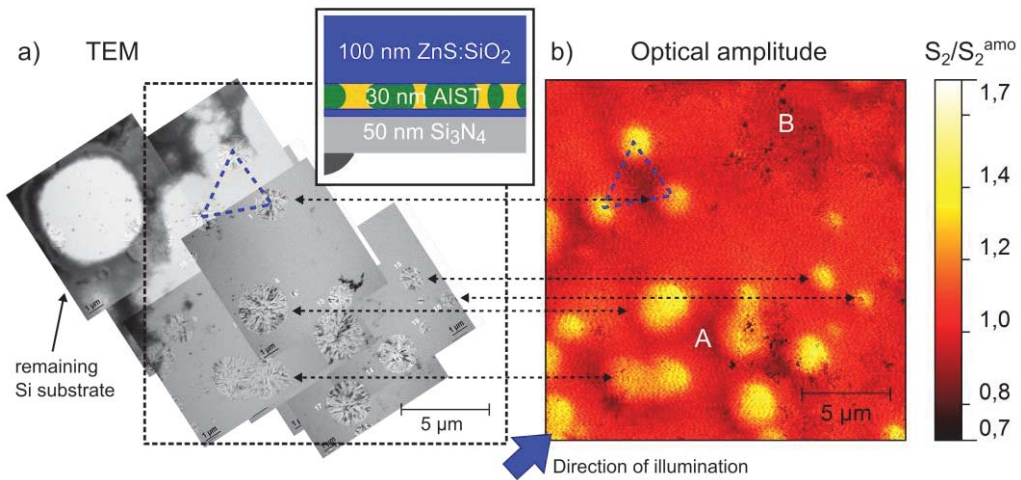


Figure 1. Correlative TEM and SNOM studies of AIST sandwiched in a special electron transparent sample design with an etched membrane window (see inset in a); [6]. (a) Multiple TEM bright field images and (b) the corresponding optical amplitude image both show buried crystalline spots in the amorphous regions ($\lambda = 8,06 \mu\text{m}$).

- ¹ Wuttig M., Yamada N. (2007), *Nature Materials.*, 6, 824-832
- ² Anbarasu M., Wuttig M. (2011), *Journal of the Indian Institute of Science.*, 91:2, 259-274
- ³ Raoux S. & Wuttig M., Eds. (2009). *Phase change materials*. Springer Science +Business Media
- ⁴ Oosthoek J.L.M., Voogt F.C., Attenborough K., Verheijen M.A., Hurkx G.A.M., Gravesteijn D.J., Kooi B.J. (2015), *Journal of Applied Physics*, 117, 064504
- ⁵ Salinga M., Carria E., Kaldenbach A., Bornhöfft M., Benke J., Mayer J., Wuttig M. (2013), *Nature Communications.*, 4:2371
- ⁵ Shportko K., Kremers S., Woda M., Lencer D., Robertson J., Wuttig M. (2008), *Nature Materials.*, 7, 653-658
- ⁷ Keilmann F., Hillenbrand R. (2004), *Philosophical Transactions of the Royal Society*, 362, 787-805
- ⁸ Atkin J.M., Berweger S., Jones A. C., Raschke M.B. (2012), *Advances in Physics*, 61 (6), 745-842
- ⁹ Goyadinov A.A., Amenabar I., Huth F., Carney P.S., Hillenbrand R. (2013), *The Journal of Physical Chemistry Letters*, 4, 1526-1531
- ¹⁰ McLeod A.S., Kelly P., Goldflam M., Gainsforth Z., Westphal A.J., Dominguez G., Thiemens M.H., Fogler M.M., Basov D.N. (2014), *Physical Review B*, 90, 085136
- ¹¹ Goyadinov A.A., Mastel S., Golmar F., Chuvilin A., Carney P.S., Hillenbrand R. (2014), *ACS Nano*, 8 (7), 6911-6921
- ¹² Taubner T., Keilmann F., Hillenbrand R. (2005), *Optics Express*, 13 (22), 8893-8899
- ¹³ Cvitkovic A., Ocelic N., Hillenbrand R. (2007), *Optics Express*, 15 (14), 8551-8565
- ¹⁴ Hauer B., Engelhardt A.P., Taubner T. (2012), *Optics Express*, 20 (12), 13173-13188

Laser based mid-infrared spectroscopic imaging for biomedical research and clinical diagnostics

Jeremy Rowlette¹, Miles Weida¹, Edeline Fotheringham¹, Matt Barre¹, David Arnone¹ and Benjamin Bird¹

¹Daylight Solutions Inc., 15378 Avenue of Science, Carmel Mountain, 02131, San Diego, USA

Keywords: QCL, microscope, infrared, imaging, biomedical.

Mid-infrared spectroscopic imaging of cells, tissue and biofluids is now a mature science with a wealth of evidence to support its adoption as an adjunctive tool for clinical research and diagnostics. However, instrumentation that provide increased sample throughput, improved image quality, a small footprint, low maintenance, and require minimal spectral expertise are essential for clinical translation to be realized.

Recently, broadly tunable mid-infrared quantum cascade lasers (QCL) have been successfully integrated within a microscope for spectral imaging across the molecular fingerprint region. The high brightness of these QCL sources enables high-resolution spectrochemical imaging from a large field of view using detector array technology that does not require cryogenic cooling. Even more notable is the realization of new imaging paradigms made possible by this emerging technology. Real-time spectrochemical imaging at discrete frequencies can be performed, allowing large samples to be surveyed rapidly at video-rates without the requirement of an imaging mosaic protocol. Furthermore, the multiplex advantage exploited by traditional Fourier Transform based systems can be computationally prohibitive, requiring large amounts of readout data to be processed before subsequent reduction to only a few key wavelengths or spectral biomarkers used for classification. However, with a tunable

laser based microscope, a pre-defined number of wavelengths can be targeted, reducing data acquisition time and increasing sample throughput. This contribution shall detail biomedical based applications of the technology that highlight some of these new imaging capabilities.

Brightfield microscopy of large biopsy tissue sections or high density tissue microarrays (TMAs) is time prohibitive for FT-IR based microscopes. Mega mosaic DF-IR images have now been acquired in the minute's timescale that provide rapid chemical contrast and microstructure information [1-5] Figure 1A) displays an example where an entire colon tissue section, several centimeters in size, was mapped in 3 minutes to provide rapid chemical visualisation of tissue structures. This type of low resolution global chemical view can serve as a rapid tool to pinpoint important FOVs that can be scrutinised at high resolution, similar to the paradigm employed by pathologists. The exploitation of high resolution DF-IR is further highlighted in Figures 1B-C that describe a typical colorectal epithelium. By probing the tissue response at twenty previously identified salient spectral frequencies, accurate tissue segmentation can be rendered using supervised PCA based imaging. Colonocytes that comprise a single cell layer that surround goblet cells of the crypts can be resolved allowing their chemical content to be confidently extracted.

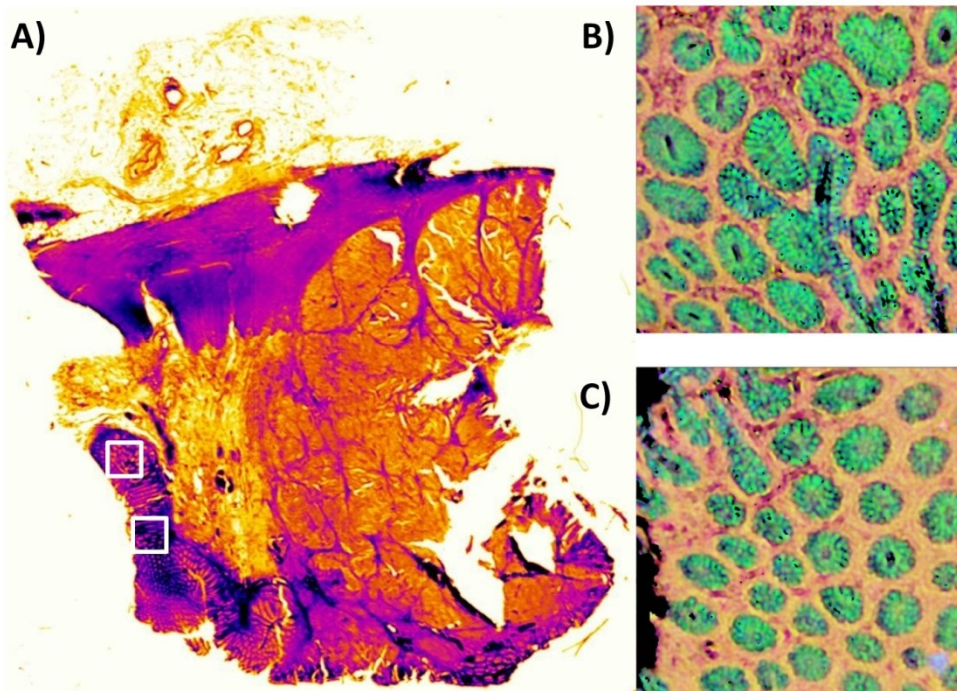


Figure 1. QCL based infrared imaging of a colorectal microtome tissue section. A) Discrete frequency chemical image of the entire tissue section recorded at 1656 cm^{-1} , highlighting the absorbance of the amide I band of proteins. This image was constructed by acquiring a 10×10 frame mosaic using the low magnification objective of the Spero microscope system. This objective has a numerical aperture of 0.15, a magnification of 4X, a pixel size of $4.25\text{ }\mu\text{m}$, and a field of view of $2\text{ mm} \times 2\text{ mm}$. A total tissue area of $2\text{ cm} \times 2\text{ cm}$ was achieved in 3 minutes.

The white squares indicate the tissue area recorded in panels B and C respectively.

B-C) RGB-PCA based chemical images constructed using the first three eigenvectors. These images were captured using a single frame of the high magnification objective of the Spero microscope. This objective has a numerical aperture of 0.70, a magnification of 12.5X, a pixel size of $1.36\text{ }\mu\text{m}$, and a field of view of $650\text{ }\mu\text{m} \times 650\text{ }\mu\text{m}$.

¹ Yeh K., Kenkel S., Liu J.N., Bhargava R., (2015), *Anal. Chem.*, 87(1), 485-493.

² Clemens G., Bird B., Weida M., Rowlette J., Baker M.J., (2014), *Spectroscopy Europe*, 26(4), 14-19.

³ Rowlette J., Weida M., Bird B., Amone D., Barre M., Day T., (2014), *Bioptics World*, March/April, 34-37.

⁴ Bassan P., Weida M., Rowlette J., Gardner P., (2014), *Analyst*, 139, 3856-3859.

⁵ Kröger N., Egl A., Engel M., Gretx N., Haase K., Herpich I., Kränzlin B., Neudecker S., Pucci A., Schönhals A., Vogt J., Petrich W., (2014), *Journal of Biomedical Optics*, 19(11), 111607.

High Spatial resolution FTIR imaging of biomedical tissue samples using a novel method of magnification enhancement

Andreas Kerstan¹, Mustafa Kansiz¹, Carol Hirschmugl², Benedict Albeni³, Catherine Liao⁴ and Kathleen Gough⁴

¹Agilent Technologies, Waldbronn, 76337, Waldbronn, Germany

²Department of Chemistry, University of Wisconsin, Milwaukee, USA

³Division of Neurodegenerative Disorders, St. Boniface Hospital Research Centre, Winnipeg, Canada

⁴Department of Chemistry, University of Mitoba, Winnipeg, Canada

Keywords: Imaging, Microscopy, tissue analysis, biomedical, fifth.

The Fourier Transform Infrared (FTIR) imaging is a well-established analytical method for obtaining spectral and spatial information simultaneously in the micron-size domain. The technique has been applied across many different application areas, from polymer science to biomedical imaging. Over recent years, interest has increased in pushing the diffraction limited spatial resolution performance of FTIR imaging systems, primarily using synchrotron based systems. In this application note, we present a novel method of magnification enhancement achieved using existing objectives. The result is an FTIR system with high spatial resolution imaging capabilities in the order of 1 $\mu\text{m}/\text{pixel}$. Uniquely, this configuration conserves the relatively large working distance of regular objectives (21 mm) by not requiring an objective change between magnification settings.

In order to assess and compare the performance of the new method, FTIR images of a biomedical sample (unfixed, cryosectioned mouse brain) were obtained using standard magnification FTIR, high

magnification FTIR and multi-beam synchrotron-based FTIR.

The results demonstrate that compared to standard magnification (5.5 μm), operating in high mode mode (1.1 μm), offers significantly added spectral and spatial detail and compared to synchrotron based high magnification systems, equivalent or better detail is observed, especially in the information rich fingerprint region, below 1800 cm^{-1} .

Additionally, image acquisition times are $\sim 10\times$ faster than the gold-standard multi-beam synchrotron instrument owing to the significantly larger field of views, together with the fact that full sized (128x128) FPAs can be used.

Furthermore, the ability to operate in standard magnification (5.5 μm) and high magnification (1.1 μm) modes without changing the objective, thus preserving the full objective working distance of 21 mm, means that users are not limited in the sample shape, size and form that can be placed and measured beneath the microscope objective.

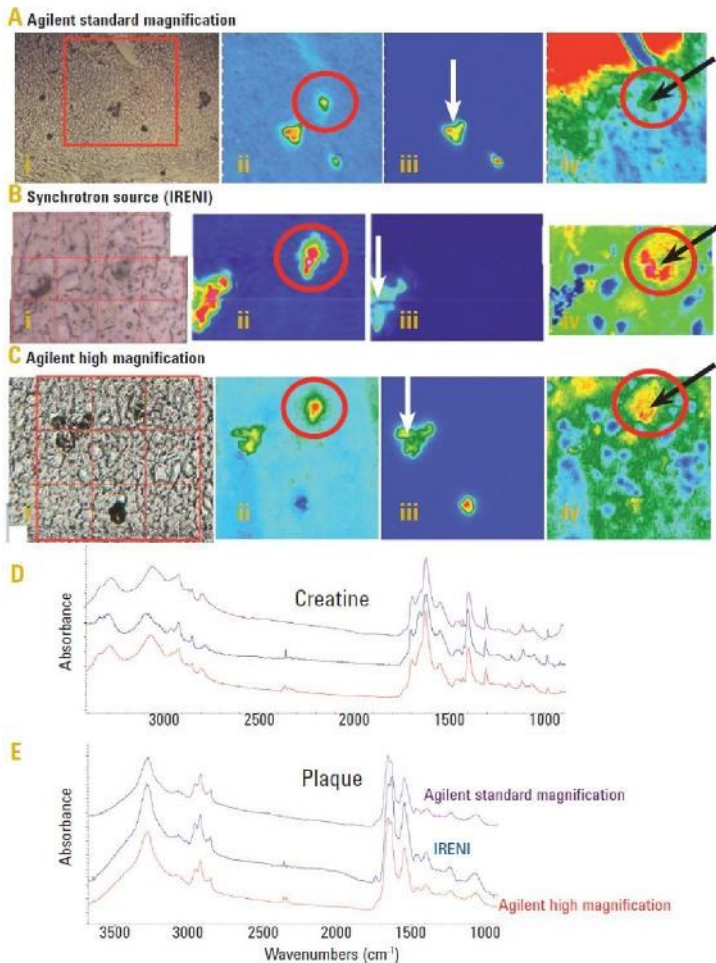


Figure 1. Excellent spectral quality from each of the 3 instruments. A, B and C: (i) visible images and chemical images of 3xTg mouse hippocampus processed for ii) Plaque and creatine (1630 cm⁻¹ band) iii) Creatine only (1305 cm⁻¹ band) iv) Lipid (2850 cm⁻¹ band). Black and white arrows point to senile plaque and creatine deposits, respectively. D and E: Spectra from (D) Creatine crystalline deposit (E) Plaque core, from each instrument (color coded text and spectra). Heavy line red circles show location of the only plaque in this sample. See further comments next page NOTE: Measurements were made approximately 12 months apart. While both spectra are similar, showing excellent S/N and spectral resolution, there are subtle differences that can be noticed. These are due to oxidation of the sample over this 12 month period. This is the sort of Figure which illustrates good agreement between theory and experiment.

¹ Nasse et al. (2011). *Nature Methods*. Vols 8 No. 5 pp. 413-418

² Liao, Rak et al. (2012), *NeuroImage*, 54 (7), 138: 3991-97

nano-FTIR: imaging and spectroscopy with 10 nm spatial resolution

Miriam Böhmler¹

¹Neaspec GmbH, Bunsenstr. 5, 82152, Martinsried (Munich), Germany

Keywords: sSNOM, near-field, nanoscopy, high resolution

Neaspec's near-field optical microscopy and spectroscopy systems (NeaSNOM, Figure 2) allow to overcoming the diffraction limit of light, enabling optical measurements at a spatial resolution of 10nm not only at visible frequencies but also in the infrared or terahertz spectral range.

This presentation will give an overview of the latest research achievements obtained with the NeaSNOM system, demonstrating the versatile scientific fields that now get accessible. This includes infrared and THz nano-spectroscopy of hot topic materials like graphene, inorganic semiconductors, polymers and biomaterials.

Development of a dedicated Fourier-transform detection module for analyzing light scattered from the tip which is illuminated by a broadband laser source enabled IR spectroscopy of inorganic and organic materials (nano-FTIR, Figure 1). As an example, a study of complex polymer nanostructures and identification of individual contaminants will be demonstrated². Other applications show characterization of embedded structural phases in biominerals³ or organic semiconductors. The patented modular system design allows for tailored system configurations where the ultimate spectral coverage can be achieved by using synchrotron-based broadband IR light sources⁴ or pump-probe measurements at 10 nm spatial resolution⁵.

Near-field imaging can be performed at time scales of 30-300s per image. Use of material-selective frequencies in the mid-IR

spectral range can be exploited to fully characterize polymer blends⁶ or phase change materials with nanometer-scale domains. Quantification of free-carrier concentration and carrier mobility in doped semiconductor nanowires⁷, analysis of graphene nanostructures⁸, or study phase propagation mechanisms in energy storage materials is achieved by amplitude- and phase-resolved infrared near-field imaging.

Latest developments which open new scientific research areas will be presented: THz-TDS in combination with the NeaSNOM system now allows experiments with 25 nm spatial resolution at THz frequencies – better than $\lambda/12000$! Besides these new capabilities in the THz spectral region, Neaspec also pushes the frontiers of sSNOM in terms of spectral resolution: our nano-FTIR system, equipped with the ultrafast upgrade, already provided first tip-enhanced and time-resolved results.

Method: Scattering-type Scanning Near-field Optical Microscopy (s-SNOM)¹ employs an externally-illuminated sharp metallic AFM tip to create a nanoscale hot-spot at its apex. The optical tip-sample near-field interaction is determined by the local dielectric properties (refractive index) of the sample and detection of the elastically tip-scattered light yields nanoscale resolved near-field images simultaneous to topography.

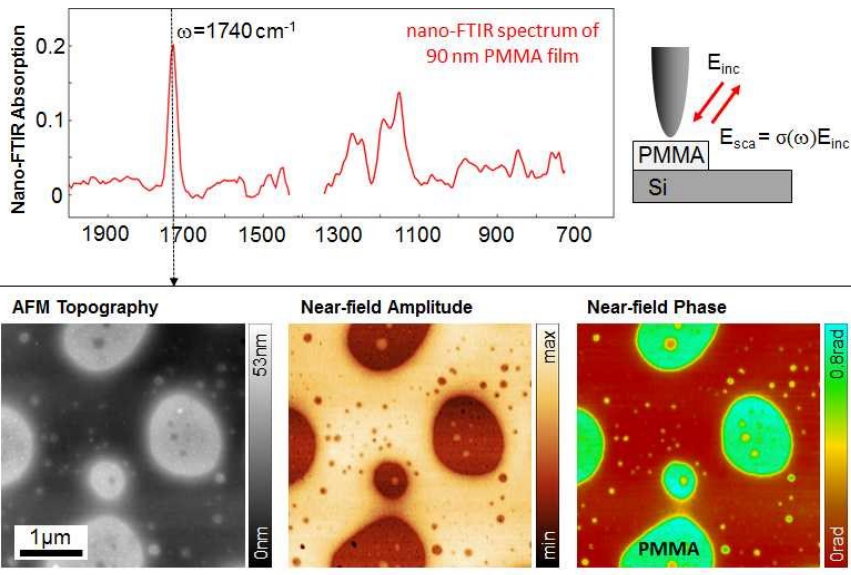


Figure 1. nano-FTIR spectroscopy and imaging of a polymer sample. The spectrum reproduces typical PMMA peaks. Imaging at 1740 cm^{-1} allows mapping of the PMMA in a polymer blend.



Figure 2. NeaSNOM system with Imaging and Spectroscopy units.

- ¹ F. Keilmann, R. Hillenbrand, (2004) *Phil. Trans. R. Soc. Lond. A* 362, 787.
- ² F. Huth, et al., (2012) *Nano Lett.* 12, 3973.
- ³ S. Amarie, et al., (2012) *Beilstein J. of Nanotech.* 3, 312.
- ⁴ P. Herrmann, et al., (2013) *Optics Exp.* 21, 2913.
- ⁵ M. Eisele, et al., (2014) *Nature Phot.* 8, 841.
- ⁶ T. Taubner, et al., (2004) *APL* 85, 5064.
- ⁷ J. Stiegler, et al., (2012) *Nature Comm.* 3, 1131.
- ⁸ J. Chen, et al., (2012) *Nature* 487, 77.

High speed infrared nanospectroscopy with sub-monolayer sensitivity

Craig Prater¹, Eoghan Dillon¹, Qichi Hu¹, Honghua Yang¹, Curtis Marcott², Feng Lu³,
Mingzhou Jin³, Mikhail Belkin³, and Kevin Kjoller¹

¹Anasys Instruments, 93101 Santa Barbara, CA USA ²Light Light Solutions, Athens GA USA
³University of Texas, Austin TX USA

Keywords: AFM, infrared spectroscopy, AFM-IR

AFM-based infrared spectroscopy (AFM-IR) pioneered by Dazzi¹ has been a critical innovation in the field of vibrational spectroscopy. Using the tip of an atomic force microscope to detect IR absorption, AFM-IR has provided ~100X improvement in spatial resolution over conventional infrared microspectroscopy, enabling widely applicable chemical analysis at the nanoscale. AFM-IR has already been successfully applied to many applications, including polymer composites and films,^{2, 3} photonic devices,^{4, 5} fuel cell membranes,⁶ and bacteria for biofuels applications⁷ and other applications. This contribution will focus on recent key advances in AFM-IR that have dramatically improved sensitivity, spatial resolution, measurement speed and the range of samples that can be measured.

The AFM-IR technique illuminates with pulses from an IR laser and uses the tip of an atomic force microscope to detect thermal expansion resulting from IR absorption. The thermal expansion from each laser pulse induces resonant oscillations in the AFM cantilever. Absorption spectra are created by measuring the cantilever oscillation as a function of wavenumber of the IR laser source. Chemical imaging may be performed by measuring the cantilever oscillation across the sample with the IR laser tuned to a specific absorption band.

Recent innovations in AFM-IR have dramatically improved the sensitivity,

spatial resolution and measurement speed, while also expanding the range of samples that can be successfully measured. Sensitivity and spatial resolution enhancements have been achieved through resonance enhanced AFM-IR⁸, which has achieved sub-monolayer sensitivity IR nanospectroscopy and chemical imaging with sub-20 nm spatial resolution. Figure 1 shows example measurements of resonance enhanced AFM-IR on a 5 nm thick biological membrane. These measurements demonstrate the ability to perform spectral analysis on extremely small amounts of biological and other organic materials.

We have recently also made dramatic improvements in measurement speeds, such that AFM-IR spectra can be acquired in a few seconds. These innovations significantly improve the measurement throughput and pave the way for high resolution IR hyperspectral imaging.

Recent advances have also overcome previous limitation that required samples to be thin-sectioned and mounted on IR transparent prisms. These advances have enabled measurements on arbitrary substrates, including composites, metals, semiconductors, minerals and other samples.

In this presentation we will review the recent AFM-IR advances and discuss examples in material and life sciences applications, including advanced polymers, fibers, biological cells, amyloids, protein secondary structure and others areas.

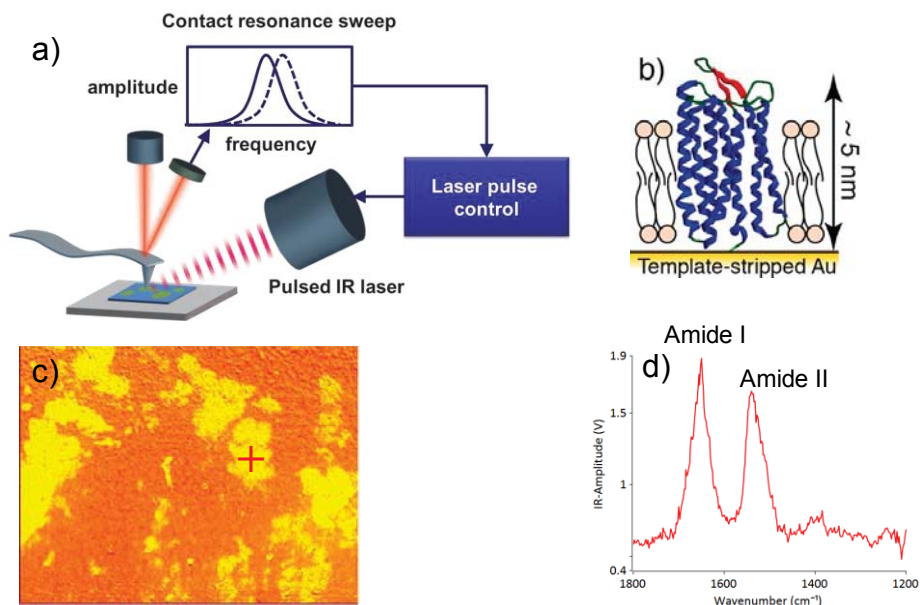


Figure 1. (a) Schematic of resonance enhanced AFM-IR. b) molecular model of purple membrane from *Halobacterium salinarum*; (c) AFM-IR chemical image of purple membrane patches at 1540 cm^{-1} , corresponding to amide II absorption band; (d) resonance enhanced AFM-IR spectrum on 5 nm thick patch of purple membrane patch.

1. Dazzi, A., Prazeres, R., Glotin, F. and Ortega, J.M., (2005) *Opt. Lett.* 30 (18), 2388-2390.
2. Prater, C., Kjoller, K., Cook, D., Shetty, R., Meyers, G., Reinhardt, C., Felts, J., King, W., Vodopyanov, K. and Dazzi, A., (2010) *Microscopy and Analysis* 24 (3), 5-8.
3. Dazzi, A., Prater, C.B., Hu, Q., Chase, D.B., Rabolt, J.F. and Marcott, C., (2012) *Appl. Spectrosc.* 66 (12), 1365-1384.
4. Lahiri, B., Holland, G., Aksyuk, V. and Centrone, A., (2013) *Nano Letters* 13 (7), 3218-3224.
5. Felts, J.R., Law, S., Roberts, C.M., Podolskiy, V., Wasserman, D.M. and King, W.P., (2013) *Applied Physics Letters* 102 (15), 152110-152115.
6. Awatani, T., Midorikawa, H., Kojima, N., Ye, J. and Marcott, C., (2013) *Electrochemistry Communications* 30 (0), 5-8.
7. Deniset-Besseau, A., Prater, C.B., Virolle, M.-J. and Dazzi, A., (2014) *The Journal of Physical Chemistry Letters* 5 (4), 654-658.
8. Lu, F., Jin, M. and Belkin, M.A., (2014) *Nat Photon* 8 (4), 307-312.

Orientation and disentanglement in electrospun polystyrene fibers using vibrational spectroscopy

Christian Pellerin and Marie Richard-Lacroix

Department of Chemistry, University of Montreal, Montreal H3C 3J7, QC, Canada

Keywords: Electrospun fibers, Disentanglement, Molecular orientation, Diameter dependence

Electrospinning is a widely used technique to prepare polymer fibers with a diameter on the order of a few hundreds nm to a few microns. They are produced by applying a high voltage on a diluted (although entangled) polymer solution. During their formation, the electrospinning jet is submitted to extremely high stretching forces while a rapid solvent evaporation simultaneously occurs. This leads to a drastic diameter reduction and to the kinetic freezing of an out-of-equilibrium structure.

It is now well-known that electrospun fibers show a complex variety of diameter-dependent properties, including an exponentially increasing modulus with decreasing diameter. Chain orientation, confinement, and partial disentanglement of the polymer chains are the three main factors that have been proposed to explain these phenomena. However, our understanding of the factors giving rise the unusual properties of electrospun fibers remains fragmentary, mainly due to the lack of appropriate molecular level characterization tools enabling studies at the single fiber level.¹

Disentanglement of the chains is particularly difficult to probe experimentally but it can be detected using IR or Raman spectroscopies for some polymers, thanks to the appearance of “new” bands in the spectra of samples showing a lower level of entanglement. This is the case for atactic polystyrene (PS), for which such bands have been observed for samples freeze-dried from

diluted solutions and associated to a conformation made possible by chain disentanglement.²

Here, we report the observation of the same bands in the spectra of electrospun PS fibers. Figure 1 presents the first experimental evidence supporting the occurrence of the phenomenon in electrospun fibers using IR spectroscopy. The association of the 1262 cm^{-1} band to incomplete entanglement was confirmed by eliminating other possibilities.³ The main electrospinning parameters governing its appearance were identified, in particular the solution concentration and the electrospinning time.

We will further show our capability to probe the phenomenon at the single fiber level using confocal Raman spectroscopy. This technique has the advantage of enabling to study directly the link between disentanglement and fiber diameter. It also enables mapping the longitudinal and radial distribution of the additional bands. The right panel of Figure 1 shows the heterogeneous radial distribution of one of the bands identified as being related to disentanglement in an individual PS fiber. The phenomenon is shown to be highly localized on the edges of the fiber, suggesting a core-shell distribution of characteristics.

The difference of intensity between the two polarized Raman spectra (XX and ZZ, parallel and perpendicular to the fiber axis, respectively) show that the chains giving

rise to the additional bands are oriented, most likely along the fiber axis. We further propose a procedure enabling the semi-quantitative evaluation of the evolution of the bands between samples and apply it to more than 100 fibers showing a broad range of diameters. This enables us to correlate the disentanglement phenomenon to some of the diameter-dependent properties of electrospun fibers such as the exponential increase of their modulus.

Molecular orientation, a parameter that is also known to strongly influence the

properties of polymeric materials, was also quantified at the single fiber level using the same polarized Raman spectra. Our results suggest a direct orientation/disentanglement correlation due to the extremely close similarity of their diameter dependence. The statistical significance of the results and the rich information extracted from the spectra enable us to draw a clearer picture of the organization of the chains in PS fibers and to better explain some of their unusual properties.

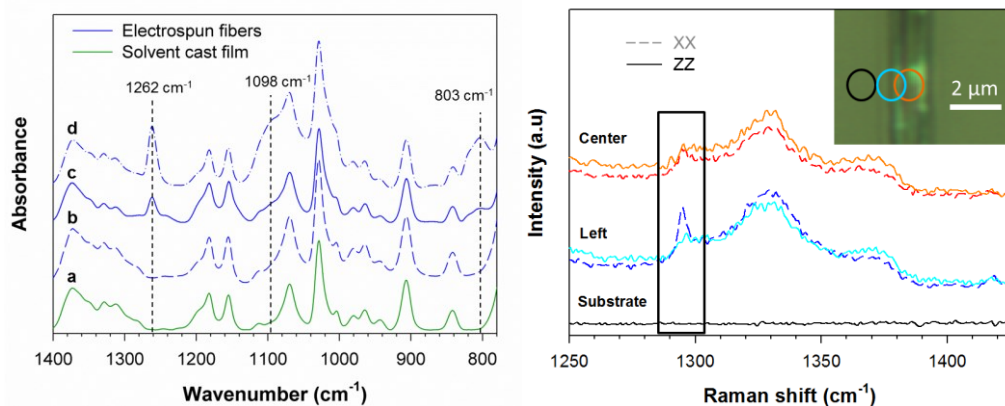


Figure 1. Left: Infrared spectra of a solvent-cast polystyrene film produced from a chloroform solution (a) and of electrospun fibers without (b) and with (c-d) the additional bands associated with a conformation made possible by partial disentanglement of the PS chains. **Right:** Confocal Raman spectra obtained at different radial locations on an individual PS fiber. The band in the frame is related to disentanglement.

- (1) Richard-Lacroix, M.; Pellerin, C. *Macromolecules* **2013**, *46*, 9473.
- (2) Sasaki, T.; Tanaka, M.; Takahashi, T. *Polymer* **1997**, *38*, 4765.
- (3) Richard-Lacroix, M.; Pellerin, C. *Macromolecules* **2015**, *48*, 37.

Different types of polaronic absorptions in organic conjugated polymers induced by distinct doping techniques

Sandra Enengl¹, Christina Enengl¹, Marek Havlicek¹, Markus C. Scharber¹, Helmut Neugebauer¹, Kurt Hingerl², Eitan Ehrenfreund³ and Niyazi S. Sariciftci¹

¹Linz Institute for Organic Solar Cells (LIOS), Physical Chemistry, Johannes Kepler University, Altenbergerstraße 69, 4040, Linz, Austria

²Center for Surface and Nanoanalytics (ZONA), Johannes Kepler University, Altenbergerstraße 69, 4040, Linz, Austria

³Department of Physics and Solid State Institute, Technion-Israel Institute of Technology, Technion City, 32000, Haifa, Israel

Keywords: organic conjugated polymers, polaron, bipolaron, 2D delocalized polaron, *in situ* spectroscopy.

Polarons are charge carriers in organic conjugated polymers and they are extensively studied over the last decades¹. Especially in doped organic conjugated polymers different kinds of polarons have been demonstrated². These organic materials are either semiconductors or insulators in their undoped, pristine form and show almost metallic properties upon doping³. Doping in these polymers leads to formation of polarons, bipolarons or 2D delocalized polarons and the geometry changes from benzenoid to quinoid-like structure. While polarons have a spin 1/2, bipolarons are spinless⁴. During doping of conjugated polymers new polaronic absorption bands in the infrared and UV-VIS range as well as very strong infrared bands, called infrared active vibrations (IRAVs), appear.

In this work we show the occurrence of various polarons *i.e.* polaron, bipolaron and 2D delocalized polaron⁵ in poly(3-hexylthiophene-2,5-diyl) (P3HT) (Figure 1), depending on the used doping technique. We focus on *in situ* chemical and electrochemical p-doping (oxidation) as well as on photoinduced doping in the infrared and UV-VIS range. Each doping technique

gives specific response in electronic as well as in vibrational absorptions.

For our investigations we use *in situ* infrared spectroscopy, working in the attenuated total reflection (ATR) mode. In the infrared range the broad absorption band arises during oxidation. As the oxidation proceeds the maximum of this polaronic band shifts, while the new IRAV modes hardly change. We trace the shifting of the maximum of the polaronic absorption band with the oxidation level in cyclic voltammogram.

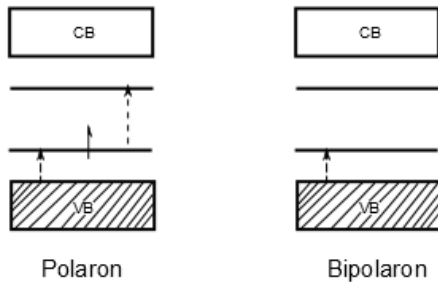
We apply *in situ* transmittance spectroelectrochemistry in the UV-VIS range, where a new transition appears which is assigned to polaron formation. This absorption changes after reaching a certain potential. The obtained results are correlated with electron paramagnetic resonance (EPR) spectroscopy. Interestingly, a change of the EPR signal follows after a certain potential. The same measurement techniques have been used by chemical doping using iodine as oxidation agent, where similar results have been observed.

Additionally, these results are compared with results obtained by photoinduced doping, where a laser light

excites the polymer. Österbacka et al.⁵ introduced the 2D delocalized polaron for photoinduced doping. Our results are supported by their theory.

Photoinduced doping shows different spectroscopic behaviors than electrochemical or chemical doping, this leads to a different formation of polarons. Possible explanations are presented.

chemical and electrochemical doping:



photoinduced doping:

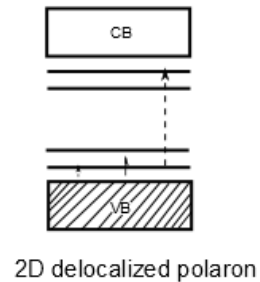


Figure 1. General schemes of the formation of positive polaron, positive bipolaron and 2D delocalized polaron⁵ by doping of P3HT. The dashed arrows show electronic transitions either in the infrared or UV-VIS range.

- ¹ Heeger A.J., Kivelson S., Schrieffer J.R., Su W.P. (1998), *Reviews of Modern Physics*, 60, 781-786.
- ² Furukawa Y. (1996), *Journal of Physical Chemistry*, 100 (39), 15644-15653.
- ³ Bredas J.L., Street G.B. (1985), *Accounts of Chemical Research*, 18 (10), 309-315.
- ⁴ Nowak M., Rughooputh S.D.D.V., Hotta S., Heeger A.J. (1987), *Macromolecules*, 20 (5), 965-968.
- ⁵ Österbacka R., An C.P., Jiang X.M., Vardeny Z.V. (2000), *Science*, 287 (5454), 839-842.

The effect of chain length and non-covalent interactions on blending of polymers

Adriana Šturcová, Jaroslav Kratochvíl, Jiří Dybal and Antonín Sikora

Institute of Macromolecular Chemistry, Academy of Sciences of the Czech Republic,
Heyrovsky Sq. 2, 162 06, Prague, Czech Republic

Keywords: inter-polymer complex, hydrogen bonding, FTIR, DSC.

Polymer blends are physical mixtures of structurally different homopolymers and/or copolymers. A blend is termed miscible in the thermodynamic sense if the two polymers in the amorphous phase exist as a single phase of intimately mixed segments. Hydrogen-bonded interpolymer complexes are representatives of such highly miscible polymer blends.

Complexation of two given polymers is a diffusion-controlled process that is strongly dependent on the chain length/molar mass of the polymer components in addition to other factors such as concentration and the nature of the solvent.

Often, a gel-like interpolymer complex is prepared in a hydrogen-bond-neutral solvent or in a solvent that is a weak proton acceptor. Soluble complex aggregates (soluble blends) are usually formed in a solvent that is a strong proton acceptor.

The differences between the interpolymer complex and the soluble blend in the glass transition temperature T_g , in the heat capacity change at T_g , in thermal stability and mechanical properties are often interpreted as the difference in their structure. It is usually assumed that the gel-like interpolymer complex is ladder-like and results from a network of co-operating hydrogen bonds. On the other hand, soluble blends are thought to have structure that consists of loose and random hydrogen bonds. Alterations in hydrogen bonding

affect the characteristic vibrational frequency of functional groups involved in such interactions; therefore vibrational spectroscopy can be used to differentiate between the two hydrogen-bond patterns.

In the work presented in this contribution, blends of poly(*N*-methyl-dodecano-12-lactam) (PMDL) with poly(4-vinylphenol) (PVPh) were prepared either from low-molar-mass (LM) polymer pair or from a high-molar-mass (HM) polymer pair. The two polymers have a difference in T_g of approximately 200 °C.

In the case of the LM pair, which is soluble in tetrahydrofuran (THF), a single T_g dependent on the composition was found by differential scanning calorimetry (DSC). Attenuated-total-reflection (ATR) FTIR spectroscopy indicated that the polymers were miscible due to hydrogen bonds between hydroxyl groups of PVPh and carbonyl groups of PMDL, especially in the blends with PVPh content above about 0.28 weight fraction. In the low-PVPh blends, the intermolecular mixing was enabled by conformational entropy.¹

In the case of the HM polymer pair in THF, a gel-like interpolymer complex precipitated from the solution, while leaving a LM residual phase dissolved in the solvent. Both types of associates were characterized by various techniques and relatively small differences were found in their respective T_g , in their thermal stability and in the heat capacity change.² FTIR

spectroscopy and DFT calculations were used to study in detail the interactions between the two polymers. The findings indicated that the different thermal properties were caused by the longer chain length in the interpolymer complex and resulted from fractionation rather than from higher density of hydrogen bonding. It was also suggested that, upon complexation, there is a change in the thermodynamic quality of the solvent used.³

Gel-like complexes and soluble blends of two chosen polymers are rarely directly

compared. In addition, such studies rely on comparison of the two types of associates each prepared in different solvent and/or with different molecular weight. Since in our work the interpolymer complex and the soluble blend were prepared from one solution, the direct comparison was possible. This new insight obtained by vibrational spectroscopy into polymer blending and complexation can be used in the design of new materials prepared from synthetic as well as bio-polymers.

- ¹ Kratochvíl J., Šturcová A., Sikora A., Dybal J. (2011), *Journal of Polymer Science Part B: Polymer Physics*, 49 (14), 1031-1040.
- ² Kratochvíl J., Šturcová A., Sikora A., Dybal J. (2014), *Polymer International*, 63 (8), 1406-1413.
- ³ Šturcová A., Kratochvíl J., Sikora A., Dybal J. (2014), *European Polymer Journal*, 59, 200-207.

Polymer hydration in poly(2-(2-methoxyethoxy)ethyl methacrylate) hydrogels differ on network architecture

Marcin Kozanecki¹, Magdalena N. Olejniczak¹, Jakub Saramak¹

¹Department of Molecular Physics, Lodz University of Technology, Zeromskiego 116, 90-92, Lodz, Poland

Keywords: thermoresponsive hydrogels, water structure

Thermo-responsive polymer hydrogels exhibiting Volume Phase Transition (VPT) are one of the most interesting groups of water-containing systems. They reveal abrupt change of their properties if the temperature pass through the critical threshold commonly corresponds to the polymer Lower or Upper Critical Solution Temperature (LCST and UCST respectively) in water. Because of that unique behavior thermo-responsive hydrogels attract a great attention from both practical and cognitive point of view.

According to model proposed by Maeda and Kitano¹ water in polymer hydrogels may be divided into three types: (1) hydration (bound) water, (2) interstitial water and (3) bulk water. Water hydrating the most polar hydrophilic groups is called “primary bound water”, whereas “secondary bound water” directly interact with hydrophobic segments.

In the present studies, an influence of the architecture of poly(2-(2-methoxyethoxy)ethyl methacrylate) (PMEO₂MA) network on its hydration is discussed. Three various PMEO₂MA materials (Fig 1) with various structure will be presented as follow: (i) random network obtained via radiation-induced free radical polymerization (FRP), (ii) regular network formed by Atom Transfer Radical Polymerization (ATRP), (iii) regular network decorated by additional dangling chains. The Raman spectroscopy was used to evaluate water-polymer interactions and to estimate the fraction of primary and secondary bound. Analysis of the Raman spectra was supported by Density Functional Theory (DFT) calculations.

It was found that for all investigated systems an amount of water formed the hydration shell around PMEO₂MA chains is equal 11±1 H₂O molecules/mer unit apart from polymer topology. However an

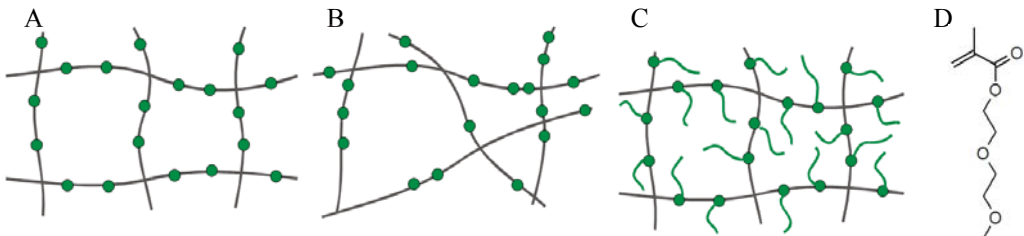


Figure 1. Architecture of studied PMEO₂MA hydrogel networks: (A) irregular obtained by FRP, (B) regular obtained by ATRP, (C) regular decorated, (D) chemical structure of PMEO₂MA.

accessibility of the most hydrophilic, C=O groups to water is lower in the cross-linked systems (only 40 % of C=O groups are hydrated) in comparison to linear chain, where 60 % of C=O groups are hydrated.

The network architecture strongly influence the range of water-polymer interactions. The number of water molecules influencing the vibrational dynamics of single carbonyl group is equal only 2 in the case of regular network, while for irregular one containing numerous free chain ends - 4. Additional dangling chains in regular system

brings about increase to 5 H₂O/mer that is the same as in the case of linear chain.

Performed DFT calculations allowed to interpret the Raman spectrum of PMEO₂MA and to point out analytical bands useful to monitor hydration of particular parts of this polymer:

This work was financially supported by the following project: 2013/09/B/ST4/03010 (Polish National Science Centre)

¹ Maeda Y., Kitano H. (1995) *Spectrochimica Acta Part A*, 51, 2433-2446

Characterization of a Polyethylene – Polyamide Multilayer Film Using Nanoscale Infrared Spectroscopy and Imaging

Curtis Marcott¹, Mauritz Kelchermans², Michael Lo³, Eoghan Dillon³, Craig Prater³, and Kevin Kjoller³

¹Light Light Solutions, Athens, GA, 30608, USA

²ExxonMobil Chemical Europe, B-1831 Machelen, Belgium

³Anasys Instruments, Santa Barbara, CA, 93101, USA

Keywords: AFM-IR, multilayer films, tie layers, polyethylene, polyamide.

Atomic force microscopy (AFM) and infrared (IR) spectroscopy have been combined in a single instrument (AFM-IR) capable of producing IR spectra and absorption images at sub-micrometer spatial resolution¹. This new device enables cross sections of multilayer films to be spectroscopically characterized at levels not previously possible². In particular, it was possible to observe nanoscale IR spectroscopic differences, as well as thermal and mechanical property differences, in the tie layers located between the individual polyethylene and polyamide layers of a multilayer film of unknown structure. It also appears that a two- μm -thick barrier layer between two polyamide layers near the center of the multilayer film consist of an ethylene (vinyl alcohol) (EVOH) copolymer. Mechanical stiffness and thermal property differences are also observed between the various layers in the film. This powerful capability should prove generally useful for reverse engineering complex unknown multilayer film materials, as well as in aiding the intelligent design of superior multilayer film materials.

Figure 1 shows a tapping mode AFM height image and AFM-IR spectra from seven layers of a multilayer film sample consisting of polyethylene (PE) and polyamide (PA) layers. The colored marker locations on the AFM image are locations

where the corresponding AFM-IR spectra of the same color were obtained. IR spectra collected from layers labelled A and F are consistent with PE, while spectra collected from layers C, E, and G are consistent with a PA. The IR spectrum recorded from what may be a barrier layer (D) in the film is consistent with EVOH.

Figure 2 shows a contact mode AFM height image and AFM-IR spectra from the boundary region between the PE and PA layers. The colored marker locations on the AFM image are locations where the corresponding AFM-IR spectra of the same color were obtained (100-nm spacing). The spectra recorded within 200 nm of the boundary have significantly sharper CH_2 -stretching bands with lower peak wavenumber than the areas of the PE further away from the boundary. This is graphically shown on the right-hand side of Figure 2 for the antisymmetric CH_2 -stretching band, in particular. This is consistent with the nanoscale thermal analysis results (not shown) and suggests a more highly ordered (or less branched) PE-like tie layer was used to help improve the adhesion between the PE and PA layers. This example also demonstrates that subtle band width and peak position changes can be used to provide insights into nanoscale AFM-IR data in the same way they are applied in conventional IR spectroscopy.

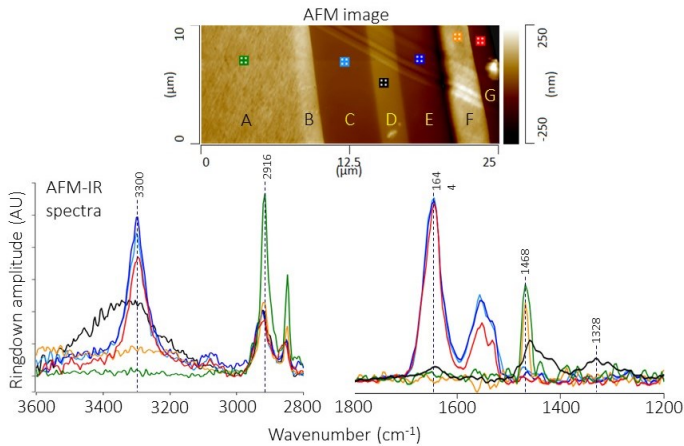


Figure 1. AFM height image and AFM-IR spectra collected from the locations shown a 7-layer multilayer film sample.

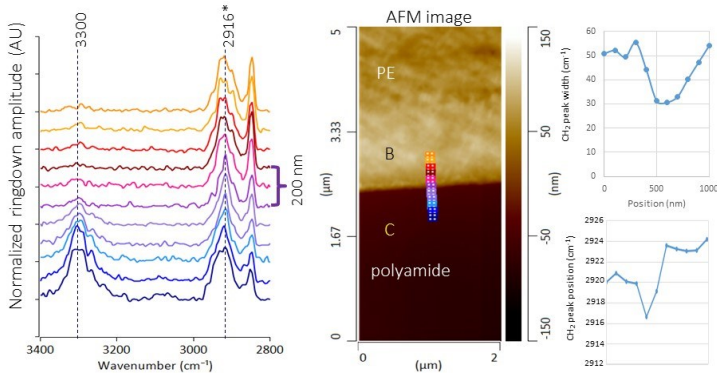


Figure 2. Contact mode AFM height image (center) and AFM-IR spectra (right) collected from the locations shown on the image (100-nm spacing). The plots on the right show the peak width (FWHM) and center-of-mass peak positions of the antisymmetric CH₂-stretching band.

- ¹ Dazzi A., Prater C.B., Hu Q., Chase D.B., Rabolt J.F. & Marcott C. (2012), *Applied Spectroscopy*, 66 (12), 1365-1384.
- ² Eby T., Gundusharma U., Lo M., Sahagian K., Marcott C. & Kjoller K. (2012), *Spectroscopy Europe*, 24 (3), 14-17.

Low-frequency Raman spectroscopy as a probe of order: from pharmaceuticals to organic solar cells.

Keith C. Gordon

Department of Chemistry and Dodd-Walls Centre, University of Otago, Dunedin, 9010, New

Keywords: low-frequency Raman, crystallization, solar cell.

The low frequency region of the vibrational spectrum contains a number of interesting spectral features. These include transitions associated with phonon and torsional modes and low-frequency stretches such as metal-chelate atoms in metal polypyridyl complexes. Phonon modes can be a powerful way to detect crystallization in materials such as amorphous drugs. Torsional and phonon modes can also be used to probe order in plastics such as organic photovoltaic (OPV) cells. Metal complexes have utility in solar cell materials and as photocatalysts, and the low frequency region can inform on structural changes.

For almost a decade THz absorption techniques have been used very successfully in the analysis of pharmaceutical materials, the utility of this spectral region has been demonstrated in both imaging and quantitative analysis.¹ More recently the possibility of combining the relatively high sensitivity of CCD-based Raman spectroscopy with the low frequency regime has been realized with the introduction of volume Bragg gratings. These permit Rayleigh line rejection down to 9 cm^{-1} with minimal modification of normal Raman experiments. We have used two systems to investigate low-frequency Raman spectra for a number of systems, one of these allows for the simultaneous measurements of Raman scattering from $9 - 2400\text{ cm}^{-1}$, the second through the use of a number of grating types can measure spectral windows as small as 200 cm^{-1} thus boosting spectral resolution.

In a study on griseofulvin², the level of crystallinity in tablets containing amorphous drug was quantified using low-frequency Raman spectroscopy and compared with other methods, in concert with chemometrics. The data were obtained simultaneously in the low- and mid-frequency regimes. The data were also compared with conventional FT-Raman spectroscopy. With chemometric analysis it was possible to get a root mean squared error of prediction (RMSEP) of 0.65 % using FT-Raman. Using the CCD-based system equipped with volume Bragg gratings a RMSEP = 1.2 % was obtained from the low-frequency region data ($5 - 120\text{ cm}^{-1}$) and RMSEP = 1.4 % for the mid-range frequencies ($520 - 1740\text{ cm}^{-1}$). The recrystallization profiles determined using the various Raman techniques and their associated models were similar. The FT-Raman and the low frequency Raman systems were able to detect and quantify crystallinity in stored amorphous samples earlier than the mid-frequency 785 nm Raman system. It appears that low-frequency Raman spectroscopy has comparable performance to mid-frequency Raman for quantitative analysis of crystallinity in the pharmaceutical setting. More generally, the much stronger Raman scattering in the low-frequency region, combined with the intrinsic spectral differences between amorphous and crystalline materials (Figure 1), may prove advantageous for some analyses.

The utility of the low frequency region is shown in a study of OPV materials. The low-frequency spectrum of annealed polythiophene shows an amorphous spectrum; however upon heat treatment at 110 °C, the appearance of phonon modes are clearly distinguishable. The interpretation of these bands is complicated by the nature of the material and rather than attempt that directly we have undertaken a systematic study of OPVs in which the cell

performance has been measured at a range of temperatures. Using chemometric analysis we have developed correlations between spectral response and performance. Raman spectroscopy may be used in this scenario as a quality control and a screening method for the most interesting materials which are then subjected to more intensive investigation using synchrotron-based techniques.

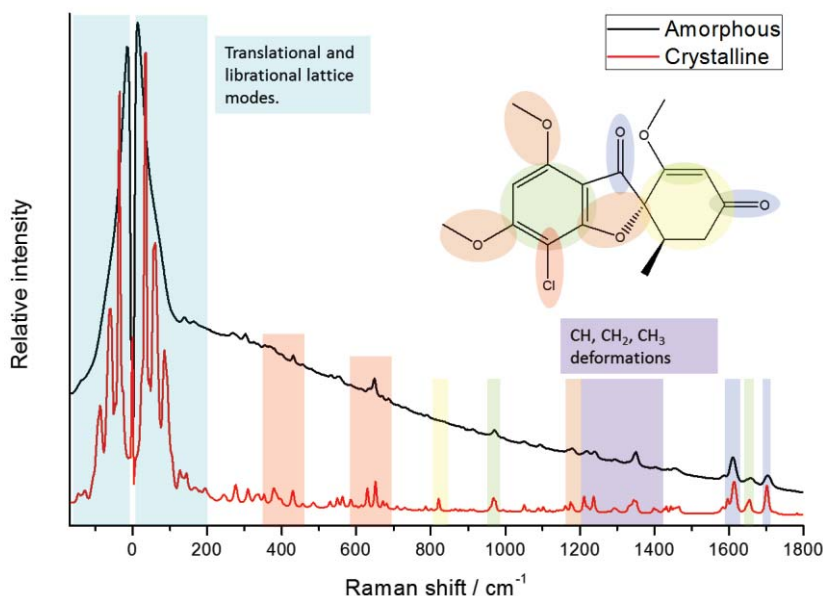


Figure 1. The crystalline and amorphous states of griseofulvin.

- ¹ Haaser, M., Gordon, K. C., Strachan, C. J., Rades, T. (2013). *International Journal of Pharmaceutics*, 457, 510-520.
- ² Mah, P. T., Fraser, S. J., Reish, M. E., Rades, T., Gordon, K. C., Strachan, C. J. (2015). *Vibrational Spectroscopy*, 77, 10-16.

Orientation quantification by confocal Raman spectroscopy: improved methodology and applications

Marie Richard-Lacroix and Christian Pellerin

¹Department of Chemistry, University of Montreal, Montreal H3C 3J7, QC, Canada

Keywords: Confocal Raman spectroscopy, Orientation parameters, polymer nanofibers

Molecular orientation has a large impact on several materials properties such as their modulus and strength, optical properties, electron conductivity, etc. Our capability to control and characterize properly this parameter for polymeric materials is thus critical because it often defines their potential applications.

Vibrational spectroscopies are among the most powerful tools enabling the characterization of this parameter because they provide both molecular (and/or chemical groups within a molecule) and phases specificity. Confocal Raman spectroscopy is particularly useful for small size materials and/or localized mapping due to its micron to nanoscale spatial resolution. However, its use is often associated with severe experimental and theoretical complexity that compromises the accuracy of the quantification when compared to IR spectroscopy.

We have recently developed an experimentally simplified procedure for orientation quantification by Raman spectroscopy that also improves the accuracy of the quantification. It is based on the approximation that the orientation distribution in the system is the most probable one (the MPD method).^{1,2}

Our numerical simulation results reveal the effectiveness of the MPD method for samples showing all possible combinations of orientation parameters, $\langle P_2 \rangle$ and $\langle P_4 \rangle$ (top of Figure 1). The green region illustrates that this method lead to

satisfactory results even if the orientation distribution function (ODF) is fairly different from the most probable one (represented by the red curve). We highlight here the efficiency of this new methodology by applying it on a broad range of polymer samples, such as polymer films and large fibers of poly(ethylene terephthalate) (PET) and polystyrene (PS), covering the full orientation range.

We then apply it in on more challenging materials such as electrospun nanofibers. Electrospinning is a common technique to produce polymer fibers of diameter on the order of a few hundred nm to a few microns. A major problem in characterizing these materials resides in the averaging of the information when using techniques, such as IR spectroscopy, that require bundles of well-aligned fibers, especially if these fibers show a broad distribution of diameters and, thus, of structural characteristics. Our understanding and opportunity to control these materials characteristics therefore rely on our ability to develop characterization tools enabling individual fiber measurements.

We have first developed an experimental procedure enabling credible orientation quantification on single fibers with diameters down to 500 nm.³ Using this protocol in association with the MPD quantification method now allows us to gain highly localized molecular level information on fibers of several different polymers such as PET, PS and poly(ethylene oxide) (PEO)

The bottom of Figure 1 gives an example of the four polarized spectra required to quantify molecular orientation measured on a PEO fiber of approximately 700 nm of diameter. They are highly repeatable and show an impressively good signal to noise ratio.

We will present the impact of several experimental parameters such as the

electrospinning collector used and the effect of the diameter on the orientation of different phases in those fibers. The development of these methodologies now allows us to extract rich and often surprising information from the Raman spectra and to revisit some of the preconceived ideas in the field of electrospun fibers.

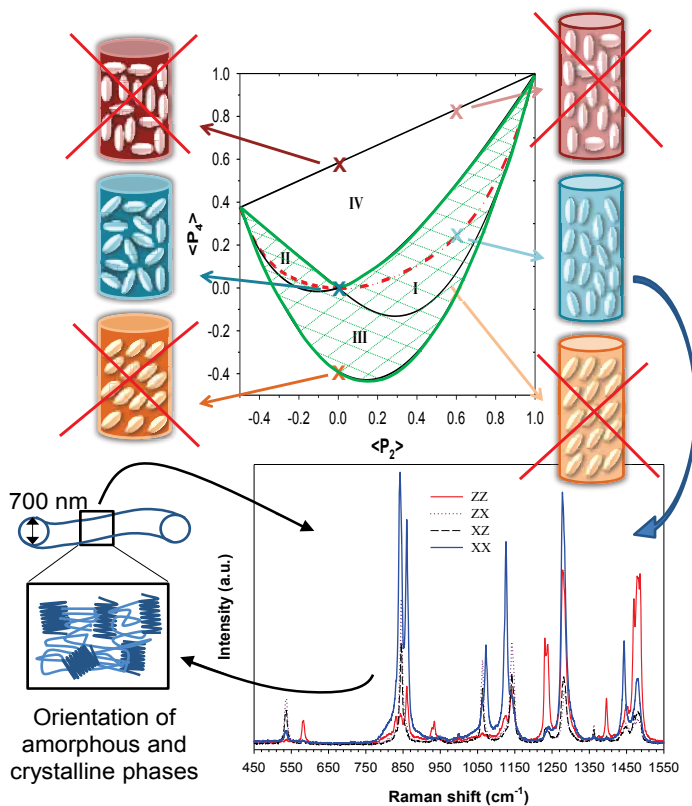


Figure 1. Top: Numerical simulation of the $\langle P_2 \rangle$ - $\langle P_4 \rangle$ diagram using the MPD method and a schematic representation of different possible ODFs associated with different $\langle P_2 \rangle$ values

The green region represents simulated samples for which the MPD method leads to satisfactory orientation values. **Bottom:** Polarized Raman spectra of a single PEO fiber of 700 nm diameter providing information on the orientation of the different phases.

- (1) Richard-Lacroix, M.; Pellerin, C. *Appl Spectrosc* **2013**, *67*, 409.
- (2) Richard-Lacroix, M.; Pellerin, C. *Macromolecules* **2013**, *46*, 5561.
- (3) Richard-Lacroix, M.; Pellerin, C. *Macromolecules* **2012**, *45*, 1946.

Regularity modes in ethylene and propylene copolymers: the comonomer content and temperature dependences.

K.A. Prokhorov¹, G.Yu. Nikolaeva¹, E.A. Sagitova¹, Yu.V. Zavgorodnev^{1,2}, P.P. Pashinin¹, P.M. Nedorezova³, A.N. Klyamkina³, T.M. Ushakova³, L.A. Novokshonova³, E.E. Starchak³, P. Donfack⁴, and A. Materny⁴

¹Prokhorov General Physics Institute, Russian Academy of Sciences, Vavilov St. 38, 119991 Moscow, Russia

²“MATI”—Tsiolkovsky Russian State Technological University, Orshanskaya 3, 121552 Moscow, Russia

³Semenov Institute of Chemical Physics, Russian Academy of Sciences, Kosygin St. 4, 119991 Moscow, Russia

⁴Department of Physics and Earth Sciences, Jacobs University Bremen, Campus Ring 1, 28759 Bremen, Germany

Keywords: Raman spectroscopy, regularity mode, copolymer, ethylene, propylene.

Vibrational spectroscopy is a powerful method to analyze polymer structure in terms of chemical and phase compositions, contents of different configurational and conformational states, and orientational order of macromolecules. As compared to infrared absorption, Raman spectroscopy does not require complicated sample preparation and is not limited by the sample state and surface quality.

Information about the content and length distribution of sequences of conformationally ordered segments of macromolecules can be obtained from the analysis of the so-called regularity modes. The behavior of the regularity modes of isotactic polypropylene (PP) as a function of temperature increase was investigated.¹⁻⁴ Despite some inconsistency between the results reported by different authors, it was established that the appearance of the Raman lines at 973, 998, 841, 1218 and 809 cm⁻¹ can be correlated to critical isotactic sequence lengths of 5, 10, 12, 14 and 15 monomer units, respectively.

K. Tashiro *et al.*⁵ studied the regularity modes of polyethylene (PE) in the

Raman spectra of random copolymers of ethylene and deuterated ethylene, n-alkanes and in the Raman spectra of neat PE as a function of temperature increase. It was found that critical sequence lengths of *trans*-conformers related to the appearance of the Raman lines at 2883 and 1062 cm⁻¹ are 4-6 and 6-8, and at 1170, 1130, and 1295⁶ cm⁻¹ 18 CH₂ units, respectively.

In this work, we investigate the behavior of the regularity modes of isotactic PP (Figure 1) and PE (Figure 2) in the Raman spectra of the neat polymers and of a wide range of recently synthesized random copolymers of propylene or ethylene with olefins. The dependence on both the content and chemical structure of the incorporated monomer as well as on the temperature is analyzed in detail. The comparison with model substances such as n-alkanes and alkylammonium salts is also presented.

This work is supported by the Russian Foundation for Basic Research (14-02-00832-a) and the Grant of the President of the Russian Federation for the Support of Leading Scientific Schools (451.2014.2).

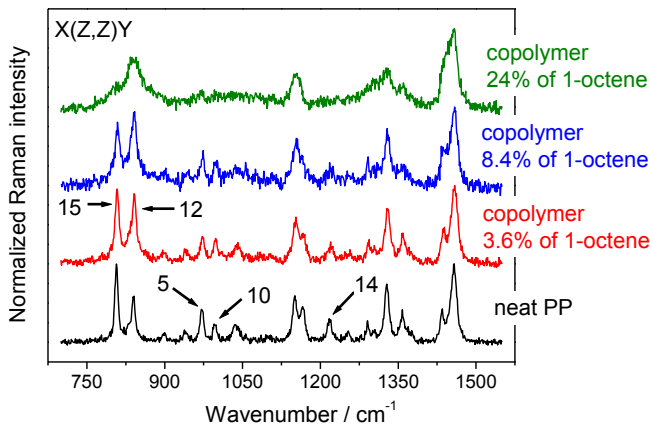


Figure 1. Raman spectra of the films of random propylene/1-octene copolymers. The numbers indicate the critical lengths of isotactic sequences related to the appearance of specific Raman lines.

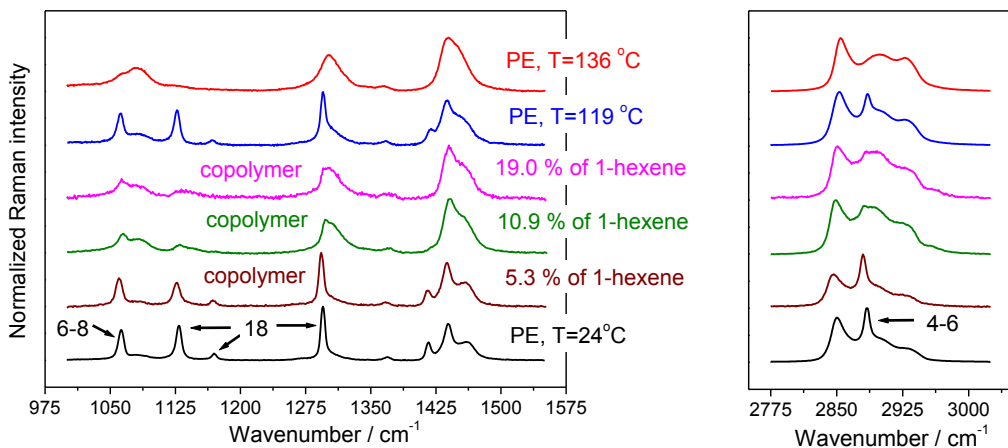


Figure 2. Raman spectra of the nascent form of random ethylene/1-hexene copolymers. The numbers indicate the critical lengths of *trans*-conformer sequences for the corresponding Raman line appearance.

¹ Khafagy R.M. (2006), *J. Polym. Sci. B*, 44 (15), 2173-2182.

² Brookes A., Dyke J.M., Hendra P.J., Meehan S. (1997), *Spectrochim. Acta A*, 53 (13), 2313-2321.

³ Zhu X., Yan D., Fang Y. (2001), *J. Phys. Chem. B*, 105 (50), 12461-12463.

⁴ Zhu X., Yan D., Yao H., Zhu P. (2000), *Macromol. Rapid Commun.*, 21 (7), 354-357.

⁵ Tashiro K., Sasaki S., Kobayashi M. (1996), *Macromolecules*, 29 (23), 7460-7469.

⁶ In accordance with our experimental data.

Investigation of carbon dioxide sorption in poly(methyl methacrylate) plate by in-situ near-infrared spectroscopy and FT-IR imaging

Yuta Hikima¹, Koji Hamada¹ and Masahiro Ohshima¹

¹Department of Chemical Engineering, Kyoto University, Katsura Campus, Nishikyo-ku, 615-8510, Kyoto, Japan

Keywords: Near-Infrared Spectroscopy, FT-IR Imaging, PMMA, CO₂

1. Introduction

Supercritical carbon dioxide (Sc-CO₂) has been applied to several polymer-processing processes, such as foaming, drying and dyeing processes aiming to replace the organic solvents and reduce the environmental burden of the processes. One of the key factors of successful application of Sc-CO₂ to these processes is to command the plasticization effects of CO₂ on polymers. Thus, understanding the sorption or diffusion behavior of CO₂ in polymer and interaction between CO₂ and polymer molecules is significantly important to optimize the processes. In this study, near-infrared (NIR) spectroscopy was employed as an in-situ measurement scheme of CO₂ sorption and diffusion process in polymer. Guadagno et al.¹ reported the in-situ NIR measurement of CO₂ sorption behavior in molten polymers. We applied NIR to investigate CO₂ sorption behavior in polymer in a solid state at temperature near the glass transition temperature, T_g, where chemical interaction between CO₂ and polymer molecules is more prominent.

2. Experimental

The plate-shaped samples of poly(methyl methacrylate) (PMMA) were prepared by compression molding at 150°C from powder (M_w ~ 120,000, Aldrich). The size of plates was 25 mm x 25 mm x 2 mm. The plates were then dried at 50°C for 24 hours.

A NIR spectrometer (FIR1000L, Yokogawa) was connected via optical fibers to a high-pressure transmission cell equipped with sapphire windows. The path

length was 4 mm. The spectra were recorded with 4 cm⁻¹ spectral resolution, 128 cumulative number and 46 seconds interval.

At first, a PMMA plate was placed in the high-pressure cell and kept at a specified temperature. CO₂ was introduced into the high-pressure cell through stainless steel capillaries by a high-pressure pump (PU-2080-CO₂ Plus, JASCO) to keep the pressure at 10 MPa. The plate was kept in the pressurized cell for 12 hour while keeping the pressure and temperature to let CO₂ diffuse into PMMA from plate's surface. NIR spectra, pressure and temperature were on-line recorded simultaneously during this sorption process.

To investigate the CO₂ diffusion behavior in PMMA more precisely, CO₂ concentration profile in the thickness direction of plate was visualized by FT-IR imaging (Spotlight 400, PerkinElmer) to the PMMA plates treated for different CO₂ sorption time. The PMMA plates were taken out from the high-pressure cell after conducting CO₂ sorption for different period of time, thin film was cut out from PMMA plate in perpendicular to the plate surface or parallel to the diffusion direction. Then, the concentration profile was detected by FT-IR imaging.

3. Results and Discussion

The change in NIR spectra was monitored on-line while CO₂ pressure was increased to 10 MPa (CO₂ pressurization stage). It is also successively monitored on-line while CO₂ pressure is kept at 10MPa at the constant temperature, 40°C (CO₂ sorption stage). Three strong absorption

bands of CO₂ were detected around 5000 cm⁻¹ and their intensities were increased as the pressure was increased during pressurization stage. Fig. 1(a) shows the 2nd derivative NIR spectra around the wavenumbers range where the largest CO₂ absorption band was observed during CO₂ pressurization stage. In the pressurization stage, the band intensity drastically increased at 4980 cm⁻¹. Fig. 1 (b) shows the change of the 2nd derivative NIR spectra during CO₂ sorption stage. The spectrum at the sorption time of 716 seconds corresponded to that at 10 MPa in Fig. 1(a). In the sorption stage, the new absorption band was observed at 4970 cm⁻¹ and its intensity increased as the sorption went on. CO₂ concentration-time curve (sorption dynamics) could be obtained from the change of band intensity of the 2nd

derivative NIR spectra at 4970 cm⁻¹ against the time.

Fig. 2 (a) shows FT-IR imaging of PMMA plate treated at different sorption times. It shows CO₂ concentration map in 2 dimensional spaces in parallel to the diffusion direction of CO₂. The concentration map was obtained from the intensity ratio of 3696 cm⁻¹ (a CO₂ band) to 3436 cm⁻¹ (a PMMA band). The diffusion front was formed in PMMA plate and it was propagated from surface to inside as CO₂ sorption time went on. Figs. 2 (b) and (c) show a photograph and a CO₂ concentration map in a foamed PMMA plate treated at 80°C. Bubbles were observed at near the surface where CO₂ concentration was higher. Difference of the diffusion front position between 40°C (Fig. 2 (a)) and 80°C was little.

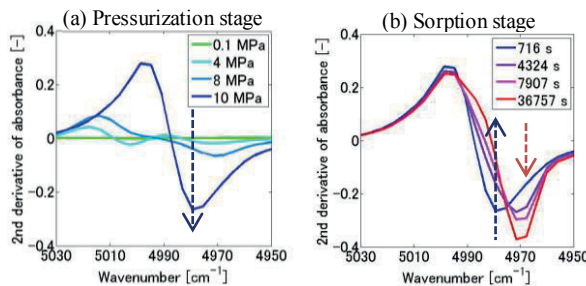


Figure 1. Change of NIR 2nd derivative spectra around the $\nu_1 + 2\nu_2 + \nu_3$ band¹ of CO₂ during (a) pressurization stage (b) sorption stage.

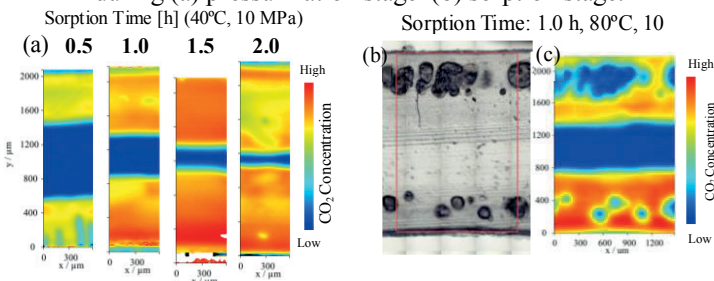


Figure 2. (a) CO₂ concentration map in the cross sectional area of PMMA plate in parallel to diffusion direction during CO₂ sorption stage (10 MPa, 40°C). (b) An optical image and (c) a CO₂ concentration map in a foamed PMMA plate after the sorption (10 MPa, 80°C)

¹ T. Guadagno, S. G. Kazarian (2004), *J. Phys. Chem. B*, 108 13995-13999.

The Stratified Dipole-Arrays (SDA) Model toward Unified Understanding of Bulk Properties of Perfluoroalkyl Compounds Studied by Infrared Spectroscopy

Takeshi Hasegawa¹, Takafumi Shimoaka¹, Yuki Tanaka¹, Nobutaka Shioya¹, Kohei Morita², Masashi Sonoyama², Toshiyuki Takagi³, Toshiyuki Kanamori³

¹ICR, Kyoto University, Gokasho, Uji, Kyoto 611-0011, Japan

² Division of Molecular Science, Faculty of Science and Technology, Gunma University, Kiryu, Gunma 376-8515, Japan

³AIST Tsukuba Central 5, 1-1-1 Higashi, Tsukuba, Ibaraki 305-8565, Japan

Keywords: SDA model, Perfluoroalkyl compounds, Two-dimensional molecular assemblies, IR MAIRS spectra.

A perfluoroalkyl (Rf) compound is known to exhibit hydrophobicity on the surface. The C–F chemical bond involved in the compound, however, has a strong electric permanent dipole that should have hydrophilicity, which sounds difficult to be correlated with the Rf-compound-specific bulk properties represented by the hydrophobic character.

Another important characteristic of an Rf compound is the fluorophilic effect. This effect corresponds to a self-assembling property of Rf groups, which is much larger than that of normal alkyl compounds. In fact, polytetrafluoroethylene (PTFE) known as Teflon, which comprises long Rf groups, has a uniquely high melting point (327 °C) as an organic compound, and this straightforwardly implies a strong molecular interaction between the Rf groups. On the other hand, as found in an Rf containing ionic liquid compound, Rf groups sometimes exhibit a very weak molecular interaction, which is inconsistent with the fluorophilic effect.

In this manner, understanding of Rf compounds in a unified manner has long been a difficult issue. In addition, the electromagnetic properties of Rf compounds such as permittivity are attributed to the low

polarizability, and the uniquely strong permanent dipoles have long been put aside, which seems unreasonable.

To overcome the confusing matters, we have proposed a new chemical model, which is named the stratified dipole-arrays (SDA) model (Figure 1). This model has the following characteristics [1].

- 1) The molecular interaction primarily depends on the dipole-dipole interaction, instead of the conventionally recognized dispersion force.
- 2) Property of a single molecule is strictly discriminated from that of a molecular aggregate.
- 3) The molecules are spontaneously aggregated when the Rf length (number of CF₂) is seven or longer, which determines the bulk property.

In the present study, the SDA model has been examined by using newly synthesized compounds: CF₃(CF₂)_n–(CH₂)_m–COOH ($n + m = 12$). According to the SDA model, the molecules would spontaneously be aggregated when n is seven or larger. Therefore, when the compound of $n = 7$ is spread on a water surface, a molecular aggregate (domain) would be generated, in which the molecules are expected to have a perpendicular stance. On the other hand, a

Resonance Raman based Cytochrome C biosensor as a tool for the evaluation of the redox properties of carbonaceous particles

Giuseppe Zerbi¹, Andrea Lucotti¹, Maurizio Gualtieri², Marina Camatini²

¹ Department of Chimica, Materiali e Ingegneria Chimica, Politecnico di Milano, P.zza L. DaVinci 32, 20133, Milano, Italy

² POLARIS Research Center, Department of Scienze Ambientali, Università Bicocca, P.zza della Scienza 1, 20126, Milano, Italy

Keywords: Raman, Resonant Raman, Cytochrome C, nanocarbon, biosensor

It is presently generally recognized that inhalation of diesel exhaust particles (DEP) is the cause of respiratory and cardiovascular diseases. So far, this effect has been ascribed to the fact that PM (particulate matter) and DEP consist of a carbonaceous/graphitic components mixed with organic molecules most of which belong to the class of polyaromatic molecules (PAH). Among the PAH's the class of quinones, formed during the combustion process, has been the target of many works which have shown that they are able to catalyze the generation of oxygen superoxide radicals ($O_2^{\cdot-}$) producing reactive oxygen species (ROS), thus inducing oxidative stress in biological systems. This reaction needs to be activated by various reducing agents such as, for example, DTT (dithiothreitol) or TCEP (tris(2-carboxyethyl) phosphine)^{1,2}.

The obvious request by the Science of the Environment has been that to exploit these experimental observations for the qualitative and quantitative evaluation (possibly with fast and in situ analysis) of the relationship between i) chemical composition and ii) size of PM and DEP and their capability of producing ROS.

It has been shown that Cytochrome C (CytC) can be taken as a very suitable biosensor for the detection and evaluation of oxygen superoxide². This fact has

prompted the development of two independent analytical methods. An electrochemical/spectrophotometric sensor has been presented by Ciriello et al³. We present here an alternative method based on Resonance Raman Spectroscopy (RRS). Spiro et al. (1972) have provided a detailed understanding of the RRS of CytC and its changes with the oxidation state of the coordinated Fe (Fe^{3+} or Fe^{2+})⁴. Thus, the use of RRS allows to monitor the reduction process of CytC in extremely small samples and even at very small concentrations (approx. 10^{-7} M of CytC).

In this research we have applied our method to study a variety of samples of carbonaceous particles namely DEP, graphite (99.99% purity) samples of ball milled HOPG for 10 and 20 hours, nanocarbon (99% purity). The commonly known Raman spectroscopic features (namely the G and D lines near 1300 and 1600 cm^{-1} respectively), observed with experiments and accounted for by theory, of carbonaceous particles are indeed observed in our samples, but show unquestionable differences. Multi-wavelength Raman experiments had been carried out on ball milled graphite to investigate the effect of varying crystallite size and defect concentration. The intensity ratio I_D/I_G has been shown to be related to the average size (or amount of edges) of the "graphitic"

platelets, which make up most of a given sample of carbonaceous particle⁵.

The experiments on these samples (pristine graphite, ball milled graphite (10 and 20 h), nanocarbon) lead to the following observations:

a) The Raman intensities plotted vs. time allow to calculate the reaction time constants τ .

b) We have measured the I_D/I_G intensity ratio and plotted τ vs I_D/I_G (Fig.1). From this figure we learn that superoxide formation is activated even by ball milled graphite. Furthermore, nanocarbon shows a value of τ well below the value obtained for 20h ball-milled graphite.

c) From Fig.1 we observe a direct proportionality of these two parameters (τ , I_D/I_G) which highlights the role of the amount of edges of the carbon particles on the superoxide formation. In other words these experiments strongly suggest, that in the presence of an activator redox reactions probably involving the disordered edges or surfaces of the graphitic platelets, can contribute to the formation of oxygen superoxide.

These results must be rationalized in terms of their biological relevance. Further work is in progress.

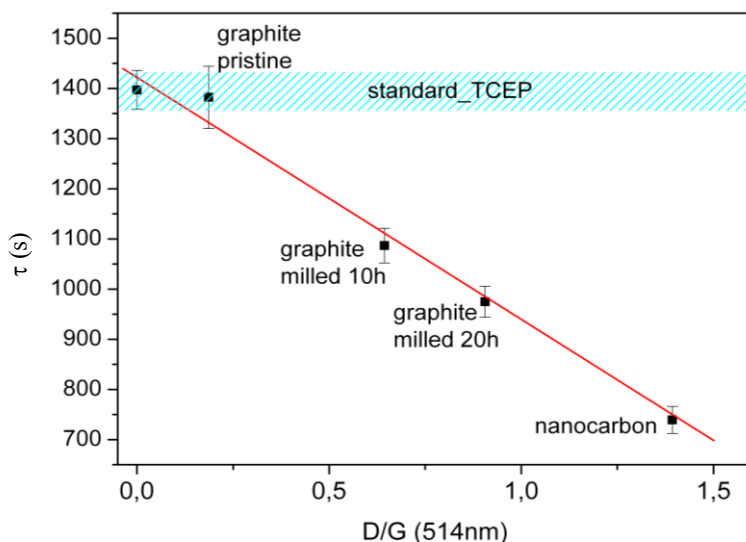


Figure 1. reaction time constant (τ) vs I_D/I_G Raman intensities for different carbonaceous materials

¹Squadrito GL., Cueto R., Dellinger B., Pryor WA. (2001), Free Rad B, 31, 1132-1138.

²Kumagai Y., Koide S., Taguchi K., Endo A., Nakai Y., Yoshikawa T., Shimojo N. (2002) Chem. Res. Toxicol. 15, 483-489

³Ciriello F., Gualtieri M., Longhin E., Ruffo R., Camatini M., Parenti P., (2015) Environ. Sci. Pollut. Res., in press

⁴Spiro T.G., Streckas T.C. (1972), Proc. Nat. Acad. Sci. USA, 69, 2622-2626

⁵Tommasini M., Castiglioni C., Zerbi G., Barbon A., Brustolon M. (2011) Chem. Phys. Lett., 516, 220-224

DSC and Raman study of phase transitions in diphenylalanine nanotubes

Pavel Zelenovskiy¹, Anton Davydov¹, Semen Vasilev¹, Alla Nuraeva¹, Kate Ryan²,
Alexander Krylov³, Maciej Wojtas⁴, Vladimir Shur¹, Andrei Kholkin^{1,5}

¹Institute of Natural Sciences, Ural Federal University, 51 Lenin Ave., 620000, Ekaterinburg, Russia

²School of Physics, University College Dublin, Belfield, Dublin 4, Ireland

³Kirensky Institute of Physics SB RAS, Akademgorodok 50/38, Krasnoyarsk, 660036, Russia

⁴Faculty of Chemistry, University of Wroclaw, Joliot-Curie 14, 50-383 Wroclaw, Poland

⁵Department of Materials and Ceramic Engineering & CICECO, University of Aveiro, 3810-193, Aveiro, Portugal

Keywords: Raman spectroscopy, DSC, Diphenylalanine, Nanostructures, Phase transitions.

Low and high temperature phase transitions occurred in diphenylalanine nanotubes are investigated by differential scanning calorimetry (DSC) and Raman spectroscopy.

Self-assembled peptide nanostructures have attracted significant interest in the recent decade. Piezoelectric micro- and nanotubes and rods of diphenylalanine (C₁₈H₂₀N₂O₃, FF) are considered as an advanced material for developing new biocompatible sensors¹, coatings, piezoelectric elements for medical equipment etc.² The first prototype of the piezoresonator based on a single FF peptide tube has been recently demonstrated³.

The formation of FF micro- and nanotubes is intensively discussed in the literature and several mechanisms are proposed^{4,5}. However, thermal behavior of FF structure is still poorly understood. An irreversible loss of piezoelectric response and second harmonic generation happened around 150°C has been attributed to phase transition from hexagonal symmetry $P6_1$ to orthorhombic P_{bca} ⁶, whereas FF cyclization provides an irreversibility of the transition^{7,8}. The detailed study of this process and low temperature phase transitions have not been investigated until now.

In this work, we studied temperature-driven phase transitions in FF nanotubes by DSC and Raman spectroscopy methods. We revealed the details of FF cyclization at 423°K by Raman spectroscopy and demonstrated for the first time by DSC phase transitions in FF nanotubes around 255° and 147°K.

Essential frequency variations of the spectral line at about 106 cm⁻¹ corresponding to lattice vibrations of FF tube have been revealed in temperature range from 200 up to 300 K. These variations demonstrate clear hysteretic behavior with temperatures of curve inflection coinciding with anomalies seen by DSC (Figure 1). No changes in Raman spectra were found near the second transition at 147 K. The role of water molecules in those low temperature transitions is discussed.

The equipment of the Ural Center for Shared Use “Modern Nanotechnology”, Ural Federal University has been used. The research was made possible by financial support of Russian Science Foundation (Grant № 14-12-00812) and by the Ministry of Education and Science of the Russian Federation (Contract 14.594.21.0011).

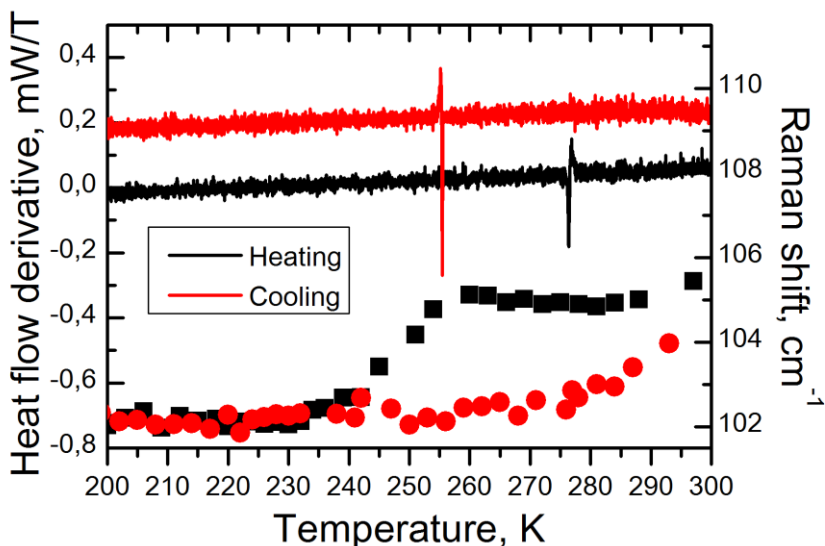


Figure 1. Superposition of DSC (lines) and Raman data (dots) in the vicinity of the phase transition in FF nanotubes.

¹ Braun H.-G. and Cardoso A. Z. (2012), *Colloids Surf. B*, 97, 43.

² Kholkin A., Amdursky N., Bdikin I., Gazit E. and Rosenman G. (2010), *ACS Nano*, 4, 610.

³ Bosne E. D., Heredia A., Kopyl S., Karpinsky D.V., Pinto A.G. and Kholkin A.L. (2013), *Appl. Phys. Lett.*, 102, 073504

⁴ Kim J., Han T.H., Kim Y., Park J.S., Choi J., Churchill D.G., Kim S.O. and Ihee H. (2010), *Adv. Mater.*, 22, 583.

⁵ Kumaraswamy P., Lakshmanan R., Sethuraman S. and Krishnan U.M. (2011), *Soft Matter*, 7, 2744.

⁶ Heredia A., Bdikin I., Kopyl S., Mishina E., Semin S., Sigov A., German K., Bystrov V., Gracio J. and Kholkin A.L. (2010), *J. Phys. D: Appl. Phys.*, 43, 462001.

⁷ Amdursky N., Beker P., Koren I., Bank-Srouer B. et al. (2011), *Biomacromolecules*, 12, 1349.

⁸ Handelman A., Beker P., Mishina E., Semin S., Amdursky N. and Rosenman G. (2012), *Ferroelectrics*, 430, 84.

Helical structures of collagen: relative stability of triple and single helix forms characterized by vibrational spectroscopy

Karl J. Jalkanen¹, Michaela Knapp-Mohammady,² Kasper Olsen,³ and Jakob Bohr³

¹Department of Technical Services, Gilead Sciences, Inc. (GSI), San Dimas, CA 91773, USA

²Division of Functional Genome Analysis, Deutsches Krebsforschungszentrum (DKFZ), Im Neuenheimer Feld 280, D-69120 Heidelberg, Germany

³Department of Micro- and Nanotechnology, DTU-Nanotech, Ørstedes Plads, Building 345B, DK-2800 Kgs. Lyngby, Denmark

Keywords: Collagen, Triple helix, Single helix, VCD, ROA.

In this work we present our second spectroscopic investigation of two helical forms of collagen in both the triple and single helical forms. In our first spectroscopic investigation¹ we investigated the use of electronic circular dichroism (ECD) to distinguish between the two helical forms of collagen proposed in the 2010 publication of Olsen and Bohr.² Although ECD could be used to distinguish between the two helical forms, the differences in the EA and ECD spectra were not as drastic as they are between the helical and beta sheet forms in proteins. In addition to ECD there are the vibrational analogues, vibrational circular dichroism (VCD) and Raman optical activity (ROA). We have previously shown that the combination of theoretical simulations and experimental VA, VCD, Raman and ROA spectra can answer previously unanswered questions about the structural stability of various conformers of peptides in various environments.³ In those works we looked at only single chains. Here we extend that work by investigating for the first time triple helical forms of collagen as modeled by the (PPG)_n model, where n is 2, 3, 6, and 9. Due to the large size of these systems, we have initially used the continuum solvent models to treat the aqueous environment as the number of explicit water molecules to completely solvate the triple helix forms of

the 3(PPG)₉ structures was resource prohibitive. We have used a combination of theoretical methods to calculate the relative stabilities of the closed pack structure of Olsen and Bohr^{1,2} and then at the optimized structures calculated the vibrational spectra: vibrational absorption (VA), vibrational circular dichroism (VCD), Raman scattering, and finally the Raman optical activity (ROA) spectra.

In addition to the question of the relative stability of the triple helix forms, there is the question of whether the conformations seen/found in the triple helical forms are stable as single helices or are the interactions which stabilize these structures such that they change the topology of the so-called potential energy surface of the backbone angles of these trimmers of PPG monomers, similar to what we say when peptides are in aqueous solution versus non polar solvents.³

Additionally, we investigate the property of H₂ storage of the closed packed structure of the collagen triple helix. Due to the larger inner cavity of the CP form of collagen, we have shown that it is possible for H₂ to fit in the cavity. As sequestration/binding of O₂, H₂ and CO₂ are important problems for both organisms and societies, the binding property of the various forms of collagen is also important.

Finally, in addition to the native form(s) of collagen, there are the additional functionalized forms due to for example biomineralization in the bones where collagen-hydroxyapatite complexation occurs. Collagen-hydroxyapatite composites need to be characterized by methods other than X-ray and neutron crystallography.

Here the combination of theoretical simulations and vibrational spectroscopy can be used an answer unanswered questions about the stability and mechanisms of formation of these composites, some of which we will discuss/present/address in this presentation.

- ¹ Jalkanen K.J., Olsen, K., Knapp-Mohammady, M., Bohr, J. (2012) Europhys. L. 93 (6), 60004.
- ² Olsen K.W. & Bohr J. (2010) Theor. Chem. Acc. 125 (3-6), 207-215.
- ³ Jalkanen K.J., Degtyarenko I.M., Nieminen R.M., Cao X., Nafie L.A., Zhu F., Barron L.D. (2008) Theor. Chem. Acc. 119 (1-3) 191-210.



Investigation of molecular structure and orientation in thin films and electrospun nanofibers of poly[(R)-3-hydroxybutyrate-co-(R)-3-hydroxyhexanoate] (PHBHx) using AFM-IR spectroscopy and imaging techniques

J.F. Rabolt, L. Gong, D.B. Chase, I. Noda, C.J. McBrin, and C. Marcott

Department of Materials Science and Engineering, University of Delaware, Newark, Delaware 19716, United States

Keywords: AFM-IR, spectroscopy, orientation, imaging, biodegradable

The combination of atomic force microscopy (AFM) and infrared (IR) spectroscopy is a powerful tool that provides chemical, conformational and molecular orientation information at a spatial resolution of 50-100 nm. Using an AFM-IR instrument, we have explored the correlation between structure, processing and chain orientation/crystallinity and tested the hypothesis that improved chain orientation in electrospun nanofibers can increase modulus and tenacity even while crystallinity is disrupted by appropriate addition of longer side-chain comonomer compositions. Nanofibers and films of poly[(R)-3-hydroxybutyrate-co-(R)-3-hydroxyhexanoate] (PHBHx) have been produced with a wide range of crystallinity and molecular orientation. They have been characterized using polarized AFM-IR spectroscopy and imaging in order to assess the role of processing on orientation and morphology. This paper will highlight the use of AFM-IR spectroscopy and imaging to characterize orientation and crystallinity changes as a function of side-chain length and comonomer concentration and illustrate the importance of obtaining rapid spatial spectroscopic images in inhomogeneous materials.

For example, AFM-IR allows direct investigation of both the crystalline and amorphous phases of ultrafine electrospun

fibers at the single fiber scale. It provides IR spectra and AFM images simultaneously of sub-100 nm features. The source is a tunable IR laser whose wavelength can be swept through the infrared “fingerprint” region in less than 1 minute. If one of the wavelengths is absorbed by the sample, then expansion of the sample occurs on the ns time scale, which causes a modulation of the oscillating AFM cantilever. This creates a “ringdown” at that particular frequency which decays as the heat dissipates. The positive amplitude of the oscillation represents the IR band intensity and hence as the frequency is tuned through the IR region ($900\text{ cm}^{-1} - 3600\text{ cm}^{-1}$), an IR spectrum is obtained at a spatial resolutions of 50 - 100 nm. More details of this instrumentation is reported elsewhere¹.

In order to test the feasibility of this technique, the IR spectra of a single fiber collected on both Al foil and a rotary disk were collected and compared with the transmission FT-IR spectra of their corresponding fiber mats (not shown). Figure 1(a) and (b) show the AFM images of the two fibers with diameters of 473 nm and 324 nm, respectively. The IR spectra of these two single fibers are displayed in Figure 1(c). As shown in the figure, the spectrum of the fiber collected on Al foil could be resolved into two features, an intense peak at 1725 cm^{-1} and a weak shoulder at 1746 cm^{-1} , corresponding to the

α crystalline phase and the amorphous phase, respectively. However, in the spectrum of the fiber collected on a rotary disk, two distinct peaks at 1728 cm^{-1} and 1740 cm^{-1} were observed, which were assigned to the more ordered α crystalline phase and the β crystalline phase, respectively. These AFM-IR spectra are in good agreement with the traditional FT-IR spectra in terms of peak/shoulder position and relative intensity. However, it is noted that the peaks in the single fiber spectra are more highly resolved, compared to the corresponding FT-IR spectra which are broadened and smeared due to averaging over multiple fibers.

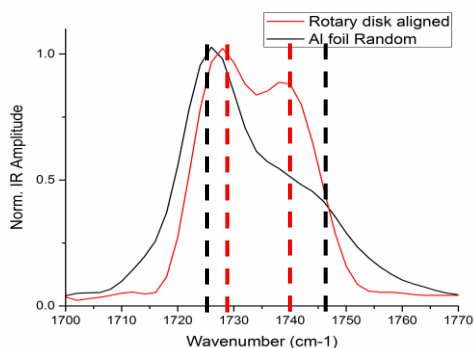
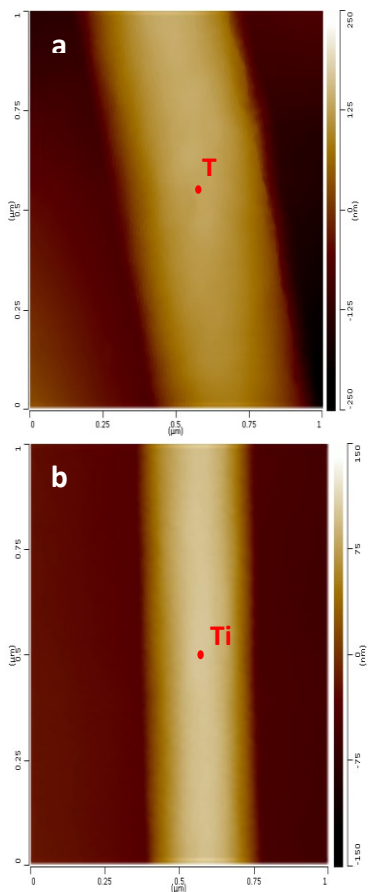


Figure 1. AFM images of single electrospun PHBHx fibers collected on (a) aluminum foil (473 nm) and (b) the tapered edge of a rotary disk (324 nm); (c) IR spectra of fibers shown in (a) and (b). The red dots on the two individual fibers indicate the position of the AFM tip.



In conclusion, the AFM-IR technique shows considerable promise as a powerful, efficient tool for the microstructural characterization of individual electrospun nanofibers. Our ongoing studies are exploring the relationship between the β -structure and the mechanical properties and processing protocols of PHBHx. The corresponding changes in the macroscopic performance of the material, together with its excellent biodegradability and biocompatibility, make PHBHx a promising material in many application areas.

1. Dazzi, A.; Prater, C. C. B.; Hu, Q.; Chase, D. B.; Rabolt, J. F.; Marcott, C. *Appl. Spectrosc.* **2012**, *66*, 1365–1384.



Medical Raman Spectroscopy

Juergen Popp^{1,2}

¹ Leibniz Institute of Photonic Technology, D-07743, Jena, Germany

² Institute of Physical Chemistry & Abbe-Center of Photonics, Friedrich-Schiller University
Jena, D-07745, Jena, Germany

Keywords: Raman, multimodal imaging, chemometrics, infectious diseases, cancer.

A comprehensive analysis to determine diagnostic, prognostic and predictive factors in a few steps or ideally in one-step requires the development of new, fast and reliable approaches that support and supplement routine medical diagnostics and therapy. In the past years, Raman spectroscopic approaches have shown their potential to meet these aforementioned challenges¹. In this contribution, we will summarize our recent results in implementing various Raman-approaches for infectious diseases and cancer, as these types of diseases harbor unmet needs regarding diagnosis and therapy.

We will start with highlighting the potential of Raman microspectroscopy for an early diagnosis and therapy of infectious diseases with special focus on sepsis. In the field of sepsis, the fast identification of pathogens, their resistances and the specific host is crucial for choosing the appropriate initial antibiotic therapy to save lives in intensive care units. It will be shown that Raman hold great promise as point-of-care approaches to address these challenging tasks²⁻⁵. In this context we will present innovative chip-based bacterial isolation strategies out of complex sample matrices (e.g. blood or urine)^{6,7}.

Besides single cells, whole tissue sections like biopsy specimens can be characterized by means of Raman-microspectroscopy enabling an objective evaluation of the tissue samples for an early diagnosis of

cancer (= spectral histopathology)⁸⁻¹⁰. The potential to couple the Raman system via optical fibers to the point of measurements has enabled within the last years besides ex-vivo Raman studies on excised tissue also in-vivo Raman studies, i.e. Raman endospectroscopy. We will introduce novel Raman fiber probes for in-vivo tissue screening to reliably diagnose and screen cancer and other diseases like atherosclerosis in internal organs like e.g. colon, stomach or aorta¹¹.

While the advantage of Raman spectroscopy are its unprecedented high specificity it suffers from its poor sensitivity. This disadvantage can be overcome by utilizing non-linear Raman phenomena like CARS = coherent anti-Stokes Raman scattering. However, these methods as standalone techniques are typically highlighting a particular detail of e.g. pathological alterations in tissues and cells. In order to improve the diagnostic result a meaningful combination of different contrast mechanism in a multimodal approach in one microscopic setting has been proven to be extremely beneficial for biomedical imaging. Here we demonstrate how the combination of CARS, second harmonic generation (SHG) and two-photon excited autofluorescence (TPEF) to a multimodal imaging approach allows one to characterize the architecture and biochemical composition, i.e., the morphochemistry of frozen section biopsy specimens from a

broad range of different cancer entities¹²⁻¹⁷. To facilitate handling and interpretation of the image data characteristic properties can be automatically extracted by advanced image processing algorithms. Overall, the presented examples show the great potential of multimodal non-linear imaging to complement established clinical pathological diagnostic tools.

Acknowledgements

Financial support of the EU, the "Thüringer Kultusministerium", the "Thüringer Aufbaubank", the Federal Ministry of Education and Research, Germany (BMBF), the German Science Foundation, the Fonds der Chemischen Industrie and the Carl-Zeiss Foundation are greatly acknowledged.

- ¹ Krafft C., Popp J. (2015) *Anal. Bioanal. Chem.* 407, 699–717.
- ² Kloß S., Kampe B., Sachse S., Rösch P., Straube E., Pfister W., Kiehntopf M., Popp J. (2013) *Anal. Chem.* 85, 697-708.
- ³ Schröder U. -Ch., Beleites C., Assmann C., Glaser U., Hübner U., Pfister W., Fritzsche W., Popp J., Neugebauer U. (2015) *Scientific Reports*, 5, 8217-1-7.
- ⁴ Große C., Bergner N., Dellith J., Heller R., Bauer M., Mellmann A., Popp J., Neugebauer U. (2015) *Anal. Chem.* 87, 2137-2142.
- ⁵ Kloß S., Rösch P., Pfister W., Kiehntopf M., Popp J. (2015) *Anal. Chem.* 87, 937-943.
- ⁶ Pahlow S., Kloß S., Blätzel V., Kirsch K., Hübner U., Cialla D., Rösch P., Weber K., Popp J. (2013) *ChemPhysChem*, 14, 3600-3605.
- ⁷ Schröder U. C., Ramoji A., Glaser U., Sachse S., Leiterer C., Cszaki A., Huebner U., Fritzsche W., Pfister W., Bauer M., Popp J., Neugebauer U. (2013) *Anal. Chem.* 85, 10717-10724.
- ⁸ Bergner N., Romeike B. F. M., Reichart R., Kalff R., Krafft C., Popp J. (2013) *Analyst*, 138, 3983-3990.
- ⁹ Bergner N., Krafft C., Geiger K. D., Kirsch M., Schackert G., Popp J. (2012) *Anal. Bioanal. Chem.* 403, 719-725.
- ¹⁰ Bergner N., Medyukhina A., Geiger K. D., Kirsch M., Schackert G., Krafft C., Popp J. (2013) *Anal. Bioanal. Chem.* 405, 8719–8728.
- ¹¹ Matthäus C., Dochow S., Bergner G., Lattermann A., Romeike B. F., Marple E. T., Krafft C., Dietzek B., Brehm B. R., Popp J. (2012) *Anal. Chem.* 84, 7845-7851.
- ¹² Krafft C., Ramoji A. A., Bielecki C., Vogler N., Meyer T., Akimov D., Rösch P., Schmitt M., Dietzek B., Petersen I., Stallmach A., Popp J. (2009) *J. Biophoton.* 2, 303-312.
- ¹³ Meyer T., Bergner N., Bielecki C., Krafft C., Akimov D., Romeike B. F. M., Reichart R., Kalff R., Dietzek B., Popp J. (2011) *J. Biomed. Opt.* 16, 021113/1-021113/10.
- ¹⁴ Meyer T., Baumgartl M., Gottschall T., Pascher T., Wuttig A., Matthaues C., Romeike B. F. M., Brehm B. R., Limpert J., Tuennermann A., Guntinas-Lichius O., Dietzek B., Schmitt M., Popp J. (2013) *Analyst*, 138, 4048-4057.
- ¹⁵ Meyer T., Chemnitz M., Baumgartl M., Gottschall T., Pascher T., Matthaues C., Romeike B. F. M., Brehm B. R., Limpert J., Tünnermann A., Schmitt M., Dietzek B., Popp J. (2013) *Anal. Chem.* 85, 6703–6715.
- ¹⁶ Meyer T., Guntinas-Lichius O., von Eggeling F., Ernst G., Akimov D., Schmitt M., Dietzek B., Popp J. (2013) *HEAD & NECK*, E280-E287.
- ¹⁷ Heuke S., Vogler N., Meyer T., Akimov D., Kluschke F., Röwert-Huber H.-J., Lademann J., Dietzek B., Popp J. *British Journal of Dermatolology*, 169, 794-803.

The latest developments and applications of spatially offset Raman spectroscopy (SORS) and transmission Raman

Benjamin Gardner¹, Martha Z. Vardaki¹, Pavel Matousek² and Nick Stone¹

¹School of Physics, University of Exeter, EX4 4QL, Exeter, United Kingdom

²Central Laser Facility, STFC Rutherford Appleton Laboratory, OX11 0QX, Oxford, United Kingdom

Keywords: Transmission Raman, Spatially offset Raman, Tissue Phantoms, Monte Carlo models

Deep Raman spectroscopy includes the techniques, spatially offset Raman spectroscopy (SORS) and transmission Raman spectroscopy. These techniques allow molecular information to be gathered from sample depths >30mm, whereas conventional Raman spectroscopy is confined to the sample surface <100µm depth. These techniques are being developed in diverse areas from biomedical / pharmaceutical applications to security services¹⁻².

The potential for non-labelled Deep Raman in disease detection has been explored, including their application in breast cancer³ and bone disease⁴.

However, these studies were limited and only explored signal intensity with increasing tissue thickness, while the spatial distribution of the Raman signal and its dependence on the optical properties were mostly neglected. Moreover, is it not always possible to design appropriate experiments to understand these parameters. This has led to the development of approaches to computationally model the interaction of light and tissue. Modelling the propagation of light through tissue with Monte Carlo (MC) methods provides a rigorous yet flexible approach to study the ballistic movement of photons.

Therefore, we have studied both experimentally and with (MC) the origins of

signals with hydroxyapatite (a cancer marker) acting as our signal and the liquid tissue phantom with varied optical properties.

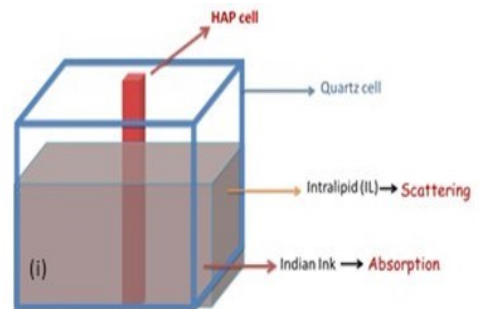


Figure 1. Schematic of the liquid tissue phantom components.

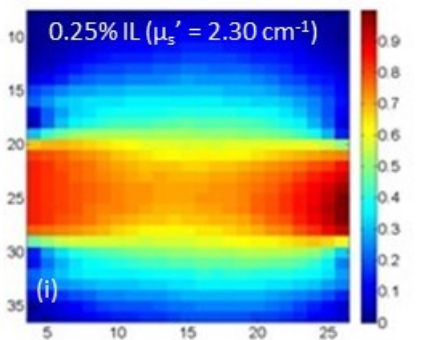
Figure 1. depicts the concept of the experimental setup, the position of HAP is systematically moved in the larger quartz cell containing the liquid phantom. This phantom consists of intra lipid (IL) which acts as the scattering agent, and India ink the absorbing agent. The concentration of both can be adjusted and the effect on the signal origins is observed.

As is shown (Figure 2.) for two extremes of tissue scattering, a 2D map of HAP intensity can be constructed, in which changes in the distribution of the collected transmission Raman signal are observed

with increasing concentration of IL. Accompanying MC simulations were also ran, which showed good agreement to the experimental results.

The purpose of this work was to help with the application of transmission Raman with non-invasive diagnostics in vivo. We also present novel developments and applications of SORS for sample measurements.

2D Raman Intensity of HAP



1D Raman Intensity of HAP

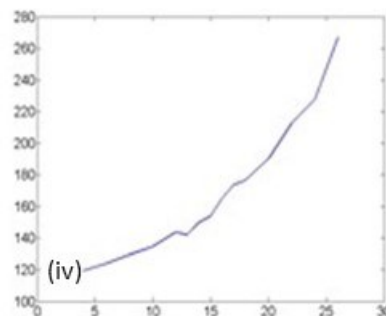
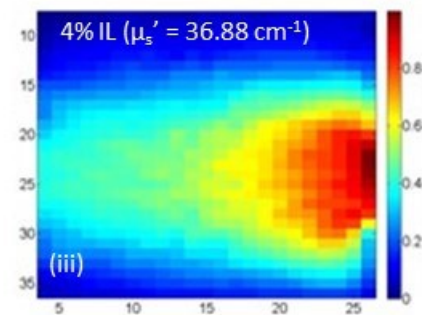
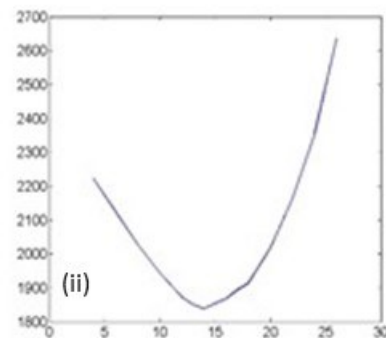


Figure 2. The distribution of the Raman HAP intensity under different IL concentrations. The 2D intensity profile of HAP intensity as a function of position in the cell (I&III) and a 1D intensity profile (II & IV) along the optical axis.

1. P. Matousek, I. P. Clark, E. R. C. Draper, M. D. Morris, A. E. Goodship, N. Everall, M. Towrie, W. F. Finney and A. W. Parker, *Appl Spectrosc*, 2005, **59**, 393-400.
2. P. Matousek and N. Stone, *J Biomed Opt*, 2007, **12**.
3. N. Stone and P. Matousek, *Cancer Res*, 2008, **68**, 4424-4430.
4. B. R. McCreadie, M. D. Morris, T. C. Chen, D. S. Rao, W. F. Finney, E. Widjaja and S. A. Goldstein, *Bone*, 2006, **39**, 1190-1195.



**Bio-accumulation of TiO₂ nanoparticles in *Caenorhabditis Elegans*:
an in-vivo model for toxicity analysis**

Luca Iannarelli¹, Andrea Mario Giovannozzi², Luisa Mandrile¹, Paolo Bigini³, Luisa Diomede³,
Valter Maurino¹, Letizia Pellutiè¹, Gianmario Martra¹, Vasile-Dan Hodoroaba⁴, Erik Ortel⁴,
and Andrea Mario Rossi²

¹Department of Chemistry, University of Turin, Via Giuria 7, 10125, Turin, Italy

²Department of Quality of Life, INRiM, Strada delle Caccie, 10135, Turin, Italy

³Molecular Biochemistry and Pharmacology Department of Mario Negri Institute, Milan, Italy

⁴Surface Analysis and Interfacial Chemistry division, BAM Federal Institute for Materials
Research & Testing, 12200, Berlin, Germany

Keywords: TiO₂ nanoparticles, Raman imaging, *C. Elegans*, metrology.

Titanium dioxide (TiO₂) represents one of the most versatile and economic semiconductor materials available at the moment and it is widely used in form of nanoparticles (NPs) for a wide range of applications such as dye sensitized solar cells, biomedical devices and photocatalysis. Besides, titanium dioxide in general is commonly used also in a lot of food products and personal care stuffs. The recent in-vivo results regarding TiO₂ toxicity^{1, 2} urged the scientific community to be questioned about TiO₂ dangerousness and its dependence on the shape and size of TiO₂ particles. Therefore, the availability of certified reference materials becomes crucial in this context. The standardization of engineered shape and size of TiO₂ NPs represents the main goal of the European FP7 project SETNanoMetro coordinated by the Italian National Institute of Metrology (INRiM).³

In order to provide robust metrology tools in toxicity analysis, the bio-accumulation of TiO₂ NPs reference materials with known shape and composition (Pure Anatase structure) was evaluated in *C. Elegans* worm model organism. *C. Elegans* specimen were fed with three different type of TiO₂ NPs: i)

commercial TiO₂ (Sigma Aldrich, 25nm sized, undefined shape, 0,2g/l); ii) home-synthesized TiO₂ NPs⁴ (50 nm, bipyramidal shape, 0,2 g/l) and iii) home-synthesized TiO₂ NPs (100 nm, bipyramidal shape, 0,2 g/l). Preliminary study devoted to determine the shape and size of different TiO₂ NPs were conducted using DLS (Dynamic Light Scattering) for NPs size distribution and T-SEM (Scanning Electron Microscopy in Transmission mode) for NPs shape. Moreover, Raman spectroscopy was exploited for NPs analysis because of the possibility of characterizing TiO₂ nanostructures according to their specific Raman fingerprint. The typical Raman spectrum of TiO₂ is shown in figure 1a. In particular in-vivo Raman Imaging analysis was performed on worms fed with TiO₂ in order to attest the bio accumulation of the NPs inside the model organism. Preliminary results regarding localization of TiO₂ NPs using Raman imaging technique are shown in figure 1b. NPs were detected along the digestive system of the worm in form of agglomerates as can be observed in figure 1c. Also confocal Raman depth profile on a TiO₂ aggregate was performed in order to obtain a 3D imaging of the model system

and to attest that TiO₂ NPs were effectively inside of the worm body and not deposited out of it.

Contextually toxicity tests of TiO₂ NPs are being conducted by the Molecular

Biochemistry and Pharmacology Department of Mario Negri Institute (Milan) in order to determine the toxicity of TiO₂ nanoparticles.

C. Elegans fed with commercial TiO₂ nanoparticles

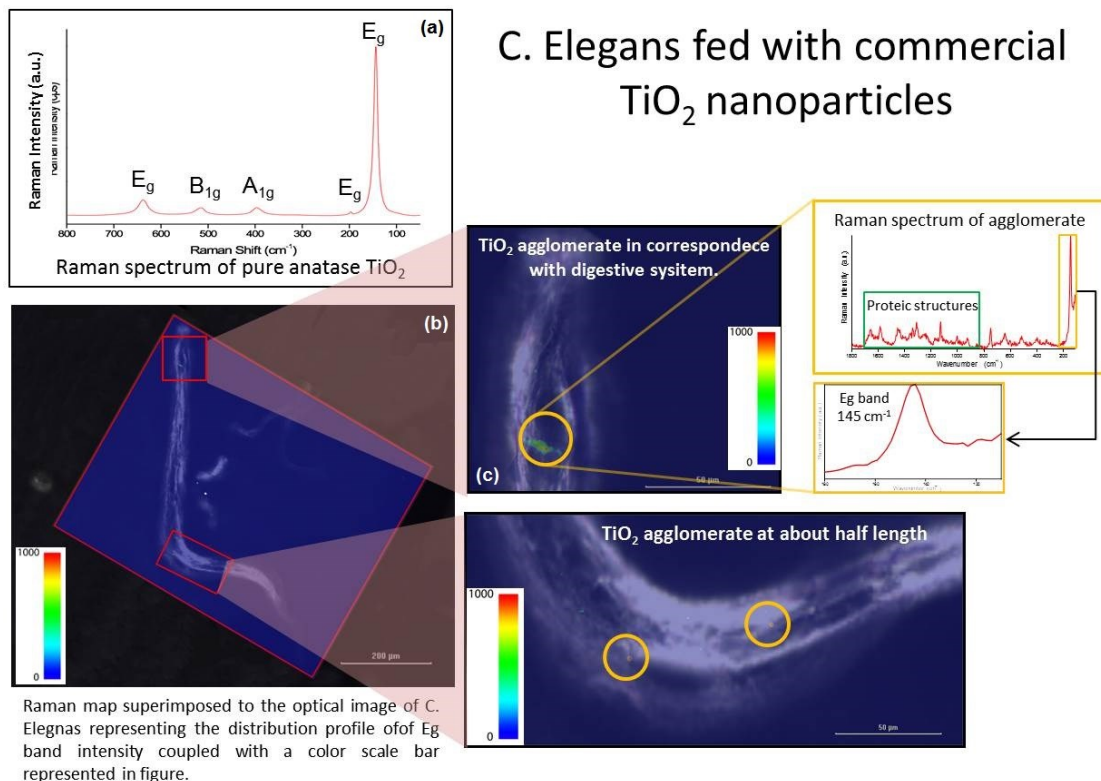


Figure 1. a) Raman spectrum of TiO₂; (b) Raman mapping of *C. elegans* worm fed with TiO₂; (c) Raman mapping particular showing TiO₂ Agglomerate detected in *C. Elegans* model system.

¹ E. D. Kuempel and A. Ruder, Titanium Dioxide (TiO₂), IARC Monograph, 2010, 93, 193-276

² <http://monographs.iarc.fr/ENG/Publications/techrep42/TR42-4.pdf>

³ <http://www.setnanometro.eu/>

⁴ C. Deiana et al., Shape-controlled TiO₂ nanoparticles and TiO₂ P25 interacting with CO and H₂O₂ molecular probes: a synergic approach for surface structure recognition and physico-chemical understanding, *Physical Chemistry Chemical Physics*, 2013, 15, 307-315

Study of tissue repair after surgical trauma by Raman microscopy

Otávio M. Gil¹, Michele A. Rocha¹, Vera R. L. Constantino¹, Ivan H. J. Koh² and Dalva L. A. de Faria¹.

¹Institute of Chemistry, University of São Paulo, Av. Lineu Prestes 748, CEP 05508-900, São Paulo, SP, Brazil

²Department of Surgery, Federal University of São Paulo, R. Pedro de Toledo 781 – 9º, 04023-062, São Paulo, Brazil

Keywords: Raman, Micro-spectroscopy, biological samples, inorganic matrix.

Inflammatory processes can be triggered by infections, foreign body and cell necrosis¹. The evaluation of tissue repair *in situ* using Raman spectroscopy (RS) can provide additional information when compared to conventional biological analysis that necessarily require physical manipulations for chemical analysis. Raman microspectroscopy is a powerful tool for characterizing tissues due to its high specificity at the molecular level, insensitivity to water interference and the advantage of allowing spatial discrimination of the studied areas, therefore, it has been used both in medical diagnostics and in the study of biochemical tissue responses to stimuli, such as healing processes².

This work aims the use of Raman microscopy for temporal analysis of the inflammatory process after surgical implantation of a lamellar inorganic material in muscle tissue compared to the natural healing processes that follow a surgical trauma.

Under general anesthesia, Wistar-EPM adult rats were submitted to implantation of an inorganic lamellar matrix in the intermuscular space of the abdominal wall through microsurgery. Biological samples of the trauma, called control group (CPO), and implanted group (IPO) were collected at 7, 21, 28 and 35 days after surgery. Reference spectrum from muscle was obtained from a

sample of the same healthy muscle. Tissues were evaluated by RS using excitation at 785 nm with low power to prevent tissue degradation.

Raman spectra of muscle tissue submitted only to the surgical trauma (CPO) are shown in Figure 1. It is clear that the spectral pattern in region between 1400 and 1200 cm^{-1} changes with time, showing that in the first periods (7 to 21 days) the inflammatory response is severe and after the end of the inflammatory acute phase (after 28 to 35 days) the spectral pattern is similar to the one produced by reference of muscle tissue, a set of bands located around 1250 cm^{-1} in the last periods can be assigned to the amide III of β -sheet and random coil conformation of structural proteins. Possibly, these bands are due to disorganization of these proteins that over time tend to organize forming the protein α -helix that have very intense and broad band in 1300 cm^{-1} . The bands appearing since 7 days located at 943, 922, 876 and 857 cm^{-1} are characteristic of collagen formed during the healing tissue³.

Figure 2 shows the Raman spectra of tissues that were in direct contact with the inorganic lamellar matrix, where the spectral pattern of the region between 1400 and 1200 cm^{-1} preserves the spectral pattern of the healthy muscle during the acute phase of the inflammatory process comprised in the first

21 days; after this period we observe the appearance of bands at 1320, 1302, 1272 and 1246 cm^{-1} assigned to collagens as well as those specified in Figure 1.

In conclusion, the RS was capable of detect the biological responses between different periods and among groups,

indicating the specificity and sensitivity to identify important components that return to tissue their physiological functionality after the tissue repair, such as the collagen fibers, denoting the applicability of RS in studies of biocompatibility/biointegration.

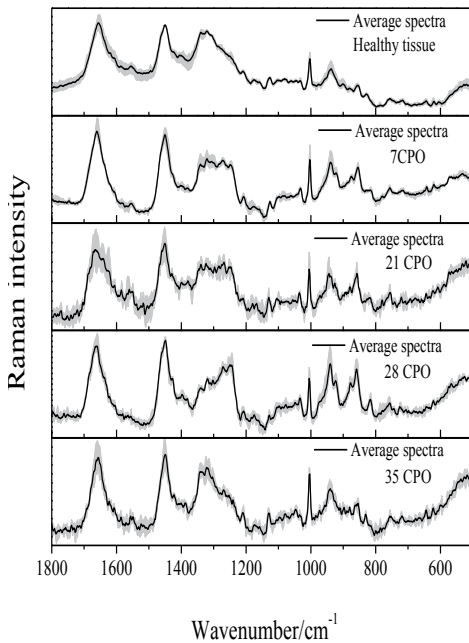


Figure 1. Average Raman spectra of control group over time.

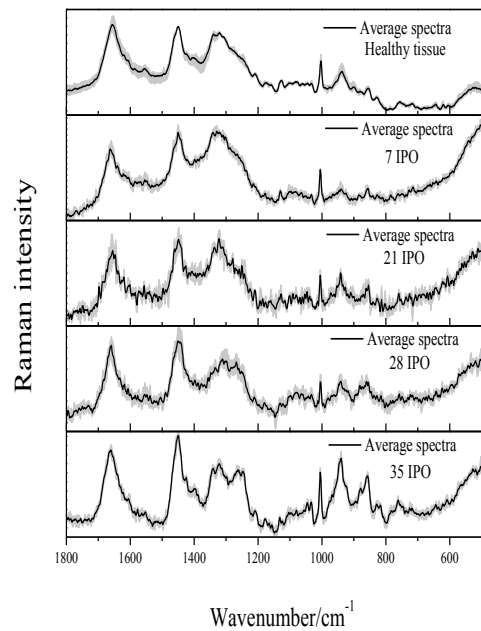


Figure 2. Average Raman spectra of implanted group over time.

¹ Medzhitov R. (2008), *Nature*, 454, 428-435.

² Jain R., Calderon D., Kierski P. R., Schurr J., Czuprynski C. J., Murphy, C. J., McAnulty J. F., Abbot N. L. (2014) *Analytical Chemistry*, 86, 3764-3772.

³ Talari A. C. S., Movasaghi Z., Rehman S., Rehman I. (2015), *Applied Spectroscopy*, 50 (1), 46-111.

Raman Spectroscopy as a tool for Bioanalytical Characterization of Biopharmaceuticals

Lorna Ashton¹, Katherine A. Hollywood² and Roy Goodacre²

¹Department of Chemistry, Lancaster University, Lancaster, LA1 4YB, UK

²Manchester Institute of Biotechnology, University of Manchester, Manchester, M1 7DN, UK

Keywords: biopharmaceuticals, proteins, 2DCOS, live cell imaging

Protein-based biopharmaceuticals are becoming increasingly popular therapeutic agents despite the fact that the bioanalytical characterization of such therapeutics continues to present numerous analytical challenges. Raman spectroscopy offers vast potential for the biopharmaceutical industry as it is non-destructive, label free and insensitive to water. This makes it an ideal technique for protein characterisation at every stage of the biomanufacturing process from protein engineering to protein production to formulation. Furthermore, with the rapid development of Raman imaging techniques it is also now possible to monitor single cell uptake of the final product.

Firstly, we will report on our research using Raman spectroscopy combined with two-dimensional correlation analysis (2DCOS) to characterise temperature-induced aggregation in antibody variants each with a different propensity to aggregate.¹ By acquiring Raman data sets for each antibody during heating from 58-78 °C differences in temperature-induced protein behaviour as a result of the various mutations could be determined. Two distinct phases of protein unfolding and a further phase of protein aggregation could be identified by comparing perturbation-correlation moving windows (PCMW) plots. Raman assignments provided information on changes in protein stability including increases and decreases in solvent exposure

of side chain residues as well as changes in H-bonding of β -structure that occurs with aggregation. This type of information can greatly aid in the initial screening for promising protein based biopharmaceuticals. By understanding the precise mechanism of aggregation for each variant, only the most promising candidates can be selected for further development.

Secondly, we will report on our recent developments in live cell Raman imaging.² Raman imaging is a label free approach that provides vast amounts of spatially resolved biochemical data from which cellular composition and subcellular components can be identified. By placing a specialized cell incubator within the chamber of the Raman microscope human keratinocytes (HaCaT) cells could be kept alive and healthy for several days. The topical anti-psoriatic drug dithranol was added to the cells and uptake and distribution was monitored using Raman imaging (Figure 1). By false-colouring the Raman images using a colour-ramp based on the overall distribution of specific peak intensities³ dithranol uptake could be observed in the live cells over a 24 h period. Analysis of the Raman maps generated from a number of cells revealed a variable response within different cells. This approach provides verification that a cell population is inherently heterogeneous in nature and thus undertaking single cell analysis is a beneficial method to understand single cell drug uptake.

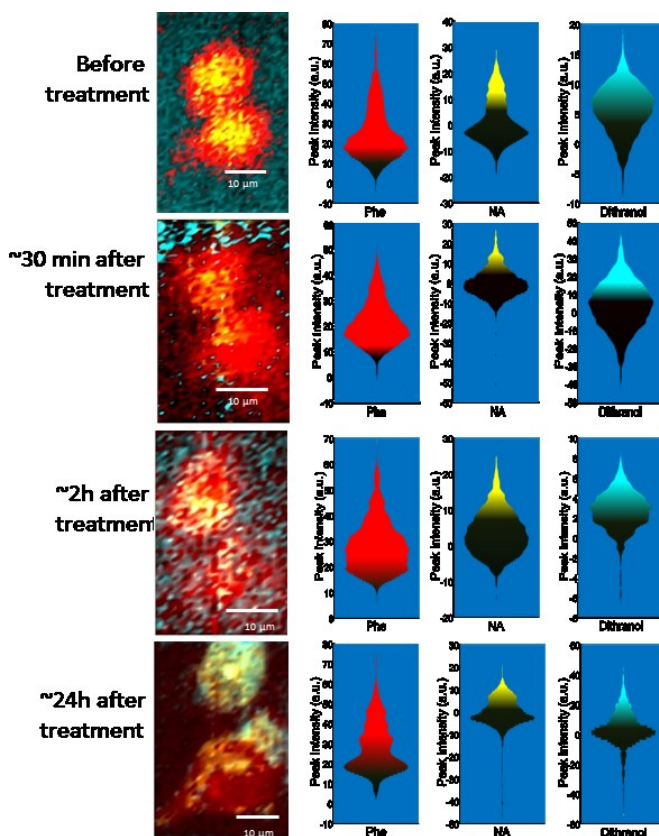


Figure 1. Raman images of live HaCaT cells collected over 24 h, before and after treatment with dithranol and the corresponding colour ramp/distribution plots. Red shading indicates peak intensity from 990-1019 cm^{-1} yellow shading peak intensity 768 – 800 cm^{-1} and cyan shading peak intensity 598-653 cm^{-1} .

- ¹ R. G. de la Cuesta, R. Goodacre & L. Ashton. (2014). *Analytical Chemistry*, 86, 11133-11140.
- ² K. A. Hollywood, K. Lau, D. I. Ellis, R. Goodacre & L. Ashton (2015), *Analytical and Bioanalytical Chemistry*, (submitted).
- ³ L. Ashton, K. A. Hollywood & R. Goodacre (2015), *Analyst*, 140, 1852-1858.

Selective-sampling Raman micro-spectroscopy for tissue diagnosis

Kenny Kong¹, Chris Rowlands¹, Faris Sinjab¹, Ioan Notingher¹

¹School of Physics and Astronomy, University of Nottingham, Nottingham, NG7 2RD, UK

Keywords: sampling, Raman micro-spectroscopy, cancer, diagnosis.

One of the main challenges in cancer surgery is ensuring that all tumour cells are removed during surgery, while sparing as much healthy tissue as possible. Histopathology is often impractical for intra-operative use because of the time-consuming tissue preparation procedures (sectioning and staining). Raman micro-spectroscopy is a powerful technique that can discriminate between tumours and healthy tissues with high accuracy, based entirely on intrinsic chemical differences. However, raster-scanning Raman micro-spectroscopy is a slow imaging technique that typically requires data acquisition times as long as several days for typical tissue samples obtained during surgery (1×1 cm²) - in particular when high signal-to-noise ratio spectra are required to ensure accurate diagnosis.

In raster-scanning the sampling points are set on a pattern without considering any properties of the sample. Indeed, for samples consisting of small regions close to the resolution-limit and for which the location cannot be estimated by other means, raster-scanning is required to ensure correct characterization and avoid under-sampling. However, in many applications, including tumour diagnosis, samples have high spatially-correlated regions and selective sampling techniques can be used to drastically reduce the number of sampling points.

In general, the basic problem in sampling is to estimate some characteristic of a population by observing only a part of the

population. The problem of establishing an optimal sampling strategy that would ensure accurate estimation of the characteristic of interest is not new to Raman micro-spectroscopy, but it has been encountered in many research fields, industry, politics, etc: finding the main reservoirs of oil or ore, estimation the number of animals in certain parts of the globe, election surveys, etc. It is clear that in such cases it is not possible or not economically viable to sample the entire population and the characteristics of interest need to be inferred from a suitably chosen sample of the population.

One strategy that can reduce the sampling points in Raman micro-spectroscopy is adaptive cluster sampling. In this technique, the sampling points for Raman spectroscopy measurements are not allocated at the start of the measurements but rather are selected depending on the values of the variable of interest observed during the measurement. Adaptive cluster sampling is a common strategy when sampling rare and clustered populations. This technique is extensively used for detection of "hot spots" in environmental pollution studies, mineral or oil reserves, rare diseases, etc ¹. In the case of Raman micro-spectroscopy, two interpolating surfaces based on pre-defined spectral features can be used to focus the sampling points in the regions of the sample with a higher level of spectral variation at the expense of the more homogenous areas².

A second sampling strategy that can be used for detection of tumours in tissue

resection specimens is stratified sampling ¹. In this technique, the sample is divided in regions (or strata) based on a given criterion and then sampling points are selected within these regions (e.g. in a survey, human population may be stratified on the basis of geographic area, socioeconomic factors, sex, age, etc). In the case of tissue samples, stratification can be achieved by using other imaging techniques, such as autofluorescence imaging to determining the optimal locations of the sampling points for Raman measurements ³. Indeed, stratified sampling can be combined with adaptive cluster sampling to optimize the diagnosis for tissue samples based on histological subtypes ⁴.

The third sampling technique that will be discussed is based on integrating the selective sampling techniques described above with multiplex Raman micro-spectroscopy. Our most recent work shows

spatial light modulators can be used to measure simultaneously tens of Raman spectra from sampling points arranged in arbitrary patterns. This technique overcomes the restrictions of other multiplex Raman techniques in which the sampling points are restricted to pre-defined rigid patterns (limitations caused mainly by the spectrometer slit, or arrays of optical fibres and slits). By integrating this new multiplex Raman microscopy technique with stratified sampling based on autofluorescence-Raman spectroscopy, it is possible to reduce the diagnosis of tumours in large tissue specimens to only few minutes.

Here we will present examples of using Raman micro-spectroscopy based on the selective sampling strategies described above to diagnose basal cell carcinomas of skin and breast ductal carcinoma.

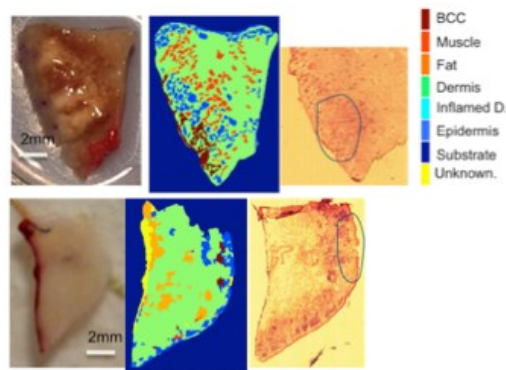


Figure 1. Diagnosis of basal cell carcinoma (BCC) of skin by Raman micro-spectroscopy using stratified sampling based on autofluorescence imaging.

¹ Thompson K.T. (2002). *Sampling*, John Wiley & Sons: New York.

² Rowlands C., Varma S., Perkins W., Leach I., Williams H., Nottingher I. (2012), *J Biophotonics*, 3, 220-229.

³ Kong K., Rowlands C.J., Varma S., Perkins W., Leach I.H., Koloydenko A.A., Williams H.C., Nottingher. I (2013), *PNAS* 2013, 110 (38), 15189-15194.

⁴ Takamori S., Kong K., Varma S., Leach I., Williams H.C., Nottingher I. (2015), *Biomed Opt. Express*, 6 (1), 98-111.

Combined fiber probe for fluorescence lifetime and Raman spectroscopy
Sebastian Dochow¹, Dinglong Ma², Ines Latka¹, Thomas Bocklitz¹, Brad Hartl², Julien Bec²,
Hussain Fatakawala², Eric Marple⁴, Kirk Urmey⁴, Sebastian Wachsmann-Hogiu³, Michael
Schmitt¹, Laura Marcu², Jürgen Popp^{1,5}

¹Institute of Physical Chemistry and Abbe Center of Photonics, Friedrich-Schiller University Jena, Helmholtzweg 4, 07743 Jena, Germany

²Department of Biomedical Engineering, University of California, Davis, 451 E. Health Sciences Drive, Davis, CA 95616, USA

³Department of Pathology and Laboratory Medicine and Center for Biophotonics, University of California, Davis, 2700 Stockton Blvd., Sacramento, CA 95817, USA

⁴EmVision LCC, 1471 F Road, Loxahatchee, Florida 33470, USA

⁵Leibniz-Institute of Photonic Technology Jena e.V., Albert-Einstein-Str. 9, 07745 Jena, Germany

Keywords: fluorescence lifetime, Raman spectroscopy, bimodal, imaging, fiber probes

Raman spectroscopy has been proven to have tremendous potential as biomedical analytical tool for spectroscopic disease diagnostics¹. The use of inelastic scattered photons lead to a specific, chemical fingerprint of each tissue which can be obtained marker free and in a nondestructive manner. The possibility to use fiber coupled Raman spectroscopy systems and according probes allows in-vivo characterization of suspicious lesions even during laparoscopies or endoscopies. However, Raman spectroscopy has the drawback of rather long acquisition times of several hundreds of milliseconds which makes scanning of larger regions quite challenging. Therefore the trend is going towards multimodal probes which combine Raman spectroscopy with a fast imaging technique like, e.g. optical coherence tomography, diffuse reflectance spectroscopy or fluorescence spectroscopy².

Fluorescence lifetime imaging (FLIm) offers a great potential for such a combination since lifetime extraction is not affected by changes in fluorescence intensity. Therefore FLIm shows minimal impact on changes in probe to target distance and allows scanning with several millimeters in distance to the sample. In certain implementations the repetition frequency can be as high as several hundred Hz which allows for fast tissue area pre

segmentation and locating the points for Raman spectra acquisition.

Here, we introduce an optical fiber probe combining FLIm and Raman spectroscopy. Fluorescence is generated via excitation with a fiber laser at 355 nm. The fluorescence emission is spectrally resolved using a custom-made wavelength-selection module (WSM)³ that separates the fluorescence into four wavelength channels coupled to four optical delay lines, generating a 45 ns delay between channels. The fluorescence photons from all 4 channels were detected using a single micro-channel plate photo-multiplier and the resulting signal output is then amplified and digitized. An embedded controller was integrated with the digitizer for readout, processing and storage of the ms-TRFS data. The excitation pulse power was set to 200 μ J and was kept constant during the whole experiments. The Raman probe excitation fiber was coupled to a 300 mW multi-mode laser emitting light at 785 nm. The overall Raman excitation power was set to 100 mW at the sample and was kept constant during all acquisitions except for the in-vivo measurements where the power was set to 50 mW to prevent sample drying. The collection fiber port was connected with a compact Raman spectrometer equipped with a 785 nm transmission grating and a Pixis400B CCD. The CCD was

thermoelectrically cooled to $-70\text{ }^{\circ}\text{C}$ and the readout was done in full vertical binning. All Raman measurements were triggered by the FLIm software, which was modified to send a line starting trigger to the CCD and each dataset was recorded using the visual basic scripting of the Winspec software and automatically saved.

The characterization of the probe resolution was determined to be $250\text{ }\mu\text{m}$ for both modalities. This value was taken as step size for several raster scans of different tissue types which were done to show the overlap of both modalities under realistic conditions. The samples were prepared by flattening their surface and fixated on a foam adaptive holder in order to preserve their flat top surface during the acquisition time of a bimodal raster scan. The sample was aligned to the scanning plane with a 2

axis tilting stage. Several raster scans in the dimensions of $50 \times 50\text{ mm}$, which corresponds to 400×400 spectra for both modalities, were acquired. The Raman acquisition time was set to 20 ms and the FLIm speed was matched to the same value in order to generate the same amount of FLIm and Raman points per line. Both modalities were acquired at the same time. Figure 1 shows an example of FLIm/Raman images of a pig sample. The different tissue regions (bone, fat and muscle tissue) are clearly separable in both modalities. Finally the probe was used for in vivo raster scans of a rat's brain and subsequently to acquire FLIm guided Raman spectra of several tissues around the craniotomy. Future development steps will be discussed.

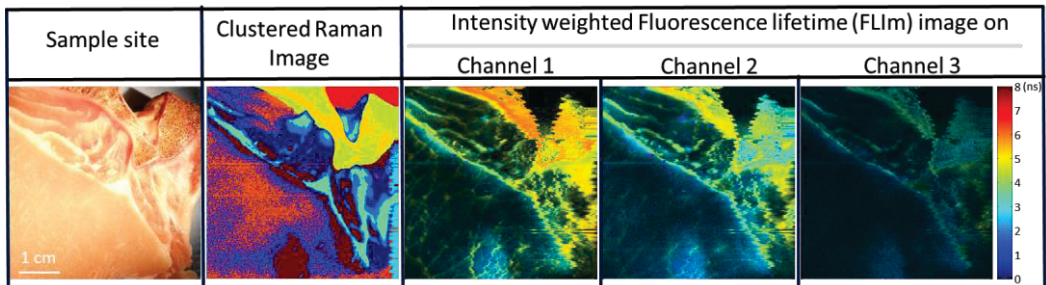


Figure 1: Comparison of the different modalities in a raster scan of a pig sample

Acknowledgement

Current study was supported in part by NIH grants R21 CA178578 and R01 CA187427.

- ¹ C. Krafft, G. Steiner, C Beleites and R. Salzer. Journal of Biophotonics 2, (2009) 13-28.
- ² I. Latka, S. Dochow, C. Krafft, B. Dietzek, J. Popp, Laser Photon. Rev. 7 (2013) 698-731.
- ³ D. R. Yankelevich, D. Ma, J. Liu, Y. Sun, Y. Sun, J. Bec, D. S. Elson, and L. Marcu, Rev. Sci. Instrum. 85, (2014) 034303.

**Fluorescence-Raman dual-modal Endomicroscopic System
for *in vivo* Real-time Multiplexed Molecular Diagnosis**

**Sinyoung Jeong¹, Yong-il Kim², Homan Kang³, Gunsung Kim¹, Myeong Geun Cha¹,
Hyejin Chang¹, Yoon-Sik Lee³, Dong Soo Lee², and Dae Hong Jeong¹**

¹*Department of Chemistry Education, Seoul National University, Korea*

²*Department of Nuclear Medicine, College of Medicine, Seoul National University, Korea*

³*School of Chemical and Biological Engineering, Seoul National University, Korea*

*E-mail: jsyl482@snu.ac.kr

Keywords: Multiplexed Molecular Imaging, *in vivo* Diagnosis, Fluorescence, Surface-Enhanced Raman Scattering (SERS), Endoscopy

Optical endoscopic imaging techniques have been widely utilized for diagnosis and treatment of specific cancers including gastric, lung, colon, prostate and bladder cancer due to their high accessibility to proximal surface of suspicious lesion with minimal invasive or non-invasive manner.¹ However, conventional white-light endoscopy has a shortcoming for diagnosis of specific cancer, because it can provide only a visualized morphological change, which is difficult to identify in early stage. Additionally, to accurately diagnose a specific cancer, the further biopsy and histopathological examination of suspicious lesion are essential.

Recently, to improve the accuracy of endoscopic diagnosis, multifunctional endoscopic techniques have been developed to provide molecular imaging by utilizing additional functionalities such as fluorescence and Raman scattering including exogenous contrast agents. The fluorescence endoscopic imaging techniques with fluorescently labeled molecular contrast agents can visualize a specific biotarget associated with a specific cancer that enhance differentiation between tumor and adjacent benign tissues.² The Raman spectroscopy based endoscopic techniques using surface-enhanced Raman scattering (SERS) nanoprobe as contrast agents can

simultaneously detect the multiple biotargets with high sensitivity to identify the pathological condition of suspicious lesion for molecular diagnosis, due to its narrow spectral band width (<1 nm) and single excitation source for multiple analytes.³

In this study, to diagnose a specific cancer at a suspicious lesion in a multiplexed way, we developed a dual modal fluorescence-Raman endoscopic system (FRES) with fluorescence-SERS active nanoprobes (F-SERS dots).⁴ Real-time, *in vivo*, and multiple bio-targets detection of a specific cancer was successful, based on the fast imaging capability of fluorescence signals and the multiplex capability of simultaneously detected SERS signals using an optical fiber bundle for intraoperative endoscopic system. The *in vitro* detection sensitivity of FRES was 1-pM of F-SERS dots. Human epidermal growth factor receptor 2 (HER2) and epidermal growth factor receptor (EGFR) on the breast cancer xenografts in a mouse orthotopic model were detected successfully in a multiplexed way, which illustrated the potential of FRES as a molecular diagnostic instrument that enables real-time tumor characterization of the receptors during routine endoscopic procedures.

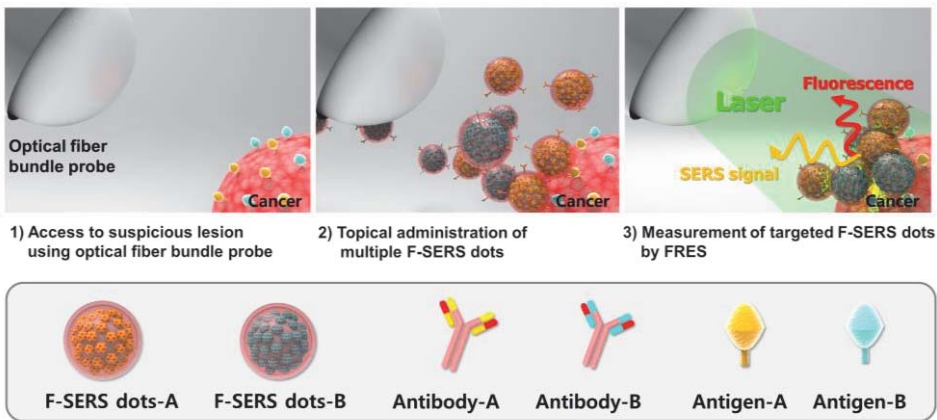
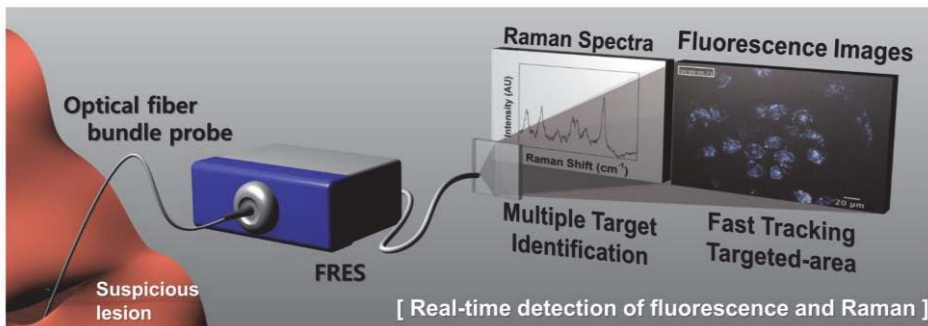


Figure 1. Schematic illustration of real-time multiplexed imaging using the fluorescence-Raman endoscopic system (FRES). (a) The mode of dual modal detection with fluorescence and Raman scattering. The real-time fluorescence imaging tracks the locations of the probe-targeted areas, and a concurrent SERS spectral analysis identifies the species of targets. (b) Illustration of the *in vivo* multiplexed molecular imaging procedure: First, access to a suspicious lesion via optical images; second, the spray-and-mix multiple F-SERS dots for topical administration; third, a multiplexed measurement of the targeted F-SERS dots with FRES.

- ¹ Khondee, S. & Wang, T.D. (2103), *J. Healthc. Eng.* 4, 1-21.
- ² R. Atreya, H. Neumann, C. Neufert, M.J. Waldner, U. Billmeier, Y. Zopf, M. Willma, C. App, T. Munster, H. Kessler, S. Maas, B. Gebhardt, R. Heimke-Brinck, E. Reuter, F. Dorje, T.T. Rau, W. Uter, T.D. Wang, R. Kiesslich, M. Vieth, E. Hannappel, M.F. Neurath, (2014) *Nat. Med.*, 20, 313-318.
- ³ C.L. Zavaleta, E. Garai, J.T. Liu, S. Sensarn, M.J. Mandella, D. Van de Sompel, S. Friedland, J. Van Dam, C.H. Contag, S.S. Gambhir, (2013) *Proc. Natl. Acad. Sci.*, 110, E2288-2297.
- ⁴ S. Jeong, Y. Kim, H. Kang, G. Kim, M.G. Cha, H. Chang, K.O. Jung, Y.-H Kim, B.-H. Jun, D.W. Hwang, Y.-S. Lee, H. Youn, Y.-S. Lee, K.W. Kang, D.S. Lee, D.H. Jeong (2015) *Sci. Rep.* 5, 9455

Prediction of poor prognosis of targeted cancer therapy by label-free Raman imaging

Samir F. El-Mashtoly, Hesham K. Yosef, Laven Mavarani, Dennis Petersen, Carsten Kötting, and Klaus Gerwert

Department of Biophysics, Ruhr-University Bochum, 44801 Bochum, Germany

Keywords: Raman imaging, colon cancer, targeted therapy, microscopy.

Mutational acquired resistance is a major challenge in cancer therapy. Somatic tumors harbouring oncogenic mutations are characterized by poor prognosis and high rate of mortality. In the present study, Raman spectral imaging as an *in vitro* marker-free approach is used to emphasize the oncogenic mutation resistance to therapy.

Targeting epidermal growth factor receptor (EGFR) is one of the effective strategies to suppress tumors in advanced stages due to its overexpression in many cancers. Panitumumab and erlotinib are EGFR inhibitors. Panitumumab antibody blocks the extracellular domain of the receptor to prevent ligand binding. On the other hand, erlotinib is a small molecule that competes with the ATP binding site of the receptor intracellular tyrosine kinase domain. Thus, they disrupt downstream signaling cascade, which is responsible for tumor growth and progression.

In the present study, we have investigated the effect of panitumumab and erlotinib on cellular components of colon cancer cells with and without K-RAS mutations. In case of cancer cells in which K-RAS is mutated, no significant alteration is observed in the Raman spectra of cells after incubation with panitumumab or erlotinib. In contrast, colon cancer cells with wild-type K-RAS showed large spectral changes that indicate changes in the biochemical composition of treated cells.

This can be attributed to the therapeutic effect of panitumumab or erlotinib those prevent auto-phosphorylation of different downstream pathways and trigger the apoptotic state. These results are in agreement with the clinical studies which have proved that patients with K-RAS mutated colon cancer have a poor prognosis and a decreased response to panitumumab and erlotinib.

In addition, we have shown the distribution of molecular targeted agent erlotinib in colon cancer cells by Raman microspectroscopy. Raman results indicated that erlotinib has strong C≡C stretching vibration at 2110 cm⁻¹, which is located in a Raman silent region of cells. Thus, it can be used as a label-free marker band for erlotinib. The Raman results also indicated that the drug in cells is metabolized to desmethyl-erlotinib.¹ These results indicate the potential of Raman microspectroscopy as a non-invasive tool to investigate pharmacokinetics.

Furthermore, we have established Raman spectral histopathology (SHP) method, which are label free and automatic classification of the biochemical state of tissues.² Excellent data quality is obtained and differentiates between healthy and cancerous tissues. Although Raman based SHP is slower, it allows a 10 times higher spatial resolution compared to Infrared. This leads to resolve erythrocytes, lymphocytes and single cell nuclei in the tissue section by

Raman imaging.² In addition to Raman scattering auto fluorescence is observed. We found that this auto fluorescence is spatially overlapped with the fluorescence of antibodies against p53 that is used in a routine immunohistochemistry in surgical pathology. This fluorescence indicates

nuclei of cancer cells with mutated p53 and allows label free assignment of cancer cells. These results open new avenues for medical diagnosis by Raman microscopy and auto fluorescence.

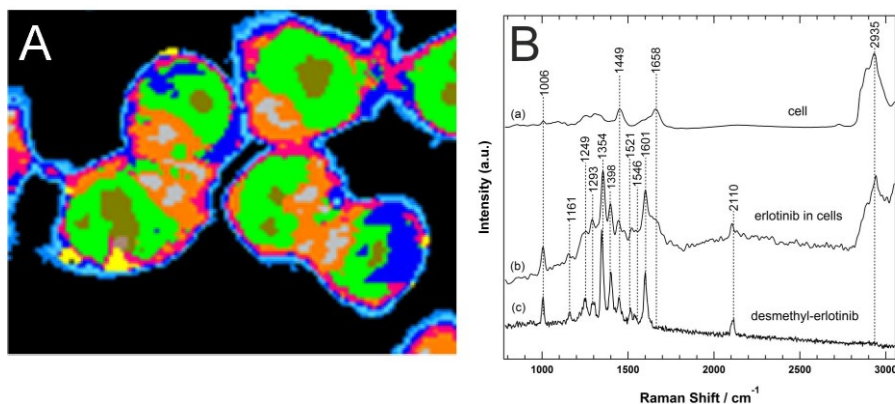


Figure 1. (A) HCA results based on the Raman dataset of SW480 colon cancer cells showing nucleus (green), lipid droplets (grey), and erlotinib (yellow). (B) Raman spectra from cells lacking drug (a), drug within cells (b), and desmethyl-erlotinib (c).

¹ El-Mashtoly, S.F., Niedieker, D., Petersen, D., Kruß, S., Freier, E., Mosig, A., Kötting, Hahn, S., Gerwert, K. (2014) *Biophysical J.*, 115, 1910-1920.

² Mavarani, L., Petersen, D., El-Mashtoly, S.F., Mosig, A., Tannapfel, A., Kötting, C., Gerwert, K. (2013) *Analyst*, 138, 4035-9039.

Studying the effects of UV radiation on human skin by *in vivo* confocal Raman spectroscopy

Alessia Quatela¹, Ali Tfayli¹, Lynda Miloudi¹, Arlette Baillet-Guffroy¹

¹ Laboratory of lipids: analytical and biological systems “Lip(sys)²”, ex: Group of Analytical Chemistry of Paris-Sud (GCAPS), Faculty of Pharmacy, University of Paris-Sud, 5 rue Jean Baptiste Clément, 92296, Châtenay-Malabry. France

Keywords: *In vivo* Raman, skin, photo-aging, UV.

Photoaging and skin cancer have been extensively studied, but the effects of UV on the critical barrier function of the outermost layer of the epidermis, the Stratum Corneum (SC), are not understood.

UV radiation is divided into three main types based on wavelength: UV_C radiation (200–280 nm) is predominately filtered by the ozone layer in the stratosphere, UV_B radiation (280–320 nm) is mainly absorbed by the epidermis, and UV_A radiation (320–400 nm) penetrates deeper into the dermis but interacts with both the SC and epidermis as well¹. Penetration of UV light into the skin results in the formation of free radicals, which immediately interact with the living cells. Free radicals can cause oxidation effects on epidermal proteins, lipids and epidermal DNA².

Here we present the effects of UV_A and UV_B exposure in suberythemal doses and over a relatively short period of time, with no clinically evident inflammation or barrier disruption. Twenty females volunteers aged 20–30 years (mean 25 years) with healthy skin were enrolled in the study. Volunteers had skin phototypes I and II. Volunteers were instructed not to apply any skin care product for at least 72 h previous to the beginning of the experiments. After an acclimation time of 10 min, a template containing three apertures (UV_A, UV_B and control) of 1 cm² each in size was attached to the volunteers' volar forearms.

The equipment used for UV irradiation was a fiber-coupled D2000 lamp source (215–400 nm) from Ocean Optics equipped with custom-made UV_A and UV_B bandpass filters. The starting UV_A and UV_B doses were 95 mJ/cm² and 15 mJ/cm², respectively.

For fast *in vivo* measurements of SC response to UV irradiation, we used a confocal Raman optical microprobe (Horiba Jobin Yvon, Villeneuve d'Asc, France). The probe, coupled to 5 μm diameter optical fiber operates at 660 nm with a laser power on the skin site of 15.0 mW. A long working distance objective MPlanFLN 100X/NA 0.75 is coupled to a piezoelectric system allowing increments of 1 μm step-size. Six measurements at different points of the selected aperture were performed for each volunteers. For each scan, a 2 s exposure time was used with 2 accumulations. Signal and spectra have been separated into two wavenumber regions: the so-called fingerprint region i.e. 600–1800 cm⁻¹ and the 2600–3100 cm⁻¹ region, normalized on Amide I band (1565–1720 cm⁻¹) and on C-H stretching band (2800–3030 cm⁻¹) respectively. The different data analysis steps were performed using Matlab (Mathworks, USA); a Savitsky-Golay filter (4th order, 9 points) was applied to smooth any spurious peaks of the spectra and reference constituting the background³.

Transepidermal Water Loss (TEWL), corneometry and temperature measurements were carried out on each point after irradiation and together with Raman sessions, they were held five times weekly.

Results (Figure 1) showed strong specific differences among volunteers. These differences are related to various molecular components, i.e. carotenoids,

hydration level, lipid conformation... In addition to that, a spectral evolution under the effects of UV radiation along the five days, indicating direct impact on the lipids organization have been observed. Proteins related bands were also affected highlighting changes in the secondary and ternary structure.

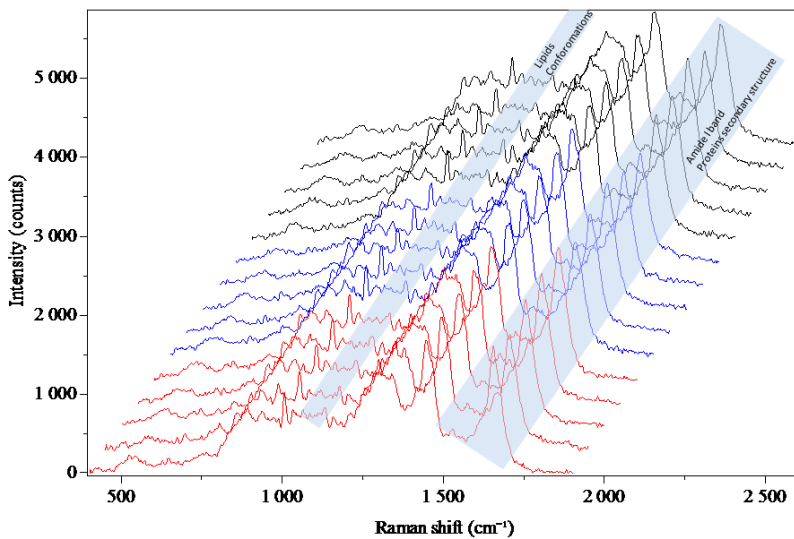


Figure 1. Five days *in vivo* evolution of UV_A- (red curves) irradiated, UV_B- (blue curves) irradiated and Control (black curves) SC.

- ¹ Biniek K., Levi K., Dauskardt R. H. (2012), *PNAS*, 109(42), 17111–17116.
- ² Darvin M.E., Gersonde I., Albretch H., Sterry W., Lademann J. (2006), *Laser Physics*, 16 (5), 833-837.
- ³ Quatela A., Tfyali A., Baillet-Guffroy A. (2015), *Skin Res. and Technol.*, in press.

“The use of 2D IR correlation spectroscopy in fragment based drug design and the identification of novel protein-targets”

Belinda Pastrana-Rios^{1,2}, Adalberto Diaz Casas² Walter Chazin³ and Eaton Lattman⁴

¹Protein Research Center, University of Puerto Rico-Mayagüez, 00681-9019, Mayagüez, PR

²Department of Chemistry, University of Puerto Rico, Mayagüez Campus, 00681-9019, Mayagüez, PR USA

³Center for Structural Biology, Vanderbilt University, 37232-8725, Nashville, TN, USA

⁴Hauptman-Woodward Medical Research Institute, BioXFEL Science and Technology Center, 700 Ellicott Street, 14203 Buffalo, New York, USA

Keywords: 2D IR correlation spectroscopy, Isothermal Titration Calorimetry, fragment based drug design, Yeast-two-hybrid, crystal screens for BioXFEL.

Centrin is a small 20 kDa calcium binding protein belonging to the EF-hand superfamily^{1,2}. Like other proteins in this superfamily it is a calcium sensor with both regulatory and structural roles. This calcium binding protein (CaBP) has also been found to be an essential protein in Eukaryotes. Centrin is required for the assembly of highly conserved structures known as centrioles, basal bodies, primary cilium and flagella. Yet, this protein has also been found localized to the nucleus along with XPC and RAD23 in the regulation of DNA excision repair³⁻⁵. More recently, centrin was found to

be involved in mRNA export⁶. Prp40 homologue A is a protein localized to the nucleus. We identified the Prp40 homologue A to contain the hydrophobic triad W₁L₄L₈ this sequence pattern was found to overlap the Nuclear Export Signal (NES) site⁷. High resolution structure determination has only been ascertained for several domains of this protein. Prp40 is comprised of two tandem WW domains followed by six FF domains, which were found to mediate Prp40-target interactions⁷⁻¹¹. The biological role of Prp40 has been linked to the assembly of the spliceosome and mRNA splicing.

Herein our group has provided molecular biophysical evidence through a fragment based drug design approach that

validates Prp40 homologue A-centrin interaction.

Different centrin-Prp40A complexes were studied by ITC and 2D IR correlation spectroscopy. The actual Prp40A peptide studied contained the NES and its sequence was comprised of the following Ac-K₅₂₄QLRKRNWEALKNILDNMANVTYS TTWSEAAQQY₅₅₆-NH₂ referred to as Prp40Ap₁ and different centrins. We performed 2D IR correlation spectroscopy of ¹³C-labelled *Chlamydomonas reinhardtii* centrin (¹³C-Crcen)-Prp40Ap₁ at 1:1 mole ratio under varying temperatures. FT-IR spectral data was acquired at 5°C intervals within the temperature range of 5-95°C. The use of isotope labelling allowed for the simultaneous monitoring of both centrin and the Prp40Ap₁ peptide. 2D IR correlation spectroscopy¹² was used to enhance the spectral resolution and ascertain the molecular events that led to complex formation. Also cross peaks were evident that confirmed the interaction between centrin and Prp40Ap₁. In addition, comparative calorimetric study between *Hscen2*-Prp40Ap₁ and *Chlamydomonas reinhardtii* centrin (Crcen)-Prp40Ap₁ complexes at 25°C were performed (Table 1). Crcen-Prp40Ap₁ complex presented the highest stability and affinity. Also, we explored the interaction

between *Crcen* and Prp40Ap₁ as a function of temperature. At a temperature near physiological condition (35°C), the complex exhibited the highest stability ($\Delta G = -9.49 \pm 0.04$ kcal/mol) and affinity ($K_a = 5.3 \pm 0.2 \times 10^6$ M⁻¹) with a favorable enthalpy ($\Delta H = -12.1 \pm 0.6$ kcal/mol) and unfavorable entropy ($-\Delta S = 2.6 \pm 0.6$ kcal/mol). From the analysis of the binding enthalpies as a function of temperature, we obtain a change in binding heat capacity (ΔC_p) of -0.2402 kcal/mol°C indicating a decrease in exposure of the hydrophobic surface as a result of the interaction between *Crcen* and Prp40Ap₁. Finally, in collaboration with the BioXFEL STC we have performed crystallization screenings of the *Crcen*-Prp40Ap₁ complex. Discussion of the biological implications will be presented.

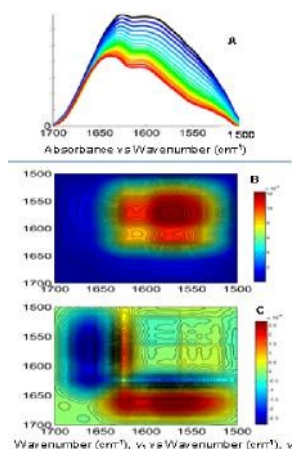


Figure 1. ¹³C-*Crcen* Prp40Ap₁ complex within the spectral region of 1700-1500 cm⁻¹ (A) FT-IR spectral overlay and 2D IR correlation analysis (B) synchronous and (C) asynchronous plots.

Table 1. Summary of the thermodynamic parameters governing binding of centrin-Prp40Ap₁.

Protein	Peptide	K_a (error)	ΔG (error)	ΔH (error)	$-\Delta S$ (error)
		(10 ⁶ M ⁻¹)	(kcal/mol)	(kcal/mol)	(kcal/mol)
<i>Crcen</i>	Prp40Ap ₁	3.7 (0.8)	-8.8 (0.1)	-9.3 (0.2)	0.6 (0.2)
<i>Hscen2</i>	Prp40Ap ₁	2.1 (0.4)	-8.6 (0.2)	-16.4 (0.8)	7.8 (0.8)

¹Nakayama S. and Kretsinger R.H. (1998) *Biometals* 11, 277-295.

²Pastrana-Rios B. Reyes M. Meza V. De Orbeta J. Rodriguez Nassif A., Narváez, D. Gómez, A.M. Almodovar R. Díaz A. Robles J. Irizarry L. Campbell M. and Colón M. (2013) *Biochemistry* 52, 1236-1248.

³Araki M. Masutani C. Takemura M. Uchida A. Sugasawa K. Kondoh J. Ohkuma Y. and Hanaoka F. (2001) *J. Biol. Chem.* 276, 18665-18672.

⁴Nishi R. Okuda Y. Watanabe E. Mori T. Iwai S. Masutani C. Sugasawa K. and Hanaoka F. (2005) *Mol. Cell. Biol.* 25, 5664-5674.

⁵Marteijn J.A. Lans H. Vermeulen W. and Hoeijmakers J.H.J. (2014) *Nat. Rev. Mol. Cell. Biol.* 15, 465-481.

⁶Resendes K.K. Rasala B.A. and Forbes D.J. (2008) *Mol. Cell. Biol.* 28, 1755-1769.

⁷Ester C. and Uetz P. (2008) *BMC Biochemistry* 9, 29 doi:10.1186/1471-2091-9-29.

⁸Berglund J.A. Chua K. Abovich N. Reed R. and Rosbach M. (1997) *Cell.* 89, 781-787.

⁹Bedford M.T. Chan D.C. and Leder P. (1997) *EMBO J.* 16, 2376-2383.

¹⁰Bedford M.T. Reed R. and Leder P. (1998) *Proc. Natl. Acad. Sci. USA.* 95, 10602-10607.

¹¹Allen M. Friedler A. Schon O. and Bycroft M. (2002) *J. Mol. Biol.* 323, 411-416.

¹²Noda, I. (2004) *Vibrat. Spectrosc.* 36, 143-165.

Early detection of colorectal cancer relapse using infrared spectroscopy in morphologically normal anastomosis

A. Salman¹, G. Sebbag², S. Argov³, R.K. Sahu^{4,5} and S. Mordechai⁵

¹Department of Physics, SCE - Shamoon College of Engineering, 84100, Beer-Sheva, Israel.

²Surgery B Department, Soroka University Medical Center, Faculty of Health Sciences, Ben Gurion University, 52900, Beer-Sheva, Israel.

³Department of Pathology, Soroka University Medical Center, 84105, Beer-Sheva Israel.

⁴Centurion University of Technology and Management, Paralakhemundi, India, 761211.

⁵Department of Physics, Ben-Gurion University of the Negev, 84105, Beer-Sheva, Israel.

Keywords: infrared spectroscopy, metastasis, local recurrences, distant recurrences, multivariate analysis

Colorectal cancer is the third most common cancer diagnosed in the United States. The American Cancer Society's most recent estimates for the number of colorectal cancer cases in the United States for 2013 are: 102,480 new cases for colon cancer, 40,340 new cases for rectal cancer, and 50,830 deaths. The estimated numbers for 2014 are: 96,830 new cases of colon cancer, 40,000 new cases of rectal cancer, causing 50,310 yearly deaths.

According to the literature, up to 55% of rectal cancer patients experience a recurrence within five years from the time of surgery resulting with a deep influence on the quality of patient's life. It causes great pain, both mentally and physically, with inconvenience induced by the need to be in proximity to the medical center. Since the margins of the removed cancerous lesion are not well determined, surgeons may occasionally leave malignant cells during the anastomosis surgery. The shoulders of the removed (diseased) colonic section lead to 83% of the local recurrences. The morphology often seems normal in standard pathology, though it is already in an early stage of abnormality in the molecular level.

Infrared spectroscopy has been widely used in medicine. It can detect abnormalities

in the colonic crypts, which are not detectable yet using standard histopathological review. The detection of abnormal crypts is essential for diagnosis of the spread of colorectal cancer and its effective management^{1, 2}. Our previous studies have shown that IR spectroscopy can detect early development of diseases at a stage when the morphology is still normal³. This important observation was named by our group as the "crypt model"^{5, 6}. Our research group has reached important milestones in the overall understanding of the complex changes that occur in single cells as well as tissues on the level of biochemical composition when a cell undergoes changes between normal and abnormal conditions^{5, 7, 8}. Our main goal in this study was to evaluate the potential of FTIR spectroscopy in tandem with multivariate analysis to detect and predict whether the patient will experience colorectal cancer recurrence by classifying the investigated crypts into three categories: control, local recurrence, and distant recurrence, based on their IR absorption spectra. Success of this idea may lead to an objective detection and assessment of free micro-metastasis shoulders of the removed

section of the colon, in order to reduce the recurrence rate.

The spectra were measured from bottom, middle, and top sites of the same crypt, respectively. Figure 1 shows the typical IR control absorption spectra measured from three different sites along the height of the longitudinal section of the same crypt—base, middle, and top in the range 850–1775 cm^{-1} before manipulation.

The main features of the spectra are due to the organic molecules such as phospholipids, proteins, lipids, carbohydrates, and nucleic acids.

We used PCA followed by LDA for the classification to differentiate among the three categories. Our results showed that it is possible to differentiate among control, local and distant recurrence crypt with more than 92% success rate.

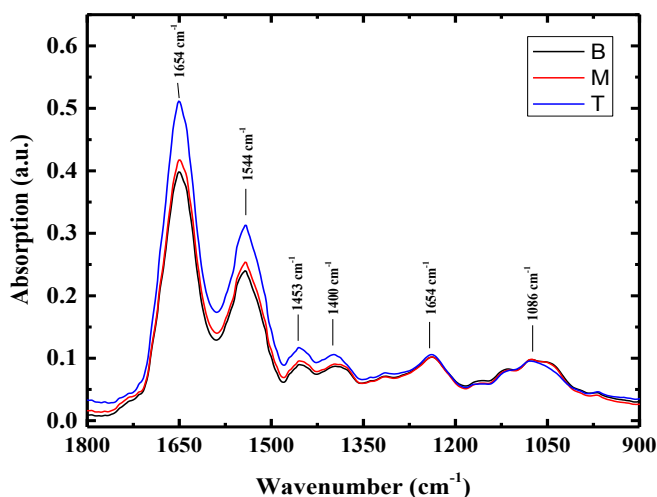


Figure 1. IR absorption spectra measured from three different sites of the same crypt, taken from the control section before manipulation. The main vibrations are assigned in the figure.

1. G. I. Zonios, R. M. Cothren, J. T. Arendt, J. Wu, J. Van Dam, J. M. Crawford, R. Manoharan and M. S. Feld, *IEEE transactions on bio-medical engineering*, 1996, **43**, 113-122.
2. T. Enomoto, M. Kuranami and A. Kakita, *Surgery today*, 2000, **30**, 711-717.
3. A. Salman, V. Erukhimovitch, M. Talyshinsky, M. Huleihel and M. Huleihel, *Biopolymers*, 2002, **67**, 406-412.
4. E. Bogomolny, S. Mordechai, A. Zwielly and M. Huleihel, *European biophysics journal : EBJ*, 2009, **38**, 971-980.
5. R. K. Sahu, S. Argov, A. Salman, U. Zelig, M. Huleihel, N. Grossman, J. Gopas, J. Kapelushnik and S. Mordechai, *Journal of biomedical optics*, 2005, **10**, 054017.
6. A. Salman, R. Sahu, E. Bernshtain, U. Zelig, J. Goldstein, S. Walfisch, S. Argov and S. Mordechai, *Vibrational Spectroscopy*, 2004, **34**, 301-308.
7. S. Argov, J. Ramesh, A. Salman, I. Sinelnikov, J. Goldstein, H. Guterman and S. Mordechai, *Journal of biomedical optics*, 2002, **7**, 248-254.
8. A. Salman, S. Argov, J. Ramesh, J. Goldstein, I. Sinelnikov, H. Guterman and S. Mordechai, *Cellular and molecular biology*, 2001, **47 Online Pub**, OL159-166.

Lipid droplets: a Raman signature of colorectal cancer stem cells

Luca Tirinato¹, Simone Di Franco², Vijayakumar P. Rajamanickam³, Patrizio Candeloro⁴, Matilde Todaro², Jan Paul Medema⁵, Giorgio Stassi², Enzo Di Fabrizio¹ and Carlo Liberale³

¹PSE Division, King Abdullah University of Science and Technology (KAUST), 23955-6900, Thuwal, Kingdom of Saudi Arabia

²Department of Surgical and Oncological Sciences, University of Palermo, Palermo, Italy

³BESE Division, King Abdullah University of Science and Technology (KAUST), 23955-6900, Thuwal, Kingdom of Saudi Arabia

⁴BioNEM Lab, Department of Experimental and Clinical Medicine, University Magna Graecia of Catanzaro, 88100, Catanzaro, Italy

⁵LEXOR, Center for Experimental Molecular Medicine (CEMM), Academic Medical Center (AMC), University of Amsterdam, 1100, Amsterdam, The Netherlands;

Keywords: Colorectal cancer stem cells, Lipid droplets, Raman spectroscopy.

Colorectal Cancer (CR) cell normally originates from clonal expansion of a single intestinal stem or progenitor cell located at the bottom of the CR crypt that undergoes genetic and /or epigenetic alterations, which appears to maintain their hierarchical organization as well as the morphogenic signals¹.

CR has been shown to contain this hierarchy with a Cancer Stem Cell (CSC) compartment at the apex. Most importantly, CSCs are more resistance to therapy than differentiated tumor cells. Thus Colorectal Cancer Stem Cells (CR-CSCs) have been recognized as a key component in CR carcinogenesis and recurrence. Their further identification and isolation become a crucial step to better understand the mechanisms that underlie their biological behavior. The most common *in vitro* methods used to detect and isolate CR-CSCs comprise, i) the analysis of CSC markers, ii) the propagation as tumor spheres and then ii) serial injections of the spheres into immune compromised mice. Unfortunately, nearly all of the CSC markers for CR-CSCs so far proposed, such as CD133, CD44, ESA (EpCAM), CD166, ALDH-1, Musashi 1

(Msi1), and LGR5 requires staining and are not completely unique for the CSC population²⁻³.

The quantification of CSC subpopulation is therefore of utmost interest both in terms of functional assays and finding markers for CR-CSC identification. For this purpose, it is highly desirable to develop an alternative, rapid and reliable technique to apply in medicine for future stem cell detection. In this context, we discovered that CR-CSCs overexpress Lipid Droplets (LDs) in comparison to differentiated colon cancer cells and normal epithelial colon cells (NECC), by using Raman micro-spectroscopy⁴. They could be considered as a CR-CSCs marker.

From a vibrational spectroscopic point of view, the large amount of LDs produces remarkable increased intensities in the Raman difference spectrum (Figure 1***) at 1300 cm⁻¹ and 2800 cm⁻¹ related to specific vibrations of lipid. This was clearly visualized in corresponding space-correlated Raman mapping. Furthermore, lipid selective visualization of CR-CSCs directly revealed that these LD Raman modes are ideal candidates as Raman signatures for a

fast, robust and label-free CR-CSC identification method. The presented results were also confirmed with classic LDs staining dyes, BODIPY493/508 and LD540 by measuring their expression with flow cytometry, and by fluorescence and electron microscopic techniques.

In addition, the higher expression of LDs in CR-CSCs content was correlated to

an over-expression of CD133 and high Wnt/ β -catenin pathway, two well-known markers for CR-CSC. This was further confirmed when CR-CSC LD High content population (CR-CSC LD^{High}) retain most tumorigenic potential after xenotransplantation experiments, evidencing that LDs could be foreseen as potential subcellular structure for novel anti-cancer target therapies.

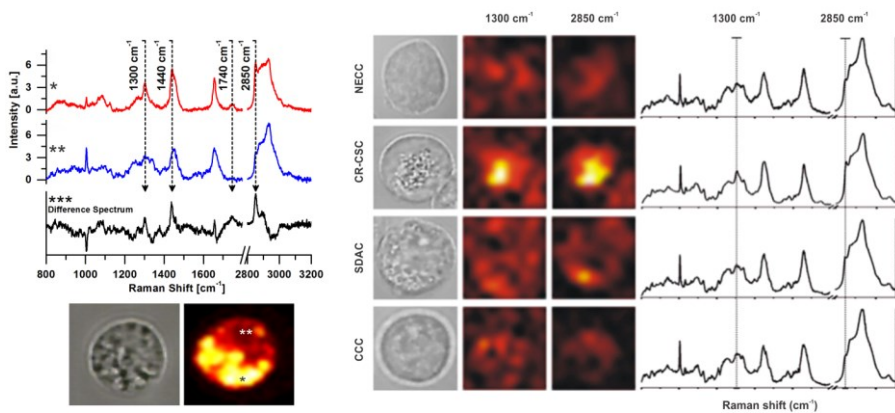


Figure 1. Label-free chemical imaging of LDs in colorectal cancer stem cell using Raman micro-spectroscopy.

Left: Two different cell regions, indicated as * and ** respectively, can be clearly identified in the cell according to their Raman spectra. The Raman differences are due to 4 main peaks located at 1300, 1440, 1740 and 2850 cm^{-1} . Typical spectra from region * (top curve) and region ** (bottom curve) show that region * has higher expression of all these aforementioned peaks compared to region **, as clearly highlighted by the Raman difference spectrum ***.

Right: Peaks related to lipidic vibrations are more pronounced in the CR-CSCs (second row) compared to sphere-derived adherent cells (SDACs) and colon cancer cell (CCCs), as it is evident both from Raman images and spectra. NECCs reported in the first row express the lowest Raman intensities of lipidic vibrations.

¹ Reya T, Morrison S.J, Clarke M.F, Weissman I.L., (2001), *Nature*, 414(6859), 105-111.

² Visvader J.E, Lindeman G.J., (2008) *Nat Rev Cancer*, 8, 755-768.

³ Ebben J.D, Treisman D.M, Zorniak M, Kutty R.G, Clark P.A, Kuo J.S., (2010) *Expert Opin Ther Targets*, 14(6), 621-632.

⁴ Tirinato L, Liberale C, Di Franco S, Candeloro P, Benfante A, La Rocca R, Potze L, Marotta R, Ruffilli R, Palanisamy Rajamanickam V, Malerba M, De Angelis F, Falqui A, Carbone E, Todaro M, Medema J P, Stassi G, Di Fabrizio E, (2015), *STEM CELLS*, 33, 35-44.

Multimodal Raman imaging and a comparison of scanning vs non-scanning approaches for spectral discrimination of immune cells

Nicholas Smith¹, Nicolas Pavillon¹, Alison Hobro¹

¹Biophotonics Lab, Immunology Frontier Research Center (IFReC), Osaka University, 565-0871, Osaka, Japan

Keywords: Raman, imaging, cell type discrimination, multimodal, high-throughput.

Raman spectroscopic imaging is an imaging modality for measuring chemical states and distributions of components in living cells. The lack of labeling can provide opportunities for unique insights into the sample nature and dynamics^{1,2}. Raman imaging is already implemented in many systems, and is providing robust data, but remains subject to a number of restrictions, due to the inherently low number of Raman-scattered photons. These limitations have been reduced by the use of new approaches such as coherent or stimulated Raman imaging modalities, but with reduced spectral resolution. Attempts to supplement the Raman data with additional information from a complementary measurement mode are possible but are also challenging since the addition of particles or fluorescent dyes can interfere with the Raman signal. Even typical brightfield or DIC phase imaging does not allow the simultaneous measurement of the Raman signal.

Our approach was to add a coherent phase imaging mode, with a laser excitation wavelength outside the Raman spectral range of interest. Using near infrared laser illumination and digital holographic microscopy (DHM)^{3,4}, we observed the quantitative phase distribution at up to video rate, while the Raman signal was simultaneously detected (at a slower frame rate). The addition of the quantitative phase not only allows a view of the sample during long Raman acquisition periods, it also allows the study of how the two sets of

label-free image data are related. Since the phase contrast is based on the density of material and the Raman contrast results from the chemical composition, this multimodal label-free imaging proves a more complete data set than either imaging modality alone.

The ability to use multimodal imaging opens up possibilities in the use of Raman spectroscopy to discriminate between cell lines, or measure changes in groups of cells. Since cells contain an enormous number of different molecules, and measured spectra contain mixed contributions of these molecules, practical use of Raman is often suited to differential measurements in cellular spectra. In Raman imaging measurements, if the entire cell is measured in an imaging mode, the laser is scanned over the entire cell, either as a point raster scan or as a line scan, exploiting the 2d nature of the detector. Each pixel then contains unique spectra that can help to discriminate between different cell targets as well as provide spatial information as to the nature of those differences.

In practice however, the signal-to-noise ratio (SNR) in Raman imaging, where the entire cell is scanned and spatially mapped, is often insufficient to discriminate between cells without some type of binning or spatial averaging of the pixel spectra. If so, then this equates to mapping the spatial distribution of the spectra across the detector and then discarding the spatial information when later averaging. This comes at a significant cost: each pixel contains

significant read noise, which will be summed (e.g. as a root-mean square) in the final averaged spectra.

By comparison, single point Raman measurements in cells can allow discrimination abilities and also a much higher throughput. Using only a single point from the cytosol or nucleus of the cell means these measurements are non-scanned. Each cell can be measured once, providing a spectrum with high SNR compared to full Raman imaging. However, the use of only a single point measurement to characterize an entire cell does not ignore the spatial variation within the cell, but instead captures it in an unknown manner (ie the precise location of the laser excitation in the cell is difficult to determine).

We therefore proposed a new approach, which we termed a ‘hybrid’ scan⁵. The beam is scanned across a region of the cell sample and then descanned by galvanometer mirror, so that the final spectra on the 2d detector is “optically binned” and collected by only a single row of pixels. This has the advantage of high SNR spectra (Fig. 1), discrimination based on a large and user-definable region of the cell, and high throughput. By using the quantitative phase mode to evaluate cellular morphology, we additionally have imaging that helps define the correct outlines of the cell so we can choose the region to spectrally evaluate.

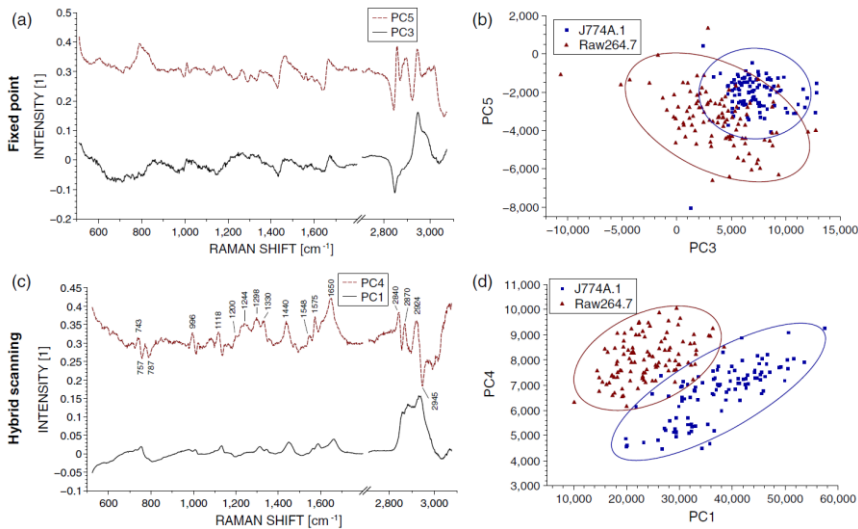


Fig 1. Fixed point (a,b) vs hybrid scan (c,d) discrimination of immune cell lines (from Ref 5.)

- ¹ M. Okada, N. I. Smith, A. Palonpon, H. Endo, S. Kawata, M. Sodeoka and K. Fujita, (2012) *P. Natl. Acad. Sci. USA* 109(1), 28-32.
- ² A. J. Hobro, N. Pavillon, K. Fujita, M. Ozkan, C. Coban and N. I. Smith, (2015) *Analyst*, in press.
- ³ N. Pavillon, A. J. Hobro and N. I. Smith, (2013) *Biophys. J.* 105(5), 1123-1132.
- ⁴ N. Pavillon and N. I. Smith, (2015) *EPJ Techniques and Instrumentation* (in press).
- ⁵ N. Pavillon and N. I. Smith, (2015) *J. Biomed. Opt.* 20(1), 016007-1-016007-10.



On-site non-invasive investigation of polychrome decorations using Raman spectroscopy: achievements and limitations

María José Ayora Cañada¹

María José de la Torre López², Ramón Rubio Domene³, Ana Domínguez Vidal¹

¹Department of Physical and Analytical Chemistry, Universidad de Jaén, Campus Las Lagunillas, E-23071, Jaén, Spain

²Department of Geology, Universidad de Jaén, EPS-Linares, Alfonso X El Sabio 28, E-23700 Linares (Spain)

³ Conservation Department, Council of The Alhambra and Generalife, Real de la Alhambra s/n, E-18009 Granada, Spain

Keywords: Raman spectroscopy, conservation science, non-destructive investigation, mobile equipment, pigment degradation

Raman spectroscopy is a versatile technique that has frequently been applied for the investigation of art objects. Advantages like its ability to identify materials at a micrometer-scale and its non-destructive character are greatly appreciated in conservation science. By using mobile Raman instrumentation it is even possible to investigate the artworks without the need for sampling, in a complete non-invasive way.

The rich polychrome decorations of the stalactite ceilings at the Alhambra complex in Granada (Spain) have been studied. These typical Arabic decorations consist of self-supporting domes built up with gypsum. Vertical gypsum prisms applied one over another are joined in multiple different arrays resembling stalactites of a cave (mocarabes). These mocarabes are decorated in red, blue, green, golden and black colors. A totally non-invasive investigation using a fiber-optic portable Raman micro-spectrometer equipped with a 785-nm laser and an optical probe head attached to a videomicroscope was carried out. The works were conducted on scaffolding platforms at a height of ca. 12 m above the ground level coinciding with conservation works. The fiber optic probe was mounted on a tripod motorized in the X–Y–Z axes with remote control. Despite working under non-

laboratory conditions which involved challenges as scaffolding vibrations, daylight, temperature differences and dust, good quality Raman spectra were obtained during this survey. It is remarkable that using mobile non-invasive techniques the investigation is not limited by sampling and more representative results can be obtained. We took hundreds of Raman spectra from different locations in the seven vaults of the Hall. Such a wide study would have been impossible by sampling even at micro scale. This advantage is clearly illustrated in the case of the degradation of the pigments. Two red pigments, cinnabar and minium, were identified in the red decorations. Both provided Raman spectra of extraordinary quality, even working on top of the scaffold with the portable instrument. Many areas decorated with minium appeared darkened. Two different alteration processes affecting minium were identified. One of the alterations led to an initial darkening by the formation of plattnerite (β -PbO₂). This darkening phase ends into a complete discoloration by transformation into the more stable white anglesite (PbSO₄). This alteration was probably induced by rain water, the degraded areas were found in the stalactite ceiling in areas with evidence of water leaking through the cracks of the

structure. On the contrary, the second kind of alteration was probably induced by sunlight penetrating from the windows and leading to the different mixed valence Pb oxides. On the other hand, chloride induced degradation of cinnabar was demonstrated through the identification of calomel (Hg_2Cl_2) in degraded areas.

Furthermore, black decorations showed always the Raman signature of carbon, although in this case the Raman spectra were weak and noisy since very low laser power had to be employed to avoid burning. Natural lapis lazuli (with a characteristic luminescence pattern¹) was identified in most of the blue motifs. In addition, synthetic ultramarine blue (which showed no luminescence bands) was detected only in one of the vaults revealing a much more recent restoration, with motifs of very poor artistic quality

The major limitation of the on-site study was due to the availability of only one laser for excitation. With the 785 nm laser it was not possible to obtain spectra from green and pale blue-greenish decorations. Thus, the on-site study was complemented by analyses in the laboratory on selected samples taking benefit of higher sensitivity, higher spatial resolution and the possibility of using different lasers. In samples with blue and green areas azurite severely degraded to clinoatacamite was identified. Other degradation products, identified in the laboratory regardless of the color of the pigment, were calcium oxalates. Finally, the laboratory studies also enabled the investigation of the stratigraphy of the pictorial layers revealing some re-decorations.

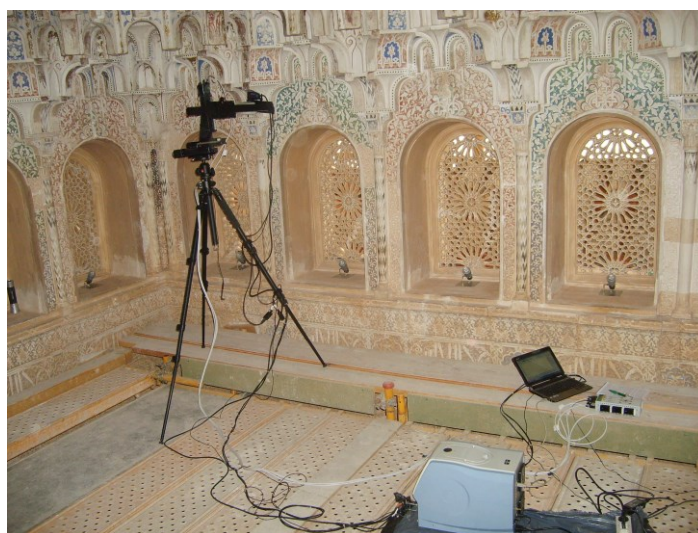


Figure 1. Experimental set-up for the non-invasive Raman spectroscopic investigation of the stalactite ceilings at the Alhambra

¹ A. Dominguez-Vidal, De La Torre-Lopez M.J., R. Rubio-Domene and M. J. Ayora-Cañada, *Analyst* **2012**; 137, 5763

Acknowledgements. This work was financed by the research project BIA2013-41686-R from the Spanish Ministry of Economy and competitiveness and FEDER funds.

Raman line scanner for automated explosive detection on hand luggage and Spatially Offset Raman Spectroscopy (SORS) for threat detection

Bernhard Zachhuber, Martin Glimtoft, Mattias Svanqvist, Ola Norberg, Niklas Johansson, Matilda Ågren, Anders Elfving and Henric Östmark

Defence and Security, Systems and Technology / Energetic materials
FOI, Swedish Defence Research Agency, 164 90, Stockholm, Sweden

Keywords: explosives, Raman spectroscopy, line scanner, aviation security, counter terrorism.

A Raman line scan system for the identification of explosive particles was developed for the analysis of particles on hand luggage. This fully automated system was integrated in the housing of an x-ray scanner common on airports. Since the luggage is investigated as it passes the setup on a conveyor belt, instantaneous detection is imperative. This requirement is met by single-shot Raman line scan spectroscopy, where a broader area on the sample is simultaneously probed, by a laser beam that is widened along one dimension. For all positions of the excited line a full Raman spectrum is obtained within a single laser shot. To rapidly adjust for the different height dimensions of individual hand luggage, a photography objective was built in to autofocus on the sample surface.

Furthermore, the system was also adapted to determine the content in containers which are non-transparent to the human eye. The combination of Spatial Offset Raman Spectroscopy (SORS) with Raman line scanning allows to collect spectral data from a broad range of different spatial offsets simultaneously. This is a significant advantage over SORS with predefined offset, since the ideal offset is unknown prior to the measurement and depends on the container material as well as the sample content¹. Here, the detection of sodium chlorate in a white plastic bottle is shown. Whereas a previously introduced

stand-off SORS imaging system required stepwise collection of the different wavelength², here the entire spectrum is collected simultaneously. For security applications, this concept can be combined with already existing stand-off Raman systems to rapidly evaluate the threat of concealed substances. Especially when investigating potentially harmful objects, such as explosives, the added distance between operator and sample is most beneficial³. For instance, the identification of trace amounts was successfully shown for a variety of threat substances using imaging Raman spectroscopy⁴ from a stand-off distance of 10 m.

In Fig. 1 (top left) the Raman raw data is illustrated. The spatial offset changes along the vertical image axis, whereas the Raman shift changes on the horizontal axis. The vertical, dark lines in the image are Raman signals from the investigated NaClO_3 powder as well as the HDPE container. It can be seen that the Raman band originating from the NaClO_3 is still comparably intense at increased offset. The signal at zero offset is most intense for both Raman bands (NaClO_3 , HDPE). The main difference is, that the signal of the content decreases much slower, due to the internal light scattering (Fig 1a).

As a consequence (Fig. 1b), the relative signal ratio (inside : outside) increases to a maximum on either side of the laser entry point (at zero offset).

This position is referred to as “ideal offset” and has a value of 4.3 mm, in this particular case.

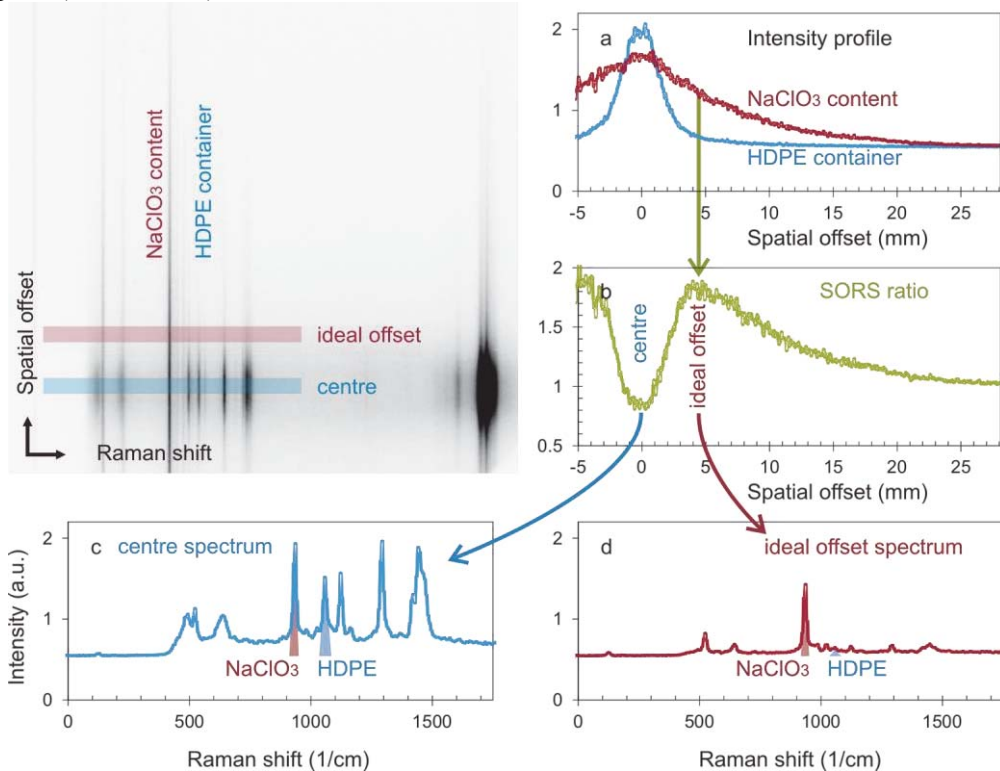


Figure 1. SORS line scan of NaClO₃ powder in white plastic container, analysed from 68 cm; image: raw data; a: change of intensity with spatial offset; b: ratio of container and content intensity shows ideal offset at 4.3 mm; c: spectrum without offset; d: spectrum at ideal offset.

It should be noted that the ideal offset is different for each individual sample, due to changing scattering parameters. That is why simultaneous collection of many offsets is beneficial when unknown samples are investigated.

The research leading to these results has received funding from the European Community’s Seventh Framework Program (FP7/2007-2013) “XP-DITE” (Grant Agreement No. 285331).

¹ Maher J.R., Berger A.J., (2010), *Applied spectroscopy*, 64 (1), 61-65.
² Zachhuber B., Östmark H., Carlsson T., (2014), *Proc. of SPIE*, 9073, 21.
³ Izake E.L., Cletus B., Olds W., Sundarajoo S., Fredericks P.M., Jaatinen E., (2012), *Talanta*, 94, 342-347.
⁴ Östmark H., Nordberg M., Carlsson T.E., (2011), *Applied optics*, 50, 5592-5599.

On the quantification of caffeine, the major impurity in legal-high stimulants, using handheld Raman spectroscopy and partial least square regression

Sulaf Assi¹, Stuart Preston² and David Osselton¹

¹Faculty of Science and Technology, Bournemouth University, Poole, BH12 5BB, UK

²Scientific and Medical Products Ltd., Cheadle, SK8 1PY, UK

Keywords: Legal high, Raman, impurities, quantitative, partial least square regression.

Legal-highs represent a major public health threat due to their unpredicted toxicity. This is because they often contain impurities in various concentrations that do not match their label claim. For instance, caffeine has been reported as the major impurity in legal-high stimulants^{1,2}. Raman spectroscopy offers a rapid and non-destructive technique for analysis of legal-high products². Therefore, this work aims at quantifying caffeine in legal-high stimulants using Raman spectroscopy and partial least square regression (PLSR).

A total of four pure substances were used, and included: 2-aminoindan hydrochloride (2AI), caffeine (CAF), lidocaine (LID) and mephedrone (MEPH). Models were constructed from binary mixtures of these substances to contain 5-95% of each constituents as follows: Model 1 (2AI/CAF), Model 2 (LID/CAF) and Model 3 (MEPH/CAF), and were stored in glass vials. Internal test sets containing mixtures of 2AI/CAF, LID/CAF and MEPH/CAF were prepared for each model³. Moreover, external test sets 10 legal high stimulants were used. Pure substances, mixtures and products were measured through glass vials using the Rigaku Xantus-1 handheld Raman instrument equipped with 785 nm laser power. Three replicates were taken per spectrum, such that each spectrum

was the sum of 4 scans over the range of 250-2000 cm^{-1} (Figure 1). The spectra were exported to Matlab R2014a where PLSR was applied.

The three PLSR models were created for each binary mixture by splitting the spectra into calibration and validation sets in the ratio 2:1. The number of factors used was four for all the three models and was chosen to give a low relative square error of prediction (RSEP). Models 1 (2AI/CAF) and 3 (MEPH/CAF) showed higher accuracy than model 2 (LID/CAF) with r^2 values above 0.98 and 0.97, for the calibration and validation sets respectively (Table 1). The root mean square errors of calibration (RMSEC) and prediction (RMSEP) values of the aforementioned two models were below 5% m/m. On the other hand, model 2 (LID/CAF) showed the least accuracy with r^2 values of 0.95 and 0.89 for the calibration and validation sets respectively. It also showed poor precision with RMSEC and RMSEP values of 6.02 and 11.7% m/m respectively. When legal high products were predicted using the three models, the lowest RSEP value observed was 16% and was observed for model 3 (MEPH/CAF) test set. This showed that the method was semi-quantitative in nature and did not fit with the pharmacopoeial requirements (within 5% RSEP).

The use of handheld Raman spectroscopy and PLSR offered a rapid and non-destructive method for the quantification of caffeine in legal high stimulants. However, the accuracy of this

method to predict drug quantity is still not satisfactory to fit with the pharmacopoeial requirements and thus further work is needed to improve quantification.

Table 1. Comparison between theoretical predictions and experimental measurements.

Model	Range (% m/m)	r ² c	RMSEC (% m/m)	r ² v	RMSEP (% m/m)	RSEP (%)
M1	5.06-95.3	0.9802	4.43	0.9713	5.03	11.2
M2	5.10-95.2	0.9527	6.02	0.8923	11.7	23.4
M3	5.03-95.4	0.9803	4.42	0.9658	4.32	8.61

M: Model, % m/m: Percentage mass per mass, r²c: correlation coefficient of calibration set, RMSEC: Root mean square error of calibration, r²v: correlation coefficient of validation set, RMSEP: Root mean square error of prediction, RSEP: Relative standard error of prediction.

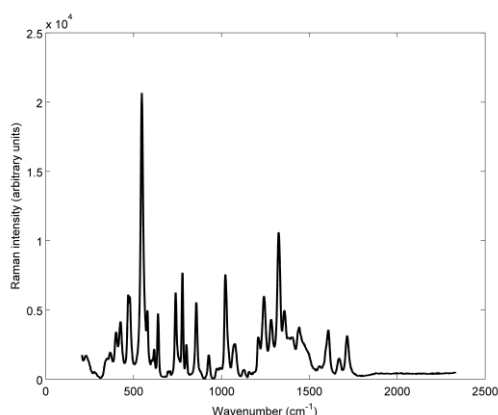


Figure 1. Raman spectrum of a mixture containing 50% 2AI and 50% caffeine.

- ¹ Davies S., Lee T., Ramsey, J., Dargan PI. (2012), *European Journal of Clinical Pharmacology*, 68 (4), 435-439.
- ² Assi, S. (2013), *American Pharmaceutical Review*, 18 (5), 25-31.
- ³ Assi S., Watt R.A., Moffat A.C. (2011), *Journal of Raman spectroscopy*, 43 (8), 1049-1057.

HAND HELD OFF-AXIS RAMAN SPECTROSCOPY FOR PROCESS ANALYSIS

Keith Carron

Snowy Range Instruments, 407 South Second Str. 82070, Laramie, WY, USA

Keywords: Process Analysis, Non-invasive, Raman, Depth Profile.

The most common collection geometry for Raman spectroscopy is 180 degrees backscattering collection. This collection geometry overcomes tedious alignment of off-axis excitation and collection. **Figure 1** illustrates an older collection geometry used for spectroelectrochemistry where off-axis collection was used to eliminate scattering or fluorescence from windows and solutions in front of the electrode [1].

The key to understanding off-axis collection is the spatial filter. Spectrographs are just imaging systems that image the entrance aperture at the focal plane. As with confocal Raman microscopy, this entrance aperture is also a spatial filter that permits only a small area of the spot illuminated by the laser beam. By exciting off-axis the window and solution in front of the sample is imaged to the side of the spatial filter (entrance aperture) and it is removed from the spectroscopic signal.

A handheld Raman instrument with Off-Axis Raman Scattering (OARS) can easily see into chemical containers to eliminate wasteful, time consuming sampling inside the container. This can be particularly useful to eliminate the handling of hazardous materials.

The technique permits us to completely resolve the container material from the contents. Identification or verification can

be performed without ever opening the container.

Figure 2 illustrates a handheld OARS system with a typical white plastic chemical bottle and a fairly weak Raman scatterer, citric acid. The OARS technique permits us to completely resolve the container material from the contents. Identification or verification can be performed without ever opening the container.

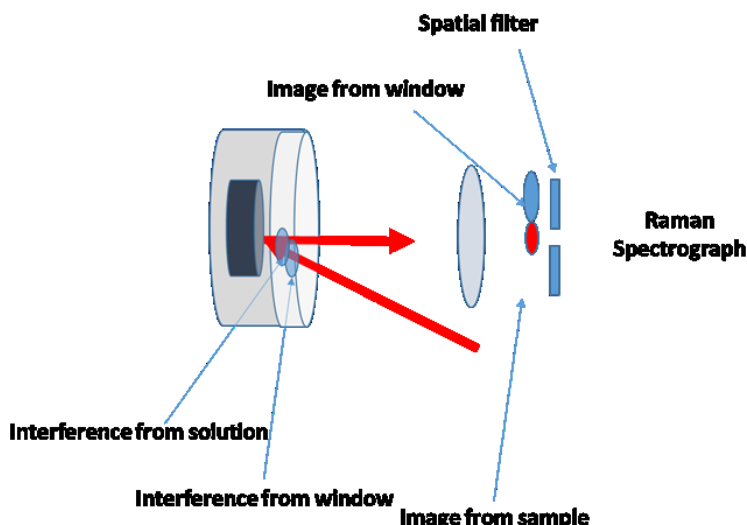


Figure 1 Illustration of angular offsets to spatial filter interferences of material before the sample.

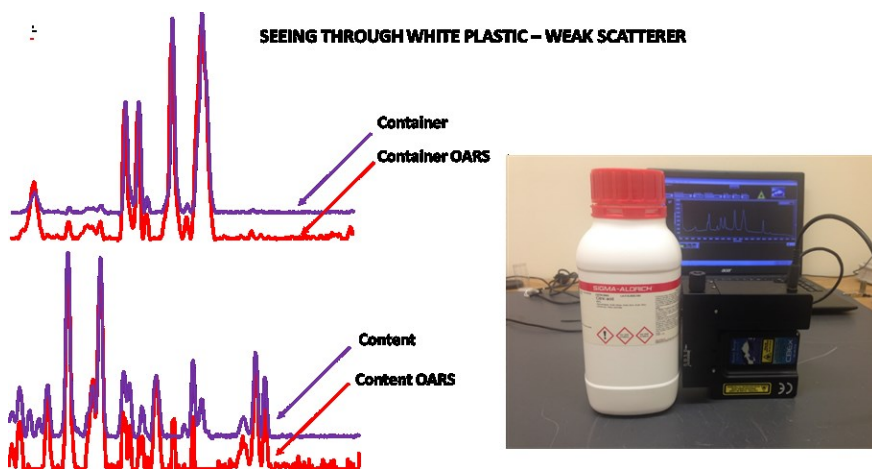


Figure 2 Examples of the OARS method to examine material inside optical dense containers. Top) violet is the Raman spectrum of the container material; red is the spectrum extracted with the OARS method. Bottom) violet is a Raman spectrum of the pure material (citric acid) and red is the spectrum of citric acid extract through the container with the OARS method.

¹Carron, K., Surface enhanced resonance Raman, resonance hyper-Raman, and hyper-Raman spectroscopy of molecules adsorbed to thin metal films, (1985) Dissertation, p. 151

BRAVO – Advances in handheld Raman spectroscopy

Felix Fromm and Armin Gembus

Bruker Optik GmbH, 76275 Ettlingen, Germany

Keywords: Raman, handheld, fluorescence, raw material, pharmaceutical

Raman spectroscopy has evolved to an important method for raw material verification. In recent years handheld devices reached the pharmaceutical industry trying to offer a fast and reliable method for warranting the quality control and assurance of incoming goods as well as throughout the whole manufacturing process. Here Raman spectroscopy is advantageous towards other analytical techniques because of its capabilities to probe a large quantity of substances in any state through packaging material, e.g. plastic or paper bags and glass. A Raman spectrum can be considered as a molecular fingerprint of a material which is stored on-board in a spectroscopic library. Therefore, the intend of a handheld instrument is to offer on-site verification of incoming raw materials, fast sampling of key manufacturing steps and finished product inspection within seconds, to be able to shape a modern and efficient production process.

Despite this strong points Raman spectroscopy for material verification using handheld systems has its device-specific limitations. In many cases the generation of reliable results is prevented by fluorescence which can vary from batch to batch. This causes problems matching results to the spectra stored in the library or the fluorescence even prevents the detection of the specific Raman fingerprint. Fluorescence can be addressed using a long wavelength for excitation (e.g. $\lambda = 1064$ nm) with a drawback in sensitivity because of the $1/\lambda^4$ dependence of the Raman intensity. This

lack in performance can be compensated using high laser output powers causing issues regarding the operators safety and which enhance the risk of alteration of the probed material, e.g. damaging through heat or even burning of the sample.

The new Bruker handheld Raman spectrometer BRAVO¹ addresses both issues fluorescence and sensitivity constituting new possibilities for handheld Raman spectroscopy. The patented fluorescence mitigation Sequentially Shifted Excitation^{2,3} (SSETM) uses temperature tuned diode lasers to acquire Raman spectra at sequentially shifted excitation energies. Subsequently, Raman signals which exhibit spectral shifts according to the changes in excitation energy are separated from signals constant in spectral space, e.g. arising from fluorescence. This allows on-device the generation of fluorescence free Raman spectra which form the basis of an unambiguous verification of the broadest range of materials.

To be able to detect Raman signals in a large range of wavenumbers from 300 cm^{-1} to 3200 cm^{-1} at the highest sensitivity BRAVO uses Duo LASERTM excitation³. Here two lasers of different excitation energy are employed to detect the Raman signals in smaller spectral range. As a further consequence, BRAVO accomplishes measurements with a low laser output power and is certificated as a class 1M laser product, even in the so-called point and shoot operation with an open beam.

This work stresses the performance of Brukers Handheld Raman spectrometer BRAVO, e.g. by comparing results to the spectra measured at state of the art benchtop systems. For example Fig. 1 compares two Raman spectra of 4-acetaminophenol measured with an FT-Raman spectrometer at 8 cm^{-1} resolution and BRAVO.

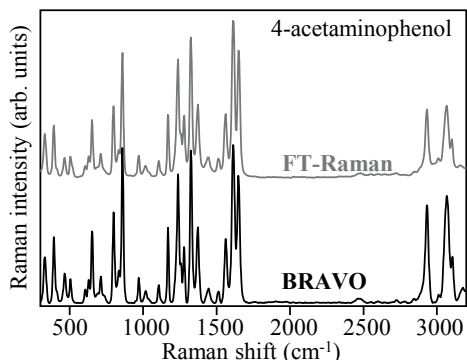


Figure 1. Raman spectra of 4-acetaminophenol measured with a benchtop FT-Raman system (top) and the handheld spectrometer BRAVO (bottom).

The exceptional quality of the Raman spectrum generated by BRAVO with a high signal to noise ratio at an integration time below 5 s is obvious. Furthermore, it is shown that BRAVO accesses the CH-stretching vibrations above 2800 cm^{-1} which is next to the high sensitivity the benefit of the Duo LASER™ excitation.

¹ www.bruker.com/bravo.

² Cooper J.B., Abdelkader M., Wise K.L. 984 (2013), *Applied Spectroscopy*, 67 (8), 973–984.

³ Cooper J.B., Marshall S., Jones R., Abdelkader M., Wise K.L. (2014), *Applied Optics*, 53 (15), 3333–3340.

In Fig. 2 the efficient working SSE™ technology is demonstrated with Raman measurements of talc, a material showing relatively weak Raman signals which are overlapped by an intense fluorescence. Using a dispersive Raman microscope at 785 nm excitation the strong fluorescence is obvious, whereas BRAVO generates a spectrum completely free of fluorescence with well resolved signatures of talc up to 700 cm^{-1} .

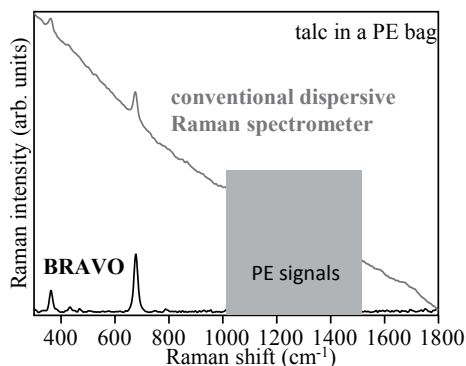


Figure 2. Raman spectra of talc measured through a PE bag using a dispersive benchtop system (top) and BRAVO (bottom). Note, that the signature at higher wavenumbers results from the PE packaging material.



Vibrational Spectroscopy of Southern Ocean Phytoplankton: a new tool for understanding drivers of primary productivity.

Olivia Sackett^{1,2}, Katherina Petrou³, John Beardall², Philip Heraud^{1,2}

¹Centre for Biopetroscopy, Monash University, Clayton, 3800, Australia

²School of Biological Sciences, Monash University, Clayton, 3800, Australia

³Plant Functional Biology and Climate Change Cluster, University of Technology Sydney, Broadway, 2007, Australia

Keywords: Primary Productivity, Phytoplankton, Southern Ocean

Each year, marine phytoplankton (unicellular microalgae) convert ~50 Tg of inorganic carbon into the building blocks of life - proteins, lipids and carbohydrates, which comprise ~95% of organic matter. This massive quantity of organic carbon, which is approximately equal in magnitude to carbon assimilation by all the terrestrial rainforests on earth, provides nutrition and energy to marine food webs and is known as primary production. As well as supporting marine fisheries worth an estimated 75 billion US\$ annually, primary production is an important component of the global carbon cycle. Hence, substantial scientific effort is devoted to its measurement. At present estimations of oceanic primary productivity are quite crude limited to biomass determination using a combination of satellite chlorophyll fluorescence imaging and ground based turbidity measurements. These current measurements lack definition in terms of quantifying species composition within the phytoplankton blooms nor do they define the physiological status of the different species and how this is affecting carbon uptake and partitioning of carbon within cells. Infrared spectroscopy is a powerful new tool in this area of research having potential for both species identification (see Figure 1) and characterisation of physiological responses of living phytoplankton to the environment

in terms of carbon partitioning at the single cell level [1].

Iron limitation is known to affect the primary productivity of phytoplankton in the otherwise nutrient rich Southern Ocean [2]. Enhanced supply of nutrient-rich waters along the coast of the subantarctic Kerguelen Island provided a valuable opportunity to examine the responses of phytoplankton to natural Fe enrichment. Synchrotron radiation Fourier Transform Infrared (SR-FTIR) microspectroscopy was used to analyse changes in the macromolecular composition of diatoms collected along the coast and plateau of Kerguelen Island. SR-FTIR microspectroscopy enabled the analysis of individual diatom cells from mixed communities of field-collected samples, thereby providing insight into in situ taxon specific responses in relation to changes in Fe availability. Phenotypic responses were taxon-specific in terms of intraspecific variability and changes in proteins, amino acids, phosphorylated molecules, silicate and carbohydrates. The highly abundant taxon *Fragilariopsis kerguelensis* displayed a higher level of phenotypic plasticity than *Pseudo-nitzschia* spp., while analysis of the data pooled across all measured taxa showed different patterns in macromolecular composition compared to those for individual taxon.

This study demonstrates that taxon-specific responses to Fe enrichment may not always be accurately reflected by bulk community measurements, highlighting the

utility of the spectroscopic measurements compared with traditional analytical approaches.

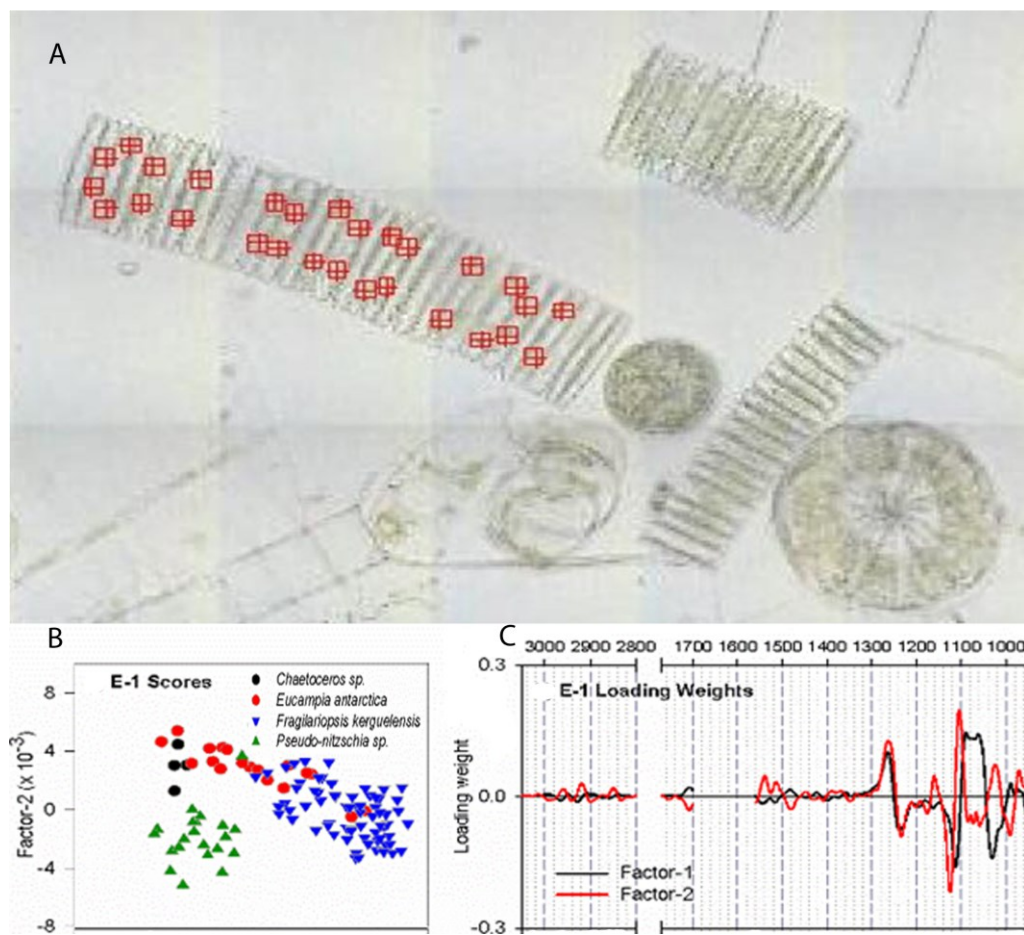


Figure 1. A. Phytoplankton sampled from the Southern Ocean targeted by synchrotron IR microspectroscopy ($5 \times 5 \mu\text{m}$ aperture). B. PLSDA scores plot showing species discrimination at the single cell level. C. Loadings plot explaining the clustering of the scores plot in (B) related mainly to differences in silica, carbohydrate and protein (units are cm^{-1}).

- ¹ Sackett O, Petrou K., Reedy B., De Grazia A., Hill R., Doblin M., Beardall J., Ralph P., Heraud P. (2013), *Plos One*, 8(11), 1-12.
- ² Sackett O., Armand L., Beardall J., Hill R., Doblin M., Connelly C., Howes J., Stuart B., Ralph P., Heraud P. (2014), *Biogeosciences*, 11, 5795-5808.

Infrared extinction spectra of polar stratospheric cloud constituents: Variation of particle phase and shape with formation conditions

Robert Wagner¹, Martin Ebert², Sandy James³, Ottmar Möhler¹, Martin Schnaiter¹, Ralf Weigel⁴

¹Karlsruhe Institute of Technology, Institute for Meteorology and Climate Research, Germany

²Institut für angewandte Geowissenschaften, Technische Universität Darmstadt, Germany

³School of Chemistry, University of Leeds, UK

⁴Institute for Physics of the Atmosphere, Johannes Gutenberg-University, Mainz, Germany

Keywords: Polar stratospheric clouds, NAD, NAT, infrared extinction, AIDA.

The formation pathways and compositions of solid HNO₃-containing cloud particles in the polar stratosphere are still controversially debated.^{1,2} Several field observations suggest that such Polar Stratospheric Cloud (PSC) particles are composed of the thermodynamically stable Nitric Acid Trihydrate (NAT),^{3,4} but it stays elusive whether NAT directly nucleates in liquid ternary H₂SO₄/HNO₃/H₂O solution droplets, or whether formation of metastable compositions like Nitric Acid Dihydrate (NAD) can occur at intermediate evolution stages. The nucleation of NAD or NAT might proceed homogeneously or involve the surface of solid particles, presumably of meteoritic origin, in a heterogeneous immersion freezing mechanism.¹ Detailed knowledge about the shape and morphology of the nucleated particles is essential for an accurate estimate of sedimentation speed and denitrification efficiency.⁵

In this work, we have investigated the homogeneous and heterogeneous nucleation of solid NAX (e.g. NAD or NAT) species from supercooled aqueous HNO₃/H₂O solution droplets with experiments conducted in the low-temperature aerosol chamber facility AIDA (Aerosol Interactions and Dynamics in the Atmosphere) of the Karlsruhe Institute of Technology. In the case of the heterogeneous nucleation

experiments, the injected aqueous HNO₃/H₂O solution droplets contained a solid nucleus of meteoritic ablation analogue or mineral dust. Nucleation of solid NAX species was then monitored at $T < 195$ K over time scales of up to 6 hours.

Infrared extinction spectroscopy was used to infer the chemical identity of the nucleated particles. Both NAD and NAT have two modifications, denoted α -/ β -NAD and α -/ β -NAT, which feature characteristic spectroscopic signatures in the mid-infrared region.⁶ T-matrix calculations were performed to investigate the effect of particle asphericity on the recorded infrared extinction spectra.⁷ Information about particle shape was independently retrieved from the analysis of the two-dimensional scattering patterns of the nucleated NAX particles, which were recorded with the latest version of the Small Ice Detector instrument (SID-3) developed at the University of Hertfordshire.

On the time scale of our nucleation experiments, we found no indication for the formation of NAT. Instead, exclusively the nucleation of the metastable NAD phase was detected. In the homogeneous nucleation experiments, α -NAD particles of needle-like shape were formed. β -NAD particles were the result of the heterogeneous immersion freezing experiments where the NAX

crystallization rate was significantly enhanced. The β -NAD crystals featured a comparably compact particle shape. In future studies, we will investigate if and how

the nucleation products change when H_2SO_4 is added to the $\text{HNO}_3/\text{H}_2\text{O}$ solution droplets.

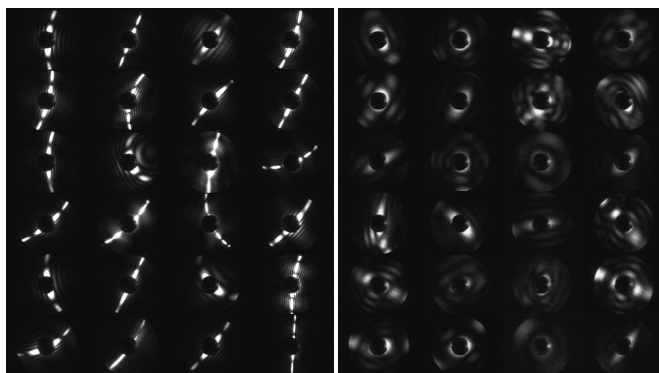


Figure 1. Two-dimensional scattering patterns recorded with SID-3 of homogeneously formed needle-like α -NAD particles (left) and more compactly shaped, heterogeneously nucleated β -NAD crystals (right).

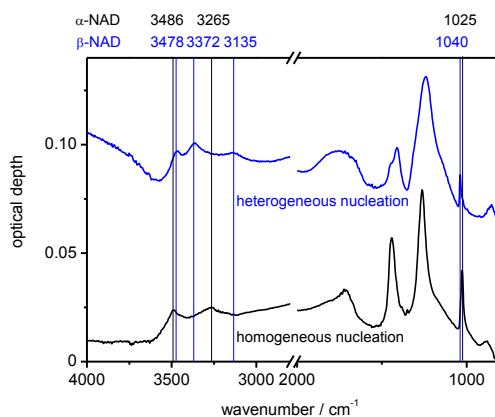


Figure 2. Infrared extinction spectra of α -NAD (black) and β -NAD (blue) particles from the homogeneous and heterogeneous nucleation experiments, respectively.

- Hoyle, C. R., I. Engel, B. P. Luo, M. C. Pitts, L. R. Poole, J. U. Groß, and T. Peter (2013), *Atmos. Chem. Phys.*, 13(18), 9577-9595.
- Grothe, H., H. Tizek, and I. K. Ortega (2008), *Faraday Discuss.*, 137, 223-234.
- Voigt, C., et al. (2000), *Science*, 290(5497), 1756-1758.
- Höpfner, M., et al. (2006), *Atmos. Chem. Phys.*, 6, 1201-1219.
- Woiwode, W., et al. (2014), *Atmos. Chem. Phys.*, 14(20), 11525-11544.
- Grothe, H., C. E. L. Myhre, and H. Tizek (2004), *Vib. Spectrosc.*, 34(1), 55-62.
- Wagner, R., O. Möhler, H. Saathoff, O. Stetzer, and U. Schurath (2005), *J. Phys. Chem. A*, 109, 2572-2581.

Studies on the photolysis of iodate salts

Oscar Gálvez¹ and Alfonso Saiz-Lopez²

¹ Departamento de Física Molecular, Institute for the Structure of Matter, IEM-CSIC, 28006 Madrid, Spain

² Atmospheric Chemistry and Climate Group, Institute of Physical Chemistry Rocasolano, CSIC, 28006 Madrid, Spain

Keywords: infrared spectroscopy, iodine chemistry, ice.

Atmospheric iodine compounds are ubiquitous in the marine and polar boundary layers¹ in which it plays a relevant role in ozone catalytic destruction² and new particle formation³. Different studies have shown that iodine concentrations in rainwater and aerosol are considerable enriched over seawater, and an appreciable fraction of iodine species are in IO₃⁻ form¹. A recent study suggests that iodate shows a substantial reactivity in frozen solutions under near-UV/visible light irradiation⁴. In this study, the irradiation of IO₃⁻ solutions form reactive gas-phase iodine species.

To study this effect, frozen samples containing iodate anions were produced through the sudden freezing of droplets of aqueous solutions of NH₄IO₃ on a cold Si substrate located inside a vacuum chamber. Solar irradiance was simulated by a Xenon Arc lamp which radiate between 350 nm to 2.5 μm, although an important fraction of the output is given below 900 nm. The vacuum chamber is coupled to FTIR spectrometer through a purged pathway, which allows motorize the evolution of the samples under irradiation.

The samples were irradiated from 100 K up to room temperature. A common behavior is observed for all samples, NH₄⁺ and IO₃⁻ bands diminish during irradiation process, which is especially evident when 1430 and 740 cm⁻¹ bands are monitored (see Fig. 1).

The calculated J value for the photolysis of iodate is $J = (4 \pm 2) \cdot 10^{-5} \text{ s}^{-1}$. Significant differences on the J values have not been observed along the samples at different temperatures (from 100 to 298 K) or in presence of water. We have also estimated the photon flux impacting on the samples values, and assuming a constant quantum yield (valor of unity), the integrated absorption cross section is calculated, yielding a value of $1.0 \cdot 10^{-20} \text{ cm}^2 \text{ nm molec}^{-1}$.

These results are of interest in iodine atmospheric chemistry, in which photolysis of iodate in frozen salt could be an impact in the budget of reactive iodine specie in the atmosphere

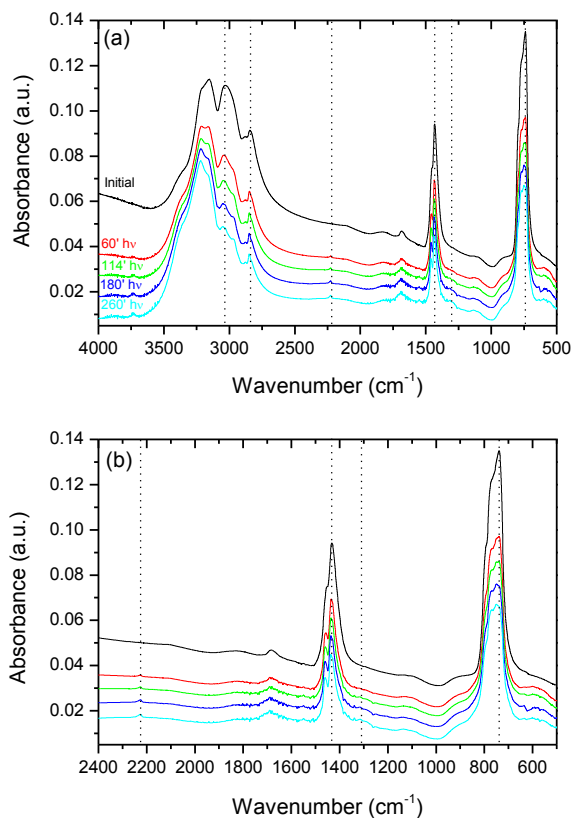


Figure 1. Evolution of the transmission mid-IR spectra of pure NH_4IO_3 at 100 K during photolysis.

¹ Saiz-Lopez A., Plane J. M. C., Baker A., Carpenter L., von Glasow R., Gómez Martín J. C., McFiggans G and Saunders R. (2012), *Chem. Rev.*, 112, 1773–1804.

² Read K. A., Mahajan A. S., Carpenter L. J., Evans M. J., Faria B. V. E., Heard D. E., Hopkins J. R., Lee J. D., Moller S. J., Lewis A. C., Mendes L., McQuaid J. B., Oetjen H., Saiz-Lopez A., Pilling M. J. and Plane J. M. C. (2008), *Nature*, 453, 1232–1235.

³ O'Dowd C. D., Jimenez J. L., Bahreini R., Flagan R. C., Seinfeld J. H., Hameri K., Pirjola L., Kulmala M., Jennings S. G. and Hoffmann T. (2002), *Nature*, 417, 632–636.

⁴ Spolaor A., Vallelonga P., Plane J. M. C., Kehrwald N., Gabrieli J., Varin C., Turetta C., Cozzi G., Kumar R., Boutron C., and Barbante C. (2013). *Atmos. Chem. Phys.*, 13, 6623–6635.

Raman spectroscopic techniques for planetary exploration: detecting microorganisms through minerals

Mattheus F.C. Verkaaik¹, Jan-Hein Hooijschuur^{1,2}, Gareth R. Davies² and Freek Arie^{1*}

¹LaserLaB, VU University, 1081 HV Amsterdam, The Netherlands

²Deep Earth and Planetary Science, VU University, 1081 HV Amsterdam, The Netherlands

Keywords: Time-Resolved Raman Spectroscopy; Resonance Raman; Depth selectivity; Extremophile bacteria;

Raman spectroscopy can provide highly specific chemical fingerprints of inorganic and organic materials, and is therefore expected to play a significant role in interplanetary missions, especially for the search of life elsewhere in our Solar System^{1,2}. A major challenge will be the unambiguous detection of low levels of biomarkers on a mineral background. In addition, these biomarkers may not be present at the surface (for instance due to high levels of UV and cosmic radiation) but rather inside or underneath minerals. Strong scattering will prevent focusing deeper into the sample.

Here we report the detection of carotenoid-containing microorganisms behind mineral layers using time resolved Raman spectroscopy (TRRS)³. Two extremophiles, the bacterium *Deinococcus radiodurans* and the cyanobacterium *Chroococcidiopsis* were detected through translucent and transparent minerals using 440-nm excitation under resonance conditions to selectively enhance the detection of carotenoids⁴. In a TRRS experiment a backscattering geometry is applied; Raman signals from the surface will reach the detector sooner than Raman signals generated deeper inside the sample. The 3-picosecond (ps) laser pulses and 250-ps gated intensified CCD camera provide depth selectivity for the subsurface

microorganisms over the mineral surface layer, and in addition lower the contribution of the fluorescent background, which has typically a much longer lifetime.

Following optimization of the TRRS setup, Raman spectra of both organisms could be detected through 5 mm of translucent calcite or 20 mm of transparent halite. Multi-layered mineral samples were used to further test the applied method. A separate tuneable laser setup for resonance Raman and a commercial confocal Raman microscope, both with continuous (non-gated) detection, were used for comparison. For these setups it was important to defocus the objective used for excitation and collection, in order to reduce the relative contribution from the surface layer⁵. The intensity of the subsurface layer is much less sensitive to focusing. Nevertheless, without time-resolved detection the fluorescence background was much stronger, and detection of bacteria was only possible through thinner layers of minerals.

This study demonstrates the capabilities of time-resolved Raman spectroscopy for the depth-selective analysis through scattering samples, which could be used in future planetary exploration to detect microorganisms or biomarkers within or behind minerals. Implications for the design of future space instrumentation will be discussed.

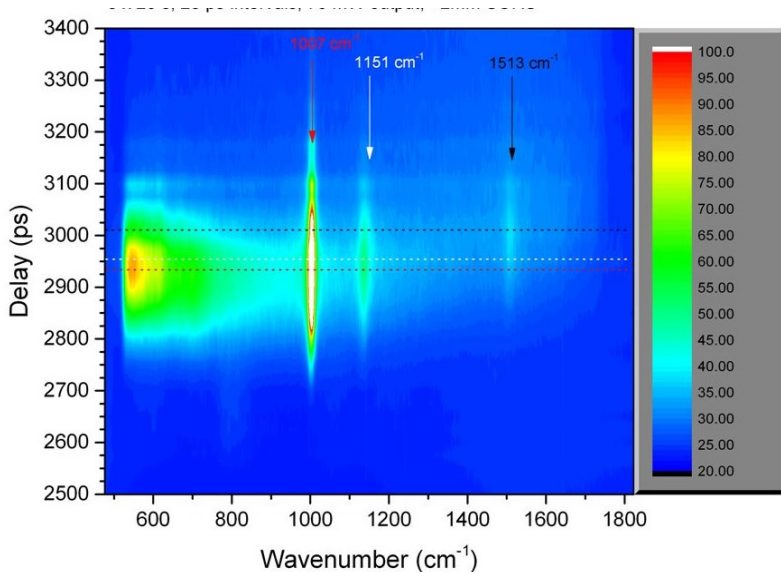


Figure 1. Time-resolved Raman Spectroscopy: contour plot of Raman spectra recorded at increasing delays of the bacterium *Deinococcus radiodurans* behind 11 mm of gypsum. The peak at 1513 cm⁻¹ is specific for the carotenoids that are abundant in this species; its signals are detected at longer delays than that of the mineral.

- ¹Wang, A., Jolliff, B. L. & Haskin, L. A., (1995) Raman spectroscopy as a method for mineral identification on lunar robotic exploration missions. *J. Geophys. Res.* 100, 21189-21199.
- ²Edwards H.G., (2010) Raman spectroscopic approach to analytical astrobiology: the detection of key geological and biomolecular markers in the search for life. *Phil. Trans. R. Soc. A* 368, 3059-3065.
- ³Hooijschuur, J. H., Iping Petterson, I. E., Davies, G. R., Gooijer, C. & Ariese, F., (2013) Time resolved Raman spectroscopy for depth analysis of multi-layered mineral samples. *J. Raman Spectrosc.* 44, 1540-1547.
- ⁴Jehlicka, J., Edwards, H. G., Osterrothova, K., Novotna, J., Nedbalova, L., Kopecky, J., Nemecek, I. & Oren, A., (2014) Potential and limits of Raman spectroscopy for carotenoid detection in microorganisms: implications for astrobiology. *Phil. Trans. R. Soc. A* 372, 1-17.
- ⁵Eliasson, C., Claybourn, M. & Matousek, P., (2007) Deep Subsurface Raman Spectroscopy of Turbid Media by a Defocused Collection System. *Appl. Spectrosc.* 61, 1123-1127.

Noble metal nanoparticles in seawater: nano risk towards aquatic organisms assessed by SERS

Simona Cinta Pinzaru^{1,2}, Csilla Müller¹, Sanja Tomšić², Ivana Ujević³, Ana Bratoš Cetinić², Bogdan I. Cozar⁴, Rares Stiufluic⁵, Monica M. Venter⁶, Branko Glamuzina²

¹Department of Biomolecular Physics, Babes-Bolyai University, Kogalniceanu 1, 400084, Cluj Napoca, Romania

²Department of Aquaculture, University of Dubrovnik, Ćira Carića 4, 20000 Dubrovnik, Croatia

³Laboratory of plankton and shellfish toxicity, Institute of Oceanography and Fisheries, PO Box 500, 21000 Split, Croatia

⁴National Institute for Research and Development of Isotopic and Molecular Technologies, 67-103 Donat, PO Box 700, 400293 Cluj-Napoca, Romania

⁵Department of Biophysics, "Iuliu Hatieganu" University of Medicine and Pharmacy, Louis Pasteur 4, 400349 Cluj-Napoca, Romania

⁶Department of Chemistry, Babes-Bolyasi University, Faculty of Chemistry and Chemical Engineering, Arany Janos 11, 400028, Cluj-Napoca, Romania

Keywords: oligotrophic seawater, SERS, AFM, diatoms, nanoparticles.

Oligotrophic seawater has been assessed concerning the SERS response in the presence of noble metal nanoparticles prepared by various methods. Unicellular photosynthetic microscopic organisms that inhabit the surface waters of almost all oceans sustaining the aquatic food web and accounting for half of the planetary photosynthetic activity as primary producers of organic compounds, revealed an unexpected primary SERS response consistent with that of pure beta-carotene at sub-micromole concentrations. We recently demonstrated that the beta-carotene exhibits a completely different SERS spectral signature on the generally known C=C, C-C and C-CH₃ vibrational modes of the polyene chain when adsorbed on the AgNPs at sub-micromole concentrations in non-resonant conditions¹. Unexpected similarity of beta-carotene SERS signal with that of natural seawater was observed in a 6 months monitoring experiment for water samples

collected from 10 different locations on the South Eastern Adriatic Coast of Croatia. To understand its origin, a series of additional SERS experiments were conducted using both natural and filtered seawater. A closer look at several phytoplankton and zooplankton species in the presence of NPs in their natural environment revealed remarkable similarities concerning their primary SERS response. Diatoms, dinoflagellates, chlorophyta cells, cyanobacteria and their vesicles they constantly release² were individually assessed concerning SERS. Drop coating deposition samples on a hydrophobic stainless steel teflon coated Spectrim plate³ were measured and compared to the SERS results in liquid state in conjunction with scanning probe microscopy analyses. Dominant carotene signal (Fig. 1) with the influence of the chlorophyll a SERS response suggested a strong interaction of the AgNPs with the live plankton bodies,

diatoms and cyanobacteria. Since beta-carotene and chlorophylls are not aqueous soluble, being located in the lipid bodies and chloroplasts respectively inside the cells, the results suggest rather a cell protective response at the cell wall membrane level,

releasing carotene than nanoparticles incubation or ingestion. Incubation was excluded since the signal was promptly recorded in seconds after nanoparticles adding. Several similar examples from various species will be discussed.

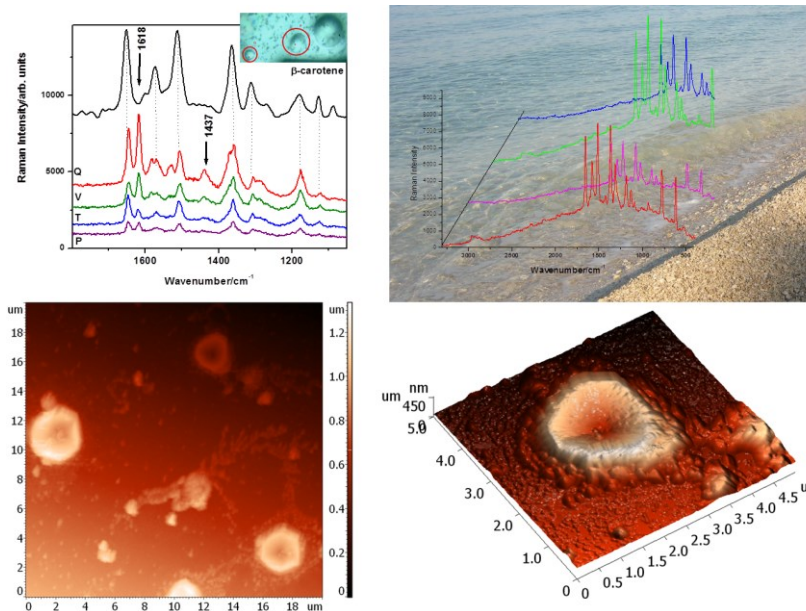


Figure 1. SERS spectra collected from the drop coating deposition of seawater with AgNPs on a Spectrim plate and AFM images of the sample revealing the diatoms and cyanobacteria surrounded by the nanoparticles (bottom). A graphical sketch in the upper right corner shows the raw SERS signal of seawater.

Acknowledgments. This study was supported from NEWFELPRO Grant Nr. 5/2014 project of the Government of the Republic of Croatia and the Ministry of Science, Education and Sport (MSES) co-financed through the Marie Curie FP7-PEOPLE-2011-COFUND. Cs. Muller acknowledges the financial support from POSDRU/159/1.5/S/132400.

- ¹ S. Cintă Pinzaru S., Müller Cs., Tomsic S., Venter M. M., Cozar B. I., Glamuzina B., (2015), *Journal of Raman Spectroscopy* . Doi: 10.1002/jrs.4713.
- ² Biller S. J., Schubotz F., Roggensack S. E., Thompson A. W., Summons R. E., Chisholm S. V. (2014), *Science*, 343 (6167), 183-186.
- ³ Cinta Pinzaru S, Peica N., Schmidt U., Kiefer W., (2007) *Journal of Optoelectronics and Advanced Materials*, 9(3), 768-771.

**New generation Raman imaging:
Confocal 3D Raman imaging meets highest spectral resolution**

Thomas Dieing, Ute Schmidt, Wolfram Ibach, and Olaf Hollricher

WITec GmbH, Lise-Meitner Str. 6, 89081 Ulm, Germany (www.witec.de)

Keywords: Raman imaging, spectral resolution.

In the past decade confocal Raman imaging gained in importance in the characterization of heterogeneous materials and is applied in almost all fields of research. In polymer science phase separation processes, polymorphism, chemical and structural composition, can be visualized (1-3). In pharmaceuticals the identification and distribution of the ingredients in tablets, lotions, powders, and medical devices plays a key factor for the development of new products (4-8). In life science imaging of cells and tissues on a molecular level is possible, without specified labeling or staining, thus allowing identification of sub-cellular components or follow processes such as drug uptake (9, 10). A lot of the above listed research areas require fast Raman imaging capabilities at highest possible lateral and spectral resolution. Until recently, the acquisition of highest lateral resolution images over large surface areas was limited by the computer memory. In addition to this, for high spectral resolution only long focal length spectrographs with comparably low light throughput were available resulting in long integration times and thus impractically long acquisition times for Raman images.

New developments in computer memory management and data acquisition routines facilitate the acquisition of hundreds of thousands Raman spectra in one data file. Fig. 1a shows a 3D Raman image of a carbon-tetrachloride - alkane - water emulsion. This image was acquired from a

sample volume of $100 \times 100 \times 10 \mu\text{m}^2$ by acquiring $200 \times 200 \times 20 = 800000$ complete Raman spectra with an integration time of 0.06 s per spectrum. These spectra were acquired with a 600 mm spectrometer equipped with a 300 g/mm grating. Modern Raman data evaluation routines allow a fast identification of the corresponding chemical or molecular species and their distribution in the analyzed sample volume. In this image green color corresponds to the alkane phase, blue to the water phase, and orange to the carbon tetrachloride and oil phase.

The high spectral resolution 2D Raman image (Fig. 1b) was acquired from a sample area of $10 \times 10 \mu\text{m}^2$ by acquiring 100x100 complete Raman spectra with an integration time of 0.08 s per spectrum. For this high resolution image the same 600 mm spectrometer was used in combination with an 1800 g/mm grating. The short integration time highlights the high throughput of the spectroscopic system. In this Raman image the distribution of carbon tetrachloride (yellow color) was imaged at room temperature. The triplet of Raman bands at 460 rel. 1/cm, characteristic for CCl_4 , could be clearly resolved (Fig. 1c).

The aim of this contribution is to present the newest achievements in confocal Raman imaging microscopy. The highlights will be cosigned with examples from various fields of applications.

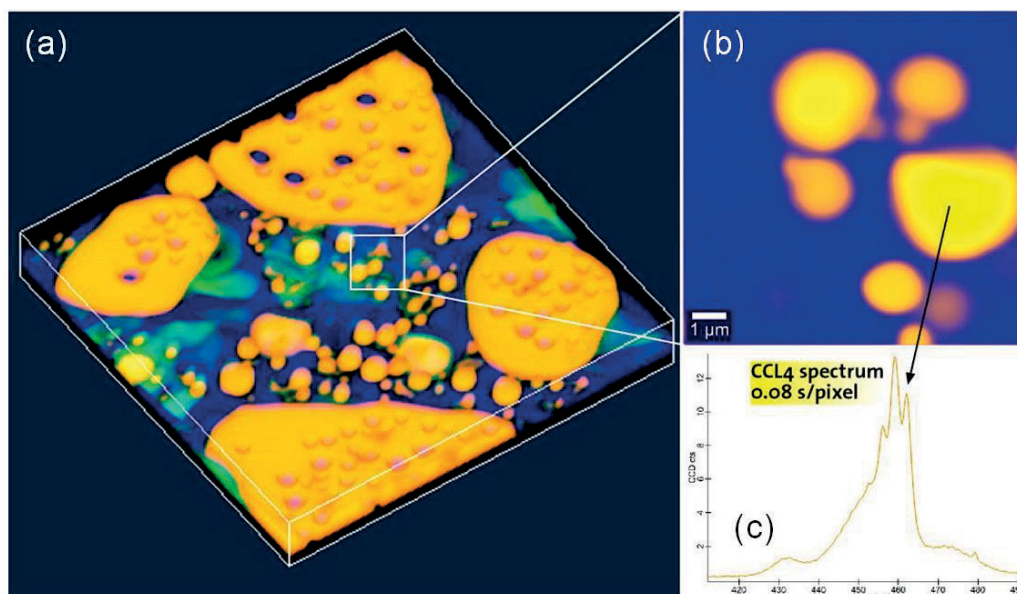


Figure 1. Confocal Raman imaging study of an emulsion consisting of carbon tetrachloride (orange), alkane (green) and water (blue): 3D Raman image (a), zoom in Raman image with high spectral resolution (b), and high spectral resolution Raman spectrum of carbon tetrachloride acquired at room temperature (c).

1. J. Zhang *et al.*, *Industrial & Engineering Chemistry Research* **52**, 8616-8621 (2013).
2. J. Yang, R. Sekine, H. Aoki, S. Ito, *Macromolecules* **40**, 7573-7580 (2007).
3. U. Schmidt, S. Hild, W. Ibach, O. Hollricher, *Macromolecular Symposia* **230**, 133-143 (2005).
4. D. Lunter, R. Daniels, *Journal of biomedical optics* **19**, 126015 (2014).
5. B. Kann, B. J. Teubl, E. Roblegg, M. Windbergs, *Analyst* **139**, 5069-5074 (2014).
6. P. D. A. Pudney *et al.*, *Applied spectroscopy* **67**, (2013).
7. B. Mostaghaci, B. Loretz, R. Haberkorn, G. Kickelbick, C.-M. Lehr, *Chemistry of Materials* **25**, 3667-3674 (2013).
8. C. Matthaus *et al.*, *Chemphyschem* **14**, 155-161 (2013).
9. K. Czamara, J. Natarska, P. Kapusta, M. Baranska, A. Kaczor, *Analyst*, (2015).
10. C. Grosse *et al.*, *Anal Chem*, (2015).

Fast, quantitative analysis of large volume bulk mixtures using transmission Raman Spectroscopy.

Pippa Law, Tim Smith, David Reece

Renishaw plc

Old Town, GL12 7DW, Gloucestershire. UK

Key words: Transmission, Raman, Mapping, Pharmaceutical, Multivariate.

In this work transmission Raman spectroscopy (TRS) was used to map large volumes, tens of centimetres cubed, of powder blends. This novel technique enables content uniformity to be statistically analysed using multivariate techniques. It was found that direct classical least squares is sufficient to quantify mixture uniformity. In doing this, it is possible to avoid complex partial least squares modelling to find pharmaceutical powder blend homogeneity.

Fast, quantitative analysis of bulk mixtures has become increasingly important in regulating pharmaceutical manufacturing processes. The analysis of statistically significant large volumes of mixtures is critical to ensure uniformity and relative amounts are accurately quantified and optimised. Achieving this provides less variation when, for example, formulations are subsequently manufactured. This potentially could reduce issues with regulatory dosage testing of batches, where amounts and distribution are not accurately known until final analysis. At this point

significant material write-off or damaging regulatory non-compliance could be avoided.

Raman spectroscopy is an attractive method for determining concentrations of these materials as it offers quick, non-destructive and highly selective quantification without the need for time consuming sample preparation. TRS presents significant benefits over the more conventional backscattering Raman Spectroscopy by providing an average through the entire sample, offering fast and effective analysis of content uniformity.

In this work we introduce a novel technique utilising TRS and Renishaw's high speed encoded stage to enable the analysis of bulk mixture volumes far larger than conventional single point TRS configurations (analysing tens of centimetres cubed). Raman transmission images demonstrate the sample volume that is measured, and the importance of being able to control sample state properties such as density and thickness. Figure 1 shows

how the compression of a caffeine powder alters the Raman spectra. Here it can be seen that by increasing the compression, the Raman intensity signal increases as expected because the more compressed the sample is the shorter the random walk is between scattering events.

Further, multivariate and chemometric analysis of the data reveals the ability to quantify mixture uniformity. Knowing the content uniformity at the mixing stage in the manufacturing process will reduce the cost of bad batches being discovered later down the line. Mapping statistically significant volume of blended material has many benefits of the traditional static TRS measurements especially when considering content uniformity of pharmaceutical tablets. Figure 2 shows direct classical least squares maps of the caffeine content in a caffeine and acetaminophen mix taken with transmission Raman. Initially in 2a) the powders are separate. Then the powders were stirred once and another transmission Raman map was taken, seen in 2b). This process was repeated down to 2f).

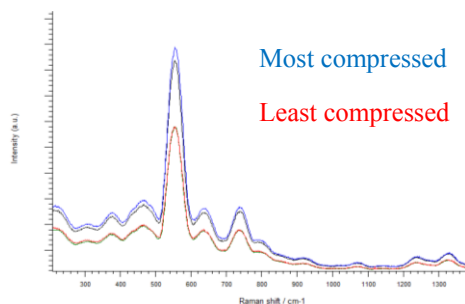


Figure 1. Transmission Raman spectra from a caffeine powder highlighting the change in spectral intensity with increase sample compression. Blue is most compressed and red is least compressed.

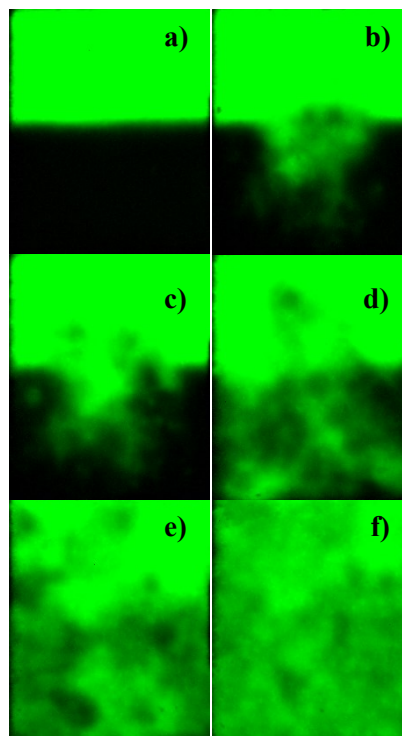


Figure 2. Multivariate DCLS analysis of transmission Raman maps showing caffeine content in an acetaminophen and caffeine mix. The level of mixing is increased from a) to f).

Structural Analysis of Conjugated Aromatic Compounds Using Low Frequency Raman Spectroscopy

James T. Carriere¹, Anjan Roy¹, Randy Heyler¹ and Peter Larkin²

¹Ondax, Inc., 850 E. Duarte Rd., Monrovia CA, 91016, USA

²Cytec Industries, 1937 W. Main St., Stamford CT, 06902, USA

Keywords: Low Frequency Raman, Low Wavenumber Raman, Structural Analysis, Lattice Vibrations, Phonon Modes.

Low frequency Raman spectroscopy is a particularly useful technique for exploring the structural properties of materials because the low energy vibrational transitions in this spectral region provide contributions from both selected molecular vibrations and crystal lattice vibrations. The crystal lattice vibrations involve movements of the entire molecule with respect to other molecules in the crystalline solid, thus providing a more direct probe of intermolecular interactions and structure. In particular, this region of the spectrum is quite sensitive to conformational changes of the molecule such as with different polymorphic forms of the same material or the effect of co-solvents/co-crystals¹.

To better understand the relationship between the physical structure of the material and these low vibrational energy modes, we present our observations of the corresponding spectral changes for a series of simple aromatic molecular species that vary systematically in their molecular form. We monitor the changes in the structural vibrational degrees of freedom of the organic molecular crystals as the complexity of the molecule increases. The polycyclic aromatic hydrocarbon family of materials containing compounds such as Naphthalene, Biphenyl, Anthracene etc. shown in Figure 1 were chosen as perfect candidates for this study because they are both well understood and modeled in the literature²⁻⁵.

While historically this low wavenumber region has been difficult to access, recent advances in volume holographic grating (VHG) based Rayleigh blocking filter technology have enabled simultaneous measurements to $\sim 5\text{cm}^{-1}$ from the laser line in both the Stokes and anti-Stokes spectra.

To measure these materials, a spectrometer with high spectral resolution ($\sim 1\text{cm}^{-1}$) was combined with several configurations of the Ondax SureBlock XLF family of low frequency Raman spectroscopy products that incorporate this VHG filter technology. The optimal excitation frequency was highly dependent upon the fluorescence properties of the samples. Figure 2 shows an example of the low wavenumber region of the spectrum for Naphthalene, Biphenyl and Anthracene to illustrate how these modes change with increasing molecular complexity. Other materials from the same family including Benz[a]anthracene, Pentacene, Perylene and Rubrene were also measured and analyzed.

The corresponding measured peak positions for each material were compared with the crystalline structure parameters of the organic molecular crystals and theoretical calculations from the literature. We differentiate the bands which derive from molecular vibrations and crystalline lattice vibrations and identify trends for these structurally related aromatic organic crystals.

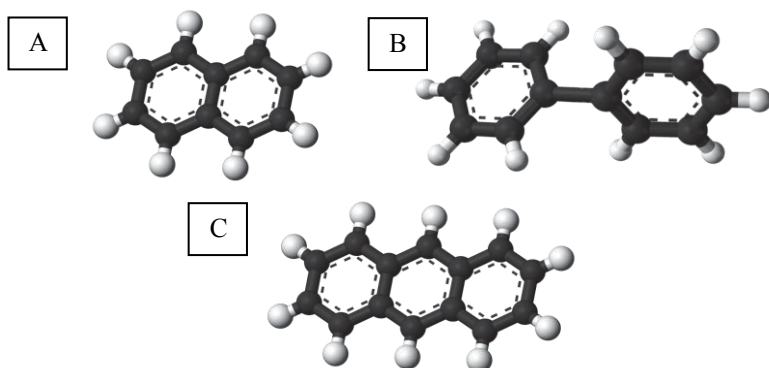


Figure 1. Molecular structure models of A) Naphthalene, B) Biphenyl and C) Anthracene showing the similarities between these compounds.

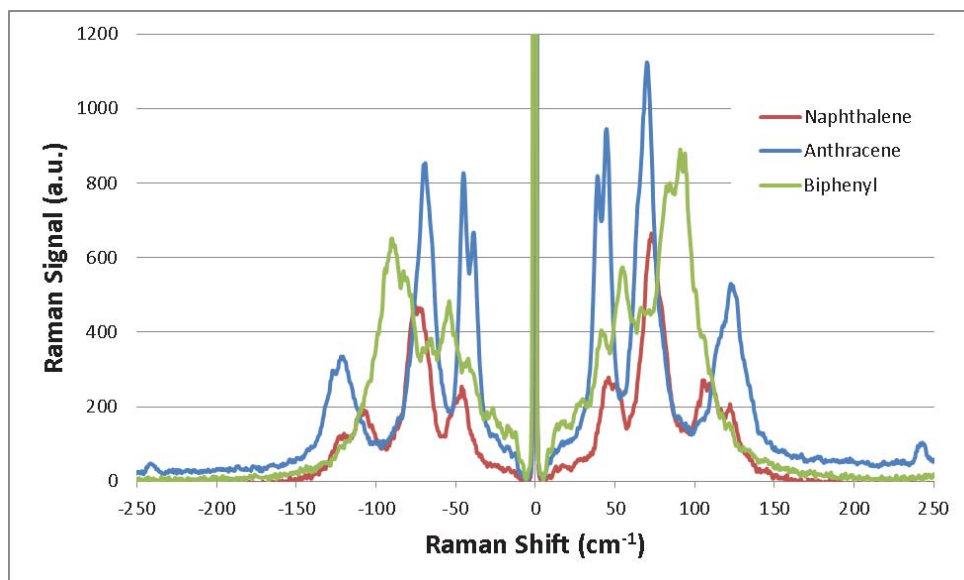


Figure 2. The low wavenumber region of the Raman spectrum is particularly sensitive to changes in the physical structure of the molecule.

- ¹ Larkin P.J., Dabros M., Sarsfield B., Chan E., Carriere J.T., Smith B.C. (2014), *Applied Spectroscopy*, 68 (7), 758-776.
- ² Schwoerer M., Wolf H.C. (2007), *Organic Molecular Solids. Ch. 5 Molecular and Lattice Dynamics in Organic Molecular Crystals*, Wiley-VCH Verlag GmbH & Co. 89-124.
- ³ Day G.M., Price S.L., Leslie M. (2003), *J. Phys. Chem. B*, 107 (39), 10919-10933.
- ⁴ Brillante A., Della Valle R.G., Farina L., Girlando A., Masino M., Venuti E., (2002), *Chem. Phys. Lett.*, 357 (1-2), 32-36.
- ⁵ Prasad P.N., Kopelman R. (1972), *The Journal of Chemical Physics*, 57 (2), 863-865.

New Electrically Gated Raman Technique for Fast Mineralogical Analyses

Lauri Kurki, Mari Tenhunen and Jyrki Savela
Timegate Instruments Oy, Teknologiantie 5B, 90590 Oulu, FINLAND

Keywords: timegated Raman, picosecond, mineral analyses.

Raw minerals' chemical and mineralogical compositions vary significantly. This is one of the main challenges for the optimized mining processes since the composition of the raw materials is very unpredictable. Currently, the exploration and mineral processing optimization is very much based on off-line, laboratory analyses of minerals' chemical and mineralogical composition. The available sampling-based methods require sample preparation, costly equipment and in some cases several steps of purification that prevent the delivery of results in real time in an industrial environment. Therefore, the cost and complexity, time and labour intensity involved in these laboratory analyses pose major barriers for mining companies to follow and control their processes, which often jeopardise the real time optimization of e.g. crushing, grinding and concentration processes.

So far, Raman spectroscopic techniques are not very widely used for mineralogical analysis because conventional Raman measurements often face the difficulty of fluorescence, which can cover totally the Raman signal.

Figure 1 shows the timegated Raman spectroscopic instrument composition and the basic principle of fluorescence rejection based on this technology. This new instrumentation is based on the use of highly specific, pulsed picosecond laser source and the fast read out detector solution. In the laser, the main drivers are short enough laser pulses with high enough energy to enable Raman scattering. The new SPAD (Single Photon Avalanche Diode) array has been used as a detector. This type of detector solution can be controlled in very short timeframes (in picoseconds class) to collect the data.

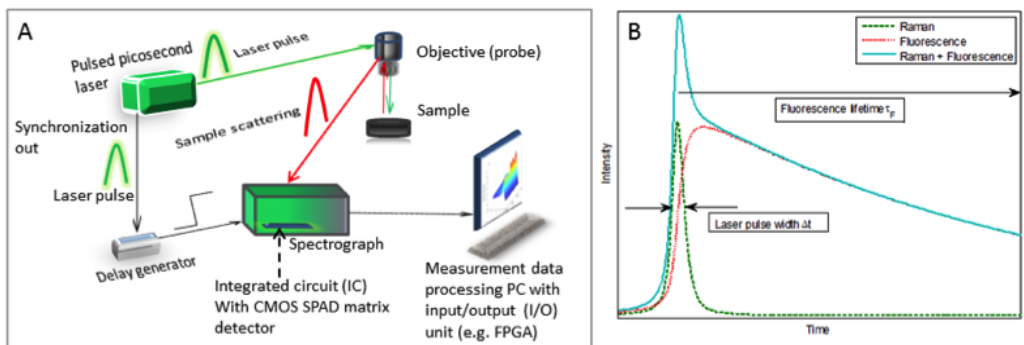


Figure 1 (A) Schematic description of timegated Raman spectrometer and (B) the fluorescence rejection principle.

The sample set contained several industrial samples with varying mineralogical compositions. The main minerals in the samples were apatite, calcite and biotite. All samples were measured using conventional (CW) Raman instruments with 532, 785 and 1064 nm excitation wavelengths, and the new timegated Raman spectrometer with 532nm pulsed laser excitation. Figure 2 shows conventional and timegated Raman spectra of industrial mineral sample.

To sum up, in this presentation, we show the power of new electrically gated Raman spectroscopic technique to catch the Raman signal before fluorescence (within a “timegate” of 100 picoseconds) so that the Raman signal can be differentiated perfectly from the fluorescence effect. This new Raman technique is therefore an ideal tool e.g. for the fast and robust mineralogical analysis of materials.

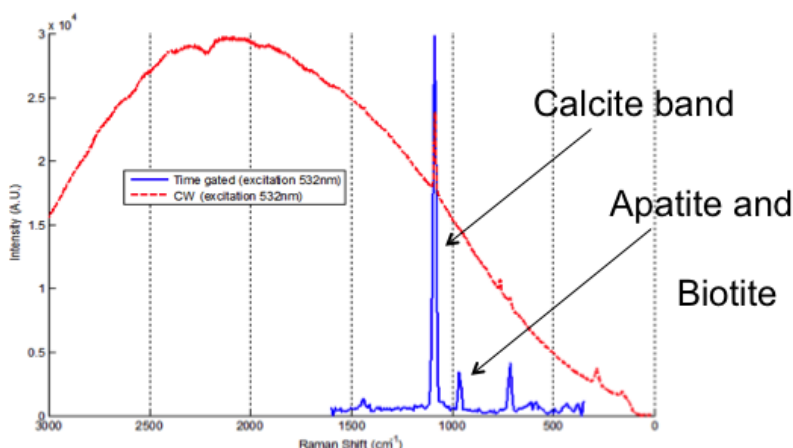


Figure 2 Conventional (red) and timegated (blue) Raman spectra of an industrial mineral sample.

Single-molecule Raman spectromicroscopy down to sub-nm resolution

Zhenchao Dong

Hefei National Laboratory for Physical Sciences at the Microscale and
Synergetic Innovation Center of Quantum Information & Quantum Physics,
University of Science and Technology of China (USTC), Hefei 230026, China

Keywords: Vibrational spectroscopy, tip-enhanced Raman spectroscopy, super-resolution imaging, single-molecule Raman scattering, plasmonics

Visualizing individual molecules with chemical recognition is a longstanding target in catalysis, bio-science, nanotechnology, and materials science. Molecular vibrations provide a valuable “fingerprint” for this identification. The vibrational spectroscopy based on tip-enhanced Raman scattering (TERS) has opened a path to obtain enhanced vibrational signals thanks to the strong localized plasmonic field at the tip apex. In this talk, I shall demonstrate single-molecule Raman spectroscopic imaging with unprecedented sub-nm spatial resolution (figure 1), resolving even the inner structure of a single molecule and its configuration on the surface¹. This is achieved by a delicate

plasmon enhanced nonlinear TERS technique that invokes a double-resonance process and resultant nonlinear optical effect, thanks to the exquisite tuning capability provided by low-temperature ultrahigh-vacuum scanning tunneling microscopy (STM)². I shall also show the powerful application of this technique for chemically distinguishing adjacent different molecules in real space and address the issue of how close and how similar these different molecules can be. These findings should open up new avenues for probing and controlling nanoscale structures, catalysis, photochemistry, and even DNA sequencing, all at the sub-nm and single-molecule scale.

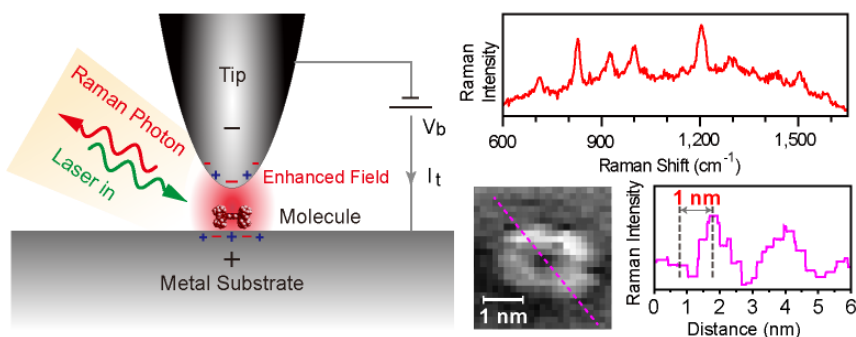


Figure 1. Single-molecule Raman imaging with sub-nm resolution by STM-controlled TERS

¹ R. Zhang, Y. Zhang, Z. C. Dong*, S. Jiang, C. Zhang, L. G. Chen, L. Zhang, Y. Liao, J. Aizpurua, Y. Luo, J. L. Yang, and J. G. Hou* (2013). *Nature* 498, 82-86.

² Z. C. Dong*, X. L. Zhang, H. Y. Gao, Y. Luo, C. Zhang, L. G. Chen, R. Zhang, X. Tao, Y. Zhang, J. L. Yang, J. G. Hou* (2010). *Nature Photonics* 4, 50-54.



Vibrational spectroscopy with laser frequency combs

Nathalie Picqué^{1,2}

1. Max-Planck-Institut für Quantenoptik, Hans-Kopfermannstr. 1, 85748 Garching, Germany
2. Ludwig-Maximilians-Universität München, Fakultät für Physik, Schellingstr. 4/III, 80799 Munich, Germany
nathalie.picque@mpq.mpg.de

Keywords: Ultrashort pulse laser, Fourier transform spectroscopy, absorption, Raman, two photon.

Laser frequency combs [1] are coherent sources which spectrum consists of several hundreds thousand sharp and evenly spaced spectral lines. A mode-locked femtosecond laser with a regular pulse train can for instance give rise to a comb spectrum of laser modes with a spacing precisely equal to the pulse repetition frequency. Fifteen years ago, such laser frequency combs have revolutionized the art measuring the frequency of light. The invention of the frequency comb technique has been motivated by precision laser spectroscopy of simple atoms. Today, frequency combs are finding applications far beyond the original purpose. Emerging applications range from fundamental research in astronomy or attosecond science to telecommunications and satellite navigation. Laser combs are becoming powerful instruments for broadband molecular spectroscopy and by creating new opportunities for Fourier transform nonlinear spectroscopy, such as two-photon spectroscopy or coherent Raman spectroscopy.

Recent experiments of multi-heterodyne frequency comb Fourier transform spectroscopy (also called dual-comb spectroscopy) have demonstrated that the precisely spaced spectral lines of a laser frequency comb can be harnessed for new techniques of linear absorption spectroscopy [2-5]. The light from a first comb is superimposed on a second frequency comb

with slightly different repetition frequency. A single fast photodetector then produces an output signal with a comb of radio frequencies due to interference between pairs of optical comb lines. The optical spectrum is thus effectively mapped into the radio frequency regime, where it becomes accessible to fast digital signal processing. The first proof-of-principle experiments have demonstrated a very exciting potential of dual-comb spectroscopy without moving parts for ultra-rapid and ultra-sensitive recording of complex broad spectral bandwidth absorption molecular spectra. Compared to conventional Michelson-based Fourier transform spectroscopy, recording times could be shortened from seconds to microseconds, with intriguing prospects for spectroscopy of short lived transient species. The resolution improves proportionally to the measurement time. Therefore longer recordings allow high resolution spectroscopy of molecules with extreme precision, since the absolute frequency of each laser comb line can be known with the accuracy of an atomic clock.

Ongoing developments will expand the range of applications of this new spectroscopy and thus they hold much promise for new approaches to sensing of gaseous, liquid and solid-state samples. Mid-infrared frequency combs [6-9] will interrogate the fundamental vibrational transitions of molecules resulting in

additional sensitivity. Miniaturized frequency comb generators [7] might even lead to chip-scale sensors.

Moreover, since laser frequency combs involve intense ultrashort laser pulses, nonlinear interactions can be harnessed. Broad spectral bandwidth ultra-rapid nonlinear molecular spectroscopy and imaging with two laser frequency combs is

demonstrated with coherent Raman effects [10,11] and two-photon excitation [12]. Real-time multiplex accessing of hyperspectral images may dramatically expand the range of applications of nonlinear microscopy. Two-photon dual-comb spectroscopy opens up opportunities [13] for Doppler-free spectroscopy of molecules.

- [1] T.W. Hänsch, Nobel Lecture: Passion for Precision, *Rev. Mod. Phys.* **78**, 1297-1309 (2006).
- [2] F. Keilmann, C. Gohle, R. Holzwarth, Time-domain mid-infrared frequency-comb spectrometer, *Opt. Lett.* **29**, 1542-1544 (2004).
- [3] I. Coddington, W.C. Swann, N.R. Newbury, Coherent Multiheterodyne Spectroscopy Using Stabilized Optical Frequency Combs, *Phys. Rev. Lett.* **100**, 013902 (2008).
- [4] B. Bernhardt, A. Ozawa, P. Jacquet, M. Jacquy, Y. Kobayashi, T. Udem, R. Holzwarth, G. Guelachvili, T.W. Hänsch, N. Picqué, Cavity-enhanced dual-comb spectroscopy, *Nature Photonics* **4**, 55-57 (2010).
- [5] T. Ideguchi, A. Poisson, G. Guelachvili, N. Picqué, T.W. Hänsch, Adaptive real-time dual-comb spectroscopy, *Nature Communications* **5**, 3375 (2014).
- [6] A. Schliesser, N. Picqué, T.W. Hänsch, Mid-infrared frequency combs, *Nature Photonics* **6**, 440-449 (2012).
- [7] C.Y. Wang, T. Herr, P. Del'Haye, A. Schliesser, R. Holzwarth, T. W. Hänsch, N. Picqué and T. J. Kippenberg, Mid-infrared optical frequency combs at 2.5 μm based on crystalline microresonators, *Nature Communications* **4**, 1345 (2013).
- [8] S. Chaitanya Kumar, A. Esteban-Martin, T. Ideguchi, M. Yan, S. Holzner, T.W. Hänsch, N. Picqué, M. Ebrahim-Zadeh, Few-cycle broadband mid-infrared optical parametric oscillator pumped by a 20-fs Ti:sapphire laser, *Laser Photonics Rev.* **8**, L86-L91 (2014).
- [9] B. Kuyken, T. Ideguchi, S. Holzner, M. Yan, T.W. Hänsch, J. Van Campenhout, P. Verheyen, S. Coen, F. Leo, R. Baets, G. Roelkens, N. Picqué, An octave-spanning mid-infrared frequency comb generated in a silicon nanophotonic wire waveguide, *Nature Communications* **6**, 6310 (2015).
- [10] T. Ideguchi, S. Holzner, B. Bernhardt, G. Guelachvili, N. Picqué, T.W. Hänsch, Coherent Raman spectro-imaging with laser frequency combs, *Nature* **502**, 355-358 (2013).
- [11] T. Ideguchi, B. Bernhardt, G. Guelachvili, T.W. Hänsch, N. Picqué, Raman-induced Kerr effect dual-comb spectroscopy, *Optics letters* **37**, 4498-4500 (2012).
- [12] A. Hipke, S.A. Meek, T. Ideguchi, T.W. Hänsch, N. Picqué, Broadband Doppler-limited two-photon and stepwise excitation spectroscopy with laser frequency combs, *Phys. Rev. A* **90**, 011805(R) (2014).
- [13] A. Hipke, S. A. Meek, G. Guelachvili, T.W. Hänsch, and N. Picqué, "Doppler-free Broad Spectral Bandwidth Two-Photon Spectroscopy with Two Laser Frequency Combs," in *CLEO: 2013, OSA Technical Digest* (online) (Optical Society of America, 2013), paper CTh5C.8.



Tip-enhanced Raman spectroscopy - a compelling device for amyloid fibril analysis

Tanja Deckert-Gaudig¹, Dmitry Kurouski², Igor Lednev³ and Volker Deckert^{1,4}

¹IPHT-Leibniz Institute of Photonic Technology, Albert-Einstein-Straße 9, 07745 Jena, Germany

²Chemistry Department Northwestern University, 2145 Sheridan rd., Evanston, IL 60208, USA

³University at Albany, State University of New York, 1400 Washington Avenue, Albany, New York 12222, United States

⁴Institute of Physical Chemistry, Friedrich-Schiller University Jena and Abbe School of Photonics, Helmholtzweg 4, 07743 Jena, Germany

Keywords: TERS, amyloid fibril, insulin, nanoscale analysis, structure characterization.

The self-assembly of proteins or peptides to elongated fiber-like structures, so-called amyloid fibrils, is a natural phenomenon that is still not completely understood. Since such structures can have a severe impact on cells and tissues a thorough characterization is in great demand. From Raman, IR, NMR and VCD it is known that a common feature of amyloid fibrils is a β -sheet spine, independent from the secondary structure of the initial protein. Since those standard techniques deliver averaged chemical information, only little is known from fibril surfaces. On the other hand a highly laterally resolved approach to chemically characterize such interfaces is of crucial interest to answer questions like what initiates fibrillation and how fibrils can be annihilated. Recent studies on insulin fibrils have demonstrated that tip-enhanced Raman spectroscopy (TERS) is a compelling device in this field.¹⁻³

TERS is the combination of scanning probe microscopy and Raman spectroscopy allowing topography imaging and chemical structure analysis simultaneously with a spatial resolution in the (sub)-nanometer range. For the presented experiments an atomic force microscopy (AFM) based

TERS setup operating in back-reflection geometry at ambient condition was used. In such measurements a commercial AFM tip is evaporated with silver and laser irradiation of the nanoparticle at the tip apex leads to a vast Raman signal intensity enhancement of sample molecules, which are in closest apex vicinity.

In this contribution the reproducibility of TERS measurements is demonstrated by spectra acquisition on 0.5 nm distant consecutive points on laterally shifted lines on a single insulin fibril. The inherent specificity of TERS enables the discrimination of amino acids, which were repeatedly detected within the spatially defined area. In Figure 1 a selection from the experiment is given where two spectral patterns along the measured line are visible. The highlighted marker bands of cysteine (cys), tyrosine (tyr) and phenylalanine (phe) enable an assignment and distinction of these amino acids. It is obvious that the chemical composition on the fibril species changes within the examined region. The detection of structural differences within such a spatially confined area can be ascribed to the high spatial resolution of TERS in the nanometer range.

Studies were extended to amyloid fibrils of different proteins and we will demonstrate that TERS is not restricted to

amino acid distinction but can also differentiate secondary structures and regions of fibril-lipid interactions.

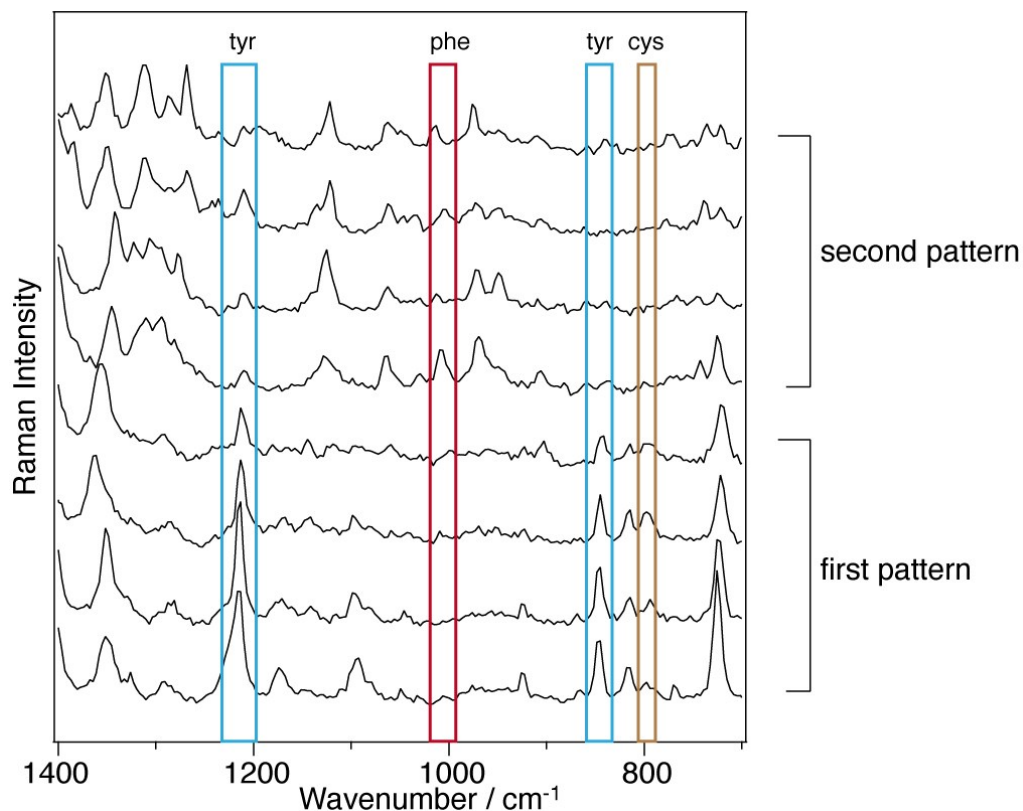


Figure 1. TERS spectra recorded on a single insulin fibril; the spectral patterns point to two chemically different regions; spectra were recorded on 0.5 nm distant consecutive points.

¹ T. Deckert-Gaudig, E. Kämmer, V. Deckert (2012), *J. Biophotonics*, 5, 215-219.

² D. Kourouski, T. Deckert-Gaudig, V. Deckert, I. Lednev (2012), *Journal of the American Chemical Society*, 134, 13323-13329.

³ D. Kourouski, T. Deckert-Gaudig, V. Deckert, I. Lednev (2014), *Biophysical Journal*, 106, 263-271.

Resonance Raman Spectroscopy Reveals a Novel Intermediate in the Catalytic Cycle of [FeFe] Hydrogenase

Sagie Katz¹, Marius Horch¹, Jens Noth², Ingo Zebger¹, Thomas Happe²

¹Department of chemistry, Technische Universität Berlin, Straße des 17. Juni 135, 10623, Berlin, Germany

²Department of biology and biotechnology, Ruhr Universität Bochum, Universitätsstraße 150, 44801, Bochum, Germany

Keywords: hydrogenase, low-temperature spectroscopy, photochemistry, electron transfer

[FeFe]-hydrogenases are the most efficient biocatalysts known for hydrogen evolution. The highly conserved active site, the so called H-cluster, consists of a [4Fe4S] cluster, which is linked to a unique [2Fe] center (Fig. 1, right). The latter is coordinated by a total of 2 CN⁻ and 3 CO ligands. In contrast to most other [FeFe]-hydrogenases, the enzyme from *Chlamydomonas reinhardtii* (HydA1), contains only the H-cluster and no other interfering cofactors, which makes it an ideal model system for spectroscopic studies.

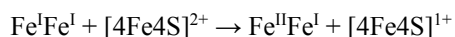
Several potential catalytic intermediates of the H-cluster can be clearly distinguished, e.g. by infrared (IR) spectroscopy, which probes the CO and CN stretching vibrations. For instance, the oxidized H-cluster (H_{ox}) is characterized by an Fe^{II}Fe^I mixed valence ground state of the [2Fe] center and an oxidized [4Fe4S]²⁺ cluster. A major reduced species (H_{red}) exhibits an oxidized [4Fe4S] cluster as well as, while the [2Fe] moiety is one-electron reduced (Fe^IFe^I). Moreover the H-cluster can be inhibited by exogenous CO.¹

In the present study we used resonance Raman (RR) spectroscopy for the first time to probe the entire H-cluster as well as the individual [4Fe4S] and [2Fe] sub-centers. Using HydA1 as a model system, as isolated (dithionite reduced), thionine oxidized, H₂ reduced, and CO treated enzyme was

characterized by this technique. Moreover, complementary low-temperature IR measurements were performed to identify contributions of individual redox states in all samples. Together, these data provide detailed insights into metal-ligand coordinates of the entire H-cluster, its cofactor building blocks, and the interactions between both sub-centers.

Despite varied compositions of different redox states, as evident from IR spectra (not shown), the marker region for Fe–CO/CN vibrations in the RR spectra (Fig 1, center) is remarkably similar for the different samples. This indicates a comparable electronic configuration of the [2Fe] moiety, i.e. this sub-center is barely affected by the different redox conditions. In contrast, considerable changes can be observed in the marker region for [4Fe4S] cluster modes (Fig 1, left). In particular, the reduction-induced intensity loss for the band at 336 cm⁻¹ indicates that reducing equivalents accumulate at the [4Fe4S] cluster rather than the [2Fe] moiety, in contrast to expectations (*vide supra*).

Since the reduction potentials of the two sub-centers are not expected to be altered by the experimental conditions, we propose that H_{red} is photoconverted by the probe laser to a kinetically trapped variant:



This metastable configuration, termed H_{red} , was previously proposed² as an intermediate in the catalytic cycle but not experimentally captured so far. Notably, this species can be assigned to the missing first intermediate of [FeFe] hydrogenase, where an electron is localized at the [4Fe4S] cluster and not yet transferred to the higher-potential [2Fe] moiety.

This study elucidates important details of the catalytic cycle of [FeFe] hydrogenase, which are essential for the understanding of biological hydrogen evolution. In a more general sense, the capability of low-temperature spectroscopy to characterize otherwise inaccessible intermediates is demonstrated.

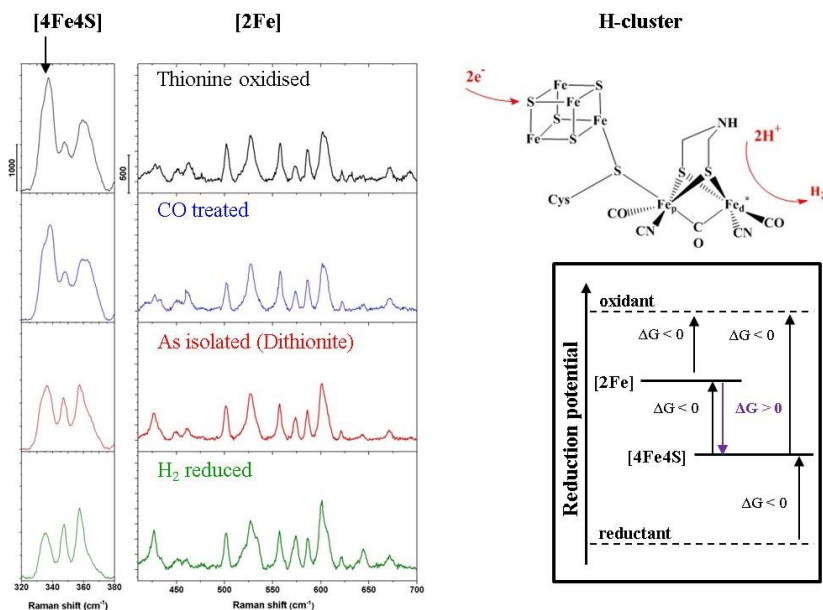


Figure 1: Cryo-RR spectra of (black) thionine-oxidized, (blue) CO-treated, (red) as-isolated (dithionite reduced), and (green) H_2 -reduced HydA1.. The middle panel shows the region specific for Fe–CO/CN vibrations of the [2Fe] moiety, while the left panel is dominated by normal modes of the [4Fe4S] cluster. The marker band for oxidized cluster at 336cm^{-1} is indicated by the black arrow. The H-cluster and its potential scheme is depicted on the right.

¹ Lubitz W., Ogata H., Rüdiger O., Reijerse E. (2014), *Chemical reviews*, 114 (8), 4081-4148.

² Mulder D. W., Ratzloff M. W., Shepard E. M., Byer A. S., Noone S. M., Peters J. W., Broderick J. B., (2013), *Journal of the American Chemical Society*, 135 (18), 6921-6929

Resonance Raman spectroscopy for analysis of amino acids

Martin Höhl^{1,3}, Merve Meinhardt-Wollweber^{1,3}, Uwe Morgner^{1,3}, Heike Schmitt^{2,3}, and Thomas Lenarz^{2,3}

¹Institut für Quantenoptik, Leibniz Universität Hannover, Welfengarten 1, 30167, Hannover, Germany

²Experimentelle Otorhinolaryngologie, Medizinische Hochschule Hannover, Carl-Neuberg-Straße 1, 30625, Hannover, Germany

³Exzellenzcluster Hearing4all

Keywords: resonance, amino acid, perilymph, fingerprint.

The work presented here was conducted within the scope of a larger project aiming at the development of a non-invasive optical technique to investigate inner ear hearing loss. Here, resonance Raman spectroscopy is applied to measure pathophysiologically relevant parameters like the peptide, protein or ion content of the inner ear fluid (perilymph). The long term aim is to implement this method as a fiber based endoscope for non-invasive measurements during surgeries (cochlear implants) making it available as a diagnostic tool.

Amino acids show strong absorption in the ultraviolet part of the spectrum. Due to the small concentrations of peptides in the perilymph, resonance Raman spectroscopy was used to increase the sensitivity¹. Figure 1 shows the increase in Raman scattered light when using ultraviolet instead of visible light.

In order to find the optimal wavelength for discriminating different peptides, resonance profiles of several amino acids are recorded. An optical parametric oscillator (OPO, Ekspla, PG122/UV) provides ns pulses tunable in the ultraviolet range (210-354 nm). The light is focused into a cuvette containing the sample. A second lens collimates the light behind the cuvette and guides it through a filter that blocks the

Rayleigh-scattered light. The Raman-signal is then focused into a fiber leading the light to a spectrometer (Andor Technology, SR-500i-D2) to record the spectra. Those can be arranged to create an excitation-emission map showing both Raman line positions and their intensity in dependence of the excitation wavelength and indicating the wavelength with the strongest Raman resonance. The gap-free tunability of the OPO allows the recording of complete resonance profiles.

We present resonance Raman maps and profiles for human amino acids (Figure 2). Due to the lack of filters in some regions of the ultraviolet, it is not possible to cover the whole range provided by the OPO.

In the future, the investigations are extended to more complex molecules like proteins and protein mixtures as expected in human perilymph. During a surgery, time is limited for measuring in vivo. Experimental parameters like exposure time need to be optimized for that purpose. For use as a diagnostic tool, the Raman data and (patho)physiological assessment need to be correlated. To achieve this, pathophysiologically relevant bio-chemical parameters and markers are identified using mass spectrometry in a partner project at the "Medizinische Hochschule Hannover" (MHH). Human perilymph can be taken

during cochlea implant surgery and is available for both mass spectrometric and Raman spectroscopic analysis.

This project is embedded in the cluster of excellence “Hearing for all” (H4A). The cluster tries to achieve better hearing for individuals with various degrees of hearing impairment (constituting more than 18% of the total population and about 50% of all

people above 65). This is why there is a need for functional individualized hearing devices. By combining basic, clinical, translational and applied research with clinical service, engineering and applications, a major breakthrough in hearing and rehabilitation technology is aimed to be achieved.

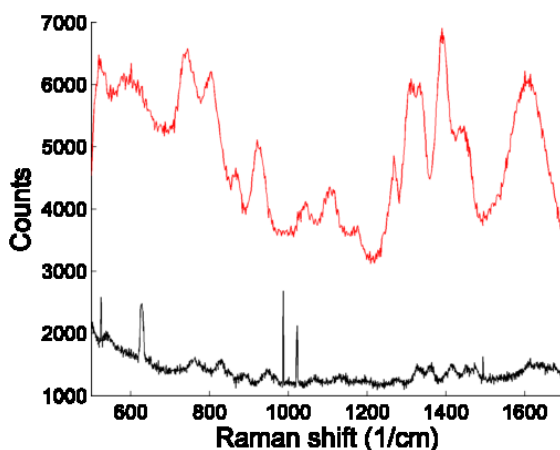


Figure 1. Raman spectra of valine ($C = 428 \text{ mM}$, black: $185 \text{ mJ @ } 528 \text{ nm}$ and red: $134 \text{ mJ @ } 321 \text{ nm}$ excitation).

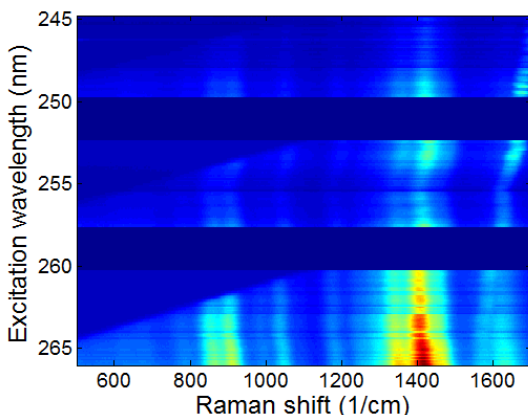


Figure 2. Raman spectra of proline continuously measured from $244.8\text{-}249.7 \text{ nm}$, $252.4\text{-}257.6 \text{ nm}$, and $260.3\text{-}266 \text{ nm}$ in 0.1 nm steps.

¹ Asher S. (1993), *Analytical Chemistry*, 65 (2), 59A-66A.

Carotenoids, hemoproteins and the “life band” – Raman microimaging
of live *Rhodotorula mucilaginosa* cells

Jan Pukalski¹, Marta Z. Pacia^{1,2}, Katarzyna Turnau³, Malgorzata Baranska^{1,2} and Agnieszka Kaczor^{1,2}

¹Faculty of Chemistry, Jagiellonian University, 3 Ingardena St., 30-060, Krakow, Poland

²Jagiellonian Centre for Experimental Therapeutics (JCET), Jagiellonian University, 14
Bobrzynskiego St., 30-048, Krakow, Poland

³Institute of Environmental Sciences and Malopolska Centre of Biotechnology, Jagiellonian
University, 7 Gronostajowa St., 30-387, Krakow, Poland

Keywords: carotenoids, yeasts, “life band”, Raman imaging, hemoproteins

“Raman signature of life”, a band at 1602 cm⁻¹, is a unique spectroscopic feature directly related to mitochondria activity and present both in yeasts and animal cells.¹⁻⁴ The life band signal is related to heme functions³ although a direct link between them is unknown. Flavohemoglobins, present in yeasts, are localized in the mitochondrial matrix and play a role as NO-detoxifying system under hypoxic conditions.⁵ Next to hemoglobins, carotenoids are pigments produced by many yeast species, responsible for defense against free radicals. *Rhodotorula mucilaginosa* is one of many yeast species capable of carotenoids *de novo* synthesis.

In order to shed some more light on the relation between carotenoid and flavohemoglobin synthesis and “life band” origin, Raman imaging of live *Rhodotorula* cells in aerobic, anaerobic conditions and upon additional stress factor (diazinone presence) were undertaken.

Raman imaging was done using a Confocal Raman Imaging system WITec alpha300 with the application of a 100× oil objective (Nikon, EPlan 100×, NA = 1.25) with the lateral spatial resolution of *ca.* 260 nm, spectral resolution of 3 cm⁻¹, laser excitation of 532 nm and integration times of 0.2 s on areas of 15 × 15 μm edge length.

The Raman images of yeast cells grown in the aerobic and anaerobic conditions were strikingly different.⁶ Obviously, the “life band” was absent in live *Rhodotorula* cells grown under anaerobic conditions. Next to it, practically no carotenoids and hemoproteins were found in yeasts cells in anaerobic environment, while they were clearly observed in cells with active mitochondria (grown in aerobic conditions, Fig. 1).

Additionally, the switch from anaerobic to aerobic environment resulted in the change of cells’ phenotype and the appearance of the “life band” and hemoproteins (rather than carotenoids). This result indicates that carotenoids and flavohemoproteins can interchange in their protective roles in the yeast cells and their ratio is dependent on environmental conditions. Possibly, the carotenoid production requires longer time to be initiated than the hemoprotein synthesis (no traces of carotenoids have been observed after 12 hours after the anaerobic-aerobic transition).⁶

The presence of diazinone further influenced distribution of hemoproteins and carotenoids in *Rhodotorula mucilaginosa* cells.

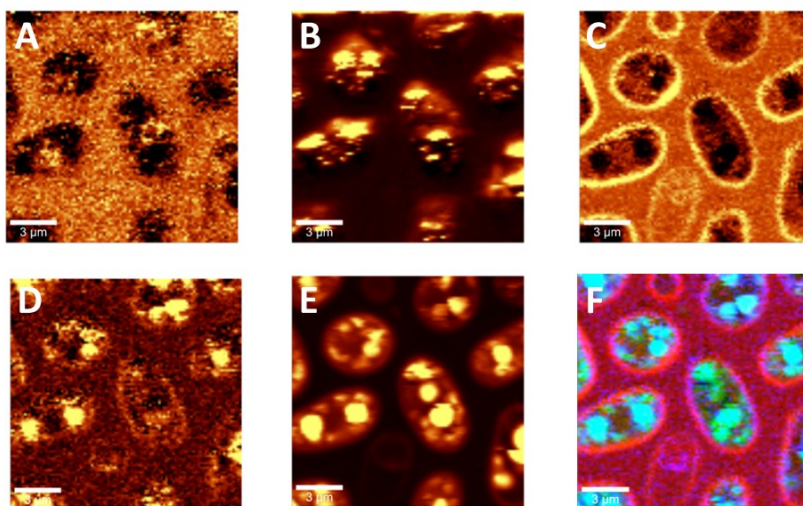


Figure 1. The representative images showing the distribution of hemoproteins (integration over the band at 750 cm^{-1} , **A**), carotenoids (1154 cm^{-1} , **B**), cell wall (1460 cm^{-1} , **C**), the “life band” (1602 cm^{-1} , **D**) lipid bodies (2857 cm^{-1} , **E**) and overlaid signal (cell wall, “life band” and lipid bodies denoted in red, blue and green, respectively) in yeast cells cultured under aerobic conditions.

Acknowledgements

This project was supported by the National Science Centre (DEC-2012/07/B/ST5/00889).

- ¹ Huang Y. S., Karashima T., Yamamoto M., Ogura T., Hamaguchi H.-O., (2004), *Journal of Raman Spectroscopy*, 35, 525–526.
- ² Chiu L. D., Ando M., Hamaguchi, H.-O., (2010), *Journal of Raman Spectroscopy*, 41, 2–3.
- ³ Chiu L. D., Hamaguchi H.-O., (2011), *Journal of Biophotonics*, 4, 30–33.
- ⁴ Tang H., Yao H., Wang G., Wang Y., Li Y.-Q., Feng M., (2007), *Optics Express*, 15, 12708–12716.
- ⁵ Vinogradov S. N., Bailly X., Smith D. R., Tinajero-Trejo M., Poole R. K., Hoogewijs D., (2013), *Advances in Microbial Physiology*, 63, 391–446.
- ⁶ Pacia M. Z., Turnau K., Baranska M., Kaczor A., (2015), *Analyst*, 140, 1809–1813.

Raman spectroscopy and SEM study on microorganisms for applications in the field of biofuels and biopolymer production

O. Samek¹, S. Obruča², A. Haronikova², Z. Pilát¹, S. Bernatová¹, K. Hrubanová¹, J. Ježek¹, V. Krzyžánek¹, I. Márová², P. Zemánek¹

¹Institute of Scientific Instruments of the ASCR, v.v.i., 61264, Brno, Czech Republic.

²Centre for Material Research, Brno University of Technology, 61200, Brno, Czech Republic.

Keywords: Raman spectroscopy, SEM, microorganisms, biofuel, food industry, biopolymer

Samples of red yeast strains (*Rhodotorula spp.*, *Cystofilobasidium spp.* and *Sporobolomyces spp.*) have been studied due to their potential applications in the field of biofuel generation and food industry. In order to utilize biomass for efficient industrial production, the optimal cultivation parameters have to be determined which in turn lead to high production of desired substances such as oil and carotenoids in the selected cell line. Main aim of our investigations was to study – using Raman spectroscopy and scanning electron microscopy (SEM) techniques – how different cultivation conditions influence production of oil and carotenoids. Raman spectroscopy can be used for the determination of the oil present in the biomass and also for the determination of carotenoids as the intensity ratios of specific, selected Raman bands. SEM uses focused electron beam to gain information about morphology of cells (biomass structure) which is very important factor to study cells response on the applied stress.

In our experiments we have observed different morphology when employing SEM/cryo-SEM to study cells of *Cystofilobasidium capitatum* which was cultivated in media with different carbon to nitrogen (C/N) ratios. Corresponding Raman spectra is also shown (Figure 1).

Here we combined information about morphology of the sample with Raman

fingerprint by which lipid and carotenoids molecules can be identified. Thus, all matrix changes within the studied cells introduced by stress response mechanisms (different C/N ratios) can be visualized (SEM) and chemically characterized/monitored (Raman).

Many bacterial strains are capable of accumulation of very high amounts of polyhydroxyalkanoates (PHAs) in cytoplasm. Consequently, increasing content of the macromolecular material will strongly affect the overall material properties of cells and it is also likely that high content of PHAs inside the cells will also influence the rest of the cell volume – the cytoplasm.

The main aim of our investigations concerning PHA study is to again utilize combination of the two modern methods - electron and Raman microscopy in the complex study on changes in physico-chemical properties of bacterial cells and cell cytoplasm with respect to intracellular content of PHA. For this purpose, we have utilized following bacterial strain *Cupriavidus necator* H16 and also its PHA none-producing mutant *C. necator* PHB⁻⁴. Raman spectroscopy seems to be very efficient tool for direct analysis of intracellular PHA content of bacteria and, furthermore as mentioned above, can be combined with SEM imaging to make it possible to measure/follow nutrient dynamics and metabolism of the cells.

Moreover, with this type of sensing one may detect variability of polymers contained within the cells which could help in elucidating different morphological features during the process of cryo scanning electron microscopy (cryo-SEM) technique (Figure 2). All Raman micro-spectroscopic experiments with above mentioned cells were carried out using inVia Renishaw system.

We believe that our study will be of significant assistance to research group being involved in study of microorganisms for biofuels, food, and biopolymer production. Our results are convincing enough to warrant more extensive investigations with larger sets of yeast/bacterial strains to evaluate combination of Raman spectroscopy and SEM/cryo-SEM.

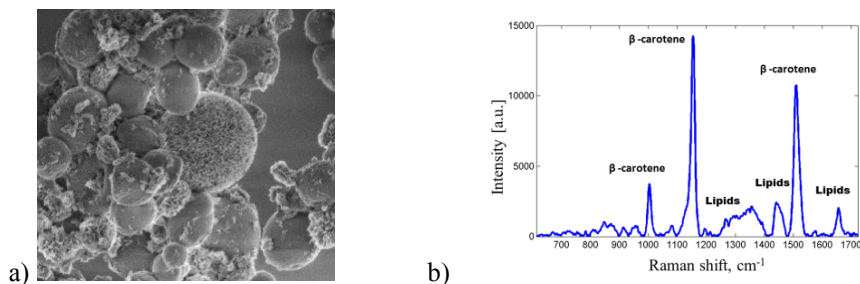


Figure 1. a) SEM image of *Cystofilobasidium capitatum* (sample was chemically fixed); b) Raman spectra of *Cystofilobasidium capitatum* cultivated in medium which contributes to increased lipid production.

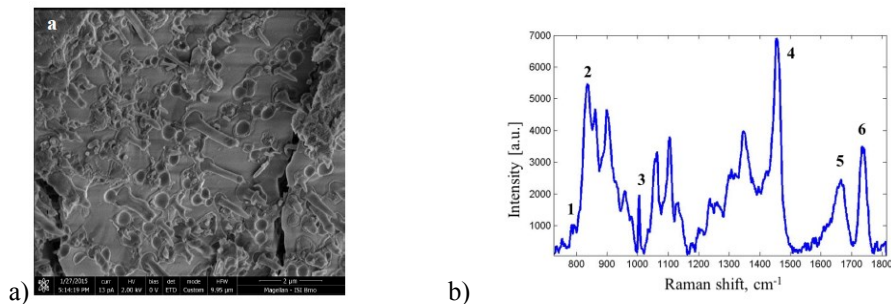


Figure 2. a). Cryo-SEM image of *Cupriavidus necator* H16. Needle-type deformations can be clearly seen on the fractured sample surface. b) Raman spectra of *Cupriavidus necator* H16. The most prominent contributions are (1) DNA, (2,4,6) PHB, (3) Phenylalanine, (5) lipids.

Acknowledgement

This work received support from the Ministry of Health, Ministry of Education, Youth and Sports of the Czech Republic (LO1212), together with the European Commission (ALISI No. CZ.1.05/2.1.00/01.0017) and the Grant Agency of the Czech Republic (GACR GA15-20645S, GA14-20012S).



Oxygen reduction and water at the semiconductor/solution interface probed by stationary and time-resolved ATR-IR spectroscopy coupled to electrochemical experiments and DFT calculations

Stefanie Pengel¹, Fang Niu¹, Simantini Nayak¹, Stefanie Tecklenburg¹, Ying-Hsuan Chen¹, Petra Ebbinghaus¹, Rainer Schulz², Lei Yang¹, P. Ulrich Biedermann¹, Francois Gygi³, Rochus Schmid², Giulia Galli⁴, Stefan Wippermann¹ and Andreas Erbe¹

¹Max-Planck-Institut für Eisenforschung GmbH, 40237 Düsseldorf, Germany

²Faculty of Chemistry and Biochemistry, Ruhr-Universität Bochum, 44801 Bochum, Germany

³Program in Applied Science, University of California, Davis, 95616, USA

⁴Institute for Molecular Engineering, University of Chicago, Chicago, 60637, USA

Keywords: spectroelectrochemistry, solvation, reaction intermediates, ion adsorption.

The electrochemical oxygen reduction (ORR) an important reaction in chemical energy conversion and corrosion science. The cathodic ORR net reaction is $O_2 + 4 e^- + 4 H^+ \rightarrow 2 H_2O$ in acidic solution, and $O_2 + 4 e^- + 2 H_2O \rightarrow 4 OH^-$ in alkaline solution. Because 4 electrons are transferred and the solvent water is also a reactant in the ORR, the reaction mechanism is complex and depends on the substrate. In this work, we investigate the intermediates of the ORR and the electrode-potential dependent change in electrode solvation on electrodes of the semiconductors silicon and germanium by attenuated total reflection IR spectroscopy.

On Ge(100), the ORR was shown to proceed via superoxide and peroxide intermediates, which have been observed in 0.1 M HClO₄, alkaline chloride and perchlorate solutions. Measurements of the linear dichroism showed the upright orientation of the intermediates, whose vibrational frequencies have been assigned on the basis of DFT computations. IR spectra show evidence for anion adsorption at negative potentials^{1,2}.

Comparing steady state ORR currents to integrated absorbance enables deeper insight into the second electron transfer step of the ORR from superoxide to peroxide. Superoxide absorbance increases with

increasing cathodic current. Comparison between Cl⁻ and ClO₄⁻ electrolytes shows that the second electron transfer step of the ORR is three times faster in perchlorate².

A quantitative analysis of the kinetics of superoxide formation is possible by time-resolved spectroscopy. Therefore, a tunable quantum cascade laser (QCL) was coupled to an electrochemical experiment³. Rate constants of superoxide decay have been determined by analysis of transients as shown in Figure 1. The control experiments in Ar are needed to separate free carrier absorption from superoxide absorption.

In acidic solution, Ge undergoes a surface transformation from a hydrophilic, OH-terminated surface a hydrophobic, H-terminated surface below a certain electrode potential. Hence, solvation of Ge is expected to change as function of potential, and indeed detected by FTIR (Figure 2). The negative difference absorbance in the OH stretching mode region below the electrode potential of the surface termination change indicates a partial desolvation of the surface at negative potentials. Also, changes in the perchlorate antisymmetric stretching mode at 1110 cm⁻¹ indicate changes in the ion adsorption at the interface.

On silicon, its tendency to form a stable amorphous oxide film complicates the

spectral analysis. In NaF, ~60% of the H-termination produced after an etching process survives exposure to the aqueous electrolyte, without major changes as function of electrode potential. More subtle changes in the electrode solvation are observed. Preliminary analysis of ab initio

molecular dynamics simulations indicate the presence of the peak typically assigned to non-hydrogen bound water at the interface.

Acknowledgment: This work is supported by the IMPRS SurMat, DAAD and the Cluster of Excellence RESOLV (EXC 1069) funded by the DFG.

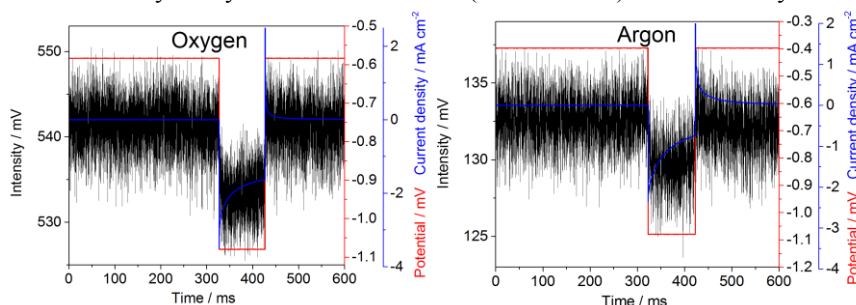


Figure 1. Current, potential and laser intensity transients in oxygen and argon-saturated NaClO_4 after an electrode potential jump of -1081 mV. The laser intensity is recorded at 1205 cm^{-1} , in an absorption band of the superoxide ORR intermediate.

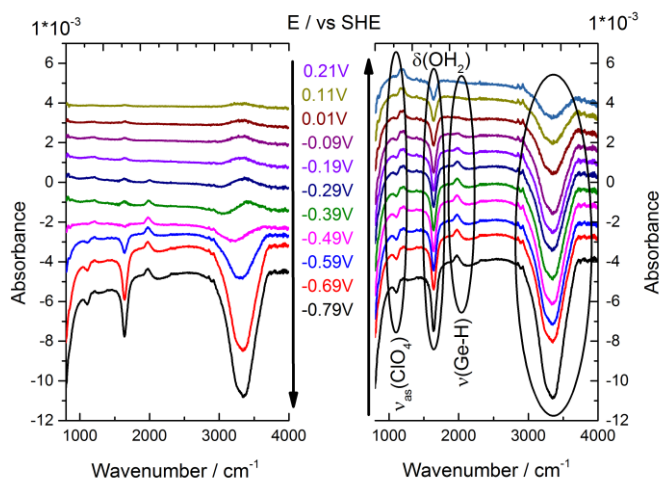


Figure 2. Difference absorbance ATR-FTIR spectra of 0.1 M HClO_4 in contact with $\text{Ge}(100)$, p-polarisation. Reference spectrum recorded at 0.21 V vs. SHE. Left decreasing, right increasing potential.

- Nayak S., Biedermann P.U., Stratmann M., Erbe A. (2013), *Physical Chemistry Chemical Physics*, 15(16), 5771-5781.
- Nayak S., Biedermann P.U., Stratmann M., Erbe A. (2013), *Electrochimica Acta*, 106, 472-482.
- Pengel S., Schönberger B., Erbe A. (2012), *Lasers, Sources, and Related Photonic Devices*,

Influence of surface structure on biofilm growth

Tasha Jarisz, Sarah Kowallik, Sandra Roy, Paul Covert, Dennis Hore

Department of Chemistry, University of Victoria, Victoria BC, V8W 3V6, Canada

Keywords: biofilms, nonlinear vibrational spectroscopy, silica, interfacial water

Complex assemblies of bacteria, known as biofilms, rapidly form when nearly any solid surface is exposed to an aqueous environment. The polymeric substance they then secrete is one of their unique features, improving adhesion and cohesion, and offering enhanced resistance to environmental stresses. Colloquially referred to as slime, this is the slippery material you feel when standing on rocks at the bottom of a river. While such marine biofilms are a natural part of aquatic ecosystems, the films may pose significant environmental and energy strains when fouling ship hulls, as the subsequent attachment of barnacles creates drag that increases fuel consumption. Biofilms are also responsible for chronic infections and dental caries, and are a primary cause of industrial fouling, clogging pipes, heat exchangers, and water filtration membranes. From a different perspective, heavy metal remediation of soil and waste water treatment rely on biofilms in natural and engineered environments. Over the past four decades, scientists have amassed considerable knowledge of the growth, composition, and structure of biofilms. However, the role of the solid surface in sequestering the bacteria and fostering the development of the film is acknowledged as a critical factor that remains largely unknown.¹

One of the primary challenges associated with this characterization lies in achieving sufficient selectivity for molecules at the surface, particularly interfacial water

molecules, as they are overwhelmed by the same species in the bulk solution phase. Second-order nonlinear techniques directly address this issue by requiring a break in inversion symmetry, thereby limiting signal to regions very close to the surface.² We have used structure-sensitive visible-infrared sum-frequency generation (SFG) spectroscopy to probe *E. coli* K12 biofilm growth at the silica-water interface. The basic experimental configuration is shown in Figure 1, where a fixed wavelength visible beam and tunable infrared beam are spatially and temporally overlapped at the buried silica surface. By tuning the IR beam over the O-H stretching region, one obtains a fingerprint of the surface hydrogen bonding network by monitoring the intensity of the up-converted light.

Our preliminary results are illustrated in Figure 2, where we draw comparisons to the effect of increasing ionic strength on the SFG signature of water at the silica surface (Fig 2a,b).^{3,4} The SFG response is greatly diminished upon replacing the water

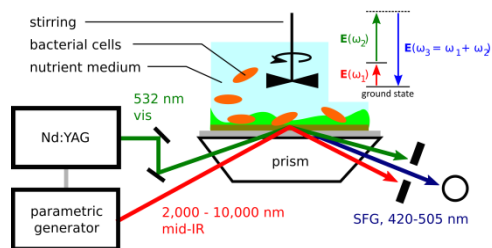


Figure 1. Schematic of the vibrational sum-frequency experiment.

with lysogeny broth (LB, Fig 2c), as may be expected from an enhanced screening of the silica surface charge. However, upon addition of the cells, the signal increased steadily over a period of three days. Based on our understanding of the silica surface, this is consistent with a model in which the accumulated cations are gradually depleted by the cells. Preservation of the relative

intensity of the 3200 cm^{-1} and 3400 cm^{-1} features is further evidence that the cells are not rearranging the structure of the interfacial water molecules as much as they are modulating the penetration of the surface potential. Optical microscopy (Fig 2d-h) provides some additional insight into the surface structural changes, together with linear vibrational measurements.

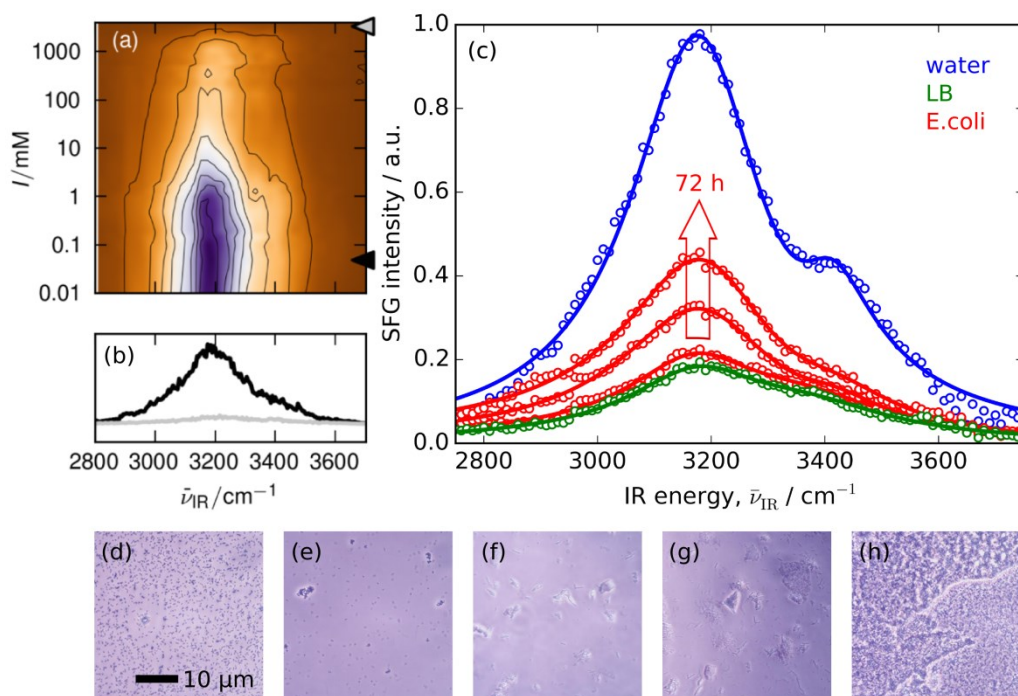


Figure 2. (a) Variation in SFG signal at the water-silica interface as a function of ionic strength with (b) 0.07 mM and 3 M NaCl spectra highlighted. (c) SFG signal for water, LB growth medium, and 72 hours of *E. coli* growth at the silica surface. (d-h) phase contrast optical microscopy images of the early stages in the biofilm growth.

¹ Costerton, J.W. (2007). *The Biofilm Primer*. Springer: Heidelberg.

² Jena K.C., Hore D.K., (2010), *Physical Chemistry Chemical Physics*, 12, 14383–14404.

³ Jena K.C., Covert P.A., Hore D.K., (2011), *Journal of Physical Chemistry Letters*, 2, 1056–1061

⁴ Covert P.A., Jena K.C., Hore D.K., (2014), *Journal of Physical Chemistry Letters*, 5, 143–148

Silanol-to-siloxane interconversion during room temperature hydration/dehydration of amorphous silica films as observed by ATR-IR spectroscopy

Suzanne L. Warring¹ and A. James McQuillan¹

¹ Department of Chemistry, University of Otago, P. O Box 56, Dunedin 9054, New Zealand

Keywords: ATR-IR, silica, surficial reactions.

Studies of silica surface chemistry by infrared spectroscopy have spanned over 50 years due to the importance of silica as a surface coating on silicon in semiconductors and as a material for chromatography. Previous studies have assigned characteristic vibrational frequencies of geminal, vicinal and isolated silanol groups in addition to siloxane bridges (Figure 1).¹⁻³ There has also been in-depth analysis and experimentation to clarify the bulk vibrational modes of the silica lattice with determination of characteristic frequencies of the transverse and longitudinal optical modes (TO and LO respectively).^{4,5}

Such studies have utilized vacua and high temperature calcination of the silica films to determine silanol condensation reactions at the silica surface. It is of interest to monitor spectral changes of silica films with the stimulus of hydration/dehydration at room temperature. These results aid in the interpretation of IR spectra of room temperature adsorption of polymeric adsorbates to silica.

The following work has utilized thin silica particle films ~300 nm thick and attenuated total internal reflection infrared (ATR-IR) spectroscopy to probe the spectral response of silica films exposed to humidified atmosphere. The use of thin silica films as a substrate avoids the intense bulk signals that would obscure the spectral signatures from surface phenomena. Spectra were recorded using argon, humidified with

water and D₂O, at relative humidity's between ~10 and ~40 %. Measured spectra had the spectrum of the silica film under dry argon subtracted from them to give the spectral results presented in Figure 2.

Absorption gains are observed in vibrational bands associated with water indicating both bulk and interfacial are present. Absorption gains are also observed in bands associated with vicinal silanol groups at 3647 and 956 cm⁻¹. These are concordant with absorption losses in vibrational bands associated with isolated silanol and surficial siloxane groups at 3736 and 876 cm⁻¹ respectively. These spectral results are indicative of siloxane-to-silanol interconversion upon exposure to humid atmosphere at room temperature. This has often been alluded to in previous IR studies, however, the results presented are the first clear illustration of this process.

An intriguing finding of these studies is the absorbance loss at 1107 cm⁻¹ concomitant with growth of a feature at 1033 cm⁻¹. A number of possible structural and experimental effects may lead to these observations. Firstly, this may be indicative of changes in the porosity of the film as a result of constrained ring size in the silica matrix. Secondly anomalous dispersion⁶ may lead to such spectral changes.

Spectral results will be presented from D₂O humidified argon providing further insight into the nature of the observed spectral features through isotopic effects.

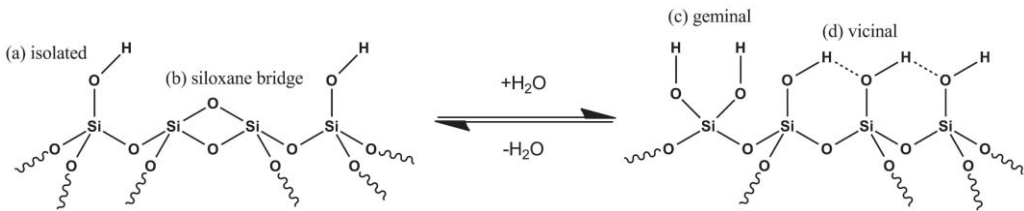


Figure 1. Schematic surficial hydroxylation of silica upon exposure to humid environments and the type of silanol groups present at the SiO₂ surface (a) isolated, (b) siloxane bridge, (c) geminal and (d) vicinal.

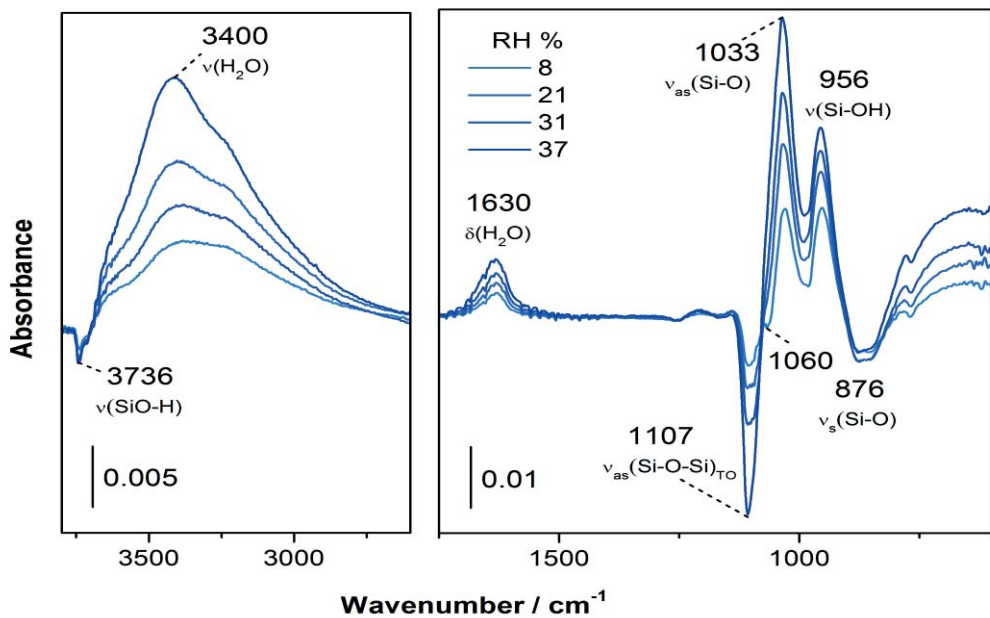


Figure 2. Aqueous silica film ATR-IR difference spectra for 8, 21, 31 and 37 % relative humidity.

- ¹ Takamura, T.; Yoshida, H.; Inazuka, K. (1964), *Kolloid-Zeitschrift Zeitschrift für Polym.*, 195, 12–16.
- ² McDonald, R. S. (1957), *J. Am. Chem. Soc.*, 79, 850–854.
- ³ Liu, W.-T.; Shen Y. (2008), *Phys. Rev. Lett.*, 101, 016101.
- ⁴ Galeener, F. (1979) *Phys. Rev. B*, 19, 4292–4297.
- ⁵ Almeida, R. M.; Pantano, C. G. (1990) *J. Appl. Phys.*, 68, 4225.
- ⁶ Harrick, N. J. *Internal Reflection Spectroscopy*; 3rd ed.; John Wiley & Sons, Inc.: New York, USA, 1987.

Immobilization of Cryptophane Derivatives onto SiO₂/Au and Au SubstratesElise Siurdyban¹, Thierry Brotin², Karine Heuzé¹, Luc Vellutini¹, and Thierry Buffeteau¹¹Institut des Sciences Moléculaires, Université de Bordeaux, 351 Cours de la libération, 33405, Talence, France²Laboratoire de Chimie, Ecole Normale Supérieure de Lyon, 46 Allée d'Italie, 69364, Lyon, France

Keywords: Cryptophanes, Surface chemistry, PM-IRRAS.

Cryptophanes are nearly spherical cage molecules composed of two cyclo-triveratrylene bowls connected by three aliphatic linkers. The rigid bowl-shaped structure of the cryptophane cavity generates a lipophilic cavity suitable for the encapsulation of guest species, such as halogenomethanes, ammonium salts, or even xenon in organic or aqueous solutions. Recently, we have shown that cryptophanes bearing hydroxyl functions could also efficiently encapsulate cesium and thallium cations in water under basic conditions.¹⁻³

The immobilization of cryptophane molecules onto surfaces could be an original and clever approach for extraction of toxic molecules or polarizable cations such as cesium or thallium. Therefore, we have investigated the grafting of cryptophane derivatives onto SiO₂/Au and Au substrates.

In this study, several ways were considered for the grafting of a model cryptophane (pentamethoxy cryptophane-A derivative) onto surfaces (Figure 1a).⁴ The first way (**SAM-1**) consists in the covalent linkage, via amide bonds, between a cryptophane derivative bearing one acid function (**cryptoMA**) and a amino-terminated self-assembled monolayer (**SAM-NH₂**). The formation of **SAM-NH₂** onto a silica surface is based on the chemistry of organosilanes (chloro- or alkoxy-silanes). Due to the electrophilic

nature of the trichlorosilane groups, it is necessary to protect the amino groups in non-nucleophilic form, using a phthalimido terminal group, for example. The deprotection of phthalimido terminal groups can be performed after the grafting of the chlorosilane molecules. Then, the cryptophane molecules can be immobilized by activation of the carboxylic acid function of the **cryptoMA** and by reaction with the amino-terminated **SAM-NH₂**. The second way (**SAM-2**) implies functionalizing the pentamethoxy cryptophane with an alkanethiol chain (**cryptoSH**) and grafting it, in one step, onto a gold substrate. The third way (**SAM-3**) is a mix of the two previous methods and involves functionalizing the activated **cryptoMA** with cysteamine coupling agent (reaction with the amino group), followed by grafting it onto a gold substrate (using the thiol group of the cysteamine).

Polarization modulation infrared reflection-absorption spectroscopy (PM-IRRAS) was used to characterize the three types of cryptophane monolayers (Figure 1b). It is a very straightforward and non-destructive method giving molecular information on these bi-dimensional systems. Surface coverage of cryptophane monolayers was estimated by comparing the IRRAS intensities of cryptophane bands with those calculated for a compact

monolayer (surface coverage of 100%), using the optical constants of **cryptoMA**.

The reaction of **cryptoMA** with amino-terminated **SAM-NH₂** was found the less efficient method, since the surface coverage did not exceed 9% (table 1). In contrast, a very efficient grafting of **cryptoSH** onto a gold surface was found,

with a surface coverage close to 100%. Finally, a good surface coverage (77%) was also obtained by using the cysteamine coupling agent to modify **cryptoMA** before its grafting onto gold surface.

Table 1. Surface Coverage of Cryptophane Derivatives onto SiO₂/Au and Au Substrates.

SAMs	Compounds	Substrate	Surface Coverage (%)
SAM-1	CryptoMA+SAM-NH ₂	SiO ₂ /Au	9 ± 3
SAM-2	CryptoSH	Au	95 ± 5
SAM-3	CryptoMA+NH ₂ (CH ₂) ₂ SH	Au	77 ± 4

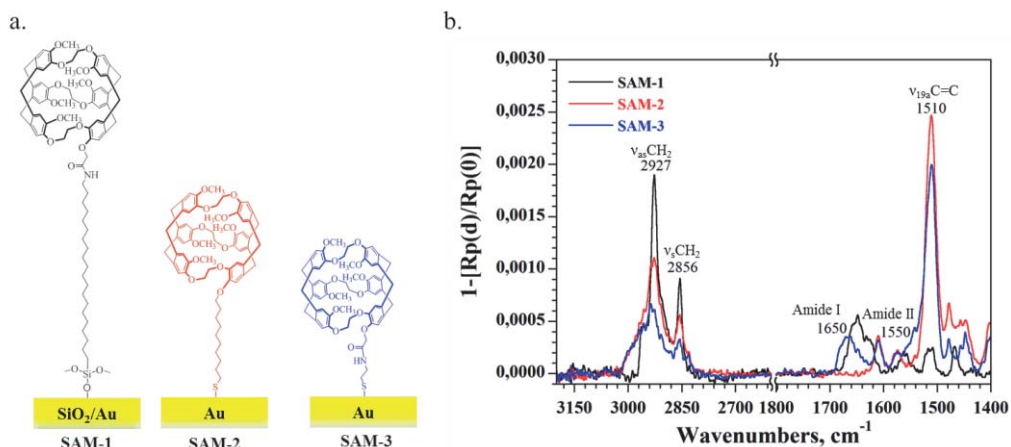


Figure 1. a) Schematic representation of cryptophane derivatives immobilized onto SiO₂/Au or Au substrates and b) PM-IRRAS spectra, expressed in IRRAS units, of **SAM-1** (black), **SAM-2** (red) and **SAM-3** (blue).

¹ Brotin T., Montserret R., Bouchet A., Cavagnat D., Linares M., Buffeteau T. (2012), *J. Org. Chem.*, 77, 1198-1201

² Brotin T., Cavagnat D., Berthault P., Montserret R., Buffeteau T. (2012), *J. Phys. Chem. B*, 116, 10905-10914

³ Brotin T., Goncalves S., Berthault P., Cavagnat D., Buffeteau T. (2013), *J. Phys. Chem. B*, 117, 12593-12601

⁴ Siurdyban E., Brotin T., Heuzé K., Vellutini T., Buffeteau T. (2014), *Langmuir*, 30, 14859-14867.

Versatility of SERS spectra potential dependence to surface equilibria

Elena V. Solovyeva, Assima Rakhimbekova, Lubov A. Myund and Anna S. Denisova

Chemistry Department, Saint-Petersburg State University, Universitetsky pr. 26, Peterhof,
Saint-Petersburg 198504, Russian Federation

Keywords: SERS, surface equilibria, potential dependence, aromatic heterocycles.

Surface enhanced Raman scattering is still actively developing optical method of investigation but is already recognized as one of the most powerful and promising tool of vibrational spectroscopy. The high demand of SERS method is derived from its unique sensitivity allowing to detect even single molecule¹. In addition to high sensitivity of analytical determination SERS is extremely valuable for the study of physical and chemical aspects of the adsorption of molecules on the surface. From this point of view the modification of method on the metal–solution boarder in the electrochemical cell is especially important. There is the additional possibility to vary the surface potential in such conditions thus valuable information inaccessible for other SERS techniques can be obtained. Based on the SERS spectra potential dependence one can judge about the orientation of adsorbate, the structure of electrical double layer, the existence of various adsorbate species.

This work presents the study of SERS spectra potential dependence for a number of azaheterocycles (1,10-phenanthroline (*phen*), acridine (*acr*), 2,2'-bipyridyl (*bpy*)) and their derivatives, and shows how to establish the relationship between the molecule structure, the type of the SERS spectra potential dependence and the form of adsorbate.

Even for the simple azaheterocycles molecules *phen* and *acr* different dependence of SERS spectra on the electrode potential is observed. In the case of *phen* the intensity of SERS spectra grows

and bands shift at electrode potential lowering. In the case of *acr* only a general decrease in the spectra intensity with a shift of potential to the negative range is observed. Such behavior of SERS spectra suggests the different ways for *phen* and *acr* molecules adsorption on the surface. A fundamental difference between surface forms for these two molecules can only consist in the type of molecule interaction with the surface: through heteroatom or via π -system of aromatic rings. Probably, *phen* due to the presence in molecule of two heteroatoms adsorbs on the surface as σ -complex and more aromatic *acr* as π -complex².

The more interesting situation arises in cases when a molecule under investigation has additional conformational possibilities. So in the dependence of *bpy* SERS spectra on electrode potential the changing of the interplanar angle in molecule comes out at shifting of potential to negative range (Figure 1). Wherein *bpy* derivatives with bulky substituents in the 5,5'-positions which molecules are limited in rotation of pyridine planes in contradistinction to *bpy* are characterized by other changes occurring in the SERS spectra at variation of surface potential.

Even more interesting results were obtained for two similar *phen* derivatives – 2,9-dimethyl-1,10-phenanthroline (*dimephen*) and 2,9-dibutyl-1,10-phenanthroline (*dibuphen*). For *dimephen* the character of SERS spectra potential dependence indicates that despite the

vicinity of the methyl groups to the heteroatoms the molecules adsorb on surface via nitrogen atoms and at lowering of electrode potential not just the molecules reorientation occurs but the appearance a new rotational conformations happens too. The new *dimephen* conformations differ in the rotation of the methyl groups relative to the aromatic fragment (Figure 1). For the *dibuphen* in comparison with *dimephen* a different character of SERS spectra dependence on electrode potential was obtained. Probably, due to more bulky aliphatic substituents the σ -complexes can not exist on the surface consequently the *dibuphen* molecules adsorb through conjugated π -system of aromatic rings and

the desorption of molecules from surface occurs at lowering of electrode potential.

Thereby the dependence of SERS spectra on electrode potential can be interpreted in terms of reorientation or reversible adsorption – desorption for planar aromatic heterocycles but the factor of conformational equilibrium should be taken into account for their derivatives. In general it may be concluded that the SERS method has a unique sensitivity even to the conformational equilibrium on the surface and allows establish the interrelation between the molecule structure and the way of its adsorption.

This work was supported by the research Grant 14-03-31656 from RFBR.

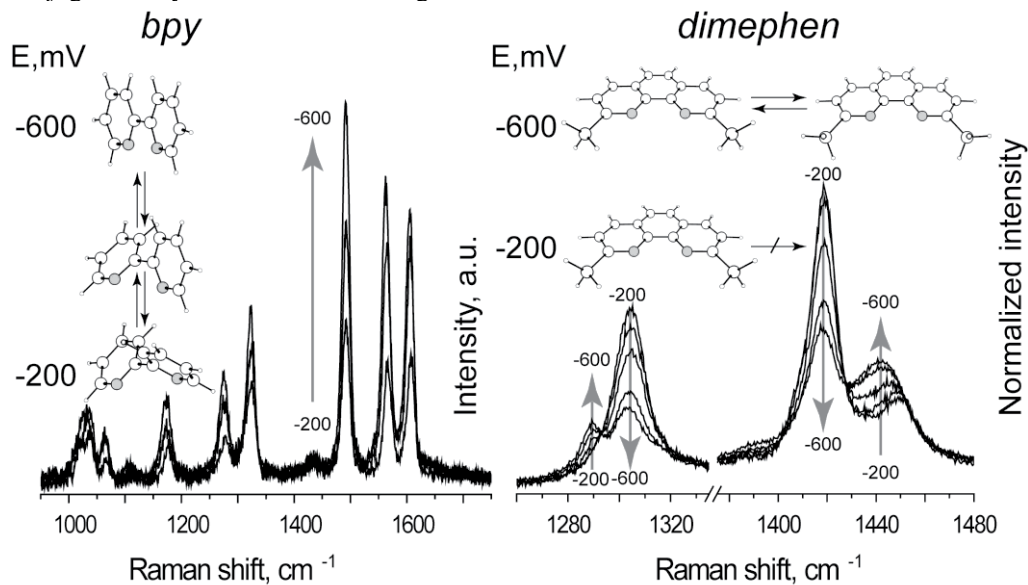


Figure 1. Potential dependence of SERS spectra of molecules with rotational degree of freedom: *bpy* – between pyridine planes, *dimephen* – around C(2,9)-CH₃

- ¹ Kneipp K., Wang Y., Kneipp H., Perelman L. T., Itzkan I., Dasari R. R., Feld M. S., (2000), *Phys. Rev. Lett.*, 78, 1667–1670.
- ² Solovyeva E.V., Myund L.A., Dem'yanchuk E.M., Makarov A.A., Denisova A.S., (2013), *J. Molecular Structure*, 1034, 19-21.

High resolution aspects of AFM based tip-enhanced Raman scattering

Volker Deckert^{1,2}, Pushkar Singh², and Steffen Trautmann²

¹Institute of Physical Chemistry and Abbe Center of Photonics, University of Jena, Helmholtzweg 4, 07743 Jena, Germany

²Leibniz Institute of Photonic Technology – IPHT, Albert-Einstein-Str. 9, 07745 Jena, Germany

Keywords: Raman scattering, plasmon, near-field optics, high resolution.

High resolution spectroscopies gained a lot of attention recently. The 2014 Nobel Prize honoring high resolution fluorescence based methods exemplifies this trend. Near-field optics provides another approach towards nanometer resolution. Here, no labels are required if vibrational techniques are utilized. Recent experimental evidence points to surprisingly high spatial resolution, in particular for tip-enhanced Raman scattering (TERS). In this contribution we intend to compare experimental evidence with theoretical modeling approaches to investigate the potential effects leading to such resolution.

Several experiments demonstrated unexpected high lateral resolution using near-field based vibrational spectroscopies.¹⁻³ The interesting feature in these cases was the fact, that the resolution was higher than the resolution predicted by standard estimations taking into account the “macroscopic” dimension of the plasmonic tip (see for instance^{4,5}). Up to now no unambiguous hypothesis of such effects has been presented and we will try to compare our experimental findings with quantum mechanical calculations as well as standard finite element calculations taking distinct tip features into account.

Two kinds of TERS experiments can reveal information regarding high resolution effects. First of all the standard resolution

test where either a line or an image is measured and the signal changes between the single steps can unambiguously assigned to a difference in molecular composition, structure or conformation. In this case only few samples can be used for such investigations in an easy way. Either the sample surface consists of sharp and defined transitions or the sample itself contains these clear molecular changes. This way a molecular ruler could be defined. A further challenge is to find the particular transitions and clearly distinct them from topographic effects. An instructive example of such topographic effects is a comparison of a scan along a DNA⁶ strand or orthogonal to a strand⁷. While a high resolution can be obtained along a strand, the convolution of tip and sample results in an apparent wide appearance of the spectra, due to the long interaction of tip and the particular sample feature. Another kind of experiment is using a different approach by using monolayers of molecules on ultra flat substrates. Here the variations in spectral position and full-width-half-maximum of the TERS data point also towards a very low number of molecules in the tip interaction area, because averaging orientation effects do not yet dominate the results.⁸

Considering the above mentioned findings we will compare such experimental findings with models that take into account for instance a crystallinity or partial

crystallinity of the near-field probes. This way the electromagnetic enhancement modeling can be pushed further towards higher resolution and the actual tip composition while less predictable is potentially modeled better.

A further way is to model the tip-sample interaction using quantum mechanical approaches. While recent

results demonstrate, that considering quantum mechanical effects leads to a blurring of the lateral resolution⁹, a more realistic modeling of the lateral resolution, taking into account “chemical effects” between tip and sample, is obviously needed to explain the experimental features. We will show how such effects can explain at least certain experimental details.

- ¹ Deckert-Gaudig, T., Kämmer, E. & Deckert, V. (2012) *J. Biophoton.* (5), 215–219 (2012).
- ² Zhang, R. *et al.* (2013) *Nature* (498), 82–86.
- ³ Chen, C., Hayazawa, N. & Kawata, S. A. (2014) *Nat Commun* (5), 3312.
- ⁴ Renger, J., Grafstrom, S., Eng, L. & Deckert, V. (2004) *JOSA* (21), 1362–1367.
- ⁵ Yang, Z., Aizpurua, J. & Xu, H. (2009) *J Raman Spectrosc* (40), 1343–1348.
- ⁶ Treffer, R. *et al.* (2012) *Biochem. Soc. Trans.* (40), 609–614.
- ⁷ Treffer, R., Lin, X., Bailo, E., Deckert-Gaudig, T. & Deckert, V. (2011) *Beilstein J Nanotechnol* (2), 628–637.
- ⁸ Singh, P. *et al.* (2015) *Phys Chem Chem Phys* (17), 2991–2995.
- ⁹ Savage, K. J. *et al.* (2012) *Nature* (491), 574–577.

Selective TERS detection in cell membranes

Zachary D. Schultz¹, Hao Wang, and Stacey L. Carrier

¹Department of Chemistry & Biochemistry, University of Notre Dame, Notre Dame, IN, 46556, USA

Keywords: TERS, plasmonics, biomembranes, chemometrics, microscopy.

Tip enhanced Raman scattering has emerged as a powerful tool for obtaining chemical information from single molecules and enabling microscopy with nanometer spatial resolution.¹ Single molecule detection typically involves a molecule located in electric field associated with a gap resonance between two coupled nanostructures.¹ Interestingly, results in ours and other labs indicate the ability of coupled nanostructures to amplify chemical specific Raman scattering from molecules beyond the gap region.²⁻³ The ability to control the interaction between plasmonic structures with tip enhanced Raman scattering (TERS) methodology, has enabled new insight into the use of plasmons for chemical analysis.

Initial results in our laboratory indicated that proteins bound to a surface could be investigated when bound to ligand-functionalized nanoparticles and detected with a TERS tip.⁴ The imaging resolution was modelled by finite element method calculations of interacting nanoparticles.⁵ Recent work in our laboratory demonstrates that controlled plasmon coupling can provide highly sensitive and selective detection of biomolecules in complex samples, specifically protein receptors in intact cellular membranes.⁶ Nanoparticles functionalized with an antagonist for a membrane receptor, generate a Raman signal characteristic of the receptor in the membrane when detected with tip enhanced Raman scattering. Results suggest that molecules in fixed orientations at the

nanoparticle probe are selectively enhanced by the plasmonic interaction between the nanoparticle and the TERS tip. Interestingly, with intact cell membranes the spectrum obtained from the tip coupling to the nanoparticle is significantly different than that observed from aggregated nanoparticles on the membrane, emphasizing the importance of a controlled interaction.

In this presentation will show our results that illustrate selective TERS detection of proteins. The membrane protein receptor $\alpha_v\beta_3$ integrin has been selectively detected within an intact cellular membrane. Chemometric analysis comparing the observed TERS signal with the SERS spectrum of the purified receptor indicates the spectrum of the receptor is selectively detected despite the presence of the diverse molecular composition found in cellular membranes.

Figure 1 illustrates our experiment and shows spectra obtained in both the TERS and reference SERS experiments. Using a nanoparticle with a ligand specific for the integrin protein, the same Raman spectrum is detected in the cell membrane and from SERS of the purified protein. The observed Raman bands can be correlated to the amino acids that are known to be involved in ligand-recognition. Control experiments indicate that this selective detection can be used to screen molecules interacting with the cell membrane.

To further understand this selectivity we have performed experiments with mutant proteins. The amino acids closest to the nanoparticle probe are key contributors to the observed Raman signal. These results

suggest a selective approach to monitoring chemical reactions relative to drug screening and chemical signalling in cells.

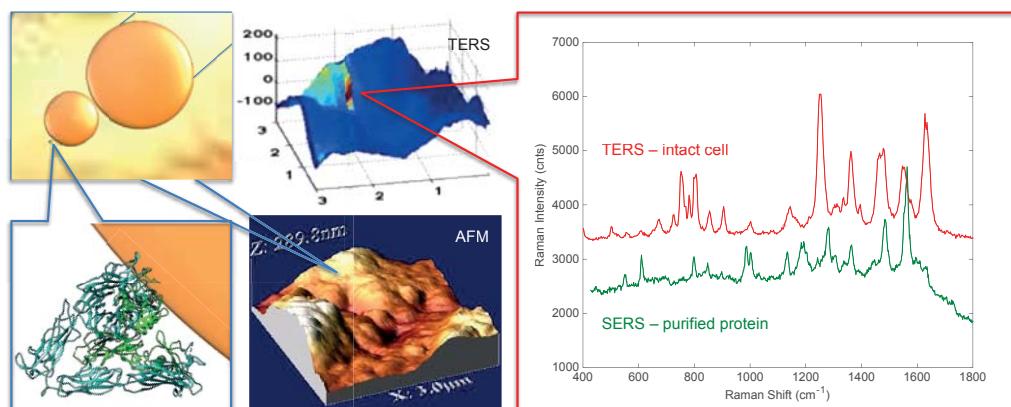


Figure 1. TERS detection of ligand functionalized nanoparticles bound to cell membranes provides selective detection of membrane receptors. Overlaying the TERS intensity onto the AFM topography enables us to correlated observed features. Nanoparticles functionalized with a peptide specific for the integrin protein give rise to the same spectral signature from both TERS in an intact cell and SERS with the purified protein in solution.

¹ Schultz, Z. D.; Marr, J. M.; Wang, H., (2014) *Nanophotonics* 3 (1-2), 91-104.

² Wang, H.; Schultz, Z. D., (2013) *Analyst* 138 (11), 3150-3157.

³ Willets, K. A.; Stranahan, S. M.; Weber, M. L., (2012) *J. Phys. Chem. Lett.* 3 (10), 1286-1294.

⁴ Carrier, S. L.; Kownacki, C. M.; Schultz, Z. D., (2011) *Chem. Commun.* 47 (7), 2065-2067.

⁵ Alexander, K. D.; Schultz, Z. D., (2012) *Anal Chem* 84 (17), 7408-14.

⁶ Wang, H.; Schultz, Z. D., (2014) *ChemPhysChem* 15 (18), 3944-9.

AFM-Tip Enhanced Near-Field Raman Imaging Analysis of Single-Molecule and Single-Electron Interfacial Electron Transfer Dynamics at Chemical and Biological Interfaces

H. Peter Lu

Bowling Green State University, Department of Chemistry and the Center for Photochemical Sciences, Bowling Green, OH 43403

Interfacial electron transfer dynamics is important for environmental and catalytic reactions. Extensive ensemble-averaged studies have indicated inhomogeneous and complex dynamics of interfacial ET reaction. To characterize the inhomogeneity and the complex mechanism, we have applied single-molecule spectroscopy and correlated AFM/STM imaging to study the Interfacial ET dynamics of dye molecules adsorbed at the surface of TiO₂ nanoparticles.¹⁻⁶ The interfacial ET activity of individual dye molecules showed fluctuations and intermittency at time scale of milliseconds to seconds. The fluctuation dynamics were found to be inhomogeneous from molecule to molecule and from time to time, showing significant static and dynamic disorders in the dynamics. Furthermore, we have applied site-specific AFM-Raman spectroscopy on analyzing ET associated mode-specific vibrational reorganization energy barriers. Our experiments revealed site-to-site variations in the vibrational reorganization energy barriers in the interfacial ET systems. We have studied ground-state single-electron self-exchange across a molecule-Metal Interface and Molecule-Substrate Electronic Coupling by Simultaneous Spectroscopic and Topographic Near-Field SERS Imaging. Single-molecule redox reaction dynamics⁷ of Hemin (Chloride) adsorbed on Ag nanoparticle surfaces has been probed by single-molecule surface-enhanced Raman

spectroscopy (SMSERS) combined with spectroelectrochemistry.⁸ Redox reaction at the molecule/Ag interface is identified and probed by the prominent fluctuations of the Raman frequency of a specific vibrational mode ν_4 , which is a typical marker of the redox state of the Iron center in a Hemin molecule. The spontaneous fluctuation dynamics of the single-molecule redox reaction is measured under no external potential across the molecule-metal interfaces, which provides a novel and unique approach to characterize the interfacial electron transfer at the molecule-metal interfaces. We have also probed single surface states and the involved interfacial charge transfer coupling on the TiO₂ surface using a tip-enhanced near-field topographic-spectroscopic imaging analysis on a Niobium-doped rutile TiO₂ (110) surface.^{9,10} The nanoscale optical images of single surface states are visualized by the strong exciton plasmon-polariton coupling localized at the sub-domain boundaries with a spatial resolution of ~ 15 nm (far beyond the optical diffraction limit). We suggest that the abundant surface states in the doped TiO₂ generate excitons under laser excitation which are strongly coupled to the surface plasmon-polaritons of the Au tip. Our demonstrated approaches are powerful for obtaining molecular electronic coupling and dynamics involving in interfacial electron transfer processes. The new information obtained is critical for a further

understanding, design and manipulation of the charge transfer processes at the molecule-metal interface or metal-molecule-metal junctions, which are fundamental elements in single-molecule electronics, catalysis, and solar energy conversion.

SERS analysis of redox proteins on *Schewanella* bacterial cell surfaces in environmental remediation applications will also be discussed.^{11,12}

- ¹ Pan, Klymyshyn, Hu, Lu, "Tip-enhanced near-field Raman spectroscopy probing single dye-sensitized TiO₂ nanoparticles," *Appl. Phys. Lett.*, 88, 093121(2006).
- ² Pan, Hu, Lu, "Probing Inhomogeneous Vibrational Reorganization Energy Barriers of Interfacial Electron Transfer," *J. Phys. Chem. B*, 109, 16390-16395 (2005).
- ³ Hu, Lu, "Single-Molecule Triplet-State Photon Antibunching at Room Temperature," *J. Phys. Chem. B*, 109, 9861-9864 (2005).
- ⁴ H. Peter Lu, "Site-Specific Raman Spectroscopy and Chemical Dynamics of Nanoscale Interstitial Systems," *J. Physics: Condensed Matter*, 17, R333-R355 (2005).
- ⁵ Biju, Micic, Hu, Lu, "Intermittent Single-Molecule Interfacial Electron Transfer Dynamics," *J. Am. Chem. Soc.* 126, 9374-9381 (2004).
- ⁶ Yuanmin Wang, Xuefei Wang, Sujit Kumar Ghosh, H. Peter Lu, "Probing single-molecule interfacial electron transfer dynamics of porphyrin on TiO₂ nanoparticles," *J. Am. Chem. Soc.* ASAP Web Released (2009).
- ⁷ Vishal Govind Rao, Bharat Dhital, Yufan He, H. Peter Lu, "Single-Molecule Interfacial Electron Transfer Dynamics of Porphyrin on TiO₂ Nanoparticles: Dissecting the Complex Electronic Coupling Dependent Dynamics," *J. Phys. Chem. C*, 118, 20209-20221 (2014).
- ⁸ Yuanmin Wang, Papatya C. Sevinc, Yufan He, H. Peter Lu, "Probing Ground-State Single-Electron Self-Exchange Across a Molecule-Metal Interface," *J. Am. Chem. Soc.*, 133, 6989-6996 (2011).
- ⁹ X. Wang, D. Zhang, Y. Wang, P. Sevinc, H. Peter, Lu, A. J. Meixner, "Interfacial Electron Transfer Energetics Studied by High Spatial Resolution Tip-Enhanced Raman Spectroscopic Imaging," *Angewandte Chemie International Edition* 50, (2011) A25-A29.
- ¹⁰ Sevinc, Papatya; Wang, Xiao; Wang, Yuanmin; Zhang, Dai; Meixner, Alfred; Lu, H. Peter, "Simultaneous Spectroscopic and Topographic Near-Field Imaging of TiO₂ Single Surface States and Interfacial Electronic Coupling," *Nano Letters*, 1490-1494 (2011).
- ¹¹ V. Biju, D. Pan, Yuri A. Gorby, Jim Fredrickson, J. Mclean, D. Saffarini and H. Peter Lu, "Correlated Spectroscopic and Topographic Characterization of Nanoscale Domains and Their Distributions of a Redox Protein on Bacterial Cell Surfaces," *Langmuir* 23, 1333-1338 (2007).
- ¹² Yuanmin Wang, Papatya Sevinc, Sara Balchik, Jim Fridrickson, Liang Shi, H. Peter Lu, "Single-Cell Imaging and Spectroscopic Analyses of Cr(VI) Reduction on the Surface of Bacterial Cells," *Langmuir*, 29, 950-956 (2013).



Understanding the TERS Effect with On-line Tunneling and Force Feedback Using Multiprobe AFM/NSOM with Raman Integration

Aaron Lewis¹, Rimma Dekhter², Patricia Hamra², Yossi Bar-David² and Hesham Taha²

¹Department of Applied Physics, The Hebrew University of Jerusalem, 91404, Jerusalem, Israel,

²Nanonics Imaging Ltd., Har Hotzvim, 97775, Jerusalem, Israel

Keywords: TERS, Raman Scattering, Multiprobe, AFM/NSOM

Tip enhanced Raman scattering (TERS) has evolved in several directions over the past years. The data from this variety of methodologies has now accumulated to the point that there is a reasonable possibility of evolving an understanding of the underlying cause of the resulting effects that could be the origin of the various TERS enhancement processes.

The objective of this presentation is to use the results thus far with atomic force microscopy (AFM) probes with noble metal coating, etching, transparent gold nanoparticles with and without a second nanoparticle [Wang and Schultz, ANALYST 138, 3150 (2013)] and tunneling feedback probes [R. Zhang et. al., NATURE 498, 82 (2013)].

We attempt at understanding this complex of results with AFM/NSOM multiprobe techniques. Results indicate that TERS is dominated by complex quantum interactions. This produces a highly

confined and broadband plasmon field with all k vectors for effective excitation. Normal force tuning fork feedback with exposed tip probes provides an excellent means to investigate these effects with TERS probes that we have shown can circumvent the vexing problem of jump to contact prevalent in conventional AFM methodology and permit on-line switching between tunneling and AFM feedback modes of operation.

Monday

Tuesday

Wednesday

Thursday

Friday

Author Index

Monday

Tuesday

Wednesday

Thursday

Friday

Author Index



Raman spectra of carriers in ionic-liquid-gated transistors fabricated with poly(2,5-bis(3-tetradecylthiophen-2-yl)thieno[3,2-b]thiophene)

Yukio Furukawa, Kotaro Akiyama, and Jun Yamamoto

Department of Chemistry and Biochemistry, Graduate School of Advanced Science and Engineering, Waseda University, Shinjuku-ku, Tokyo, 169-8555, Japan

Keywords: Raman, conducting polymer, ionic liquid, polaron, bipolaron.

A polymer transistor using a conjugated polymer and an ionic liquid as a gate electrolyte (ionic-liquid-gated polymer transistor) attracts high attention because of a large drain current at a low voltage. These polymer ionic-gated-transistors are expected to be used as electric papers. The device performance is associated with carriers generated in the polymer by electrochemical doping with an ionic liquid. The maximum in doping level is high, because the potential window of an ionic liquid is wide. A positive polaron (charge, $+e$; spin, $1/2$) and a positive bipolaron (charge, $+2e$; spin 0) are considered as carriers in a conjugated polymer. For the understanding of device properties, the detailed analysis of these doped states is necessary. Raman spectroscopy is a powerful tool for elucidating carriers generated in doped polymers.¹

Poly(2,5-bis(3-tetradecylthiophen-2-yl)thieno[3,2-b]thiophene) (PBTTT-C₁₄) is a promising conjugated polymer. In this paper, the doped states generated by electrochemical doping with an ionic liquid have been studied by Raman spectroscopy.

An ionic-liquid-gated transistor was fabricated with PBTTT-C₁₄ and ionic liquid 1-butyl-3-methylimidazolium bis(trifluoromethylsulfonyl)-imide ([BMIM][TFSI]). The schematic device structure is shown in Fig. 1. Ni and Au were deposited on the glass substrate by the vacuum evaporation method and used as the

source and drain electrodes. The length and width of a channel region were 100 μm and 1 mm, respectively. A $\sim 100\text{-nm}$ thick film of PBTTT-C₁₄ was formed on a substrate by the spin-coating method. The thickness of the [BMIM][TFSI] layer was 0.25 mm. Raman spectra were measured on a Raman microscope (RENISHAW InVia) with excitation at 785 nm.

Raman spectra of an ionic-liquid-gated transistor are shown in Fig. 2. In these measurements, the source–drain voltage was fixed to -100 mV ; the gate voltage (V_G) was changed from 0.0 to -2.2 V . The Raman spectrum at $V_G = 0.0\text{ V}$ is attributed to PBTTT-C₁₄. As the $-V_G$ bias increases, spectral changes are observed. At $V_G = -0.8\text{ V}$, the observed spectrum is attributed to positive polarons, because the spectrum is quite similar to that of positive polarons generated by chemical oxidation. As the $-V_G$ bias increases, electrochemical oxidation of the PBTTT-C₁₄ film proceeds. As the $-V_G$ bias increases further, spectral changes are observed. Above $V_G = -1.6\text{ V}$, no changes are observed. These spectra are attributable to positive bipolarons, because the spectra are quite similar to that of positive bipolarons generated by chemical oxidation. In the V_G range between -0.8 and -1.6 V , a positive polaron is oxidized to form a positive bipolaron. Thus, positive polarons and bipolarons coexist in this range.

Drain currents were measured against gate voltages for this transistor. The drain

current rose at -1.2 V, and increased rapidly. The current showed the maximum at -1.9 V. These results indicate that positive bipolarons are major carriers in the "on" state of the transistor. In most conjugated polymers, positive polarons are major

carriers. Thus, PBTTT- C_{14} is a unique conjugated polymer, where positive bipolarons are stable. We have demonstrated that Raman spectroscopy is a powerful tool for detecting in situ carriers formed in ionic-liquid-gated transistors.

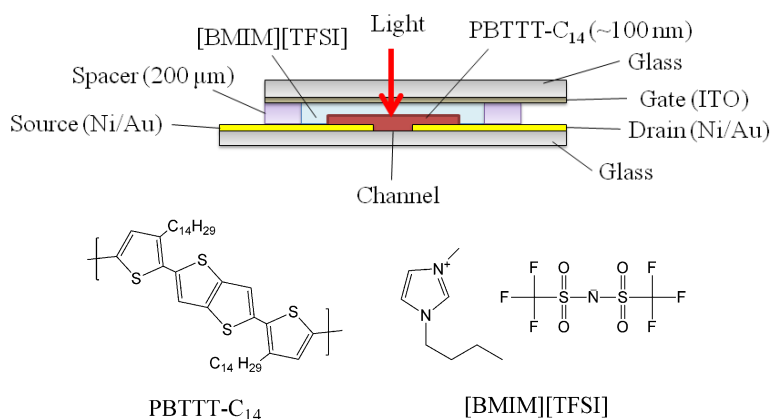


Figure 1. Schematic device structure of an ionic-liquid-gated transistor.

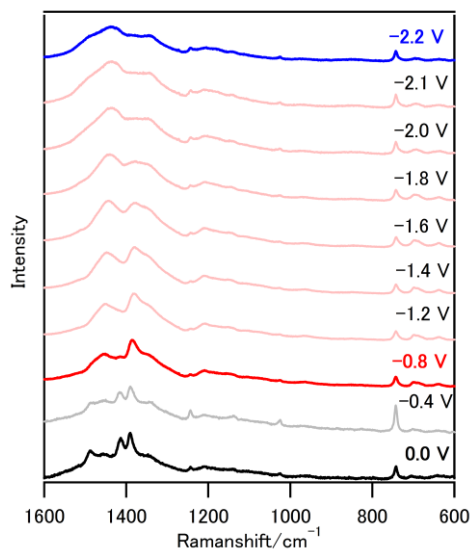


Figure 2. Raman spectra of an ionic-liquid-gated transistor fabricated with PBTTT- C_{14} and [BMIM][TFSI] as a function of V_G .

¹ J. Yamamoto and Y. Furukawa, *J. Phys. Chem. B*, in press. DOI: 10.1021/jp512654b.

Chemical mapping in light-emitting electrochemical cells

Mohammad J. Jafari¹, Jiang Liu², Isak Engquist² and Thomas Ederth^{1,*}

¹Division of Molecular physics, IFM, Linköping University, SE-581 83, Linköping, Sweden

²Dept of Science and Technology, Linköping University, SE-601 74, Norrköping, Sweden
(mohja@ifm.liu.se), Ederth (ted@ifm.liu.se)

Keywords: Infrared microscopy, Light-emitting electrochemical cell, Ion migration, MEH-PPV.

Fourier-Transform Infrared microscopy is a practical and frequently used tool for chemical mapping and imaging of samples, based on spatially resolved imaging of components' molecular vibrations, and with rational measurement and evaluation times. The infrared spectrum reveals composition and molecular bonding at a resolution of a few micrometers, and identifies molecular structure in the fingerprint region (1450-600 cm⁻¹), and diatomic stretching vibrations in the group frequency region (4000-1450 cm⁻¹) which can be used to identify functional groups. Infrared microscopy can be used for quantitative evaluation of material density changes caused by, for example, diffusion or chemical reactions.

Polymer light-emitting electrochemical cells (LECs) are solid-state electrochemical devices, which can generate light from an electrical current. These are two-terminal (planar or sandwich) devices with an organic/polymer semiconductor with mobile ions between electrodes¹. Polymer LECs take advantage of the ionic conductivity of organic semiconductors to achieve reduced charge injection barriers and low turn-on voltages². Infrared microscopy is a promising method for mapping structural changes in polymer films, and to obtain a deeper understanding about ion mobility in

LECs. To this end, we captured IR images and spectra of the region between two planar electrodes, and also attempt time-resolved imaging of ionic transport between the electrodes.

The device is a planar LEC with a 300 μm gap, consisting of the light-emitting polymer poly[2-methoxy-5-(2-ethylhexyloxy)-1,4-phenylenevinylene] (MEH-PPV) and an ion-conductive electrolyte poly(ethylene oxide) (PEO) and the salt is potassium triflate (CF₃SO₃K, or Ktri)³. Infrared measurements were carried out with a Bruker HYPERION 3000 microscope, equipped with an array detector (128x128 px resolution), giving a lateral resolution of 2 μm. Images were captured every 5 min over 1 h, between 4000-800 cm⁻¹ and with a 4 cm⁻¹ spectral resolution.

The optical micrograph of an LEC device (active film between anode and cathode) is shown in figure 1b. Figure 1a and 1c represent the distribution of the intensity at 1265 cm⁻¹, related to the asymmetric vibration of sulfonate; the density of the sulfonate indicates the volume density of triflate ions. As shown in figure 1a, triflate is homogeneously distributed before applying potential, but after applying potential (4V) for 1 hour at 60°C (figure 1c), the density of triflate ions increased at the anode side and decreased at the cathode

side. Figure 1d shows infrared spectra of the active material under zero bias (1), under forward bias at the anode (2) and cathode (3) sides, respectively. This change in triflate density demonstrates ion diffusion in the active layer. Bands at 1503 and 1413 cm^{-1} are due to C=C and C α =C β vibrations of a benzoid ring in MEH-PPV at zero bias (Figure 1d, spectrum 1). Under forward bias, the band position did not change at the cathode side (spectrum 3). At the anode side (spectrum 2), bands are shifted to 1489 and

1432 cm^{-1} , which is related to quinoid ring vibration and shows benzoid-quinoid reaction in MEH-PPV. This reaction confirms polymer doping and formation of a p-n junction in the MEH-PPV polymer, and subsequent dedoping at zero bias.

In this work, we show that infrared microscopy is a robust tool for *in-situ* characterization of electroactive organic materials and chemical reactions in soft active layers.

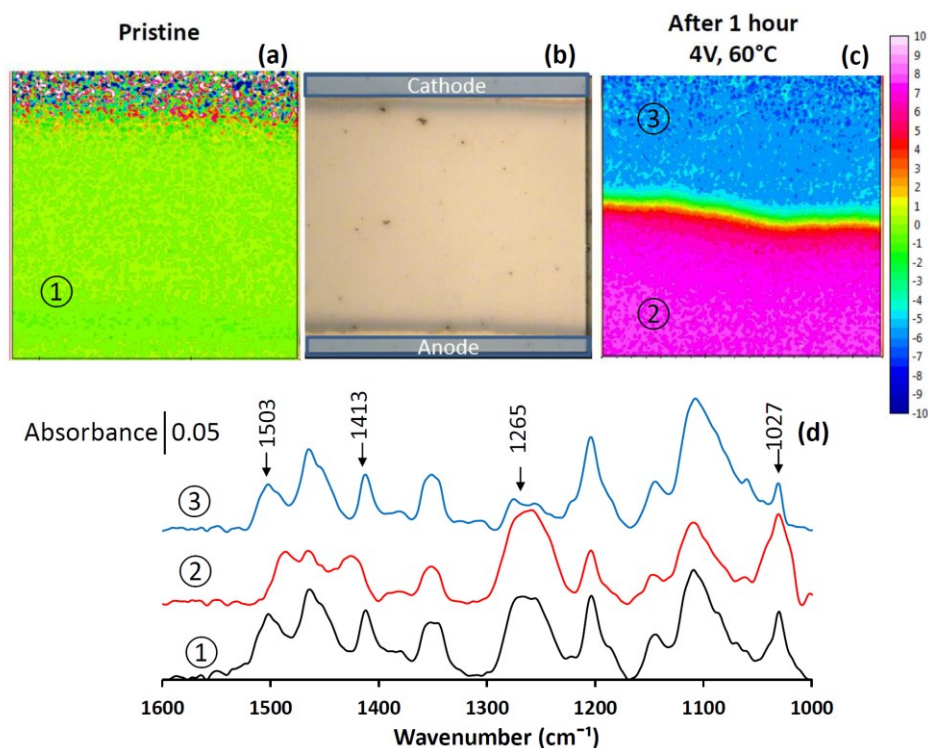


Figure 1. (b)Optical and (a, c) infrared microscopic images of LEC device, before and after applying potential, respectively, (d) infrared spectra related to pointed areas.

¹ Meier S.B. et al. (2014) *Materials Today*, 17 (5), 217-223.

² Shoji T.K. Zhu Z., Leger J.M. (2013) *Appl. Mater. Interfaces*, 5, 11509-11514.

³ Liu J., Engquist I., Crispin X., Berggren M. (2012) *JACS*, 134, 901-904.

Investigation onto the degradation mechanisms affecting long term stability of hybrid and organic photovoltaic devices by means of Raman spectroscopy

Antonio Agresti¹, Sara Pescetelli¹ and Aldo Di Carlo¹

¹C.H.O.S.E. (Centre for Hybrid and Organic Solar Energy),
Department of Electronic Engineering, University of Rome Tor Vergata, Via Giacomo Peroni
400-402, 00131, Rome, Italy

Keywords: degradation mechanisms, solar cell's stability, resonant Raman spectroscopy.

In recent years, the progress in organic and hybrid photovoltaic has been remarkable. The potential low cost of the new organic and hybrid photovoltaic technologies, even known as third generation photovoltaic, is also accompanied by their versatility in term of tunability in color and shape, transparency, flexibility, roll-to-roll production and quite high efficiencies. Beside these advantages, the feasibility of a commercialization of these technologies even requires stability under operative conditions. Since the number of the application fields is so huge and the real working conditions for a solar cell are countless and so disparate, the chemical and electrical stability remains a key point to make this technology really attracting for the market. Each type of hybrid and organic solar cell in fact suffers typical degradation mechanisms under real work conditions that need enormous efforts in designing stable chemical compounds and solar cell architectures and in developing materials and procedures for the encapsulation of the active devices against the external moisture attack.

In this optic the stability of Dye Sensitized Solar Cells (DSCs, hybrid technology) and small molecule based solar cells (SMSCs, organic technology) have been tested under real working conditions and the main degradation mechanisms have been pointed

out by mean of Resonant Raman Spectroscopy (RRS).

In particular reverse bias (RB) stress has been reproduced on a DSC in order to simulate the working condition experienced by a series-connected solar cell in a module when shadowing phenomena occur on it, and the degradations involving both dye molecules and electrolyte solution (cell structure in Fig.1a) have been investigated. Largely before complete device's breakdown, consisting in a turbulent bubbling of electrolyte solution causing electrolyte leakage from active area and strong color heterogeneity on photo-electrode, we detected polyiodides species in electrolyte solution by RRS (Fig.1b and 1c). Even the marked fluorescence background affecting the Raman spectra has been useful in order to discover and classify other degradation induced products in the electrolyte solution; various associated structures among 1-methyl-3-propylimidazolium iodide (PMII) ions were detected, giving a clear explanation about the strong I_3^- ions depletion and about the consequent strong unbalance in redox couple I/I_3^- that leads to the final device's breakdown. Furthermore RRS on a completely degraded solar cell clarified that the apparent N719 dye bleaching in particular zones of the cell active area, can be reasonably attributed to the irreversible structural changes (involving SCN^- ligand)

that affect dye molecule in some zones of photo-electrode which are not in contact with electrolyte solution, during the turbulent final stages of RB stress test¹.

On the other hand, since small molecule solar cell are at the prototype stage yet, thermal and humidity aging tests have been applied on the most customary zinc-phthalocyanine/fullerene (ZnPc/C₆₀) planar heterojunction solar cells (devices structure in Fig.1e). By comparing Raman spectra acquired on active area of fresh, thermal stressed and humidity aged devices (Fig.1d), it has been possible to demonstrate that the coarsening of C₆₀ grains induced by prolonged thermal stress (@85°C) is the responsible for the well-known burn-in phenomenon, consisting in a degradation of

the initial value device electrical parameters before to reach a stabilized value.

In conclusion this work reports a further inside investigation in the long term stability of hybrid and organic photovoltaic devices and reveals degradation mechanisms never taken into account before, by applying Raman spectroscopy. The possibility to apply the vibrational spectroscopy on sealed devices under operative conditions, the non-destructive character and the independence of the investigative technique from the device's structure give a new route to improve the reliability of the third generation photovoltaic devices and to accelerate the appearance of these innovative technologies in the global commercial scenario in a next future.

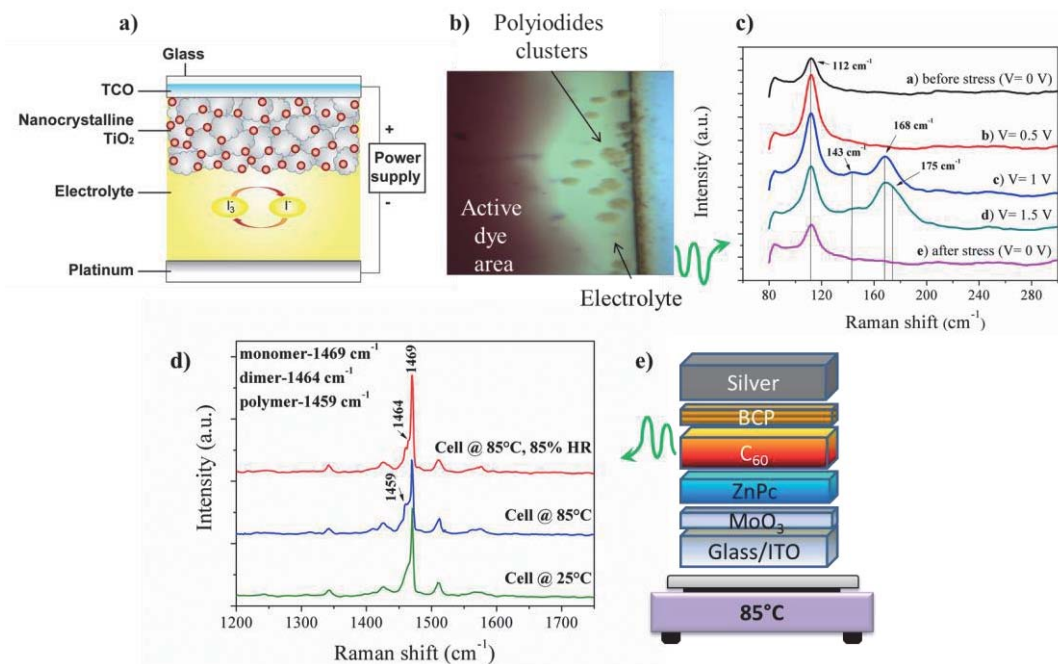


Figure 1. a) DSC scheme, b) polyiodides clusters, c) Raman spectra of polyiodides clusters under RB, d) Raman spectra of differently stressed SMSC, e) SMCS structure.

¹ Agresti A., Pescetelli S., Quatela A., Mastroianni S., Brown T.M., Reale A., Bignozzi C.A., Caramori S., Di Carlo A., (2014), *RSC Advance*, 4, 12366-12375.

FTIR-spectroscopic investigations on the absorption of metamaterial multi-arrays built by sub-micron single-structures

Gabriele C. Eder¹, Christian Brandl², Boril S. Chervnev², Astrit Shoshi³ and Hubert Brückl³

¹OFI, Austrian Research Institute for Chemistry and Technology, 1030 Vienna, Austria.

²ZFE, Graz Centre for Electron Microscopy and Nanoanalysis, 8010 Graz, Austria.

³Danube University Krems, Center for Integrated Sensor Systems, 2700 Wr. Neustadt, Austria.

Keywords: Infrared-microscopy, Absorbance, Sub-micron structures, FTIR-imaging, Metamaterials.

Metamaterials consist of artificial periodic structures with unusual optical properties. These materials can show a variable/tunable absorption behavior for electromagnetic irradiation (infrared region) in dependence on the dimensions and arrangement of the metallic sub-micron periodic structures applied on the surface [1,2].

Fourier Transform InfraRed spectroscopic (FTIR) reflection

measurements on arrays of absorber elements were performed in order to elaborate their selective absorption behavior. On the one hand, the averaged absorption on 100µm x 100µm test arrays consisting of special arrangements of sub-micron structures was investigated and the absorption maximum and intensity was determined. On the other hand the absorption of single absorber structures was probed by FTIR-Imaging. This method allows for a 2-dimensional visualization of the absorption behavior of the area under investigation with a high spatial resolution.

The spectroscopic system used for the investigations was a BRUKER Hyperion 3000 FTIR microscope equipped with Mercury Cadmium Telluride (MCT) single point and Focal Plane Array (FPA; 64x64 elements) detection systems. The

microscope is coupled to a TENSOR 27 spectrometer (BRUKER) which can be operated both, in the mid- and near-IR-region.

The averaged reflection spectra were recorded using a x15 Cassegrain objective in the range from 4000 – 600 cm⁻¹ with a spectral resolution of 4 cm⁻¹; 32 scans were coadded. The measurement range was adjusted with metal knife-edge apertures to 100µm x 100µm, and then systematically reduced down to 10µm x 10µm. For the FTIR reflection images an area of 170µm x 170µm was measured with the FPA detection system in conjunction with the above mentioned x15 Cassegrain lens. The spectral range was 4000-900 cm⁻¹ and the spectral resolution 8 cm⁻¹.

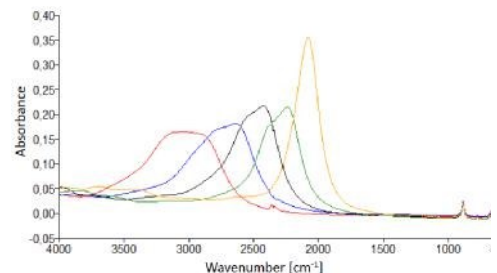


Fig.1 Absorption of test arrays varying in the diameter of the absorber structure (red = small diameter, yellow = large diameter)

The model samples were built of several multi-arrays with varying geometry. In Fig. 1 an example for the change in the absorption behavior of test arrays with increasing diameter of the individual absorber structures is given. The larger the diameter of the test structure, the lower is the wavenumber of the absorption maximum.

In addition, the absorption of single sub-micron structure points was evaluated by using the FTIR-imaging technique. Exemplarily the image of 6 individual 500nm absorber points is given in Fig.2.

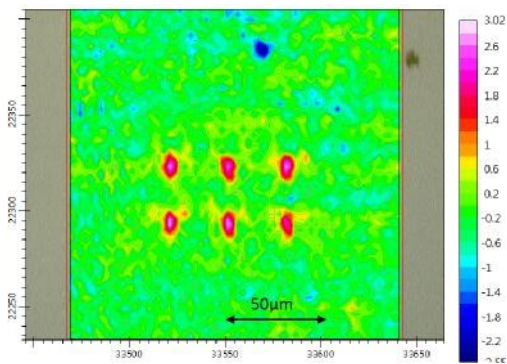


Fig.2 FTIR image of a test array containing 6 single structures (distance $\sim 30\mu\text{m}$)

Although the diameter of a single structure point is much smaller than the spatial resolution of FTIR-imaging [3], the changes in the absorption behavior of test array due

to the presence of the 6 sub-micron structures can be clearly visualized.

The FTIR spectrum of a single point was extracted from the image and the absorption maximum was determined to be at 2100 cm^{-1} , which is in good agreement with the values measured for test arrays, which have absorbance structures with the same diameter (500nm) but in much closer distance to each other (300 – 2300nm). The shape of the absorption peaks, however, changes with increasing distance between the individual structure points: the larger the distance, the sharper the peaks get.

With these results we could prove the suitability of FTIR reflection measurements for the investigation of the variable absorption behavior of metamaterials.

¹ T. Maier and H. Brückl, Opt. Lett. 34, 3012 (2009).

² T. Maier and H. Brückl, Opt. Lett. 35, 3766 (2010).

³ Review: Spatial resolution in infrared microspectroscopic imaging of tissues Peter Lasch, Dieter Naumann, Biochimica et Biophysica Acta 1758, 814 (2006).

Structurally dissimilar phase separation in $\text{La}_{5/8-y}\text{Pr}_y\text{Ca}_{3/8}\text{MnO}_3$ thin films

Dileep K Misra^{1,2}, R. Rawat² and V. G. Sathe²

¹ Department of Condensed Matter Physics & Materials Science, Tata Institute of Fundamental Research, Mumbai 400005, India,

² UGC- DAE Consortium for Scientific Research, Indore 452001, India

Keywords: Raman scattering, Phase separation, Thin films, Strain disorder

From last century, colossal magneto resistance (CMR) phenomena are under intense research investigation. Understanding of CMR is centered on the phase separation (PS). In colossal magneto resistive manganites, coupled electronic, magnetic and elastic interactions lead to energetically favorable local PS with varying lengthscales from nano meter (nm) to micro meter (μm). Underlying physics behind origin of large (μm) sized PS is debated. $\text{La}_{5/8-y}\text{Pr}_y\text{Ca}_{3/8}\text{MnO}_3$ (LPCMO) is a prototype system to study highly intriguing μm sized PS. In LPCMO, low temperature ferromagnetic metallic (FMM) phase and high temperature charge ordered antiferromagnetic insulating (CO-AFI) phases are separated by first order phase transition (FOPT). The width of the FOPT is broadened by quenched disorder and argued to be responsible for large sized PS, however there is another view point: long range strain interaction that is also suggested to be an important aspect for stabilization of μm sized PS. Recently, using magnetic force microscopy in LPCMO thin films, we have shown that nucleation and growth of the FMM phase cannot be explained solely by quenched disorder and have to consider other extrinsic causes [1]. Our further study elucidates that extrinsic disorder stabilizes low temperature FMM phase at larger length scale [2, 3]. In present work structural aspect of coexisting phases has been explored by low temperature Raman spectroscopy.

The epitaxial LPCMO ($y = 0.45$) thin films of 100nm and 200nm thicknesses on LaAlO_3 substrate are prepared by pulsed laser deposition technique. The films are well characterized using X-ray diffraction, phi-scan and reciprocal space mapping techniques and are found to be single phase, crystalline and epitaxial in nature. Strain analysis shows 100 nm thick film is fully strained while 200nm thick film has significant amount of strained phase along with relaxed phase i. e. having high degree of strain field inhomogenities termed as ‘strain disorder’. Magneto transport measurements on the films showed that on lowering temperature strained film has highly insulating character and strain disordered film shows metallic behavior below 100 K. The result is consistent with our previous studies that strain disorder favors nucleation and growth of FMM phase at low temperatures [2,3]. Therefore, below 100K strained film has insulating phase while strain disordered film possesses metallic phase. In order to investigate structural aspect of the insulating and metal phases, low temperature Raman study is performed on both films. At Room temperature both films shows identical Raman feature, revealed that both films have same structure at room temperature. On lowering temperature below 100K Raman signature of strained and strain disordered films differ significantly as shown in Figure 1(a,b). In strained film (Fig 1(a)) at 80 K,

intensity of Jahn Teller (JT) modes is found to be very intense along with appearance of new Raman peaks (shown by arrows) owing to structural change (From Pbnm to $P2_1/m$) by charge ordering revealed that insulating phase is charge ordered JT distorted. While, in strain disordered film (Fig.1(b)) JT modes suppressed below 100 K along with appearance of a new peak at 450 cm^{-1} (shown by arrow), these features signifies towards rhombohedral (R3-C) dynamical JT distorted phase. Therefore, metallic phase has R3-C like symmetries. In Raman maps shown in Figure 1(c,d), intensity of JT is

plotted as a function of spatial coordinates. For insulating film, nearly uniform spatial distribution of intensity (1%) is observed signifying the presence of predominant JT distorted CO-AFI phase. On the other hand, large spatial distribution (6%) is observed for metallic film, indicates towards presence of coexisting CO_AFI and FMM phases.

Therefore, in low temperature PS states, coexisting charge-ordered-insulating and ferromagnetic-metallic phases are structurally dissimilar and possess $P2_1/m$ and R-3C like symmetries respectively.

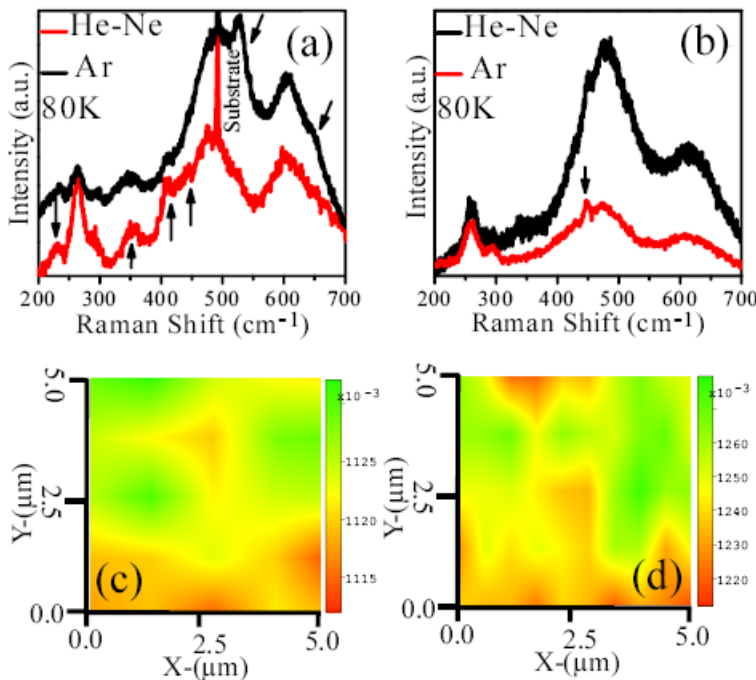


Figure1. (a,b) Raman spectra of strained and strain disordered thin film collected at 80K using Ar nm and He-Ne laser lines. (c,d) Raman mapping at 80 K on both of the films.

¹ R. Rawat, P. Kushwaha, D. K. Mishra, and V. G. Sathe, (2013), *Phys. Rev. B*, 87, 064412.

² D. K. Mishra, V. G. Sathe, R. Rawat, and V. Ganesan, (2013), *J. Phys.: Condens. Matter*, 25, 175003.

³ D. K. Mishra, V. G. Sathe, R. Rawat, V. Ganesan¹, R. Kumar, and T. K. Sharma, (2015), *App. Phy. Lett.*, 106, 072401.

Recent advances in micro and macro ATR-FTIR spectroscopic imaging

Sergei G. Kazarian

Department of Chemical Engineering, Imperial College London, South Kensington Campus,
SW7 2AZ, London, United Kingdom

Keywords: chemical imaging, internal reflection, depth profiling, polymers

Recent developments in Attenuated Total Reflection Fourier Transform Infrared (ATR-FTIR) spectroscopic imaging and their applications to a very broad range of materials made this approach into a powerful and versatile analytical tool for analysis of many systems, particularly for studies of dynamic processes.¹⁻³

The most recent developments in ATR-FTIR spectroscopic imaging and its applications will be summarized here. Two complementary approaches have been used, providing flexibility with field of view and spatial resolution: micro ATR-FTIR imaging using a microscope objective with a Ge crystal, and macro ATR-FTIR imaging using a single-reflection ATR accessory, the latter provides many opportunities for studying dynamic chemical systems. Recent advances in micro ATR-FTIR imaging include application of optical apertures for the Ge microscope objective to provide control of the angles of incidence in micro ATR-FTIR imaging.⁵ This new approach provides the possibility of depth profiling using this mode of measurement in FTIR imaging. It has been demonstrated that this approach allowed us to obtain images of polymer laminates with different depths of

penetrations.

Recent advances in macro ATR-FTIR imaging with the use of inverted prism crystals demonstrate good potential with applications to dynamic processes by collecting spectral imaging datasets as a function of time, revealing spatially resolved and chemically specific information about the samples. The ATR accessory based on diamond inverted prism is particularly suited for such studies and was beneficially used for protein aggregation and imaging of fast drying of polymeric films.⁴

The application of fast ATR-FTIR imaging to drying of latex films allowed us to spatially resolve distribution of water and chemical components of the drying films during fast drying and to reveal different stages of drying process. It has been shown that using ATR-FTIR imaging, one can clearly distinguish regions of fast and slow drying via the concentrations of water and polymer, indicative of skin formation under these drying conditions, which is important for understanding the high-speed drying of paints and adhesives, where it is desirable to minimise the drying time and energy expenditure, and produce smooth, consistent films.

¹ Kazarian S. G. Chan K. L. A. (2010) *Applied Spectroscopy* 64 (5) 135A-152A.

² Kazarian S. G. Chan K. L. A (2013) *Analyst* 138, 1940-1951.

³ Kimber A. A., Kazarian S. G. (2014) *Spectroscopy* 29(10), 34-44.

⁴ Wrobel T. P., Vichi A., Baranska, M., Kazarian S. G. (2015) *submitted*.

⁵ Boulet-Audet, M., Byrne B., Kazarian S. G. (2014) *Analytical Chemistry* 86(19), 9786-9793.

⁶ Kimber, J. A., Gerst M., Kazarian S. G. (2014) *Langmuir* 30, 13588-1359.



ATR-IR-based molecular-scale thermometer reflecting free volume changes due to azobenzene photoisomerization

Jaana Vapaavuori¹, Audrey Laventure¹, Jérémie Bourotte¹, Olivier Lebel², C. Geraldine Bazuin¹ and Christian Pellerin¹

¹Département de chimie, Université de Montréal, Montréal, QC, H3C 3J7, Canada

²Department of Chemistry and Chemical Engineering, Royal Military College of Canada, Kingston, ON, K7K 7B4, Canada

Keywords: ATR-IR spectroscopy, azobenzene, photoinduced mechanical changes

One of the most pertinent questions in the field of stimuli-responsive materials, both from the standpoint of fundamental understanding and for optimizing the materials for high-technology applications, is how repetitive photoisomerization cycles of azobenzene derivatives under illumination can drive the photo-induced motion of the material over macroscopic scales. This phenomenon can be used in all-optical fabrication of nano- and micro-structured surfaces,¹ as well as in imaging of plasmonic structures.² Multiple mechanisms on how the light renders polymeric materials malleable at temperatures well below (often 50 to 100 K) their glass transition temperature (T_g) have been proposed and there is ongoing debate on the nature of photoisomerization-induced changes in mechanical properties. The discussion is complicated by the difficulties in relating results from different methods used for measuring bulk mechanical properties to the disturbance created by photoisomerization at the molecular level of the material system. Experimental methods elucidating the latter aspects and allowing direct comparison of different material systems are thus needed.

Herein, we show for the first time that the free volume created upon photoisomerization is non-uniformly distributed at molecular scale. By employing ATR-IR spectroscopy with *in-situ* heating and illumination of the material, we follow the

photo-induced increase in the mobility of the material reflecting the free volume increase created by increased thermal motion upon heating. Trends regarding the IR wavenumber shifts for the azo-containing standard pDR1A homopolymer and a DR1-containing mexylaminotriazine molecular glass (gDR1, structure shown in Figure 1a) under illumination of nonpolarized light at 520 nm are found to correlate with the changes observed during heating of the samples in a non-uniform manner. The extent of this correlation is quantified through defining the concept of apparent temperature, as demonstrated in Figure 1b.

Our results show that different vibrational modes reach different apparent temperatures under uniform illumination conditions, indicating that more free volume is created closer to the functional groups of the photoactive molecular moiety. In sharp contrast, the apparent temperature of the pDR1A backbone and the triazine moiety of the gDR1 molecular glass remains unchanged. Through this method, the apparent temperature gradient along the molecule can be mapped and is found to exceed 100 °C under illumination of 100 mW/cm² of 520 nm light for both molecules under study. Combined with the photo-orientation ability of these molecules, these apparent temperature gradients offer a plausible explanation for the origin of directional photoinduced diffusion of the

materials below their glass transition. They also offer an experimental support for the hypothesized worm-like (directionalized along the molecular axis) diffusion motion, first proposed by Lefin and co-workers,³ and further developed by Juan et al. to account for polymer motion both upon surface relief grating formation⁴ and under nanoplasmonic fields.⁵ Along with Fang et al.,⁶ we thus advance the idea that certain parts of

molecules can “feel” being at a much warmer temperature than ambient without the total material temperature increasing above or even close to its T_g . We will also present our preliminary investigations on how the observed photomobility depends on the T_g of the photopassive matrix in supramolecular mixtures of gDR1 with molecular glasses of varying T_g .

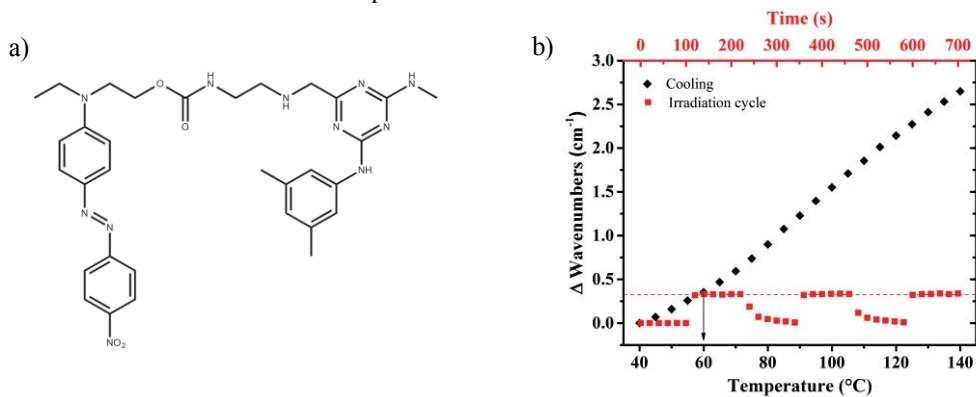


Figure 1. a) Structure of the gDR1 molecular glass and b) determination of the apparent temperature by correlating spectral shifts as a function of temperature (black) and illumination (red).

1. (a) Priimagi, A.; Shevchenko, A., Azopolymer-based micro- and nanopatterning for photonic applications. *J. Polym. Sci. Part B: Polymer Physics* **2014**, *52*, 163; (b) Lee, S.; Kang, H. S.; Park, J. K., Directional photofluidization lithography: micro/nanostructural evolution by photofluidic motions of azobenzene materials. *Adv. Mater.* **2012**, *24*, 2069
2. (a) Haggi, M.; Dridi, M.; Plain, J.; Marguet, S.; Perez, H.; Schatz, G. C.; Wiederrecht, G. P.; Gray, S. K.; Bachelot, R., Spatial confinement of electromagnetic hot and cold spots in gold nanocubes. *ACS Nano* **2012**, *6*, 1299; (b) Hubert, C.; Rumyantseva, A.; Lerondel, G.; Grand, J.; Kostchev, S.; Billot, L.; Vial, A.; Bachelot, R.; Royer, P.; Chang, S. H.; Gray, S. K.; Wiederrecht, G. P.; Schatz, G. C., Near-field photochemical imaging of noble metal nanostructures. *Nano Letters* **2005**, *5*, 615
3. P. Lefin, C. Fiorini., J.-M. Nunzi, *P. Appl. Optics* **1998**, *7*, 71
4. Juan, M. L.; Plain, J.; Bachelot, R.; Royer, P.; Gray, S. K.; Wiederrecht, G. P., Stochastic model for photoinduced surface relief grating formation through molecular transport in polymer films. *App. Phys. Lett.* **2008**, *93*, 153304.
5. Juan, M. L.; Plain, J.; Bachelot, R.; Royer, P.; Gray, S. K.; Wiederrecht, G. P., Multiscale model for photoinduced molecular motion in azo polymers. *ACS Nano* **2009**, *3*, 1573
6. Fang, G. J.; Maclennan, J. E.; Yi, Y.; Glaser, M. A.; Farrow, M.; Korblova, E.; Walba, D. M.; Furtak, T. E.; Clark, N. A., Athermal photofluidization of glasses. *Nature Communications* **2013**, *4*, 1521.

ATR-IR spectroscopic observations of water structure in zwitter-ionic polymers

Shigeaki Morita

Department of Engineering Science, Osaka Electro-Communication University, 18-8
Hatsucho, Neyagawa 572-8530, Japan

Keywords: biomaterials, betaine, wet polymer, hydration, salt addition

Water molecules play important roles in biocompatibility of medical polymers at their biointerfaces.¹ Our group has revealed hydration structures of antithrombogenic polymers at a functional group level using attenuated total reflection infrared (ATR-IR) spectroscopy.^{2,3} In the present study, water structure in three different antithrombogenic polymers having zwitter-ionic groups was investigated using ATR-IR spectroscopy.

Figure 1 shows chemical structures of zwitter-ionic polymers used in the present study. Phospho-betaine methacrylate (PBMA), calboxy-betaine methacrylate (CBMA) and sulfo-betaine methacrylate (SBMA) were used as the zwitter-ionic monomers. Note that analogous betaine structures are found in lipid molecules of living cell membranes. All the zwitter-ionic homopolymers are water soluble. Thus, their random copolymers with *n*-buthyl methacrylate (BMA) were prepared by radical polymerization. All the obtained copolymers were water insoluble and showed stable surface in water.

A film sample was prepared on a flat surface of a ZnSe prism by solvent casting. The ATR element having the polymer film was mounted on an ATR flow trough cell. All the ATR-IR spectra of wet polymer samples were recorded after 1 hour of introducing an aqueous solution into the cell.

Figure 2 shows ATR-IR spectra of hydrated P(PBMA-*r*-BMA) film in contact with NaCl aqueous solutions at different

concentrations of 0, 0.15, 0.60, 1.20, 1.71 and 2.22 M. Bold line corresponds to the spectrum contacting with pure water. A thickness of the film sample was enough thicker than penetration depth of evanescent wave generated at the prism/sample interface. Therefore, the OH stretching band in the 3700-3000 cm⁻¹ region is arising from hydrating water in a polymer matrix, excluding evidence of bulk water contacting with the surface of the film sample. Spectral shape of the OH stretching gradually change by the salt addition. The band around 3200 cm⁻¹ gradually decreases with increasing the sodium chloride concentration, while that around 3500 cm⁻¹ gradually increases. It should be noted that total area intensities of the OH stretching band in the 3700-3000 cm⁻¹ region hardly decreased. This result represents that the hydrating water in the zwitter-ionic polymer scarcely dehydrated from the polymer matrix by the salt addition. Our recent study revealed that neutral polymer of poly(2-methoxyethyl methacrylate) (PMEA) and analogous polymers easily dehydrated by the salt addition, while zwitter-ionic polymer of P(MPC-*r*-BMA) hardly dehydrated. However, water structure in the zwitter-ionic polymer matrix is perturbed by the salt addition because of the spectral shape variation. Structure change of the hydrating water in the polymer matrix will be discussed in detail.

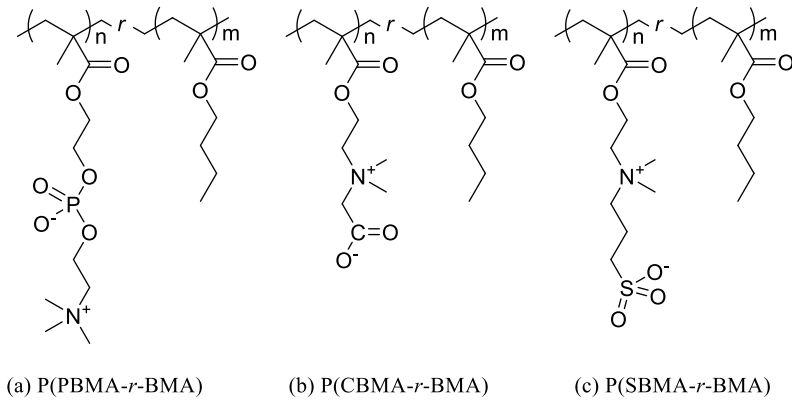


Figure 1. Chemical structures of polymers used in the present study.

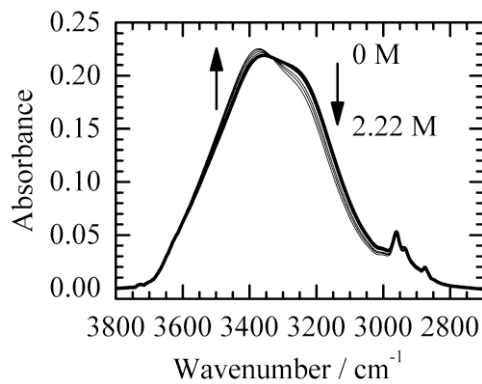


Figure 2. ATR-IR spectra of hydrated P(PBMA-*r*-BMA) film in contact with NaCl aqueous solutions. Bold line corresponds to the spectrum contacting with pure water.

- ¹ Tanaka M., Hayashi T. Morita S., (2013), *Polymer Journal*, 45, 701-710.
² Morita S., Tanaka M., Ozaki Y., (2007), *Langmuir*, 23, 3750-3761.
³ Morita S., Tanaka M., (2014), *Langmuir*, 30, 10698-10703.

Chemical Structural Analysis of an Antifreeze Solution by Using Infrared Spectroscopy with an Aid of Chemometrics

Takafumi Shimoaka¹ and Takeshi Hasegawa¹

¹Institute for Chemical Research, Kyoto University, Gokasho, Uji, Kyoto 611-0011, Japan

Keywords: Infrared Spectroscopy, Chemometrics, Ethylene Glycol (EG), Antifreeze Effect, Water/EG Complex.

Introduction: An aqueous solution of ethylene glycol (EG) is used as an antifreeze solution in various fields. Although the property should be related to a chemical structural change by the mixing, the mechanism is not revealed at a molecular level. The mixed solution should involve a constituent that is not found in the water and pure EG. To investigate the newly generated constituent in the solution in terms of a change of hydrogen(H)-bonding structure and a conformational change of the EG molecule, concentration-dependent infrared spectra are measured. Since the spectra are of multi constituents, the spectra are analyzed by using chemometrics to obtain the structure of the new constituent.

Experimental Eleven samples with various molar fractions of EG ($x_{EG}=0.0-1.0$) were prepared. IR spectra of the samples were measured by the attenuated total reflection (ATR) method using a germanium prism. The number of accumulations was 1000.

The measured spectra are analyzed by the principal component analysis (PCA) to estimate the number of constituents. To obtain the chemically independent spectra of all the constituents, the alternative least-squares (ALS) technique was employed.

Results and Discussion: In the concentration dependent spectra, with increasing x_{EG} , the vibration bands due to water decreased and disappeared, whereas

those due to EG developed. In the spectra, some isosbestic points were observed, which indicated that the spectral variation can apparently be explained by the quantity changes of the two constituents: water and EG. However, the CH_2 stretching vibration band of EG and the OH_2 bending vibration ($\nu(OH_2)$) band were accompanied by a peak shift, which suggested that the spectral variation can be related to another constituent. To estimate the number of constituents related to the spectral variation, PCA was carried out, and three or four constituents were necessary for modeling the spectral variation.

The ALS analysis considering ‘four’ constituents revealed that the spectral variation was explained by ‘three’ constituents. One of the constituents increased monotonously as a function of x_{EG} , and the corresponding spectrum denoted by (c) in Fig. 1 matches that of pure EG. There was a monotonously decreasing constituent, and the corresponding spectrum denoted by (a) matches that of bulk water. The rest constituent showed the maximum at x_{EG} of 0.3. It is interesting that the solution of $x_{EG}=0.3$ is known to show a remarkable anti-freeze effect. The corresponding spectrum (b) is shown in Fig. 1. Since this spectrum has the bands of both water and EG, the rest constituent is assigned to a ‘complex’ of the water and EG molecules. Since the amount of complex becomes dominant in the solution of $x_{EG}=0.3$ ¹, the

anti-freezing property should be correlated with the complex.

To reveal the chemical structure of the complex, the revealed spectrum is discussed in detail. First, the $\nu(\text{OH}_2)$ band is located at 1653 cm^{-1} , which is 15 cm^{-1} higher than that of pure water. This band is known to appear at a higher position when the hydrogen bonding becomes stronger. This indicates that the hydrogen bonding in the complex is stronger than that in pure water.

The antisymmetric and symmetric CH_2 stretching vibration ($\nu_a(\text{CH}_2)$, $\nu_s(\text{CH}_2)$) bands of EG in the complex appear at a higher position by 21 and 10 cm^{-1} than those of pure EG, respectively. The origin of the shift of these bands can be attributed to two possibilities: (1) the conformational change of EG molecule and (2) the changing H-bonding state about the hydroxyl (OH) group of EG. Pachler et al.², however,

reveals that the gauche conformer is dominant in both pure liquid and the solution. This indicates that a conformation of EG molecule does not change through the dissolution process in water, and the higher wavenumber shift is caused by the changing H-bonding state. In a former study, we investigated the origin of higher wavenumber shift of the CH stretching vibration band of methanol. The result reveals that the shift is caused by the hydration of the OH group in the dissolution in water; whereas the OH group forms imperfect H-bond in pure methanol.³ In the same manner, the EG molecule in the complex is fully hydrated, although the OH group forms imperfect H-bond in the pure liquid. In this way, the fully hydrated 'complex' in the solution should induce the antifreeze effect.

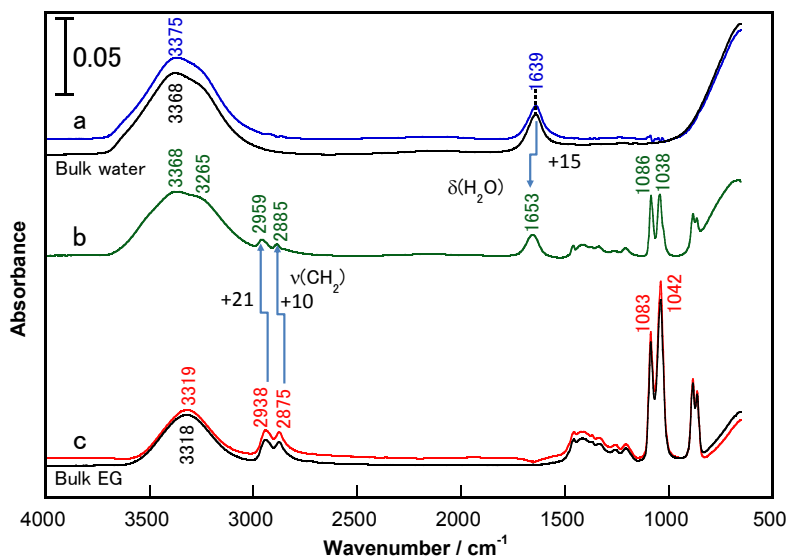


Figure 1. Decomposed spectra by the ALS method.

¹ Cordray D. R., Kaplan L. R., Woyciesjes P. M., Kozak, T. F. (1996), *Fluid Phase Equilibria*, 117, 146-152.

² Pachler K. G. R., Wessels, P. L. (1970) *J. mol. Struct.* 6, 471-478.

³ Shimoaka T., Katsumoto Y. (2010) *J. Phys. Chem. A* 114, 11971-11976.

Variable Temperature ATR-IR spectroscopy as a valuable tool for the *in situ* spin state detection of Iron(II) Spin Crossover complexes

Christian Knoll¹, Marco Seifried¹, Danny Müller¹ and Peter Weinberger¹

¹Institute of Applied Synthetic Chemistry, Vienna University of Technology,
Getreidemarkt 9/163-AC, A-1060 Vienna, Austria

Keywords: tetrazoles, iron(II) spin crossover, ATR, variable temperature.

Variable temperature vibrational spectroscopy has proved a valuable tool for structural characterization of iron(II) coordination compounds undergoing a high-spin (HS) \leftrightarrow low-spin (LS) transition. MIR- and FIR-spectroscopy of iron(II) compounds allows not only for the observation of the first order structural phase transition, but also concomitant for an *in-situ* detection of the spin state [1]. The reason for this is the drastic bond strength change of the Fe-N bonds due to the spin transition.

Especially, temperature-dependent FIR-spectroscopy is an often neglected technique, mainly due to the obstacle of sensitivity and sample preparation. It has been shown that in the FIR region there is a vibrational mode of the iron(II) coordination center towards the centroids of the coordination octahedron formed by the six coordinating nitrogen atoms of the tetrazole ligands [2]. The calculations reveal that this N3-Fe-N3' vibrational mode is almost totally decoupled from any other atomic motions of the rest of the molecule. Therefore, this absorption feature can be

used for the quantification of the high spin and low spin species, respectively, thus allowing for a very sensitive *in-situ* determination of the ratio between the high spin and low spin compounds. The molecular spin transition properties derived by variable vibrational spectroscopy is compared to complementary physico-chemical characterizations by UV-VIS-NIR spectroscopy, SQUID/VSM and ⁵⁷Fe-Mössbauer spectroscopy [3]

Herein we present an innovative custom-made setup for both temperature-dependent MIR and FIR-spectroscopy based on a PIKE Technologies ATR-Unit with a Perkin Elmer Spectrum 400 FT-MIR/FIR combination (see Fig. 1).

The resulting spectra during the observation of a phase transition using the novel ATR-setup are compared to calculated spectra for detailed assignments using DFT. The DFT calculations implemented in the Gaussian 09 software package [4] used for the free ligands the basis set 6-311G++ (2d,3p) and SDD for the complexes for the B3LYP functionals.



Figure 1. Variable temperature MIR/FIR-ATR unit

Acknowledgements:

We gratefully acknowledge financial support of Danny Müller by the Austrian Science Fund (FWF), project P24955-N28. Financial support of the COST project CM 1305 providing a short time scientific mission of Christian Knoll in the University of Warwick (UK) and a summer school at the university of Groningen (The Netherlands) is acknowledged. The computational results presented have been achieved using the Vienna Scientific Cluster VSC-1 and VSC-3.

¹ Weinberger P., Matthias G., (2004) *Vibrational Spectroscopy* 34(1), 175-186.

² Valtiner M., Paulsen H., Weinberger P. and Linert W., (2007) *MATCH Communications in Mathematical and in Computer Chemistry*, 57, 749-761.

³ Reissner M., Weinberger P., Wiesinger G., Hilscher G., Mereiter K., Linert W., (2009) *Hyperfine Interactions*, 191, 81-86.

⁴ Gaussian 09, Revision C.01, M. J. Frisch et al. Gaussian, Inc., Wallingford CT, (2010)

Detection of Virulence Markers in Highly Pathogenic Influenza by SERSRichard A. Dluhy¹, Joo-Young Choi¹, S. Mark Tompkins², and Ralph A. Tripp²¹Department of Chemistry, University of Georgia, Athens, GA 30602 USA²Department of Infectious Disease, University of Georgia, Athens, GA 30602 USA

Keywords: plasmonics, SERS, influenza, biomarkers

H5N1 avian influenza, a highly pathogenic strain of avian influenza, has raised concerns due to its potential for increased virulence in poultry and humans, with pandemic potential. Avian influenza virus (AIV) is transmitted to hosts through two viral surface glycoproteins, hemagglutinin (HA) and neuraminidase (NA). HA recognizes receptors on target cells to initiate virus infection, while NA plays a critical role in assisting virus release from infected cells and entry to new cells by removing the terminal sialic acids from oligosaccharide side chains.

The NA glycoprotein consists of four different domains, a cytoplasmic, transmembrane domain, stalk, and the globular head. The NA stalk region is located between an enzymatically and antigenically active globular head and the hydrophobic viral membrane anchored domains. This region varies in length and sequence among strains in the same subtype of NA. Many studies have suggested that insertion, deletion, or mutation of amino acids in the NA stalk region correlates with increasing the virulence of virus, host range, and replication of virus. (insert refs) NA stalk-motifs have been increasingly observed in H5N1 isolates; for example, the number of NA stalk motifs found in highly pathogenic H5N1 influenza viruses increased ~85% from 2000 to 2007. Thus, a better understanding of the correlation between the structure of NA stalk-motif and

its biological characteristics related to influenza virulence is critical.

Six different stalk motifs exist in the NA stalk region of all N1 subtype influenza virus A. These six different stalk-motifs are A/Gs/Gd/1/96/H5N1-like (with no amino acid deletion), A/WSN/33/H1N1-like (16 amino acid deletion from 57 to 72), A/Puerto Rico/8/34/H1N1-like (15 amino acid deletion from 63 to 77), A/Chicken/Italy/1067/99/H7N1-like (22 amino acid deletion from 54 to 75), and A/chicken/Hubei/327/2004/H5N1-like (20 amino acid deletion from 49 to 68).

PCR has been widely used for a rapid, sensitive, and selective screening for virulence markers. However, this method is based on the amplification of analyte for detection and relies on the design of primers, which is time-consuming and costly. Moreover, detection of new, emerging pathogens can be a problematic. This technique is also prone to false-positives or false-negatives caused by the carry-over contamination. For these reasons, there is a critical need for development of a biosensing tool to identify emerging influenza viruses in a rapid and sensitive manner with a high specificity.

Our research group has previously demonstrated a feasibility of surface-enhanced Raman spectroscopy (SERS) as a rapid, sensitive, and specific tool for detecting oligonucleotide probe-RNA target complexes in a direct and label-free manner.^{1,2} The intrinsic properties of

Raman spectra provide a unique spectral signature of SERS, sensitive enough to identify the extent of hybridization between DNA and target sequences. This method has become a widely used technique for diagnostic applications. Our recent work demonstrated a detection of DNA-RNA binding by using oligonucleotide-modified Ag nanorod array based SERS and differentiated DNA probe-complementary RNA strains from the DNA probes with non-complementary RNA sequence via multivariate analysis.

The current work aims to identify potential influenza virulence factors that occur from deletion of amino acid sequences in the NA stalk region using SERS. 5'-thiolated ssDNA oligonucleotides were immobilized onto a hexadecyl trimethyl ammonium bromide (CTAB) coated Au nanoparticle (AuNP) substrate. Three synthetic RNA sequences corresponding to specific amino acid deletions in the influenza NA stalk region were attached to the CTAB-modified AuNPs; two of these sequences were putative high virulence sequences with 20 and 15 amino acid deletions, and one was a low virulence sequence with no amino acid deletions. Hybridization of matched and mismatched DNA-RNA complexes were detected based on the intrinsic SERS spectra.

Multivariate feature selection methods were employed to determine which wavenumbers in the Raman spectra contributed the most information for class discrimination. A one way analysis of variance (ANOVA) test identified 884 and 1196 wavenumbers as being highly significant in the high and low virulence spectra, respectively ($p < 0.01$). A post-hoc Tukey Honestly Significance Difference (HSD) test identified the wavenumbers that played a major role in differentiating the DNA-RNA hybrid classes. An estimate of the spectral variability, based on the Wilcoxon rank sum test, found the major source of variation to be predominately between the different classes, and not within the classes, thus confirming that the spectra reflected real class differences and not sampling artifacts. Multivariate classification methods such as partial least squares discriminant analysis (PLS-DA) and support vector machine discriminant analysis (SVM-DA) were able to distinguish between the DNA-RNA complementary target hybrids and the hybridization of non-complementary sequences with ~95% sensitivity and specificity. This study demonstrated the feasibility of SERS for direct identification of influenza NA stalk virulence markers without sample amplification or labeling.

¹ Negri, P, Dluhy, R (2013). *Analyst*. 138, 4877-4884.

² Negri, P, Choi J-Y, Jones, C, (2014), *Analytical Chemistry*, 86, 6911-6917.

Statistical analysis of large areas of Raman mapped DNA functionalized gold coated silicon nanopillar SERS substrates

Kasper B. Frøhling¹, Tommy S. Alstrøm², Michael Bache¹, Michael S. Schmidt¹, Mikkel N. Schmidt², Jan Larsen², Mogens H. Jakobsen¹ and Anja Boisen¹

¹Department of Micro- and Nanotechnology, Technical University of Denmark, Ørsted's Plads, 2800, Kgs. Lyngby, Denmark

²Department of Applied Mathematics and Computer Science, Technical University of Denmark, Asmussens Alle, 2800, Kgs. Lyngby, Denmark

Keywords: SERS, area map, peak fitting, statistics, sensor

Detection of small molecules at low concentration by Surface Enhanced Raman Spectroscopy (SERS) has mostly been done using metal nanoparticles¹, where data is normally limited to a few measurements of different clusters. The emergence of SERS substrates with well-defined, uniform 2D layers of nanostructures has created an opportunity to increase the amount of data tremendously. The amount of data calls for new approaches for data processing and data visualization, especially when batches of large area maps are collected. However to our knowledge only limited statistical analysis on SERS maps have been published²⁻⁴.

In this work we demonstrate new ways to analyze DNA and 6-mercapto-1-hexanol (MCH) surface functionalization of a uniform gold covered silicon nanopillar SERS substrate⁵ (Figure 1; SEM images) by using a peak-fitting approach on 30x10 point area maps. Using the fitted model it is possible to observe behavior of peak creation and peak shifts during different functionalization steps. Direct characterization of a DNA and MCH functionalized SERS substrate is of high value for use in different diagnostic assays^{3,6,7}.

The analysis is carried out by jointly fitting a Voigt profile (a combination of

Lorentzian and Gaussian shaped curve) and a linear baseline correction to a given spectral window (Figure 1; graph).

The gold heads of the SERS substrate were functionalized with thiolated 75-mer DNA. The remaining gold binding sites were subsequently blocked with the small molecule MCH (Figure 1; schematic). The SERS signal was then captured in a 30x10 point area map using a 780 nm laser with 0.1 mW power and a 50x objective.

By analyzing the large amount of data, it is possible to get a statistical view of the position of SERS peaks for a given surface functionalization. Current data shows the appearance of a specific DNA peak after 15 minutes incubation in thiolated DNA solution (data not shown). Incubation for longer time does not narrow the peak position distribution nor increase the intensity distribution of the peaks. Data on MCH backfilling show significant change in peak position of the DNA peak for different MCH concentrations (Figure 1; histogram). Smaller concentrations show only a slight shift of the DNA peak position, while the largest show only the MCH peak.

The statistical tool presented allows for direct inspection, interpretation and comparison of batches of SERS maps on uniform SERS substrates that would otherwise not be possible.

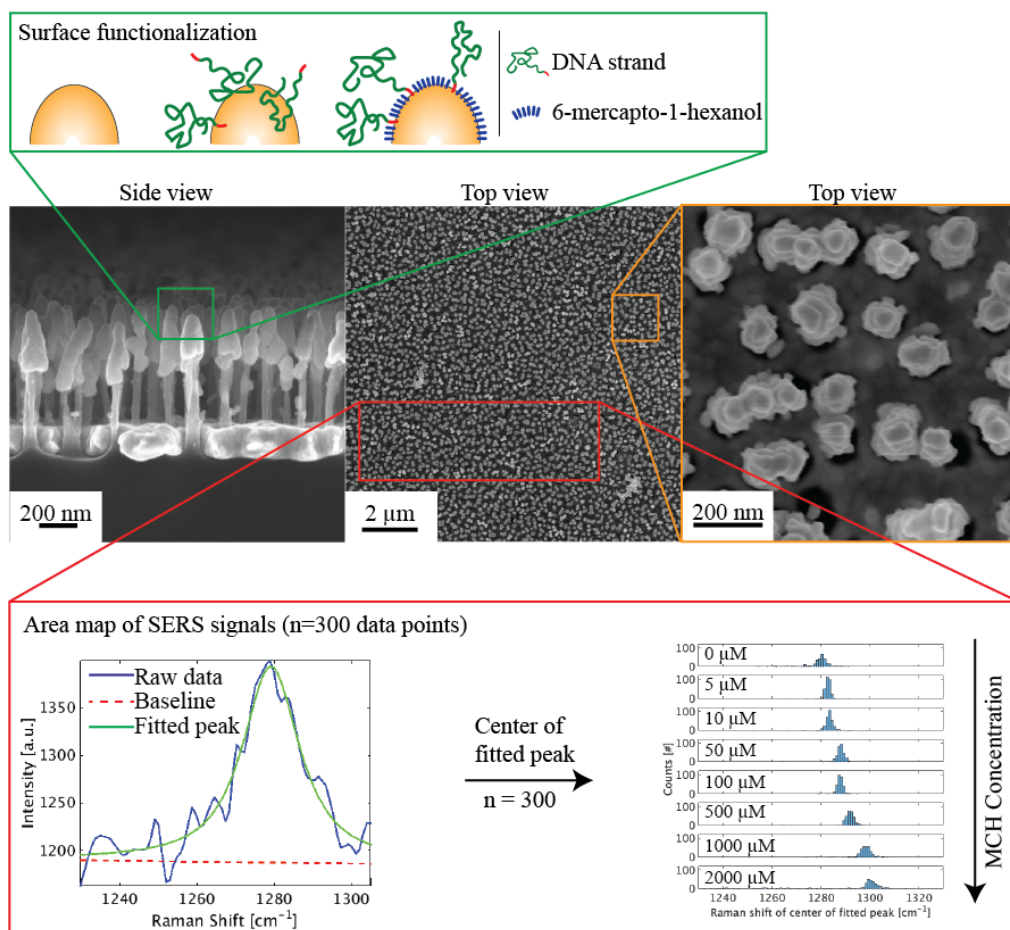


Figure 1. Top: schematic of the surface functionalization used in the experiments. Thiolated DNA was conjugated to the gold covered silicon nanopillar heads followed by backfilling with 6-mercapto-1-hexanol (MCH). Middle: SEM images of the SERS substrate seen from the side (left) and the top (middle and right). The gold heads of the silicon nanopillars are clearly seen. Bottom: overview of the peak-fitting model (left) used on 300 individual SERS spectra. The histogram (right) shows a clear shift of center peak position as a function of MCH concentration.

- 1 B. Sharma, M. Fernanda Cardinal, S. L. Kleinman, N. G. Greeneltch, R. R. Frontiera, M. G. Blaber, G. C. Schatz and R. P. Van Duyne, (2013), *MRS Bull.*, 38, 615–624.
- 2 C. M. S. Izumi, M. G. Mo and A. G. Brolo, (2011), *J. Phys. Chem. C*, 115, 19104–19109.
- 3 J. Yang, M. Palla, F. Bosco, T. Rindzevicius, T. S. Alström, M. S. Schmidt, A. Boisen, J. Ju and Q. Lin, (2013), *ACS Nano*, 7, 5350–5359.
- 4 T. S. Alström, K. B. Fröhling, J. Larsen, M. N. Schmidt, M. Bache, M. S. Schmidt, M. H. Jakobsen and A. Boisen, in *24th International Workshop on Machine Learning for Signal Processing (MLSP)*, IEEE, 2014.
- 5 M. S. Schmidt, J. Hübner and A. Boisen, (2012), *Adv. Mater.*, 24, OP11–OP18.
- 6 M. Culha, D. Stokes, L. R. Allain and T. Vo-Dinh, (2003), *Anal. Chem.*, 75, 6196–201.
- 7 E. A. Josephs, T. Ye, N. Sciences and U. States, (2013), *ACS Nano*, 7, 3653–3660.

Reporter-free surface-enhanced Raman spectroscopy for studying the differentiation of adult stem cells

Justyna P. Smus², Anna Huefner¹ and Sumeet Mahajan^{1,2}

¹University of Southampton, Institute of Life Sciences and Department of Chemistry, Highfield, SO17 1BJ, Southampton, UK, ²University of Cambridge, Sector for Biological and Soft Systems, Cavendish Laboratory, JJ Thompson Avenue, CB3 0HE, Cambridge, UK.

Keywords: SERS, gold nanoparticles, intracellular, biological cells, biosensors

Fluorescence microscopy is the most prolific technique used in cellular imaging. However, its scope is limited by photobleaching and the requirement of labelling of target molecules, besides the fact that it does not deliver information regarding the molecules themselves. This limitation is exacerbated for cells which are morphologically similar and only differ in slight biochemical composition as multiple labels or stains are needed to identify the correct cells such as those required in grafts and cell-based therapies. Moreover, the use of labels or stains would render the cells useless for therapeutic purposes.

Gold nanoparticles, taken up voluntarily by cells through the endolysosomal uptake pathway, can be used as intracellular surface-enhanced Raman spectroscopy (SERS) sensors. We have demonstrated the use of SERS by employing intracellular gold nanoparticles (AuNPs) to sense the complex molecular environment inside cellular organelles and the cytoplasmic matrix of adult stem cells.^{1,2} We were also able to determine the spectral characteristics inside the nucleus of cells using functionalized SERS probes. The aim of the functionalization was to help AuNPs escape the endolysosomal pathway and direct the nanoparticles towards the target organelle rather than act as a reporter. This enabled the chemical environment of the

organelles inside cells to be spectrally mapped by SERS.

Adult stem cells can differentiate into different cell types under different treatments. We use differentiated neural cell types each of which differ in the biochemical composition. In this work the differences are explored by using our strategy of reporter-free intracellular SERS and the role of functionalization of AuNPs is studied. We use a combination of functionalization and size control of the nanoparticles to make them escape the endosomes in which they are initially trapped and then either remain free in the cytoplasm or are directed to different organelles. The results for functionalization by different short peptide sequences such as the nuclear localization signal (NLS) peptide will be presented. It has been found that control of the level of functionalization was important for the selectivity of spectral characteristics and thus for allowing the biochemical differences between the different cell types to be observed. Furthermore, we find that the functionalization of the SERS probes improves the distinction ability between the different cell types compared to non-functionalized probes. The observed spectral differences are correlated to the differentiation process in order to understand their biochemical origins.

Thus, the reporter-free intracellular SERS approach is firmly established in its ability to sense biochemical differences between different cells and the role of functionalization of the nanoparticle probes has been explored. This SERS strategy

sheds light on the intracellular mechanisms of differentiation complementing existing technologies. Finally, the reporter-free SERS methodology offers an alternative to distinguish cells for cell-based therapeutics.

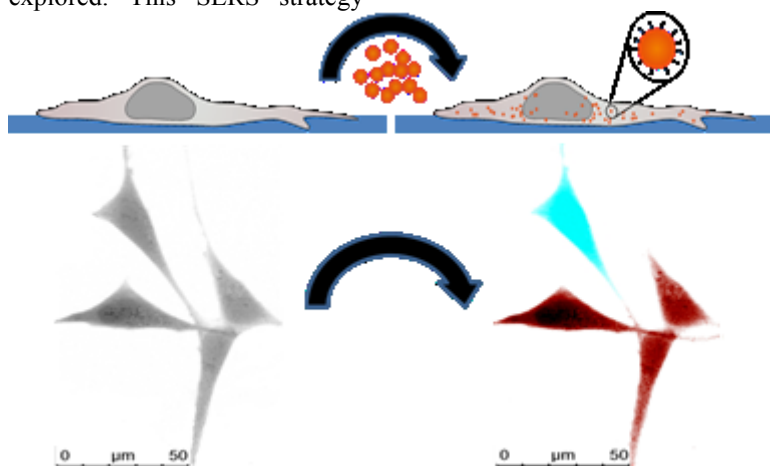


Figure 1. Schematic of the methodology of the intracellular SERS experiment (top) described in this work. The reporter-free intracellular SERS methodology allows distinguishing cell types which appear morphologically similar but are biochemically different (bottom).

¹Huefner, A., Kuan, W.-L., Barker, R. A. & Mahajan, S. Intracellular SERS Nanoprobes For Distinction Of Different Neuronal Cell Types. *Nano Lett* **13**, 2463-2470, doi:10.1021/nl400448n (2013).

²Huefner, A., Septiadi, D., Wilts, B. D., Patel, I. I., Kuan, W.-L., Fragniere, A., Barker, R. A. & Mahajan, S. Gold nanoparticles explore cells: cellular uptake and their use as intracellular probes. *Methods*, 1-20, doi:10.1016/j.ymeth.2014.02.006 (2014).

SERS study of thiocarbonyl compounds adsorbed on metal nanoparticles

J. L. Castro, J. Roman-Perez, J. C. Otero, M. R. Lopez-Ramirez¹¹Department of Physical Chemistry, Faculty of Science, University of Málaga, E-29071-Málaga, Spain

Keywords: thiobenzoic acid, thiobenzamide, SERS, metal nanoparticles.

Thiocarbonyl compounds have been reported to exhibit interesting biological and pharmacological properties but they are many often characterized by their toxicological effects. However the chemistry of thiobenzoic acid (TBA) and thiobenzamide (TB) has not been fully studied yet. Some of the biological studies of TBA are related to the tautomerism of thiocarboxylic acids and the important role that the $-C(=O)-S$ and $-C(=S)-O$ functional groups play in the catalytic activities of enzymes such as cysteine or serine proteases.¹ On the other hand, TB and derivatives are well known hepatotoxins and have been used as inhibitor in enzymatic reactions and in pharmacy due to their microbial activity.²

From a chemical point of view, thiocarboxylates are an interesting type of molecules having two different donor atoms, a soft sulfur donor atom and a hard oxygen donor one. The presence of these unlike groups can lead to the bonding with metal surfaces. Likewise the interaction of thiobenzamide and their derivatives with metals is of great interest because both the sulfur and nitrogen atoms are also able to coordinate with the surface. Therefore the high affinity of these molecules for metal surfaces makes them suitable SERS target adsorbates. Taking advantage of the fact that SERS spectroscopy is both surface selective and highly sensitive we have attempted to determine the molecular structure of TBA and TB once they are adsorbed on the metal.

The main objective of this work is focussed on discussing the observed vibrational wavenumber shifts of TBA and TB upon adsorption on silver nanoparticles. In this work the SERS substrates have been prepared by using different colloidal silver solutions according to the method described by Creighton et al.³ and Leopold and Lendl.⁴

The analysis of the vibrational wavenumbers shifts of the Raman and SERS spectra allow us to know the adsorption process (Figure 1). In the case of TBA, the wavenumber of the SERS band assigned to $\nu(C=O)$ vibrational mode shows an important blue shift up to 40 cm^{-1} with respect to the Raman whereas the $\nu(C-S)$ band undergoes a red shift up to 40 cm^{-1} . These results suggest a unidentate coordination of TBA to the silver surface through the sulfur atom.

On the other hand, the SERS band assigned in the case of TB to Amide III (mainly $\nu(CN)$) exhibits a significant blueshift up to 41 cm^{-1} , and the SERS band assigned to Amide I (mainly $\nu(CS)$) shows a red shift up to 11 cm^{-1} . These wavenumber shifts indicate that TB interacts to the silver surface through the sulfur atom. Interestingly, in previous SERS studies of pyridinecarboxamides and benzamide we have observed that some SERS bands assigned to $1; \nu_{ring}$, Amide I (mainly $\nu(C=O)$) and Amide III (mainly $\nu(C-N)$) show wavenumber shifts of $+50$, -50 and $+10\text{ cm}^{-1}$, respectively, which were attributed to the deprotonation of carboxamide group.^{5,6}

Finally, in order to verify experimental results DFT calculations have been carried out for different silver complexes of TBA and TB concluding that the unidentate

coordination is the most likely interaction of both of them.

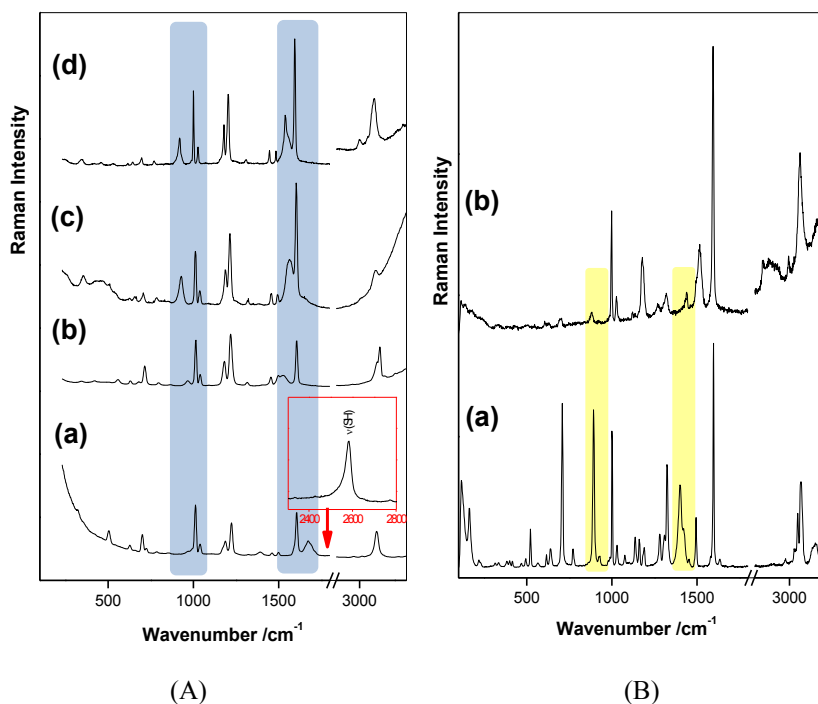


Figure 1.(A) Raman spectra of TBA in the neat liquid (a) and 1 M aqueous solution at pH 14 (b); SERS spectra of 5×10^{-4} M of TBA on Ag NPs obtaining by reduction with sodium borohydride (c) and by reduction with hydroxylamine hydrochloride (d); (B) Raman spectra of solid TB (a), SERS spectrum of 5×10^{-4} M of TB on Ag NPs obtaining by reduction with hydroxylamine hydrochloride (b). An excitation wavelength of 514.5 nm was used.

- Carey P.R. Eds. (1982). *Biochemical Applications of Raman and Resonance Raman Spectroscopy*. Academic Press: London.
- Yu K.L., Torri A.F., Luo G., Cianci C., Grant-Young K., Danetz S., Tiley L., Krystal M., Meanwell N.A. (2002), *Bioorg. Med. Chem. Lett.* 12, 3379-3382.
- Creighton J.A., Blatchford C.G., Albrecht M.G. (1979), *J. Chem. Soc. Faraday Trans. II*, (75), 790-798.
- Leopold N., Lendl B. (2003), *J. Phys. Chem. B*, 107 (24), 5723-5727.
- Castro J.L., Lopez-Ramirez M.R., Arenas J.F., Soto J., Otero J.C. (2012), *Langmuir*, (28) 8926-8932.
- Castro J.L., Arenas J.F., Lopez-Ramirez M.R., Soto J., Otero J.C. (2013), *J. Colloid Interface Sci.*, 396, 95-100.

Tip-enhanced Raman scattering study on the nanoscale features of epitaxial graphene

Sanpon Vantasin¹, Toshiaki Suzuki¹, Yoshito Tanaka¹, Tamitake Itoh², Tanabe Ichiro¹, Yasunori Kutsuma³, Tadaaki Kaneko³, and Yukihiro Ozaki¹

¹Department of Chemistry, Kwansei Gakuin University, 2-1 Gakuen, Sanda, 669-1337, Japan

²National Institute of Advanced Industrial Science and Technology (AIST),
2217-14 Hayashi-cho, Takamatsu, Kagawa 761-0395, Japan

³Department of Physics, Kwansei Gakuin University, 2-1 Gakuen, Sanda, 669-1337, Japan

Keywords: TERS, graphene, nanostructure, strain, AFM

Characterizations of graphene are becoming more and more important. For epitaxial graphene, which is a desirable type of graphene for graphene-based electronic nanodevices due to its large sheet area and low defect, the characterizations are not only required in the circuit scale, but also in the nanoscale. The necessity comes from the variations in each local domain of graphene. Even though the number of layers and doping level can be precisely controlled with high homogeneity, there are still strain differences in nanoscale, which can significantly affect both physical and electronic attributes of graphene.

This strain difference is suspected to originate from nanostructures on graphene sheet since there is a correlation between the strain variation in Raman studies and nanostructures occurrence in AFM/STM studies. However, since the spatial resolution of normal Raman spectroscopy, which is the conventional method for graphene characterization, is not enough to resolve each individual single nanostructure of epitaxial graphene, the effect of an individual nanostructure on the strain in local domain is never measured spectroscopically. To overcome this limitation, we employed tip-enhanced Raman spectroscopy (TERS) technique. With the near field enhancement from the

plasmon resonance between etched silver nanotip and excitation laser, a spatial resolution exceeding the diffraction limit was achieved and each individual structure can be investigated. The setup we used is top-illumination top-collection. The tips were controlled by non-contact mode AFM.

This study consists of two parts. In the first part¹, we demonstrated that TERS can probe strain variations in nanoscale using the shift of G band and G' band. We also found a correlation of ΔFWHM and $\Delta\omega$ between (normal) far-field Raman and TERS spectra. The enhancement factor of 1000 was achieved.

In the second part², we studied TERS on step, ridge, and cracks sub-micro/nanostructures. The result shows that the step nanostructure did not significantly affect TERS spectra. On the ridge nanostructure, 8.7 cm^{-1} downshift of G' band was observed and then calculated into a strain difference of 1.6×10^{-3} . This indicates a weaker compressive strain compared to neighbor areas, which confirms a speculation of previous studies that nanoridges form as a compressive strain relief during the cooldown after the high-temperature synthesis. On the crack sub-microstructure, the reduced intensity ratio between graphene and SiC peak was found,

suggesting lower graphene content in the crack.

The TERS results in every studied local domain indicate that there is high homogeneity of strain among flat area. The only places where significant strain variations occur are on the nanostructures themselves. Therefore, we can conclude that

the origin of strain variations in local domains is the nanostructures.

All of these results cannot be observed in far-field Raman spectra due to the limit in the spatial resolution, thus demonstrating the powerfulness of TERS in nanoscale study of epitaxial graphene.

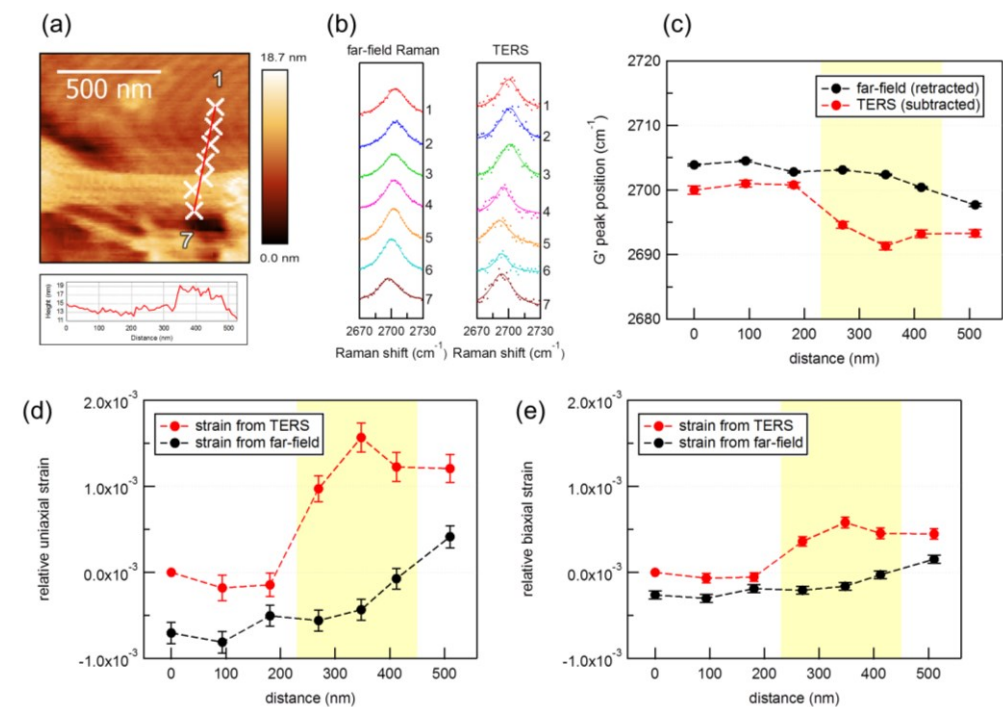


Figure 1. (a) AFM topography of graphene nanoridge with line profile showing ~ 6 nm ridge height. (b) G' band in far-field Raman and TERS spectra from each point in (a). (c) Plot of G' band position in far-field Raman and TERS spectra against distance in the line profile. (d),(e) Calculated relative strain using band position in (c) in uniaxial and biaxial model, respectively.

- ¹ Suzuki T., Itoh T., Vantasin S., Minami S., Kutsuma Y., Ashida K., Kaneko T., Morisawa Y., Miura T., Ozaki Y. (2014) *Phys. Chem. Chem. Phys.*, 16 (37), 20236–20240.
- ² Vantasin S., Tanabe I., Tanaka Y., Itoh T., Suzuki T., Kutsuma Y., Ashida K., Kaneko T., Ozaki Y. (2014) *J. Phys. Chem. C*, 118 (44), 25809–25815.

Application of Raman spectroscopy and in situ Raman spectroelectrochemistry in the studies of isotopically labeled graphene heterostructures

Martin Kalbac¹, Johan Ek Weis,¹ Sara Costa,¹ Jana Vejpravova,² Mildred Dresselhaus³

¹J. Heyrovský Institute of Physical Chemistry, AVCR, Dolejskova 3, Prague 8, Czech Republic.

²Institute of Physics, AVCR., Na Slovance 2, Prague, Czech Republic.

³Department of Materials Science and Engineering, MIT, Cambridge, Massachusetts, USA.

Keywords: Raman spectroscopy, graphene, isotope labelling

Raman spectroscopy plays an important role in graphene research since the discovery of this material. It allows to distinguish between monolayer and AB stacked bilayer, determine number of defects, doping level¹ or mechanical strain in graphene.

Recent advances in graphene synthesis allowed to prepare ¹³C enriched graphene samples. The change in the carbon isotope results in a change of the frequency of the Raman bands due to different mass of the isotope. In this case it is possible to address individual layers of graphene since the layers with different isotope exhibit different frequency of all Raman features (Figure 1).² This approach can be further extended to prepare in general isotopically labeled multilayer graphene samples.^{3,4} The application of isotope labelling in the doping experiments is of particular importance. The differently charged graphene layers of bilayer graphene are important prerequisite for a proper function of new type of graphene based bilayer pseudofield effect transistors. The Raman spectra of doped graphene samples reflect both the changes in the C-C bond strength and the changes in the concentration of charge carriers in this material. The Raman spectrum of neutral graphene exhibit a downshift and broadening of the G line due to the Kohn anomaly. The doping of graphene leads to

shift of the Fermi level which prevents the electron-hole excitations by phonons, hence the Kohn anomaly effect is removed. Consequently, the G mode is narrowed and upshifted. Since the area of the G mode remains constant at low doping levels, the narrowing of the G mode causes an increase of its amplitude. The G' mode also reflects the changes in the doping of graphene. The intensity G' mode is decreased with increasing doping since the larger amount of charge carriers increases electron-electron interactions and the resonance is weakened. The isotopic labeling of graphene can be also used in graphene based heterostructures. An example of such a system can be graphene/BN/graphene heterostructure. If the isotopically labeled graphene is used one can follow the behavior of the top and bottom layer independently. Figure 2 shows an example of the electrochemical doping of ¹²C/BN/¹³C heterostructure. It can be seen that both the top and bottom graphene layer are increasingly doped as the applied electrode potential is increased. This is indicated by a change of the Raman frequencies of the G mode and the decrease of the intensity of the G' mode of both the top and bottom layers. Furthermore, it seems that the changes are very similar for the top and bottom layer, which indicates similar doping level of both layers at all applied electrode potentials. This is not intuitive

since the top and the bottom layer are separated by insulating BN layer and it is more difficult for electrolyte ions to compensate charge in the bottom layer. This behavior is essentially the same as observed for two layered graphene.² Obviously, the charge transfer between turbostratic graphene layers is possible even if they are separated by a thin dielectric layer.

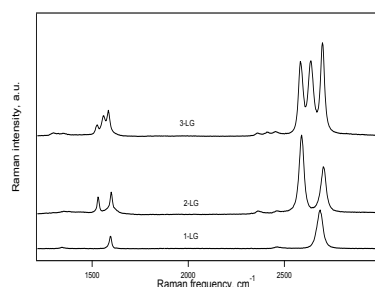


Figure 1. The Raman spectra of 1-LG (one layer graphene) and isotopically labeled 2-LG (two layered graphene) and 3-LG (three layered graphene).

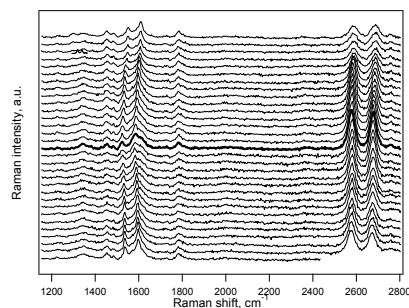


Figure 2. The Raman spectra of $^{12}\text{C}/\text{BN}/^{13}\text{C}$ heterostructure at electrode potentials between -1.5 and 1.5V. The middle bold spectrum was loaded at electrode potential of 0V. The spectra above are loaded with positive potentials and the spectra underneath are loaded at negative electrode potentials. The potential step between adjacent spectra is 0.1V.

In summary we prepared a new isotopically labeled $^{12}\text{C}/\text{BN}/^{13}\text{C}$ heterostructure and measured its Raman spectra (in situ) at different electrode potentials. We showed that both the top and the bottom graphene layers are charged simultaneously.

Reference List

1. Kalbac, M.; Reina-Cecco, A.; Farhat, H.; Kong, J.; Kavan, L.; Dresselhaus, M. S. (2010), *Acs Nano*, 4 (10), 6055-6063.
2. Kalbac, M.; Farhat, H.; Kong, J.; Janda, P.; Kavan, L.; Dresselhaus, M. S. (2011), *Nano Letters*, 11 (5), 1957-1963.
3. Frank, O.; Kavan, L.; Kalbac, M. (2014), *Nanoscale* 6 (12), 6363-6370.
4. Kalbac, M.; Kong, J.; Dresselhaus, M. S. (2012), *J. Phys. Chem. C*, 116 (35), 19046-19050.

The authors acknowledge the support of MSMT ERC-CZ project (LL 1301).

Resonance Raman Spectroscopy of Extreme Nanowire Systems

Joseph Spencer¹, Liam McDonnell¹, Reza J. Kashtiban², Gavin Bell², Eric Faulques³, Jeremy Sloan² and David C. Smith¹

¹School of Physics and Astronomy, University of Southampton, Southampton SO17 1BJ, United Kingdom,

²Department of Physics, University of Warwick, Coventry, CV4 7AL, United Kingdom

³ Institut des Matériaux Jean Rouxel, University of Nantes CNRS, UMR6502, F-44322 Nantes, France.

Keywords: Resonance Raman, 1D Materials, Carbon Nanotubes, Extreme Nanowires

Resonance Raman Spectroscopy gives an insight to the nature of optical transition states of extreme nanowires, wires at the fundamental limit of the nanoscale mere atoms in diameter that no other single optical characterization tool can provide. There is a wide range of interest for both fundamental physics and technological applications of extended, crystalline 1D quantum systems, also known as nanowires. Such nanowires can be manufactured in a variety of ways, these include vapour-liquid-solid grown semiconductor nanowires¹, lithographically defined nanowires², template grown nanowires in materials such as anodic alumina and many others.

A reason for such interest in these systems is that they combine large quantum confinement effects with the ability for electrons and other excitations to move freely along 1 dimension of the structure. It has been shown that behavior of such nanowire systems in some cases differs from unconfined material, producing effects such as ballistic transport, but in generally nanowires behave as slightly modified versions of a bulk material and possess the same crystal structures. However as the dimensions of the confined directions are reduced to a few atoms nanowires with entirely new bonding can occur forming never previously seen allotropes³. These 'extreme nanowires' are extreme in the sense they are the true limit of the nanoscale and their properties differ from their bulk counter-parts^{4,5}. This is scientifically

interesting in two senses, one for the obvious addition to the understanding of physics these materials can provide, but also poses limits on an ever increasing demand for miniaturization of nano-electronics. Such extreme nanowires can be formed using melt infiltration into single walled carbon nanotubes⁶. This technique produces high yield filling of continuous single crystals within the central pore of a SWCNT and therefore the ideal method for probing structures, because of the ease of sample generation and high yield.

Resonance Raman Spectroscopy is a tool widely used to identify Carbon Nanotubes⁷, and because of the van Hove singularities appearing in low-dimensional structures is a necessary tool to observe individual nanotubes. In our previous report⁵, we demonstrate new Raman modes (Fig 1) appearing in a crystal structure of extreme quantum confined Mercury Telluride embedded down the central pore of a Carbon Nanotube. This structure was shown to have completely different Raman characteristics that are not simply modifications of the LO and TO phonon modes observed in bulk HgTe⁸. The observed modes were also shown to possess a strong resonance with a narrow line-width, highlighting not only the power of resonant Raman spectroscopy for such experiments but make it a necessary tool for characterization of extreme nanowire structure. We now develop this measurement on HgTe@SWCNTs and

further investigate, using Resonance Raman Spectroscopy temperature dynamics of the new phonon modes observed. We demonstrate a striking temperature dependence that indicates a decrease of the spectral weight of the observed modes as a

function of temperature that cannot be explained by line-width broadening of the modes. We also demonstrate the use of CRS as a method to stimulate the excitation of the observed modes.

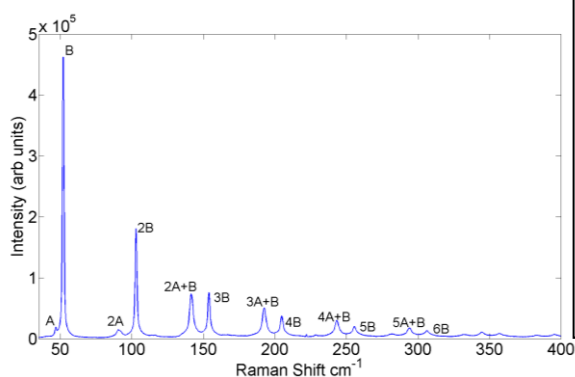


Figure 1 (left): Representative Raman Spectra of HgTe@SWCNT at 4K excited at resonance of 1.77eV. Multiple overtones and combination modes of fundamental modes can be observed up to 7th order; these modes are not merely modifications of LO or TO phonons observed in bulk HgTe or HgTe nanowires.

- 1 Gudiksen, M. S., Lauhon, L. J., Wang, J., Smith, D. C. & Lieber, C. M. Growth of nanowire superlattice structures for nanoscale photonics and electronics. *Nature* **415**, 617-620, doi:10.1038/415617a (2002).
- 2 Hisamoto, D. *et al.* FinFET-a self-aligned double-gate MOSFET scalable to 20 nm. *Electron Devices, IEEE Transactions on* **47**, 2320-2325, doi: 10.1109/16.887014 (2000).
- 3 Sloan, J. *et al.* A One-Dimensional BaI2 Chain with Five- and Six-Coordination, Formed within a Single-Walled Carbon Nanotube. *Angewandte Chemie International Edition* **41**, 1156-1159, doi:10.1002/1521-3773
- 4 Sloan, J., Kirkland, A. I., Hutchison, J. L. & Green, M. L. H. Integral atomic layer architectures of 1D crystals inserted into single walled carbon nanotubes. *Chemical Communications*, 1319-1332, doi:10.1039/B200537A (2002).
- 5 Spencer, J. H. *et al.* Raman Spectroscopy of Optical Transitions and Vibrational Energies of ~1 nm HgTe Extreme Nanowires within Single Walled Carbon Nanotubes. *ACS Nano* **8**, 9044-9052, doi:10.1021/nm5023632 (2014).
- 6 Ebbesen, T. W. Wetting, filling and decorating carbon nanotubes. *Journal of Physics and Chemistry of Solids* **57**, 951-955, doi:http://dx.doi.org/10.1016/0022-3697(95)00381-9 (1996).
- 7 Dresselhaus, M. S., Dresselhaus, G., Saito, R. & Jorio, A. Raman spectroscopy of carbon nanotubes. *Physics Reports* **409**, 47-99, doi:http://dx.doi.org/10.1016/j.physrep.2004.10.006 (2005).
- 8 Ingale, A., Bansal, M. & Roy, A. Resonance Raman scattering in HgTe: TO-phonon and forbidden-LO-phonon cross section near the E1 gap. *Physical Review B* **40**, 12353-12358, doi:10.1103/PhysRevB.40.12353 (1989).

The structure of metal - carbon nanotube's coating interface, the effect of interaction with albumin.

Aleksandra Weselucha-Birczyńska¹, Ewa Stodolak-Zych², Sylvia Turrell³, Franciszek Cios¹, Magdalena Krzus¹, Aleksandra Benko², Wiktor Niemiec² and Marta Błażewicz²

¹Faculty of Chemistry, Jagiellonian University, 30-060 Kraków, Poland

²Faculty of Materials Science and Ceramics, AGH-University of Science and Technology, 30-059 Kraków, Poland

³Laboratoire de Spectrochimie Infrarouge et Raman, Université des Sciences et Technologies de Lille, Lille, France

Keywords: multi-walled carbon nanotube (MWCNTs) coatings, Raman micro-spectroscopy, atomic force microscopy (AFM), scanning electron microscopy (SEM), electrophoretic deposition (EPD).

The application of multi-walled carbon nanotubes (MWCNTs), as a modifying phase for the surface of biomedical materials, can constitute an attractive material for the production of implants and supports in the human body or implantable electrodes for modern therapies¹. The biocompatibility of carbon nanoforams depends on their structural arrangement and the surface chemical state.

The aim of this study is to analyze the interface of the titanium support and carbon nanotube layer deposited on the titanium surface (i.e. the electrophoresis, EPD). In an attempt to analyze accurately the impact subjected to material in a living organism the interaction with albumin was modeled. The adsorption of albumin may constitute the early stages of implant surface modification supported cell adhesion. The interface seems, in this context, to be important.

The electrophoretic deposition (EPD) routine was applied to cover the metal support within the carbon nanotube layer forming a relatively uniform microstructure⁴. However, this layer was so modeled, that the titanium plate was coated with varying degrees of nanotubes (Figure 1A, SEM image). Multi-walled carbon nanotubes (NanoAmor Inc., USA) were combined with a mixture of concentrated acids to obtain highly oxidized CNTs, which were later deposited on the titanium plates, forming a metal support, for 30 sec, at a voltage of 30V.

Raman spectroscopy is well established as a sensitive technique for the characterization of carbon materials. Raman spectra were obtained while the sample was excited using: 266, 473, 514.5 and 785 nm laser lines. The G peak, corresponding to the E_{2g} phonon at the Brillouin zone center, and the D peak, due to the breathing modes of the atom rings and requiring a defect for its activation, appear around 1580 and 1350 cm⁻¹, respectively. Peak intensities and full width at half-maximum carries information of sample structural arrangement, at the same time also of disorder. According to Ferrari⁵ disorder classification, based on spectral features, the studied coatings may be positioned on graphite to a nanocrystalline graphite

trajectory site. The defect distance L_D for the phase boundary layer, excited with 473 nm, is equal to 4.3 and 4.7 nm, for the bottom and top layer, respectively. The layer of carbon nanotubes shows a smaller disorder, L_D = 5.6 and 4.8 nm, for the bottom and top layer, respectively. A similar relationship is observed for excitation line 514.5 nm. The L_D value for the phase boundary layer is equal to 4.8 and 4.9 nm, for the bottom and top layer, respectively. The carbon nanotube coating shows a smaller disorder, L_D = 5.3 and 5.0 nm, for the bottom and top layer, respectively (Figure 1B).

Additionally, the 2D (G*) Raman band shift can be related to the mechanical deformation of the nanotubes⁶. These shifted frequencies, relative to the surface (top) layer of the carbon coating 2D band position, can be directly related to the mechanical strain exerted on the composite material. The downshift of the 2D band position with simultaneous bandwidth increase for the phase boundary layer in comparison to carbon nanotube coating indicates greater surface strain at the transitional layer⁷.

In order to verify the interaction between the CNT layer deposited on a titanium substrate and protein (albumin) test measurements were carried out by Raman spectroscopy. They showed albumin conformational changes dependent on the surface condition (Ti, Ti-interface CNT, CNT coating). Additionally, a complementary study showed the diversity of the topography of the surface covered with albumin (AFM, SEM). The wettability profile confirmed the physico-chemical changes in the surface of an interface boundary layer and stresses resulting from the presence of the carbon layer/coating (Raman spectroscopy).

Studies using Raman spectroscopy allows for the tracking of changes in the structure of the CNT layer on a titanium substrate (thickness profile, the amount of CNT on the surface). Depending on the thickness of the CNT layer, the interaction between the CNT and the protein is different, which is reflected in the albumin conformational changes.

These studies can be considered as a model for the interaction of carbon nanotubes with protein

confirmed by spectroscopic, microscopic and physicochemical analyses.

Acknowledgements. The project was financed from the National Science Centre (NCN, Poland) granted on the basis of decision number DEC-2013/09/B/ST8/00146 and 2011/01/B/ST5/06424.

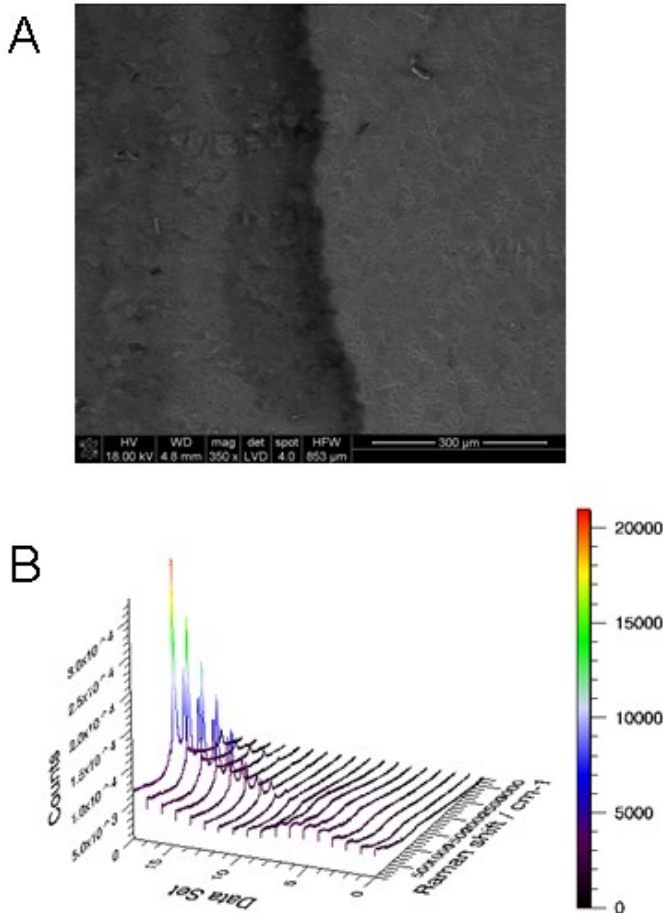


Figure 1. Metal - carbon nanotube's coating interface; (A) SEM image, magnification $\times 350$; (B) The Raman line mapping, 785 nm laser line, $\times 100$ objective magnification, step 1 μm .

- 1 Luo X., Weaver C. L., Zhou D. D., Greenberg R., Cui X. T., (2002). *Biomaterials*. 32 (24), 5551-5557.
- 2 Fraczek-Szczypta A., Długon E., Weselucha-Birczynska A., Nocun M., M. Błażewicz, (2013), *Journal of Molecular Structure*, (1040) 238–245.
- 3 Bareket-Keren L., Hanein Y., (2012), *Frontiers in Neural Circuits*, 6 /122/ 1-16.
- 4 Ferrari B., Moreno R. (2010), *Journal of the European Ceramic Society*, 30, 1069–1078.
- 5 Ferrari A.C., Robertson j., (2000), *Physical Review B*, 61, 14095-14107.
- 6 Zhao Q., Wagner H. D., (2004), *Philosophical Transactions of the Royal Society of London A*, 362, 2407–2424.
- 7 Cooper C.A., Young R.J., Halsall M., (2001), *Composites: Part A* 32, 401–411.

Infrared attenuated total reflection spectroscopy for the characterization of gold nanoparticles in solution

Ángela I. López-Lorente^{1,2}, Markus Sieger¹, Miguel Valcárcel² and Boris Mizaikoff¹

¹Institute of Analytical and Bioanalytical Chemistry, University of Ulm, 89081, Ulm, Germany

²Department of Analytical Chemistry, University of Córdoba, Campus of Rabanales, 14071, Córdoba, Spain

Keywords: attenuated total reflection, infrared spectroscopy, gold nanoparticles.

Gold nanoparticles (AuNPs) are characterized by exceptional physical properties, which have promoted their use in a diverse range of areas including biomedical imaging and diagnostic assays, catalysis, and for applications based on the enhanced optical properties of nanoparticles such as surface-enhanced Raman scattering (SERS) for analyzing adsorbed molecules.

In general, AuNPs do not show pronounced mid-infrared absorptions, unless they are functionalized with organic ligands attached to the particle surface. Hartstein et al.¹ were the first reporting on the so-called surface-enhanced infrared absorption (SEIRA) effect. Two enhancement mechanisms –electromagnetic and chemical– are thought to mainly contribute to the total enhancement in SEIRA spectroscopy. The electromagnetic mechanism increases the local electric field at the surface, while the chemical enhancement assumes an increase of the absorption due to chemical interactions between molecules and gold nanoparticles.

In the present study, the adsorption of water molecules at gold nanoparticles has been utilized for in situ monitoring of the synthesis of bare gold nanoparticles via surface-enhanced infrared attenuated total reflection (SEIRA-ATR) spectroscopy².

Gold nanoparticles were directly synthesized inside the ATR unit taking advantage of the stainless steel ring establishing the confining walls of the liquid cell, as previously demonstrated^{3,4}. While AuNPs are

formed, they sediment at the ATR waveguide surface until Coulombic repulsion from already adsorbed AuNPs leads to an equilibrium. Despite the IR inactivity of AuNPs, it was found that their formation could still be monitored via IR spectroscopy by analyzing the increase of the water absorption features during the synthesis process, which arises from a SEIRA effect. Figure 1 shows a series of in situ IR-ATR spectra recorded during in situ gold nanoparticle synthesis within the ATR unit.

According to literature⁵, the vibrational modes of water in the infrared region are the H₂O bending mode at 1644 cm⁻¹, the combination of H₂O bending and libration at 2128 cm⁻¹, and an absorption around 3404 cm⁻¹. The latter is composed from the overtone of the bending mode at 3250 cm⁻¹, the symmetric OH stretch at 3450 cm⁻¹, and the antisymmetric OH stretch at 3600 cm⁻¹. As gold nanoparticles are formed and deposited at the ATR surface, an increase in the H₂O bending and the OH stretching bands is observed, despite a decrease in the amount of water molecules present in the evanescent field during the deposition, as water molecules are displaced by gold nanoparticles. This increase is attributed to the so-called SEIRA effect of water molecules in the enhanced field created by formed nanoparticles. This enhanced near-field decays with increasing the distance from the particle surface, and it compensates the loss of water molecules replaced by nanoparticles.

A similar effect has been observed in the case of gold nanoparticles synthesized in deuterium oxide with its absorption bands revealing similar enhancement during the formation of AuNPs.

Moreover, the generic suitability of SEIRA-ATR spectroscopy for the investigation of gold nanoparticle solutions has been studied via the evaluation of effects such as the addition of salts or variation of the pH on the aggregation state of gold nanoparticles in solution, as well as monitoring the involved

sedimentation processes. As IR spectra are sensitive to variations of the chemical environment, next to nondestructively monitoring the synthesis of gold nanoparticles one may furthermore analyze changes in aggregation or stability of the obtained AuNP dispersions.

Thus, in the present study IR-ATR spectroscopy is confirmed as an innovative analytical tool applicable for the characterization of bare AuNPs providing a straightforward and nondestructive characterization strategy.

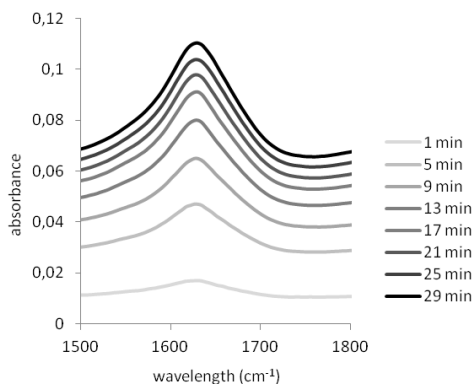
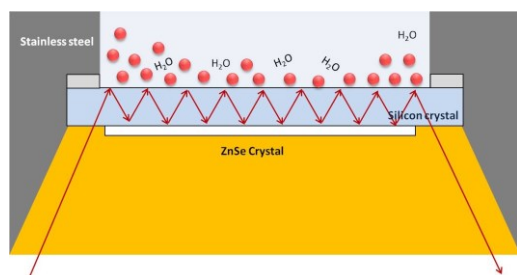


Figure 1. Left: Scheme of the ATR configuration used within the present study. The walls of the cell are composed of stainless steel, which acts as a reducing agent leading to the in situ formation of AuNPs^{3,4}. Right: *In situ* ATR-SEIRA H₂O bending mode spectra during the synthesis of gold nanoparticles inside the ATR unit in an aqueous environment (from a 200 mg dL⁻¹ HAuCl₄ solution).

- Harstein, A., Kirtley, J.R., Tsang, J.C. (1980) *Physical Review Letters*, 45 (3), 201-204.
- López-Lorente, A.I., Sieger, M., Valcárcel, M., Mizaikoff, B. (2014), *Analytical Chemistry*, 86 (1), 783-789.
- López-Lorente, A.I., Simonet, B.M., Valcárcel, M., Eppler, S., Schindl, R., Kranz, C., Mizaikoff, B. (2014), *Talanta*, 118, 321-327.
- López-Lorente, A.I., Simonet, B.M., Valcárcel, M., Mizaikoff, B. (2013), *Analytica Chimica Acta*, 788, 122-128.
- Venyaminov, S.Y., Pendegast, F.G. (1997) *Analytical Biochemistry*, 248 (2), 234-245.

Unraveling the sum-frequency generation signatures of functionalized surfaces using quantum chemical calculations

Vincent Liégeois¹, Conrard Giresse Tetsassi Feugmo¹, Benoît Champagne¹

¹Department of Chemistry, University of Namur (UNamur), rue de Bruxelles 61, 5000, Namur, Belgium

Keywords: sum frequency generation, functionalized surfaces, simulation, ab-initio, DFT.

Vibrational spectroscopies are powerful tools to study the structures of molecules, polymers, self-assembled monolayers, interfaces, ... Indeed, each normal mode of vibration provides information about their structure: the composition, the configuration, the conformation, or the supramolecular arrangement. Last but not least, there exists a broad range of vibrational spectroscopies: Infrared (IR), Raman, Vibrational Circular Dichroism (VCD), Raman Optical Activity (ROA), Hyper-Raman, Resonant Raman (RR), Sum Frequency Generation (SFG), which all provide specific signatures.

Among them, infrared-visible sum-frequency generation (SFG) spectroscopy has been employed to monitor interface formation, to determine the structure of the interface, and therefore to help improve the efficiency of the immobilization of biomolecules.¹ Indeed, SFG spectroscopy presents the advantage of being sensitive only to the regions of the material where the inversion symmetry is broken. Moreover, theoretical approaches promote an increased understanding of molecular interactions at the interface through the elucidation of its structure by means of the spectral assignment of the vibrational signatures. Therefore, the complexity of the spectra calls for the development of simulation and interpretation tools.²

Among the tools and code designed for this purpose, the Pyvib2 program, first

developed by Fedorovsky in Fribourg university (Switzerland), provides original tools to unravel the structure/spectra relationships. Some of its key features are i) the decomposition scheme³ introduced by Hug that divides the intensity into group coupling matrices (GCMs) or atomic contribution patterns (ACPs) and ii) the interface to analyze the coupling between normal modes of two similar molecules,^{4,5} iii) and the recent implementation of the localized mode method⁶ originally developed by Jacob and Reiher.⁷ This program was released as an open-source program and is used by the scientific community worldwide.

In this contribution, we present recent developments on the simulation of the sum frequency generation (SFG) spectra and its applications to study the structure and dynamics of organic layers at interfaces. A general method has been developed. It combines density functional theory calculations to evaluate the molecular properties with a three-layer approach to determine the macroscopic response of the organic monolayer. The later step, which accounts explicitly for the nature of the surface, has been implemented in a homemade code. In addition to its detailed presentation, the method is illustrated in the case of 1-dodecene covalently bonded to hydrogen-terminated Si(111).⁸ We demonstrate that the consideration of the nature of the surface greatly improves the

agreement with experiment, which allows using the comparison between theory and experiment to unravel the monolayer structure (Figure 1). So, the tilt angles of the alkyl chain and of the terminal CH_3 with respect to the surface normal (laboratory Z axis) are estimated to 43° and 67° , which is close to the 35° and 70° literature values, respectively. Moreover, the analysis of the evolution of the normal mode intensities with the orientation of the molecule at the surface (defined by the tilt and twist angles) has shown that the intensity ratio between the symmetric and anti-symmetric CH_3

stretching modes is directly related to the twist angle. This can be justified by looking to the orientation of the derivative of the dipole moment with respect to the normal mode. At last, we propose a graphical user interface (within Pyvib2 program) to simulate the sum-frequency generation (SFG) spectra function of both the tilt and twist angles, which enables a direct correlation between the SFG signatures and the orientation of the molecule (and its normal modes) at the surface.

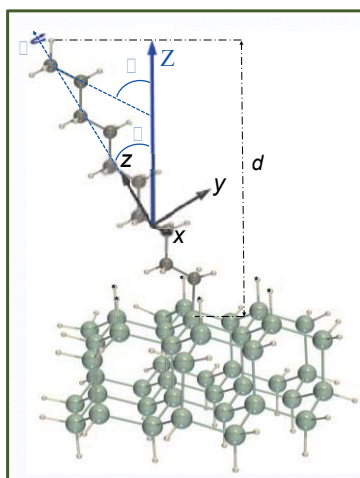


Figure 1. Optimized structure ($\omega\text{B97X-D/6-311G}^*$) of the Si cluster- $(\text{CH}_2)_9\text{CH}_3$ system. θ and α are the alkyl chain and methyl tilt angles, respectively; ξ is the Euler twist angle; and d is the monolayer thickness.

- ¹ Asanuma H., Noguchi H., Uosaki K., Yu H.-Z., (2008), *J. Am. Chem. Soc.*, 130, 8016–8022.
- ² Tetsassi Feugmo C.G., Champagne B., Caudano Y., Cecchet F., Chabal Y.J., Liégeois V., (2012), *J. Phys.: Condens. Matter*, 24, 124111.
- ³ Hug W., (2001), *Chem. Phys.*, 264, 53–69.
- ⁴ Hug W., Fedorovsky M., (2008), *Theor. Chem. Acc.*, 119, 113–131.
- ⁵ Fedorovsky M., (2006), *Computing Letters*, 2, 233–236.
- ⁶ Liégeois V., Champagne B., (2012), *Theor. Chem. Acc.*, 131, 1284.
- ⁷ Jacob Ch. R., Reiher M., (2009), *J. Chem. Phys.*, 130, 084106.
- ⁸ Tetsassi Feugmo C.G., Liégeois V., Champagne B., (2015), *J. Phys. Chem. C*, 119, 3180–3191.

Generalized dispersion analysis of arbitrarily cut crystals with unknown orientation

Sonja Höfer¹, Jürgen Popp^{1,2} and Thomas G. Mayerhöfer^{1,2}

¹Leibniz-Institut für Photonische Technologien e.V., Albert - Einstein - Str. 9,
D-07745 Jena, Germany

²Institut für Physikalische Chemie, Lessingstraße 10, Friedrich-Schiller-Universität,
D-07743 Jena, Germany

Keywords: Crystal systems, dispersion analysis, IR-spectroscopy.

Dispersion analysis is the determination of oscillator parameters of a material. It is also the basis to determine the dielectric tensor function of this material¹. Based on the examples of the triclinic crystals coppersulfate² $\text{CuSO}_4 \cdot 5\text{H}_2\text{O}$ and potassium dichromate³ $\text{K}_2\text{Cr}_2\text{O}_7$ we presented the first successful dispersion analyses of triclinic crystals recently. Since in triclinic crystals the orientations of the transition moments is a priori unknown we concluded that with a similar formalism it should be possible to perform dispersion analysis for uniaxial, orthorhombic and monoclinic crystals with a priori unknown orientation.

To be successfully applied, for each crystal class the evaluation scheme must follow certain constraints according to the crystal symmetry. These constraints are necessary to reduce the parameter space significantly, which makes it much easier for the fit to end at meaningful dispersion parameters.

For the uniaxial crystal systems the occurrence of degenerate oscillators is characteristic. This degeneracy is no longer present in the orthorhombic system. The orthorhombic and monoclinic system is distinguishable by the lifted condition of mutual orthogonality of the oscillators in the monoclinic *a-c*-plane: While in the orthorhombic system the transition moments

are aligned parallel to the crystal axes, in the monoclinic system the orientation of the transition moments fans out in a plane normal to the last remaining predominant direction. The monoclinic and triclinic system in turn can be distinguished by the vanished predominant direction that is present in the monoclinic system.

To develop the measurement and evaluation scheme for the generalized dispersion analysis we employed at least two crystals of each crystal system with different properties to test the developed scheme. The crystals were either grown in the laboratory or naturally occurring crystals. The sample preparation comprised the optical polishing of three different, not coplanar, crystal faces. The spectra sets for uniaxial crystals were measured in the same way triclinic crystals, of which 12 spectra of three perpendicular crystal faces are recorded in the measurement scheme developed in².

In case of the orthorhombic and monoclinic crystals the spectra sets need to be supplemented by cross polarization measurements in order to yield unambiguous results concerning the crystal orientation. The formalism is designed in a way that the calculation of the additional cross polarization spectra does not require extra computing capacity and time.

The crystal orientation can be found within $\pm 2^\circ$ error depending on the

complexity of the spectra and the spectral distance of the oscillators. Except for very weak oscillators the oscillators are correctly oriented by the fit routine. Figure 1 shows the employed crystals to develop the measurement and evaluation scheme.

The calculated dispersion parameters were verified by using these parameters to predict spectra of a crystal in principal cut and compare the predicted spectra to the

measured ones. This work is an important step towards being able to perform dispersion analysis without any prior knowledge of crystal class and orientation.

We gratefully acknowledge funding from the Deutsche Forschungsgemeinschaft (MA 2616/5-1). We would like to thank Mr Frank Hänshcke for his help with the spectroscopic measurements

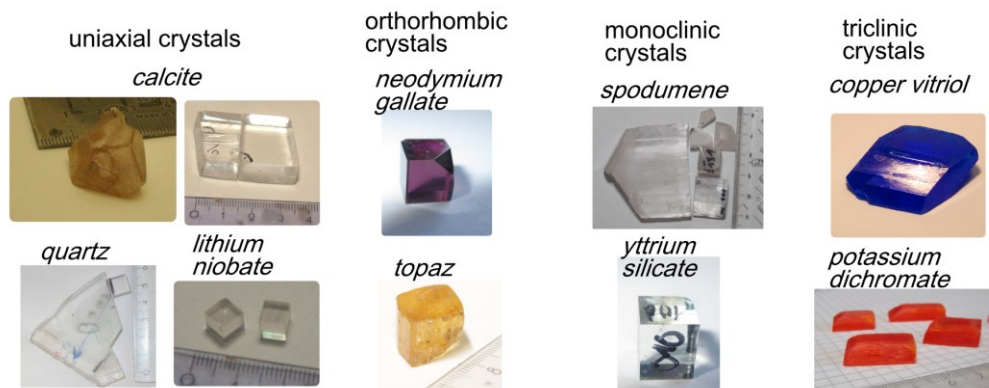


Figure 1. Dispersion analysis can now be performed for arbitrarily cut crystals of all crystal systems with a priori unknown orientation.

¹ Spitzer, W. G., Kleinmann, D. A. (1961), *Physical Review A*, 121, 1324-1335

² Höfer, S., Popp, J., Mayerhöfer, T. G. (2013), *Vibrational Spectroscopy*, 67, 44-45

³ Höfer, S., Popp, J., Mayerhöfer, T. G. (2014), *Vibrational Spectroscopy*, 72, 111-118

Investigation of band gap effect and dephasing on Raman line broadening for the highest A_g mode in comparison with $SrWO_4$ and $SrMoO_4$

Jun Suda¹ and Petr. G. Zverev²

¹Department of Electrical and Electronic Engineering, School of Engineering, Chukyo University, 101-2 Yagoto Honmachi, Showa-ku, Nagoya-shi, 466-8666, Japan

²A.M. Prokhorov General Physics Institute Russian Academy of Sciences, 38 Vavilov Street, 119991, Moscow, Russia

Keywords: Raman spectroscopy, band gap, anharmonicity, Raman laser, Raman gain.

In recent years, scheelite crystals (e.g. $SrWO_4$, $BaWO_4$, $PbWO_4$ and $SrMoO_4$) have attracted the interest of several research groups as promising and potentially efficient materials for technological applications using the highest-frequency A_g mode in Raman laser.¹ Very recently, we clarified that the highest A_g mode has significant effect for the dephasing in scheelite crystals.²⁻⁴ We found that there is an energy gap of more than 350 cm^{-1} between high- and low-frequency bands in $BaWO_4$ and $SrMoO_4$ by the lattice dynamical calculations approach.²⁻⁴ The temperature dependence of linewidth of the highest A_g mode well describes the observed ones in this temperature range by both the cubic term and the dephasing term. The relative ratio of the dephasing effect in linewidth for this mode in $SrMoO_4$ is greater than that in the case of $BaWO_4$.³ This indicates the impact of the dephasing is related to the size of band gap.²⁻⁵

The steady state Raman gain coefficient is inversely proportional to the Raman mode linewidth.¹ During the operation of a Raman laser these scheelite crystals are heated due to the Stokes losses, which results in both the line broadening and lowering of the Raman gain.¹ The obtained results allowed us to predict the temperature dependence of the Raman gain during the operation of the Raman lasers with scheelite crystals.¹⁻⁵

However, the dephasing effects with respect to the difference between Mo-O and W-O vibrations have not been clarified up to now. This will lead to design the scheelite Raman laser with more excellent Raman gain.

The aim of this study was to investigate anharmonicities of the highest A_g mode (921-cm^{-1} peak) in $SrWO_4$ with comparison with $SrMoO_4$ by both the lattice dynamical calculations and spontaneous Raman spectroscopy. The phonon dispersion relations (Fig. 1) of $SrWO_4$ were calculated using the same model.² Temperature dependence of calculated linewidth of the highest A_g mode well described the observed ones below room temperature (Fig. 2) by using both the cubic term and the dephasing term. The size of a band gap ($\sim 410\text{ cm}^{-1}$) in $SrWO_4$ equals to that in $SrMoO_4$ approximately. So the most effect due to this down-conversion process contributes to the line broadening for this mode. However, the bands for internal mode above band gap in $SrWO_4$ are broader than those for $SrMoO_4$.³ Comparing with the case of $SrMoO_4$, this creates more number of the up-conversion in $SrWO_4$ is that this mode is produced by interaction between higher frequency bands with very lower bands.

Therefore, the relative ratio of the dephasing effect in linewidth in $SrWO_4$ is smaller than that in $SrMoO_4$.

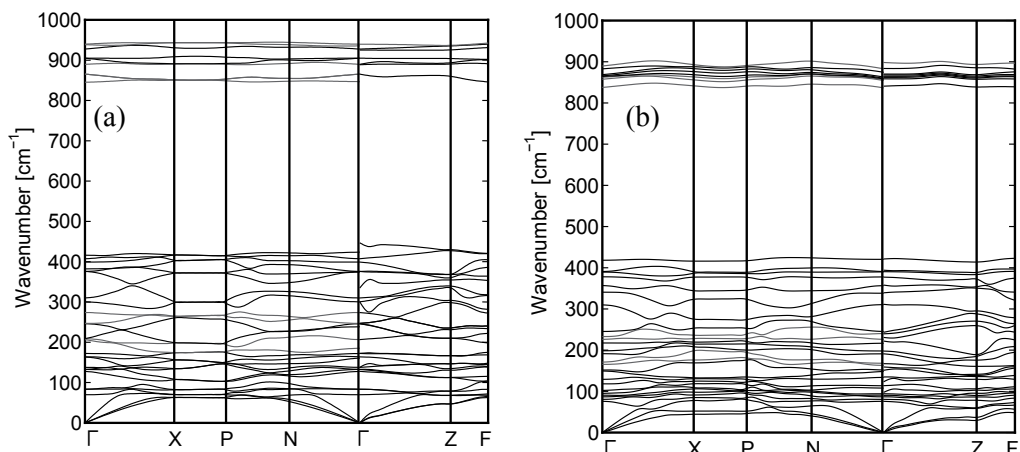


Figure 1. Calculated phonon dispersion curves for SrWO₄ (a) and SrMoO₄³ (b).

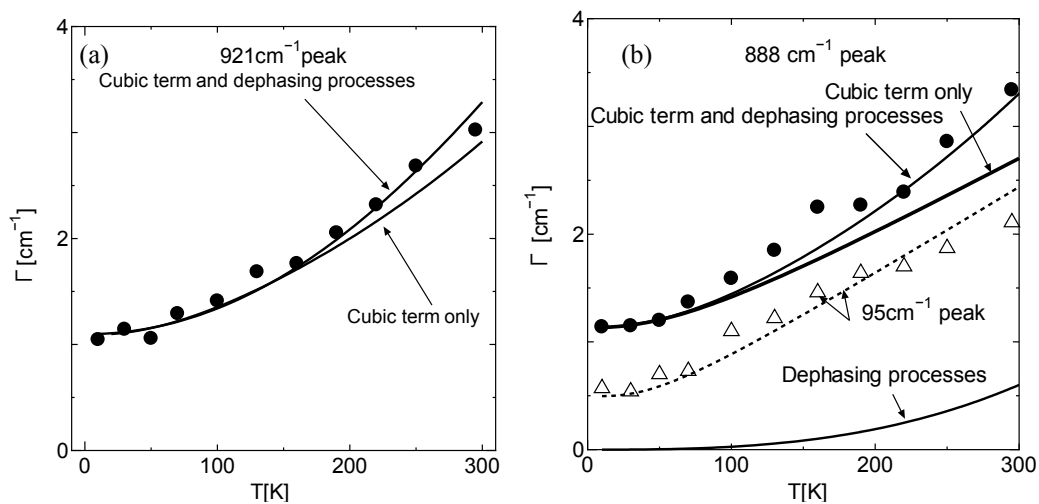


Figure 2. Calculated curves and experimental data (dots) for the linewidth of the highest-frequency *A_g* mode in SrWO₄ (a) and SrMoO₄³ (b).

- ¹ Basiev T., Doroshenko M., Ivleva L., Voronina I., Konjushkin V., Osiko V., Vasilyev S., (2009), *Optics Letter*, 34, 1102-1104.
- ² Suda J., Zverev P., (2012), *Vibrational Spectroscopy*, 62, 85-91.
- ³ Suda J., Zverev P., (2014), *Vibrational Spectroscopy*, 71, 6-11.
- ⁴ Suda J., (2014), *Vibrational Spectroscopy*, 72, 33-36.
- ⁵ Suda J., Kamishima O., Kawamura J., Hattori T., (2014), *Solid State Communications*, 72, 36-41.

General vibrational spectroscopies with Wilson

Magnus Ringholm¹, Dan Jonsson¹ and Kenneth Ruud¹

¹CTCC, Department of Chemistry, UiT The Arctic University of Norway, NO-9037, Tromsø, Norway

Keywords: 2D-IR, elastic, general, frequency-domain, anharmonic.

The program Wilson aims to offer a complete frequency-domain treatment of any elastic vibrational spectroscopy where the incident lasers are either in the infrared (IR) or in the ultraviolet/visible (UV/VIS) range, detuned from any electronic resonance.

The starting point of the program is the Liouville equation, from which the sum-over-states expression for the response function¹ at the appropriate order considering the number of incident laser pulses is derived by a schematic, recursive approach² developed in our group. Next, the vibrational contributions to this response function are determined by a method based on that of Bishop, Kirtman, and Luis³⁻⁵. The resulting expressions are developed into working expressions involving normal-mode derivatives of polarization properties through the so-called double perturbation treatment. Finally, these expressions are evaluated for a general setup of polarization vectors and time-ordering of the incident lasers. In accordance with the number of independent variables (i.e. frequencies or frequency differences/sums in the IR range) chosen, the program outputs spectra of the appropriate dimensionality, up to and including animated two-dimensional spectra for the case of three independent variables.

Due to the recursive and general nature of the program, all eligible experiments are treated on an equal footing and the method

can in principle be applied to treat experiments involving any number of incident lasers at any order of anharmonicity, such that the only practical limitations are the computational capacity available and the possibility of obtaining the normal-mode derivatives necessary for evaluation of the spectra.

The program is still being developed, and we will present some preliminary results to demonstrate the functionality of the code and the feasibility of the approach used. Among the spectroscopic phenomena that could be studied with the program are sum-frequency generation (SFG) and doubly vibrationally enhanced two-dimensional IR (DOVE-2D-IR) processes and coherent anti-Stokes Raman spectroscopy (CARS). In addition to this, there is the possibility to treat other exotic phenomena such as three-dimensional IR spectroscopies and processes combining various features from the aforementioned groups. Future work could extend the approach to inelastic processes.

For the purpose of obtaining the normal-mode derivatives used in the evaluation of the spectra, our group has developed the recursive and open-ended response theory⁶ code⁷ OpenRSP, which can manage the fully analytic calculation of any such property at the Hartree-Fock (HF) and density-functional (DFT) levels of theory, getting necessary integral and exchange-correlation contributions from external

routines. In the present setup, OpenRSP can be used to calculate high-order normal-mode derivatives of the energy and electric dipole polarization properties^{7,8}, and support for calculation of not only these properties, but also normal-mode derivatives of magnetic

and higher-order electric multipole properties, is being developed. Work on incorporating molecular environment effects through the polarizable embedding⁹ (PE) and the polarizable continuum model¹⁰ (PCM) approaches is ongoing.

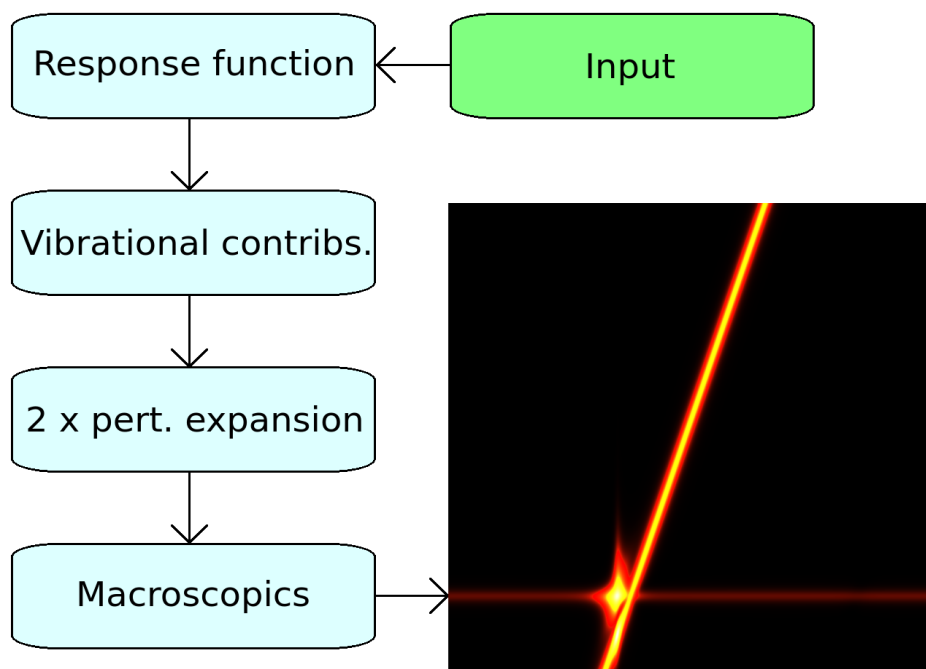


Figure 1. The progression through the main parts of the program Wilson.

¹ Norman, P., “Exact State Response Theory” (book chapter), unpublished

² Ringholm, M., Ruud, K., unpublished

³ Bishop, D. M., Kirtman, B., *J. Chem. Phys.* **95**, 2646 (1991)

⁴ Bishop, D. M., Kirtman, B., *J. Chem. Phys.* **97**, 5255 (1992)

⁵ Bishop, D. M., Luis, J. M., Kirtman, B., *J. Chem. Phys.* **108**, 10013 (1998)

⁶ Thorvaldsen, A. J., Ruud, K., Kristensen, K., Jørgensen, P., Coriani, S., *J. Chem. Phys.* **129**, 214108 (2008)

⁷ Ringholm, M., Jonsson, D., Ruud, K., *J. Comput. Chem.* **35**, 622 (2014)

⁸ Ringholm, M., Jonsson, D., Bast, R., Gao, B., Thorvaldsen, A. J., Ekström, U., Helgaker, T., Ruud, K., *J. Chem. Phys.* **140**, 034103 (2014)

⁹ Steindal, A. H., Ruud, K., Ringholm, M., List, N. H., Kongsted, J., Olsen, J. M. H., *in preparation*

¹⁰ Di Remigio, R., Cornaton, Y., Beerepoot, M. T. P., Ringholm, M., Frediani, L., Ruud, K., *in*

Vibrational spectra of the isotopic species of nitrosyl halides : a study using the U(4) algebraic model

Nirmal Kumar Sarkar

Department of Physics, Karimganj College, Karimganj-788710, India

Keywords: Vibrational spectra, Lie algebra, isotopic species, nitrosyl halides.

Since the last part of the 20th century, an algebraic approach¹⁻² has been used in the study of the molecular spectra. The approach has been found effective in the analysis and interpretation of experimental rovibrational spectra of small and medium-sized molecules. This approach is based on the idea of dynamical symmetry and is expressed through the language of Lie algebras. The algebraic approach can account for any specific mechanism relevant for the correct characterization of the molecular dynamics and spectroscopy. Applying algebraic techniques, in this approach, one obtains an effective Hamiltonian operator that conveniently describes the rovibrational degrees of freedom of the physical system. The algebraic approach is especially useful when the potential energy surface is unknown or when it is too difficult to calculate the spectrum by starting with the potential surface using the traditional approaches. For example, in a large molecule (larger than a diatomic), the potential surface is a very complex function, composed of a discouragingly large number of coordinates. Under such circumstances, the traditional approaches face a tremendous difficulty in approximating the molecule as soon as we consider the highly excited levels. Further, a large number of parameters are also required here to obtain meaningful results. On the other hand, the algebraic approach needs a much more economical set of parameters to

provide the fits of the spectra. This is a very important practical advantage of the algebraic approach over the traditional approaches. In algebraic approach, there are general forms of algebraic Hamiltonian and by using a common Hamiltonian entire classes of molecules can be approximated by changing only the parameters (typically, linear) for different molecules. This is another remarkable advantage of the algebraic approach over the traditional approaches. Finally, we note the comparative ease of the algebraic operations used in the algebraic approach – a technical advantage of the algebraic approach over the traditional approaches.

In the study of vibrational spectra of polyatomic molecules, both U(2) and U(4) algebraic models¹⁻² have been attracting a wider scientific community of the globe in recent years. The models already have been applied in the study of vibrational spectra of linear triatomic, linear tetratomic and some other small, medium and large-sized molecules³⁻⁵. In many aspects, the U(4) and U(2) algebraic models are in advantageous positions with respect to their traditional counterparts in the study of vibrational spectra of a molecule.

However, it is to be noted that the U(2) algebraic model is one-dimensional in nature and it does not take into account rotational motions of a molecule. Simply to provide a global vibrational picture of a

certain molecule, the rotational degrees of freedom are completely disregarded in the U(2) algebraic model. Such a drawback is overcome with the introduction of the U(4) algebraic model. The full treatment of molecular rovibrational degrees of freedom can be achieved in the three-dimensional framework of the U(4) algebraic model. The three dimensional framework of the U(4) algebraic model leads us to a more complex and realistic picture of a molecular system as well as producing a more exacting algebraic treatment.

The three-dimensional algebraic model is definitely much more difficult to manipulate than the one-dimensional one, purely for algebraic aspects. Due to this reason, the U(4) algebraic model could proceed till today only up to the approximation of linear tetratomic

molecules⁴. So far the cases of bent polyatomic molecules are concerned, successful applications⁶⁻⁷ of the U(4) algebraic model could be reported so far only for a few bent triatomic molecules. Thus, for the U(4) algebraic model, more or less, the entire kingdom of the bent polyatomic molecules is left unattended till today.

In this study, a successful application of the U(4) algebraic model has been reported in the vibrational spectral analysis of the isotopic species of nitrosyl halides. With a detail spectral analysis, it has been shown in this study that all the isotopic species of NOF, NOCl, NOBr and NOI can be approximated very well using the U(4) algebraic model.

¹ R.D. Levine, C.E. Wulfman, (1979) Chem. Phys. Lett. 60, 372-376.

² F. Iachello, (1981) Chem. Phys. Lett. 78, 581-585.

³ N. K. Sarkar, J. Choudhury, S. R. Karumuri and R. Bhattacharjee, (2009) Eur. Phys. J. D. 53, 163-171.

⁴ N. K. Sarkar, J. Choudhury, S. R. Karumuri and R. Bhattacharjee, (2008) Mol. Phys. 106, 693-702.

⁵ S. Oss, (1996) Adv. Chem. Phys. 93, 455-649; R. Sen, A. Kalyan, N. K. Sarkar and R. Bhattacharjee, (2014) Fullerenes, Nanotubes and Carbon Nanostructures, 22, 914-920.

⁶ F. Iachello and S. Oss, (1990) J. Mol. Spectrosc. 142, 85-107.; N. K. Sarkar, J. Choudhury, S. R. Karumuri and R. Bhattacharjee, (2011) Vib. Spectrosc. 56, 99-104; N. K. Sarkar, J. Choudhury and R. Bhattacharjee, (2012) Vib. Spectrosc. 60, 63-67.

⁷ Sarkar, Nirmal Kumar; Sen, Rupam; Kalyan, Ashim; Das, Raghunandan; Roy, Subha Gaurab; Choudhury, Joydeep; Karumuri, Srinivasa, (2015). Indian Journal of Pure & Applied Physics (in press).

SURFACE-ENHANCED AND NEAR-FIELD IR SPECTROSCOPIES TO STUDY BIOMEMBRANES AND MEMBRANE PROTEINS

Kenichi Ataka, Ramona Schlesinger and Joachim Heberle

Department of Physics, Freie Universitaet Berlin, Arnimallee 14, 14195 Berlin

Keywords: membrane proteins, SEIRAS, SNIM, FTIR, photobiology.

Membrane proteins are the target of more than 50% of all drugs and are encoded by about 30% of the human genome. Electrophysiological techniques, like patch-clamp, unravelled many functional aspects of membrane proteins but suffer from structural sensitivity. We have developed Surface Enhanced Infrared Absorption Spectroscopy (SEIRAS) to probe potential-induced structural changes of a protein on the level of a monolayer^{1,2}. A novel concept is introduced³ to incorporate membrane proteins into solid-supported lipid bilayers in an orientated manner via the affinity of the His-tag to the Ni-NTA terminated gold surface. General applicability of the methodological approach is shown by tethering photosystem II to the gold surface⁴. In conjunction with hydrogenase, the basis is set towards a biomimetic system for H₂-production⁵. FTIR difference spectra of a monolayer of sensory rhodopsin II were

recorded under voltage-clamp conditions⁶. This approach opens an avenue towards mechanistic studies of voltage-gated ion channels with unprecedented structural and temporal sensitivity. The expression, insertion and folding of membrane proteins traced by SEIRAS. In this novel approach, the complex reaction sequence is time-resolved on the level of a monolayer of a biomembrane.

Finally, scanning near-field IR microscopy will be introduced and applied to study the structure of biomembranes⁷. Mapping of protein structure with 30 nm spatial resolution and sensitivity to individual protein complexes by Fourier transform infrared nano-spectroscopy (nano-FTIR) will be demonstrated. We present the first broadband infrared spectra of purple membranes indicating their local α -helical structure.

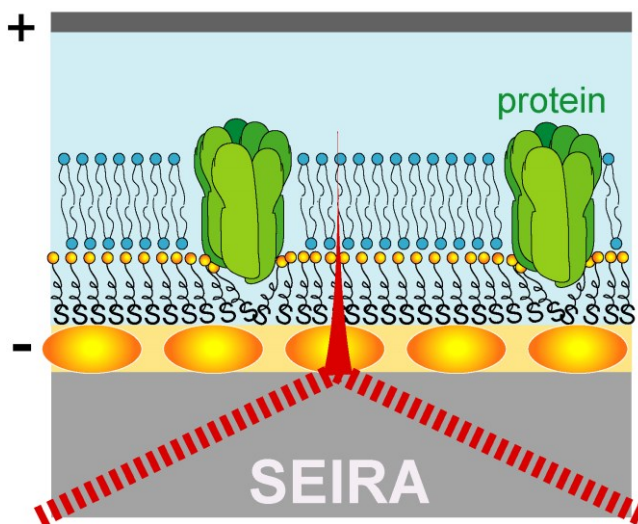


Figure 1. Surface-reconstituted biomembrane probed by SEIRAS.

References:

- ¹ Ataka, K., & Heberle, J. (2003), *J. Am. Chem. Soc.* 125, 4986-4987
- ² Ataka, K., Kottke, T., & Heberle, J. (2007), *Angew. Chem. Int. Ed.* 122, 5544 - 5553
- ³ Ataka, K., Giess, F., Knoll, et al. (2004), *J. Am. Chem. Soc.* 126, 16199-16206
- ⁴ Badura, A., Esper, B., Ataka, K., et al. (2006), *Photochem. Photobiol.* 82, 1385-1390
- ⁵ Krassen, H., Schwarze, A., Friedrich, B., et al. (2009), *ACS Nano* 3, 4055-4061
- ⁶ Jiang, X., Zaitseva, E., Schmidt, M., et al. (2008), *Proc. Natl. Acad. Sci. USA* 105, 12113-12117
- ⁷ Ataka, K., Stripp, S., and Heberle, J. (2013), *Biochim. Biophys. Acta* 1828, 2283-93
- ⁸ Amenabar, I, Poly, S, Nuansing, W, Hubrich, EH, Govyadinov, A, Huth, F, Krutokhvostov, R, Zhang, L, Knez, M, Heberle, J, Bittner, A, Hillenbrand, R. (2013), *Nat. Commun.* 2013 Dec 4;4:2890. doi: 10.1038/ncomms3890.

New developments in ATR-FTIR difference spectroscopy of protein monolayers

Jonas Schartner¹, Jörn Güldenhaupt¹, Klaus Gerwert¹ and Carsten Kötting¹

¹Department of Biophysics, Ruhr-University Bochum, Bochum, 44801, Bochum, Germany

Keywords: ATR-FTIR, protein immobilization, surface modification, protein interactions, monolayers.

The attenuated total reflection Fourier transform infrared spectroscopy (ATR-FTIR) allows a detailed analysis of immobilized proteins, including their secondary structure, reaction mechanism, orientation and interactions with small molecules or other proteins.¹ We optimized an ATR-FTIR system based on a germanium crystal to perform stimulus induced difference spectroscopy of monolayers without depending on the surface enhance effect. The aim of our study is the development of a universal immobilization technique on germanium for all kinds of proteins. We recently showed the specific immobilization of N-Ras and Photosystem I on a silane modified germanium surface.² We obtained high quality stimulus induced difference spectra from the monolayer, proving the integrity of the immobilized proteins.

We now present a new approach employing thiol chemistry on germanium (Figure 1).^{3,4} On one hand, due to the large diffractive index, germanium crystals provide a great signal-to-noise ratio in ATR-FTIR. On the other hand, protein immobilization via thiol chemistry is well-established, because it is the standard method for modifications of gold surfaces

e.g. in surface plasmon resonance. Here, we combine the best of both worlds and report on germanium surface functionalization with different thiols which allowed for specific immobilization of histidine-tagged proteins with over 99% specific binding. The great advantage of using thiols in comparison with silanes is that a huge variety of thiols with functional groups for many kinds of protein immobilizations are readily available. Nativity of the protein fold was confirmed by secondary structure analysis. Stimulus induced difference spectra were obtained for immobilized Channelrhodopsin 2, the small GTPase N-Ras and the phosphocholine-transferase AnkX, which demonstrated protein function at the atomic level (Figure 1).⁴ The immobilized proteins are active for several days.

Alternatively a model membrane can be attached to the germanium and membrane anchored proteins can be investigated in its natural environment.⁵ With this system we investigated membrane anchored Rab proteins.⁶ We showed that GDI (guanaine dissociation inhibitors) genuinely accelerates the intrinsic Rab membrane dissociation. The dissociation kinetics depends on the C-terminal sequence and the charge of the GTPase.

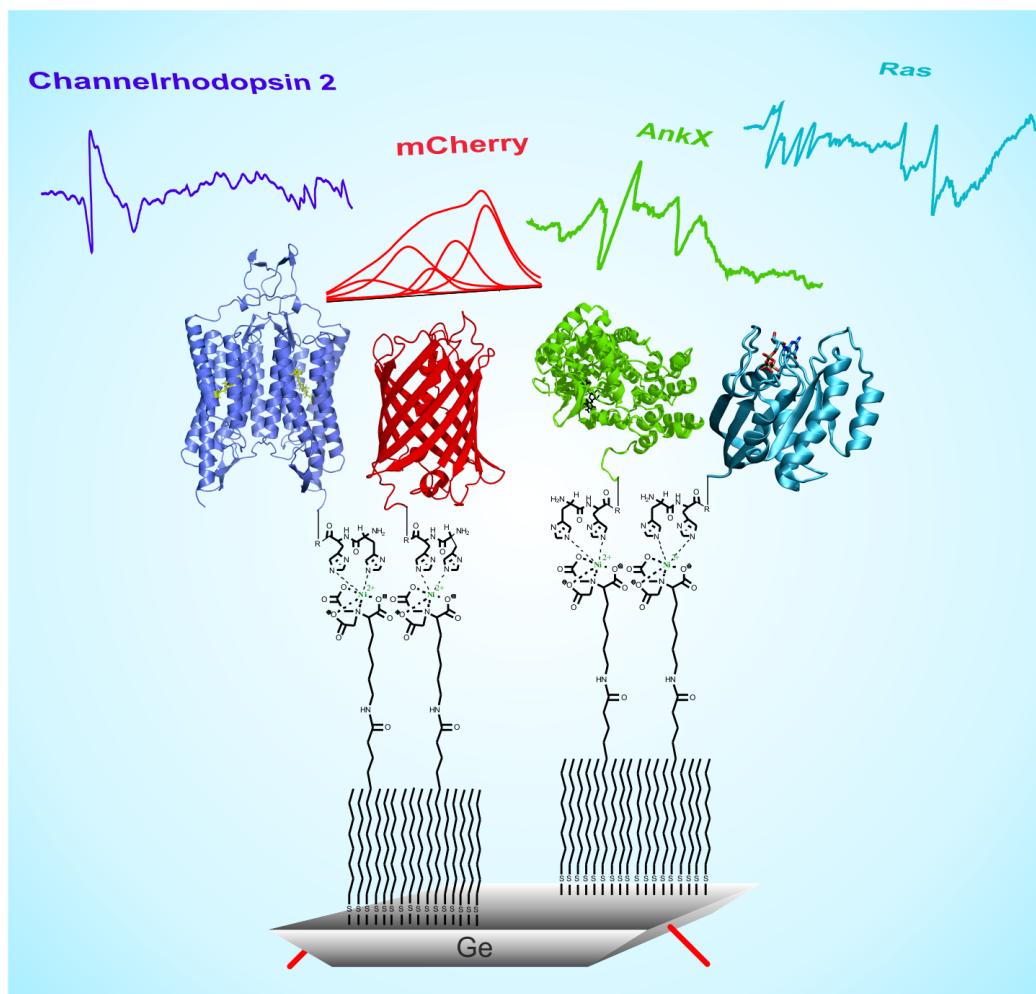


Figure 1. Schematic representation of various proteins immobilized by thiol chemistry at an ATR-germanium crystal. The proteins are active for several days. Stimulus induced infrared difference spectra with excellent signal/noise ratio can be obtained.

- ¹ Glassford, S. E.; Byrne, B.; Kazarian, S. G. (2013) *Biochim. Biophys. Acta BBA - ProteinsProteomics* 2013, 1834, 2849.
- ² Schartner, J.; Güldenhaupt, J.; Mei, B.; Rögner, M.; Muhler, M.; Gerwert, K.; Kötting, C. (2013) *J. Am. Chem. Soc.* 135, 4079.
- ³ Hanrath, T.; Korgel, B. A. (2004) *J. Am. Chem. Soc.* 126, 15466.
- ⁴ Schartner, J.; Gavriljuk, K.; Nabers, A.; Weide, P.; Muhler, M.; Gerwert, K.; Kötting, C. (2014) *ChemBioChem* 15, 2529.
- ⁵ Kötting, C.; Güldenhaupt, J.; Gerwert, K. (2012) *Chem. Phys.* 396, 72.
- ⁶ Gavriljuk, K.; Itzen, A.; Goody, R. S.; Gerwert, K.; Kötting, C. (2013) *Proc. Natl. Acad. Sci. U.S.A.* 110, 13380.

Infrared micro-spectroscopy combined with microfluidics is promising to monitor *in situ* the enzymatic degradation of plant tissues

Fabienne Guillon¹, William André², Estelle Bonnin¹, Brigitte Bouchet¹, Sylvie Durand¹, Camille Alvarado¹, Paul Robert¹, Luc Saulnier¹, Frédéric Jamme² and Marie-Françoise Devaux¹.

¹UR1268 BIA, INRA, F-44300 Nantes.

²Synchrotron SOLEIL, BP 48 F- 91192 Gif-sur-Yvette.

Keywords: infrared microspectroscopy, microfluidic, plant tissue, enzymatic degradation, polysaccharides.

The enzymatic conversion of lignocellulosic materials for the production of fine and bulk chemicals in place of the pretroleum feedstock is a very promising approach due to enzyme high selectivity and mild use conditions. However, the complex architecture of cell walls, consisting of a network of cellulose micro-fibrils embedded in a matrix of hemicelluloses and encrusted by lignin make them very resistant to degradation. A huge heterogeneity is observed according to cell types with different amount and type of lignins inside¹ leading to difficulties to interpret this resistance. There is still a knowledge gap between the plant cell wall structure and composition and the enzymatic mechanisms that lead to degradation.

Infrared microspectroscopy is an efficient technique to analyse *in situ* polysaccharides and lignin in lignocellulosic tissues^{2,3} Using synchrotron source, a spatial resolution compatible with the cell and cell wall sizes (10-50 μm , 1-5 μm resp.) can be attained⁴.

In the present work, we propose to take advantage of a microfluidic device to obtain time-lapse information of the evolution of cell wall composition during enzymatic degradation. Cell wall degradation was studied according to cell types in maize stem tissues using cocktails with cellulase and hemicellulase activities.

A microfluidic device was adapted for enzymatic degradation of 16 μm thick maize section (Figure 1). ZnS windows were retained to analyse the sugar fingerprint region. Masks of 20 μm thickness were designed for fluid circulation and sample positioning. Different cell types were followed in maize stem sections (Figure 1). Cell wall spectra could be obtained by taking the aqueous medium as background.

In vascular bundles, sclerenchyma and xylem fibres were not degraded while phloem and xylem parenchyma largely disappeared (Figure 2). Differences in parenchyma were evidenced depending on their localisation in the stem. Some cell walls were totally degraded while the most central were recalcitrant to enzyme actions. Degradation is attested by a general decrease of absorbance. Variations in peak decrease were also observed within spectra for the parenchyma close to the rind.

Infrared microspectroscopy using a microfluidic device and the synchrotron radiation was proved efficient to obtain time-lapse spectra of different cell wall types during enzymatic degradation. The technique is very promising to have a comprehensive insight in the enzyme actions on heterogeneous biological material.

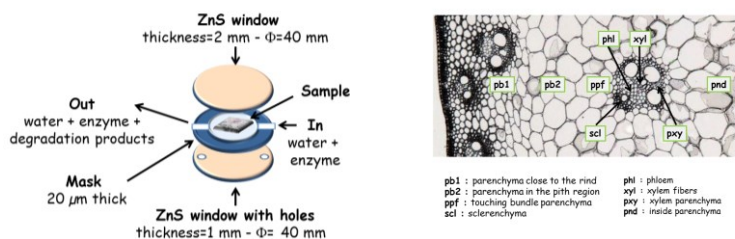


Figure 1. Microfluidic cell characteristics and cell types in maize stem section.

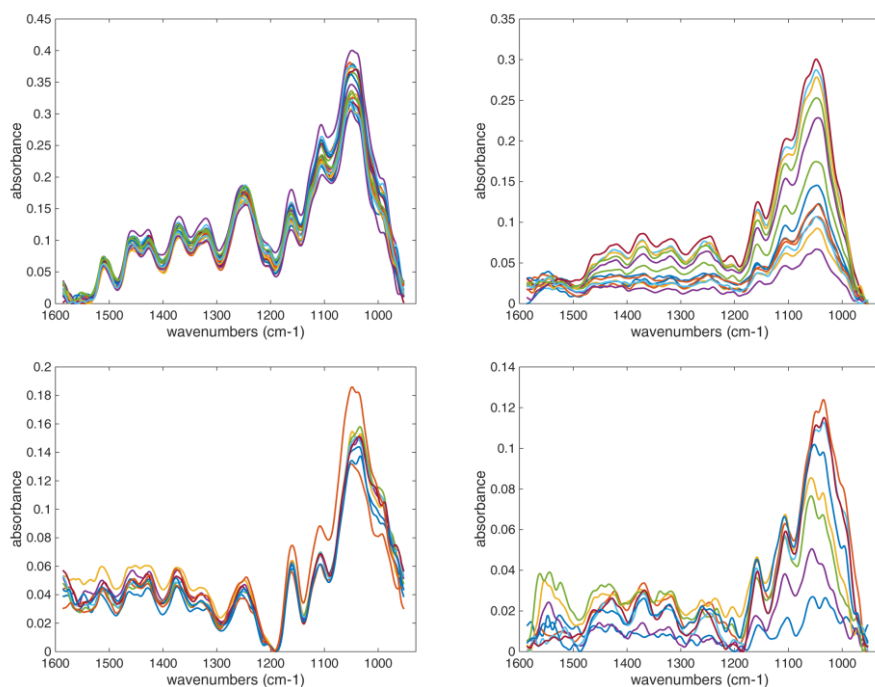


Figure 2. Examples of infrared spectra evolution. From top left to bottom right: sclerenchyma and phloem in vascular bundles, parenchyma towards stem center and near the rind.

- ¹ Anderson W.F. & Akin D.E. (2008). *Journal of Industrial Microbiology & Biotechnology*, 35, 355-366.
- ² McCann M.C., Defernez M., Urbanowicz B.R., Tewari J.C., Langewisch T., Olek A., Wells B., Wilson R.H., Carpita N.C. (2007). *Plant Physiology*. 143(3), 1314-26.
- ³ Olsson M.M., Bjurhager I., Gerber L., Sundberf B., Salmén L. (2011). *Planta*, 232,1277-1286.
- ⁴ Allouche F., Hanafi M., Jamme F., Robert P., Barron C., Guillon F., Devaux M.-F. (2012). *Chemometrics and Intelligent Laboratory systems*. 117, 200-212.

Infrared spectroscopic and electrochemical approaches for the study of the reaction mechanism of membrane proteins from the respiratory chain immobilized on nano structures

Frédéric Melin, Sébastien Kriegel, Thomas Meyer, Petra Hellwig

Laboratoire de bioelectrochimie et spectroscopie, UMR 7140, Chimie de la matière complexe, Université de Strasbourg, hellwig@unistra.fr

Keywords: SEIRAS, Nanomaterials, Spectroelectrochemistry, Membrane Proteins

Abstract: Spectroelectrochemical techniques are developed to study the reaction mechanism of membrane proteins from the respiratory chain immobilized on nanostructured electrodes. Different immobilization techniques for the proteins are compared and electrochemically induced FTIR difference have been successfully obtained from SEIRAS.

Energy supply mechanisms are central to life and living cells and are in focus of our research. Although the architectures of several membrane proteins in respiration and photosynthesis as well as the basic chemical reactions have been described, the interactions on molecular level, the curiously high diversity of mechanisms and their high efficiency, need to be clarified. In order to understand the molecular basis of energy transduction, experiments have been developed which reveal how protons, other ions and water molecules are drawn through proteins and how they are coupled to electron transfer.

The visualization of the redox reaction and coupled protonation reactions is possible when combining bio-electrochemical approaches with infrared and Raman spectroscopic techniques. In the obtained data the observation of protein action at the level of single functional groups within large proteins is possible and

thus provides essential knowledge's for the understanding of the mechanism of the studied enzymes. Information is obtained on the changes in conformation and in protonation state upon the induced redox reaction. Modes specific for a specific residue may be identified.¹

Electrochemical studies on membrane proteins need to take into account the large size of the proteins, the high distance between the active site and the electrode of often more than 10 Å as well as the necessity to work with lipids or detergent to stabilize the extracted proteins. In order to obtain a redox response for proteins in solution, mediators (like for example quinones) are added in a sub stoichiometric manner and the reaction then followed spectroscopically.¹ Direct electron transfer between electrode and sample is possible when the proteins are immobilized on an electrode. It was found that an excellent electrochemical response can be obtained even for large membrane proteins, when nanostructured materials are used, since they ensure a high protein density on the surface and allow even studies on the catalytic reaction of the protein.^{2,3}

Within these lines, the direct immobilization of membrane proteins from the respiratory chain have been performed on different nanomaterials, including gold nanoparticles and carbon nanotubes.^{2,3}

Insights into the redox properties in the presence and absence of substrate and inhibitors to the proton channels in the studied enzymes can be obtained.⁴

Different approaches are presented and compared to functionally probe different enzymes from the respiratory chain, as for example the proton pumping NADH: ubiquinone reductase and the cytochrome c oxidase. The proteins are immobilized on a gold layer, deposited on an ATR-crystal and studied by surface enhanced IR spectroscopy (SEIRAS). Different immobilization methods were probed, all based on the creation of a high affinity Self-Assembled Monolayer (SAM). We made for example use of the affinity of Ni-NTA towards a hexahistidine tag that is often genetically engineered into membrane proteins for purification purposes. Alternatively a linker is introduced that exploits the affinity of the enzyme towards its natural substrate, here NADH.⁵ Interestingly, several approaches were found to be successful despite the different

distance and orientation towards the electrode.

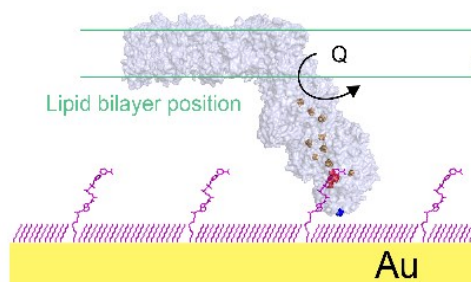


Figure 1. Schematic view on the immobilization of complex I for SEIRAS studies

The electrochemically induced FTIR difference spectra obtained are presented for the approaches tested and the effect of inhibitors on the proton channels, like Zn^{2+} investigated.

References

- ¹Melin, F.; Hellwig, P., 'Recent Advances in the Electrochemistry and Spectroelectrochemistry of membrane proteins' (2013) *Biol. Chem.*, **394**, 593-609.
- ²Melin, F.; Noor, M. R.; Pardieu, E.; Boulmedais, F.; Banhart, F.; Cecchini, G.; Soulimane, T.; Hellwig, P. 'Investigating the Thermostability of Succinate: Quinone Oxidoreductase Enzymes by Direct Electrochemistry at SWNTs-Modified Electrodes and FTIR Spectroscopy' (2014) *Chemphyschem*, **15**, 3572-3579.
- ³Meyer, T.; Melin, F.; Xie, H.; von der Hocht, I.; Choi, S. K.; Noor, M. R.; Michel, H.; Gennis, R. B.; Soulimane, T.; Hellwig, P. 'Evidence for distinct electron transfer processes in terminal oxidases from different origin by means of protein film voltammetry' (2014) *J. Am. Chem. Soc.*, **136**, 10854-1085
- ⁴Meyer, T.; Melin, F.; Richter, O.-M.H.; Ludwig, B.; Kannt, A.; Müller, H.; Michel, H.; Hellwig, P. 'Electrochemistry suggests proton access from the exit site to the binuclear center in *Paracoccus denitrificans* cytochrome c oxidase pathway variants' (2015) *Febs. Lett.*, **589**, 565-568.
- ⁵Kriegel, S.; Uchida, T.; Osawa, M.; Friedrich, T.; Hellwig, P. 'Biomimetic Environment to Study *E. coli* Complex I through Surface-Enhanced IR Absorption Spectroscopy' (2014) *Biochemistry*, **53**, 6340-6347.

Recent advances in EC-QCL technology and its use in spectroscopic sensing

J. Wagner¹, R. Ostendorf¹, J. Grahmann², A. Merten², S. Hugger¹, L. Butschek¹, F. Fuchs¹, D. Boskovic³ and H. Schenk²

¹Fraunhofer Institute for Applied Solid State Physics IAF, Tullastrasse 72, 79108 Freiburg, Germany

²Fraunhofer Institute for Photonic Microsystems IPMS, 01109 Dresden, Germany

³Fraunhofer Institute for Chemical Technology ICT, 76327 Pfinztal, Germany

Keywords: quantum cascade lasers, laser spectroscopy, mid-infrared spectroscopy, spectroscopic sensing, external cavity laser.

Widely tunable quantum cascade lasers (QCL) are ideal light sources for spectroscopic sensing exploiting characteristic finger print absorption of molecules in the mid-infrared (MIR) spectral range. Such broadband tunability can be achieved by placing a QCL chip with a broad gain spectrum into an external cavity (EC-QCL), using e.g. a diffractive grating as wavelength-dependent feedback-element. This way wavelength tuning over >25% of the central wavelength can be achieved routinely in the MIR spectral range. EC-QCLs deliver a well collimated low-divergence output beam with high spectral brightness, which enables a range of new applications. These include on- and in-line MIR spectroscopic sensing of substances in aqueous solutions and MIR backscattering spectroscopy for stand-off detection of hazardous substances. On-line and in particular in-line spectroscopy requires analytical data to be taken at high sampling rates, which in turn requires analytical MIR spectra to be taken at a high succession rate.

Here, we report on recent advances in broadband-tunable MIR EC-QCL technology as well as their use in spectroscopic analysis. First results are presented on rapid scan EC-QCL,

employing a custom-made MEMS scanning grating in Littrow-configuration as wavelength-selective optical feedback element (Fig. 1). This way, a scanning rate of 1 kHz was achieved, which corresponds to 2000 full wavelength scans per second¹.

Next, as an initial test for the use of a MEMS EC-QCL as a spectroscopic light source, the transmission spectrum of a polystyrene sheet was measured, placed between the output collimating lens of the EC-QCL and a fast thermoelectrically cooled photovoltaic MIR detector. The MEMS grating was operated close to its resonance frequency at 975 Hz, covering a spectral scan range from 1000-to-1250 cm⁻¹. 1000 transmission spectra, recorded at those points in time when the MEMS grating was scanning from longer to shorter wavelengths, were accumulated and averaged, resulting in a total data acquisition time of 1 sec. The resulting transmission spectrum is displayed in Fig. 2, together with a reference spectrum of the same polystyrene sheet recorded with a conventional FTIR spectrometer. The characteristic absorption bands of polystyrene are well resolved also in the spectrum recorded using the optical MEMS-based μ EC-QCL.

As a case study for chemical in-line process analysis, the evolution of a prototypical catalytic chemical reaction, the so-called Knoevenagel condensation, was studied using time-resolved EC-QCL based MIR fingerprint spectroscopy, this time using still a conventional slow-scan EC-QCL module. Fig. 3 shows how the MIR absorption spectrum, resulting from a



Fig. 1 Detailed view of an EC-QCL module employing a MEMS scanning grating in Littrow-configuration as wavelength-selective optical feedback element.

superposition of the fingerprint spectra of the educts and the product, evolves with time as the chemical reaction progresses¹. It is evident that, with availability of the above rapid-scan large tuning range MEMS EC-QCL, chemical reactions can be followed and monitored on a second and even sub-second time scale.

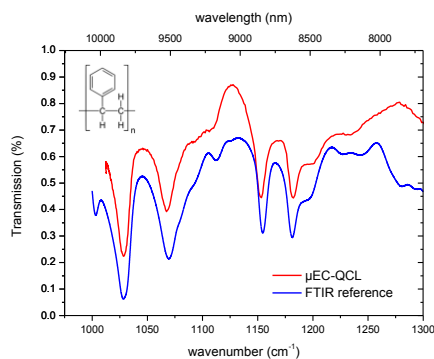


Fig. 2 Transmission spectrum (red curve) of a polystyrene recorded using a MOEMS EC-QCL. The blue curve shows a reference spectrum recorded with a FTIR spectrometer.

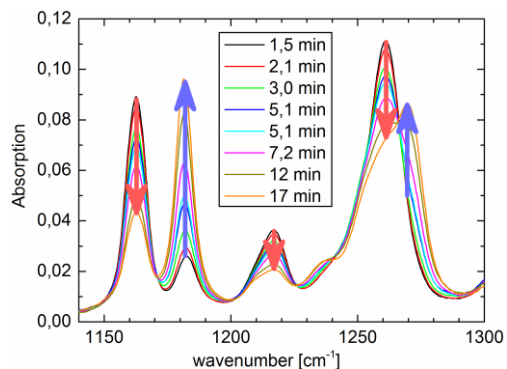


Fig. 3 MIR spectroscopic monitoring of a Knoevenagel condensation reaction using a conventional EC-QCL.

¹ Wagner J., Ostendorf R., Grahmann J., Merten A., Hugger S., Jarvis J.P., Fuchs F., Boskovic D., and Schenk H., Proc. SPIE Vol. 9370, 937012 (2015).

Monolithic tunable MIR-lasers from mirSense

Mathieu Carras, Gregory Maisons, Clement Gilles, Mickael Brun

mirSense, 86 Rue de Paris, 91400 Orsay, France

Keywords: quantum cascade lasers, monolithic, tunable.

Quantum Cascade Lasers are coherent light sources in the MIR range, attracting great interest in covering the MIR for sensing applications [1]. Currently, Distributed Feedback (DFB) QCLs provide a narrow-linewidth single-mode emission spectrum which is perfectly suited for trace gas detection, requiring wavelength tuning of a few tens of wavenumbers to detect multiple gases. DFB QCLs have demonstrated wide wavelength range operation from the MIR to the Terahertz and achieve high output powers in continuous-wave operation at room temperature. The main drawback to date is that each individual DFB QCL exhibits a limited tuning range typically of about 5.4 cm^{-1} , usually associated to temperature variations changing the index of refraction thus a spectroscopic system based on these emitters can only detect one or two molecules of interest. In order to overcome this issue, arrays of DFB QCL, composed of tenths of emitters have been developed as a solution for broad tunability [2]

One major objective of mirSense is to develop MIR Photonic Integrated Circuit (PIC) based sources through the monolithic integration of the QCL array and a multiplexer scheme achieving a widely tunable, low cost and reliable source in the MIR range suitable for laser spectroscopy

mirSense follows two approaches, one on using integration on InP, one using silicon.

We will present to two approaches, and the corresponding advantages, and performances of each of them..

For full InP based sources, we present simulation and experimental results for an adiabatic coupler realized on a double-waveguide structure. We presents the characterization results for the fabricated multiplexer structure and section 5 encompasses the most significant results of this characterization effort. Along this work we highlight the use of Echelle gratings as the optimum multiplexer solution, as they present advantages such as size reduction and minimized diffraction aberrations as well as size advantage in comparison to other multiplexer schemes; which make them ideal for compact low cost applications [3], [4], [5].

For the silicon based approach, we'll show the performances of our products, based on hybrid integration.

We thank MIRIFISENS funded by the European Commission under reference 317884.

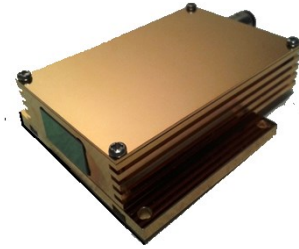


Figure 1. Product of mirSense : tunable monolithic laser source.

- [1] Faist, J.; Hugi, A.; Riedi, S.; Bismuto, A.; Hinkov, B.; Gini, E.; Blaser, S.; Beck, M., "Mid-infrared quantum cascade lasers combs for spectroscopy," Semiconductor Laser Conference (ISLC), 2012 23rd IEEE International , vol., no., pp.2,3, 7-10 Oct. 2012.
- [2] Lee, Benjamin G.; Zhang, H.A.; Pflugl, C.; Diehl, L.; Belkin, M.A.; Fischer, M.; Wittmann, Andreas; Faist, J.; Capasso, F., "Broadband Distributed-Feedback Quantum Cascade Laser Array Operating From 8.0 to 9.8 μm ," Photonics Technology Letters, IEEE , vol.21, no.13, pp.914,916, July1, 2009.
- [3] Nicoletti, S.; Barritault, P.; Boutami, S.; Brun, M.; Gliere, A.; Labeye, P.; Rouxel, J.; Czarny, J.; Lhermet, H.; Carras, M.; Maisons, G., "Challenges in the realization of a fully integrated optical lab-on-chip," SENSORS, 2014 IEEE , vol., no., pp.649,652, 2-5 Nov. 2014.
- [4] Maisons, G.; Gilles, C.; Simozrag, B.; Carras, M.; Brun, M.; Labeye, P.; Barritault, P.; Nicoletti, S.; Orbe, L.Jorge; Barrio, G.Carpintero Del, "Advances Toward Monolithic Tunable Source," Semiconductor Laser Conference (ISLC), 2014 International , vol., no., pp.169,170, 7-10 Sept. 2014
- [5] Orbe, L. J.; Gordon, C.; Carpintero, G.; Maisons, G.; Carras, M.; "InGaAs/InP-based Echelle mirror multiplexer using dual Rowland circle gratings for DFB QCL arrays in the mid-long infrared range," Proc. SPIE 9002, Novel In-Plane Semiconductor Lasers XIII, 90021O (February 27, 2014).

Ring quantum cascade lasers for infrared spectroscopy

Rolf Szedlak¹, Martin Holzbauer¹, Donald MacFarland¹, Tobias Zederbauer¹, Hermann Detz¹, Aaron Maxwell Andrews¹, Werner Schrenk¹ and Gottfried Strasser¹

¹Institute for Solid State Electronics, Vienna University of Technology
Floragasse 7, 1040 Vienna, Austria

Keywords: quantum cascade laser, ring, infrared, spectroscopy, metamaterial

Quantum cascade lasers [1] (QCLs) have become powerful and reliable tools for many applications in a variety of fields like imaging, astronomy and free space optical communication. Due to their customizable emission wavelengths they are also the perfect candidates for various spectroscopic applications like trace gas sensing, chemical sensing of liquids and many more. In QCLs electrons emerge through a semiconductor heterostructure with multiple cascading active regions. The electrons are recycled and emit as many photons as cascades are present in the structure.

Previously, we reported on vertically emitting ring quantum cascade lasers [2] providing improved electrical and power characteristics compared with conventional Fabry-Pérot devices. In addition, ring QCLs exhibit a strongly collimated and rotationally symmetric emission beam. This narrow light beam is attributed to the large emitting area. A distributed feedback grating (DFB) provides optical feedback and vertical light outcoupling. Using substrate emitting lasers, it is possible to manipulate the emitted light with a gradient index based metamaterial [3] fabricated into the bottom side of the chip. We observed a maximum intensity increase by a factor of more than six (see Fig. 1) due to the focusing effect of this metamaterial. Such devices significantly increase the sensitivity of spectroscopic

absorption measurements. Modified DFB gratings like abrupt and continuous Pi-Shifts or off-centered gratings provide far fields with a central intensity maximum. This could further improve the sensitivity of spectroscopic measurements.

Usually, the spectroscopy of substances in a composition requires more than one wavelength. Therefore, QCL arrays can be used. Each laser in such an array emits at a different frequency. Conventional ring QCL arrays consist of a rectangular arrangement of multiple rings. This means that the different wavelengths originate from slightly different positions under unequal angles. Therefore, special beam combining optics are required. We propose a novel array design, where the lasers are arranged in a concentric pattern as shown in Fig. 2. Though due to the different sizes of the rings different beam divergences are expected, our calculations predict only very small variances. The utilization of Pi-Shifts at different angular positions opens the door for polarization-based spectroscopy. Since the central lobe of Pi-Shift ring QCLs is linearly polarized, concentric ring lasers with Pi-Shifts at different angular positions can be used for multicolor spectroscopic measurements, where the wavelength can be selected by an external polarizer. This could decrease the necessary time for such measurements.

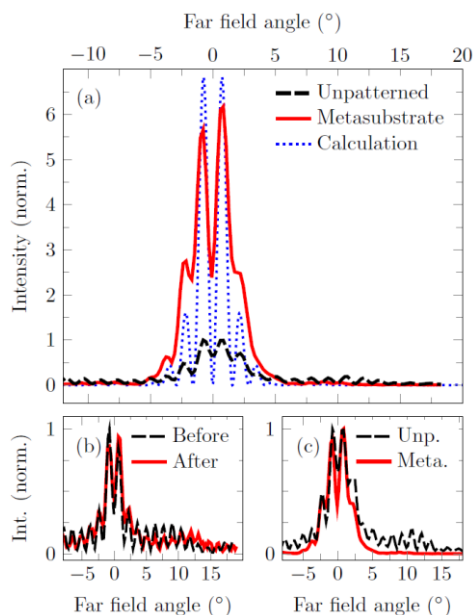


Figure 1. (a) Farfield with (red) and without (black) metasubstrate. (b) Farfield of reference laser. (c) Normalized far fields from (a).

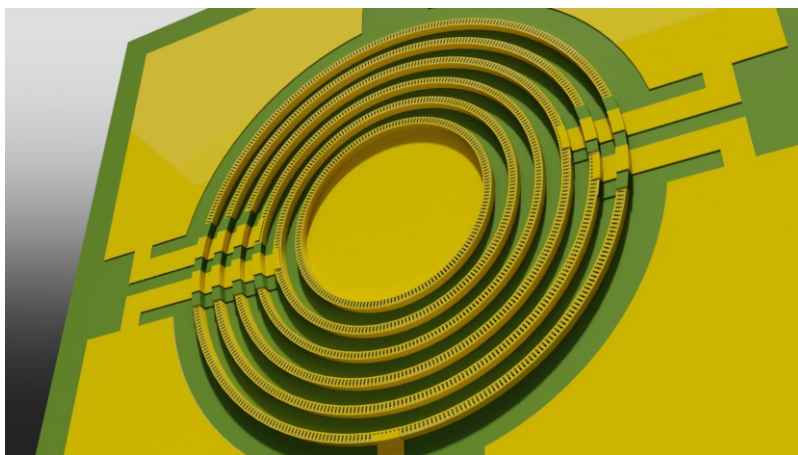


Figure 2. Concentric arrangement of 6 ring QCLs. Each ring can be equipped with a different emission wavelength.

J. Faist, F. Capasso, D. L. Sivco, C. Sirtori, A. L. Hutchinson, and A. Y. Cho, *Science* 264, 553 (1994).
 E. Mujagic, L. Hoffmann, S. Schartner, M. Nobile, W. Schrenk, M. Semtsiv, M. Wienold, W. Masselink, and G. Strasser, *Appl. Phys. Lett.* 93, 161101 (2008).
 R. Szedlak, C. Schwarzer, T. Zederbauer, H. Detz, A. M. Andrews, W. Schrenk, and G. Strasser, *Appl. Phys. Lett.* 104, 151105 (2014).

Recent results on performance optimization of QCLs for spectral coverage, heat dissipation, and output power

Antoine Müller¹, Alfredo Bismuto¹, Stéphane Blaser¹, Tobias Gresch¹, Olivier Landry¹, Richard Maulini¹ and Romain Terrazzi¹

¹Alpes Lasers SA, 2000 Neuchâtel, Switzerland

Keywords: QCL, tuning, spectroscopy, broad gain, low dissipation.

Quantum Cascade Lasers have been available commercially for 16 years now. They are commonly used in multiple applications, such as atmospheric monitoring, urban, rural and industrial emission control and medical applications such as breath analysis. Yet large scale deployment similar what has been seen in the last decades for visible and near-infrared diode lasers is still out of reach. Major differences include the comparatively low efficiency of QCLs and their high electrical dissipation and the small spectral tunability of monolithically integrated devices. In this presentation the results of recent optimization efforts performed at Alpes Lasers SA to overcome these barriers will be presented. For applications such as hand held battery powered apparatus, devices with total dissipation lower than one Watt are presented. Focus will also be put on applications related to extended tuning devices, showcasing DFB devices with up to 10 cm⁻¹ of tuning. Finally watt level output power in the 4 to 5 micron region will be presented.

Most QCLs create 5 to 15 W of electrical dissipated power at their operation point; the thermoelectrical temperature control systems required for stable operation can bring the overall power needs up to 100W. Conversely, output powers of a few mW are sufficient for a large array of

applications. By optimizing the grating coupling and the facet coatings to aim for short and narrow low-power devices, Alpes Lasers has succeeded¹ in developing QCLs which require less than 1W of electrical power such as shown in Fig. 1. In particular, this allows CW devices to be used in the smaller and less expensive TO3 housings.

Standard DFB lasers can scan a range of 1 to 2 cm⁻¹ through electrical tuning; this is sufficient to scan through one, sometimes two gas lines. Many applications require a larger tuning range, either to resolve wide lines or multiple lines rapidly. The new extended tuning devices (QC-ET) use a dual current control to extend the mode-hop free tuning to more than 0.4% of the central wavelength (>6 cm⁻¹ at 1270 cm⁻¹). While the first laser input allows direct intensity modulation in the same manner as standard DFB lasers, the integrated heater current IT allows to offset the wavelength much faster than the temperature change of the heatsink temperature would do. An example of such a laser scanning through 11 absorption lines of N₂O is shown in Fig. 2.

Finally, QCLs with more than 1W of output power are showcased. Available in a collimated HHL package with a dedicated driver, these lasers can be used for free-space optical communications, energy deposition, illumination and IR countermeasures.

Monday

Tuesday

Wednesday

Thursday

Friday

Author Index

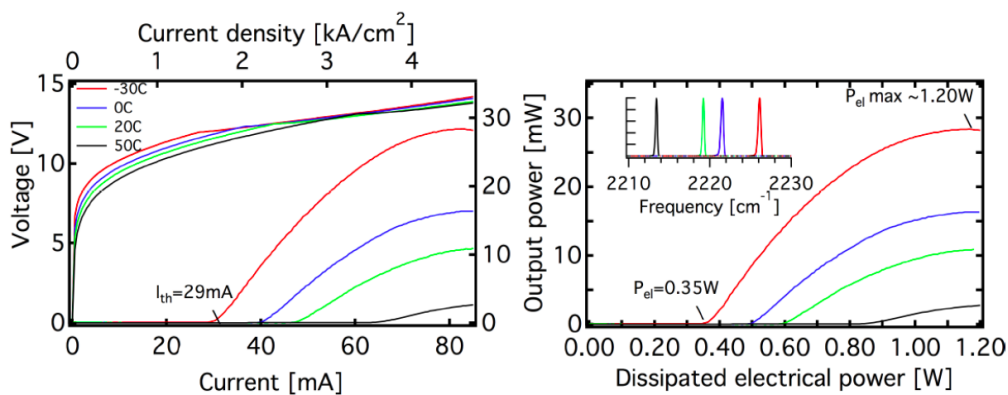


Figure 1. Low dissipation laser

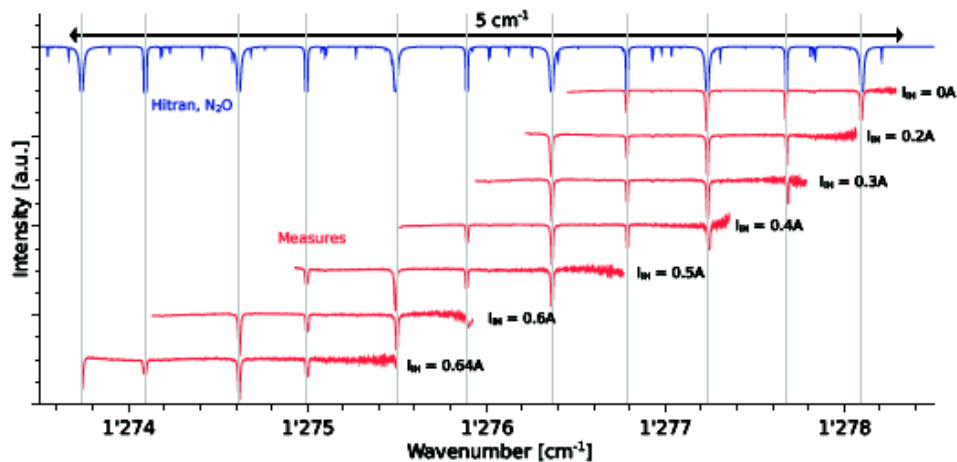


Figure 2. Example of wide scanning of a N₂O gas cell, with fast I_L scans and independent I_T values.

¹ Bismuto, A. et al., *Optics Express*. Vols 3 No 5 p. 5477, OSA 2015.

QCL frequency comb technology for mid-infrared sensing

Markus Mangold^{1,2}, Andreas Hugi^{1,3}, Markus Geiser^{1,3}, Gustavo Villares³, Jérôme Faist³,
Lukas Emmenegger²

¹ IRsweep GmbH, c/o ETH Zürich, Institute for Quantum Electronics, HPT H4.1, Auguste-Piccard Hof 1, 8093 Zürich

² Empa, Laboratory for Air Pollution and Environmental Technology, Überlandstr. 129, 8600 Dübendorf, Switzerland

³ Institute for Quantum Electronics, ETH Zürich, Auguste-Piccard-Hof 1, 8093 Zürich, Switzerland

Keywords: Mid-infrared; absorption spectroscopy; quantum cascade laser; frequency combs.

Mid-infrared (MIR) laser spectroscopy is highly suitable for trace substance monitoring in industrial, medical, and environmental applications. Also known as the spectral fingerprint region, MIR is especially attractive because it contains the strong fundamental ro-vibrational bands of many molecules. Applying high-resolution spectroscopy techniques allows for outstanding selectivity and sensitivity.

In order to fully exploit the potential of MIR spectroscopy, we are developing a measurement platform based on semiconductor quantum cascade laser frequency combs.¹ Frequency combs emit light of many, clearly defined wavelengths in a broad spectral range. In a dual-comb spectroscopy setup, two optical frequency comb sources are superimposed on a detector, as shown in Figure 1a.² The multi-heterodyne detection relies on down-mixed beat notes of the two combs with very similar repetition rates, effectively mapping the optical frequencies (THz) down to the radio-frequency domain (up to GHz, Figure 1b). The heterodyne beatnotes can be measured with conventional electronics, allowing for spectral analysis without refractive, diffractive, or movable elements.

However, the parallel acquisition of dual-comb spectrometers comes at the price

of enormous data-rates. We use free-running QCL combs to improve the system scalability, robustness, and optical simplicity. Therefore, no complicated optical locking mechanisms are required. To reach high signal-to-noise ratios, we are developing an algorithm, which is based on combination of coherent and non-coherent averaging. This algorithm is specifically optimized for free-running, high-repetition rate comb sources. As a consequence, our system generates data at rates of up to 3.2 GB/sec. These data-rates need to be reduced by several orders of magnitude in real-time in order to be useful for spectral fitting algorithms.

We present the development of a data-treatment solution, which reaches a single-channel throughput of 22% using a standard laptop-computer. Using a state-of-the art desktop computer, the throughput is increased to 43%. This is combined with a data-acquisition board to a stand-alone data processing unit, allowing real-time industrial process observation and continuous averaging to achieve highest signal fidelity. Our development goes towards a small size and robust measurement platform. The platform's key features will be an unmatched combination of optical bandwidth (100 cm^{-1}), spectral resolution

(100 kHz), and measurement speed (100 μ s). Combining the dual-comb spectroscopy with a multipass reflection cell will considerably increase the sensitivity of the

absorption measurement,³ opening doors to beforehand unreachable applications.

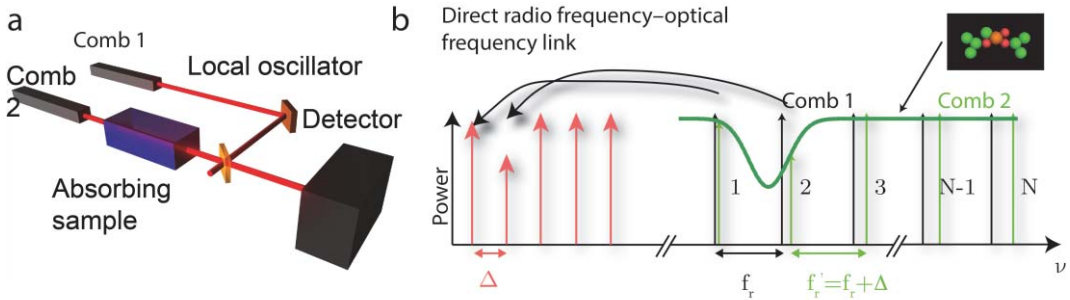


Figure 1. (a) Schematic representation of a dual comb spectroscopy setup. (b) The heterodyne beatnotes of the two combs with slightly different repetition frequencies result in a radio-frequency signal which is measurable with conventional electronics.

- ¹ Andreas Hugi, Gustavo Villares, Stéphane Blaser, H. C. Liu, and Jérôme Faist (2012), *Nature*, 492, 229–233.
- ² Gustavo Villares, Andreas Hugi, Stéphane Blaser and Jérôme Faist (2014), *Nature Communications*, 5, 5192.
- ³ Béla Tuzson, Markus Mangold, Herbert Looser, Albert Manninen, and Lukas Emmenegger (2013), *Optics Letters*, 38, 257.

Broadband high-resolution multi-heterodyne ro-vibrational spectroscopy of gases with quantum- and interband cascade lasers

Jonas Westberg, Eric Zhang, Andreas Hangauer, and Gerard Wysocki*
Electrical Engineering Department, Princeton University, 08544 Princeton, NJ
*email: gwyssocki@princeton.edu

Keywords: multi-heterodyne spectroscopy, mid-IR spectroscopy, quantum cascade lasers, interband cascade lasers, broadband laser sources

Mid-IR is considered a molecular fingerprint region that is particularly suitable for sensitive chemical detection. In the recent years quantum cascade lasers (QCLs) and interband cascade lasers (ICLs) become semiconductor sources of choice for high resolution spectrometry in the mid-IR. A common problem of simultaneous spectroscopic detection of large molecules with broad ro-vibrational spectra, and small molecules with well-resolved narrow spectral lines requires both broadband optical frequency coverage ($>50\text{ cm}^{-1}$) and high resolution ($<0.01\text{ cm}^{-1}$) to perform accurate spectral measurements. So far the most common laser technologies that could address the broadband spectral coverage have been external cavity (EC) QCLs and EC-ICLs providing $>100\text{ cm}^{-1}$ tuning ranges and narrow linewidths in the mid-IR¹. However EC lasers are rather complex opto-mechanical systems, which are vibration-sensitive, and construction of robust transportable systems is difficult.

In this work we are investigating a new method of performing broadband mid-IR spectroscopy using free-running Fabry-Perot (FP) QCLs² or ICLs. This measurement method is based on down-conversion of optical signals to the RF domain through a multi-heterodyne process (used in dual-comb spectroscopy³). In this paper we will discuss the configuration of the experimental set-up (Fig. 1) of a robust dual-FP-laser multi-heterodyne spectrometer that is all electrically driven, contains no moving

parts and assures high opto-mechanical stability. The application of intrinsically small semiconductor devices shows great potential for development of simple and compact broadband spectrometers that are able to access the fundamental molecular absorption bands in the mid-IR with high resolution ($\leq 2\text{ MHz}$, free-running and the ultimate linewidth limit of $<200\text{ kHz}$ demonstrated in Fig. 2).

In this paper we will be present performance studies of the multi-heterodyne spectrometers based on QCLs and ICLs as well as demonstration of chemical sensing capabilities. Examples will include broadband multi-mode direct absorption spectroscopy measurements and high-resolution ($\sim 15\text{ MHz}$ or $\sim 0.0005\text{ cm}^{-1}$) spectroscopy of NH_3 and N_2O (Fig. 3). The evaluation of the amplitude and phase noise observed in the multi-heterodyne signals revealed a clear $1/f$ trend. Therefore modulations techniques such as wavelength modulation spectroscopy (WMS) have a potential to reduce the technical noise in the measured absorption spectrum and thus improve sensitivity of the spectral measurements. Here we will present the first implementation of WMS technique applied to multi-heterodyne spectral measurement (Fig. 3). The WMS allows accessing the region of lower intensity noise at modulation frequencies $>5\text{ kHz}$ and achieve relative intensity noise of $\sim 6 \times 10^{-5}/\text{Hz}^{1/2}$ for QCLs and $\sim 3.5 \times 10^{-4}/\text{Hz}^{1/2}$ for ICLs.

In summary, multi-heterodyne spectroscopy with multi-mode semiconductor lasers enables a multitude of spectroscopic applications that could cover the entire mid-IR region and even free running FP-QCLs (1.9 MHz linewidth) or FP-ICLs (11MHz linewidth) show an excellent potential for

high resolution multi-heterodyne spectroscopy of gases at reduced and/or atmospheric pressures.

Acknowledgements: The authors gratefully acknowledge funding by the U.S. EPA (RD-83513701-0), and by the NSF ERC MIRTHE (EEC-0540832).

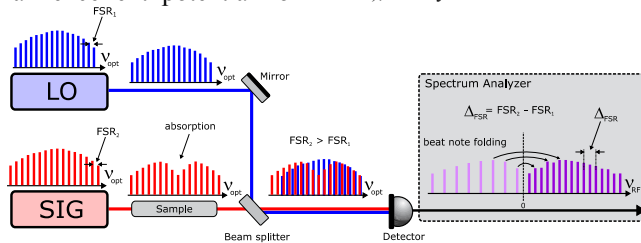


Figure 1. The experimental layout of multi-heterodyne spectrometer based on two Fabry Perot laser pairs (8.5 μm QCLs and 3.5 μm ICLs) with slightly different free-spectral range. The insets show cartoons of emission spectra of individual lasers and the down-converted RF spectrum (with frequency folding effect).

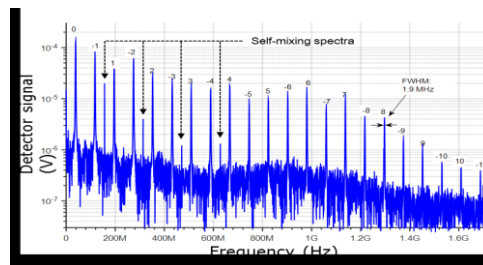


Figure 2. Multi-heterodyne beatnote spectrum for the QCL emitting at 8.5 μm . The spectrum contains 21 beatnotes corresponding to optical modes separated by 1.4 cm^{-1} providing instantaneous spectral bandwidth of $\sim 30 \text{ cm}^{-1}$.

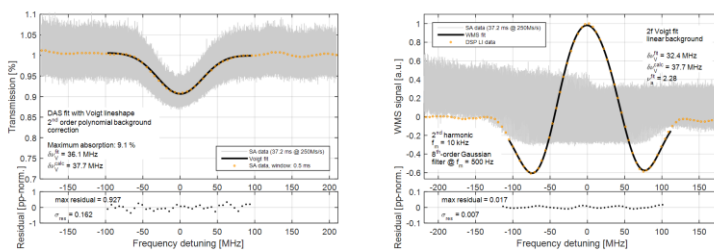


Figure 3. Absorption spectrum of N_2O acquired with the beatnote #0 in Fig. 2 in a direct laser absorption spectroscopy (left) and WMS mode (right). The data are fitted with a spectral model using HITRAN database (black line).

- ¹ M. Bo, and W. Qi Jie, "Broadly tunable single-mode mid-infrared quantum cascade lasers," *Journal of Optics* 17, 023001 (2015).
- ² Y. Wang, et al., "High-resolution multi-heterodyne spectroscopy based on Fabry-Perot quantum cascade lasers," *Appl. Phys. Lett.* 104, 031114 (2014).
- ³ S. Schiller, "Spectrometry with frequency combs," *Opt. Lett.* 27, 766 (2002).

Interband cascade lasers with spectrally single mode emission in the mid-infrared wavelength range from 3 to 5 microns

Julian Scheuermann¹, Michael von Edlinger¹, Robert Weih², Lars Nähle¹, Marc Fischer¹, Johannes Koeth¹, Martin Kamp² and Sven Höfling^{2,3}

¹nanoplus Nanosystems and Technologies GmbH, Oberer Kirschberg 4, 97218, Gerbrunn, Germany

²Technische Physik, Physikalisches Institut and Wilhelm-Conrad-Röntgen-Research Center for Complex Material Systems, Universität Würzburg, Am Hubland, 97074, Würzburg, Germany

³School of Physics and Astronomy, North Haugh, St Andrews, KY16 9SS, United Kingdom

Keywords: mid-infrared absorption spectroscopy, distributed feedback, interband cascade laser, gas sensing.

Compared to the near-infrared, many technologically and industrially relevant gas species have absorption features in the mid-infrared (MIR), with more than an order of magnitude higher absorption strength. This includes combustion gases like carbon oxides, many hydrocarbons and also volatile organic compounds used e.g. as cancer indicators in breath analysis.

Laser emission in the MIR wavelength range can in principle be achieved by three approaches. Based on GaSb diode lasers, long wavelength emission up to 3.7 μm was reported¹ whereas quantum cascade lasers, which show best performances at higher wavelengths, were published down to emission wavelengths around 3 μm ^{2,3}. The third approach is based on interband cascade lasers (ICLs), which have evolved over the last years into important laser sources in the MIR wavelength region. Especially distributed feedback (DFB) ICLs with application grade performance have recently become available in the spectral range from 3 to 5 μm ⁴.

These DFB ICLs are a perfect tool for tunable laser absorption spectroscopy

(TLAS) or other spectroscopic applications, which has already been proven by various experiments^{5,6}.

This presentation will focus on the fabrication and application of DFB ICLs. By depositing a lateral metal grating along the ridge waveguide which couples to the evanescent field of the fundamental laser mode, spectrally single mode emission is achieved. Recorded spectra show setup limited signal to noise ratios of around 30 dB (Figure 1). The ebeam defined metal grating approach enables exact realization of the targeted emission wavelength.

All devices operate in continuous wave (cw) mode at least up to room temperature, some even up to 80 °C. With cw output powers up to 20 mW the devices offer sufficient power for use in TLAS applications. Figure 2 shows temperature dependent light-current characteristics of a device with room temperature threshold currents below 15 mA. Devices in the 3.4 micron wavelength range showed an overall tuning range of up to 25 nm, with respective current tuning rates of around 0.22 nm/mA.

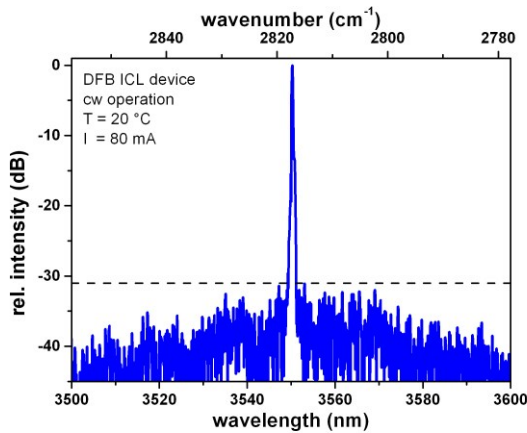


Figure 1. Spectrum of a single mode ICL with setup limited signal to noise ratio >30 dB operating in cw mode.

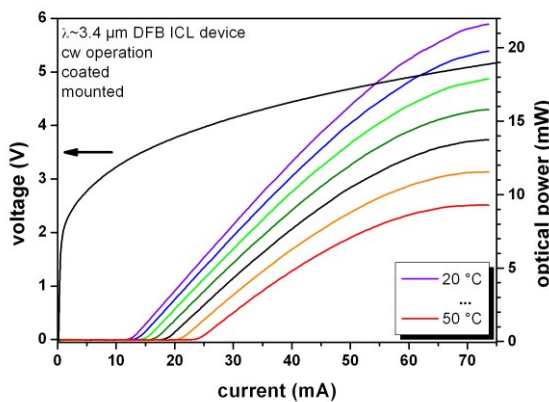


Figure 2. Performance characteristics of a DFB ICL with room temperature threshold current below 15 mA and output power up to 20 mW.

Vizbaras C.K., Amann M.C. (2012), *Semiconductor Science and Technology*, 27, 032001.
 Pandey N., Bai Y., Tsao S., Nida S., Slivken S., Razeghi M. (2012), *Applied Physics Letters*, 101, 241110.
 Volf J.M., Bismuto A., Beck M., Faist J. (2014), *Optics Express*, 22, 2111-2118
 Burgaftman I., Bewely W.W., Canedy C.L., Kim C.S., Kim M., Merritt C.D. Abell J. Meyer J.R. (2013), *Selected Topics in Quantum Electronics*, 19, 1200210.
 Lundqvist S., Kluczynski P., Weih R., v. Edlinger M., Nähle L., Fischer M., Bauer A., Höfling S., Koeth J. (2012), *Applied Optics*, 51, 6009.
 Nyssocki G., Bakhirkin Y., So S., Tittel F.K., Hill C.J., Yang R.Q., Fraser M.P. (2007), *Applied Optics*, 46, 8202.

Improvements of a capillary Raman system for trace gas analysis and rapid process control

Simone Rupp¹, Timothy M. James¹, Andreas Off¹,
Hendrik Seitz-Moskaliuk² and Helmut H. Telle³

¹ Institute of Technical Physics, Tritium Laboratory Karlsruhe, Karlsruhe Institute of Technology, 76021 Karlsruhe, Germany

² Institute of Experimental Nuclear Physics, Karlsruhe Institute of Technology, 76021 Karlsruhe, Germany

³ Instituto Pluridisciplinar, Universidad Complutense de Madrid, Paseo Juan XXIII-1, 28040 Madrid, Spain

Keywords: Raman spectroscopy, capillary, gas analysis, process control, high sensitivity.

Raman spectroscopy is a flexible tool for compositional analyses of solid, liquid and gaseous samples. The technique allows one to measure compositions in a contact-free and inline way, and to detect multiple species simultaneously using only one excitation wavelength. On the downside, the small excitation cross-sections pose a challenge in low-pressure (low total particle density) applications. In particular, for real-time process monitoring or the detection of trace gases at total pressures in the mbar/sub-mbar range, measurement systems of extremely high sensitivity are required.

A simple, robust approach to enhance the Raman signal utilizes a hollow tube / capillary with a reflective inner surface as the gas cell, through which the laser beam passes longitudinally¹. The Raman light is collected in a backward configuration, with the tube greatly increasing the interaction region as the scattered light is reflected and collected over the full tube length. Recently, we demonstrated the use of such a capillary system for dynamic process monitoring, achieving sub-mbar detection limits in sub-second recording times.² However, despite the implementation of fluorescence reduction measures, the signal-to-noise ratios (SNRs) of the systems described therein and

in Rupp *et al*³ were limited by shot-noise from the still non-negligible background, counter-acting the gain in Raman signal.

In Figure 1a the measurement setup^{2,3} is shown, with the components contributing to the fluorescence background marked in red: namely, the capillary itself, the dichroic beam-splitter, the window and the (optional) back-reflecting mirror.

The capillary was a silver-lined hollow glass fiber with an inner diameter of 1 mm, which matched the aperture of the dot-to-slit fiber bundle imaging the collected light onto the spectrometer slit. Glass fibers are commonly used in such systems as their smooth surface provides excellent reflection properties; however, fluorescence light originating from the glass walls could not be fully suppressed. Therefore, we investigated whether non-fluorescing metal tubes could be used instead. The main caveat is that small-diameter tubes are hard to polish internally to a smooth, mirror-like finish, while larger diameters lead to reduced light collection. We compared metal tubes of different diameters and materials; despite some signal reduction, the SNR could be increased by a factor of 3 for gold tubes, of 20 cm length and inner diameter 2 mm, due to the substantially reduced shot noise.

Commonly, a beam splitter separates the laser beam and the scattered light, with little loss in the Raman signal. As alternatives, (i) a 2 mm pick-off mirror and (ii) an off-axis metal-substrate parabolic mirror with a central hole (to pass the laser into the capillary) were tested. In both configurations parts of the Raman light are “blocked”, but the associated small signal loss is more than compensated by the significant fluorescence reduction. Using the second approach instead of the dichroic beam splitter, the SNR could be increased by a factor of 5.1.

Assuming that a full-metal mirror is less prone to damage in corrosive atmospheres (like e.g. T_2) than a dielectric coating, it could be placed inside the gas system, as shown in Figure 1b. Now the laser enters through one window in front of the mirror with hole, which blocks the generated flu-

orescence almost completely. The Raman light exits the gas system through a second window which is not in contact with laser light. In addition, the mirror at the capillary end was replaced by a window to simplify the alignment. Fluorescence previously generated by the back-reflected laser beam is eliminated completely; and fluorescence from the end component back through the tube can be minimized by a suitably-placed diaphragm and by tilting the window by 45° .

The fluorescence reduction measures described here increased the SNR by a factor of 10.8. Based on this, a limit of detection (3σ) of 0.21 ± 0.03 mbar in 50 x 0.1 s was achieved for N_2 in a prototype setup, demonstrating the suitability of capillary Raman systems as robust and simple real-time gas analysis tools.

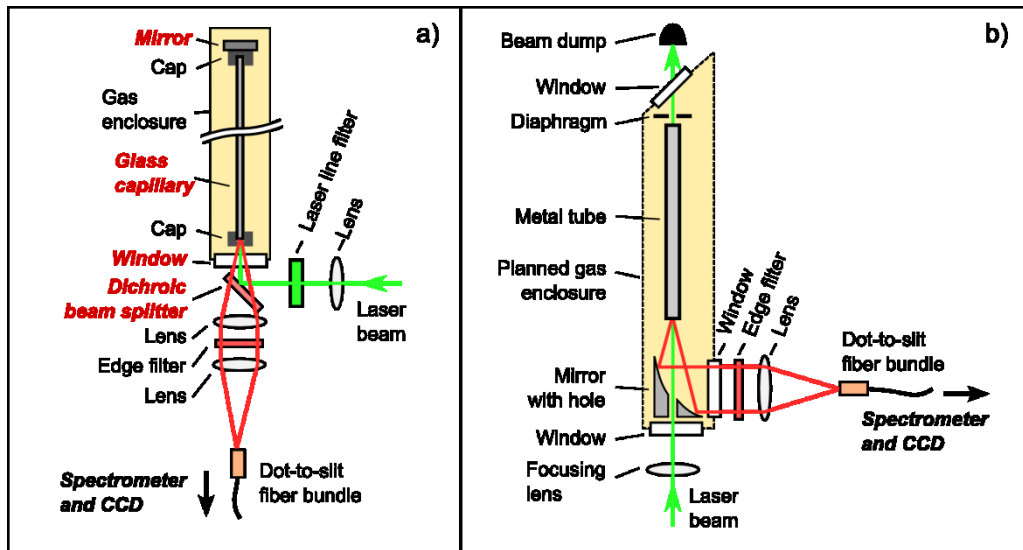


Figure 1: Schematic sketch of (a) previous Raman setup and (b) improved prototype.

¹ Carlsen W.F., Simons T.D., Pittaro R.J., Hopkins G.W., Gray D.F. (1996), *System for collecting weakly scattered electromagnetic radiation*, US Patent No. 5506678, 25p.

² James T.M., Rupp S., Telle H.H. (2015), *Anal. Methods*, 7, 2568-2576, doi: 10.1039/c4ay02597k.

³ Rupp S., James T.M., Telle H.H., Schlösser M., Bornschein B. (2015), *Fusion Sci. Technol.*, 67, 547-550, doi: 10.13182/FST14-T76.

Fiber and cavity enhanced Raman spectroscopic analysis of breath and environmental gases

Torsten Frosch^{1,2}, Tobias Jochum¹, Di Yan¹, Anne Bachmann¹, Timea Bögözi¹, Stefan Hanf¹, Robert Keiner¹, and Juergen Popp^{1,2,3}

¹Leibniz Institute of Photonic Technology, Albert-Einstein-Str. 9, 07745 Jena, Germany;

²Friedrich Schiller University, Institute for Physical Chemistry, Helmholtzweg 4, 07743 Jena, Germany;

³Friedrich-Schiller University, Abbe Centre of Photonics, Max Wien Platz 1, 07743 Jena, Germany;

Keywords: fiber-enhanced Raman spectroscopy (FERS), cavity-enhanced Raman spectroscopy (CERS), breath analysis, environmental monitoring

Fiber-enhanced Raman spectroscopy (FERS) and cavity-enhanced Raman spectroscopy (CERS) were proven as versatile new techniques for online and real-time monitoring of disease markers in exhaled breath¹⁻³. Biogenic gases play also an important role in the biosphere. The continuous online monitoring of gas compositions and exchanges helps to reveal complex biogeochemical processes⁴⁻⁸. Non-consumptive Raman gas spectroscopy enables the characterization of ecosystems without disturbance^{5, 7, 8}.

Conventional Raman spectroscopy provides excellent chemical sensitivity for the identification of multi-gas compositions (all gases except noble gases can be measured), but is a weak scattering process. Recently innovative optical hollow fibers⁹ and power build-up cavities⁷ were developed for strong enhancement of the Raman signals and improved analytical sensitivities down to low ppm concentrations^{2, 3, 7}.

FERS was introduced for early-stage, non-invasive, point-of-care breath gas diagnosis of metabolic diseases, based on combined rotational and ro-vibrational Raman spectroscopy^{1, 2}. A compact device was developed which provides excellent linearity and a dynamic range of five orders

of magnitude^{2, 3}. The abilities of this new device were proven with the precise monitoring of H₂ and CH₄ in the concentration range between 5 and 50 ppm in order to demonstrate the potential for the diagnosis of malabsorption disorders, including lactose intolerance, fructose malabsorption, and bacterial overgrowth syndrome².

CERS has unique potential for continuous onsite monitoring of complex gas mixtures⁴⁻⁸, including: (i) the analysis of bioremediation of benzene contaminants in soil⁴, (ii) monitoring of intermediate states and mass balance of nitrogen during denitrification of fertilizer by soil microorganisms⁵, (iii) monitoring the photosynthetic uptake of ¹³CO₂ in order to investigate the flow of resources in plants⁶, (vii) the quantification of gas exchange rates from climate sensitive ecosystems (here water-saturated peat bog) for the determination of important ecosystem parameters such as the maximum photosynthesis rate of the sphagnum as well as the extent of soil and plant respiration⁷, and (iv) the study of the live cycle of important biomineral precipitating cave bacteria⁸.

The global nitrogen cycle is highly impacted by humans and understanding

rates and processes of microbial N transformation, is of great importance in environmental chemistry research. Nitrogen is a fundamental component of living organisms and human activities, e.g. in fertilizer use. The investigation of changes in N cycling has been very challenging so far due to difficulties with measuring gases such as N₂ and N₂O simultaneously. Here CERS was applied for tracing the stepwise reduction of ¹⁵N-labelled nitrate by the denitrifying bacteria *Pseudomonas stutzeri*⁵. The unique capabilities of Raman multi-gas analysis enabled real-time, continuous, and non-consumptive quantification of the relevant gases (¹⁴N₂, ¹⁴N₂O, O₂, and CO₂) with one single measurement. Using this new methodology, it was possible to quantify the kinetics of the formation and degradation for all gaseous compounds (educts and products) and thus study the reaction orders⁵. The gas quantification was complemented with the analysis of nitrate and nitrite concentrations for the online monitoring of the total nitrogen element

budget⁵. The simultaneous quantification of all gases also enabled the contactless and sterile online acquisition of the pH changes in the *P. stutzeri* culture by the stoichiometry of the redox reactions during denitrification and the CO₂-bicarbonate equilibrium⁵. Continuous pH monitoring – without the need to insert an electrode into solution – elucidated e.g. an increase in the slope of the pH value coinciding with an accumulation of nitrite, which in turn led to a temporary accumulation of N₂O, due to an inhibition of nitrous oxide reductase⁵.

In summary, CERS and FERS are extremely versatile analytical techniques for fast and continuous onsite multi-gas analysis. This new techniques provide unique features for the elucidation of complex biochemical processes and for the estimation of climate-relevant gas budgets⁴ ⁸. Regarding the early-stage, non-invasive monitoring of disease markers in exhaled breath - CERS and FERS may develop into new point-of-care devices¹⁻³.

Acknowledgement: Funding by the Collaborative Research Centre 1076 “AquaDiva” from the Deutsche Forschungsgemeinschaft (DFG) is gratefully acknowledged. We thank our collaboration partners¹⁻⁹.

¹ Bögözi T., Popp J., Frosch, T. (2015), *Bioanalysis*, 7 (3), 281–284

² Hanf S., Bögözi T., Keiner R., Frosch T., Popp J. (2015), *Analytical Chemistry*, 87, 2, 982–988.

³ Hanf S., Keiner R., Yan D., Popp J., Frosch T. (2014), *Analytical Chemistry*, 86, 11, 5278–5285.

⁴ Jochum T., Michalzik B., Bachmann A., Popp J., Frosch T. (2015), *Analyst*, DOI: 10.1039/C5AN00091B.

⁵ Keiner R., Herrmann M., Küsel K., Popp J., Frosch T. (2015), *Analytica Chimica Acta*, 864, 39–47.

⁶ Keiner R., Frosch, T., Massad T., Trumbore S., Popp J. (2014), *Analyst*, 139, 16, 3879–3884.

⁷ Frosch T., Keiner R., Michalzik B., Fischer B., Popp J. (2013), *Analytical Chemistry*, 85, 1295–1299.

⁸ Keiner R., Frosch T., Hanf S., Rusznyak A., Akob D.M., Küsel K., Popp J. (2013), *Analytical Chemistry*, 85, 8708–8714.

⁹ Hartung A., Kobelke J., Schwuchow A., Wondraczek K., Bierlich J., Popp J., Frosch T., Schmidt M.A. (2014), *Optics Express*, 22, 16, 19131–19140.

New developments in THz quartz-enhanced photoacoustic spectroscopy

Vincenzo Spagnolo¹, Pietro Patimisco¹, Angelo Sampaolo^{1,3}, Gaetano Scamarcio¹, Miriam S. Vitiello², Frank K. Tittel³

¹Dipartimento Interateneo di Fisica, Università e Politecnico di Bari, CNR-IFN UOS BARI, Via Amendola 173, Bari, Italy,

²NEST, CNR-Istituto Nanoscienze and Scuola Normale Superiore, Piazza San Silvestro 12, I-56127 Pisa, Italy

³Department of Electrical and Computer Engineering, Rice University, 6100 Main Street, Houston, TX 77005, USA

Keywords: Quartz-enhanced photoacoustics, THz spectroscopy, Gas Sensing.

Recent advances in terahertz (THz) photonics and nanotechnology have opened the way to gas sensing applications in an increasingly wide variety of fields, such as environmental monitoring including atmospheric chemistry, climate modelling, volcanic emissions, rural emission measurements associated with agriculture and forestry, medical diagnostics and the life sciences, industrial process monitoring related to the petrochemical, semiconductor, and pharmaceutical industries, law enforcement and defense. THz gas spectroscopy is a very promising tool for in-situ and remote gas sensing, since many molecules of interest with distinct spectral fingerprints and strong absorption bands fall in the THz spectral region. For example, gas species such as water, hydrogen sulphide, hydrogen fluoride, hydrogen bromide, nitrogen compounds, possess their strongest absorption bands in the THz spectral range.

Among trace-gas detection techniques, quartz-enhanced photoacoustic spectroscopy (QEPAS) is capable of record sensitivities using a compact and relatively low-cost acoustic detection module¹. Efficient QEPAS sensors have been demonstrated for trace detection of several gas chemical species¹ with a minimum detection limit down to a few parts per trillion in volume.² The THz spectral range can be considered

the most suitable for the QEPAS technique, because rotational levels are mainly involved in THz absorption processes and their relaxation rates are up to three orders of magnitude faster with respect to vibrational levels in the mid-IR spectral range. Moreover, the THz region offers advantages in terms of selectivity, because gas molecules have distinct spectral “fingerprints” absorption spectra, arising from rotational quantum transitions. These spectra allow unambiguous, more efficient and accurate detection compared to the characteristic ro-vibrational complex structures in the mid-IR.

Due to the difficulty of a proper focalization of the long-wavelength THz laser beam between the prongs (300 μm) of standard quartz tuning fork (QTF), only recently, the QEPAS technique has been extended in the THz range by using a custom QTF having the same geometry of the standard but six times larger³.

The performance of QEPAS sensors can be compared in terms of normalized noise equivalent absorption (*NNEA*), taking into account the available optical laser power, the selected absorption line strength and the integration time. As shown in Figure 1, the in THz range have been reported the smallest *NNEA* values for QEPAS sensors,

confirming the efficacy of this technique in the THz range.

We will review our recent developments in the realization of THz QEPAS sensors^{3,4}. Specifically, on the design and realization of new QTFs with different geometries in terms of the spacing between the prongs, their length, width and thickness, leading to an enhancement of optoacoustic generation efficiency and on the results obtained using these new QTFs in QEPAS sensors systems

for hydrogen sulphide and methanol detection.

With the THz QEPAS based methanol sensor, a record normalized noise equivalent absorption coefficient $NNEA = 3.75 \times 10^{-11} \text{ cm}^{-1}\text{W}/\text{Hz}^{1/2}$ was achieved which is one order of magnitude better than what was previously obtained³ using a custom QTF with a standard geometry (see Figure 1).

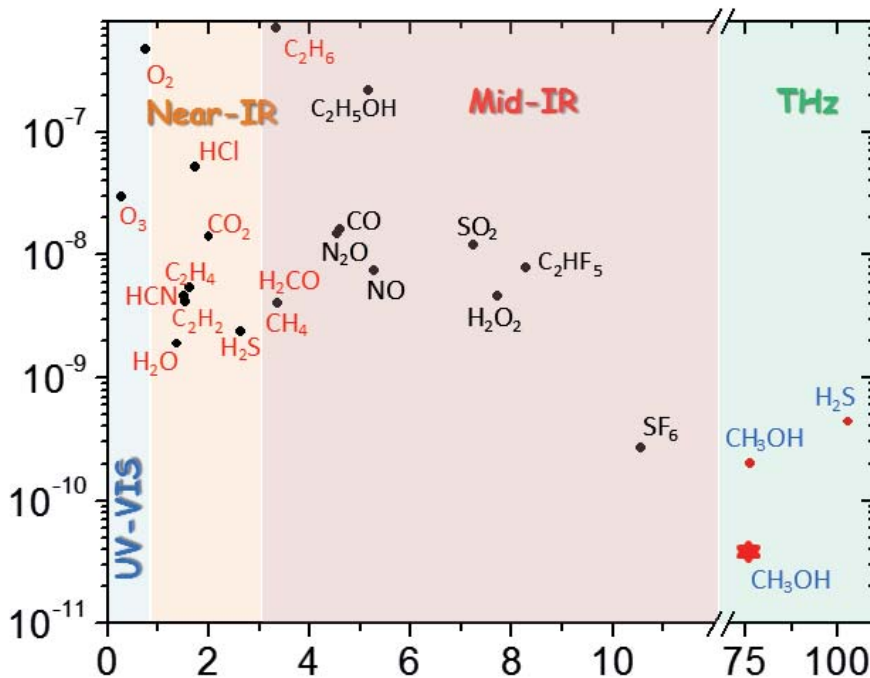


Figure 1. NNEA results obtained with QEPAS sensor for the gas species reported versus employed laser wavelength, in the UV-Vis, near-IR, mid-IR and THz spectral ranges. The red star symbol (*) marks the result obtained with the custom QTF with new geometry.

¹ Patimisco P., Scamarcio G., Tittel F.K., Spagnolo V. (2014), *Sensors*, 14, 6165-6205.

² Spagnolo V., Patimisco P., Borri S., Scamarcio G., Bernacki B.E., Kriesel J. (2012), *Opt. Lett.*, 37, 4461-4463.

³ Borri S., Patimisco P., Sampaolo A., Vitiello M.S., Beere H.E., Ritchie D.A., Scamarcio G., Spagnolo V. (2013), *Appl. Phys. Lett.*, 103, 021105.

⁴ Spagnolo V., Patimisco P., Pennetta R., Sampaolo A., Scamarcio G., Vitiello M.S., Tittel F.K., (2015), *Opt. Express*, 23, 7574-7582.

Biomedical applications of IR spectroscopy - from FT-IR to QCLs

Andreas Roth¹ and Werner Mäntele¹

¹Institute of Biophysics, Goethe-University Frankfurt, Max-von-Laue-Straße 1,
D-60438 Frankfurt am Main, Germany

Keywords: QCL, ATR, photoacoustic spectroscopy, photothermal deflectometry, biomedical applications.

IR spectroscopy is a very specific technique for qualitative and quantitative determination of ingredients in multi-compound systems. Especially for biomedical applications, the sample interface is of great importance because both *in vitro* and *in vivo* samples are normally aqueous solutions with all known challenges in IR spectroscopy. We want to present different approaches for biomedical applications such as dialysis or the non-invasive measurement of blood glucose for diabetes patients, starting with ATR-systems and FT-IR spectroscopy ranging to photoacoustic spectroscopy and photothermal deflectometry with QCLs.

A great challenge in today's healthcare systems is point-of-care diagnostics and continuous monitoring of different parameters. To address these problems, an IR spectroscopic system has to be small, transportable and independent of laboratory equipment such as liquid nitrogen or dried air. We used a small FT-IR spectrometer to build an analysis system, which can be used for discrete μL -samples as well as for flow-through measurements with flow rates up to 1 L/min. As sample interface, we built a multi-reflex ATR-cell because of the small penetration depth and the easily cleanable surface. We could show that such a device can be used to monitor the detoxification of a dialysis patient continuously during the dialysis process. Multivariate methods are used to obtain different parameters, for

instance urea, glucose, creatinine and lactate¹. Because of the general sample interface, this system can also be used for a wide range of body fluids such as blood or urine².

Diabetes is a very serious disease, which requires as much measurements of the blood glucose level as possible in order to fit the glucose or insulin uptake and to avoid hypo- or hyperglycemic conditions respectively. This is not only a problem of inconvenience because of the frequent blood draw but also of cost for the amount of needed test strips. The worldwide growing number of diabetes patients shows the lack of a non-invasive system to determine the blood glucose level. Our first solution for this is photoacoustic spectroscopy in combination with a tunable quantum cascade laser. The tuning range of the QCL is about $1000 - 1200 \text{ cm}^{-1}$ which covers the whole fingerprint region of glucose. The absorption of the QCL impulses results in periodical thermal expansion of the sample, which generates sound waves that can be detected by a microphone. The repetition frequency is in the ultrasound range to minimize the influence of disturbing noise. To improve the signal-to-noise-ratio, the photoacoustic cell was designed to be resonant in the used frequency range. This setup together with multivariate methods can be used for non-invasive monitoring of the blood glucose level in human epidermis³. To evaluate such a system,

Monday
Tuesday
Wednesday
Thursday
Friday
Author Index

several oral glucose tolerance tests were performed, in which a test person takes up an amount of glucose orally and the blood glucose level is monitored constantly by both photoacoustic spectroscopy and conventional test strips. These measurements showed clearly the ability of our setup to obtain the blood glucose level non-invasively.

To improve this setup, we developed a new technique called TIR-PTD spectroscopy, which is an IR-pump/VIS-probe method for the measurement of IR absorption spectra by means of photothermal deflectometry (PTD) enhanced by total internal reflection (TIR). It overcomes the limitations of IR and ATR spectroscopy for the study of opaque samples and allows molecular fingerprinting of IR-active liquids or solids. Another important advantage of this approach over traditional IR spectroscopy methods is the ability to obtain IR information by means of VIS detection, which is generally much cheaper and easier to handle than IR detection. After the absorption of IR light by a sample, the radiationless deexcitation of

the vibrational–rotational states produces a temperature increase of the irradiated spot. If the produced heat diffuses to a material in contact with the sample, a temperature gradient resulting in a thermal lens is generated in the coupled material; as seen for instance in the ‘mirage-effect’ in the air layer next to a sun-exposed street. We were able to enhance the ‘mirage-effect’ by guiding the probe beam directly to the photothermally produced heat source by means of total internal reflection. This was done using an internal reflection element (IRE) as probe beam guidance also acting as the coupling material (Figure 1). As excitation source we used the same tunable quantum cascade laser as in the photoacoustic system. We were able to demonstrate the potential of this method for the analysis of biofluids or any other IR-active liquid or solid sample. We also could demonstrate the correlation of blood glucose with glucose levels in the epidermis of a type 1 diabetic patient. This IR sensor principle is therefore the very promising basis for non-invasive glucose measurement for diabetes patients⁴.

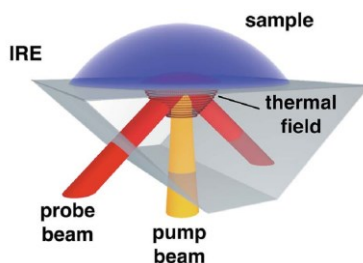


Figure 1: Principle of the TIR-PTD spectrometer.

- ¹ Roth A., Dornuf F., Klein O., Schneditz D., Hafner-Gießauf H., Mäntele W. (2012), *Analytical and Bioanalytical Chemistry*, 403 (2), 391-399.
- ² Hoşafçı G., Klein O., Oremek G., Mäntele W. (2007), *Analytical and Bioanalytical Chemistry*, 387 (5), 1815-1822.
- ³ Pleitez M.A., Lieblein T., Bauer A., Hertzberg O., von Lilienfeld-Toal H., Mäntele W. (2013), *Review of Scientific Instruments*, 84 (8), 084901.
- ⁴ Pleitez M.A., Hertzberg O., Bauer A., Seeger M, Lieblein T., von Lilienfeld-Toal H., Mäntele W. (2015), *Analyst*, 140 (2), 483-488.

Active Hyperspectral Imaging using broadly tunable Quantum Cascade lasers for standoff detection of explosives

S. Hugger, F. Fuchs, J. Jarvis, Q. K. Yang, M. Rattunde, R. Ostendorf, C. Schilling, R. Driad, W. Bronner, R. Aidam, and J. Wagner

Fraunhofer Institute of Applied Solid State Physics, Tullastr.72, 79106 Freiburg, Germany

Keywords: External Cavity Quantum Cascade Lasers, Hyperspectral Imaging, Standoff detection

Broadly tunable external cavity quantum cascade lasers (EC-QCLs) are compact, wavelength-versatile and powerful mid-infrared (MIR) light sources, bearing great potential to extend the range of applications of MIR spectroscopy. In this contribution we report on the use of EC-QCLs for active hyperspectral imaging in the 7.5 μm -10 μm spectral range. This technique is employed for contactless identification of solid contaminations on surfaces over distances of up to 20 meters. It may also be applied to thin liquid films on appropriate substrates. The main purpose of our system is standoff-detection of explosives [1] and their precursors, a task that until today has remained unresolved by established techniques. Due to the spectroscopic nature of our approach, it is easily extended to any substance that exhibits a sufficiently characteristic reflectance spectrum in the MIR.

EC-QC Lasers: The EC-QC lasers used in this work were developed and produced at Fraunhofer IAF. Control of the emission wavelength over the entire gain spectrum is obtained via an external cavity setup using the common Littrow-configuration with a diffraction grating as wavelength-selective intra-cavity feedback element. The lasers are operated at room temperature in pulsed mode. The maximum

tuning range exceeds 300 cm^{-1} for chips centered at 1200 cm^{-1} i.e. $\Delta\lambda/\lambda \sim 25\%$. The linewidth in pulsed operation is typically about 1 cm^{-1} , which is sufficiently narrow for spectroscopy on solids or liquids. The maximum average power at the center of the tuning curve reaches about 50 mW. Compact and rugged EC-QCL modules well suited for field use have been realized. For extended spectral coverage, we combined two of these modules via a dichroitic mirror (figure 1)

Imaging Backscattering Spectroscopy: In our detection scheme, the area of interest is illuminated by a tunable QC laser, and the diffusely backscattered radiation is collected by a MCT camera, synchronized with the spectral tuning of the laser source. Thus, a hyperspectral data cube, containing the spatially resolved spectroscopic information of the scene, is obtained. For distances up to a few meters, the camera is equipped with a f/2 lens ($f=100\text{mm}$ or 200 mm). For larger distances of up to 20 m, the lens is replaced by a modified Cassegrain telescope ($f=1\text{m}$, 12.5" aperture). Detection results are improved by beam shaping, aiming for a flat-top laser profile, and, even more importantly, by taking measures to reduce speckle formation, stemming from the coherent nature of the laser illumination. We address

this issue by a combination of a 2D fast moving mirror and an optical fiber or waveguide. The collected data is analyzed by appropriate algorithms, capable of finding the target substances even on scattering substrates with a priori unknown spectrum [2]. Synchronization of the laser with the low integration duty cycle of the camera results in a low total time-averaged output power density of well below $1 \text{ mW} / \text{cm}^2$, i.e. more than two orders of magnitude below the limiting value for eye safety ($100 \text{ mW}/\text{cm}^2$).

Results: Over short distances of $\sim 2\text{m}$, residues of e.g. PETN on the order of $10 \mu\text{g}$ could be detected on different substrates, while quantities of some $100 \mu\text{g}$ to 1 mg are

detectable over up to 20m . As an example, we show a result from a recent field test, where residues of precursors of explosives had to be detected on a parked car at a distance of 13 m . Fig. 2 shows the output of our detection software, i.e. the chemically selective image of such a deliberately contaminated area, overlaid to the visible image of the scene. The time required for acquiring the full spectral set of MIR images was $<30 \text{ s}$. The presence of residues of DNT located on the left rear tire of the car is unambiguously identified, in spite of the adverse weather conditions, which were high humidity and rain fall. No false alarms for the other substances in the target list were obtained.

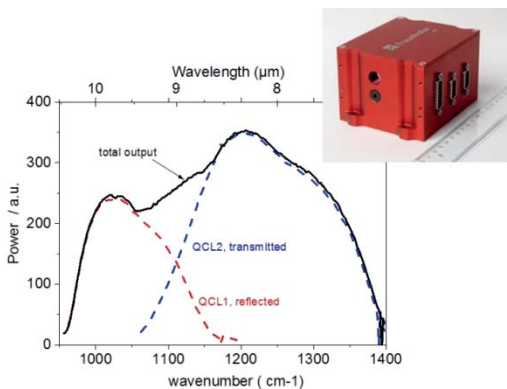


Fig. 1 Inset: IAF EC-QCL laser module. Two such modules were combined via a dichroitic mirror. Solid black line: Combined Output. Dotted lines: Reflected and transmitted laser beams measured separately.

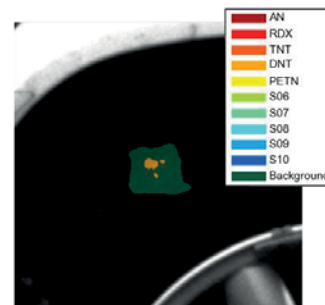


Fig. 2 Traces of DNT identified on the tire of car parked 13 m away. Detection results are overlaid on the vis image of the scene. Green: Part of the illuminated area where no target material was present.

¹ Fuchs, F., Hugger, S., Jarvis, J., Blattmann, V., Kinzer, M., Yang, QK, Ostendorf, R., Bronner, W., Driad, R., Aidam, R., and Wagner, J., Proc. of SPIE Vol. 8710, 87100I-1 (2013)

² Jarvis, J. et.al, in: 9th Future Security 2014, pp. 241-247, Fraunhofer Verlag, Stuttgart (2014)

Developing Discriminant Frequency Infrared (DFIR) Diagnostics

Caryn S. Hughes¹, Graeme Clemens¹, Benjamin Bird², Matt Barre², Miles Wieda², Jeremy Rowlette² and Matthew J. Baker¹

¹WestCHEM, Department of Pure and Applied Chemistry, University of Strathclyde, 295 Cathedral Street, Glasgow, G1 1XL, UK

² Daylight Solutions Inc., 15378 Avenue of Science, San Diego, CA 92128, USA

Keywords: Infrared, Imaging, Discrete Frequency, Biomedical

Mid-infrared spectroscopic imaging is an emerging technique for clinical diagnostics. Spectroscopic analysis allows for the label-free objective classification of biological material on the molecular scale. This technique has been applied to histology, cytology and surgical pathology and can detect subtle changes in the proteome and metabolome¹⁻³. This addition of spectral biochemical information has the potential to improve patient outcome through the identification of earlier stages of disease, drug resistance, disease states and high-risk populations³.

Recently, broadly tunable mid-infrared quantum cascade lasers (QCLs) have been successfully integrated within a microscope for spectrochemical imaging across the molecular fingerprint region.^{4,5} The combination of a broadly tunable laser source, refractive-based high numerical aperture objectives and a large format detector system has enabled high-definition diffraction-limited resolution, without a trade-off in signal to noise and field of view when compared to FTIR-based microscope systems. In addition, the use of a tunable laser source provides new opportunities for data collection including real-time and data collection for discrete frequency infrared (DFIR) imaging.

Recently DFIR has been shown as a powerful technique to provide spectroscopic images with fidelity, definition and importantly collection time relevant to

clinical needs using discrete frequency protocols.⁶ Clemens *et al.* have exemplified this on serum and tissue samples related to brain cancer diagnostics.⁶ Recent work has demonstrated the collection of a protein chemical image based upon the amide I band at 1655 cm⁻¹ of a breast tissue microarray with over 200 cores in 9 minutes.⁷

This paper will discuss recent applications in the development and validation of DFIR with a focus on cancer diagnosis from serum. In particular it will discuss a proof of principle study on hand applied 1 microlitre drops to investigate the impact of DFIR on the spectrum and the ability of spectral diagnostics to discriminate samples based upon discrete frequencies of the most salient information obtained from the dataset, including data analysis techniques to enable this.

Importantly we will discuss the use of piezojetted serum spots (Figure 1 (A)) combined with DFIR imaging (Figure 1 (B)) to enable rapid spectral diagnostics observing the reproducibility and repeatability (Figure 1 (C)) obtained when implementing different levels of a DFIR regime.

Acknowledgements

MJB and GC gratefully acknowledge the support of CLIRSPEC - EPSRC funded

Clinical Infrared and Raman Spectroscopy Network, EP/L012952/1 for funding in order to undertake these experiments.

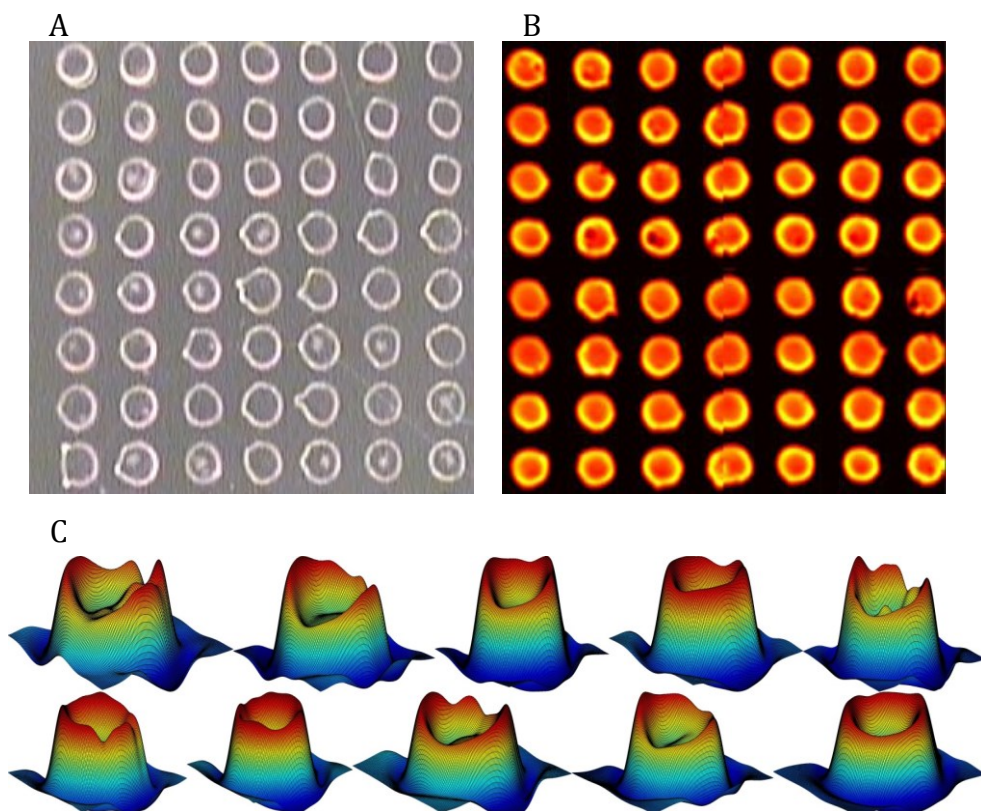


Figure 1. (A) Optical image of Piezojetted serum drops (B) DFIR Image of total spectral intensity (C) 3D mesh plots of total spectral intensity to observe reproducibility and repeatability of individual drops

- ¹ Clemens, G, Flower K.R, Henderson A.P., Whiting A., Przyborski S.A., Jimenes-Hernandez M., Bassan, P., Cinque C., and Gardner, P., (2013), *Mol. Biosystems*, 9, 677-692
- ² Petibois C., and Deleris G., (2006) *Trends Biotech*, 24(10), 455-462
- ³ Levin I.W., and Bhargava, R., (2005), *Ann. Rev. Phys. Chem.* 56, 429-474
- ⁴ Rowlette J., Weide M., Bird B., Arnone D., Barre M., and Day T., (2014) *BioOptics World*, 7(2), 34-37
- ⁵ Yeh K., Kenkel S., Liu J.N., and Bhargave R (2014), *Anal. Chem.* DOI:10.1021/ac5027513
- ⁶ Clemens, G., Bird, B., Weida, M., Rowlette, J., and Baker, M.J. (2014), *Spectroscopy Europe*, 26(4), 14 - 20
- ⁷ Bassan,P., Weida, M.J., Rowlette, J. and Gardner, P (2014), *Analyst*, 139, 3856-3859

Recent advances of mid-infrared semiconductor laser based trace gas sensor technologies for environmental monitoring

F. K. Tittel¹, L. Dong¹, C. Li¹, Y. Yu¹, P. Patimisco², A. Sampaolo², G. Scamarcio² and V. Spagnolo²

¹Electrical and Computer Engineering Department, MS-366, Rice University, Houston, TX 77005-1827, USA

² Dipartimento Interateneo di Fisica, Univerita e Politecnico di Bari, Via Amendolo 173, Bari, Italy

Keywords: Trace gas sensing, Interband cascade lasers, Quantum cascade lasers, Quatz enhanced photoacoustics, Laser absorption spectroscopy.

Recent advances of sensor systems, based on mid-infrared interband cascade lasers (ICLs) for the detection of trace gas species and their application in atmospheric chemistry, medical diagnostics, life sciences, petrochemical industry, and national security will be reported [1].

The development of compact ICL based trace gas sensors will permit the targeting of strong fundamental rotational-vibrational transitions in the mid-infrared which are one to two orders of magnitude more intense than transitions in overtone and combination bands in the near-infrared. Specifically, the spectroscopic detection and monitoring of four molecular species, methane (CH₄) [2], ethane (C₂H₆), formaldehyde (H₂CO) and hydrogen sulphide (H₂S) will be described.

CH₄, C₂H₆ and H₂CO can be detected using two innovative detection techniques: mid-infrared tunable laser absorption spectroscopy (TDLAS) using a novel, compact multi-pass gas cell and quartz enhanced photoacoustic spectroscopy (QEPAS). Both techniques utilize state-of-the-art mid-IR, continuous wave, distributed feedback ICLs and QCLs. TDLAS was performed with an ultra-compact 57.6 m effective optical path length innovative

spherical multipass cell capable of 459 passes between two mirrors separated by 12.5 cm.

TDLAS and QEPAS can achieve minimum detectable absorption losses in the range from 10⁻⁸ to 10⁻¹¹ cm⁻¹/Hz^{1/2}. Several recent examples of real world applications of field deployable gas sensors will be described. For example, an ICL based TDLAS sensor system is capable of detecting CH₄ and C₂H₆ concentration levels of 1 ppb in a 1 sec. sampling time, using an ultra-compact, robust sensor architecture.

Future work will include the detection of other important target analytes. For example, H₂S detection can be realized with a THz QEPAS sensor system using a custom quartz tuning fork (QTF) with a new geometry and a QCL emitting at 2.913 THz [3]. Furthermore, two new approaches aimed to achieve enhanced detection sensitivities with QEPAS based sensing can be realized. The first approach will make use of an optical power buildup cavity. The second approach will use custom produced QTFs of different geometries. The development of cavity-enhanced optical feedback-assisted QEPAS will lead to significantly lower minimum detectable gas concentration levels of < 10 pptv.

Table 1. Near-IR & mid-IR QEPAS performance for trace gas species (2015)

Molecule (Host)	Frequency, cm^{-1}	Pressure, Torr	NNEA, $\text{Cm}^{-1}\text{W/Hz}^{1/2}$	Power, mW	NEC (t=1s), ppbv
C ₂ H ₂ (N ₂)	6523.88	720	4.1×10^{-9}	57	30
NH ₃ (N ₂)	6528.76	575	3.1×10^{-9}	60	60
C ₂ H ₄ (N ₂)	6177.07	715	5.4×10^{-9}	15	1,700
CH ₄ (N ₂ +1.2% H ₂ O)	6057.09	760	3.7×10^{-9}	16	240
N ₂ H ₄	6470.00	700	4.1×10^{-9}	16	1,000
H ₂ S (N ₂)	6357.63	780	5.6×10^{-9}	45	5,000
HCl (N ₂ dry)	5739.26	760	5.2×10^{-8}	15	700
CO ₂ (N ₂ +1.5% H ₂ O)	4991.26	50	1.4×10^{-8}	4.4	18,000
C ₂ H ₆	2976.8	200		1.8	.74
CH ₂ O(N ₂ :75% RH)	2804.90	75	8.7×10^{-9}	7.2	120
CO(N ₂ +2.2% H ₂ O)	2176.28	100	1.4×10^{-7}	71	2
CO (propylene)	2196.66	50	7.4×10^{-8}	6.5	140
N ₂ O (air+5%SF ₆)	2195.63	50	1.5×10^{-8}	19	7
C ₂ H ₅ OH (N ₂)	1934.2	770	2.2×10^{-7}	10	90,000
NO (N ₂ +H ₂ O)	1900.07	250	7.5×10^{-9}	100	3
H ₂ O ₂	1295.6	150	4.6×10^{-9}	100	12
C ₂ HF ₅ (N ₂)	1208.62	770	7.8×10^{-9}	6.6	9
NH ₃ (N ₂)	1046.39	110	1.6×10^{-8}	20	6
SF ₆	948.62	75	2.7×10^{-10}	18	0.05 (50 ppt)

[1] P. Patimisco, G. Scaramarcio, F.K. Tittel, and V. Spagnolo, Sensors: Special Issue, Gas Sensors-2013, 14, 6165-6206, 2014

[2] W. Ren, W. Jiang, and F.K. Tittel, Appl. Phys Lett. 104, 041117, 2014

[3] V. Spagnolo, P. Patimisco, R. Penetta, A. Sampaolo, G. Scaramarcio, M.S. Vitiello and F.K. Tittel, Opt. Exp. 23, 7574-7582, 2015

Peptide Conformations and Solvent Environments Obtained from Raman Optical Activity

Shigeki Yamamoto¹

¹Department of Chemistry, Graduate School of Science, Osaka University
Machiakaneyama 1-1, Toyonaka, Osaka 560-0043, Japan

Keywords: ROA, Vibrational optical activity, Quantum mechanical calculation.

Conformations of peptides and its surrounding solvent environments can be elicited from Raman optical activity (ROA) spectra. We present here our ROA studies¹⁻⁷ on peptides and a small protein by comparisons of the experimental spectra to quantum-mechanically calculated ones which can give information about structures of conformers, conformer populations and also solvent permittivity. A new assignment on extended amide III ROA bands is proposed based on good theoretical reproductions of the experimental spectra¹.

ROA spectra of isotropic solutions may be measured as small differences in Raman scattering intensities corresponding to right and left circularly polarized light.⁸ Applications of ROA have been expanded to include the structural analyses of peptides and proteins in solutions, especially denaturing or unfolding proteins and their intermediates which are difficult to analyze by the other measurement techniques³. However, some important spectral features of peptide ROA spectra are still not fully understood. For example, as will be discussed in this lecture, extended amide III ROA bands of α -helical structure seems not well-explained by a conventional explanation⁹, a geometrical change of helices between solvated and unsolvated α -helical structures.

The most effective way to interpret the ROA spectra is its comparisons to quantum-mechanically simulated ones. Owing to the

developments of the software and the hardware, nowadays it is possible to calculate reliable ROA spectra of small- and medium-sized molecules in an acceptable time. However, for bigger and flexible molecules, it is still difficult to calculate the spectra with high accuracy because of the high cost. We successfully applied the quantum mechanical calculations of ROA of peptides and a small protein, insulin, with the aid of the Cartesian-coordinate tensor transfer (CCT) method¹⁰⁻¹² which can dramatically reduce computational time with retaining nearly ab-initio accuracy.

By applying this method, the experimental ROA pattern in the extended amide III region of PLA was successfully reproduced at the first time¹. Our calculations on the PLA indicate that the change in dielectric constant of the surrounding solvent is the main factor to change the spectral intensity ratio, whereas the conformational change is a minor one.

The ability of the ROA bands to distinguish solvent dielectric constant around α -helix will be valuable to study proteins in solutions as they often undergo conversion of hydrated α -helices during their denaturation. The secondary-structural changes of the amyloid fibril of insulin and its naturing intermediates were explored based on the experimental ROA spectra with the empirical assignments³. The vanishing of the hydrated α -helical ROA band at ~ 1340 cm^{-1} in unfolding processes of proteins can

be interpreted in terms of the solvent-exposure.

We also successfully applied the ROA calculation with the CCT method to the native insulin molecule² (insulin contains about 1600 atoms in its dimer state) in order to verify the assignments of the ROA bands and to know the details of the signal generation of ROA. The CCT methodology yielded spectra of insulin monomer and dimer with nearly ab initio quality, while at the same time reproducing the experiment very well. The link between the spectra and the protein structure could thus be studied in detail. Spectral contributions from the peptide backbone and the amino acid side chains were calculated. Besides, specific

intensity features originating from the α -helical, coil, β -sheet, and 3_{10} -helical parts of the protein could be assigned. The assignment of the Raman and ROA bands to intrinsic molecular coordinates revealed their origin and degree of locality. Alternatively, the relation of the structural flexibility of insulin to the smoothing of spectral bands was studied by a combination of CCT and molecular dynamics.

The work was partly supported by the JSPS Grants-in-Aid for Young Scientists (A) (26708017), that for Scientific Research (A) (26246037), and Yamada Science Foundation.

- ¹ S. Yamamoto, T. Furukawa, P. Bouř, and Y. Ozaki, *J. Phys. Chem. A*, 2014, *118*, 3655-3662
- ² S. Yamamoto, J. Kaminsky, and P. Bouř, *Anal. Chem.*, 2012, *84*, 2440-2451
- ³ S. Yamamoto, H. Watarai, *Chirality*, 2012, *24*, 97-103
- ⁴ S. Yamamoto, J. Kaminsky, P. Bouř, *ChemPhysChem*, 2011, *12*, 1509-1518
- ⁵ S. Yamamoto, M. Straka, H. Watarai, P. Bouř, *Phys. Chem. Chem. Phys.*, 2010, *12*, 11021-11032
- ⁶ S. Yamamoto, H. Watarai, *J. Raman Spectrosc.* 2010, *41*, 1664-1669
- ⁷ S. Yamamoto, *Anal. Bioanal. Chem.*, 2012, *403*, 2203-2212
- ⁸ L.D. Barron. 2014, *Molecular light scattering and optical activity*, 2nd ed., Cambridge University Press: Cambridge.
- ⁹ I.H. McColl, E.W. Blanch, L. Hecht, L.D. Barron, *J. Ame. Chem. Soc.*, 2004, *126*, 8181-8188
- ¹⁰ P. Bouř, T.A. Keiderling, *J. Chem. Phys.* 2002, *117*, 4126-4132
- ¹¹ P. Bouř, J. Sopková, L. Bednárová, P. Maloň, T.A. Keiderling, *J. Comput. Chem.* 1997, *18*, 646-659
- ¹² S. Yamamoto, X. Li, K. Ruud, P. Bouř. *J. Chem. Theory Comput.*, 2012, *8*, 977-985

Marker-free cancer annotation by FTIR imaging

Klaus Gerwert¹

¹Department of Biophysics, Ruhr-University Bochum, 44801, Bochum, Germany

Keywords: FTIR imaging, Raman imaging, CARS, spectral histopathology, cancer

Infrared, Raman and CARS are emerging tools for label-free, non-invasive characterization of tissue, cells and body fluids.¹ Thereby the pathological annotation of tissue and liquid biopsies maybe performed in automated workflow with high sensitivity and specificity over 95% respectively.

Vibrational spectra are used as fingerprints to identify and annotate cancer in tissue, living cells and body fluids. The approach is applied to fresh frozen and formalin fixed paraffin embedded tissue samples. For the entities colon, bladder and lung, data bases are established to characterize tissue in an automated way with sensitivity and specificity of over 90%.²⁻³ A bioinformatics workflow and a corresponding power-full computer cluster is established.⁴ While IR provides fast annotation of larger tissue sections,³ Raman is slower but allows a 10 times higher spatial resolution as compared to IR. This leads to resolve erythrocytes, lymphocytes and single cell nuclei in tissue sections by Raman imaging.²

The approach is extended for IR and Raman from tissue to small biopsies using thin fiber optics. Thereby, the measuring time is reduced to few seconds and can be used to annotate not only at the bench but now also at the bedside.

We have used furthermore a combination of CARS, fluorescence, and multivariate analysis to identify in living cells automatically the nuclei, nucleoli, lipid droplets, endoplasmic reticulum, Golgi apparatus, and mitochondria in an automated way in short measuring time.⁵

In addition in blood-plasma the approach was able to distinguish between the inflammation and bladder cancer with sensitivity and specificity over 90%.⁶⁻⁷

In a hypothesis driven approach using the conformation of the a-beta protein as biomarker we were able to distinguish between Alzheimer and non-Alzheimer diseased patients. An ATR-based sensor with functionalized surface is developed. The patent application is submitted (EP14155138) and will be published.⁸

¹ Gerwert K., Großerüschkamp F., Ollesch J. (2014), *SPIE Newsroom*, DOI: 10.1117/2.1201-312.005297.

² Mavarani L., Petersen D., El-Mashtoly S.F., Mosig A., Tannapfel A., Kötting C., Gerwert K. (2013), *Analyst*, 138(14), 4035-9.

³ Kallenbach-Thieltges A., Großerüschkamp F., Mosig A., Diem M., Tannapfel A., Gerwert K. (2013), *J. Biophotonics*, 6(1), 88-100.

⁴ Zhong Q., Yang C., Großerüschkamp F., Kallenbach-Thieltges A., Serocka P., Gerwert K., Mosig A. (2013), *BMC Bioinformatics*, 14, 333.

- ⁵ El-Mashtoly S.F., Niedieker D., Petersen D., Krauss S.D., Freier E., Mosig A., Kötting C., Hahn S., Gerwert K. (2014), *Biophys J.*, 106(9), 1910-20.
- ⁶ Ollesch J., Drees S.L., Heise H.M., Behrens T., Brüning T., Gerwert K. (2013), *Analyst*, 138(14), 4092-102.
- ⁷ Ollesch J., Heinze M., Heise H.M., Behrens T., Brüning T., Gerwert K. (2014), *J. Biophotonics*, 7(3-4), 210-21.
- ⁸ Nabers A., Ollesch J., Schartner J., Kötting C., Haußmann U., Klafki H., Wiltfang J., Gerwert K. (2015), *Journal of Biophotonics*, accepted.

Practical cancer histopathology by advancing spectroscopic imaging instrumentation and analytical methods

Rohit Bhargava^{1,2}, Kevin Yeh,¹ Andre Balla,³ Shachi Mittal,¹ Saumya Tiwari,¹ Tomasz Wrobel,¹ L. Suzanne Leslie¹ and David Mayerich^{1,4}

¹Department of Bioengineering and Beckman Institute for Advanced Science and Technology, University of Illinois at Urbana-Champaign, Urbana, IL 61801 USA

²Departments of Chemical & Biomolecular Engineering, Electrical & Computer Engineering, Mechanical Science & Engineering and Chemistry, University of Illinois at Urbana-Champaign, Urbana, IL 61801 USA

³Department of Pathology, University of Illinois at Chicago, Chicago, IL 60612 USA

⁴Present address: Department of Electrical and Computer Engineering, University of Houston, Houston, TX 77004 USA

Keywords: infrared spectroscopy, FT-IR imaging, microscopy, cancer pathology

Modern IR spectroscopic imaging can become a more useful tool for biomedical tissue analysis with many recent innovations in instrumentation and methods. In particular, the analysis of cancer in complex tissue is an active and potentially very rewarding area. However, the diversity of optics, sampling modes and methods also creates challenges in fragmenting efforts that make results tough to interpret and confidence in results somewhat shaky in the absence of very expensive and extensive validation. Thus, first, an understanding the image formation process is highly desirable. Since IR imaging is a new technology, it must provide solutions to some problems that hasten its adoption. Second, we describe an example of a clinically-relevant problem that is now possible. Finally, results obtained from this technique must relate to the knowledge base of the targeted audience, namely, clinicians and biomedical researchers. Hence, third, we describe a new approach to relate IR spectroscopic imaging data to common clinical knowledge. Together these concepts form a core platform to devise practical protocols for the translation of IR spectroscopic imaging to clinical applications.¹

We first describe a combination of theory, model experiments and statistical analyses to devise fast IR imaging protocols. Conventional Fourier transform infrared (FT-IR) spectroscopic imaging systems typically employ an incoherent global source and achieve spectral specificity through interferometry. While this approach is suitable for many general applications, recent advancements in broadly tunable external cavity Quantum Cascade Lasers (QCL) offer new approaches and new possibilities for IR imaging. We present results from a discrete frequency infrared (DFIR) microscope based on a QCL source and demonstrate wide-field imaging employing a 128x128 pixel liquid nitrogen cooled mercury cadmium telluride (MCT) focal plane array (FPA) detector and high NA lenses with a sub-micron effective pixel size.² The images obtained demonstrate high resolution, diffraction limited capabilities as well as several unique features due to coherence effects from the laser source. Instrumentation is tightly integrated with recent developments in theory that allow us to move with confidence from a correlative design of experiments to understanding the effects of different parameters on samples.

Precise Outcome prediction is crucial to providing optimal cancer care across the spectrum of solid cancers – we show how this need can be addressed by IR imaging. We report an approach to predict the risk of prostate cancer recurrence, at the time of initial diagnosis, using a combination of IR imaging and a diagnostic protocol that focuses on both the tumor and its microenvironment, and data analysis of frequent patterns in molecular expression. We analyzed data from a patient cohort that is mid-grade dominant – which is the largest cohort of patients in the modern era and in whom prognostic methods are largely ineffective. Our approach outperforms the two clinical tools, Kattan nomogram and CAPRA-S score in a head-to-head comparison.³

Dyes such as hematoxylin and eosin (H&E) and immunohistochemical stains have been widely used to visualize tissue composition in research and clinical practice. We developed an alternative approach to obtain the same information⁴ using stain-free IR imaging and its combination with a computational prediction algorithm. An example is shown in Figure 1. Stainless computed histopathology can enable a rapid, digital, quantitative and non-perturbing visualization of morphology and multiple molecular epitopes simultaneously in a variety of research and clinical pathology applications. Together, the development of IR imaging technology, theory, practical assays and deployable protocols is moving us closer to making the technology practical for users.

Figure 1. Breast tissue is computationally stained to demonstrate conventional staining and molecular staining simultaneously on the same samples. From left, the image shows a Hematoxylin and Eosin stain (pink-blue), molecular staining for epithelial cells (brown color indicating cytokeratin) and Masson's trichrome (blue, red at right). All three stains are computationally generated using IR imaging and without actually staining the tissue.



¹ Bhargava R. (2012). *Applied Spectroscopy* 66 (10), 1091–1120.

² Yeh K., Kenkel S., Liu J.-N., Bhargava R. (2015) *Analytical Chemistry* 87, 485–493.

³ Kwak J. T., Kajdacsy-Balla A., Macias V., Walsh M. J., Sinha S., Bhargava R. (2015) *Scientific Reports* 5, 8758.

⁴ Mayerich D., Walsh M. J., Kajdacsy-Balla A., Ray P. S., Hewitt S. M., Bhargava R. (2015) *Technology* 3 (1) 1-5.

Can we image platelets by means of FTIR spectroscopy?

Ewelina Wiercigroch¹, Aleksandra Krawczyk², Emilia Staniszewska-Slezak^{1,2}, Andrzej Fedorowicz¹, Stefan Chlopicki^{1,3}, Malgorzata Baranska^{1,2}, Kamilla Malek^{1,2}

¹ Jagiellonian Centre for Experimental Therapeutics (JCET), Jagiellonian University, Bobrzynskiego 14, 30-348, Krakow, Poland

² Faculty of Chemistry, Jagiellonian University, Ingardena 3, 30-060 Kraków, Poland

³ Department of Experimental Pharmacology (Chair of Pharmacology), Jagiellonian University, Grzegorzeczka 16, 31-531, Krakow, Poland

Keywords: FTIR spectroscopy imaging, platelets, pulmonary hypertension.

FTIR spectroscopy is considered to be a non-invasive, rapid and cost-saving method. There is enough evidence that this technique is useful in identifying biochemical changes in biosamples such as cells, tissues and blood and can be a reliable tool in diagnosis of pathological states. For instance, we have recently reported FTIR plasma markers of pulmonary arterial hypertension (PAH)¹. However, this disease involves, apart from pathological remodeling and vasoconstriction, alternations in hemostasis, coagulation and platelet activation. In PAH platelet activity is enhanced and well-recognized as an indicator of cardiovascular disease². Thus, an increasing attention is paid to search for new markers of PAH thrombosis and its origin. In routine testing, PLT (platelet count) and thromboxane A2 and B2 are determined as markers for platelet-derived vasoconstrictor mediators^{2,3} using platelet rich plasma (prp). Platelets are usually small in size (human: 1-2 μm , mouse: 0.5 μm ;) and undergo easily activation³.

The aim of this study was to optimize the preparation of platelet rich plasma for FTIR spectroscopy imaging, and then comparison of FTIR profile of prp in a mice model of pulmonary hypertension at an early and advanced stages. It is clear that spatial resolution of FTIR imaging does not allow

to discriminate single platelets but enables collection of FTIR spectra of the entire prp smear and consequently selection of a platelet-rich area. In the first step we examined an effect of fixation of prp on infrared spectra. Then, transmission FTIR technique was used for identification of spectral changes appeared in prp during the development of PAH (the 3rd and 6th week of PAH progression).

Several fixation methods were employed. Among them, we simply air-dried prp smear as well we applied thermal fixation and typical fixation agents such as paraformaldehyde (PAF) and formalin. Additionally, the separated prp was washed out with saline and PBS (phosphate buffered saline). However, fern-like pattern and strong obstruction of FTIR bands by PBS were observed, respectively. Figure 1A and B presents optical images of prp samples, which show the accumulation of platelets within the outer area of the smear. FTIR spectra from this region were further examined. The comparison of average second derivative FTIR spectra for control group of platelets shows that the fixation methods does not significantly affect the spectral profile. Some differences correspond to bands attributed to lipids and tyrosine-rich proteins (Fig. 1D). In turn, FTIR spectra of control and PAH groups

exhibited more pronounced spectral changes, FTIR spectra of prp fixed using the thermal method are shown in Fig. 1E. Reproducibility of spectral information is confirmed by almost identical spectra for two control groups (magenta and blue traces) whereas the early stage of PAH

progression (pink trace) does not provide a distinct IR features comparing to the control group and the fully developed disease (red trace). We discuss these changes and other issues of FTIR imaging of platelets in our presentation.

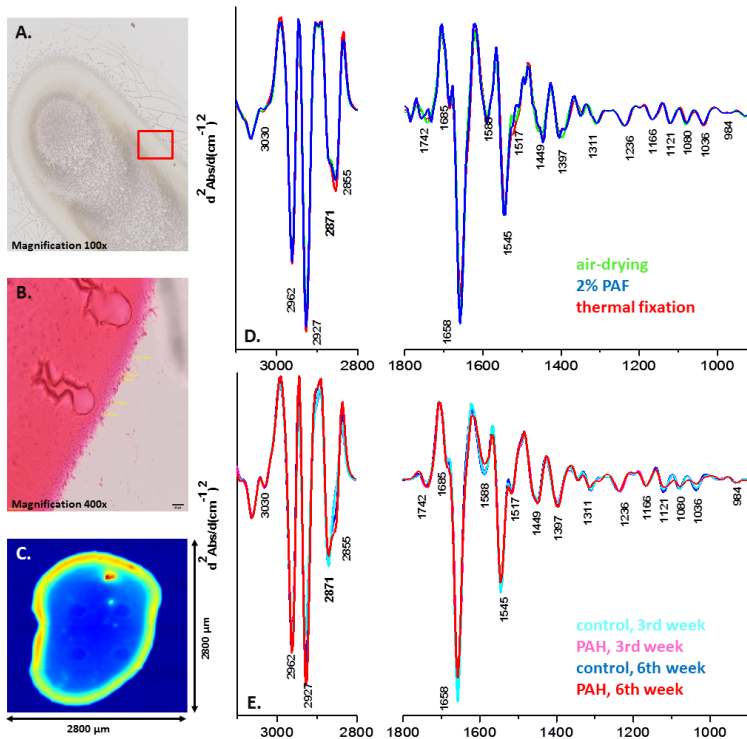


Figure 1. Optical images of prp before (1A) and after hematoxylin/eosin staining (1B), (ROI in FTIR imaging is labeled in red); chemical image (for amide I band) of prp smear (1C); average second derivative FTIR spectra of fixed prp (1D) and the comparison of control and PAH groups at the early (3rd week) and an advanced stage of the disease (6th week).

- ¹ Staniszewska-Slezak E., Fedorowicz A., Kramkowski K., Leszczynska A., Chlopicki S., Baranska M., Malek K., (2015), *Analyst*, DOI: 10.1039/c4an01864h
- ² Lannan K. L., Phipps R. P., White R. J. (2014), *Drug Discov. Today*, 9, 1230-1235
- ³ Schmitta A., Guichard J., Massé J. M., Debili N., Cramer E. M. (2001), *Experimental Hematology*, 29, 1295–1302

This work was supported by National Center of Science (DEC-2013/08/A/ST4/00308) and by the European Union from the resources of the European Regional Development Fund under the Innovative Economy Programme (grant coordinated by JCET-UJ, No POIG.01.01.02-00-069/09).

Analysis of DNA conformation and nuclear ultrastructure with synchrotron FTIR, Soft X-ray Tomography, NanoIR and TERS

Bayden R. Wood¹, Donna Whelan¹, Don McNaughton¹, Phil Heraud¹, Jason Zhang² and Dilworth Y. Parkinson²

¹Centre for Biospectroscopy, School of Chemistry, Monash University, 3800, Victoria, Australia

²Advanced Light Source, Lawrence Berkeley National Laboratory, 1 Cyclotron Road, Berkeley, California, 94720, United States

Keywords: DNA conformation, nanoIR, synchrotron radiation X-ray tomographic microscopy, TERS

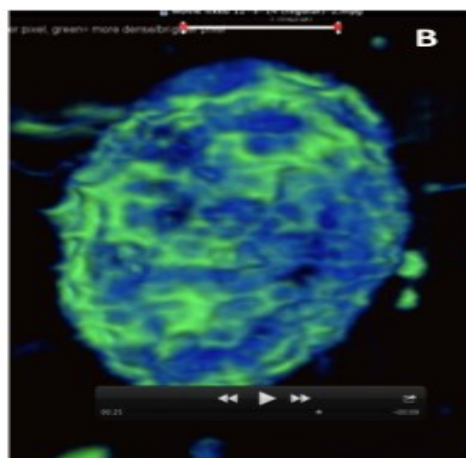
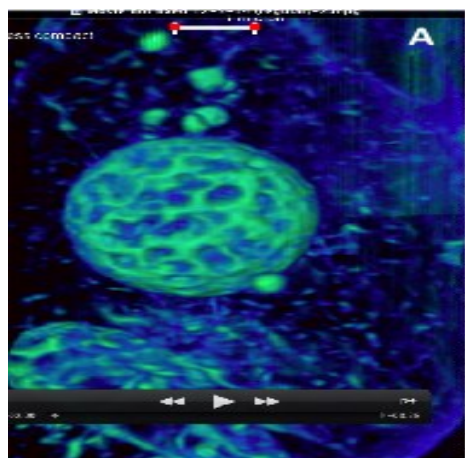
The combination of synchrotron Fourier transform infrared (SFTIR) spectroscopy, synchrotron radiation X-ray tomographic microscopy (SRXTM), nanoIR and Tip Enhanced Raman Scattering (TERS) was used to investigate the DNA conformation and ultrafine structure in the nucleus of avian erythrocytes fixed and under physiological conditions. We have recently shown using SFTIR that upon desiccation the DNA in eukaryotic cells changes from the B-DNA conformation to the A-DNA conformation and in the case of air-drying this conformation can be reversed. Interestingly upon the B-DNA to A-DNA conformational a change in the intensity of the symmetric stretching phosphodiester backbone vibration of DNA at $\sim 1080\text{ cm}^{-1}$ dramatically diminishes and the band assigned to the asymmetric phosphodiester mode shifts from $\sim 1220\text{ cm}^{-1}$ to 1240 cm^{-1} .^[1] The change in intensity of the symmetric phosphodiester vibration is due to change in the molar extinction coefficient going from the more ordered B-DNA form where the dipole moments are more aligned to the narrow and disordered A-DNA form where the dipole moments associated with the phosphodiester groups are less aligned. The integrated intensity of the symmetric phosphodiester band can be

used to quantify the amount of DNA at the single cell level^[2] and can also be used to follow the progression of the cell cycle.^[3] While this reversible DNA conformation appears to have no biological relevance in eukaryotic cells the conformation may play an important protective role of the DNA in certain prokaryotes and other desiccant tolerant organisms. In a land-mark study we demonstrated that bacterial DNA also undergoes this conformational change, however, unlike other eukaryotic cells bacteria can remain functional and reproduce after the conformational change.^[4] It appears the DNA conformational change to the A-DNA form upon desiccation may play a protective role to enable the genome to survive hostile environmental conditions. It also may explain how bacteria can become functional and infect people after contact with dry surfaces for long periods of time.

SRXTM utilizes a synchrotron X-ray source, which provides a brilliant and intense X-ray beam. The high X-ray brilliance enables high-resolution 3D imaging of single cell resulting in low-noise data with optimal contrast approaching 50 nm spatial resolution.^[5] The specimen in SXT is illuminated using photons with energies that in water window region of

the electromagnetic spectrum. The attenuation of these photons follows the Beer–Lambert Law, and is therefore linear, quantitative and dependent on chemical species and thickness.^[5] Carbon and nitrogen — major constituents of DNA and protein — attenuate the transmission of X-rays an order of magnitude more strongly than water.^[5] We have investigated the interphase nucleus of an avian erythrocyte in isotonic saline and after 4% formalin fixation to investigate the ultrastructure of histone packing. The 3D movies of the cell in isotonic saline (Figure 1A) shows a very spherical nucleus with clusters of chromosomal material linked through an intricate 3D network of tubular structures of various diameters. After fixation (Figure 1B) the nucleus is elliptical and the nuclear material appears more dispersed accumulating around the nuclear envelope.

The movies demonstrate the dramatic effects fixative has on the nuclear structure of cells and more importantly shows the nuclear ultrastructure to be a network of integrated clusters of nuclear material linked together by thread like structures of various diameters. The work demonstrates how a combination of synchrotron-based techniques, nanoIR and TERS can be used to obtain information on both the ultrafine structural architecture of the nuclear material and the molecular conformation of DNA under various environmental conditions.



References

- ¹ Chalmers J.M. & Griffith P.R., Eds. (2002). *Handbook of Vibrational Spectroscopy*. Vols 1-5, John Wiley & Sons: London.
- ² Lendl B., Ehmoser H., Frank J., Schindler R. (2000), *Applied Spectroscopy*, 54 (7), 1012-1018.
- ³ Gasser C., Waclawek P., Moser H., Wieland K., Ramer G., Koch C., Ofner J., Kraft M., Lendl B., (2014), *Abstract Template for ICAVS 8*, 2p.

Raman spectroscopy of blood serum for differential diagnosis of Alzheimer's disease

Lenka Halámková¹, Elena Ryzhikova¹, Oleksandr Kazakov¹, Earl A. Zimmerman², Igor K. Lednev¹

¹ Department of Chemistry, University at Albany, SUNY, 1400 Washington Avenue, Albany, NY 12222, USA

² Alzheimer's Center of Albany Medical Center, Albany, NY

Keywords: Alzheimer's disease, blood serum, Raman spectroscopy, artificial neural network, support vector machine

Alzheimer's disease (AD) is the most widespread neurodegenerative disease in elderly population of the world and is characterized by symptoms that progress from mild memory loss to profound cognitive failure. There is an urgent need for a noninvasive or minimally invasive test for AD detection. Currently the AD diagnosis is mainly based on cognition and behavior assessment, the analysis of medical and family history, and structural and functional neuroimaging. Early disease recognition would be a remarkable addition in preclinical early diagnosis since it may prevent cognitive decline once therapeutics have been identified. We expect that these pathological processes that leads to AD causes subtleties in peripheral biomarkers and can be captured and used for serum sample classification. Spectroscopic methods are considered as a specific and sensitive technique allowing for monitoring the biomolecular alterations associated with the diseases.

Raman spectroscopy (RS) provides specific information on structure, conformation and composition unique for

each molecule. RS allows for probing the entire biochemical composition of the blood at once. Therefore, RS enables the extraction of fingerprinting type of information for the current biochemical state of blood. Serum spectral data with various pathological attributions can then be differentiated based on their different Raman spectroscopic signatures of patient under evaluation. This technique has great potential to detect small changes specific to AD at the very early stages.

Here we describe a new method to diagnose AD based on the blood serum via near infrared (NIR) RS in combination with advanced multivariate statistics for the selective identification of AD. The serum samples were analyzed with a Renishaw inVia confocal Raman spectrometer equipped with a research-grade Leica microscope. All measurements were performed via automatic mapping using the lower plate of a Renishaw PRIOR automatic stage system. The spectra were recorded over the range of 400-1800 cm^{-1} using laser source at 785 nm and 55mW for excitation. NIR Raman

spectra were measured from blood serum samples of 20 patients diagnosed with AD, 18 patients with other neurodegenerative dementias (OD) and 10 healthy control (HC) subjects. The method developed in this work allowed the differentiation of the spectral profiles of AD patients versus those of either subjects with other types of degenerative dementia or healthy control subjects with high selectivity. Artificial neuron networks (ANN) and support vector machine (SVM) allowed for the differentiation of AD and HC subjects based on single spectrum with accuracy of

95% (Table 1) and 92% (Figure 1) respectively. The network with the optimal performance was able to distinguish OD and AD with accuracy of 96%. Our classification models showed high discriminative power suggesting that the method has a great potential for AD diagnosis. The reported Raman spectroscopic examination of blood serum can complement current clinical tests making early AD detection fast, accurate and inexpensive. Further method validation on a larger sample scale would be beneficial.

Table 1. Classification results achieved using multilayer perceptron (MLP) and radial basis function network (RBF) for discrimination between Alzheimer’s disease and healthy controls.

#	Class	RBF				MLP			
		CV sensitivity / %		CV specificity / %		CV sensitivity / %		CV specificity / %	
		Spectrum	Subject	Spectrum	Subject	Spectrum	Subject	Spectrum	Subject
1	Healthy	82-95	72-88	86-92	65-87	86-97	68-87	91-96	65-90
2	AD	86-92	65-87	82-95	72-88	91-96	65-90	86-97	68-87

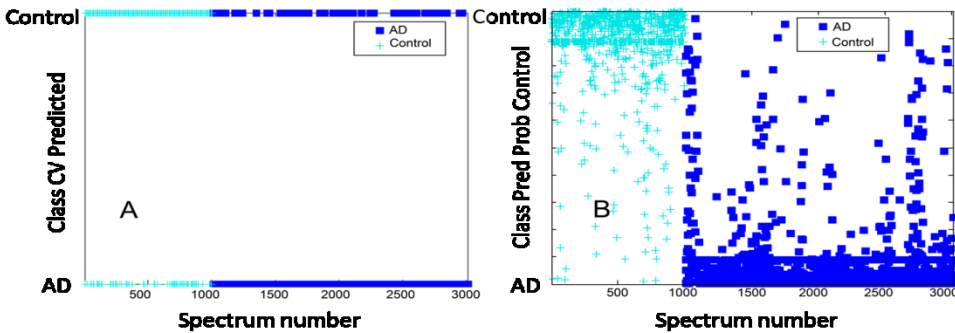


Figure 1. SVM classification of Raman spectra of blood serum. (A) Cross-validated classification of Raman spectra. Dark blue squares (light blue crosses) represent Raman spectra originated from Alzheimer’s disease (healthy control) subjects. (B) Calculated probability for single Raman spectrum to be classified as a spectrum acquired from blood serum of healthy control subjects.



Direct determination of low molecular weight biothiols in umbilical cord whole blood employing Surface Enhanced Raman Spectroscopy

Julia Kuligowski¹, Marwa R. EL-Zahry^{2,3}, Ángel Sánchez-Illana¹, Guillermo Quintás^{4,5}, Máximo Vento^{1,6}, Bernhard Lendl²

¹Neonatal Research Unit, Health Research Institute Hospital La Fe, 46026, Valencia, Spain

²Institute of Chemical Technologies and Analytics, Vienna University of Technology, A-1060, Vienna, Austria

³Department of Pharmaceutical Analytical Chemistry, Faculty of Pharmacy, Assiut University, 71526 Assiut, Egypt

⁴Bio In Vitro Division, Leitat Technological Center, 46026, Valencia, Spain

⁵Unidad Analítica, Health Research Institute Hospital La Fe, 46026, Valencia, Spain

⁶Division of Neonatology, University & Polytechnic Hospital La Fe, 46026, Valencia, Spain

Keywords: Surface Enhanced Raman Spectroscopy (SERS), glutathione (GSH), whole blood, oxidative stress, neonatology.

Monitoring of the redox status in newborns is of key importance for the diagnosis and treatment of diseases associated with oxidative stress. Biothiols such as glutathione play an essential role in a number of biological processes including detoxification, metabolism and the antioxidant defence network¹. A reliable and rapid tool for the direct determination of thiols in small volume whole blood samples is therefore desirable for its application in clinical practice.

This study shows the feasibility of Surface Enhanced Raman Spectroscopy (SERS) using a silver colloid prepared by reduction of silver nitrate using hydroxylamine², as SERS substrate for the quantification of thiols in whole blood samples after a simple precipitation step for

protein removal. Thiol bands shown in Figure 1 (790, 714 and 642 cm⁻¹) were strongly enhanced by the employed SERS substrate and the specificity of the detected SERS signal was proofed for molecules presenting -SH functional groups³. The SERS effect was not influenced by the type of anti-coagulant (i.e. EDTA or heparin) used during blood sample collection. A strong correlation between the obtained SERS signals and the thiol concentration could be demonstrated in whole blood samples as compared to a chromatographic reference method⁴.

The developed approach uses small blood sample volumes (50 µL), which is important for point of care sensor, especially in the field of neonatology.

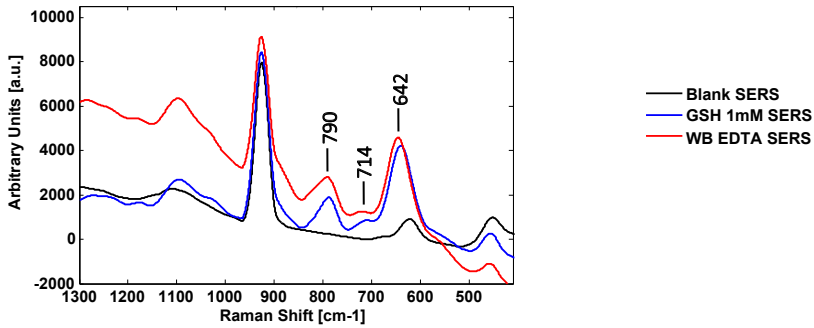


Figure 1. SERS spectra of a GSH standard solution and a K_2 -EDTA whole blood sample in comparison to a H_2O blank

- ¹ Viña J, Vento M, García-Sala F, Puertes IR, Gascó E, Sastre J, Asensi M, Pallardó FV (1995), *The American Journal of Clinical Nutrition*, 61, 1067–1069.
- ² Leopold N., Lendl B. (2003), *The Journal of Physical Chemistry B*, 107, 5723–5727.
- ³ Lv M., Gu H., Yuan X., Gao J., Cai T. (2012), *Journal of Molecular Structure*, 1029, 75–80.
- ⁴ Moore T., Le A., Niemi A-K., Kwan T., Cusmano-Ozog K., Enns GM., Cowan TM. (2013), *Journal of Chromatography B*, 929, 51–55.

Raman Spectroscopy of Graphene

Cinzia Casiraghi

School of Chemistry, University of Manchester, Manchester, UK

Keywords: Raman spectroscopy, graphene, 2D-crystals, nanoribbons

When one writes by a pencil, thin flakes of graphite are left on a surface. Some of them are only one angstrom thick and can be viewed as individual atomic planes cleaved away from the bulk. This strictly 2-dimensional (2D) material called graphene was presumed not to exist in the free state and remained undiscovered until a few years ago. In fact, there exists a whole class of such two-dimensional crystals. The most amazing things about graphene probably is that its electrons move with little scattering over large (submicron) distances as if they were completely insensitive to the environment only a couple of angstroms away. Moreover, whereas electronic properties of other materials are commonly described by quasiparticles that obey the Schrödinger equation, electron transport in graphene is different: It is governed by the Dirac equation so that charge carriers in graphene mimic relativistic particles with zero rest mass. The very unusual electronic properties of this material as well as the possibility for its chemical modification make graphene a promising candidate for future electronic applications.

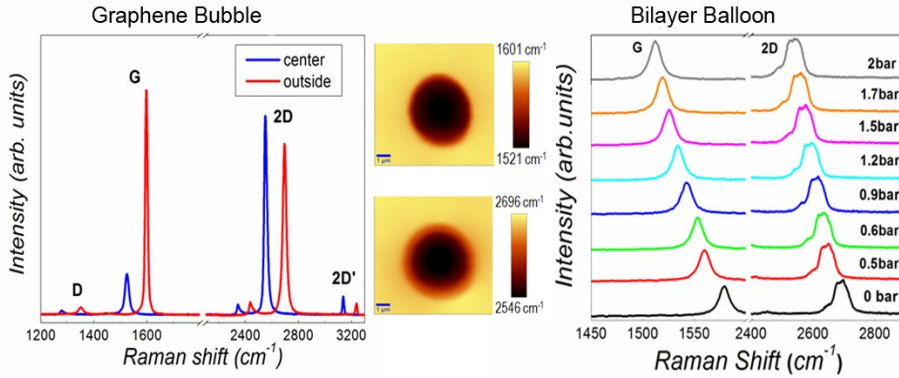
Micro-mechanical or chemical exfoliation can also be successfully applied to other layered materials such as $\text{Bi}_2\text{Sr}_2\text{CaCu}_2\text{O}_x$, NbSe_2 , BN , MoS_2 , Bi_2Te_3 and other *dichalcogenides*, therefore a

family of 2D crystals exist. The properties of those crystals might be very different from those of their 3D precursors. Furthermore, as we have full control over the 2D crystals, we can also create stacks of these crystals according to our requirements. Insulating, conducting, probably superconducting and magnetic layers can all be combined in one layered material as we wish, the properties of such heterostructures depending on the stacking order and easily tuneable, introducing a new concept in material engineering – Materials on Demand.

However, before thinking about making graphene-based products or heterostructure-based devices, we have to be able to identify 2D crystals and to probe their changes in properties while processing. Being “all surface”, the crystals are extremely sensitive to the environment and to external perturbations.

Raman Spectroscopy is the most used technique to probe the properties of graphene. In this talk I will give an overview on the use of this technique to identify graphene, and to probe amount of defects, doping, strain and superlattices [1-5]. I will also show preliminary results on graphene nanoribbons, small stripes of graphene, which could be used in transistors [6-7].

Figure 1. Example of Raman spectrum and map of a graphene bubble (left and central panel) and Raman spectrum taken at the center of a graphene balloon (right panel). This shows that Raman spectroscopy can probe biaxial strain in graphene.



- ¹ Ferrari et al. (2006), *Phys. Rev. Lett.* 97, 18740
- ² Pisana et al (2007), *Nature Materials*, 6, 198
- ³ Zabel et al (2011), *Nano Letters*, 12, 617
- ⁴ Eckmann et al (2012), *Nano Letters*, 12, 3925
- ⁵ Eckmann et al (2013), *Nano Letters*, 13, 5242
- ⁶ Narita et al (2014), *Nature Chemistry*, 6, 126
- ⁷ Narita et al (2014), *ACS Nano*, 8, 11622



Hyperbolic phonon polaritons in hBN for near-field optical imaging, focusing and waveguiding

Peining Li¹, Martin Lewin^{1,2}, Andrey V. Kretinin³, Joshua D. Caldwell⁴, Kostya S. Novoselov³, Takashi Taniguchi⁵, Kenji Watanabe⁵, Fabian Gaussmann², Thomas Taubner^{1,2}

¹Institute of Physics (IA), RWTH Aachen University, 52056 Aachen, Germany

²Fraunhofer Institute for Laser Technology ILT, 52074 Aachen, Germany

³School of Physics and Astronomy, University of Manchester, Oxford Rd, Manchester, UK

⁴U.S. Naval Research Laboratory, 4555 Overlook Ave, S.W., Washington, D.C. USA

⁵National Institute for Materials Science, 1-1 Namiki, Tsukuba, Ibaraki 305-0044, Japan

Keywords: Phonon polariton, Natural hyperbolic media, Hexagonal boron nitride, Infrared near-field imaging, super-focusing.

Natural hyperbolic materials (NHMs) exhibit sub-diffractive, highly directional, volume-confined polariton modes¹⁻⁵. Here we report that hyperbolic phonon polaritons (HPs) allow for a flat slab of hexagonal boron nitride (hBN) to enable novel near-field optical applications, including unusual imaging phenomenon (such as an enlarged reconstruction of investigated objects) and sub-diffractive focusing. Both the enlarged imaging and the super-resolution focusing are explained based on the volume-confined, wavelength dependent propagation angle of HPs. With infrared scattering-type scanning optical microscope (s-SNOM) and state-of-art mid-infrared laser sources, we demonstrated and visualized these unexpected phenomena for the first time in both Type I and Type II hyperbolic conditions, with both occurring naturally within hBN. These efforts have provided a full and intuitive physical picture for the understanding of the role of HPs in near-field optical imaging, guiding, and focusing applications⁴.

As an example, the enlarged imaging phenomenon was demonstrated in the Type II hyperbolic band of the hBN by using the combination of the s-SNOM and a line-tunable, monochromatic quantum cascade laser. The s-SNOM is used to image a Au strip (about 1 μm long, 100 nm wide, as sketched in Fig. 4a) that is covered by the 150 nm hBN layer (AFM topography in Fig. 1b). Because the deeply sub-diffractive width ($< \lambda/70$) of the stripe, no optical information cannot be recorded at the frequency outside the hyperbolic band, as shown in Fig. 1c. In contrast, we clearly observe enlarged optical patterns formed by the HP (Figs. 1d-f). Qualitatively, these elliptical, rectangular patterns carry and reflect the shape information of the original object. Quantitatively, from the measured width and length of the patterns, in conjunction with the known HP propagation angle, we can extract the geometric size of the investigated object. We note that our presented results are also reported independently by another group⁵.

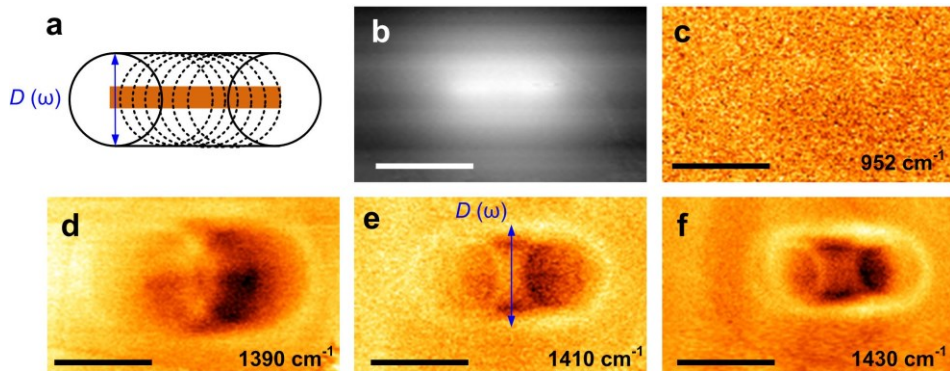


Figure 1. Experimental demonstration of enlarged imaging of a Au stripe with tunable HPs in the Type II band of hBN. (a), Sketch of the imaged object - a Au stripe (not to scale), located below the 150 nm thick hBN flake. The dashed rings result from launched HPs from the edges of the stripe. These HPs form an enlarged outline that reveals the object information. (b), AFM topography taken from the hBN top surface. (c), the s-SNOM image taken at the wavenumber of 952 cm^{-1} outside the hyperbolic band. No optical feature is observed from the underlying structure. (d - f), Spectroscopic imaging the stripe in the Type II hyperbolic band. The bright outlines found in the images are formed by the HP cones, which are enlarged compared to the original structure. The scale bars indicate 1000 nm.

¹ Jacob Z. (2014). *Nature materials*, 13(12): 1081-1083.

² Dai S, et al. (2014). *Science*, 343(6175): 1125-1129.

³ Caldwell J D, et al. (2014) *Nature communications*, 5.

⁴ Li P. et al. (2015) *arXiv:1502.04093*.

⁵ Dai S, et al. (2015) *arXiv:1502.04094*

Inelastic Neutron Scattering (INS) and Raman spectroscopic study of lattice modes for KSiH_3 and RbSiH_3 and their deuterated analogues

Janos Mink^{1,2} Yuan-Chih Lin,³ Maths Karlsson,³ Carin Österberg³, Henrich Fahlquist⁴, Ulrich Häussermann⁴,

¹ Research Center of Natural Sciences, Hungarian Academy of Sciences, P.O. Box 286, H-1519, Budapest, Hungary

² Research Institute of Chemical and Process Engineering, Faculty of Information Technology, University of Pannonia, P.O. Box 158, H-8201 Veszprém, Hungary

³ Department of Applied Physics, Chalmers University of Technology, SE-41296 Gothenburg, Sweden

⁴ Department of Materials and Environmental Chemistry, Stockholm University, SE-10691 Stockholm, Sweden

Keywords: low frequency- low temperature Raman, INS, DFT, lattice vibrations, external force constants.

The alkali metal silyl hydrides $\alpha\text{-KSiH}_3$ and $\alpha\text{-RbSiH}_3$ (ASiH_3) and their deuteride analogues (ASiD_3) were prepared as potential candidates for hydrogen storage systems. The crystal structure of ASiH_3 consists of alkali metal ions and pyramidal, closed shell, silyl hydride anions SiH_3^- . At room temperature ions are arranged in a NaCl-type structure where SiH_3^- units are randomly oriented. At temperatures below 200 K ASiH_3 exist in a low temperature (β) modification. The structures of $\beta\text{-KSiH}_3$ (space group $Pnma$, $Z = 4$) and $\beta\text{-RbSiH}_3$ (space group $P2_1/m$, $Z = 2$) were optimized for ASiH_3 by density functional theory (DFT) calculations and phonons for the optimized structures were computed within the quasi-harmonic approximation. Raman spectra of $\beta\text{-ASiH}_3$ and $\beta\text{-ASiH}_3$ were obtained at 200 and 100 K and Raman bands found to be in good agreement with DFT calculated vibrational energies. Silyl anions in $\beta\text{-ASiH}_3$ possess a local C_s symmetry but deviate only slightly from their ideal C_{3v} symmetry. Previous study we characterized the structural and vibrational properties of SiH_3^- in KSiH_3 and RbSiH_3 (see references therein). In this work analysis of external (lattice) modes, i.e. librations and translations in

low temperature spectra, based on Raman and INS.

Experiment: For Raman spectroscopy powdered samples were sealed in 0.3 mm capillaries. Room temperature spectra were measured using a Labram HR 800 spectrometer. The instrument is equipped with an 800 mm focal length spectrograph and a back thinned CCD detector. Samples were excited using an air cooled double frequency Nd:YAG laser (532 nm) and applying an input laser power of 0.56 mW. Low temperature spectra (at 200 and 100 K) were measured with a Dilor XY-800 triple grating spectrometer with double subtractive configuration. This spectrometer is equipped with a Ar^+/Kr^+ laser (647 nm). The sample chamber of the stage was evacuated to about 10^{-3} mbar in order to avoid the condensation of water on the capillary and the sample window. A cooling rate of 3 K/min was applied. Data covering the spectral range $30\text{-}4000\text{ cm}^{-1}$ were collected in 18 spectral windows.

For INS spectroscopy the hydride samples were loaded into an aluminum sample holder under a He atmosphere. The sample holder was subsequently sealed and mounted in a cryostat. The spectra of the two hydrides were measured at 4 K on the filter-analyzer neutron spectrometer (FANS) instrument at the NIST center for Neutron Research (USA).

Computation. Density functional theory (DFT) calculations were performed in the framework of the frozen core all-electron Projected Augmented Wave (PAW) method, as implemented in the program VASP using the generalized gradient approximation (GGA) with the PBE parameterization for the exchange-correlation effects. The crystal structures of orthorhombic β -KSiH₃ and monoclinic β -RbSiH₃ were relaxed with respect to volume, lattice parameters and atomic positions and atomic parameters.

Results of factor group analysis:

External modes of β -KSiH₃ (Pnma):

SiH₃⁻ libration modes (12): $A_g + 2B_{1g} + 2B_{2g} + B_{3g} + 2A_u + B_{1u} + 2B_{2u} + B_{3u}$

SiH₃⁻ translation modes (12): $2A_g + B_{1g} + 2B_{2g} + B_{3g} + A_u + 2B_{1u} + B_{2u} + 2B_{3u}$

K⁺ translation modes (9): $2A_g + B_{1g} + 2B_{2g} + B_{3g} + A_u + B_{1u} + B_{3u}$

RbSiH₃ (P2₁/m):

SiH₃⁻ libration modes (6): $A_g + 2B_g + 2A_u + B_u$

SiH₃⁻ translation modes (6): $2A_g + B_g + A_u + 2B_u$

Rb⁺ translation modes (3): $2A_g + B_g$

All Raman active lattice modes were observed and assigned e.g. 24 for KSiH₃ and 9 for RbSiH₃ and similarly for

deuterated species. The mass effects of cations, the isotope effects (both the mass and moment of inertia differences) together with DFT calculation results were used in interpretation of lattice modes. For example in case of RbSiH₃ sequence of Raman libration modes at 378, 304 and 274 cm⁻¹ refers to B_g, B_g and A_g modes, respectively. The INS features at 400, 311 and 291 cm⁻¹ can be assigned to A_u, A_u, and B_u libration modes, respectively. The scaled DFT results are 385, 356, 350, 339, 313 and 274 cm⁻¹ for B_g, A_u, B_g, A_u, A_g and B_u, respectively (Fig.1). Better agreement was observed between calculated and experimental lattice modes for KSiH₃.

An approximate cation translational force constant (f) can be calculated from averaged translational mode, 79 and 62 cm⁻¹ for KSiH₃ and RbSiH₃, respectively. We obtain $f(K^+) = 0.032 \text{ Ncm}^{-1}$ and $f(Rb^+) = 0.026 \text{ Ncm}^{-1}$, which weakening is responsible for further frequency downshift of translational modes.

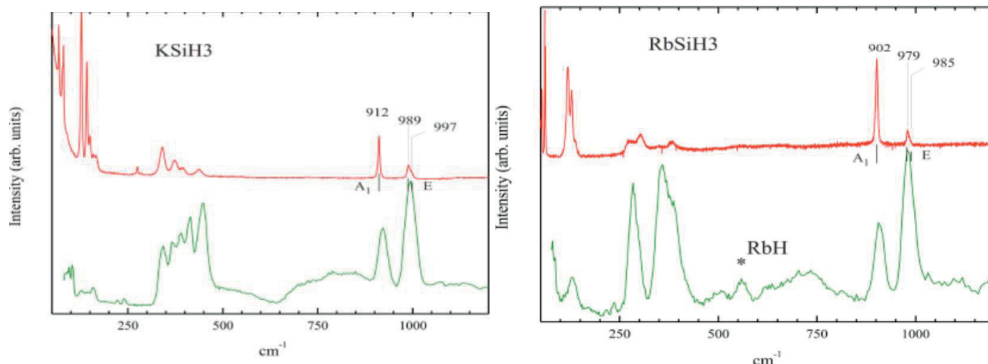


Figure 1. Raman (red) and INS (green) spectra of KSiH₃ and RbSiH₃

¹ Kranak V.F., Lin Y.C., Karlsson M., Mink J., Norberg S.T., Häussermann U. (2015), *Inorg. Chem.*, 54 (5), 2300-2309.

Phase transitions in fluorides with elpasolite structure

Alexander Krylov¹, Alexander Vtyurin¹, Sergey Goryainov², Vladimir Voronov¹ Svetlana Krylova¹

¹L.V.Kirensky Institute of physics SB RAS, 660036, Krasnoyarsk, Russia,
slanky@iph.krasn.ru

²V.S.Sobolev Institute of geology and mineralogy SB RAS, 630090, Novosibirsk, Russia

Keywords: Raman spectroscopy, phase transition, single crystal, low temperature, high pressure.

Crystals of fluoride-containing elpasolites with a common formula A_2BMeF_6 (space group of the high-symmetry G_0 phase $Fm\bar{3}m$, $Z=4$, the structure is shown in Fig. 1) belong to perovskite-like structures which have intensively been studied in the last decades. This interest is, on one hand, due to the variety of their structures and extremely wide variety of their phase transitions observed [1]; on the other hand, they represent a new perspective class of optical materials: they possess a wider range of transparency than traditional oxides and their spectral proper-ties can easily be varied by a partial or full substitution of the Me^{3+} ion. Phase transitions in the perovskite-like structures are usually associated with the lattice instability to the displacement of the central ion in the MeX_6 octahedron or with the rotation of these octahedra induced by «soft» phonon condensation.

The samples were cut along the crystallographic axes of the cubic phase. The samples were transparent and did not have any colored defects or inclusions visible under the microscope. The backscattered Raman spectra were acquired using a Jobin Yvon – Horiba T-64000 spectrometer equipped with a liquid nitrogen-cooled CCD detector. To reduce the elastic scattering wing, low frequency spectra were taken in the subtractive dispersion mode with cutting frequencies

below 8 cm^{-1} ; a high frequency part of the spectrum was acquired with the additive dispersion. The spectral width of the scattering matrix element was equal to $650/1024\text{ cm}^{-1}$ for the subtractive dispersion and $220/1024\text{ cm}^{-1}$ – for the additive one. The spectrum accumulation time was 600 sec. The spectrum was excited by the Ar+ laser line (at 514.5 nm, 500 mW). The temperature stabilization during the spectrum accumulation was either equal to or higher than 0.1 K.

High pressure spectra were obtained from non-oriented samples in a diamond anvil cell (see, for example, [2]) using the mixture of ethyl and methyl alcohols (4:1) as a pressure-transmitting medium and a ruby luminescence doublet as a pressure indicator (the accuracy of the pressure recording was 0.05 GPa). The Raman spectra were also excited by the Ar+ laser radiation (514,5 nm) and re-corded using a Raman spectrometer OMARS 89 (Dilor) (in the Rb_2KScF_6 crystal) and a spectrometer T-64000 (Horiba, Jobin Yvon) (in the crystals Rb_2KInF_6 , Rb_2NaYF_6). Due to small size of the samples and strong diffuse scattering the high-frequency part (higher than 200 cm^{-1}) of the spectrum was recorded, excluding the Rb_2NaYF_6 crystal which enabled us to acquire polarized spectra. The do-main structure and effects of birefringence in the sample were simultaneously observed using a polarization microscope. The contour

decomposition was performed using the Lorentzian function. To estimate the frequencies of the possible soft modes and to determine their nature, attempts were made to use a simple empirical model of hard ions traditionally used to simulate the crystal lattice dynamics of perovskites (all the model calculations were carried out using the software package LADY. As a result, a good quantitative agreement between the calculative and experimental results was obtained. Using these parameters of the potential, calculations were made of the dispersion phonon curves for the crystals under study in the main directions of the Brillouin zone of the cubic phase.

Structural phase transitions in the studied crystals Rb_2KScF_6 , Rb_2KInF_6 and Rb_2NaYF_6 are induced by the condensation of soft phonon modes and are not connected with the lattice ordering processes. The critical soft mode is associated with the rotations of the octahedral groups and belongs to the low-lying flat phonon branch in the direction $\Gamma-X$. According to the results of the spectroscopy of hard high frequency modes the behaviour of the main order parameter is typical for the transitions of the second kind or those of the first kind close to the tricritical point. In the low frequency area, a strong interaction of the

fluctuations of the main order parameter with the uncritical hard low frequency modes was found. Raman spectra measurement are made of the crystals Rb_2KScF_6 , Rb_2KInF_6 , Rb_2NaYF_6 at 295 K, pressure up to 7 GPa, 5.3 GPa and 4.33 GPa, respectively. Phase transitions from the cubic phase $\text{Fm}\bar{3}\text{m}$ to a lower-symmetry phase under pressure of 1 GPa were observed in the Rb_2KScF_6 crystal and under pressure of about 0.9 GPa in the Rb_2KInF_6 crystal. The analysis of the changes in the spectral parameters allows one to argue that the transitions to the distorted phase are accompanied by the increase (more likely, by two times) of the primitive cell volume of the initial phase. The calculated spectra of the lattice vibrations are in good agreement with the experimental results. It is established that the phase transitions in these crystals are associated with the rotation of the octahedral groups ScF_6 and InF_6 , and a more probable high pressure phase is the phase with the space group C2/m . The investigations in the Rb_2NaYF_6 crystal reveal the absence of changes in the spectra due to phase transitions. The lattice dynamics calculation in the Rb_2NaYF_6 crystal shows the absence of phase transitions up to 10 GPa.

¹ Alexandrov K.S., Beznosikov B.V. (1997), *Perovskite-like crystals*. Nauka: Novosibirsk.

² Munro R. G., Piermarini G. J., Block S. and Holzapfel W. B. (1985) *J. Applied Physics*, 57, 165.

COMPLEMENTARITY OF RAMAN SPECTROSCOPY AND QUANTUM CHEMICAL CALCULATIONS IN THE INTERPRETATION OF INTERPARTICLE INTERACTIONS IN MIXTURES OF 1-*N*-BUTYL-3-METHYLIMIDAZOLIUM HEXAFLUOROPHOSPHATE AND GAMMA-BUTYROLACTONE

Oleg N. Kalugin¹, Bogdan A. Marekha^{1,2}, Volodymyr A. Koverga¹ and Abdenacer Idrissi²

¹Department of Inorganic Chemistry, V.N. Karazin Kharkiv National University, Svoboda sq., 4, 61022 Kharkiv, Ukraine

²Laboratoire de Spectrochimie Infrarouge et Raman (UMR CNRS 8516), University of Lille 1, Science and Technology, 59655 Villeneuve d'Ascq Cedex, France

Keywords: 1-*n*-butyl-3-methylimidazolium hexafluorophosphate, γ -butyrolactone, Raman spectroscopy, generalized two-dimensional correlation spectroscopy analysis, DFT calculations.

We have analyzed the ion-ion, ion molecular and intermolecular interactions in mixtures of imidazolium-based room temperature ionic liquid (IL) 1-*n*-butyl-3-methylimidazolium hexafluorophosphate, BmimPF₆, with polar aprotic molecular solvent γ -butyrolactone (γ -BL), in terms of competition between different types of interactions between the constituents by using Raman spectroscopy coupled with quantum-chemical calculations.

Fig. 1 shows Raman spectra of the neat components of the studied mixture. It is apparent that in the lower wavenumber region (below 1600 cm⁻¹) there is significant overlap between the spectral contributions of the IL and the solvent. This makes this spectral region not informative and difficult to study apart from a couple of strong spectral features: a contribution at around 741 cm⁻¹ due to symmetrical P-F stretching vibration mode of the anion of BmimPF₆ (region III in Fig. 1) and a ring breathing mode of γ -BL / CH₂ rocking at 931 cm⁻¹.

The 741 cm⁻¹ band was shown to be rather sensitive to interionic interactions

both in IR and in Raman and was thus selected for consideration in the present study, at the same time the 931 cm⁻¹ band is known to be insensitive to intermolecular interactions and it was used in the normalization procedure for generalized two-dimensional correlation spectroscopy (2DCoS) analysis.

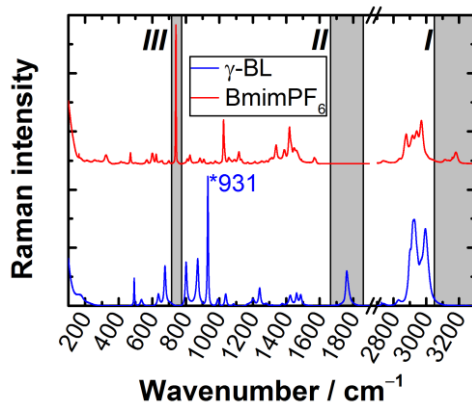


Figure 1. Raman spectra of BmimPF₆ (top) and γ -BL (bottom). The band at 931 cm⁻¹ was used for normalization. Shaded areas

indicate spectral regions of interest corresponding to *III* – P-F s. str. of BmimPF₆, *II* – C=O str. of γ -BL, and *I* – ring C-H str. of BmimPF₆.

Region *II* in Fig. 1 highlights the C=O stretching mode of γ -BL at *ca.* 1760 cm⁻¹. This donating group is known to be quite sensitive IR and Raman probe for solvation interactions in different electrolyte solutions. Taken together with the fact that there are no interfering bands due to BmimPF₆ it makes this region interesting to follow.

In this investigation we used the imidazolium ring C-H stretching at 3050-3300 cm⁻¹ (highlighted as region *I* in Fig. 1) as a probe of the interactions in BmimPF₆- γ -BL mixture though it is still not so well explored by Raman spectroscopy.

Quantum chemical calculations of optimal structures followed by harmonic vibrational analysis were performed in order to rationalize experimental results in terms of optimized configurations of ILs (isolated ions, ion pair and ion pair dimer), solvent (isolated molecule and its dimeric complex), and IL-solvent complex (cation-solvent, anion-solvent, ion pair-solvent). The revealed lowest energy structures were obtained both in vacuum and in polar solvent medium treated via implicit solvation approach.

All quantum chemical calculations reported here were conducted using density functional theory (DFT). We employed a hybrid meta exchange functional M06-2X from Truhlar's group coupled with Pople-type split-valence triple-zeta basis set augmented with diffuse and polarization functions both on hydrogens and heavier

elements 6-311++G(d,p). Selection of this level of theory was dictated by anticipated complexity of the intermolecular interactions in the studied model systems that should be adequately taken into account.

The main results can be summarized as following¹.

Symmetrical P-F stretching vibration of IL anion was found to be insensitive to changes in mixture concentration in contrast to C=O stretching vibration of γ -BL and the imidazolium ring C-H stretching vibrations of IL cation. Each of these vibrational profiles was decomposed in various spectral contributions and their number was rationalized by the results of quantum-chemical calculations and/or by previous controversial published data. Progressive redshift of the ring C-H stretching wavenumbers was referred to pronounced solvation of cation at the imidazolium ring site accompanied with H-bond formation. This is especially pronounced at $x_{IL} < 0.18$.

Complicated variations in intensities of individual contributions of the C=O profile was treated as a manifestation of the changing with concentration pattern of intermolecular interactions. Self-association of γ -BL molecules and distinct cation solvation as dominant intermolecular interactions at low IL content are replaced with weaker cation solvation and ion association at high concentrations of BmimPF₆. Possible representative molecular structures are proposed on the basis of DFT calculations.

¹ Marekha B.A., Kovrega V.A, Moreau M., Kiselev M., Takamuku T., Kalugin O.N. and Idrissi A. (2015), *J. Raman Spectrosc.*, Article first published online : 21 JAN 2015, DOI: 10.1002/jrs.4640.

Towards a standardized characterization of solution phase protein structure using Raman optical activity: Implementation of comprehensive structural databases

Carl Mensch and Christian Johannessen

Department of Chemistry, University of Antwerp, Groenenborgerlaan 171, 2020, Antwerp, Belgium

Email: Christian.Johannessen@uantwerpen.be

Keywords: Raman optical activity, Protein structure, conformation, similarity

In the age of proteomics, obtaining detailed structural information on proteins, and causally linking this information to protein function (the so-called structure-function paradigm), has become a vital part of biochemistry and pharmacology. The quest for understanding and categorizing protein structural motifs is in no small part fuelled by the emergence of neurodegenerative diseases (where misfolding of proteins play a major role) as social diseases in an aging world, but also due to many new pharmaceutical compounds being peptide or protein based. Unfortunately, traditional methods for structure elucidation in proteins, e.g. X-ray diffraction and nuclear magnetic resonance (NMR) spectroscopy, have some limitations. While X-ray diffraction is immensely powerful by directly generating a 3D structure of a protein through interpretation of the diffraction patterns from the experiment alone, this technology requires perfect protein crystals, which are time consuming and often difficult to generate. While NMR measures directly in solution, the free induction decay times required for high resolution NMR measurements are relatively long, which means that proteins with less rigid structural motifs are difficult to study using this technique. Hence, complementary techniques for studying protein structure are required.

Over the last 20 years, Raman optical activity (ROA) spectroscopy has shown much promise experimentally as a candidate for this role.¹⁻² The technique, measuring a small intensity difference in right- and left-circularly polarized photons Raman scattered by chiral molecules, is extraordinarily sensitive to differences in the back bone torsion angles of peptides and proteins and thus gives a direct indication of the secondary structure of the protein being studied. The main limitation of ROA, traditionally, has been the general requirement for optical spectroscopic methods to be supported by quantum mechanical calculations, limiting detailed structural analysis to smaller molecules. This limitation is now being pushed back by advances in computational chemistry and computer power, which means that larger peptides³⁻⁴, or even whole proteins⁵ can be studied in detail by a combination of theoretical and experimental ROA.

Here, we outline the first large scale systematic study of ROA spectral signatures and how these are related to protein conformation. By generating libraries of peptide models long enough to adapt secondary structure motifs, all with repeating back bone torsion angles, and subsequently calculating the ROA property tensors of each of these peptides, the influence of the back bone conformation on

the ROA profile can be studied in detail (see figure 1). Furthermore, the predicted Raman and ROA spectra in this data base can, by means of similarity indices, be compared to experimental Raman and ROA data of peptides with known secondary structure. This allows for an unprecedented insight into the actual solution phase conformational landscape of these peptides.

The library approach to generating ROA data also allows us to include regions

of the Ramachandran plot that are hard to come by experimentally, e.g. in regions that are not associated with the traditional definition of “order”. The addition of these disordered protein regions has the potential to redefine the structure-function paradigm, by including protein motifs usually thought of as “non-functional” and thus adding to our understanding of protein misfolding in neurodegenerative diseases.

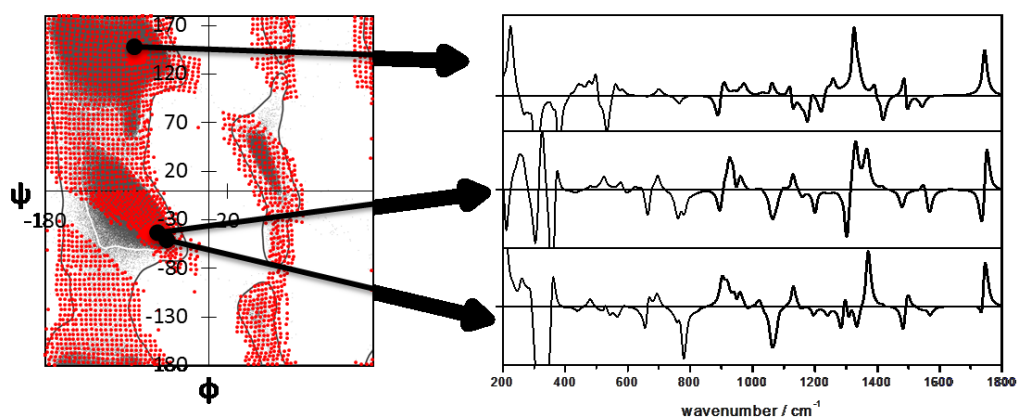


Figure 1. Ramachandran plot showing the ROA library of simulated spectra (left) and three selected spectra in the PPII region (top) and in the α -helical region (middle and bottom) of the Ramachandran plot (right)

- ¹ Barron, L.D., Buckingham, A.D. (2010), *Chemical Physics Letters*, 492, 199-213.
- ² Ramirez, F.J., Nieto-Ortega, B., Casado, J., Navarrete, J.T.L. (2013), *ChemComm*, 49, 8893-8895.
- ³ Jacob, C.R., Lubner, S., Reiher, M. (2009), *Chemistry, a European Journal*, 15(48), 13491-13508.
- ⁴ Profant, V., Baumruk, V., Li, X., Safarik, M., Bour, P. (2011), *Journal of Physical Chemistry B*, 115, 15079-15089.
- ⁵ Yamamoto, S., Kaminsky, J., Bour, P. (2012), *Analytical Chemistry*, 84, 2440-2451.

Vibrational Optical Activity: Chirality in Molecular Vibrations

Laurence A. Nafie

Department of Chemistry, Syracuse University, Syracuse, New York, 13244, USA

Keywords: VCD, ROA, absolute configuration, protein fibrils

Vibrational optical activity (VOA) consists of two major subfields, infrared vibrational circular dichroism (VCD) and vibrational Raman optical activity (ROA). VCD and ROA are measures of the difference in infrared (IR) absorption and Raman scattering for left circularly polarized (LCP) versus right circularly polarized (RCP) radiation. The first VOA measurements, ROA in 1973 and VCD in 1974, were reported and independently confirmed approximately 40 years ago.^{1,2} Since those early days, there have been many advances in instrumentation, theory, calculations and applications of VOA.^{3,4} In particular, the commercial availability of instrumentation for VCD in 1997 and ROA in 2003, followed by software for calculations of VCD in 1998 and ROA in 2003 opened the field VOA to a wide variety of scientists interested in molecular structure analysis of chiral molecules, including bio-molecules. In 2008 a series of VOA conferences began in Manchester, UK, followed Albany, New York, USA in 2010, Pisa, Italy in 2012 and now Baoding, China, 2014. Today, applications of VOA continue to widen as for example the widespread use of VCD for the determination of the absolute configuration of pharmaceutical and natural product molecules,⁵ the unusual sensitivity of VCD to the supramolecular structure of amyloid fibrils,⁶ and the enhanced sensitivity of ROA to higher-order protein structure where it is being used to assess the structural integrity of

biopharmaceuticals and biosimilars.⁷ Given this wide-ranging global progress with over 100 new publications each year, VOA can now be regarded a mature field of molecular spectroscopy.

1 Barron, L.D.; Bogaard, M.P.; Buckingham, A.D. *J. Am. Chem. Soc.* **1973**, *95*, 603; Hug, W.; Kint, S.; Bailey, G.F.; Scherer, J.R.; *J. Am. Chem. Soc.* **1975**, *97*, 5589.

2 Holzwarth, G.; Hsu, E.C.; Mosher H.S.; Faulkner, T.R.; Moscovitz, A. *J. Am. Chem. Soc.* **1974**, *96*, 252; Nafie, L.A.; Cheng, J.C.; Stephens, P.J. *J. Am. Chem. Soc.* **1975**, *97*, 3842.

3 Barron, L.D. *Molecular Light Scattering and Optical Activity*, second edition, Cambridge University Press, **2004**.

4 Nafie, L.A. *Vibrational Optical Activity: Principles and Applications*. Wiley, Chichester, **2011**.

5 He, Y.; Wang, B.; Dukor, R.K.; Nafie, L.A. *Appl. Spectrosc.* **2011** *65*, 699.

6 Kurouski, D.; Lu, X.; Popova, L.; Wan, W.; Maruda, S.; Stubbs, G.; Dukor, R.K.; Nafie, L.A. *J. Am. Chem. Soc.* **2014**, *136*, 2302.

7 Li, C.; Li, T. *Curr. Pharm Biotech.* **2009**, *10*, 391.

Monday

Tuesday

Wednesday

Thursday

Friday

Author Index



Surface enhanced resonance ROA (SERROA) as a novel probe of chirality transfer

Saeideh Ostovar Pour¹, Louise Rocks², Karen Faulds², Duncan Graham², Václav Parchaňský^{3,4}, Petr Bouř⁴ and Ewan W. Blanch^{1,5}

¹Faculty of Life Sciences and Manchester Institute of Biotechnology, University of Manchester, 131 Princes Street, Manchester, M1 7DN, U.K.

²Centre for Molecular Nanometrology, WestCHEM, Department of Pure and Applied Chemistry, University of Strathclyde, Glasgow G1 1XL, U.K.

³Department of Analytical Chemistry, Institute of Chemical Technology, Technická 5, 16628 Prague, Czech Republic

⁴Institute of Organic Chemistry and Biochemistry, Academy of Sciences, Flemingovo náměstí 2, 16610 Prague, Czech Republic

⁵Current address: School of Applied Sciences, RMIT University, GPO Box 2476, Melbourne, VIC, 3001, Australia

Keywords: ROA, SERS, chirality transfer, resonance, nanosensors.

The sensitivity of Raman optical activity (ROA) to stereochemistry and structure has led to its becoming a powerful probe of biological molecules. However, the inherent weakness of the ROA effect, typically 3-5 orders of magnitude smaller than the parent Raman scattering, has restricted its application to relatively high sample concentrations and long data accumulation times. The use of surface enhancement strategies, paralleling the development of SERS, has long been suggested as a potential approach to boost ROA. Unfortunately, the distortion of the circularly polarized light, that ROA measurements rely upon, by the plasmon resonances responsible for SERS, made measurement of surface enhanced ROA (SEROA) highly challenging.¹ Several years ago we were able to obtain reliable SEROA spectra by controlling the aggregation rate of nanoparticles using a hydrogel matrix, so minimizing birefringent distortions.² In this paper, we report a different strategy for measuring SEROA that appears to have revealed a novel form of chirality transfer and proposes the potential of new stereochemically sensitive nanoprobcs.³

In this latest work, we use nanotags consisting of a silver nanoparticle core with a silica coating, decorated with

benzotriazole azo dye reporter molecules and tether chiral analytes (either ribose or tryptophan) to the nanotag using a chemical linker. The observed SERRS response is dominated, as expected, by the benzotriazole reporter molecules, and a mirror image SERROA response for opposing enantiomers, which is expected for any chiroptical technique, is observed. What is surprising, however, is that the stereochemical response is evident from the SERRS bands of the benzotriazole dye, which is achiral so should not generate a ROA signal, and not from the parent SERS spectrum of the chiral analyte. Quantum mechanical modeling confirmed these astounding results, and indicated the existence of a new long distance and through-space mechanism of chirality transfer as being responsible.

Chirality gives stereochemically attuned nanosensors the potential to revolutionise the study of biomolecular processes. Our results demonstrate that single nanoparticle plasmonic reporters can enable a stereochemical response to be transmitted from a chiral analyte to an achiral benzotriazole dye molecule in the vicinity of a plasmon resonance generated by an achiral metallic nanostructure. This is the first report of colloidal metal

nanoparticles in the form of single plasmonic substrates displaying an intrinsic chiral sensitivity once attached to a chiral molecule. Furthermore, the observed mechanism of chirality transfer is an original

and remarkable fundamental effect which can provide a new route for engineering chiral plasmonic nanomaterials based upon vibrational optical activity.

- ¹ Etchegoin, P.G., Galloway, C., Le Ru, E.C. (2006) *Physical Chemistry Chemical Physics*, 8, 2624-2628.
- ² Ostovar pour, S., Bell, S.E.J., Blanch, E.W. (2011), *Chemical Communications*, 47, 4754-4756.
- ³ Ostovar pour, S., Rocks, L., Faulds, K., Graham, D., Parchaňský, V., Bouř, P., Blanch, E.W. (2015), *Nature Chemistry*, accepted.

Monday

Tuesday

Wednesday

Thursday

Friday

Author Index

Raman optical activity and vibrational circular dichroism of amino acid based chiral ionic liquids (CILs)

Patric Oulevey¹, Birte Varnholt¹, Sandra Lubert² and Thomas Bürgi¹

¹Department of Physical Chemistry, University of Geneva,
Quai Ernest-Ansermet 30, 1211 Geneva 4, Switzerland

²Department of Chemistry, University of Zurich,
Winterthurerstrasse 190, 8057 Zurich, Switzerland

Keywords: vibrational optical activity, ionic liquids, combined experimental and theoretical study, vibrational investigation.

Ionic liquids¹ (ILs) consist of positively and negatively charged ions, as any salts. Their melting point is considerably lower than for conventional salts due to selective choice of their ions, i.e., below 100 °C or even below room temperature. The first preparation of ionic liquids goes back as to the beginning of the last century; but they experience an increased interest in recent years, especially because of their favorable application as green solvents and electrolyte materials.

Further, chiral ILs (CILs), where usually only one of the ions is chiral, are promising in the field of stereochemistry, e.g., as solvents for enantioselective photoisomerization². Representing the molecular building blocks of life, scientists have always been fascinated by amino acids, which can be used as anions for CILs. With respect to vibrational optical activity, spectra of amino acids were recorded, for both ROA and VCD, shortly after the development of the corresponding measurement techniques^{3,4}.

The route for the synthesis of CILs from amino acids with 1-ethyl-3-methyl-imidazolium ([Emim]) as cation was presented a decade ago⁵. We have synthesized Emim-based CILs for the L-/D-pairs of alanine, valine, and leucine; hereafter labeled [L-/D-

Ala][Emim], [L-/D-Val][Emim], and [L-/D-Leu][Emim]. ROA and VCD spectra for these six compounds were measured (see Figure 1. (a) and (b)).

Two different and complementary proceedings for the vibrational analysis were chosen. At first all spectra of the three pairs of CIL-enantiomers were compared to each other and, for the Raman and IR spectra, to two ILs from literature⁶. In a second attempt, the optical activity spectra in particular were compared to the ones of their amino acids (and the Raman and IR spectra to the ones of [Emim]); computations on the individual ions helped to analyze the recorded spectra.

Additional insight into the origin of observed spectral bands — with emphasis on the dependence of molecular conformation to the generated optical activity — was obtained for the sample case of [L-Ala][Emim] through a Born-Oppenheimer molecular dynamics (BOMD) simulation⁷. The simulation box comprises 20 [L-Ala][Emim] pairs; Figure 1. (c) depicts an extract of an [L-Ala][Emim]-4-pairs cluster. In total three different [L-Ala][Emim]-4-pairs and five different [L-Ala][Emim]-1-pair were used to investigate the influence of the conformation on the optical activity of this CIL.

Results of this study are presented.

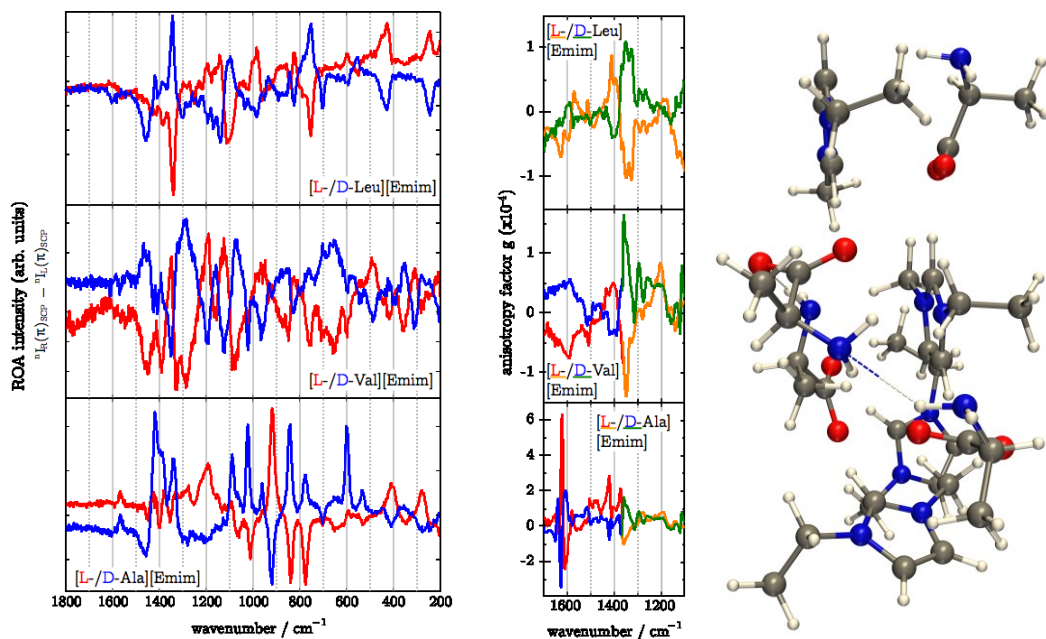


Figure 1. (a) ROA and (b) VCD spectra of [L-Ala][Emim] and [D-Ala][Emim], [L-Val][Emim] and [D-Val][Emim], and [L-Leu][Emim] and [D-Leu][Emim]. The different colors in VCD spectra (orange instead of red, and green instead of blue) reflect different spacers used in the sample cell. (c) An [L-Ala][Emim]-4-pairs cluster from a snapshot of the BOMD simulation.

¹ Welton, T. (1999). *Chemical Reviews*, 99(8), 2071–2084.

² Ding, J., Desikan, V., Han, X., Xiao, T. L., Ding, R., Jenks, W. S., & Armstrong, D. W. (2005). *Organic Letters*, 7(2), 335–337.

³ Diem, M., Gotkin, P. J., Kupfer, J. M., Tindall, A. G., & Nafie, L. A. (1977). *Journal of the American Chemical Society*, 99(24), 8103–8104.

⁴ Gargaro, A. R., Barron, L. D., & Hecht, L. (1993). *Journal of Raman Spectroscopy*, 24(2), 91–96.

⁵ Fukumoto, K., Yoshizawa, M., & Ohno, H. (2005). *Journal of the American Chemical Society*, 127(8), 2398–2399.

⁶ Kiefer, J., Fries, J., & Leipertz, A. (2007). *Applied Spectroscopy*, 61(12), 1306–1311.

⁷ Luber, S., Iannuzzi, M., & Hutter, J. (2014). *The Journal of Chemical Physics*, 141(9), 094503.

(a)

(b)

(c)

Determining the enantiomeric ratio by Raman spectroscopy

Johannes Kiefer^{1,2}

¹Technische Thermodynamik, Universität Bremen, 28359, Bremen, Germany

²School of Engineering, University of Aberdeen, AB24 3UE, Aberdeen, UK

Keywords: Chiral molecules, enantioselective discrimination, quantitative measurement.

Experimental tools for simultaneous structural and quantitative analysis that allow enantioselective discrimination as well as are very rare. Raman Optical Activity (ROA) is such a tool;¹ however, ROA is an extremely weak effect and this means a number of disadvantages when it comes to monitoring of a process, for instance. On the other hand, conventional Raman spectroscopy, which is a common method for analyzing molecular structure and performing quantitative measurements, was believed to be incapable of distinguishing between enantiomers for a long time. This ‘myth’ was very recently busted by the development of enantioselective Raman spectroscopy.²

Enantioselective Raman spectroscopy utilizes the optical activity of chiral molecules. It can be experimentally realized in a conventional Raman spectroscopy setup with polarization-resolved signal detection as illustrated in Figure 1. The beam of a linearly polarized laser passes the sample in a cuvette and is eventually blocked in a beam dump. In direction perpendicular to the laser, the scattered light is collected and collimated using an achromatic lens. The collimated light passes a half-wave retarder, e.g. an achromatic half-wave plate or a Fresnel rhomb, before its vertically and horizontally polarized components are separated in a polarizing beam splitter. Each signal component is spectrally dispersed and recorded in a spectrometer.

The key component is the half-wave retarder. Using the setup without the retarder would lead to identical signals for both enantiomers of a chiral substance. This is because the rotation angles of the laser and signal polarization would have the same absolute values for symmetry reasons. The different sign cannot be distinguished by the polarization-resolved detection since the vertical and horizontal projections of the intensity vectors are identical. The retarder, however, can break the symmetry and leads to detectable changes in the intensities. Consequently, enantioselective discrimination is possible.

The present work utilizes this approach and makes the next step by developing it further towards quantitative measurements, in particular the determination of the enantiomeric ratio. In order to allow extracting quantitative information, the effects of the main experimental parameters on the signal are investigated in detail. These parameters are

- the retarder orientation,
- the Raman depolarization ratio, and
- the target species concentration.

Regarding the latter, two scenarios are studied: (1) an enantiopure system with varying concentration, and (2) mixtures of both enantiomers of a notional chiral substance with varying composition.

A systematic variation of the above parameters allows identifying an optimal configuration that eventually facilitates the determination of the enantiomeric ratio in a

mixture of the two enantiomers. Figure 2 shows iso-intensity contour lines of the vertically and horizontally polarized signal components as function of the concentrations of the L- and D-enantiomer in the binary mixtures. It is clear that for a measured pair of intensities, a unique point in the diagram can be found, giving the enantiomeric ratio unambiguously.

In conclusion, the results demonstrate that enantioselective Raman spectroscopy can be a quantitative method for measuring enantiomer concentration and enantiomeric ratio. These capabilities make Raman

spectroscopy a unique tool for monitoring chiral systems. In principle, the method provides simultaneous structural and compositional analysis combined with enantiomeric selectivity.

The author would like to thank Kristina Noack for helpful discussions. He would also like to acknowledge membership of the Erlangen Graduate School in Advanced Optical Technologies (SAOT), which is funded by the German Research Foundation (DFG) in the framework of the German Excellence Initiative.

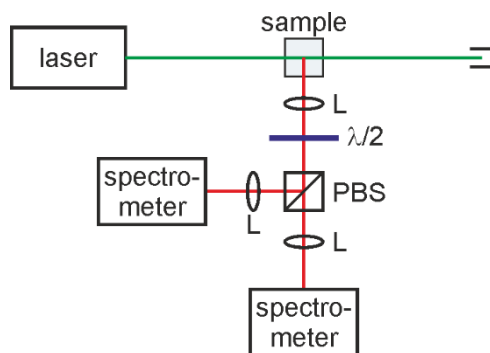


Figure 1. Schematic experimental setup. L = lens, $\lambda/2$ = half-wave retarder, PBS = polarizing beam splitter.

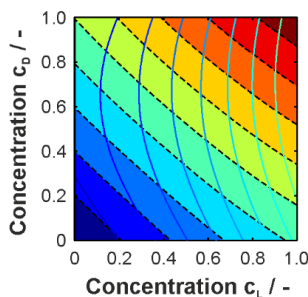


Figure 2. Iso-intensity contour lines of the vertically (dashed lines) and horizontally (solid lines) polarized signal components for the optimized half-wave plate orientation angle.

¹ Mutter S.T., Zielinski F., Popelier P.L.A. and Blanch E.W. (2015). *Analyst*, in print, DOI: 10.1039/C1034AN02357A.

² Kiefer J., Noack K. (2015). *Analyst* 140, 1787-1790.

Recent advances in infrared spectroscopic natural product analysis

Christian W. Huck

Institute of Analytical Chemistry and Radiochemistry, Leopold-Franzens University, Innrain
80/82, 6020 Innsbruck, Austria

Keywords: Near infrared, attenuated total reflection, imaging/mapping, TCM, natural products

Natural product's properties are related to certain classes of compounds such as alkaloids, flavonoids, essential oils and others. Traditionally used analytical techniques mainly used for quality (and quantity) control, including thin layer chromatography (TLC), liquid chromatography (LC), gas chromatography (GC) and capillary electrophoresis (CE) even hyphenated to mass spectrometry (MS) are time consuming and expensive¹. Therefore, infrared spectroscopic techniques enjoy a good reputation, because of the fast and non-invasive analysis enabling the measurement of physicochemical parameters simultaneously.

In food industry, spectroscopic investigations using infrared radiation have been carried out to monitor and evaluate the composition and quality already since the early sixties². During the last four decades near-infrared (NIR) and attenuated total reflection (ATR) have become one of the most attractive and used methods to determine the geographic provenience and species in parallel to the concentration of several ingredients (Figure 1)³. This technique allows on one side to avoid deception of consumers, on the other side products from cheap producing countries can be easily detected. In the field of medicinal plant analysis including traditional Chinese medicine (TCM) this

technique additionally allows to analyze health relating properties, e.g., antioxidative potential etc. Additionally, the development of customized hand-held instruments represents an important technological progress for an easy quality control directly at the market being also highly attractive for in-field measurement in order to determine the optimum harvest time⁴.

Fourier transform infrared (FTIR) spectroscopic imaging/mapping is suitable not only for the differentiation of different plant species, but also to distinct various ingredients within a (plant) sample. This technique enables molecular imaging of complex samples and therefore the detection and characterization of the molecular components of biological tissue. Based on the absorption of IR radiation by vibrational transitions in covalent bonds, the FTIR spectroscopic imaging technique offers the major advantage of the acquisition of local molecular expression profiles, while maintaining the topographic integrity of the tissue by avoiding time-consuming extraction, purification and separation steps⁵.

In the present contribution, the principle, technique and methodology of the different infrared spectroscopic methods are described followed by a discussion of quantitative and qualitative applications.

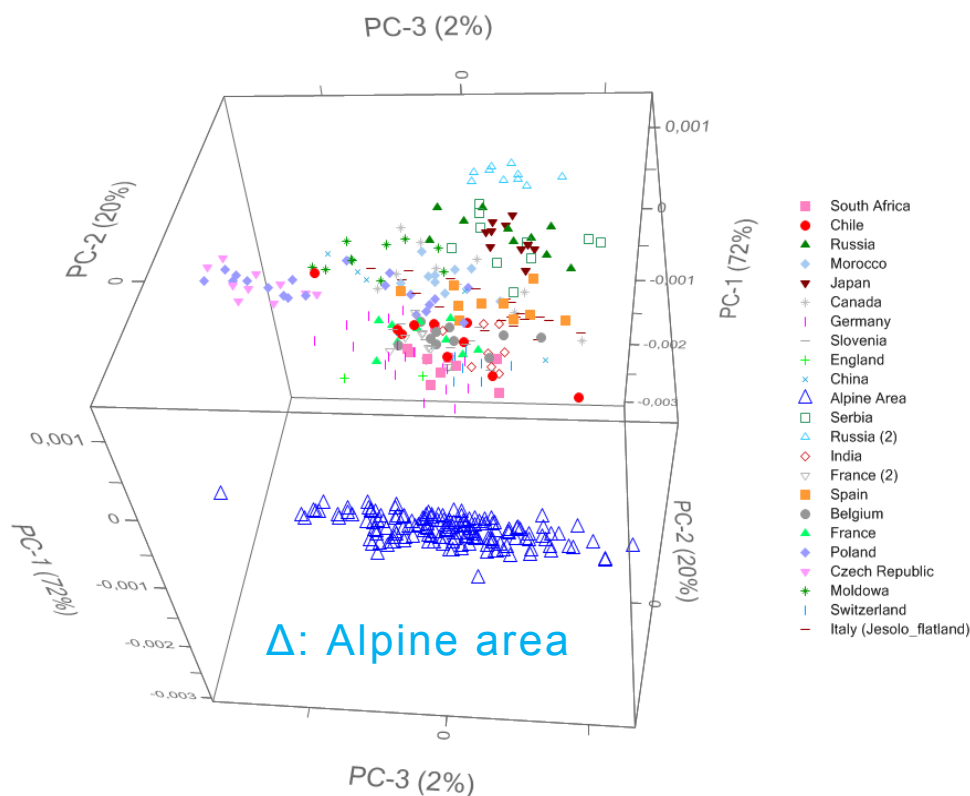


Figure 1. NIR spectroscopic differentiation of apples provenience

- ¹ Stecher G., Huck C.W., Stoeggel W.M., Bonn G.K. (2003), *Trends in Analytical Chemistry* 22, 1 – 14.
- ² Guggenbichler W., Huck C.W., Kobler A., Popp M., Bonn G.K. (2006), *Journal of Food and Agricultural Environment* 4, 98 – 106.
- ³ Huck-Pezzei V.A., Bittner L.K., Pallua J.D., Sonderegger H., Abel G., Bonn G.K., Huck C.W. (2013) *Analytical Methods* 5, 616 – 628.
- ⁴ De Benedictis L., Schmutzler M., Karer R., Eisenstecken D., Huck-Pezzei V., Robatscher P., Oberhuber M., Mimmo T., Capici C., Scampicchio M., Cesco S., Kerschbaumer L., Kaser A., Buchberger P., Huck C.W. (2012) *NIR News* 8, 12 – 15.
- ⁵ Huck-Pezzei, V.A., Pallua J.D., Pezzei C., Bittner L.K., Schoenbichler S.A., Abel G., Popp M., Bonn G.K. (2012) *Analytical and Bioanalytical Chemistry* 404, 1771 – 1778.

Direct quantitative chemical imaging of mixtures of irregular solids

David L. Wetzel and Mark D. Boatwright

Department of Biochemistry & Molecular Biophysics, Kansas State University,
Chalmers Hall Room 141, 66506, Manhattan, KS, USA

Keywords: 81,920 pixel image, Chemical pixel identity, Pixel quantitation, Near infrared focal plane array, Unit process control.

Heterogeneous mixtures of irregular solids have heretofore been an unaddressed analytical challenge. This problem has been acute for industrial processes engaged in refinement of the desired product from inorganic impurities found in the raw material. The same is true for deliberately formulated mixtures from naturally occurring base material and a chemically differing added enrichment to meet a desired specification. At long last, the pixel by pixel quantitative chemical imaging procedure described enables an array of 81,920 individual spectra revealing the distribution in the selected field of view¹. Each resulting spectrum enables identification and estimation of the prevalent chemical species for each x, y coordinate of the image.

Counting the pixels of the analyte and comparing to the total number of pixels in the particular field of view (FOV) provides a cursory population fraction of the analyte from a 1 or 0 binary census. A more precise quantitative value for the FOV is routinely achieved by a partial least squares (PLS) data treatment pixel by pixel. In such case, unlike binary (1 or 0) gross classification, the individual spectrum of a given pixel may exhibit a partial analyte composition (i.e. 0.6). Another pixel within the same FOV having less than half of the analyte (i.e. 0.4) provides a numerical value for the richness of the analyte pixel by pixel. The summation of the PLS analyte scores within the FOV results in direct quantitative chemical imaging².

The utility of this spectroscopic imaging approach has been demonstrated on natural materials, where the designation of analyte and nonanalyte may be assigned and when distinct spectroscopic features distinguish the two. The two near infrared chemical images (Figure 1) reveal the heterogeneous distribution of a binary mixture based on protein or carbohydrate wavelength absorption bands, respectively. Such an imaging routine is useful to indicate the distribution, uniformity, or a lack thereof in a deliberately formulated product following a mixing stage.

In the industrial process of wheat milling, the objective is the separation of wheat endosperm from other botanical parts of the kernel. This includes the bran that covers the outside of the wheat kernel as well as the germ. The refining process consists of many successive operational stages designated as breaks, middlings, and sizings. Within each operational stage, multiple repetitive unit processes operate at their individual optimal grinding settings. Each grinding step is followed by sequential sieves stacked in descending order of opening size to separate product or byproduct fractions based on particle size.

The relative product concentration (% endosperm) of different individual millstreams is determined (Figure 2). The efficiency of two different unit processes (Figures 3 and 4) illustrates the utility of imaging to compare various operational parameters for sequential processes.

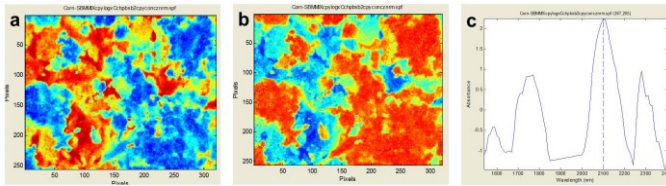


Figure 1. In Figure 1a red (warm) false color highlights high protein content at 1740 nm. The Figure 1b mirror image results from the carbohydrate band at 2100 nm. Figure 1c is a spectrum with absorption bands of both components.

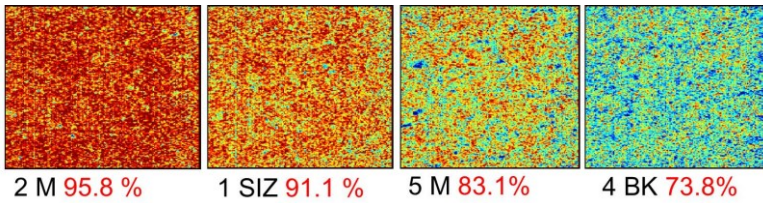


Figure 2. Quantitative near infrared images of select flour streams (red=endosperm).

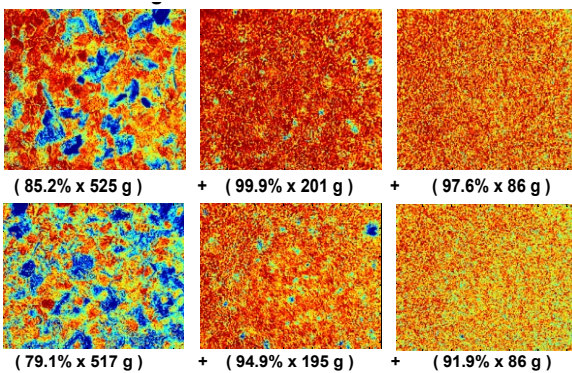


Figure 3. Quantitative images of the 1st, 2nd, and 3rd break system products. Top: Optimum adjustment products going to “sizings”, “reduction”, and “flour” streams respectively. The % endosperm and weight of each product is listed. The weighted summation of endosperm is 73%. Bottom: For the inferior break settings, the corresponding images produce % endosperm and weight values for a 67% endosperm yield.

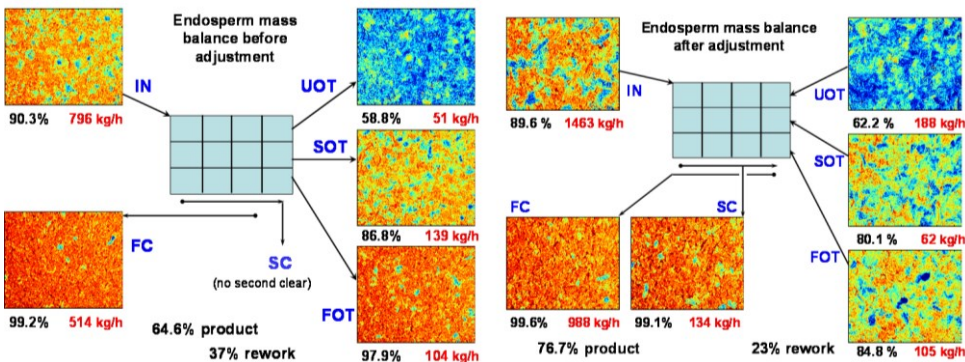


Figure 4. Unit process efficiency before and after optimization from 64.6 → 76.7% product.

¹Kidder, L., Dubois, J., Lewis, E., (2007). *Pharm. Sol. Update*. Spring, 48.

²Wetzel, D., Posner, E., Dogan, H., (2010), *Appl. Spectrosc.*, 64(10), 1320-24.

Raman spectra of samples with different particle sizes and influence on particle size on accuracy of quantitative analysis

Duy Pham Khac and Hoeil Chung

Department of Chemistry, Hanyang University, Seongdong-Gu, 133-791, Seoul, Korea

Keywords: Particle size, Mie scattering, Quantitative representation, Raman spectroscopy

Raman spectroscopy has been extensively utilized for analysis of diverse samples since it provides rich information on molecular structure with simple and non-destructive measurement. When Raman spectroscopy is employed for compositional analysis of solid samples, the variations in physical properties of samples such as particle size and packing density have confounding effects on resulting spectral features. Especially, the propagation of laser radiation and Raman scattering events could sensitively vary depending on particle size, Raman spectral features would be dissimilar for samples with different particle sizes although their compositions are same. This is a critical issue to consider when quantitative analysis based on Raman spectroscopy intends.

We have evaluated the variation of accuracy for the concentration determination of a component when the particle size of samples changes. For the evaluation, binary mixture samples of ambroxol and lactose were prepared with 4 different particle sizes of lactose (under-50, 50-100, 100-150 and over 150 μm , designated as L1, L2, L3 and L4, respectively), while the particle size of ambroxol maintained constant (15-30 μm). The ambroxol concentrations in the samples varied from 9.0 to 15 wt% with increments of 0.5 wt%. Back-scattering Raman spectra of the samples were acquired and the spectral features were examined in relation with the particle size. Figure 1 (a) shows Raman spectra of 12.5% ambroxol samples

with 4 different particle sizes of lactose. As shown, the magnitude of baseline offset becomes larger with the increase of particle size due to the greater degree of Mie scattering. To evaluate the sample representation of spectra, the baselines of spectra were corrected and the intensity ratio of 1062 cm^{-1} peak (circle, ambroxol) over 357 cm^{-1} peak (star, lactose) was calculated as shown in Fig. 1 (b) The peak intensity ratio decreases with the increase of particle size, indicating the decrease of the ambroxol peak relative to the lactose peak. When the particle size of lactose is larger, a chance for ambroxol to be exposed to laser irradiation becomes smaller, so it explains the relative intensity decrease of ambroxol peak.

Using each dataset, partial least squares (PLS) was performed to determine the ambroxol concentrations. Out of a total of 15 samples, 10 samples were randomly selected as a calibration set and remained samples were used for a validation set. Table 1 shows standard error of predictions (SEPs) resulted by 10-fold cross validation when the particle size of sample varies. The error is highest when the samples prepared with the largest lactose particles are measured, while the SEP decreases as the particle size becomes smaller. When the particle size is larger, uncertainty of photon propagation in a sample increases. So, it could degrade accuracy of quantitative representation of sample composition as well as reproducibility of measurement. To check the reproducibility, relative standard deviations (RSDs) of the lactose peak

intensity at 1062 cm⁻¹ (star) in each case were calculated as shown in Fig. 1 (c). The reproducibility becomes degraded as the particle size of samples increases. Fig. 2 (d) shows the calculated RSDs based on Monte-Carlo simulation. The simulation results are well accordance with those of experimental observations.

In conclusion, the variation of particle size needs to critically consider for reliable quantitative analysis. A strategy, so called a particle-size tolerant measurement, able to maintain consistent spectral feature by reflecting particle size information in prior is under development as a continuing study.

Table 1. SEPs (Standard Error of Predictions) for determination of ambroxol contents when the particle size of sample varies

Particle Size	L1	L2	L3	L4
SEP (%)	0.06	0.07	0.23	1.32

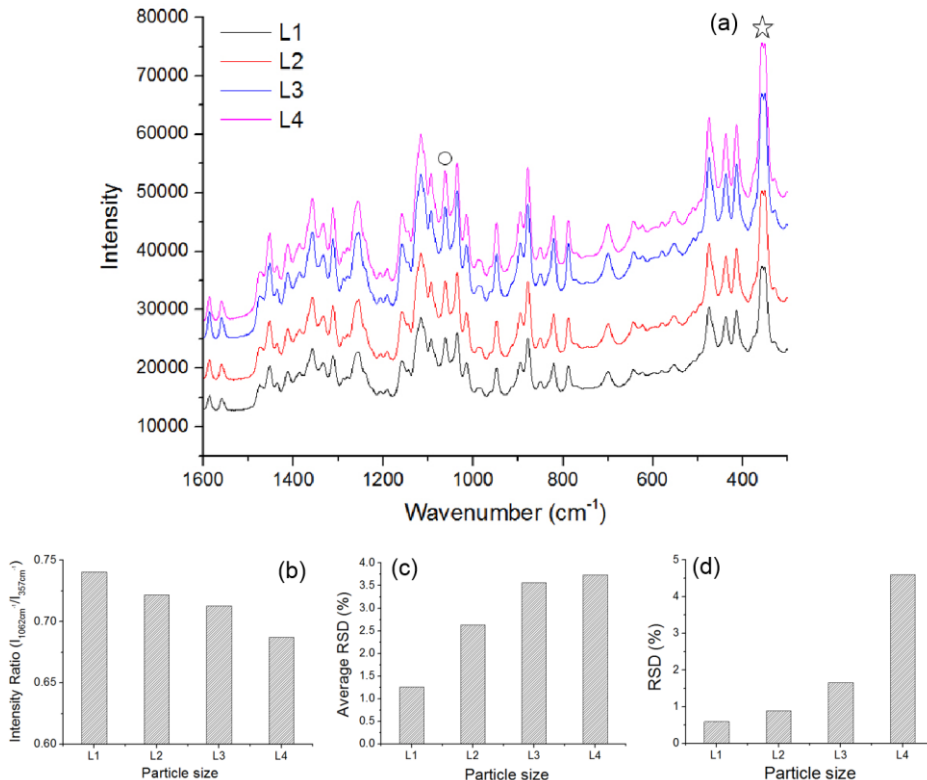


Figure 1. (a) Raman spectra of 12.5% ambroxol samples with 4 different particle sizes of lactose and (b) the corresponding intensity ratios of 1062 cm⁻¹ (circle) over 357 cm⁻¹ peak (star). RSDs of the lactose peak intensity (star) calculated from actual experimental data (c) and Monte-Carlo simulation (d) are also shown.

Optimisation of mixing time in powder blending processes using near-infrared spectroscopy

A. Barone¹, G. Montague², E. Martin¹, S. Dawson³

¹ Biopharmaceutical Bioprocessing Technology Centre, Newcastle University, Newcastle Upon Tyne, Tyne and Wear, NE1 7RU, UK

² School of Science & Engineering, Teesside University, Middlesbrough, Tees Valley, TS1 3BA, UK

³ British Bakels Ltd, Bicester, Oxon, OX26 4JT, UK

Keywords: near infrared, mixing time, food industry, pre-treatment, optimisation.

Near-infrared (NIR) spectroscopy is employed as an in-line control system to continuously monitor the blending of powder products and optimise blending time. Blending time has to date been based on experimental experience and generally extended far beyond the time when full homogeneity was indicated to accommodate natural variability and perceived risk; with this work the aim is to decrease blending time, so increasing mixer throughput, reducing the waste of energy and man hours involved in unnecessary blending.

Homogeneity is assessed for different food powder blends: bread and roll concentrates, confectionery mixes, baking and dough powders, and sponge and cake emulsifiers. A non-contact NIR fiber-optic probe is installed in a conical screw mixer and spectra are collected every few seconds in real time. In all the experiments the change of spectra over time is observed, eventually converging to the same steady state spectrum: thus blending time is clearly indicated when a constant value is reached.

In making this assessment, rigorous techniques for data pre-treatment need to be employed. First the data are truncated to eliminate the noisy areas which could influence the analyses. Then scattering effects are removed employing several chemometric techniques such as derivatives,

detrending, normalization and standard normal variate. Best results are obtained when combining more techniques together and best combination depends on the nature of the product.

After this initial work, two methods are investigated to provide with an estimation of the mixing time. The first method sees the calculation of the standard deviation of the Moving Block Standard Deviation (MBSD): plot of it against time shows how spectra profiles change with each other, until reaching the same final composition which is indicated by a flat line (Figure 1). The second method is dissimilarity, which focuses instead on the variance over time of the difference between each spectrum and the steady state fully mixed spectrum (Figure 2). The two methods show a good agreement providing the same mixing time. Finally a calibration model is built to measure concentration of in-line spectra and to assess whether composition gets stable after the estimated mixing time, therefore validating the results obtained from standard deviation and dissimilarity.

This work demonstrates the capability of near-infrared spectroscopy to be employed in food industry as a safe, non-invasive and quick technique for optimising the mixing time. NIR opens new doors to powder blends analyses as it provides a

Monday
 Tuesday
 Wednesday
 Thursday
 Friday
 Author Index

better understanding of the system and a detailed description of the process in real-time. Future studies will focus on in-line quality monitor and control: using the same NIR probe we will test the quality of both blends and finished products, so to check during the production that every substance in the mixture is the desired ingredient in the

right amount. This will help in detecting eventual contamination and prevent batches to be wasted. As we believe NIR potential is not only towards powder mixes, we will eventually apply NIR control to liquid and gel production lines.

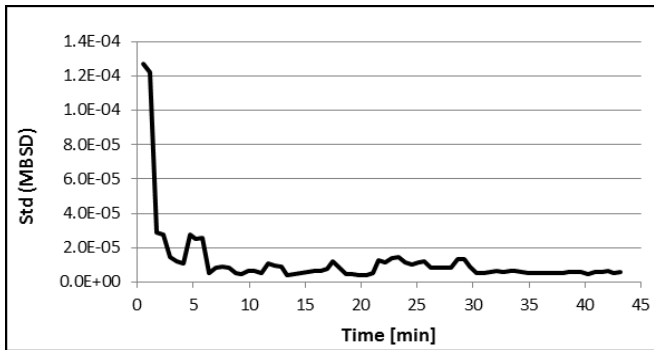


Figure 1. Plot of standard deviation of MBSD vs time: spectra profiles change with each other, until reaching the same final composition. Homogeneity is indicated by a flat line.

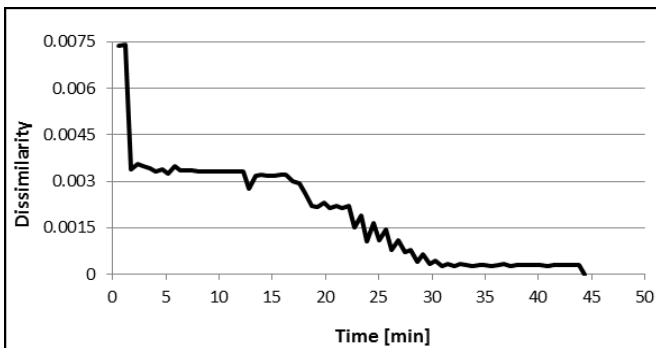


Figure 2. Plot of dissimilarity vs time: the difference between each spectrum and the steady state fully mixed spectrum decreases over time. Homogeneity is given by the starting point of the flat line.

Imaging the Desolate Microscopic Landscape of Processed Cheese Using Raman MicroscopyGeoffrey P.S. Smith¹, Keith C. Gordon¹ and Steve E. Holroyd²¹Department of Chemistry, Dodd Walls Centre, University of Otago, Union Place West, 9016, Dunedin, New Zealand²Fonterra Research and Development Centre, Dairy Farm Road, 4472, Palmerston North, New Zealand

Keywords: Raman microscopy, high resolution imaging, principal component analysis, cheese, dairy products.

Imaging microscopic objects can be a difficult task especially when they are set in landscapes which contain domains of a similar size, colour and appearance. Difficulty increases when your sample is resistant to being stained or when it reacts adversely with the colourant. When studying cheese, these problems are commonplace. An image of cheese through a light microscope could easily be mistaken for the surface of Mars, albeit with a slightly yellowish hue. Despite its initial appearance, the content of cheese can be quite diverse containing fat, protein, water, carbohydrates as well as preservatives and emulsifiers in the case of processed cheese.

Raman microscopy has proven to be an effective method for locating the majority of these components, without the use of invasive dyes or preparation methods. The purpose of this study is to determine whether Raman microscopy is an effective method for imaging the microstructure of processed cheese and whether it would also be possible to identify and locate the various additives which might be present therein. This involved collating a library of additives and obtaining their Raman spectra. These

additives were then incorporated into cheese samples with concentrations as close as possible to those which might be present within processed cheese bought in stores. Imaging was initially conducted point by point (whisk-broom method) over an area of 50 x 50 μm with 400 spectral points. This low resolution method (see figure 2) was effective in finding the locales of each component within the image but the resolution could not distinguish smaller fat globules. This resulted in images where only the largest fat globules were resolved and the presence of what appeared to be fat channels. Principal component analysis was used on this data and found to be an effective method for distinguishing regions which contained the weaker additive bands, while band integrals were sufficient for separating spectra based on fat or protein content. Imaging was then performed line by line (push-broom method) which allowed many more spectral points to be collected within a relatively small time frame. Over an area of 50 x 50 μm , 22,500 spectra were collected. This provided images in which the smaller fat globules were resolved and the

true crystal-like structure of the emulsifier, trisodium citrate (TSC), was observed.

Raman microscopy was effective for imaging fat, protein, water, starch and trisodium citrate. The preservative, sorbic acid, was not located -possibly because of its low concentration. Raman microscopy might therefore be able to find use for

studying other food products, especially other dairy products. The ability to obtain Raman spectra of a large number of dairy product components without producing intrusive fluorescence and avoid the use of staining dyes should encourage the growth of the technique for future use in the food industry.

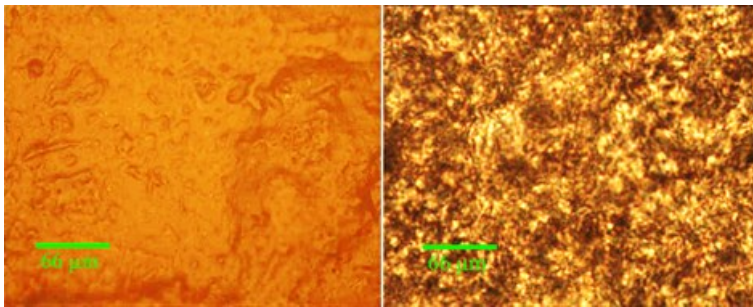


Figure 1. Viewing unsliced cheese illuminated from the top (left) and sliced cheese illuminated from the bottom (right).

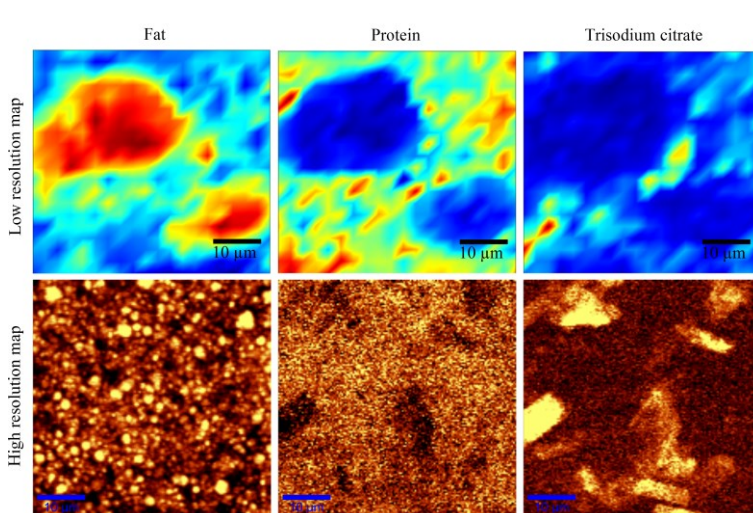


Figure 2. Raman images of three components within store-bought processed cheese, created using both high and low resolution imaging methods (different areas).

Surface-Enhanced Raman Spectroscopy and Imaging with Tailor-Made Plasmonic Nanoparticles

Wei Xie, Yuying Zhang, Mohammad Salehi, Bernd Walkenfort, Sebastian Schlücker

Physical Chemistry I, Faculty of Chemistry, University of Duisburg-Essen, 45141 Essen,
Germany

Keywords: SERS, cancer diagnostics, tissue imaging, heterogeneous catalysis, reaction kinetics

Surface-enhanced Raman scattering (SERS) has become a mature vibrational spectroscopic technique during the last decades and the number of applications in the chemical, material, and in particular life sciences is rapidly increasing.¹

In addition to normal Raman spectroscopy, SERS requires plasmonically active materials, for instance noble metal colloids, which support localized surface plasmon resonances.

This lecture gives an overview on the rational design and synthesis of functionalized noble metal colloids for chemical and bioanalytical applications of SERS. After a brief introduction on the theoretical foundations of SERS, two different topics from the chemical sciences with results from our group will be covered. In both cases plasmonic nanostructures with tailor-made physical and chemical properties play a key role.

Immuno-SERS microscopy (iSERS) for tissue-based cancer diagnostics employs target-specific colloidal SERS probes in combination with Raman microspectroscopy. SERS-labeled antibodies allow the selective and sensitive localization of the corresponding antigen in tissue specimens. The properties of the colloidal SERS probes² (Figure 1) are crucial for the success of iSERS experiments. Signal brightness, stability and robustness as well as steric accessibility for bioconjugation are few very important aspects. For instance,

small Raman reporter-functionalized clusters of noble metal nanoparticles (NPs) are very bright SERS labels due to plasmonic coupling. Small clusters of AuNPs were further used for iSERS imaging on prostate biopsies. Current work in our laboratories and future developments of this innovative iSERS imaging approach will be discussed.

The second part of the lecture covers label-free monitoring of chemical reactions catalyzed by Pt, Au and Ag nanoparticles. Bifunctional nanoparticles exhibiting both high plasmonic and catalytic activity are required, but not routinely available. We designed and synthesized Au/Pt nanoraspberries as well as Au/Au and Ag/Ag core/satellite superstructures for this purpose (Figure 2).³⁻⁴ Electron microscopy demonstrates the high uniformity of the particles. Computer simulations predict very high plasmonic activity due to plasmonic coupling, resulting in several hot spots. For proof-of-concept studies 4-nitrothiophenol, which is present as a self-assembled monolayer on Au and Ag surfaces, was chosen. The reduction to 4-aminothiophenol can be achieved either by chemical hydride agents or by a combination of hot electrons and protons. Current work from our group on temperature-controlled microfluidics for kinetic reaction monitoring as well as future directions for the use of hot electrons for driving chemical reactions will be discussed.

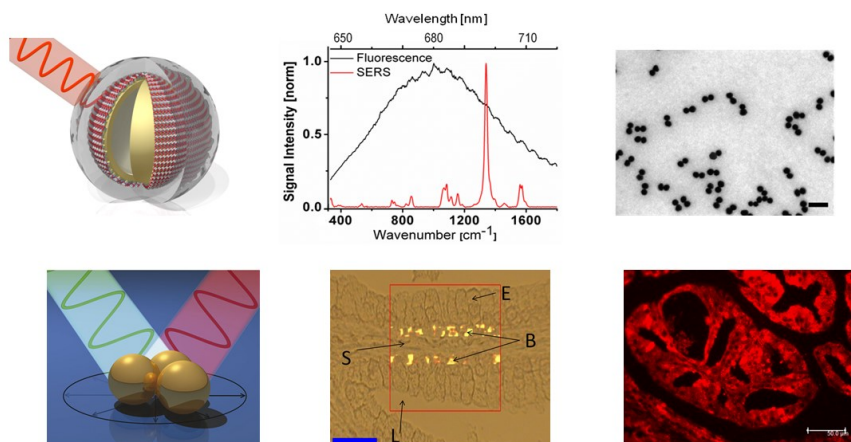


Figure 1. SERS nanoparticle labels for use in immuno-SERS (iSERS) microscopy for tissue-based cancer diagnostics. Spectral multiplexing is possible due to the small linewidth of vibrational Raman bands compared to fluorescent dyes. Correlative SEM/SERS experiments on single small AuNP clusters demonstrate their high SERS signal strength.

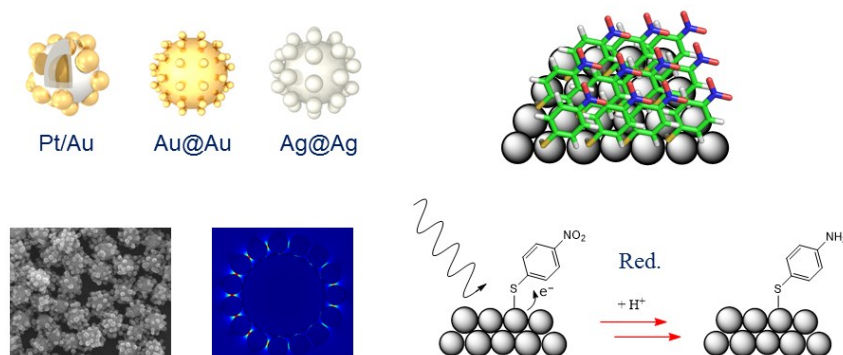


Figure 2 Bifunctional noble metal nanoparticles with plasmonic and catalytic activity (left).

Self-assembled monolayer of 4-nitrothiophenol on a metal surface for reduction to 4-aminothiophenol either by chemical hydride agents or by hot electrons and protons (right).

¹ S. Schlücker, *Angew. Chem. Int. Ed.*, **2014**, 53, 4756-4795.

² B. Küstner, M. Gellner, M. Schütz, F. Schöppler, A. Marx, P. Ströbel, P. Adam, C. Schmuck, S. Schlücker, *Angew. Chem. Int. Ed.* **2009**, 48, 1950-1953.

³ W. Xie, C. Herrmann, K. Kömpe, M. Haase, S. Schlücker, *J. Am. Chem. Soc.* **2011**, 133, 19302-19305.

⁴ W. Xie, B. Walkenfort, S. Schlücker, **2013**, *J. Am. Chem. Soc.*, 135, 1657-1660.

**Perspectives in Process Analysis:
PAT and the workhorse vibrational spectroscopy**

Rudolf W. Kessler

STZ Process Control and Data Analysis, Herderstr. 47, 72762 Reutlingen, Germany

Keywords: Process Analytical Technology (PAT), spectroscopy, sensitivity, spectral imaging,

Process analysis is a transdisciplinary technology. Process chemists, process engineers, chemometricians, and many other technologists must work together. Process Analysis includes process design (Quality by Design (QbD)) of the used technology, process analytics (Process Analytical Technology (PAT)), process control units as well as the economic evaluation of the process including supply chain management. Optical spectroscopy together with chemometrics will play an important role in the transition of a re-active industrial production into a pro-active industrial system¹. As spectroscopic techniques can simultaneously detect all morphological and chemical features, the complete fundamental functionality of a compound is inherent in every spectrum.

Sensitivity, selectivity and robustness of each individual technology in combination with the used wavelength range has its limitations due to the structure of the measured specie and the used optical configuration. In any application, a key issue is to find the causal link between the measured spectral features and the final target quality. In spectral imaging the spatial distribution in the x-, y- and possibly z-direction may be also of interest².

Optical spectroscopy covers a broad wavelength range with different sensitivities and selectivities. The major advantage of near infrared spectroscopy (NIR) is that the absorption cross sections are lower in comparison to the mid infrared (MIR) and therefore the penetration depth of the

photons are higher in particulate systems. As a result, the technique can be used to analyse components even at high concentrations in an industrial environment without the need of pre-processing the sample. The typical detection limits in NIR spectroscopy lie in the lower percentage region, 0.1 % (esp. water) up to 5. In contrast to NIR, MIR spectroscopy enables the analysis of concentrations as low as 0.01%, standard detection limits can be as low as 0.001% Due to the high absorption cross sections, special arrangements like Attenuated Total Reflectance (ATR) are developed to lower the pathlengths at higher concentrations or to use lasers with a high photon flux. The strength of the water absorption in the NIR and MIR may limit the broad use in many biotechnological applications. Although Raman absorption cross sections lie typically around 10 orders (or more) of magnitude lower than in the MIR, due to recent development of extraordinarily sensitive detection systems and its high selectivity and robustness, Raman spectroscopy may approach the performance of FTIR spectrometers in the near future, especially in aqueous systems³.

Ultraviolet-, and visible (UV/VIS) spectroscopy as well as fluorescence spectroscopy are highly sensitive techniques to measure electronic transitions, but lack selectivity. Table 1 shows a rough qualification of the used techniques in PAT with respect to sensitivity, selectivity, robustness and their general suitability for inline control.

Special emphasis in the future will be given to measure not only the chemical entities but also their lateral distribution in an object. Spectral Imaging, or also called Chemical Imaging, is an emerging field with applications ranging e.g. to find biomarkers in a tissue but also to control and qualify 100% of tablets or food². Pushbroom Imaging systems are ideally suited for inline control and in the meantime they are available in almost every wavelength range. A pushbroom imager is a line scanning system and acquires the full spectral information for all lateral x-coordinates simultaneously in a single line, often of several thousand pixels.

Process analysis together with spectroscopy and intelligent data analysis

will play a more important role in the future of the processing industry than it has in the past. According to the Industry 4.0 concept of the German government, the future of industrial automation will be “arbitrarily modifiable and expandable (flexible), connect arbitrary components of multiple producers (networked), enabling its components to perform tasks related to its context independently (self-organizational) and emphasizes ease of use (user-oriented)”³. Spectroscopy and its “workhorse” vibrational spectroscopy will be an important toolbox and enabling technology to realize this concept.

Table 1. Qualification of the different techniques for their suitability in PAT-applications

	UV/VIS/	NIR	MIR	Fluorescence	Raman
Selectivity	+	++	+++	++	+++
Sensitivity	+++	+(+)	+++	+++(+)	+++(+)
Sampling	+++	+++	+	++	+++
Working in aqueous media	+++	+	+	++	+++
Applicability	+++	++	+	+	+
Process analytical tool	+++	+++	+	+	+++
Light guide glass	+++	+++	(+)	+++	+++
Signal	Absorption	Absorption	Absorption	Emission	Scattering
Sampling online/inline	s, l, g	s, l	s, l, g	s, l (g)	s, l (g)
Techniques	Transmittance Reflectance ATR	Transmittance Reflectance ATR	ATR (Transmittance)	Reflectance Transmittance	Reflectance Transmittance
Relative costs	1	3 - 5	6 - 10	4 - 6	8 - 12

¹ Bakeev K A. (Ed.), Process Analytical Technology, (2nd edn) Wiley: 2010.

² B. Boldrini, W. Kessler, K. Rebner and R. W. Kessler, Hyperspectral imaging: a review of best practice, performance and pitfalls for inline and online applications, Journal of Near Infrared Spectroscopy 2012, 20, 438–508, doi: 10.1255/jnirs.1003.

³ R. W. Kessler, Perspectives in process analysis. J. Chemometrics, 2013, 27: 369–378. doi: 10.1002/cem.2549.



Multiplexing cellular redox potential and pH measurements in 3D breast cancer tumour models using SERS nanosensors

Lauren E. Jamieson¹, Aleksandra Jaworska^{2,3}, Pierre Bagnaninchi⁴, Kate Fisher¹, Jing Jiang¹, David. J. Harrison⁵ and Colin J. Campbell²

¹EaStCHEM, School of Chemistry, University of Edinburgh, Edinburgh, EH9 3FJ, UK

²Faculty of Chemistry, Jagiellonian University, 3 Ingardena Str., 30-060 Krakow, Poland

³Jagiellonian Centre for Experimental Therapeutics (JCET), Jagiellonian University, 14 Bobrzynskiego Str., 30-348 Krakow, Poland

⁴MRC Centre for Regenerative Medicine, Chancellor's Building, University of Edinburgh, Edinburgh, EH16 4SB, UK

⁵Medical and Biological Sciences Building, University of St Andrews, St Andrews, KY16 9TF, UK

Keywords: redox, SERS, pH, MTS, OCT.

Cellular redox potential is incredibly important for the control and regulation of a vast number of processes occurring in cells. It is a measure of the oxidising or reducing capacity of the cellular environment and exists as a delicate balance between many species including reactive oxygen species (ROS) and antioxidant enzymes and small molecules. When the fine redox potential balance within cells is disturbed it can lead to the progression of many diseases. For example, oxidative stress has been well documented to contribute to the progression of diseases such as heart disease, neurodegenerative disease and ageing.

Of particular interest to my research is the redox gradient that develops in cancer tumours where the internal regions are further from vascular blood supply and become starved of oxygen and hypoxic. This makes treatment of these areas a lot more challenging as chemotherapy approaches rely on the presence of oxygen and with a poor vascular blood supply, drugs delivered through the blood stream will have poor access to these regions.

To aid the development of drugs and therapies to overcome this problem a system that gives a quantitative map of redox

potential changes through a tumour would be a vital tool. Our technique uses redox sensitive molecules, in particular NQ and AQ (Figure 1), attached to gold nanoshells (NS, Figure 2A), which are delivered to cells and give signals using surface enhanced Raman scattering (SERS).¹⁻³ As redox potential is pH dependent, intracellular pH measurements are also required and can be made using a SERS system with a pH sensitive molecule such as mercaptobenzoic acid (MBA) (Figure 1).⁴

Intracellular redox and pH measurements have been successfully multiplexed in monolayer culture using SERS (Figure 1).⁵ Measurements are now being extended to a 3D model, multicellular tumour spheroids (MTS, Figure 2), to analyse the gradients that develop. Photothermal optical coherence tomography (OCT) has been used to reveal the 3D distribution of NS in MTS, which can be altered to monitor spatial changes in pH and redox. Transmission electron microscopy (TEM), helium ion microscopy (HIM, Figure 2) and confocal fluorescence microscopy have also been used extensively to monitor cellular uptake of NS under different conditions.

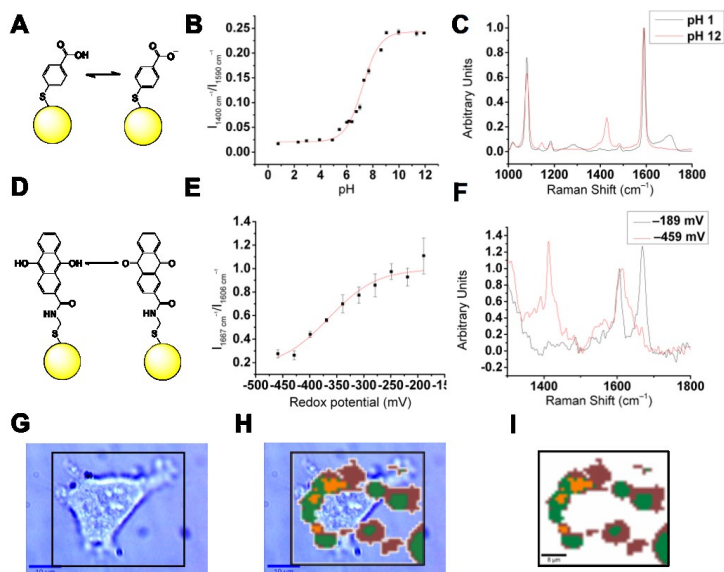


Figure 1. shows how SERS was used to multiplex intracellular pH and redox measurements. Gold NS (yellow spheres) were functionalized with pH active MBA, A, and redox active AQ, D. Calibration curves for the sensors are shown in B and E respectively and representative spectra in C and F respectively. G illustrates an example of multiplexing intracellular measurements in a cell (G) where both sensors were delivered and SERS mapped. Cluster analysis and processing were performed to give the clusters shown (I) overlaid with the cell image (H) where green = pH 7.0, yellow = pH adjusted redox -272 mV and brown = pH adjusted redox -332 mV.

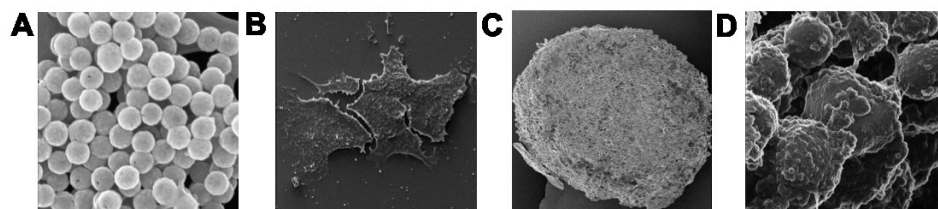


Figure 2. show HIM images of AQ-NS, A, MCF7 cells growing in monolayer culture, B, and MCF7 cells growing as MTS, C and D.

- Ochsenkühn M.A., Jess P.R.T, Stoquert H., Dholakia K., Campbell C.J. (2009), *ACS Nano*, 3 (11), 3613-3621.
- Auchinvole C.A.R., Richardson P., McGuinees C., Mallikarjun V., Donaldson K., McNab H., Campbell C.J. (2012), *ACS Nano*, 6 (1), 888-896.
- Jiang J., Auchinvole C., Fisher K., Campbell C.J. (2014), *Nanoscale*, 6, 12104-12110.
- Jaworska A., Jamieson L.E., Malek K., Campbell C.J., Choo J., Chlopicki S. & Baranska M. (2015), *Analyst*, DOI: 10.1039/c4an01988a.
- Jamieson L.E., Jaworska, A., Jiang, J., Baranska M., Harrison D.J. & Campbell C.J. (2015), *Analyst*, DOI: 10.1039/c4an02365j.

***In situ* hydrazine reduced silver colloid synthesis for reproducible SERS measurements**

Vera Dugandžić^{1,2}, Izabella Jolan Hidi^{1,2}, Karina Weber^{1,2}, Dana Cialla-May^{1,2}, Jürgen Popp^{1,2}

¹ Institute of Physical Chemistry and Abbe Center of Photonics, Friedrich Schiller University, 07743 Jena, Germany

² Leibniz Institute of Photonic Technology Jena, 07745, Jena, Germany

Keywords: *In situ*, LOC-SERS, silver colloids, hydrazine, adenine.

Surface enhanced Raman spectroscopy (SERS) is in recent time recognized as promising tool for detection and quantification of a large variety of analytes¹. Silver and gold colloidal nanoparticles are the most often used SERS substrates since their plasmon resonance frequencies are in the visible and near infrared region of the electromagnetic spectrum.

Modern analytical requirements strive for simple, inexpensive and high throughput methods for fast quantification, wherein SERS is being widely explored as a prominent candidate. Moreover, droplet based Lab-on-a-chip approach (LOC-SERS) has shown great potential for rapid monitoring of relevant analytes for medical² and environmental³ application. However, the establishment of SERS as a quantitative analysis technique requires high over time stability of synthesized colloids as well as reproducible synthetic procedure. One approach to make the colloid synthesis more reproducible might be *in situ* preparation in a chip³.

Within this contribution, we report a novel strategy for *in situ* synthesis of the silver colloids for LOC-SERS application. Silver nanoparticles were synthesized in a glass microfluidic chip (Figure 1) coupled with computer controlled neMESYS Ceti high performance syringe pump system. The chip is equipped with total of 6 ports². The synthesis was performed by pumping

solution A (containing AgNO₃, NH₄OH and trisodium citrate) and solution B (hydrazine) in equal flowrates to mix the solutions within the chip. The formation of the droplets was assured by pumping oil as separation medium through the chip.

The total reaction can be described by the equation:



Citrate was used only as a protecting agent and does not partake in the reaction. The addition of ammonia provides the possibility for kinetic control over the reaction, since the formation of stable diamminesilver(I) complex ion decreases the reduction potential of silver, making the reaction time directly proportional to the ammonia concentration. Additionally, the colloids are stabilized upon addition of ammonia⁴. Even though, molecular nitrogen is formed by oxidation of hydrazine. Due to the low concentration of the reactants, the formed molecular nitrogen probably stays dissolved in water since no gaseous bubbles are formed. The *in situ* synthesized colloids were characterized by UV-VIS spectroscopy, SEM and TEM.

To test the SERS performance of the synthesized colloids, adenine was used as a model analyte. A range of concentrations was measured. Day to day reproducibility was tested by repeating the same measurements in two consecutive days using

the same solutions A and B and plotting the area of a peak at 726 cm^{-1} assigned to ring breathing against concentration (Figure 2). The results indicate that measurements performed with *in situ* synthesized colloids

present lower standard deviation as well as better day to day reproducibility as compared to measurements performed with colloids prepared by conventional strategies.



Figure 1. LOC-SERS setup used for colloid synthesis and adenine measurements.

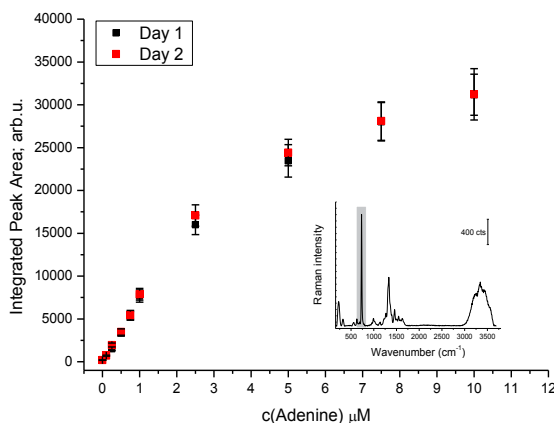


Figure 2. Day to day reproducibility of the integrated peak areas of the Raman mode at 726 cm^{-1} against concentration. Inset: Mean SERS spectrum of $1\text{ }\mu\text{M}$ adenine.

Acknowledgement:

The funding of the PhD project of Vera Dugandžić within the framework “Carl-Zeiss-Strukturmaßnahme” is gratefully acknowledged. Funding the projects “QuantiSERS” and “Jenaer Biochip Initiative 2.0” within the framework “InnoProfile Transfer – Unternehmen Region“ the Federal Ministry of Education and Research, Germany (BMBF) is gratefully acknowledged.

¹Cialla D., März A., Böhme R., Theil F., Weber K., Schmitt M., Popp J. (2012). *Anal Bioanal Chem* 403, 27–54

²Hidi I.J., Mühlig A., Jahn M., Liebold F., Cialla D., Weber K., Popp J. (2014), *Anal. Methods*, 6, 3943–3947

³Gao R., Choi N., Chang S., Lee E.K, Choo J. (2014), *Nanoscale*, 6, 8781–8786

⁴Gorup L.F., Longo E., Leite E.R., Camargo E.R. (2011), *Journal of Colloid and Interface Science*, 360, 355–358

Ultrahigh sensitivity of quasi-three-dimensional paper-based SERS substrates prepared by single-shot laser treatment

Yi-Chuan Tseng, Chen-Chieh Yu, Sin-Yi Chou, Shao-Chin Tseng, Yu-Ting Yen and Hsuen-Li Chen

Department of Materials Science and Engineering, National Taiwan University, No. 1, Sec. 4, Roosevelt Road, Taipei, 10617, Taiwan

Keywords: SERS, paper-based substrates, quasi-three-dimension, attomolar sensitivity, eco-friendly substrate.

Paper has traditionally been used for writing, wrapping, and wiping, yet has found new applications in modern technology—for example¹, in paper-based electronic devices, displays, and light emitting diodes. In a previous study, we developed a colorimetric test paper by nanoparticle containing photographic paper that provided qualitative information for an analyte². Surface-enhanced Raman scattering (SERS) is employed widely in chemical and biological sensing because it can provide abundant molecular information³. In this study, we developed an eco-friendly paper substrate that provides extremely high SERS sensitivity as a result of the formation of NPs through a single-shot laser-induced photo-thermal effect. This hydrophobic SERS filter paper could efficiently concentrate analytes and, thereby, provide intense Raman signals relative to those found on Si and glass substrates. Moreover, because the NPs were distributed on the quasi-three-dimensional fibril structures of paper, there were many electromagnetic hot spots within the range of the depth of focus (DOF) of a Raman microscope, effectively contributing to the large intensity of the Raman signals. Accordingly, we could apply this SERS filter paper to the detection of attomolar concentrations of analytes, thereby

approaching single molecule detection capability.

Fig. 1a provides a schematic representation of the use of the laser-induced photothermal effect for the fabrication of NPs on various substrate, we selected glass, Si, and paper substrates for comparison. Fig. 1b-d display the surface morphologies and distributions of the Ag NPs that formed on the glass, Si, and filter paper substrates after different numbers of shots of laser illumination. Fig. 1e presents SERS spectra of 10^{-6} M R6G that had been dried on these NP-containing substrates. The SERS performance of the filter paper substrates, featuring highly dense and uniform NPs, was superior to that of the other two substrates, presumably because of the low densities of NPs on the surfaces of the glass and Si. In Fig. 2a-d, we used the three-dimensional finite-difference time domain (3D-FDTD) method to simulate the electric field intensity of hot spots distributed in 2D, quasi-3D, and 3D arrays. In performing the simulations, we focused a plane wave through a lens to simulate a real Raman microscope setup. The SERS spectra in Fig. 2e reveal that the Raman signals of 4-ATP on the SERS filter paper were enhanced dramatically, with the limits of detection at a concentration as low as the attomolar (10^{-18} M) level, thereby approaching single molecule detection.

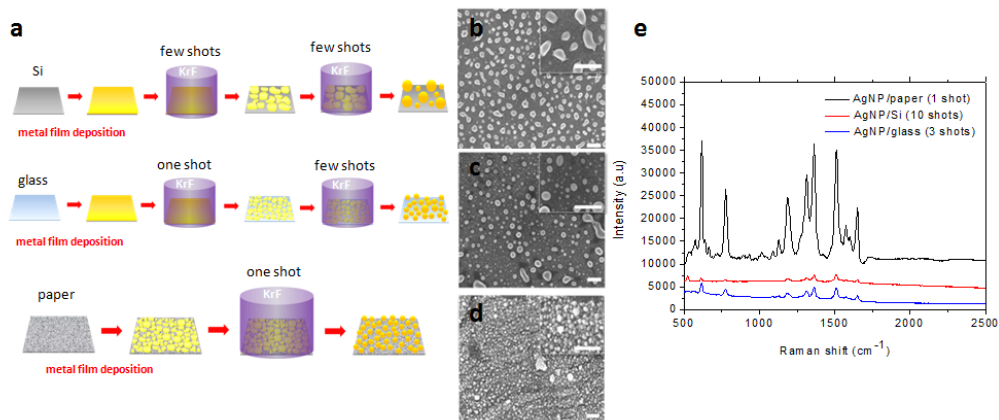


Figure 1. (a) Schematic representation of the fabrication of NPs on Si, glass, and paper by taking advantage of the laser-induced photothermal effect; SEM images of the distributions of Ag NPs formed on (b) Si with 10 shots, (c) glass with 3 shots, (d) paper with 1 shot; (e) SERS spectra of 20- μ L R6G (10^{-6} M) droplets that had been dried on various hydrophobic SERS substrates.

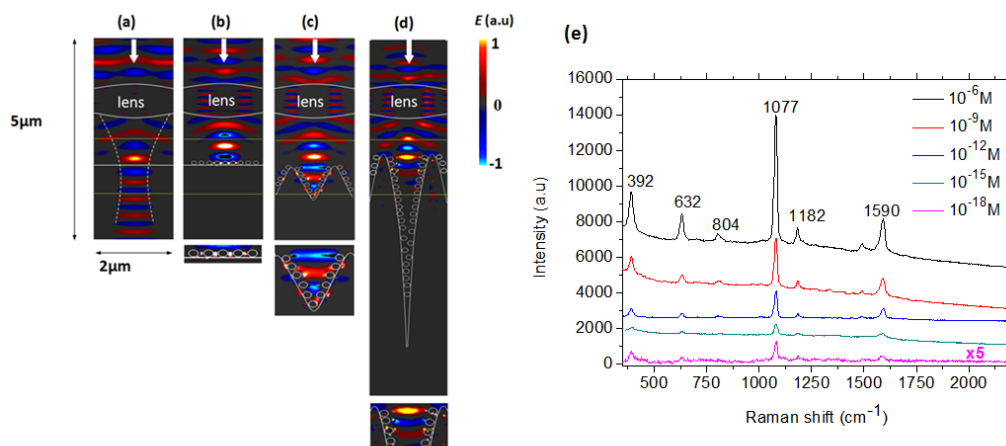


Figure 2. 3D-FDTD simulations of electric field amplitudes on (a) a flat SiO₂ substrate and (b–d) Ag NPs distributed in (b) 2D, (c) quasi-3D, and (d) 3D arrays. The bottom images in (b–d) display enlarged views of the electromagnetic hot spots; (e) SERS spectra of various concentrations of 4-ATP dried on SERS filter paper, demonstrating attomolar detection ability.

¹ Tobjörk D., Österbacka R., (2011), *Adv. Mater.*, 23, 1935–1961.

² Tseng S. C., Yu C. C., Wan D. H., Chen H. L., Wang L. A., Wu M. C., Su W. F., Han H. C., Chen L. C., (2012), *Anal. Chem.*, 84, 5140–5145.

³ Campion A., Kambhampati P., (1998), *Chem. Soc. Rev.*, 27, 241–249.

Semiconductor-enhanced Raman scattering for detection of small inorganic molecules and ions

Wei Ji¹, Wei Song^{1,2}, Ichiro Tanabe¹, Yue Wang², Bing Zhao² and Yukihiro Ozaki¹

¹Department of Chemistry, School of Science and Technology, Kwansai Gakuin University, Sanda, Hyogo 669-1337, Japan

²State Key Laboratory of Supramolecular Structure and Materials, Jilin University, Changchun 130012, P. R. China

Keywords: SERS, semiconductor-enhanced Raman scattering, sensor.

Great effort is currently being devoted to the development of methods to monitor contaminants in water, air, and foods to satisfy the ever-growing demand for better treatment and control of environmental issue. Surface-enhanced Raman scattering (SERS) spectroscopy is an ultrasensitive technique that allows the detection of analytes in a wide variety of matrices. Recently, numerous SERS sensors have been proposed for the detection of organic molecules, inorganic molecules, and ions. These SERS sensors usually utilize metal materials, such as Au and Ag, as substrates for Raman enhancement. These substrates, although highly sensitive, are often unstable and not reproducible, because they are easy to be oxidized or have a strong tendency to form agglomeration.¹ Thus, the robustness of SERS sensor has become one of the main drawbacks that restrict their application.

Recent advances in semiconductor-enhanced Raman scattering have endowed semiconductor materials as promising candidates for developing SERS sensors.² In spite of their lower sensitivity as compared to noble metal substrates, many semiconductor substrates are much more stable as well as reproducible. Meanwhile, their mature fabrication technology, high uniformity, and low cost have also assured them potential application in novel photonic,

electronic, and biological sensing. However, the application of these materials in SERS-based quantitative measurements is still matter of debate, because of their specific dependence on molecular electronic structure and relatively weak enhancement of SERS signals.

Here, we present a “turn-off” strategy and demonstrate that this strategy can be used as an efficient methodology to realize semiconductor-based SERS sensing for quantitative analysis of small inorganic molecules and ions. We will discuss some examples of quantitative analysis based on semiconductor-enhanced Raman scattering, standing as a proof of concept for authenticating the advantages of semiconductor materials for design of SERS sensors.

The alizarin red-sensitized colloidal TiO₂ system was used as a Raman probe for chromium(VI) determination (Figure 1).³ We take advantage of photocatalytic property of semiconductor to catalyze the degradation of a labeled molecule, and resulting in a decrease in the SERS signal. Quantitative analysis of chromium (VI) was achieved by monitoring the “turn-off” SERS signals. This result indicate that the “turn-off” SERS strategy can be an effective way to increase the sensitivity of semiconductor-based SERS sensing. Moreover, we attempt to utilize such “turn-off” SERS strategy, but

whereby the first-layer effect of chemical enhancement, to design a simple semiconductor-based SERS sensor for selective detection of phosphate anions in an aqueous solution. Meanwhile, the stability and reproducibility of semiconductor-based

sensor was systematically discussion. On the basis above, semiconductor-enhanced Raman scattering has great potential to develop robust SERS sensor with excellent stability and reproducibility.

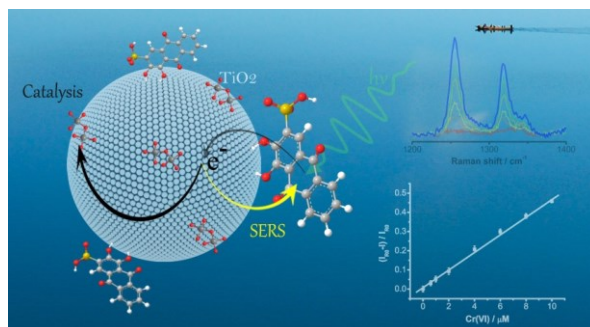


Figure 1. Schematic illustrations of the sensing mechanism of semiconductor-driven “turn-off” SERS spectroscopy for chromium(VI) detection.

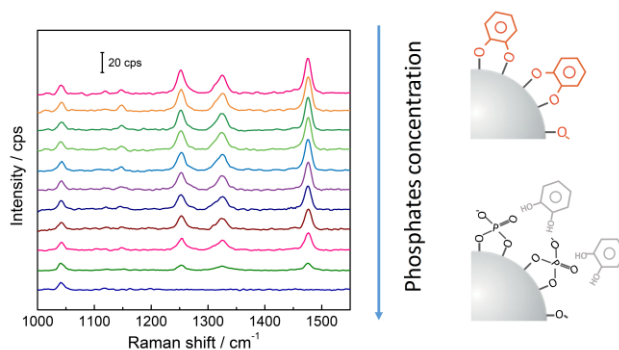


Figure 2. SERS spectra of pyrocatechol on colloidal TiO_2 nanoparticles in the presence of phosphate anions with different concentrations and its sensing mechanism.

- Ji W., Chen L., Xue X. X., Guo Z. N., Yu Z., Zhao B., Ozaki, Y. (2013), *Chemical Communications*, 49, 7334-7336.
- Zhao B., Xu W. Q., Ruan W. D., Han X. X., (2008), *Chemical Journal of Chinese Universities*, 29, 2591-2596.
- Ji W., Wang Y., Tanabe I., Han X. X., Zhao B., Ozaki Y. (2015), *Chemical Science*, 6, 342-348.

Variability of surface-enhanced vibrational spectra: Profits and drawbacks

Pavel Matejka¹, Alzbeta Kokaislova², Marcela Dendisova¹, Michaela Grafova², Marie Svecova² and Tereza Helesicova²

¹Department of Physical Chemistry, University of Chemistry and Technology Prague, Technická 5, 166 28, Prague, Czech Republic

²Department of Analytical Chemistry, University of Chemistry and Technology Prague, Technická 5, 166 28, Prague, Czech Republic

Keywords: surface enhanced Raman scattering, surface enhanced infrared absorption, natural products, spectroelectrochemistry, temperature

Surface-enhanced vibrational spectroscopy (SEVS) is based on two of several surface-enhanced (mostly plasmonic) optical phenomena, i.e. surface-enhanced Raman scattering (SERS) and surface-enhanced infrared absorption (SEIRA). SEVS techniques represent powerful tool for both physico-chemical studies of the metal-adsorbate interface and analytical applications.

The frequently observed variability of SEVS data is well-known. At first sight, such spectral unpredictability causes low repeatability/reproducibility representing a significant analytical drawback. However, a depth view shows several specific physico-chemical phenomena responsible for the observed spectral differences, e.g. the type of plasmonic metal used, its chemical reactivity, nano-/micro-morphology of SEVS substrate, presence of local “hot spots”, adsorption/desorption dynamics, surface potential, orientation and uniformity of adsorbed layer, molecular structure including electron density distribution, intermolecular interactions, molecular photophysical and photochemical properties, and excitation wavelength in the case of SERS. Comprehensive investigations of individually selected phenomena require

either stabilization or defined changes of other influences. The sets of experiments should be well-designed and carefully done; various model theoretical calculations (e.g. DFT results obtained for individual molecules interacting with metal, i.e. Ag, Au and Cu clusters) improve significantly the interpretation of experimental data.

Large data sets of SERS and SEIRA spectra recorded in our laboratory on plasmonic Ag, Au and Cu substrates (mostly electrodes and nanoparticles) for various molecules (predominantly natural products¹) during last decade (aimed recently mainly at the elucidation of the effects of variable or stabilized (i) temperature^{2,3} and (ii) electrode potential⁴⁻⁶) represent a substantial experimental basis to discuss selected issues from both physico-chemical and analytical point of view, to draw some general conclusions and to suggest future perspectives.

Exploratory, classification and quantification multivariate chemometric methods, i.e. principal component analysis (PCA), discriminant analysis (DA) and partial least square (PLS) regression were applied to clarify details of spectral variability and the relationships to mentioned physico-chemical phenomena.

Generally, varying electrode potential was applied in discrete steps forming cycles from positive values to negative and backward⁴⁻⁶. Observed spectral features in *in-situ* SERS spectra, measured under ambient conditions at varying potentials, have been changing very significantly for different type of chemical compounds including heterocyclic water-soluble vitamins, phenolic acids, flavonoids and other natural antioxidants.

At first sight, the experimental results of several temperature-dependent studies are rather controversial; some studies shows a significant increase of enhancement at increased temperatures (e.g. 50°C) while other experiments demonstrate a dramatic increase of signal caused by temperature decrease (below room temperature). Several temperature programs (in the range from 5°C to 50°C) were proposed and performed^{2,3} to investigate the effects of the temperature (i) increase, (ii) decrease, (iii) cycles and (iv) long-term stability. The spectral changes caused by temperature variation are rather tiny compared to effects of potential variation. The temperature variation in the specified range does not lead to a disappearance of spectral bands or an appearance of new spectral features.

However, the observed changes of band intensity ratios are systematic and repeatable showing the crucial role of specific molecular properties (different for different types of substances) compared to relatively minor role of the effects of the metal surface itself. Furthermore, we demonstrate the effects on band widths related to the increase or decrease of the order of adsorbed molecular layer. From other point of view, it can be shown that changes of surface plasmon resonance and collision frequency of plasmonic metal substrate are negligible in the studied temperature interval. The re-orientation of individual adsorbed molecules and the changes in the architecture of the surface molecular layer can be identified as the main source of band intensities and widths variation in the spectra under temperature changes.

Considering the individual pair of nanostructured metal surface (Ag, Au, Cu) and adsorbed substance, the detection limit, data repeatability/reproducibility (both in time and space domain) and suppression of interfering features can be improved by selection of an optimal value of surface electrochemical potential and sample temperature.

¹ Havlíček V. & Spižek J., Eds. (2014). *Natural Products Analysis: instrumentation, methods, and applications*. John Wiley & Sons: Hoboken, New Jersey, ISBN 978-1-118-46661-2.

² Kokaislova A., Kalhousova M., Grafova M., Matejka P. (2014), *Journal of Molecular Structure*, 1075, 609-619.

³ Kokaislova A., Helesicova T., Oncak M., Matejka P. (2014), *Journal of Raman Spectroscopy*, 45 (9), 750-757.

⁴ Dendisova M., Havranek L., Oncak M., Matejka P. (2013), *Journal of Physical Chemistry C*, 117 (41), 21245-21253.

⁵ Dendisova-Vyskovska M., Kokaislova A., Oncak M., Matejka P. (2013), *Journal of Molecular Structure*, 1038, 19-28.

⁶ Dendisova-Vyskovska M., Broncova G., Clupek M., Prokopec V., Matejka P. (2012), *Spectrochimica Acta Part A - Molecular and Biomolecular Spectroscopy*, 99, 196-204.

Plasmonic Nanoantennas on Nanopedestals for Ultra-Sensitive Vibrational IR-Spectroscopy

Dordaneh Etezadi^{1,2}, Arif E. Cetin^{1,2,3} and Hatice Altug^{1,2}

¹ Bioengineering Department, Ecole Polytechnique Federale de Lausanne, SWITZERLAND

² Department of Electrical and Computer Engineering, Boston University, USA

³ Koch Institute for Interactive Cancer Research, Massachusetts Institute of Technology, USA

Keywords: Plasmonics, SEIRA, Nanofabrication, vibrational spectroscopy, FDTD.

Surface Enhanced IR Absorption (SEIRA) spectroscopy provides unique opportunities in bioapplications as it enables direct access to rich vibrational information of most organic molecules. The use of SEIRA for label-free and ultra-sensitive spectroscopy as well as high-resolution microscopy, is still at its early stages. For applications associated with extremely low signal levels, such as biosamples with ultralow analyte concentrations, high signal-to-noise ratio is required for reliable spectroscopic analysis within minimum detection time. Under such circumstances, to increase the SEIRA signal levels, it is highly important to (i) maximize the field overlap with the target biosample and (ii) preserve the maximum number of photons interacting with the sample. In this work, we introduce a polarization-insensitive mid-IR nanoring antenna system fabricated on a dielectric nanopedestal to provide maximum field overlap with the target biomolecules. Our strategy of exposing antenna tips supporting larger and highly accessible nearfields is also important for applications demanding strong light-matter interactions.¹

Figure 1a-b show the schematic and scanning electron microscopy (SEM) image of the gold nanoring antenna on the silicon nitride nanopedestal. The antenna response can be tuned by changing the circumference, as the plasmonic resonance scales linearly with the radius. The symmetric nature of the nanoring antennas eliminates the need for the use of polarizers in the measurements and provides an alignment insensitive design

that can utilize the total power of the source. Figure 1c is the cross-sectional profile of the nearfield intensity enhancement distribution supported by the nanoring antennas in FDTD simulations. For the two antennas engineered for the same protein vibrational mode (Amide I band), the antennas on the nanopedestals provide ~1.5 times larger field enhancements. Moreover for the nanoantennas on the substrate, significant portion of the local fields resides within the substrate, thus not accessible for the target biomolecules while for the nanoantennas on nanopedestals realized through our isotropic etching technique, the tip ends of the antennas and hence the full mode volume of the hot spots are available for biodetection.

For calculating the absorption signals using the antennas, we numerically model a bilayer of protein A/G and IgG antibody. Our experimental surface chemistry protocols ensure that the protein bilayer only covers the gold antennas which can be modeled by defining an 8 nm thick dielectric layer (Figure 1d). Figure 2a shows the response of the ring antenna on the nanopedestal with and without the protein model. The Amide I and II vibrational signatures are observed as spectral dips in the reflection response. In addition to the spectral dips due to the absorption from the imaginary part of the complex protein permittivity, we observe a red-shift in the antenna response due to the real part of the protein permittivity. We can replace the initial response with the reflection spectrum from the antennas covered with a reference material with the real part of the refractive

index of the protein bilayer and no absorption. Figure 2b shows the reflection difference spectrum calculated from the antennas engineered for Amide I vibrational band, for the antenna on the silicon nitride nanopedestal and on the silicon nitride substrate, indicating an additional enhancement in the reflection difference for antennas on pedestals as large as 2.6 times. This enhancement in the signals is due to the improved sensing volume and the large local electromagnetic fields associated with it.

Figure 2c show the experimental spectral response of the nanoring antennas on the silicon nitride substrate and on

nanopedestals. Figure 2d shows the experimental reflection difference spectra of the ring antennas on the silicon nitride nanopedestal and substrate. Interestingly, even though the antenna system on the substrate favors the plasmonic excitations more (by covering Amide I and II better), our antenna system still supports larger absorption signal due to its highly accessible large local electromagnetic fields. The antennas on the nanopedestals give 30 mOD and 18 mOD absorption signals at the Amide I and II bands, respectively, while the antennas on substrate provide only 3 mOD for Amide I and 7 mOD for Amide II.

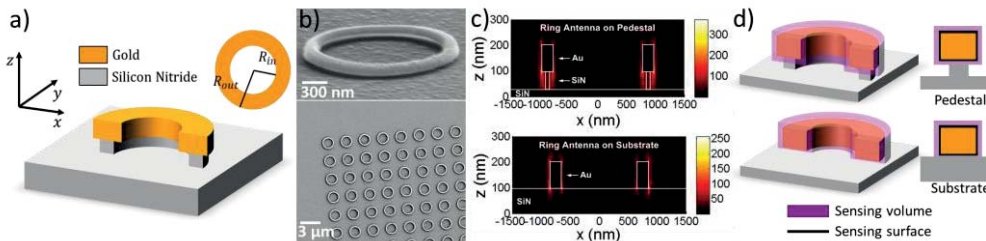


Figure 1. (a) Schematic and (b) SEM image of the gold nanoring antenna on the nanopedestal. (c) E field intensity profile for the antennas on (top) nanopedestal and (bottom) substrate. (d) Schematic cross-sectional profile of the available surface for biomolecules. We optimize the silicon nitride thickness and the antenna dimensions to for a robust pedestal (height = 70 nm).

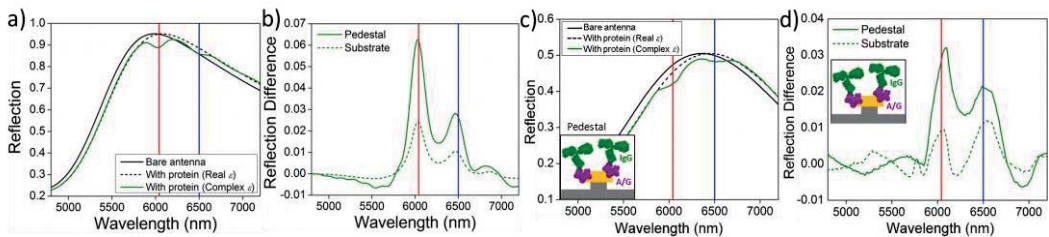


Figure 2. (a) Calculated reflection spectrum of the antenna on pedestal with no protein (black), coating of the protein bilayer model with real (black dashed) and complex (green) permittivity. (b) Calculated reflection difference spectra for the antennas on the pedestals (green) and on the substrate (dashed green). (c) Experimental reflection spectra of the nanorings on the nanopedestals before (black) and after (green) the coating of the protein. Dashed black curve shows a correction using a polynomial fit to compensate the refractive index shift. (d) Experimental reflection difference spectra for the nanoring antennas on the nanopedestal (green) and substrate (dashed green). Red and blue lines show the Amide I and II vibrations.

¹ Cetin A., Etezadi D., Altug H. (2014), *Advanced Optical Materials*, 2, 866

Angle-tuning of antenna arrays for optimization and flexible application in surface enhanced infrared absorption spectroscopy

Tobias W.W. Maß¹ and Thomas Taubner¹

¹Ist Institute of Physics (IA), RWTH Aachen University, 52056, Aachen, Germany

Keywords: Angle-tuning, SEIRA, infrared, antenna, spectroscopy.

Metallic structures can efficiently couple light into a region of subwavelength size. In these regions, large local field enhancements can occur and enable an increased absorption of molecules which are placed in these so called "hot spots". Arrays of metallic structures which are designed for surface enhanced infrared absorption spectroscopy (SEIRA) enable the detection of molecular vibrations with high sensitivity^{1,2}.

Metallic strip gratings can provide a significant field enhancement at the edges along the strips. In a previous publication we showed the spectral tuning of gold strip grating resonances by varying the grating period and demonstrated significant enhancement of a PMMA absorption band at a wavelength of $5,7 \mu\text{m}^3$. Such grating resonances can also be spectrally tuned by varying the angle of incidence and thus be matched to absorption bands of interest⁴.

In contrast, infrared metallic antenna arrays are usually tuned to specific resonance wavelengths by e.g. varying the antenna length or the refractive index of the substrate material^{2,6}. Nevertheless, by changing their periodicity, resonances of infrared antenna arrays can be optimized in terms of field enhancement by realizing collective excitations¹. In principle, this means that the antenna resonances should be close to, but still at higher wavelength compared to the spectral position of the first grating order. Fulfilling this condition, the local field enhancement can be increased by

one order of magnitude and thus enables even higher sensitivity for SEIRA¹.

FTIR microscopy is a suited method for the characterisation of metallic micrometer-sized structures and for SEIRA using arrays of these antennas. FTIR microscopy enables a spatial resolution of several tens of micrometers which allows to define a measurement area with both homogeneous antenna geometries and pattern. In order to focus the infrared light onto a sample, Schwarzschild-objectives with different numerical apertures (NA) and thus different angles of incidence are commonly used.

Concerning the collective excitation of infrared antenna arrays, the angular range of a Schwarzschild-objective can cause certain difficulties. E.g. light focused by a 15x objective with a NA of 0.4 can have incident angles between 10° and 24° . As a result, a grating resonance of an infrared antenna arrays can be distributed over a broad spectral range. Previous theoretical work shows that due to the impact of such a Schwarzschild-objective, the performance of an infrared antenna array can be significantly reduced⁵.

In our work, we use the angular range of a Schwarzschild-objective for a tuning of the antenna array performance in order to optimize the enhancement of vibrational bands of a self-assembled monolayer. Focused Ion Beam (FIB) milling is applied in order to fabricate gold antenna arrays of high quality on a CaF₂ substrate (inset in

Figure 1). The period of this antenna array is chosen to support a collective excitation of the antennas up to 20° incident angle of the exciting light. On the gold antennas, a self-assembled monolayer of 13-MHDA molecules with C-H vibrational bands in the spectral range of 3,4 μm - 3,5 μm is placed. The enhancement of the C-H vibrational bands is compared for measurements using a 15x and a 36x objective (blue and red lines in Figure 1b), as well as for more defined incident angles, respectively. Our experiments show, that the measurement

with a 15x objective leads to a significant higher signal enhancement compared to the measurement with a 36x objective. This can be attributed to the higher incident angles and thus the detuning of the array in the case of the 36x objective. Furthermore, we show that the variation of a defined incident angle can be used to tune the resonance of the infrared antenna array to optimize the enhancement of the investigated vibrational bands.

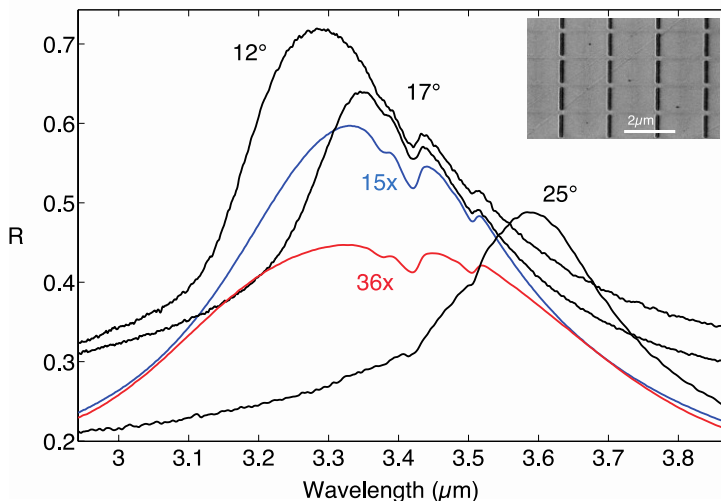


Figure 1. FTIR reflectance spectra of an infrared antenna array. Microscopic measurements are done with a 15x objective (blue), 36x objective (red) and with defined incident angles (black). The inset is an SEM image of the gold antenna array.

- ¹ R. Adato, A. A. Yanik, J. J. Amsden, D. L. Kaplan, F. G. Omenetto, M. K. Hong, S. Erramilli, and H. Altug, (2009), *P. Natl. Acad. Sci. Usa* **106**(46), 19227–19232.
- ² F. Neubrech, A. Pucci, T. W. Cornelius, S. Karim, A. Garcia-Etxarri, and J. Aizpurua, (2008), *Phys. Rev. Lett.* **101**(157403), 157403.
- ³ T. Wang, V. H. Nguyen, A. Buchenauer, U. Schnakenberg, and T. Taubner, (2013), *Opt Express* **21** (7), 9005–9010.
- ⁴ J. W. Petefish and A. C. Hillier, (2014) *Anal. Chem.* **86**, 2610–2617.
- ⁵ V. Liberman, R. Adato, A. Mertiri, A. A. Yanik, K. Chen, T. H. Jeys, S. Erramilli, and H. Altug, (2011), *Opt Express* **19** (12), 11202–11212.
- ⁶ J. M. Hoffmann, X. Yin, J. Richter, A. Hartung, T. W. W. Maß, and T. Taubner, (2013), *J. Phys. Chem. C* **117**, 11311–11316.

In situ SEIRAS study of cinchonidine adsorbed on platinum in organic solvents, a model of enantioselective hydrogenation catalysts

Kenta Motobayashi, Ryota Tomioka, Taro Uchida and Masatoshi Osawa*

Catalysis Research Center, Hokkaido University, Sapporo 001-0021, Japan

Keywords: SEIRAS, cinchonidine, molecular orientation, enantioselective catalysis.

Platinum catalysts modified with some organic molecules exhibit high enantioselectivity in hydrogenation reactions. A widely accepted concept for the enantioselectivity is that the adsorption of chiral modifier molecules on metal surfaces provides chiral adsorption sites for reactants and reactive hydrogen species approach to the adsorbed reactants from a specific direction. Therefore, the structure and orientation of the chiral modifier molecule are crucial.

Cinchonidine (CD) is the most typical effective modifiers, and hence its adsorbed structure on Pt has been studied extensively mostly by IR. However, the results reported in the literature are rather controversial. In this study, we have examined the orientation of CD adsorbed on Pt in 1,2-dichloroethane by surface-enhanced IR absorption spectroscopy in the ATR mode (ATR-SEIRAS).¹ ATR-SEIRAS enables the in situ analysis of the adsorbed CD without a serious interference from the bulk solution. The effect of H₂, a reactant in hydrogenation, on the orientation of CD is especially focused.

Experimental details of ATR-SEIRAS were described elsewhere.² A Pt thin film chemically deposited on a Si prism³ was used as the substrate.

Figure 1 shows the IR spectra of the solvent (a) and CD (b), and ATR-SEIRA spectra of CD on the Pt thin film in Ar-saturated (c-e) or H₂-saturated (f-h) 1,2-

dichloroethane containing 10⁻⁶, 10⁻⁵, or 10⁻³ M CD. All the SEIRA spectra were referenced to the spectrum of the bare Pt measured in Ar-saturated pure solvent. Therefore, adsorbed CD gives positive bands, while the solvent that was removed from the surface by adsorption of CD gives negative bands.

In Ar-saturated solutions (Figs. 1c-e), all the positive vibrational bands in the range of 1400-1700 cm⁻¹ are assigned to adsorbed CD. The spectral features are similar to that observed for quinolone (QN) adsorbed on Pt, suggesting that CD is adsorbed on Pt via the QN moiety. The significant broadening of the ν(C=C) of the vinyl group at 1635 cm⁻¹ suggests that CD is adsorbed also via the vinyl moiety. The band intensities are independent of CD concentration in the solutions, indicating that adsorbed CD was selectively observed and that CD coverage is saturated as low as 10⁻⁶ M.

In H₂-saturated solution (Figs. 1f-h), three different features are observed. First, the vinyl ν(C=C) band at 1635 cm⁻¹ (as well as the vinyl ν(C-H) at 3070 cm⁻¹) observed in the Ar-saturated solution are missing, indicating the hydrogenation of the vinyl group. Second, the relative band intensities of the in-plane ring modes of QN moiety are largely different from those in the Ar-saturated solution: The bands at 1570 cm⁻¹ and 1464 cm⁻¹ are much stronger, while those at 1593, and 1512 cm⁻¹ are weaker in

H₂-saturated solutions. Different from the Ar-saturated case, the band intensities depends on CD concentration, i.e., CD coverage is saturated at a higher CD concentration.

The orientations of CD in Ar- and H₂-saturated solution estimated using the surface selection rule in SEIRAS^{1,4} are shown in Figure 1i (nearly flat π -bonded orientation) and 1j (N-bonded upright orientation), respectively. The saturation of CD coverage at a lower concentration in Ar-saturated solution can be ascribed to the flat orientation.

Similar spectral changes as observed in the organic solvent by the introduction of H₂ were also observed in aqueous solution

without H₂ under electrochemical environment at electrode potentials where H atom is adsorbed on Pt and the Pt surface is negatively charged. On this basis, we ascribe the change in the orientation of CD in the organic solvent to the dissociative adsorption of H₂ to H atoms, which negatively charges the Pt surface. The repulsive interaction between the π -orbital of QN and the negatively charged surface rises up the QN plane from the π -bonded flat-on orientation to the N-bonded upright orientation. The hydrogenation at the vinyl moiety also facilitates the reorientation of CD.

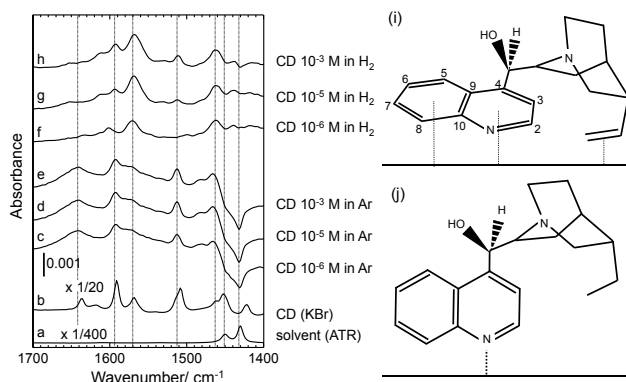


Figure 1. (a) ATR-IR spectrum of 1,2-dichloroethane. (b) Transmittance IR spectrum of CD in a KBr tablet. (c)-(h) SEIRA spectra of CD on a Pt thin film surface. CD concentrations were 10⁻⁶ M for (c) and (f), 10⁻⁵ M for (d) and (g), 10⁻³ M for (e) and (h). SEIRA spectra were obtained from 1,2-dichloroethane solution saturated with Ar (c)-(e) or H₂ (f)-(h). (i)-(j) Right column shows the schematic drawings of adsorbed structures of CD proposed from the SEIRA spectra; (i) “nearly parallel” π -bonded structure in Ar-saturated solution and (j) N-bonded “upright” structure in H₂-saturated solution.

¹ Osawa M. (1997), *Bull. Chem. Soc. Jpn.*, 70, 2861.

² Osawa M. in *Diffraction and Spectroscopic Methods in Electrochemistry* (2006), Alkire R.C., Kolb D. M., Lipkowski J. & Ross P. N., (2000), Rds., Wiley-VCH: Weinheim.

³ Miki A., Shen Y., Osawa M. (2002), *Chem. Commun.*, 1500.

⁴ Osawa M., Ataka, K., Yoshii K. & Nishikawa Y. (1993), *Appl. Spectrosc.*, 47, 1497.

Combined SERR, SEIRA and electrochemistry to study the influence of calcium on catalysis of cellobiose dehydrogenase immobilized on electrode

Patrycja Kielb¹, Lo Gorton², Roland Ludwig³, Ingo Zebger¹ and Inez M. Weidinger¹

¹Institut für Chemie, Technische Universität Berlin, Strasse des 17. Juni 135, 10623, Berlin, Germany

²Department of Biochemistry and Structural Biology, Lund University, PO Box 124, 221 00 Lund, Sweden

³Department of Food Science and Technology, BOKU University of Natural Resources and Life Science, Muthgasse 18, 1190 Vienna, Austria

Keywords: electron transfer, biocatalysis, SERRS, SEIRA, cellobiose dehydrogenase.

In the field of biosensors and biofuel cells it still remains challenging to construct devices with preserved high catalytic activity and efficient electron transfer between enzyme and electrode.

Cellobiose dehydrogenase (CDH) is an enzyme that catalyzes the oxidation of sugars. It consists of dehydrogenase domain with a FAD cofactor connected by a flexible linker with a heme containing domain. Cellobiose is oxidized at the catalytic FAD center reducing the flavin with two electrons, which can be further transferred via internal electron transfer (IET) to heme.

When the enzyme is immobilized on the electrode, it exhibits direct electron transfer between the surface exposed heme group and the electrode making it an excellent candidate for use in novel classes of bio-devices.

Moreover, it was shown that its catalytic performance could be significantly increased by presence of Ca^{2+} . Interestingly, such an effect is much less pronounced in the presence of Na^+ , suggesting that divalent ions are of significance for this effect.¹

We employed for the first time combined electrochemistry with surface enhanced vibrational (SERR and SEIRA) spectroscopic methods to study in detail the catalytic performance of CDH immobilized

on electrodes (nanostructured silver electrode for SERR and nanostructured gold electrode for SEIRA). In particular, SERRS was used to selectively probe the heme, whereas SEIRA spectroscopy is sensitive for the changes of the whole protein.

The spectro-electrochemical measurements show that immobilization of CDH on a polymer-coated electrode does not change the native structure of the heme. Furthermore, CDH remains catalytically active, performing good intramolecular electron transfer and electronic communication with the electrode (Figure 1).

To study the influence of Ca^{2+} ions on catalysis of the immobilized enzyme we performed and compared all experiments in a standard conditions (50 mM buffer), increased ionic strength conditions (200mM buffer) and in presence of Ca^{2+} .

For immobilized CDH at high ionic strength conditions, electrostatic interaction between the positively charged polymer and the negatively charged surface of an enzyme is weakened. This results in higher mobility of the heme domain such that the enzyme can adopt orientations which establish faster electron transfer (k_{HET}) (Table 1).

The presence of Ca^{2+} , however, has a different influence. The midpoint potential

of the heme is upshifted (E^0). Moreover, electron transfer between the heme and electrode is not altered. However, SERR intensity largely decreases upon heme reduction while the intensity of the SEIRA spectra remains potential independent (Table 1). On the basis of these findings we propose that binding of the Ca^{2+} happens most probably to the solution exposed heme

propionate group This binding induces the heme reorientation resulting in tuned redox potential and loss of SERR intensity (Figure 2).

Furthermore, the presence of Ca^{2+} , based on electrochemical measurements results in promotion of an alternative electron transfer pathway between the flavin and the electrode (Table 1 and Figure 2).

Table 1. Redox parameters of CDH immobilized on PDADMAC-coated Ag.electrode.

Conditions	E^0 (mV)	k_{HET} (1/s)	IP (catalytic turnover) (mV)
50mM	-55	5	-72
200mM	-73	14	-92
50mM+10mM Ca^{2+}	-15	7	-100

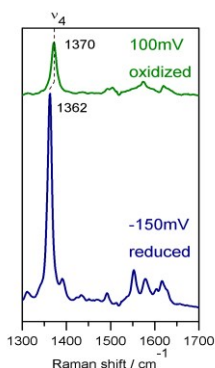


Figure 1. High frequency SERR spectra of CDH immobilized on electrode, recorded with 413 nm excitation wavelength, at 100 mV and -150 mV applied potential (vs. Ag|AgCl).

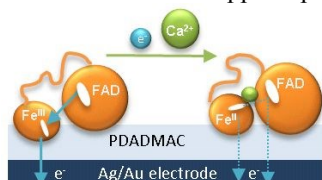


Figure 2. Proposed model of Ca^{2+} ions induced changes in orientation and electron transfer mechanism of CDH immobilized on electrode.

¹ Schulz, C., Ludwig, R., Micheelsen, P. O., Silow, M., Toscano, M. D., Gorton, L. (2012), *Electrochem. Commun.* 17, 71-74.

OPTOFLUIDIC CHIP INTEGRATING SILVERED POROUS SILICON MEMBRANES FOR MULTIANALYTE SURFACE ENHANCED RAMAN SPECTROSCOPY

Chiara Novara¹, Andrea Lamberti¹, Paola Rivolo¹, Alessandro Virga¹, Alessandro Chiadò¹, Francesco Geobaldo¹ and Fabrizio Giorgis^{1,2}

¹Department of Applied Science and Technology, Politecnico of Torino, C.so Duca degli Abruzzi 24, I-10129, Torino, Italy

²Center for Space Human Robotics, Italian Institute of Technology, C.so Trento 21, I-10129, Torino, Italy

Keywords: SERS, microfluidics, porous Silicon, plasmonics, biodetection.

Patterned Surface Enhanced Raman Scattering (SERS) substrates are currently developing in order to enable the label free detection of trace amounts of different compounds on the same chip¹. With this aim highly SERS efficient silver nanoparticles (AgNPs) stripe patterns have been recently synthesized on porous silicon (pSi) platforms by inkjet printing, exploiting the reactivity of the freshly etched silicon surface toward silver nitrate based inks². As a matter of fact, many advantages arise from the integration of SERS substrates in microfluidics, such as minimization of required volumes and higher homogeneity of analyte spreading³. Moreover, working in separate chambers would greatly improve silvered pSi performances in terms of preparation, functionalization and analysis steps, aimed to multiplexed detection.

In this work we present a novel multi-chamber SERS active silvered pSi-PDMS optofluidic device, made of porous silicon, patterned through a PDMS mask, and transferred onto a self-standing PDMS membrane. Actually, this all-PDMS microfluidic system with stable plasmonic properties is applied for SERS analysis, where AgNPs, can be synthesized either before or after the sealing of the device, by

immersion plating in aqueous AgNO₃ or in flow conditions.

Mesoporous silicon single layers 2 μm thick and with 66% porosity are electrochemically anodized in HF solution and then partially detached from the silicon substrate. An incompletely cross-linked PDMS membrane is placed in contact on the sample and the porous membrane is removed upon peeling. After a thermal treatment to complete the cross-linking reaction, the top of the porous layer is irreversibly bonded to the PDMS support.

Silver nanoparticles synthesized by dipping in aqueous silver nitrate show a morphology characterized by small and very densely packed nanostructures, which provide a great SERS enhancement, higher than 10 orders of magnitude, when the substrates are tested with Rhodamine 6G in molecular resonance conditions at 514 nm (Figure 1).

Beside the optimization of the pSi membrane detachment, the masking procedure with PDMS, inspired by micro contact printing, is also shown. A PDMS membrane with four microfluidic chambers is used as a stamp to leave a thin layer of the PDMS mixture on a silicon dice. After curing, the mask is stable both during the

growth and the detachment of the porous layer and silicon is etched according to the design of the chambers.

Combining the masking and the bonding processes the porous silicon pattern is transferred onto the PDMS substrate, which is easily aligned and irreversibly bonded with the PDMS cover (Figure 2).

As a proof of concept the AgpSi-PDMS chip is employed for the simultaneous detection of model DNA oligos (polyA, polyC, polyG, polyT) injected into the different chambers.

In summary, the potential for multianalyte SERS detection in biological assays is demonstrated with the application of an all-microfluidic chip. Preliminary results dealing with the in-flow synthesis of silver nanoparticles show promising improvements with respect to the immersion plating technique, besides the possibility to follow the reaction in situ by transmission UV-Vis spectroscopy.

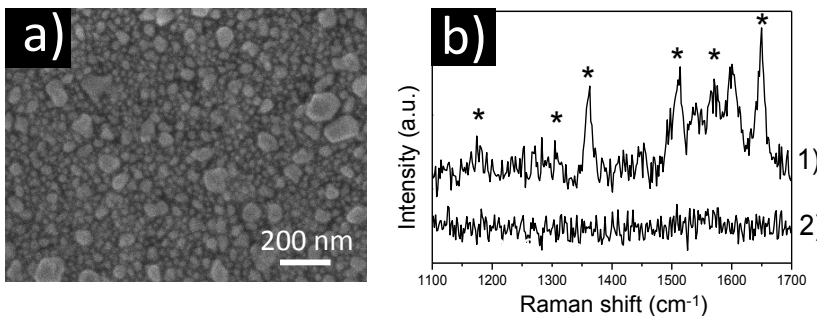


Figure 1. a) FESEM image of AgNPs on pSi/PDMS b) Raman spectra of R6G: 1) 10^{-14} M on AgpSi/PDMS (R6G peaks are marked by asterisks), 2) 10^{-4} M on bare pSi/PDMS.

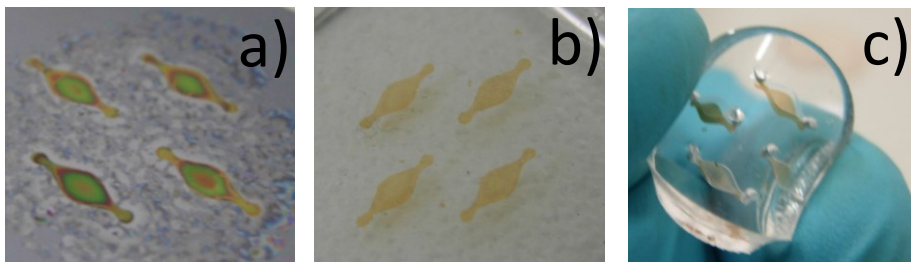


Figure 2. a) pSi pattern after masked etching b) pattern transferred onto a PDMS membrane c) the optofluidic chip.

¹ Li Q.L., Li B.W., Wang Y.Q. (2013), *RSC Advances*, 3, 13015-13026.

² Novara C., Petracca F., Virga A., Rivolo P., Ferrero S., Chiolerio A., Geobaldo F., Porro S., Giorgis F. (2014), *Nanoscale Research Letters*, 9, 527.

³ Lamberti A., Virga A., Angelini A., Ricci A., Descrovi E., Cocuzza M., Giorgis F. (2015), *RSC Advances*, 5, 4404-4410.

Lighting up the Raman Signal of Molecules in the Vicinity of Graphene Related Materials

Xi Ling¹, Shengxi Huang¹, Shibin Deng², Nannan Mao², Jing Kong¹, Mildred S. Dresselhaus^{1,3}
and Jin Zhang²

¹ Department of Electrical Engineering and Computer Science, Massachusetts Institute of Technology, Cambridge, Massachusetts 02139, USA

² Center for Nanochemistry, Beijing National Laboratory for Molecular Sciences, Key Laboratory for the Physics and Chemistry of Nanodevices, State Key Laboratory for Structural Chemistry of Unstable and Stable Species, College of Chemistry and Molecular Engineering, Peking University, Beijing 100871, P.R. China

³ Department of Physics, Massachusetts Institute of Technology, Cambridge, Massachusetts 02139, USA

Keywords: Surface enhanced Raman scattering, Chemical mechanism, Graphene, Organic molecule, 2D material

Surface enhanced Raman scattering (SERS) is a popular technique to detect the molecules with high selectivity and sensitivity. It has been developed for 40 years, and many review papers have been published to summarize the progress in SERS. Nevertheless, how to make the SERS signals repeatable and quantitative, and how to have deeper understanding on the chemical enhancement mechanism are still big challenges. Recently, graphene, as well as the other two dimensional (2D) materials, were developed to be used as a Raman enhancement substrate, which can light up the Raman signals of molecules, and these substrates were demonstrated to be a promising for micro/trace species detection. This effect was named as “graphene enhanced Raman scattering (GERS)”. GERS technique offers significant advantages for

studying molecular vibrations due to the ultraflat and chemically inert 2D surfaces, which are newly available, especially in developing a quantitative and repeatable signal enhancement technique, complementary to SERS. Moreover, GERS is a chemical mechanism dominated effect, which offers a valuable model to study the details of the chemical mechanism. As a practical technique, the combination of GERS with a metal substrate incorporates the advantages from both the conventional SERS and GERS. The introduction of graphene to the Raman enhancement substrate extended SERS applications in a more controllable and quantitative way. In this talk, I will introduce this novel technique and our recent progress on GERS.

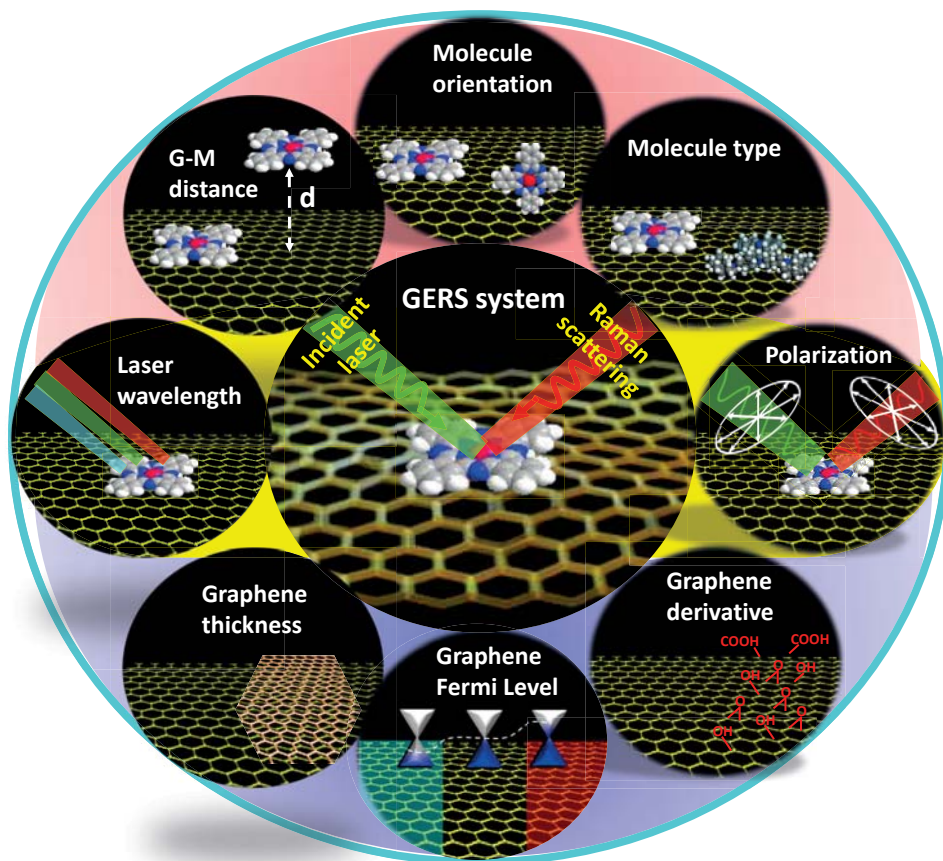


Figure 2. Overview of the factors investigated in the GERS system.

1. Ling, X.; Xie, L.; Fang, Y.; Xu, H.; Zhang, H.; Kong, J.; Dresselhaus, M. S.; Zhang, J.; Liu, Z. (2010), *Nano Lett.* 10, 553–561.
2. Xie, L.; Ling, X.; Fang, Y.; Zhang, J.; Liu, Z. (2009), *J. Am. Chem. Soc.* 131, 9890–9891.
3. Ling, X.; Fang, W.; Lee, Y.-H.; Araujo, P. T.; Zhang, X.; Rodriguez-Nieva, J. F.; Lin, Y.; Zhang, J.; Kong, J.; Dresselhaus, M. S. (2014), *Nano Lett.* 14, 3033–3040.

Probing the Properties of Random Nanometric Systems by Single Molecule Surface-Enhanced Raman Scattering

Diego P. dos Santos¹, Marcia L. A. Temperini² and Alexandre G. Brolo³

¹ Departamento de Físico-Química, Instituto de Química – Universidade Estadual de Campinas. CP 26.077, CEP 05513-970, Campinas, SP, Brazil.

² Departamento de Química Fundamental, Instituto de Química – Universidade de São Paulo. CP 26.077, CEP 05513-970, São Paulo, SP, Brazil.

³ Department of Chemistry, University of Victoria, P.O. Box 3065, Victoria, BC, V8W 3V6, Canada.

Keywords: Raman spectroscopy, plasmonics, SERS, nanostructures.

Single-molecule surface-enhanced Raman scattering (SM-SERS) is now a well-established phenomenon confirmed in different laboratories¹⁻³. The SM-SERS phenomenon is characterized by strong fluctuations in the intensities of the scattering³. These fluctuations carry information about the nanoscopic environment visited by individual molecules⁴. The SERS effect results from enhanced electric field strength observed in certain areas of the surface of metallic nanostructured systems. These very small areas of highly concentrated field are known as SERS hot spots. In a random substrate, such as an roughened metallic surface or an aggregated colloidal system, there is a distribution of hot spots with different optical (and geometrical) characteristics. We will demonstrate here that an analysis of the SERS intensity fluctuations in SM regime can provide insights into the physical characteristics of the hot spots.

First of all, the distribution of SERS intensities is not only related to both the density and the efficiency of the hot spots (field localization), but also to the adsorption characteristics of the molecule. We have demonstrated that by controlling the surface charge of a nanostructured metallic surface (roughened silver electrode⁵ and silver colloids), it is possible to tune the

intensity fluctuation distributions. These results were confirmed using a simple Monte-Carlo approach.

Information about the resonance characteristics of the hot spots was obtained by analyzing fluctuations in the ratio between the anti-Stokes and the Stokes scattering intensities at the SM level. A semi-empirical protocol was developed that interpret the strong deviations of the anti-Stokes to Stokes ratio from the expected thermal value as resulting from the surface plasmon characteristics of regions of high field concentration in the nanostructured metallic surface.

Finally, we have also shown that the anti-Stokes to Stokes analysis provides information about the hot spot structure in a random medium. Figure 1a shows a typical Monte Carlo result of a simulation of a dynamical Ag colloidal system aggregation. The different types of aggregates were quantified and analyzed. An example of a numerical calculation of the hot spots around those aggregated structures is shown in Figure 1b. The simulated enhanced field distribution is then compared to an experimental SERS spectrum in Figure 1c. The SERS background matched the resonance expected from the calculations. A correlation was also found between different types of particle aggregates in a colloid

(determined by SEM) with the distribution of anti-Stokes to Stokes ratios at SM level. These results show the potential of SM-SERS to provide a comprehensive picture of

the metallic nanometric environment that include hot spot efficiency, resonance and geometry.

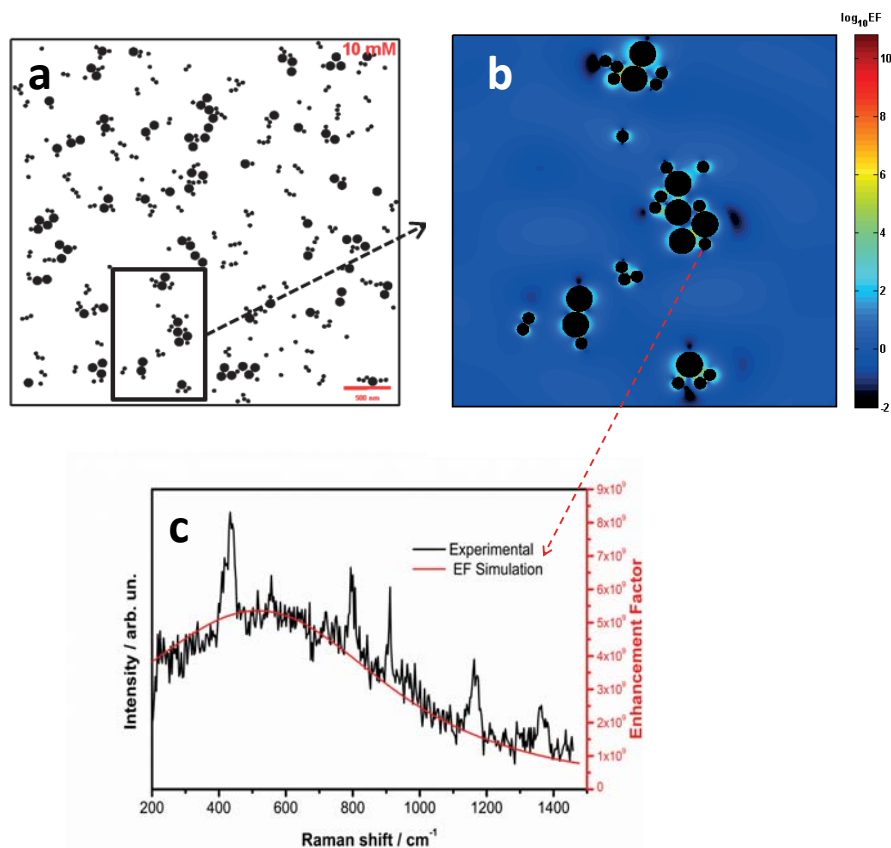


Figure 1: a) Monte Carlo simulation of aggregation in the colloidal system. Simulations were performed using the Derjaguin, Landau, Verwey and Overbeek (DLVO) potential energy; b) Generalized Mie theory calculation of the SERS enhanced factor around Ag aggregates; c) experimental SM-SERS of crystal violet and comparison with the numerical calculations.

¹ Nie S., M., Emory S.R. (1997) *Science*, 275, 1102-1106

² Etchegoin P. G., Meyer M., Blackie E., Le Ru E. C. (2007), *Analytical Chemistry*, 79, 8411-8415.

³ Dieringer J. A., Lettan R. B., Scheidt K. A., van Duyne R. P., (2007), *Journal of the American Chemical Society*, 129, 16249-16256.

⁴ dos Santos D. P., Andrade G. F. S., Brolo A. G., Temperini M. L. A., (2011) *Chemical Communications* 47, 7158-7160.

⁵ dos Santos D. P.; Temperini M. L. A.; Brolo A. G., (2012), *Journal of the American Chemical Society*, 134, 13492-13500

Localized plasmonic catalysis by SERS and TERS

Zhenglong Zhang, Volker Deckert*

Institute of Photonic Technology, Albert-Einstein-Str. 9, 07745 Jena, Germany

Keywords: SERS, TERS, Plasmonic catalysis

With the help of plasmon-induced hot electrons, plasmonic catalysis was recently designed as a new exciting topic of heterogeneous catalytic reaction. Our recent research indicates that plasmonic catalysis opens a route to concentrate and direct the energy of visible light to adsorbed molecules, hence, enhancing the rate of chemical reactions and offering a pathway to control reaction selectivity. The plasmonic catalysis of dimerization of p-nitrothiophenol (pNTP) was observed by surface enhanced Raman scattering (SERS) in 2011. As shown in Fig. 1, we report on a new plasmon catalyzed cleavage reaction of pNTP at a single molecule (SM) level using a gold nanoparticle dimer to avoid the usual dimerization.¹ Our newest experiments indicate that TP molecules can also react to

oNTP and pNTP by SERS. Tip-enhanced Raman scattering (TERS) is a technique that provides molecular information at the nanoscale. A controlled plasmonic catalysis of dimerization of pNTP was monitored by AFM and STM TERS.² Especially, the temperature of plasmonic catalysis can be obtained by comparing Stokes and anti-Stokes TERS directly at the site of interest.

In addition to the above mentioned reactions, already more reactions based on plasmonic catalysis such as the dissociation of DMAB and bond-selective dissociation of malachite green molecules were investigated by using TERS and will be discussed.³

Funding by the Deutsche Forschungsgemeinschaft (DEP4TERS, FR1348/19-1), the Thüringer Aufbau Bank (No. 2011SE9048) and the Alexander von Humboldt foundation are gratefully acknowledged.

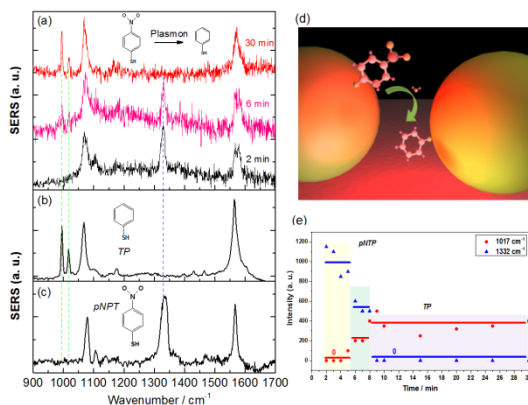


Fig. 1. Comparison of time dependent SERS spectra of pNTP (a), TP (b) and pNTP (c), reaction scheme (d) and time dependent track on a single molecule level (e).

¹Z. Zhang et al., Chem Comm, 2015, 51,3069.

²E. van S. Lantman, et al., Nat Nanotechnol, 2012, 7, 583; M. Sun, et al., Sci Rep, 2012, 2, 647.

³Z. Zhang et al. Nanoscale, 2013, 5, 3249-3252; Z. Zhang et al. Nanoscale, 2014, 6, 4903-4908.

Emails: volker.deckert@ipht-jena.de ; zhenglong.zhang@ipht-jena.de

Monday

Tuesday

Wednesday

Thursday

Friday

Author Index



Investigating SERS particles with integrated correlative Raman electron microscopy.

F.J. Timmermans¹, A.T.M. Lenferink¹, H.A.G.M. van Wolferen², C. Otto¹

¹ University of Twente, Medical Cell BioPhysics, Drienerlolaan 5, 7522 NB, Enschede, the Netherlands

²University of Twente, MESA+, Drienerlolaan 5, 7522 NB, Enschede, the Netherlands

Keywords: Integrated Correlative light and electron microscopy (iCLEM), Raman microscopy, SERS.

We present a system employing an integrated commercial Raman microscope¹ in a dual beam Focused Ion Beam – Scanning Electron Microscope (FIB - SEM). Figure 1 shows the integrated components in the FIB - SEM chamber. Sample analysis is performed by high resolution morphological SEM imaging and correlative 3D chemical specific Raman microscopy. The combination of FIB micromachining and Raman microscopy enables further analysis after material processing, in which material deformations and structural or crystal defects can be detected.

An example study to the use of Raman spectroscopy for the analysis of FIB induced damage has been performed. Figure 2 shows a pattern that has been milled in a Silicon substrate. For the corresponding Raman analysis the first order Silicon peak has analyzed. The spectral full width at half maximum (FWHM), peak position and intensity of this peak have been recovered and are shown in the images.

The system enables new workflow strategies through fast localization with SEM of regions of interest to be analysed with Raman microscopy. This makes it an ideal system for Raman analysis of nanometer to sub-micrometer particles. SEM enables the fast localization and identification of sub-diffraction particles,

after which spectral analysis of these particles is performed. This strategy is very promising for the analysis of SERS active particles and structures. The SEM can be used to locate plasmonic nanoparticles of different sizes and shapes, and single particles or clusters. This enables an accurate study of the effect of these parameters on the SERS signal strength. Furthermore the stability of the signal and repeatability for multiple SERS particles can be verified using this system.

Results on the enhancement factor are verified and experiments are planned using discrete dipole approximation scattering (DDSCAT) package. Discrete dipole approximation (DDA) enables the computation of radiation scattering and near field strength of particles of arbitrary shape. The combination of near field calculations and the ability to locate clusters of varying sizes offers the opportunity to investigate signal strength based on cluster size. Figure 3 shows a SEM image of a three particle cluster, the calculated near field strength, and recorded Raman cluster image.

This research is financially supported by the STW (Stichting voor de Technische Wetenschappen), HybriScan Technologies B.V. and MESA+ Institute for Nanotechnology.

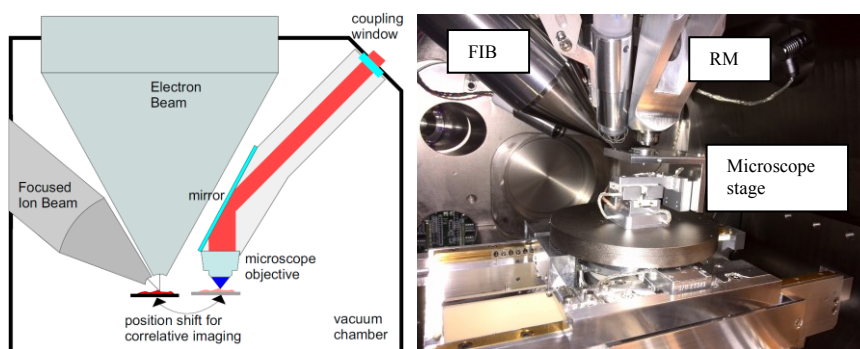


Figure 1. (Left) Schematic of the integrated Raman microscope in the Focused Ion Beam – Scanning Electron Microscope. (Right) Picture of the optical microscope objective and translation stage mounted in the system chamber.

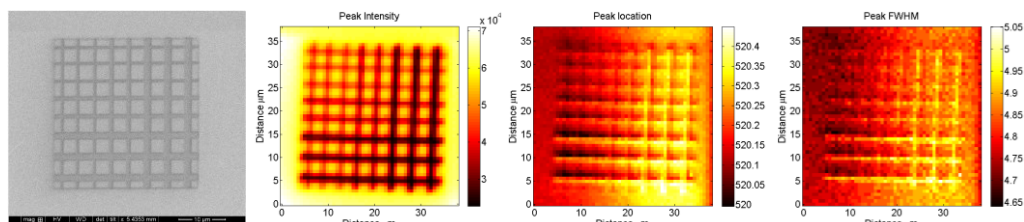


Figure 2. (A) SEM image of FIB patterned Si substrate. (B) Raman amplitude of the 1st order Si peak. (C) retrieved spectral location of the 1st order Si peak. (D) retrieved FWHM of the 1st order Si peak.

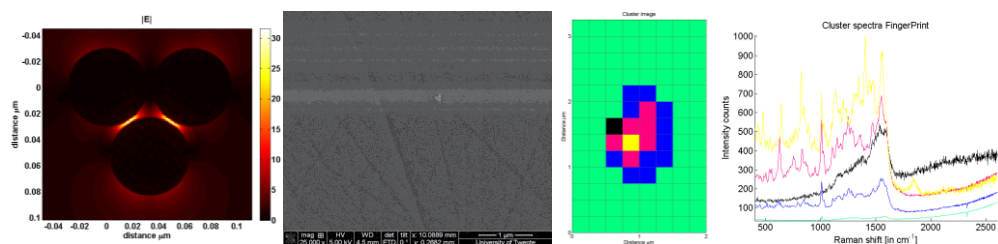


Figure 3. Sample containing 3 gold beads of 60 nm diameter. (A) DDA calculation of the near field enhancement at vertical polarization excitation. (B) SEM image of the gold nanoparticles. (C) cluster image of Raman microscopic data. (D) Average spectra corresponding to the Raman clusters.

¹ <http://www.hybriscan.com/products/hybrid-microscopes>

Coherent Raman Imaging Measurement of Stem Cell Differentiation

Young Jong Lee,¹ Sebastián L. Vega,² Parth J. Patel,³ Khaled A. Amer,¹ Prabhas V. Moghe,^{2,3} Marcus T. Cicerone¹

¹National Institute of Standards and Technology, Gaithersburg, MD 20899, USA

²Department of Chemical and Biochemical Engineering, Rutgers University, Piscataway, NJ 08854, USA

³Department of Biomedical Engineering, Rutgers University, Piscataway, NJ 08854, USA

Keywords: stem cell, coherent Raman, differentiation, CARS microscopy.

Broadband coherent anti-Stokes Raman scattering (BCARS) microscopy is used to characterize lineage commitment of individual human mesenchymal stem cells (hMSCs) cultured in adipogenic, osteogenic, and basal culture media.¹ We demonstrate robust metrics for differentiation by processing hyperspectral BCARS images in two independent ways. In one approach, pixel counts corresponding to functional markers, lipids and minerals, are used to classify individual cells as belonging to one of three lineage groups: adipocytes, osteoblasts, and undifferentiated stem cells. In the second approach, we use multivariate analysis of Raman spectra averaged exclusively over cytosol regions of individual cells to classify the cells into the same three groups, with consistent results. The high speed of spectral imaging with BCARS allows us to chemically map a large number of cells with high spatial resolution, revealing not only phenotype of individual cells, but also population heterogeneity in the degree of phenotype commitment.

Characterization of stem cell pluripotency and phenotype commitment is critical in many of biological science and engineering areas. Although it is currently possible to characterize cell pluripotency and phenotype commitment, the methods in use are typically intrusive or provide information only averaged over entire

populations. Use of invasive, endpoint methods necessitate assumptions about correlations between materials sampled and those not sampled, and these assumptions can lead to incorrect findings when working with heterogeneous tissues and cell cultures.

It is also important to measure dynamic population heterogeneity, which is intrinsic to biological systems, by analyzing a sufficient number of cells. In this study we acquired high-resolution BCARS images (see Fig. 1) comprising a total of 1.3 million spectra over a total of 9 hours imaging time. A similar study using confocal spontaneous Raman imaging would have been possible, but perhaps not practical, as it would require > 150 h of imaging time using integration times required for sufficient signal quality that individual spectra can be analyzed and used for image contrast, as is done here.

As shown in Fig. 2, the statistical analysis of more than 100 images reveals large population heterogeneity in the cells through the wide distribution of expression of the lineage-specific functional markers. We analyze the spectral image data in two independent ways, by counting image pixels corresponding to line-age-specific functional markers, and by performing a multivariate analysis of Raman spectra of the cytosol. Both approaches provide similar outcomes, with some complimentary information.

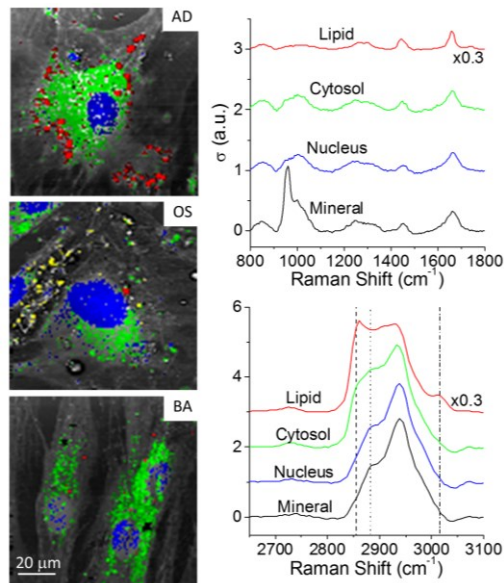


Figure 1. BCARS images of hMSCs cultured in (a) adipogenic (AD), (b) osteogenic (OS), and (c) basal (BA) growth media for two weeks. BCARS spectral maps are pseudo-colored for nuclei (blue), cytosol (green), lipids (red), and mineralization (yellow).

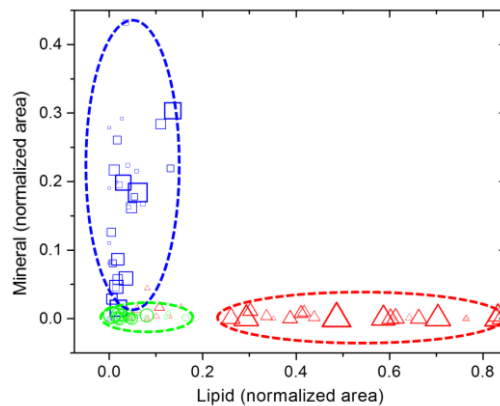


Figure 2. Scatter plot of the number of lipid and mineral pixels observed in BCARS images of the AD, OS, and BA samples. The amount of lipid and mineral per cell is represented as the number of phenotypic image pixels divided by the total number of pixels assigned to the cell. The size of the symbols represents the total number of pixels.

¹ Y. J. Lee, S. L. Vega, P. J. Patel, K. A. Aamer, P. V. Moghe, M. T. Cicerone, *Tissue Eng. Part C*, 20, 562 (2014).

Differential interference contrast stimulated Raman scattering microscope

Hiroharu Yui, Motohiro Banno and Takayuki Kondo

Department of Chemistry, Faculty of Science, Tokyo University of Science,
1-3 Kagurazaka, Shinjyuku, 162-8601, Tokyo, Japan

Keywords: stimulated Raman scattering, microscope, differential interference.

Measurement techniques for obtaining chemically-contrasted topographic images for buried interfaces or layered material in multi-layered materials with non-invasive and destructive manners have been strongly desired for both scientific and industrial purposes. Especially, for medical and industrial purposes, sub-micrometer spatial precision and resolution are often required. Optical coherence tomography (OCT), which has become inevitable tool in the fields of biology, medicine, and material science and technology, is one candidate for obtaining such topographic images of buried thin materials and interface with non-destructive manners¹. However, it has been difficult to obtain chemical contrasted images because the OCT images are constructed with the Rayleigh scattering from the target interfaces and/or materials.

To achieve the purpose, we have constructed Stimulated Raman scattering (SRS) interferometer, which can obtain chemically-contrasted OCT images. The images are obtained by the interference between the SRS and reference laser light. Since the SRS has molecular selective information and phase information, it can provide interferometric images like OCT.

In the present study, we have further improved a SRS interferometer for more simple and robust microscope, namely differential interference contrasted which is a key component for the chemical-contrast SRS microscope (DIC- μ SRS) for obtaining such chemically-contrasted images.

Schematic diagram of the developed DIC- μ SRS is shown in Figure 1. Two optical parametric oscillators (OPO) are excited by a Ti:Sapphire (Ti:S) oscillator (76 MHz, 2 ps). The output from one OPO was used as a pump pulse, and the output from the other OPO was used as a Stokes pulse. When the wavenumber difference between the pump and the Stokes pulses is the same as the wavenumber of a certain target molecular vibration, the Stimulated Raman Loss (SRL) signal overlaps the pump pulse. Local oscillator (LO) is generated by a Wollaston prism and the stimulated Raman loss signal of the pump pulse reflected from the sample surface was made collinear with a reflected LO by the Wollaston prism. The amplitude of the Stokes pulse is modulated at 3MHz with electro-optic modulator (EOM) for lock-in amplification detection.

Figure 2 shows a DIC- μ SRS image from the buried interface between liquid crystal molecules (5CB) and silicon mold with sub-micrometer-scale periodic grooves (3 μ m width and 200 nm depth, 4 μ m pitch). The upper panel is obtained when the wavenumber difference between the pump and the Stokes pulses is 1606 cm^{-1} , which is in resonant to the stretching vibration of a phenyl ring in 5CB. The lower one is obtained when the wavenumber difference is set to be 520 cm^{-1} (Si lattice stretching mode). We can clearly see the chemically contrasted topographic images with spatial resolution of sub-micron scale in depth direction.

Recently, coherent Raman microscopes have been intensively applied to biological samples to obtain molecular images with micrometer scale². The developed SRS interferometer and DIC- μ SRS will also be

useful tool for industrial and biomedical tool, where one is required the measurements of buried interface or chemical layers with non-invasive manner and sub-micrometer scale resolution.

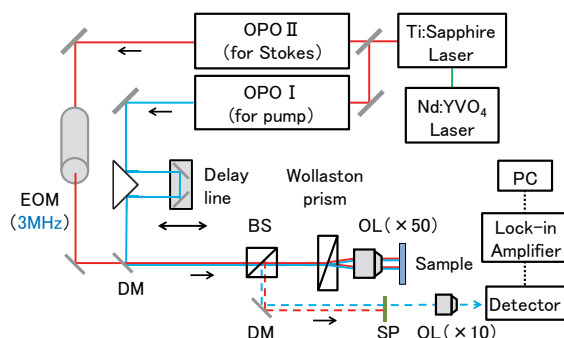


Figure 1. Schematic diagram of the differential interference contrast stimulated Raman scattering microscope (DIC- μ SRS). OPO: optical parametric oscillator, EOM: electro-optic modulator, DM: dichroic mirror, BS: beam splitter, SP: short pass filter, and OL objective lens

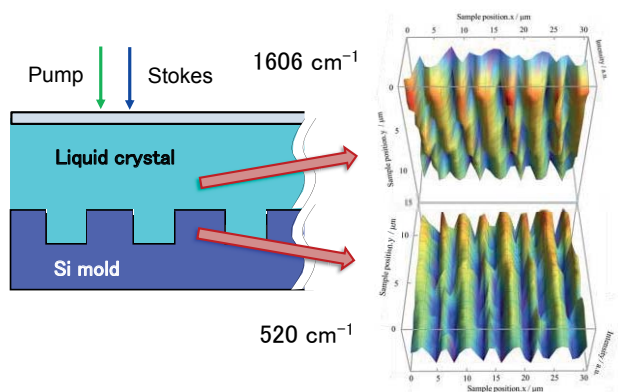


Figure 2. Left panel: schematic image of the test sample (Si mold with periodic grooves with 200 nm depth fulfilled with liquid crystal (5CB)). Right panels: DIC- μ SRS topographic images with chemical contrast. (Upper) 1606 cm^{-1} for 5CB and (Lower) 520 cm^{-1} one for Si mold.

¹ Boas D. A., Pitris C. & Ramanujam N., Eds. (2011). *Handbook of Biomedical Optics*, CRC Press: New York.

² Cheng J. -X. & Xie X. -S. Eds. (2013). *Coherent Raman Scattering Microscopy*, CRC Press: New York.

Spectral Processing Challenges in Coherent Raman Spectroscopy and Microscopy with Applications

Laszlo Ujj

Department of Physics, University of West Florida, Florida, 32514, Pensacola, USA

Keywords: CARS, Raman, DCVJ, MEM, TDKK.

After prosperity of pioneering works on picosecond coherent Raman spectroscopy and its biological applications during the 1990s (e.g. Ujj et al.¹⁻²), coherent Raman microscopy emerged at the beginning of the 21st century (e.g. Evans and Xie³). It is reaching unprecedented results mostly attributed to the technological advancements in photonics and laser technology (Camp et al.⁴).

Broadband Coherent anti-Stokes Raman scattering (BCARS) microscopy is able to record the spatial distributions of several molecular species simultaneously by measuring a wide range of vibrational spectra. Ultrashort (femto-picosecond) laser pulses with high repetition rate (e.g. 100 MHz) generate the signal from thin samples scanned across the focused beams. The wavelengths are in the near infrared range, therefore almost all of the applications generate non-electronic resonance BCARS signals. If the spectral response of the measuring system removed from the spectra, model independent phase retrieval mathematical methods (Maximum Entropy Method (MEM) or Kramers-Kronig transformations (TDKK)⁴) are applied to generate Raman like spectra, the imaginary part of the third order susceptibility.

In the case of electronic resonance enhancement, however, the line-shape remains dispersive after phase retrieval. It is shown here that Raman like spectra can be generated under the condition of electronic resonance enhancement (Figure 1). The idea

of the local phase approximation was borrowed from nonlinear fitting type of spectral retrieval used to derive the vibrational information from the measured modulus of the electronic susceptibility¹.

9-Dicyanovinyljulolidine⁵ (DCVJ) is selected to measure electronic resonance enhanced BCARS spectra with a table top CARS spectrometer⁶. DCVJ is one of the molecules that undergo viscosity dependent photo-isomerization or rotation upon photo-excitation. In order to prevent intermolecular rotation and tune the electronic transition closer to the excitation wavelength (532 nm) the molecules were dispersed in a solid polymer (NOA63, Norland, UV curable adhesive). The fluorescence intensity was enormously increased ($\sim 10^4$) relative to methanol solution (data not shown). This increase made measuring Raman spectra with 532 nm excitation impossible. Polarization sensitive resonance BCARS spectra were able to reveal the vibrational structure of the sample (Figure 1). The BCARS spectrum presented here is measured using 90° excitation geometry probing only the 1212 component of the third order nonlinear susceptibility.

Spectra are processed with an in-house written LabView program applying MEM for phase retrieval. Once the real and imaginary part of the susceptibility is available, an e^{i0} local mixing decouples the real and imaginary part of the resonances (insets A and B in Figure 1). This method makes possible to selectively enhance the

contrast of the image of specific molecular species in CARS microscopy.

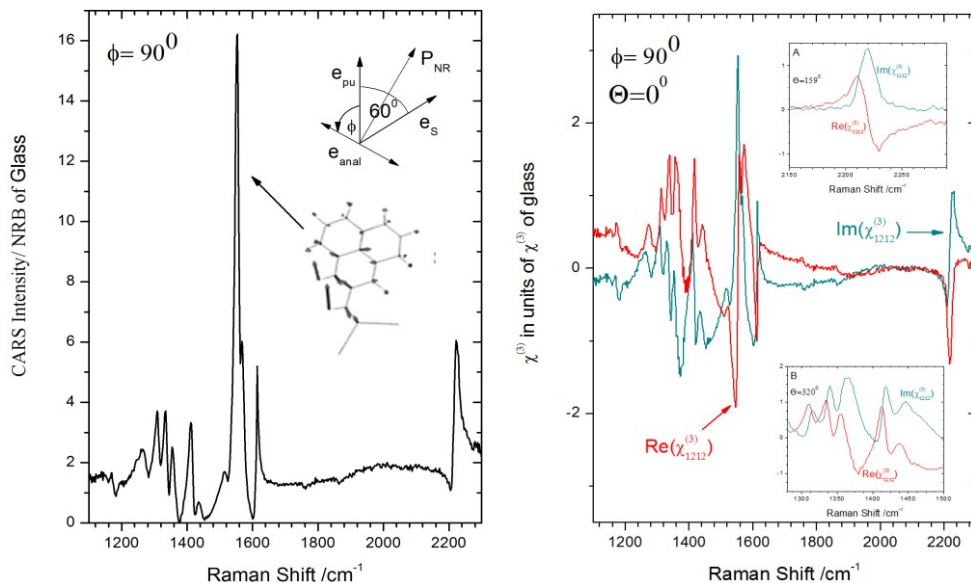


Figure 1. Left Panel: Polarization Sensitive BCARS spectrum of DCVJ in solid polymer. The normal mode associated to the most intense vibrational mode is also presented. Right Panel: Retrieved imaginary and real part of the third order susceptibility with no phase adjustment ($\theta=0$). MEM is used for phase retrieval. Inserts A and B show spectra of specific spectral regions with local phase corrections. Phases are selected to maximize the imaginary part of the signal at the vicinity of the origin of the vibrational modes (e.g. (A) CN stretch at 2220 cm^{-1} .)

- ¹ Ujj L., Jager F., Atkinson G. H., (1998), *Biophysical Journal*, 74, 1492-1501.
- ² Ujj L., Atkinson G. H., (2002) in *Handbook of Vibrational Spectroscopy*, J.M. Chalmers and P.R. Griffiths (Eds), John Wiley & Sons, Ltd. Vol. 1, 585-595.
- ³ Evans C. L., Xie, X. S. (2008), *Annual Review of Analytical Chemistry*, 1, 883-909.
- ⁴ Camp C. H. et al (2014), *Nature Photonics*, 8, 627-634.
- ⁵ Jee AY., Bae E., Lee M., (2009), *J. Phys. Chem. B*, 113, 16508-16512.
- ⁶ Lawhead C., Cooper N., Anderson J., Shiver T., Ujj L., Characterization and calibration of a combined laser Raman, fluorescence and coherent Raman spectrometer, *Proceedings of APS March Meeting 2014*, Volume 59, Number 1, Denver, Colorado.

Insights into health and disease using coherent Raman Imaging

Tual Monfort¹, Justyna Smus¹, Alan Hunt², Mark Jones², Anthony Postle² and Sumeet Mahajan¹

¹Institute of Life Sciences and Department of Chemistry, University of Southampton, Highfield, SO17 1BJ, UK
²Clinical & Experimental Sciences, University of Southampton, Southampton General Hospital, SO16 6YD, UK

Keywords: Coherent Raman, CARS, Multimodal, Imaging, Biomedical.

Coherent anti-Stokes Raman scattering (CARS) is increasingly becoming an established tool for label-free ‘chemically selective’ imaging in the life sciences. It is particularly being utilized to image lipids in cells, tissues and organisms^{1,2}. We have utilized CARS imaging earlier to monitor lipid droplets in cells generated as a result of treatment to help evaluate efficiency of chemotherapeutics³. In this talk our recent investigations on ex vivo tissue samples and model organisms to understand disease mechanisms, correlate metabolic changes to behavior and develop clinical diagnostics using multimodal CARS imaging will be highlighted.

Pulmonary alveolar proteinosis (PAP) is a condition of excess accumulation of lung surfactant which occurs due to the dysfunction in its metabolism. The breakdown of lung surfactant is regulated by a growth factor, granulocyte macrophage colony stimulating factor (GMCSF). We have studied ex vivo lung tissue from mice models in which GMCSF has been knocked out. In addition the cells, primarily macrophages, obtained by lung lavage have been examined. Since lung surfactant is essentially a lipoprotein it can be easily monitored by CARS imaging. Furthermore, second harmonic microscopy (SHM) provides information on the collagen lining

the alveoli. Together CARS and SHM results indicate an increase in lipid and collagen amount in the case of GMCSF knock-out mice compared to controls. Analysis of CARS images for the size and distribution of surfactant deposits also clearly show differences in the intracellular and extracellular accumulations. While the role of GMCSF is clear in PAP, the observation of increased collagen suggests fibrosis occurring together in lungs. Simultaneous monitoring of liver tissue from the same animals indicates a correlation between the development of disease in the lungs and lipid metabolism in the liver.

On similar lines we have studied ex vivo tissue samples of lung tissue from patients potentially suffering from idiopathic lung fibrosis (IPF). The causes of IPF are currently being debated and its definitive diagnosis is currently difficult; various histopathological stains and dyes are being tried. Using our multimodal CARS imaging approach we have studied the chemical and structural components of fibrotic and healthy tissue. Our preliminary results indicate clearly an increase in collagen fibers as imaged by SHM while CARS suggests changes in the relative protein, lipid and glycogen content in IPF tissue

harvested from patients compared to healthy controls.

In addition numerous other studies based on multimodal CARS imaging have been and are being carried out in our lab. Taken together all these studies demonstrate the immense utility of multimodal CARS in not only providing an increased

understanding of disease mechanisms but also aiding the development of imaging based clinical diagnostics.

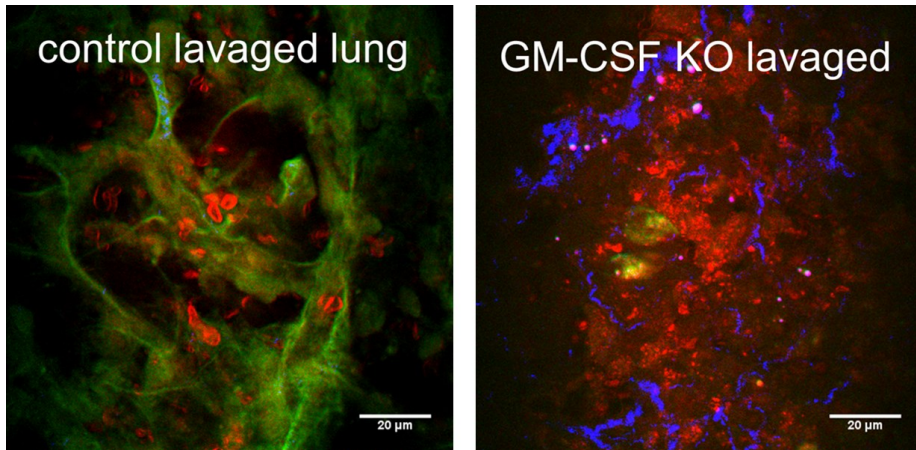


Figure 1. Representative multimodal images of lung tissue are shown above. CARS (red) shows the signal distribution at the $-\text{CH}_2$ stretching frequency of 2850 cm^{-1} to map out the surfactant. Autofluorescence is shown in green and SHM is shown in blue. GMCSF KO mice tissue clearly shows increased lipid deposits and collagen.

¹ Le T.T., Yue S.H., Cheng J.X. (2010), *J Lipid Research*, 51, 3091-3102.

² Hellerer T., Axang C., Brackmann C., Hillertz P., Pilon M., Enejder A. (2007), *Proc Natl Acad Sci U S A*, 104 (37)14658-63.

³ Steuwe C., Patel I. I., Ul-Hasan M., Schreiner A., Boren J., Brindle K., Reichelt S., Mahajan S. (2014), *J Biophotonics*, 7 (11-12), 906-913.

Resonance Raman Spectroscopy for Probing Carotene-Porphyrin Triplet States

Elizabeth Kish¹, Junming Ho², Dalvin D. Mandez-Hernandez², Ana L. Moore³, Victor S. Batista², Bruno Robert¹ and Thomas Moore³

¹Department of Life Sciences, CEA Saclay, 91191, Gif sur Yvette, France

²Department of Chemistry, Yale University, 06520, New Haven, USA

³Department of Chemistry and Biochemistry, Arizona State University, 85287, Tempe, USA

Keywords: Raman spectroscopy, carotenoid, triplet, energy transfer

Photosynthesis is the process by which certain organisms, including most plants and many bacteria, obtain their energy for survival. During photosynthesis, photons are “captured” by chromophores in light harvesting complexes and start an electron transfer chain that ultimately results in the formation of an adenosine triphosphate molecule (ATP), the energy molecule of the cell. When there is light, there will ultimately be harmful species like singlets and triplets formed; it has been found that carotenoids are efficient quenchers of these harmful species in photosynthetic apparatuses. These processes are complex and differ greatly depending on the organism, but they all have one common characteristic, energy transfer.

Energy transfer mechanisms in photosynthetic machinery have become more and more studied because they represent possibilities for next generation energy sources. Although so far enzymatic energy trapping has been highly unsuccessful on an industrial scale, there are still many who are trying to understand and develop it. These processes are still largely being studied fundamentally, and there is still much debate on the actual physical mechanism by which they work.

In our work, we have synthesized molecules (carotene-porphyrins¹) to mimic certain photosynthetic pigments and used

them to study the energy transfer mechanisms that should be similar to those found in nature. Often in light harvesting complexes, a carotenoid molecule will quench a triplet coming from a chlorophyll molecule in its vicinity. Here, we have used porphyrins as a model for chlorophyll and covalently linked them to carotenoids in different orientations to mimic the pigments in photosynthetic proteins and studied them spectroscopically.

Resonance Raman spectroscopy (RRS) is a technique that has been widely exploited to study carotenoids. It gives information on molecular vibrational states; when a molecule’s electronic transition coincides with the incident wavelength of laser used, the technique becomes “resonant”. This amplifies the signal by up to a factor of 10^6 .

Carotenoids have four characteristic bands when considering RRS spectra; they are denoted ν_1 to ν_4 . Roughly, ν_1 represents stretching vibrations of C=C bonds; ν_2 represents stretching vibrations from C-C bonds coupled to H in-plane bending modes, ν_3 represents methyl in-plane rocking vibrations, and ν_4 represents C-H out-of-plane wagging modes.

We have used RRS to study the carotene-porphyrins, specifically in their triplet forms. Depending on the relative orientation of the carotenoid to the porphyrin, we have seen that the triplet-

triplet energy transfer triggers changes in nearly all bands of the RRS spectra. Specifically, the ν_1 band (the stretching frequency of the conjugated C=C moiety) noticeably downshifts when associated with a more delocalized triplet (and consequently more efficient triplet-triplet energy transfer). Though the band shifts are not so intense compared to the typical ν_1 band, they represent the importance of molecular

proximity to energy transfer mechanisms and give some insight into how this process may truly physically occur. We have done extensive modelling to corroborate our experimental results with calculations.

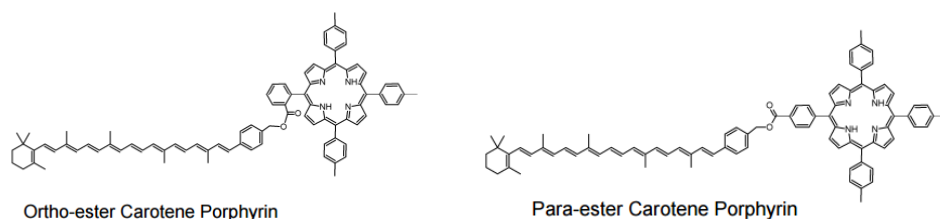


Figure 1. Carotene-porphyrin dyads that were investigated in this study.

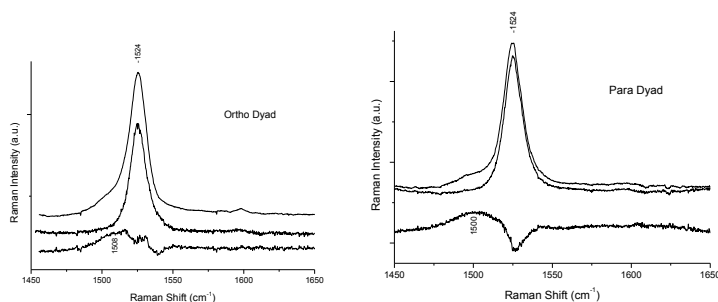


Figure 2. Results from RRS experiments. Triplet spectra are the farthest upshifted on the graph; the middle spectrum is the normal spectrum of the dyad without triplet, the lowest spectrum is a subtraction, triplet spectrum-normal spectrum, to show the differences.

¹Bensasson, R. V., Land, E. J., Moore, A. L., Crouch, R. L., Dirks, G., Moore, T. A., Gust, D. (1981) *Nature*, 290, 329–332.

In Situ Raman Study of Silicene: From Monolayer To Multilayers

Dmytro Solonenko¹, Patrick Vogt², Ovidiu D. Gordan¹, and Dietrich R. T. Zahn¹

¹Technische Universität Chemnitz, D-09126 Chemnitz, Germany

²Technische Universität Berlin, D-10623 Berlin, Germany

Keywords: silicene, multilayers, *in situ*, Raman spectroscopy

Silicene, the Si analogue of graphene, received great interest in the last years due to the peculiar electronic properties and application prospects in semiconductor technology¹. Similarly to its counterpart graphene, silicene is a one-atom-thin two-dimensional crystalline layer, with a honeycomb atomic structure. Contrary to graphene, DFT calculations reveal that free-standing silicene possesses a low-buckled structure, accounting for the preferential sp²/sp³ hybridization of Si atoms. However, the charge carriers still behave like massless relativistic Dirac fermions².

On the other hand, the sp²/sp³ hybridization causes a higher chemical reactivity, as compared to graphene, hindering the formation, processing, and analysis of silicene in ambient conditions. However, it was demonstrated that silicene can be synthesized on a supporting Ag(111) substrate under ultra-high vacuum (UHV) conditions via quasi-epitaxial growth⁴. The successful synthesis of silicene was also reported on Ir(111)⁵ and ZrB₂⁶ single crystals. Very recently the first silicene-based field-effect transistor was reported³, a remarkable result taking into account that only 2.5 years after the first synthesis of silicene have passed. Also in this case the silicene was grown on a Ag(111) layer prior to its processing.

By looking in more detail at the formation of Si-structures on Ag(111) it turns out that the structure formation strongly depends on the growth parameters,

such as the growth rate and the substrate temperature. For different conditions different 2-dimensional (2D) Si monolayers can form, and yet only the one with a (4x4) symmetry has conclusively been demonstrated to refer to silicene.

In order to get further insight into the formation of 2D Si structures on Ag(111) vibrational spectroscopy provides reliable structural information supplementing electron spectroscopies-based techniques. We carried out *in situ* Raman measurements of the different 2D Si structures on Ag(111) in order to elucidate the nature and the vibrational properties of these structures. Silicene sheets were grown in UHV conditions (base pressure < 2·10⁻¹⁰ mbar) for different substrate temperatures. Coupled to the UHV chamber, a triple-monochromator Dilor XY spectrometer was used to record the Raman spectra. For excitation different wavelengths of Ar⁺ and Kr⁺ lasers (514.5 nm and 647.1 nm) were employed. For both lines a power density of 10 μW/μm² was chosen.

Our results demonstrate that only the (4x4) structure exhibits distinct Raman modes, indicative of silicene. Others 2D-Si structures (e.g. '2√3x2√3') resemble a Raman signature similar to bulk silicon or to a superposition of several fingerprints.

After the situation for monolayer silicene sheets on Ag(111) becomes clear, we proceed with the investigation of multi-layer silicene stacks. Previously reported results⁷ show that silicon adlayers, deposited

on top of silicene, possess a multilayer structure. The number of layers depends on the deposited Si amount and both symmetry and atomic arrangement are very different from the first silicene layer. These multilayers are technologically interesting because they are electronically decoupled from the metallic substrate exhibiting properties closer to free-standing silicene, such as a linear energy-momentum dispersion at the K points. Moreover, scanning tunneling spectroscopy results confirm the absence of a bandgap for multilayer silicene. However, the atomic structure of these multilayers is controversially discussed in the literature, ranging from silicene stacks to bulk-like Si(111) or Ag-terminated bulk-like Si(111).

Our Raman investigation of the multilayer stacks demonstrates an evident difference of its fingerprint from the one of bulk silicon. Step-wise monitoring of multilayer silicene growth shows a temperature dependent formation of silicene layers with a $\sqrt{3}\times\sqrt{3}$ symmetry. We discuss the stacking order of these layers, and their thermal stability. At higher temperatures the results demonstrate a phase transition from multilayer silicene to a bulk-like Si structure at the temperature around 400°C. Atomic force microscopy before and after annealing confirms a morphological change of the silicene multilayer into bulk-like Si clusters, in agreement with the Raman measurements.

¹ Q. Tang and Z. Zhou, (2013), *Prog. Mater. Sci.* **58**, 1244.

² S. Cahangirov, M. Topsakal, E. Aktürk, H. Şahin, and S. Ciraci, (2009), *Phys. Rev. Lett.* **102**.

³ L. Tao, E. Cinquanta, D. Chiappe, C. Grazianetti, M. Fanciulli, M. Dubey, A. Molle, and D. Akinwande, (2015), *Nat Nano* **10**, 227.

⁴ P. Vogt, P. De Padova, C. Quaresima, J. Avila, E. Frantzeskakis, M.C. Asensio, A. Resta, B. Ealet, and G. Le Lay, (2012), *Phys. Rev. Lett.* **108**.

⁵ L. Meng, Y. Wang, L. Zhang, S. Du, R. Wu, L. Li, Y. Zhang, G. Li, H. Zhou, W.A. Hofer, and H.-J. Gao, (2013), *Nano Lett.* **13**, 685.

⁶ A. Fleurence, R. Friedlein, T. Ozaki, H. Kawai, Y. Wang, and Y. Yamada-Takamura, (2012), *Phys. Rev. Lett.* **108**.

⁷ P. Vogt, P. Capiod, M. Berthe, A. Resta, P. De Padova, T. Bruhn, G. Le Lay, and B. Grandidier, (2014), *Appl. Phys. Lett.* **104**, 021602.

Raman spectroscopic study of phase transitions in rare earth ferroborate multiferroic crystals under temperature and high-pressure.

Alexander Krylov, Svetlana Sofronova, Irina Gudim, Svetlana Krylova and Alexander Vtyurin

L.V. Kirensky Institute of Physics SB RAS, 660036, Krasnoyarsk, Russia

Keywords: multiferroic, phase transition, magnetic ordering, temperature, high-pressure.

Multiferroic materials showing the coexistence of at least two ferroic orders ((anti)ferroelectric, (anti)ferromagnetic and (anti)ferroelasticity) are expected to find potential applications in many devices. Amongst these properties the coexistence of ferroelectricity and ferromagnetism is highly desired. Besides their coexistence, of utmost importance is a strong coupling between the two ferroic orders. In multiferroic materials, the coupling interaction between the different order parameters can produce additional functionalities. The application of multiferroics will make possible to significantly enlarge the functional possibilities of spintronics.

Crystals of the $RFe_3(BO_3)_4$ family (R is rare earth ion) were reported to possess multiferroic features, demonstrating both structural and magnetic phase transitions [1–4], where transition points may be varied by rare earth composition. In this work we used Raman spectroscopy to study $Ho_{1-x}Nd_xFe_3(BO_3)_4$ ($x = 0, 0.25, 0.5, 0.75$) single crystals.

Temperature measurements were performed in the temperature range 10–400 K. The aim of this study is to investigate possible existence of a soft mode related to structural order parameter and effects of magnetic transitions on Raman spectra (Figure 1). Structural transitions manifest clearly by soft mode restoration and new Raman lines appearance below 366 K and 203 K for $x = 0$ и $x = 0.25$ compositions

respectively. In Nd-doped crystals significant modification of Raman scattering was induced by magnetic ordering below the Neel temperature (about 40 K), that include both magnon scattering and strong intensity redistribution of high frequency lattice modes. Analysis of vibrational spectra and its numerical simulation demonstrate that bigger cell volume of Nd-containing solid solutions provides bigger displacements of oxygen ions in a BO_3 groups below the Neel temperature that results in stronger magnetoelastic interactions. This leads to the appearance of additional lines in the Raman spectra and rapid increase of their intensity with increasing magnetic order.

Raman measurements on $HoFe_3(BO_3)$ crystal were carried out at pressures up to 7 GPa and at temperatures up to 680 K by using a diamond anvil cell in order to determine the pressure–temperature phase diagram. From the changes in the Raman spectrum at the phase transition, the stability regions of phases I, II were investigated (Figure 2). After reaching 675 K and 2.5 GPa Raman spectra lines disappear and formation of a new crystalline form was discovered. This form persists ambient condition after removing high pressure and temperature.

The work was supported by Grant of the Ministry of Education and the Russian Foundation for Basic Research Grants 13-02-00825.

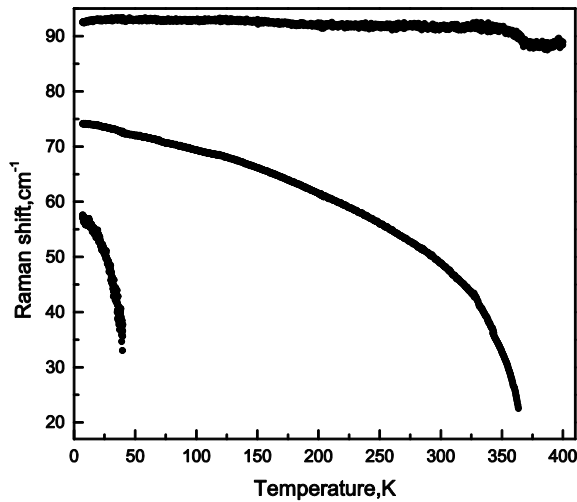


Figure 1. Soft modes restoration below magnetic and structural phase transitions in $\text{HoFe}_3(\text{BO}_3)_4$

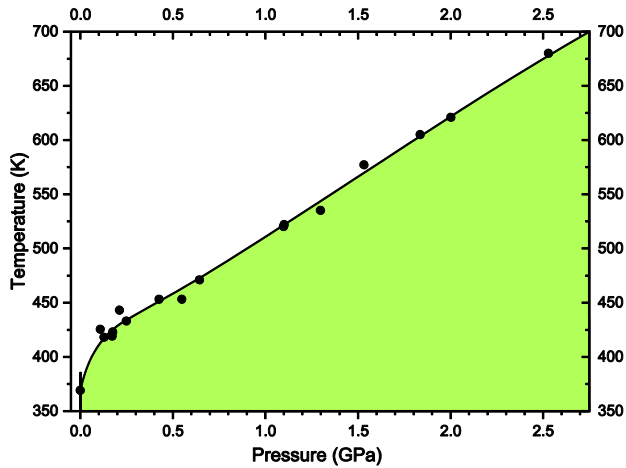


Figure 2. Pressure–temperature phase diagram in $\text{HoFe}_3(\text{BO}_3)_4$

- ¹ Zvezdin A.K., Krotov S.S., Kadomtseva A.M., Vorob'ev G.P., Popov Yu.F. et al. (2005) *JETP Lett.* 81, 272.
- ² Fausti D., Nugroho A.N., Paul H.M. van Loosdrecht (2006) *Phys. Rev. B* 74, 024403.
- ³ Kuz'menko A.M., Mukhinn A.A., Ivanov V.Yu., Kadomtseva A.M. Bezmaternykh L.N. (2011) *JETP Lett.* 94, 294.
- ⁴ Krylov A.S., Sofronova S.N., Gudim I.A., Vtyurin A.N. (2013) *Solid State Commun.* 174, 26.

Probing structural phase transformation in BiFeO₃ thin films by polarized micro Raman spectroscopy

Anju Ahlawat¹, S. Satapathy¹, P. K. Gupta¹ and V. G. Sathe²

¹Laser Materials Development & Device Division, Raja Ramanna Centre for Advanced Technology, 452013, Indore, India

²UGC-DAE Consortium for Scientific Research, University Campus, Khandwa Road, 452 017, Indore, India

Keywords: Multiferroics, BiFeO₃, thin film, Raman Spectroscopy, crystal structure.

Currently, Magnetic ferroelectrics, having coexisting magnetic and ferroelectric ordering have attracted much attention from both fundamental and practical point of view¹. BiFeO₃ (BFO) is a model multiferroic system which exhibits interesting multiferroic properties i.e ferroelectricity and ferromagnetism at room temperature². BFO possesses a rhombohedrally distorted perovskite structure with space group R3c, which gives many challenges in controlling meaningful multifunctionality of this material. Therefore efforts are being made to modify the structure of BFO other than the rhombohedral symmetry.

It is however possible to modify the structure of BFO by chemical doping or by epitaxial constraints, which in turn reduce the conductivity and improve magnetization at room temperature³. Therefore we focused the present study on the structural changes observed in BFO thin films induced by Nd, La co-doping. The most important issue of local symmetry change due to doping and elastic strain in thin films can be effectively probed by Raman spectroscopy⁴. In this context, pure as well as co doped Bi_{0.8}La_{0.1}Nd_{0.1}FeO₃ (BLNFO) epitaxial films were prepared and extensively studied using polarized Raman spectroscopy.

While it is difficult to examine the change in crystal structure of the films using X-ray Diffraction, Raman spectroscopy has been used for the evolution of structure. The room-temperature structure of BFO crystal is a highly distorted rhombohedral perovskite structure with space group R3c. But due to strain and doping, the BFO transformed to different structure (most probably either tetragonal or monoclinic). Raman spectra illustrate that for BLNFO film, numbers of peaks are larger than that of the BFO film indicating lowering of symmetry as compared to that for BFO films. In order to discern the changes in symmetry due to La and Nd doping in BFO structure, polarization dependent measurements were performed for BFO and BLNFO films. The polarization dependent measurements were performed with parallel (XX) (the wave vector of scattered light is parallel to the incident light wave vector) as well as cross polarization configuration (XY) (the wave vector of scattered light is perpendicular to the incident light wave vector). Thus the parallel and cross polarization configuration corresponds to $Z(XX)\bar{Z}$ and $Z(XY)\bar{Z}$ geometry respectively (as shown in the inset of the figure 1). According to the Raman selection rules for rhombohedral structure, only A₁ modes are expected to appear in the $Z(XX)\bar{Z}$ configuration and should not be seen in

$Z(XY)\bar{Z}$ configuration. On the other hand E modes are allowed in both $Z(XX)\bar{Z}$ and $Z(XY)\bar{Z}$ configuration. Figure 1 shows that while A_1 modes (72, 140, 175, and 220 cm^{-1}) get suppressed, E modes (277, 355, 378, 473, 526, 569 and 616 cm^{-1}) were observed in $Z(XY)\bar{Z}$ configuration for BFO film which confirm its rhombohedral structure. However for BLNFO films, our polarization analysis suggest monoclinic structure. Group theoretical calculations for Raman

intensity for monoclinic symmetry Bb suggest that intensity of A' modes (71, 138, 170, and 218 cm^{-1}) should be non zero for parallel polarization geometry $Z(XX)\bar{Z}$ and cross polarization geometry $Z(XY)\bar{Z}$. Our results on pure BFO films show zero intensity for A_1 modes in cross polarization geometry while a non zero intensity of A' modes for BLNFO film. The observation of intensity for these mode suggest that BLNFO films have monoclinic structure.

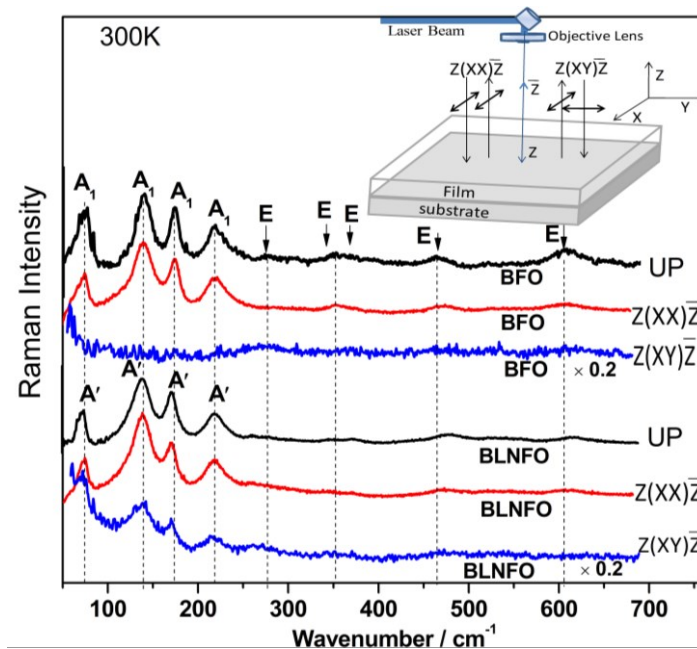


Figure 1. Polarization dependent room temperature Raman spectra of (a) $\text{BiFeO}_3/\text{SrRuO}_3/\text{SrTiO}_3$ and $\text{Bi}_{0.8}\text{La}_{0.1}\text{Nd}_{0.1}\text{FeO}_3/\text{SrRuO}_3/\text{SrTiO}_3$ films.

- ¹ R. Ramesh and N. A. Spaldin, Nat. Mater. 2007, 6, 21.
- ² P. Fischer, M. Połomska, I. Sosnowska, and M. Szymański, J. Phys. C: Solid State Phys. 1980, 13, 1931.
- ³ V. Zaleskiĭ, A. A. Frolov, T. A. Khimich, and A. A. Bush, Phys. Solid State 2003, 45, 141.
- ⁴ G. Gouadec and P. Colombar. Progress in Cryst. Growth Charact. Mater. 2007, 53, 1.

New insights into the crystal structures and vibrational properties of germanates comprising $[\text{Ge}_3\text{O}_{10}]^{8-}$ and $[\text{Ge}_4\text{O}_{12}]^{8-}$ anions from Raman microscopy and periodic *ab initio* calculations

Ivan I. Leonidov^{1,2}, Vladislav P. Petrov², Vladimir A. Chernyshev², Olga A. Lipina¹, Ludmila L. Surat¹, Alexander P. Tyutyunnik¹, Emma G. Vovkotrub³, Anatoliy E. Nikiforov² and Vladimir G. Zubkov¹

¹Institute of Solid State Chemistry, UB RAS, 620990, Ekaterinburg, Russia

²Ural Federal University, 620002, Ekaterinburg, Russia

³Institute of High-Temperature Electrochemistry, UB RAS, 620990, Ekaterinburg, Russia

Keywords: germanates, Raman microscopy, FTIR spectroscopy, DFT calculations.

In the last few years, the lanthanide-doped $\text{CaY}_2\text{Ge}_4\text{O}_{12}$ ¹, $\text{CaY}_2\text{Ge}_3\text{O}_{10}$ ² and $\text{Ca}_2\text{Ge}_7\text{O}_{16}$ ³ germanates have been studied as efficient laser systems, promising phosphors for light upconversion, pLED applications, and persistent luminescent materials. The present report will be an overview on crystal structure features and lattice dynamics of $\text{CaY}_2\text{Ge}_3\text{O}_{10}$, $\text{CaY}_2\text{Ge}_4\text{O}_{12}$, and $\text{Ca}_2\text{Ge}_7\text{O}_{16}$ comprising either $[\text{Ge}_3\text{O}_{10}]^{8-}$, or $[\text{Ge}_4\text{O}_{12}]^{8-}$ anionic units. A combined experimental-theoretical approach has been applied in the study included FTIR spectroscopy, Raman microscopy and periodic *ab initio* calculations in the DFT framework using the CRYSTAL code.

Structural chemistry of $\text{CaY}_2\text{Ge}_4\text{O}_{12}$ can be considered with two space groups $P4/nbm$ and $Cmme$. The former corresponds to a mixed (0.5 Ca + 0.5 Y) distribution at the octahedral sites found from the results of Rietveld refinement of room temperature (RT) powder X-ray diffraction (XRD) pattern, the latter refers to the model of crystallographically nonequivalent Ca and Y atomic setting in distorted oxygen octahedrons on the results of DFT calculations. A series of LDA, GGA and hybrid functionals has been employed. While the most accurate geometry description has been found with the recently

established WC1LYP and PBE ($n = 6$) hybrids, the B3LYP calculation provides the best agreement between the recorded and computed infrared and Raman spectra⁴.

Afterwards, the WC1LYP and B3LYP functionals have been applied to analyze the crystal structure and vibrational properties of $\text{Ca}_2\text{Ge}_7\text{O}_{16}$. A more clear assignment of experimentally observed infrared bands and Raman lines to certain internal vibrations of the $[\text{Ge}_4\text{O}_{12}]$ ring and lattice modes has been facilitated by the performance of periodic *ab initio* calculations combined with the conventional factor group analysis.

Finally, vibrational spectroscopy results allow revealing the local changes in the anionic and cationic sublattices of $\text{CaRE}_2\text{Ge}_3\text{O}_{10}$ ($RE = \text{Y}, \text{La}-\text{Yb}$) which belong to a new series of compounds whose crystal structures comprise isolated $[\text{T}_3\text{O}_{10}]^{8-}$ ($T = \text{Si}, \text{Ge}$) anions. Rietveld refinement of RT powder XRD patterns shows that these germanates crystallize in the monoclinic system (S.G. $P2_1/c$, $Z = 4$) and have two morphotropic transitions⁵. The calcium and rare earth atoms are distributed among three nonequivalent sites and form layers along the $[001]$ direction connected into a framework through $[\text{Ge}_3\text{O}_{10}]$. The morphotropic transitions are accompanied by changes in the site occupancy factors of

metal cations and by variation in the first and second coordination spheres of $\text{Ca}^{2+}/\text{RE}^{3+}$. The obtained results are useful not only for multiphonon relaxation estimations for germanate optical hosts, but also for further lattice dynamics studies of

arsenates, phosphates, vanadates and silicates, whose crystal structures comprise either $[\text{A}_4\text{O}_{12}]^{4-}$ ($\text{A} = \text{As}, \text{P}, \text{V}, \text{Si}; n = 4, 8$) or $[\text{T}_3\text{O}_{10}]^{8-}$ ($\text{T} = \text{Si}, \text{Ge}$) anion units.

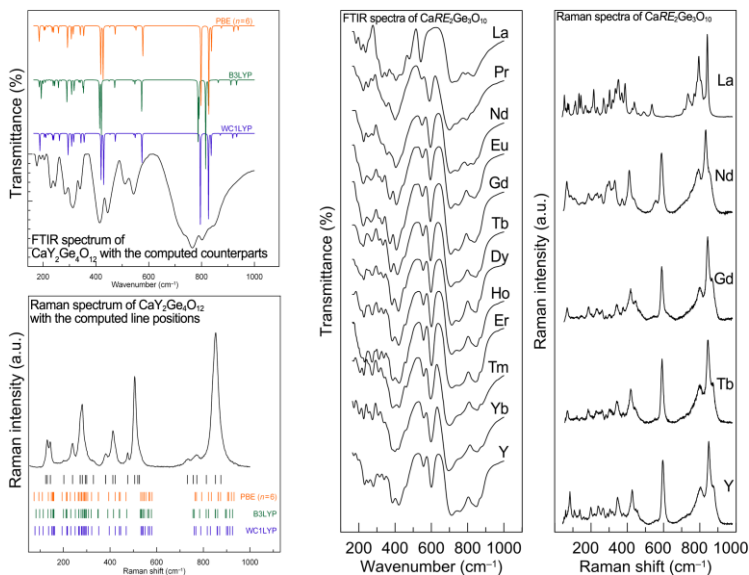


Figure 1. FTIR and Raman spectra of $\text{CaY}_2\text{Ge}_4\text{O}_{12}$ (with the computed counterparts) and $\text{CaRE}_2\text{Ge}_3\text{O}_{10}$ ($\text{RE} = \text{Y}, \text{La}-\text{Yb}$).

I.I.L. and V.P.P. are grateful to the RFBR Grant No. 14-03-31324-mol_a. The partial support from the FASO (Program No. 01201364479), RFBR (Grant No. 13-03-00047a), URAN Computing Platform (IMM UB RAS, Ekaterinburg, Russia), and the Ministry of Education and Science of Russia (Grant No. 3.571.2014/K) is strongly acknowledged.

- ¹ Leonidov I.I., Zubkov V.G., Tyutyunnik A.P., Tarakina N.V., Surat L.L., Koryakova O.V., Vovkotrub E.G. (2011), *Journal of Alloys and Compounds*, 509, 1339–1346.
- ² Lipina O.A., Surat L.L., Melkozerova M.A., Tyutyunnik A.P., Leonidov I.I., Zubkov V.G. (2013), *Journal of Solid State Chemistry*, 206, 117–121.
- ³ Leonidov I.I., Goldyreva E.I., Ishchenko, A.V. (2015), *RSC Advances*, (in preparation).
- ⁴ Leonidov I.I., Petrov V.P., Chernyshev V.A., Nikiforov A.E., Vovkotrub E.G., Tyutyunnik A.P., Zubkov V.G. (2014), *Journal of Physical Chemistry C*, 118, 8090–8101.
- ⁵ Lipina O.A., Surat L.L., Tyutyunnik A.P., Leonidov I.I., Vovkotrub E.G., Zubkov V.G. (2015), *CrystEngComm*, doi: 10.1039/C5CE00063G.

Raman Spectroscopic Investigation of CuGaTe₂ at High Pressures

Swayam Kesari, Nilesh P. Salke and Rekha Rao*

Solid State Physics Division, Bhabha Atomic Research Centre, Trombay, Mumbai - 400085, India

Keywords: High pressure, Raman spectroscopy, Phase transition, Chalcopyrite.

The ternary chalcopyrite semiconductors of I-III-VI₂ family are of interest due to their technological applications, particularly in the fabrication of solar cells, non-linear optical devices, photodiodes as well as for their thermoelectric properties.^{1,2} A few high pressure studies have been carried out on this family of compounds with an interest to find, whether the high pressure phase has cation disorder or not. High pressure XRD studies of CuGaTe₂ have reported a series of structural transitions. The first high pressure phase was tentatively assigned to be disordered simple cubic (d-sc) phase which appears along with the ambient chalcopyrite phase.³ At 11.5 GPa, chalcopyrite phase disappears completely and at 15.3 GPa, CuGaTe₂ shows second phase transition into disordered *Cmcm* (d-*Cmcm*) phase.³ AgInTe₂ and CuInTe₂ show structural transition directly to d-*Cmcm* phase at 6.2 and 3.6 GPa respectively, without intermediate d-sc phase.^{2,3} Earlier high pressure Raman study on CuGaSe₂, reported structural transition at 14.5 GPa from chalcopyrite phase to d-*Cmcm* phase,

which is also accompanied by decrease in energy gap.^{4,5} In the present study we have carried out Raman spectroscopic investigation on CuGaTe₂ at high pressures up to 24 GPa to understand phonon behaviour across the phase transition.

Raman spectroscopic measurements of CuGaTe₂ at high pressures were carried out from inside a diamond anvil cell (Diacell B-05). To maintain hydrostatic environment inside sample chamber, methanol-ethanol-water mixture in the ratio 16:4:1 was used as pressure transmitting medium. Pressure was measured using ruby fluorescence method. Raman spectrum of polycrystalline sample was excited using 532 nm laser of power ~25 mW. Backscattered light was analyzed using a home built 0.9 m single monochromator, coupled with an edge filter and detected by a cooled CCD. Entrance slit was kept at 50 μm, which gives a spectral band pass of 3 cm⁻¹.

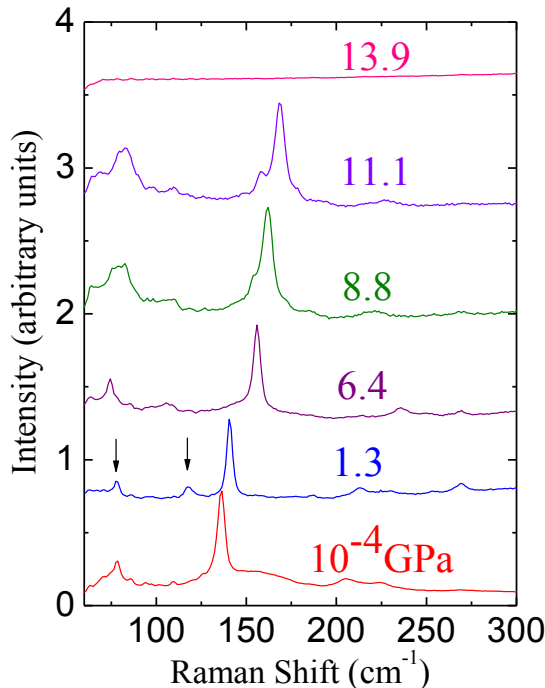


Figure 1. Raman spectra of CuGaTe₂ at high pressures. Arrows indicate soft modes.

Monday
Tuesday
Wednesday
Thursday
Friday
Author Index

Chalcopyrite CuGaTe_2 has tetragonal structure with space group $I\bar{4}2d$. Unit cell of CuGaTe_2 contains eight atoms, which give 24 normal modes of vibration. At the zone centre, 21 optical modes transform as $\Gamma = A_1 + 2A_2 + 3B_1 + 3B_2 + 6E$. Of this, B_2 and E modes are infrared active. On the contrary, all these modes, except the A_2 , are Raman active. Figure 1 shows the Raman spectrum of CuGaTe_2 at high pressures. The ambient Raman spectra match with the reported spectra. At moderate pressures of about 0.4 GPa, a mode around 117 cm^{-1} appears. This mode is identified as A_2 mode, appearing due to structural disorder which is actually a silent mode in the ambient structure.¹ Two of the low frequency modes show softening with increase in pressure. Softening of the mode could be correlated with structural instability. At 9 GPa, new modes emerge around 100 and 135 cm^{-1} , which is possibly due to the reported emergence of d-sc phase along with chalcopyrite phase. Beyond 11 GPa, we could not follow any Raman spectra. This fact is consistent with reported disappearance of chalcopyrite phase at 11.5 GPa and

emergence of metallic d- $Cmcm$ phase. The present Raman spectroscopic studies on CuGaTe_2 indicate that the softening of the lowest frequency E mode is related to the structural transition at high pressures.

References

- ¹ Rincón C., Wasim S. M., Marín G., Hernández E., Galibert J., (2001), *J. Phys. Chem. Solids*, 62, 847.
- ² Bovornratanaraks T., Kotmool K., Yoodee K., McMahon M. I., Ruffolo D., (2010), *J. Phys.: Conf. Series*, 215, 012008.
- ³ Mori Y., Ikai T., Takarabe K., (2003), *phys. stat. sol. (b)* 235, 317.
- ⁴ Gonjalez J., Rincón C., (1990), *J. Phys. Chem. Solids*, 51, 1093.
- ⁵ Gonjalez J., Chervin J. C., (1993), *Jpn. J. Appl. Phys.*, 32, 575.

* rekhar@barc.gov.in

Synergy between theory and experiment for an in-depth analysis of the Layered Double Hydroxides vibrational properties.

Erwan Andre, Jean Fahel, Arnaud Di Bitetto and Cedric Carteret

Laboratoire de Chimie Physique et Microbiologie pour l'Environnement (LCPME), UMR7564 CNRS – University of Lorraine, 405 rue de Vandoeuvre, 54602, Villers-lès-Nancy, France.

Keywords: DFT, LDH, Infrared, Raman, periodic calculations.

Layered Double Hydroxides (LDH) is a group of lamellar compounds that are well known for their proprieties of anion exchanger, pollutant scavenger, or catalyst precursors¹. Such properties are closely related to the interactions between the different parts of these chemical systems: The layers composition, the stacking sequence or the structuration of the interlayer domain. While the X-Ray Diffraction technic (XRD) is commonly used to characterize the structural properties of these materials at the crystal scale (stacking sequence, interlayer spacing...), vibrational spectroscopies (Infrared and Raman) can give access to *in-situ* information, at molecular scale, of both the anionic and cationic parts of these systems and of their interactions.

The quantum simulation of vibrational properties is now a common approach to assist in interpreting the complex signature of molecular systems. But the development of the corresponding tools for periodic systems and in particular the computation of Raman intensities is much more recent (2006 for codes using plane waves² and 2013 for codes using local basis sets³).

The aim of this work is to show how quantum mechanical calculations, realized on periodic systems at DFT level, can be used in synergy with experimental data to validate a model structure, to assign the experimental spectra and to give access to various properties related to the electronic

distribution. In the case of the LDH systems, challenges were both on theoretical and experimental sides: i) The construction of a reliable model within the limitations of the computational methods (ideal structure, no partial occupation) and the capability to model weak interactions for the theory. ii) The control the synthesis conditions (to work with pure samples) and of the analysis conditions for the experiment. In particular the recording of vibrational spectra (Infrared and Raman) has been obtained over a large spectral domain (from 40 to 4000 cm⁻¹) and under different conditions (air at ambient temperature or vacuum at liquid nitrogen temperature).

To illustrate this methodology, a focus will be made on $[M_2Al(OH)_6]^+ \cdot A^-$ (with $A^- = F^-, Cl^-, Br^-, I^-$ and $M = Mg^{2+}$ or Zn^{2+}). The choice of the halide series is motivated by the fact that, as atomic species, they do not possess any internal vibration modes which make them good probes of the layer vibrational signatures. In a second time, by changing the nature of the divalent cation (from Mg^{2+} to Zn^{2+}) we will show how the layer's vibrational fingerprint is influenced by the cationic couple. Finally, a few examples will be given for more complex systems ($A^- = NO_3^-, \frac{1}{2} CO_3^{2-}, R-COO^-$), where anions possess internal vibration modes. The influence of the confined environment of the interlayer domain on their vibrational signature will emphasize the versatility of the host-guest interactions.

Table 1. Comparison between calculated and experimental (XRD) parameters for $[\text{Mg}_2\text{Al}(\text{OH})_6]^+ \cdot \text{Cl}^-$ (lengths [Å], angles [°], cell volume V [Å³] and interlayer spacing C_z).

HTC	Experiment	Theory
a	3.048	3.048
c	22.314	22.410
α	90.0	89.2
γ	120.0	119.9
V	179.5	180.4
C_z	7.438	7.469

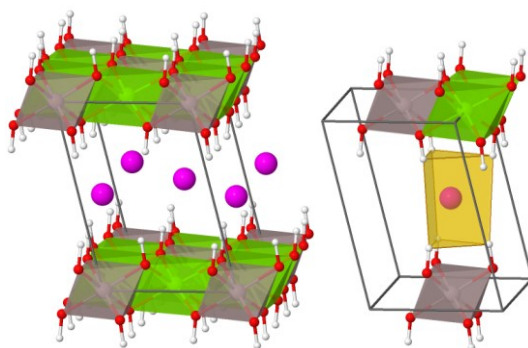


Figure 1. Supercell used to model $[\text{Mg}_2\text{Al}(\text{OH})_6]^+ \cdot \text{Cl}^-$ and highlight of anion's prismatic site.

Raman spectra

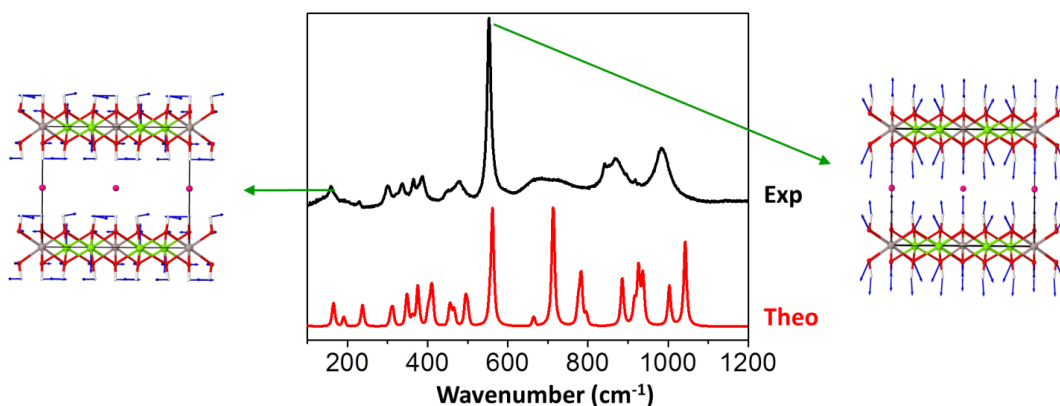


Figure 2. Comparison between experimental and calculated Raman spectra of $[\text{Mg}_2\text{Al}(\text{OH})_6]^+ \cdot \text{Cl}^-$ along with vibration modes of characteristic pics.

- ¹ Duan X. and Evans D. G. (2006). *Layered Double Hydroxides*. Springer Science & Business Media.
- ² Refson K. (2006), *Physical Review B*, 73 (15), 155114.
- ³ Maschio L., Kirtman B., Rérat M., Orlando R., Dovesi R. (2013), *The Journal of Chemical Physics*, 139 (16), 164101 and 164102.

Computational vibrational spectroscopy for various IR probes

Jun-Ho Choi^{1,2} and Minhaeng Cho^{1,2}

¹Center for Molecular Spectroscopy and Dynamics, Institute for Basic Science, Seoul 136-713, Republic of Korea

²Department of Chemistry, Korea University, 136-713, Seoul, Republic of Korea

Keywords: IR, 2D IR, MD simulation, QM calculation.

Various IR probes such as -CN, -SCN, -N₃ compounds, amide I in peptide and CO in MbCO were widely used to obtain information on protein structure and dynamics from their vibrational spectrum. The band shape and peak position are found to be sensitive to the local electrostatic environment around a given IR probe. The 2D IR spectroscopic measurement can be used in probing protein conformational change in time and protein unfolding pathway by employing femtosecond laser pulses. But, it is not straightforward to extract directly useful information on peptide structure and dynamics from experimental results obtained by vibrational spectroscopic measurements mainly due to congestion of vibrational bands. Therefore, the theoretical approach based upon the vibrational analysis is needed. There are a variety of complicated issues to be resolved in describing numerically vibrational spectrum, that is, the solvatochromic frequency shift due to interaction between peptide and water, motional narrowing, intermolecular vibrational coupling between neighboring peptides.¹

To tackle these issues, QM mechanical calculation has successfully used for a given molecular system. For the proteins under solution, the structure is constantly changed making hydrogen bonding interaction with water molecules and interaction between neighboring

peptides. This solvent or peptide induced interactions cause the frequency shift and change of band shape in the vibrational spectrum. But it is not practical to carry out QM calculation considering explicitly solvent molecules for protein-solvent system because of computational cost due to its large molecular size and varying configurations under solution.

Recently, we have developed a systematic way to numerically simulate linear and nonlinear vibrational spectrum considering fully solvent effects and peptide-peptide interaction by the hybrid method combining electronic structure calculation, molecular dynamics (MD) simulation, and theoretical models for vibrational solvatochromism.¹ This theoretical approach has been widely applied to simulate linear and nonlinear vibrational spectra of amide I vibrational modes of proteins,¹ various IR probes containing -CN, -SCN, -N₃ groups^{2,3}, and CO stretch mode in MbCO protein⁴. It was shown that the distributed interaction site model developed by us work properly in describing solvent induced frequency shift as well as calculating fluctuation amplitude of a variety of IR probe frequencies in liquid water. For MbCO protein system, the vibrational substates associated with different conformations of CO bound Myoglobin were investigated performing MD simulation studies for the wild-type and the double mutant. The numerically

simulated IR and 2D IR spectra for MbCO mutant are plotted in figure 1. Comparing to experimentally measured IR and 2D IR spectra for various IR probes, it is shown that this theoretical method can be successfully used in reproducing the protein vibrational spectra and extracting critical

information on protein structure and dynamics with the vibrational analysis.

Acknowledgement(s) This work was supported from Korea University Grant and NRF fund (Grant No.: 2014063491 and 2014044452).

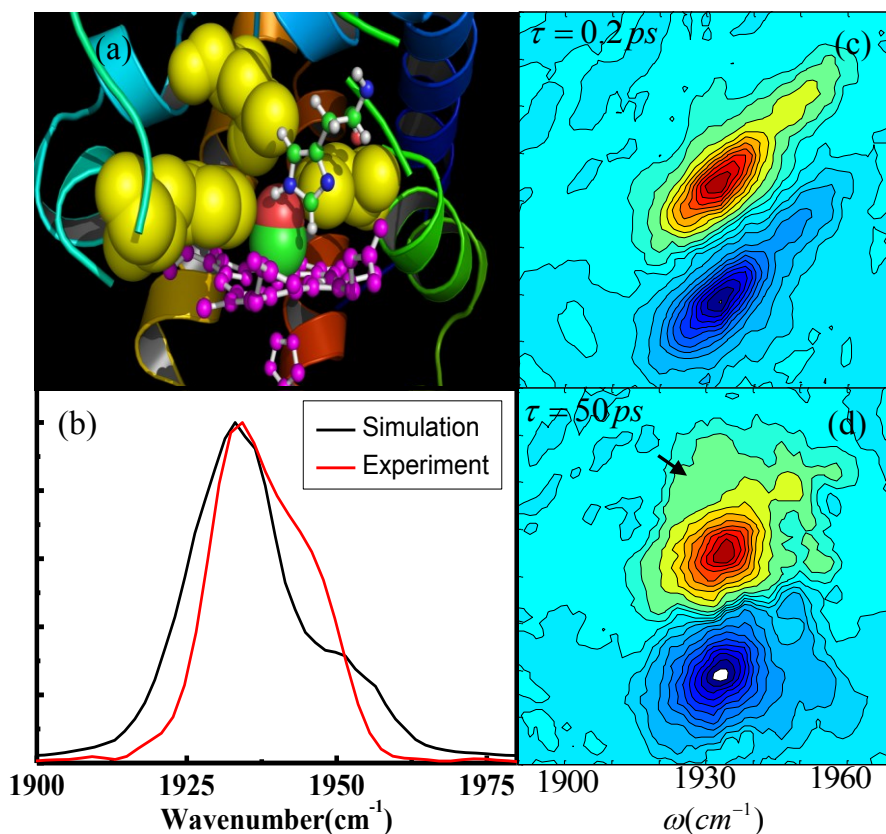


Figure 1. Snap shot structure of active site (a), simulated IR spectrum in (b), and 2D IR spectrum in (c) and (d) of the double mutant MbCO. The arrow represents growth of cross peak in the 2D IR spectrum.

References

- ¹ Jeon J., Yang S., Choi J.-H., Cho M. (2009), *Acc. Chem. Res.*, 42, 1280-1289.
- ² Choi J.-H., Oh K.-I., Cho M., (2008), *J. Chem. Phys.*, 129, 174512.
- ³ Choi J.-H., Raleigh D., Cho M., (2011) *J. Phys. Chem. Lett.* 2, 2158.
- ⁴ Choi J.-H., Kwak K.-W., Cho M., (2013) *J. Phys. Chem. B* 117, 15462.

The C-O vibrational frequency as a measure of the protein electric field in the heme pocket of carbonmonoxy heme proteins

Solomon S. Stavrov

Sackler Institute of Molecular Medicine, Department of Human Molecular Genetics and Biochemistry, Sackler Faculty of Medicine, Tel Aviv University, Tel Aviv, Israel

Keywords: protein dynamics, myoglobin, quantum chemistry

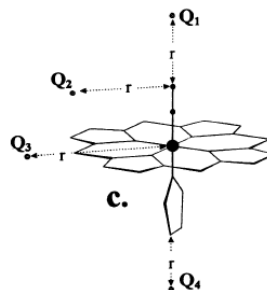
It is known that protein electric field (PEF) strongly affects chemical reactions taking part in the protein active center, see for example¹. In carbonmonoxy heme proteins (HPs) PEF was shown to strongly affect vibrational frequency of carbon monoxide molecule coordinated by the heme iron of HPs (ν_{CO}) both experimentally^{2,3} and theoretically^{4,5}. The same PEF was shown to affect affinity of HPs⁶ to different ligands, this result manifesting essential contribution of PEF into mechanism of functioning of heme proteins.

Dynamics of PEF stems from motion of amino acids, forming the heme pocket. Therefore, study of temporal dependence of ν_{CO} can provide the researcher with very specific information about the protein dynamics. This dependence was studied by using ultrafast two-dimensional infrared vibrational echo spectroscopy⁷. To interpret the experimental results it was assumed that ν_{CO} is controlled by the Stark-effect and linearly depends on the electric field on CO⁸. However, this approach failed to describe the protein dynamics of carbonmonoxy myoglobin^{9,10}.

On the other hand, it was shown earlier, that major contribution to ν_{CO} stems from the electron density transfer to the anti-bonding $2\pi^*$ orbital of CO^{4,5}.

In works^{4,5} the effect of different charges Q_1 , Q_2 , Q_3 and Q_4 located at different positions (see Scheme 1) on ν_{CO} was computed. The results of these studies

are used to check if the dependence of ν_{CO} on PEF can be described in the frameworks of Stark effect.



Scheme 1. Schematic representation the carbonmonoxy heme complex with different charges Q_i .

The results showed that in cases Q_2 and Q_3 the ν_{CO} dependence on r and charge cannot be described in terms of the Stark-effect. Changes in the positions and magnitudes of axial charges Q_1 and Q_4 linearly depend on the electric field on CO, however the coefficients of the linear dependence in cases of Q_1 and Q_4 are very different. It follows from these results that the Stark-effect approach to the problem of the field dependence of ν_{CO} is limited to the case of axial charges, and the coefficients of the linear dependence are very different for charges located on different sides of the porphyrin ring. To study such a dependence one has to use quantum chemical approach.

This approach is used to study effect of different sub-structures¹¹ of the distal

histidine observed in X-ray studies (see Fig. 1) on ν_{CO} . It is shown that ν_{CO} is very sensitive to the distal environment, and, in particular, the observed different X-ray sub-

structures correspond to the A_0 , A_1 , and A_3 conformational substates of the protein

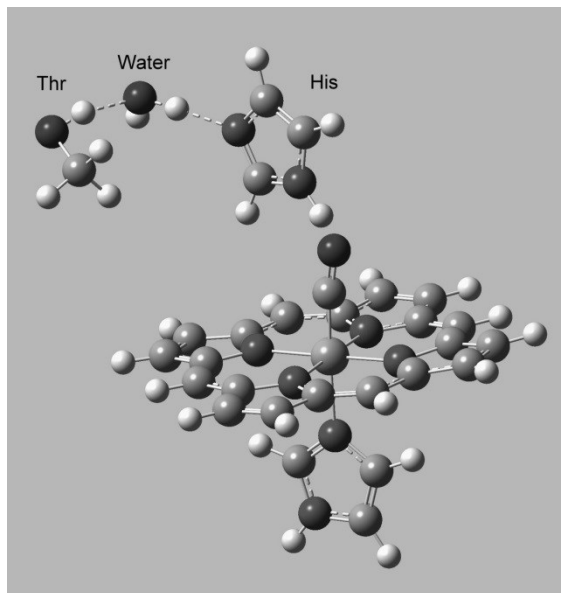


Figure 1. Active center of carbonmonoxy myoglobin.

¹ Fried, S. D., Bagchi, S., Boxer, S. G. (2014), *Science*, *346*, 1510.

² Park, K. D., Guo, K., Adebodun, F., Chiu, M. L., Sligar, S. G., Oldfield, E. (1991), *Biochemistry*, *30*, 2333.

³ Li, X. Y., Spiro, T. G. (1988), *J. Am. Chem. Soc.*, *110*, 6024.

⁴ Kushkuley, B., Stavrov, S. S. (1996), *Biophys. J.*, *70*, 1214.

⁵ Kushkuley, B., Stavrov, S. S. (1997), *Biophys. J.*, *72*, 899.

⁶ Phillips, G. N., Teodoro, M. L., Li, T. S., Smith, B., Olson, J. S. (1999), *J. Phys. Chem. B*, *103*, 8817.

⁷ Thielges, M. C., Fayer, M. D. (2012), *Acc. Chem. Res.*, *45*, 1866.

⁸ Gottfried, D. S., Stocker, J. W., Boxer, S. G. (1991), *Biochim. Biophys. Acta*, *1059*, 63.

⁹ Merchant, K. A., Noid, W. G., Thompson, D. E., Akiyama, R., Loring, R. F., Fayer, M. D. (2003), *J. Phys. Chem. B*, *107*, 4.

¹⁰ Finkelstein, I. J., Goj, A., McClain, B. L., Massari, A. M., Merchant, K. A., Loring, R. F., Fayer, M. D. (2005), *J. Phys. Chem. B*, *109*, 16959.

¹¹ Vojtechovsky, J., Chu, K., Berendzen, J., Sweet, R. M., Schlichting, I. (1999), *Biophys. J.*, *77*, 2153.

Investigating SERS particles with integrated correlative Raman electron microscopy.

F.J. Timmermans¹, A.T.M. Lenferink¹, H.A.G.M. van Wolferen², C. Otto¹

¹ University of Twente, Medical Cell BioPhysics, Drienerlolaan 5, 7522 NB, Enschede, the Netherlands

²University of Twente, MESA+, Drienerlolaan 5, 7522 NB, Enschede, the Netherlands

Keywords: Integrated Correlative light and electron microscopy (iCLEM), Raman microscopy, SERS.

We present a system employing an integrated commercial Raman microscope¹ in a dual beam Focused Ion Beam – Scanning Electron Microscope (FIB - SEM). Figure 1 shows the integrated components in the FIB - SEM chamber. Sample analysis is performed by high resolution morphological SEM imaging and correlative 3D chemical specific Raman microscopy. The combination of FIB micromachining and Raman microscopy enables further analysis after material processing, in which material deformations and structural or crystal defects can be detected.

An example study to the use of Raman spectroscopy for the analysis of FIB induced damage has been performed. Figure 2 shows a pattern that has been milled in a Silicon substrate. For the corresponding Raman analysis the first order Silicon peak has analyzed. The spectral full width at half maximum (FWHM), peak position and intensity of this peak have been recovered and are shown in the images.

The system enables new workflow strategies through fast localization with SEM of regions of interest to be analysed with Raman microscopy. This makes it an ideal system for Raman analysis of nanometer to sub-micrometer particles. SEM enables the fast localization and identification of sub-diffraction particles,

after which spectral analysis of these particles is performed. This strategy is very promising for the analysis of SERS active particles and structures. The SEM can be used to locate plasmonic nanoparticles of different sizes and shapes, and single particles or clusters. This enables an accurate study of the effect of these parameters on the SERS signal strength. Furthermore the stability of the signal and repeatability for multiple SERS particles can be verified using this system.

Results on the enhancement factor are verified and experiments are planned using discrete dipole approximation scattering (DDSCAT) package. Discrete dipole approximation (DDA) enables the computation of radiation scattering and near field strength of particles of arbitrary shape. The combination of near field calculations and the ability to locate clusters of varying sizes offers the opportunity to investigate signal strength based on cluster size. Figure 3 shows a SEM image of a three particle cluster, the calculated near field strength, and recorded Raman cluster image.

This research is financially supported by the STW (Stichting voor de Technische Wetenschappen), HybriScan Technologies B.V. and MESA+ Institute for Nanotechnology.

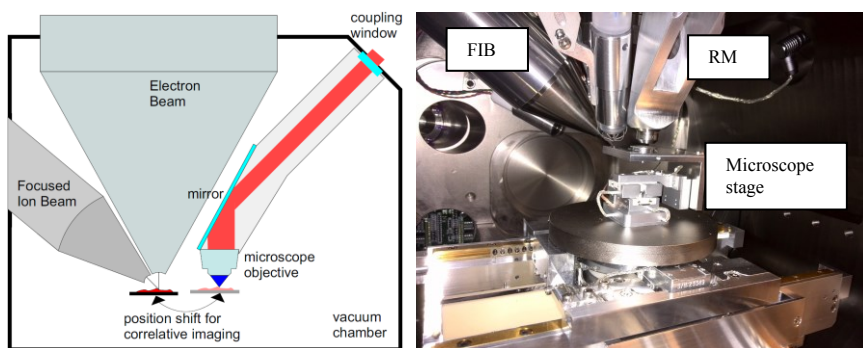


Figure 1. (Left) Schematic of the integrated Raman microscope in the Focused Ion Beam – Scanning Electron Microscope. (Right) Picture of the optical microscope objective and translation stage mounted in the system chamber.

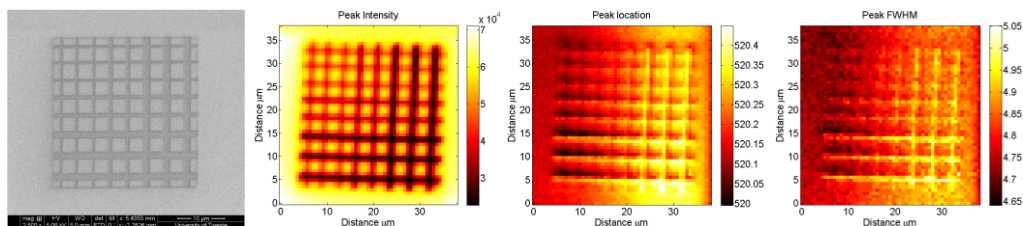


Figure 2. (A) SEM image of FIB patterned Si substrate. (B) Raman amplitude of the 1st order Si peak. (C) retrieved spectral location of the 1st order Si peak. (D) retrieved FWHM of the 1st order Si peak.

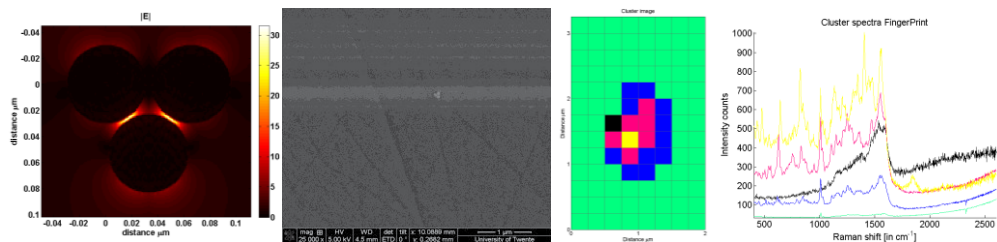


Figure 3. Sample containing 3 gold beads of 60 nm diameter. (A) DDA calculation of the near field enhancement at vertical polarization excitation. (B) SEM image of the gold nanoparticles. (C) cluster image of Raman microscopic data. (D) Average spectra corresponding to the Raman clusters.

¹ <http://www.hybriscan.com/products/hybrid-microscopes>

FTIR Hyperspectral Imaging for Rapid Identification of Pathogenic Microorganisms

Peter Lasch

Robert Koch-Institut, ZBS 6 “*Proteomics and Spectroscopy*” 13353 Berlin, Nordufer 20, Germany

Keywords: IR Imaging, Microorganisms, Identification, Neural Networks

The past decade has witnessed substantial progress towards the application of infrared (IR) microspectroscopic imaging as an useful diagnostic tool for characterization of microbial, cytological and histological specimens. In this presentation the application of mid-IR hyperspectral imaging for rapid, objective and cost effective diagnosis of pathogenic microorganisms will be illustrated

The proposed method involves a relatively short cultivation step of microorganisms under standardized conditions, transfer of the material onto suitable IR windows by a replica method, IR hyperspectral imaging measurements and image segmentation analysis by means of artificial neural networks (ANNs).

For this purpose, aliquots of the initial microbial cell suspension are sufficiently diluted to guarantee single colony growth on solid agar plates. After an incubation period of 6-8 hours microbial microcolonies have typically diameters between 30 and 150 μm . Microcolony imprints can be subsequently produced by using a specifically developed stamping device. The stamping technique allows spatially accurate transfer of the microcolonies' upper cell layers onto IR windows, usually CaF_2 , glued in specific Teflon® holders. The stamping device is equipped with a plastic hose that prevents twisting or lateral displacement during stamping. Using this device, stamping is carried out by gently lowering the holder

onto the agar plates. After stamping, the microcolony imprints are allowed to dry and are then transferred to the IR imaging device. Dried sample spots are measured operator-controlled by means of video techniques for specifying regions of interest and for documentation purposes. FTIR hyperspectral imaging measurements are carried out by employing an Agilent Cary 620 focal plane array (FPA) microspectroscopic imaging system (Agilent Technologies, Santa Clara, USA) which is equipped with a 128×128 multi-element MCT (HgCdTe) FPA detector. The pixel size of each single detector element is about $5.5 \times 5.5 \mu\text{m}^2$ giving an effective lateral spatial resolution of approximately $12 \mu\text{m}$ at 1000 cm^{-1} . Spectral data analysis involved application of supervised ANN models. These models are required to be trained and validated in an initial teaching phase by means of labeled subsets of teaching spectra. In the test phase false-color ANN segmentation images are obtained by converting the ANN output functions to color values and combining them with the available spatial information: ANN imaging involves plotting of colored pixels at the spatial coordinates at which the individual pixel spectra were measured. The resulting segmentation maps thus encode the spatial distribution of taxon-specific spectral patterns.

An example of how the IR microspectroscopic imaging technique can be

used in combination with the ANN image segmentation method is given in Figure 1. The left column of this figure shows microphotographs of stamping imprints obtained from a mixed culture of *Escherichia coli*, *Bacillus subtilis* and *Staphylococcus aureus*. The right column of Figure 1 illustrates the results of ANN image segmentation. Blue colored regions (3) illustrate the presence of spectra with the typical features of *St. aureus*, while red

areas (1) encode regions where spectra of *E. coli* are found. Black colored pixels denote regions with unclassifiable spectra. Currently we are systematically examining much larger spectral data sets to prove the hypothesis that spectra obtained from microbial microcolonies can be used to differentiate, classify and identify very small amounts of microorganisms at the genus, species and at the strain level.

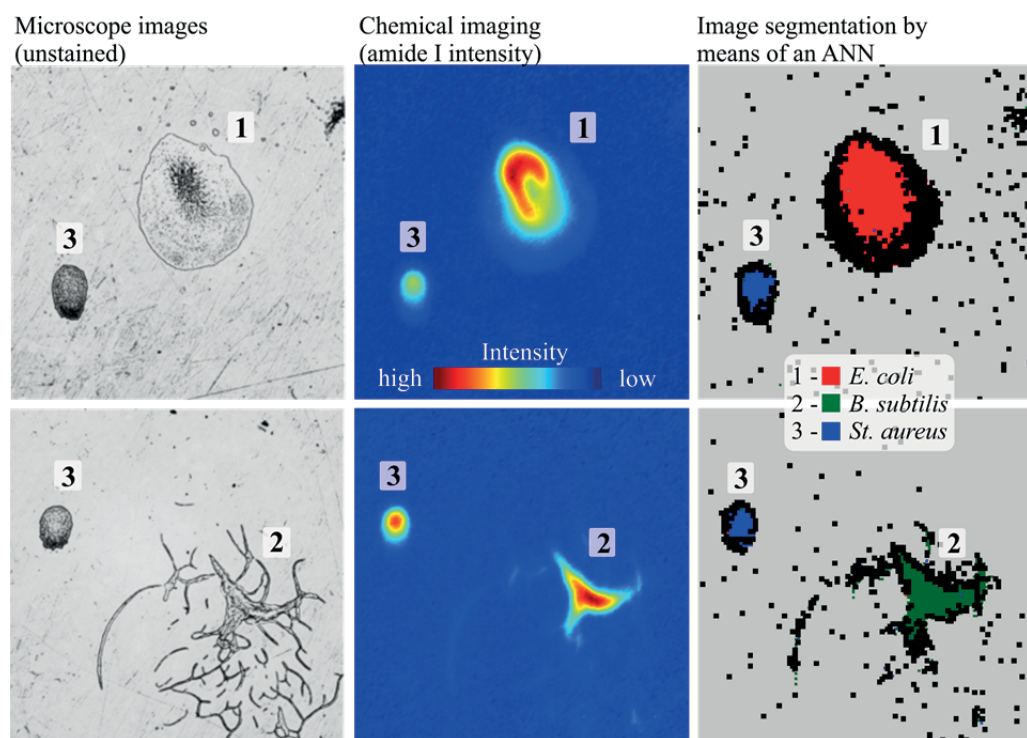


Figure 1. Characterization of microcolony imprints using mid-IR microspectroscopic imaging data collected by means of a 128×128 FPA FTIR imaging system, chemical imaging and a segmentation approach based on artificial neural network (ANN) analysis.

Left column: light microscopy images of microcolony imprints from mixed cultures of *Escherichia coli*, *Bacillus subtilis* and *Staphylococcus aureus*. Area size: 700×700 μm

Central column: chemical images obtained from FPA measurements on the basis of the amide I band intensity in the spectral region between 1620 and 1690 cm⁻¹.

Right column: An IR image segmentation approach using analysis of IR microspectral fingerprints by an ANN.

**Solute-Solvent and Pigment-Protein Interactions in Carotenoids.
A Combined Resonance Raman, step-scan FTIR, DFT/COSMO and
QM/MM Study of Peridinin**

Alberto Mezzetti^{1,2}, Elizabeth Kish², Daniele Bovi³, Riccardo Spezia⁴, Bruno Robert²,
Rodolphe Vuilleumier⁵, Marie-Pierre Gageot⁴, Leonardo Guidoni³.

¹Laboratoire Spectrochimie Infrarouge et Raman LASIR, UMR 8516, Univ. Lille, France

²Service Bioénergétique Biologie Structurale et Mécanismes, UMR 8221, CEA-Saclay, France

³Dept. of Physics, University of Rome « La Sapienza », Italy ;

⁴Laboratoire Analyse Modélisation pour la Biologie et l'Environnement, Univ. Evry, France ;

⁵Dept. Chemistry, Ecole Normale Supérieure et Université Pierre et Marie Curie, Paris, France

Keywords: Peridinin; Step-scan FTIR; QM/MM; Resonance Raman; carotenoids

Peridinin (Per) is the main light-harvesting carotenoid found in dinoflagellates, and shows peculiar photophysical properties, which are strongly dependent on the protein microenvironment. We used Resonance Raman and time-resolved step-scan FTIR difference spectroscopy (two techniques that can give precise information on pigment-protein and solute-solvent interactions, and on the mechanism of photochemical reactions at an atomic scale^{1,2}), coupled to QM/MM and Conductor-Like Screening Model (COSMO) DFT calculations, to investigate how Per interacts with its environment in Peridinin-Chlorophyll-a-Proteins (PCPs) and in several organic solvents with different physicochemical properties (which were used as prototypical environments^{3,4}). Thanks to effective normal mode analysis, we were able to assign the Raman and IR bands, and to clarify the effect of the solvent on band shifts. In particular, experiments in organic solvents showed that the stretching frequency of the lactonic C=O of Per is extremely sensitive to its surrounding environment due to three key factors:

I) H-bonding dynamics between hydrogen-bond donor solvents and the lactonic C=O moiety³ ;

II) the effect of the dielectric constant of the solvent³ ;

III) a Fermi resonance effect between the C=O and a C-H wagging mode⁴.

The lactonic C=O becomes therefore a tool to distinguish among different Pers in PCPs (where up to eight Pers are simultaneously present⁵). This made it possible to follow more deeply PCP photophysics, in particular the process of triplet formation. This is very difficult using conventional time-resolved UV-vis spectroscopy, given the overlap of electronic bands. Using time-res. step-scan FTIR spectroscopy, we found evidence that at 100 K the triplet is localized on Per 612 and/or Per 622 (whose C=O group is in a polar but aprotic environment^{3,4,6}). This result is of particular relevance, as previous step-scan FTIR studies had suggested that at 298 K the triplet state is delocalized over the Chlorophyll molecules present in PCP⁷. Several marker bands for Per in its normal and excited triplet state were also identified in PCP, and their relevance in the study of PCP photophysics have been discussed⁸.

From a methodological point of view, this work represents an interesting case study for the following reasons:

A) The interplay between the different techniques (Resonance Raman, FTIR, step-scan differential FTIR, QM/MM, DFT/COSMO) has been demonstrated;

B) Specific effects intrinsically related to the solute-solvent interaction dynamics (e.g. the

formation and disruption of hydrogen bonds) have been rationalized thanks to the QM/MM molecular dynamics simulations³; C) The extreme sensitivity to the environment polarity of the Fermi resonance coupling between the C=O stretching and a C-H wagging mode can be effectively exploited to discriminate between different Pers in proteins and solvents⁴; D) The effect of undesired heating effect and sample integrity during step-scan FTIR experiments has been investigated^{5,6}. This effect has been largely underestimated in the

literature and can therefore help to rationalize previously obtained results. The results will be discussed in the framework of the study of light-harvesting and photoprotective mechanism in photosynthesis (especially through time-resolved FTIR, ultrafast IR and Resonance Raman spectroscopy), as well as in the framework of the technological applications of Per and PCPs⁵ (and refs therein). Preliminary results on the carotenoprotein OCP (recently characterized by static differential FTIR⁹) will also be presented.

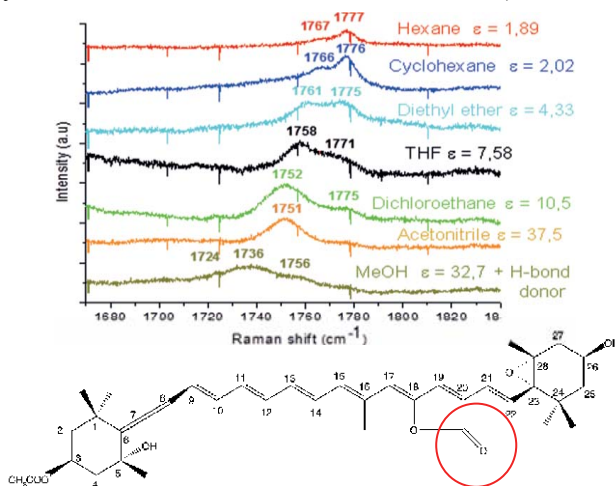


Figure 1. Resonance Raman spectra of Per in various solvents. The effects of I) H-bond formation; II) solvent polarity; III) Fermi resonance determine the position and the shape of the C=O stretching band. These effects have been rationalized by QM/MM and DFT calculations

- ¹ Gall A., Pascal AA, Robert B. (2015) *Biochimica Biophysica Acta Bioenergetics* 1847, 12-18
- ² Radu I., Schlegler M., Bolwien C., Heberle J. (2009) *Photochem. Photobiol. Sci.* 8, 1517-28.
- ³ Bovi D, Mezzetti A, Vuilleumier R, Gaigeot MP, Chazallon B, Spezia R, Guidoni L. (2011) *Physical Chemistry Chemical Physics*. 13, 20954-64.
- ⁴ Kish E., Mendes Pinto MM., Bovi D., Basire M., Guidoni L., Vuilleumier R., Robert B., Spezia R., Mezzetti A. (2014) *Journal of Physical Chemistry B*. 118, 5873-81.
- ⁵ Carbonera D., Di Valentin M., Spezia R., Mezzetti A. (2014) *Current Protein Peptide Science* 15, 332-50.
- ⁶ Mezzetti, A., Spezia, R. (2008) *Spectroscopy*, 22, 235-250.
- ⁷ Alexandre MT., Lühns DC., van Stokkum IH., Hiller R., Groot ML., Kennis JT., van Grondelle R. (2007) *Biophysical Journal* . 93, 2118-28.
- ⁸ Mezzetti A., Kish E., Robert, B., Spezia, R, *Journal of Molecular Structure* (2015) in press.
- ⁹ Wilson A, Gwizdala M, Mezzetti A, Alexandre M, Kerfeld CA, Kirilovsky D. (2012) *Plant Cell*. 24, 1972-83.

An infrared sensor analysing label-free the secondary structure of the Abeta peptide in presence of complex fluids

Andreas Nabers, Julian Ollesch, Jonas Schartner, Carsten Kötting, Klaus Gerwert

Department of Biophysics, PURE (Protein research Unit within Europe), Ruhr-University Bochum, Universitätsstraße 10, 44780 Bochum, , Germany

Keywords: Amyloid-beta, neurodegeneration, label-free ATR-FTIR spectroscopy, complex fluid, biosensor.

Protein misfolding and aggregation can be associated with a range of degenerative diseases. Especially in neurodegenerative diseases like Alzheimer's (AD) or Parkinson disease (PD), a secondary structure change of specific biomarker candidates into beta-sheet enriched conformations occurs. According to the amyloid cascade hypothesis, an early and critical event in the onset of AD is the accumulation of Amyloid-beta (Abeta) peptides in the central nervous system. In human cerebrospinal fluid (CSF), five different carboxyterminal variants of Abeta are present with a total physiological concentration of approximately 15 ng/ml. Thus, Abeta can be used as diagnostic marker for an early state of the disease. Especially the Abeta42 species indicates a high propensity to aggregate including a structural transition to conformations enriched in beta-sheet secondary structures.

To determine such secondary structure changes, Fourier-transform infrared (FTIR) spectroscopy has been proven as a powerful technique. In particular, time-resolved FTIR-difference-spectroscopy demonstrated the excellent sensitivity of this technique. Using the attenuated total reflection (ATR) technique, an evanescent IR wave invades only few micrometers into the sample layers on the surface of the internal reflection element (IRE).

For the secondary structure analysis of a specific protein within a complex body

fluid, the protein of interest has to be selectively and specifically bound to the surface.

Here, this was achieved with an antibody-functionalized internal reflection element.¹ The IRE was mounted within a customized flow-through-ATR-setup. The flow-through cuvette is covered with a quartz-window, which allows parallel control-measurements by fluorescence spectroscopy.

However, the performance of a fast and marker-free ATR-FTIR set-up for the secondary structure analysis of Abeta peptides in the presence of a biological fluid with Abeta concentrations close to those found in CSF was presented. The successful capture of Abeta peptides was verified by parallel fluorescence measurements. 1 ng/ml Abeta, which is clearly below the physiological concentration of 15 ng/ml in CSF, was detected with an excellent signal-to-noise ratio. The secondary structure analysis of Abeta selected from neuronal cell-culture medium provided a similar secondary structure as the monomeric synthetic Abeta peptide under the given measurement conditions.

In sum, the ATR-FTIR-spectroscopic set-up might become a new diagnostic tool to identify Alzheimer's disease at an early state.

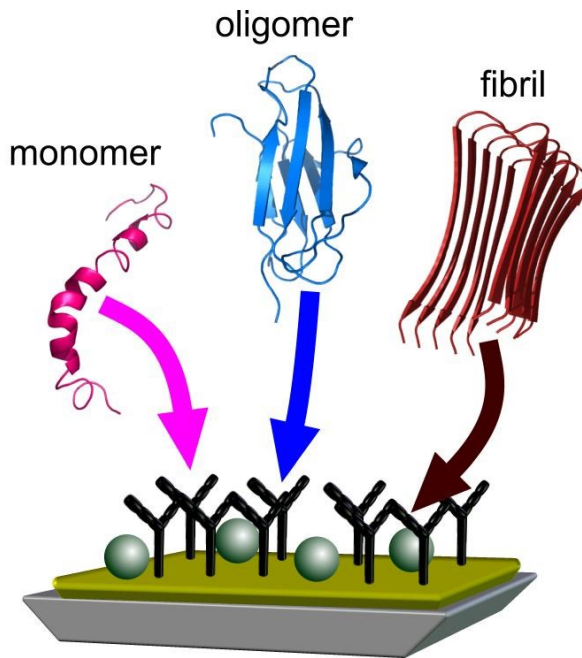


Figure 1. Antibody mediated protein immobilization of different Abeta conformations on the immuno-ATR-FTIR-biosensor from a complex fluid

¹ Nabers A., Ollesch J., Schartner J., Kötting C., Haußmann U., Klafki H., Wiltfang J., Gerwert K., (2015). *Journal of Biophotonics*, accepted.

PURE is financed by the state of North Rhine-Westfalia

Using IR and Raman spectra to explain the catalytic activity of the Fe(II)/Fe(III) pair toward the cleavage of peptide bonds

Felipe G. Camacho and Wagner A. Alves

Departamento de Química Inorgânica, Universidade Federal do Rio de Janeiro, 21941-909, Rio de Janeiro, Brazil

Keywords: IR spectra, Raman spectra, Iron (II), Iron (III), Formamide.

Cleavage of peptides and proteins is undoubtedly a subject of special interest in chemistry and biology. In this context, metal ions have an important role to promote cleavage of the polypeptide backbone under non-denaturing conditions of temperature and pH, since they activate the peptide bond whose process occurs by either a hydrolytic or an oxidative pathway.¹ Our research group has demonstrated that the vibrational spectral pattern of some divalent transition metal ions is always the same and leads to the stabilization of an ionic amide structure, which is the active species for catalysis.²⁻⁴ Here, we present IR and Raman data for solutions of a protic amide containing Fe(II) and Fe(III) salts in order to distinguish the spectral pattern as a function of their oxidation states. The motivation for the choice of the mentioned pair is due to Fe(II)-catalyzed oxidative cleavage of polypeptides, where the formation of Fe(III) requires the addition of a reducing agent to recycle the whole process.⁵

Formamide (FA) has been used as the simplest model to describe the peptide bond and its liquid structure is often considered as a mixture of monomers and dimers, which are identified in a vibrational spectrum by the respective bands at ~ 1690 and ~ 1675 cm^{-1} at the ν_{CO} region. As a Fe(II) salt is added, a new band at 1645 cm^{-1} is observed in the IR spectra and its intensity is dependent on the salt composition. In the 1400 - 1300 cm^{-1} range, two new bands are

seen at 1380 and 1340 cm^{-1} besides the original FA bands at 1390 (δ_{CH}) and 1309 cm^{-1} (ν_{CN}). The downshift of the ν_{CO} mode and the upshift of the ν_{CN} vibration, in the presence of Fe(II), are in excellent agreement with those observed for other divalent ions and are assigned to FA molecules coordinated to the metal ion through the O atom, which is the only active site of an ionic FA structure.²⁻⁴

In contrast to the ferrous ion, the addition of Fe(III) to FA causes upshifts of both ν_{CO} and ν_{CN} modes, as can be seen in Fig. 1. Particularly, the new bands at 1747 and 1349 cm^{-1} have their intensities increased as the salt concentration goes from 0.5 to 1.5 molal, suggesting that they are due to FA molecules coordinated to Fe(III), but in a way different from that observed for Fe(II). In fact, the observed upshifts lead to stabilization of a neutral FA structure, in which both O and N atoms may be involved in the coordination process.⁶ Other new band at 1376 cm^{-1} can be also seen, but it corresponds to the δ_{CH} vibration of coordinated FA.

The present investigation reveals that the spectral pattern of an FA solution with Fe(II) is fully distinct from that exhibited by Fe(III). Hence, both ionic and neutral amide structures may also coexist in oxidative cleavage processes of polypeptides and proteins, where the Fe(II)/Fe(III) pair is present. We believe that the similarity in the relative size of some divalent transition

metal ions is the explanation for the stabilization of an ionic amide structure, which is the active species for catalysis. All

these findings are very well corroborated by biological studies and ensure our vibrational predictions reported so far.

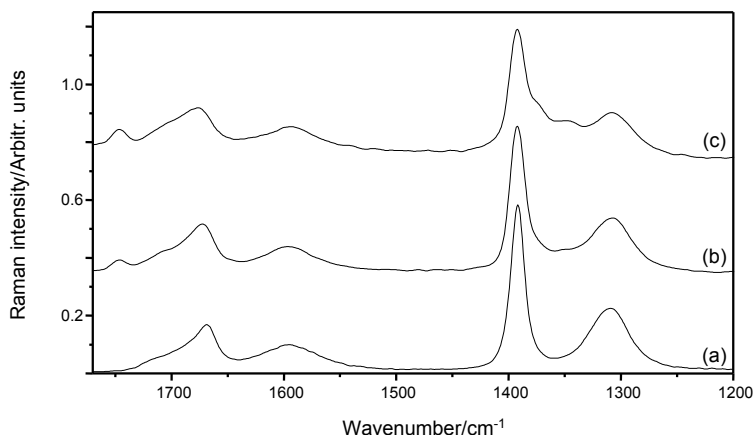


Figure 1. Raman spectra of pure liquid formamide (FA) and its Fe(III) solutions in the 1770 – 1200 cm^{-1} region. Molal concentrations: (a) solvent; (b) 0.5; (c) 1.5.

- ¹ Grant K.B. & Kassai M. (2006), *Current Organic Chemistry*, 10, 1035.
- ² Freire A.I. & Alves W.A. (2012), *Spectrochimica Acta A*, 89, 259.
- ³ Silva E.F. & Alves W.A. (2012), *Vibrational Spectroscopy*, 62, 264.
- ⁴ Freire A.I. & Alves W.A. (2014), *Vibrational Spectroscopy*, 73, 73.
- ⁵ Soundar S. & Colman R.F. (1993), *Journal of Biological Chemistry*, 268, 5264.
- ⁶ Campos T.B.C., Silva E.F. & Alves W.A. (2013), *Vibrational Spectroscopy*, 65, 24.

A Vibrational Spectroscopic Approach to the Human Mind: Expanding the Applications of Biomedical Spectroscopy

Henry Horst Mantsch

Professor Emeritus, Ottawa, Canada

Today vibrational spectroscopy is solidly entrenched as a tool in medicine, its applications ranging from the spectroscopy of body fluids, spectral cyto- and histopathology to the analysis of spectral imaging maps obtained from cells, tissues or entire body parts. However one part of the body that has escaped such vibrational spectroscopic explorations is the human mind. And here I don't mean the physical brain and the various diseases that can afflict it such as Alzheimer's disease, but I mean that part of us humans which controls our consciousness and self-awareness and which makes each of us a unique individual. This immediately raises the question of the nature of the mind, clearly a more philosophical question than a medical one. Countless minds, from Plato to present day spiritual healers, have wrestled with this question and libraries the world over are filled with works on this subject.

In keeping with the title of this conference, *Advances in Vibrational Spectroscopy*, I intend to talk about such a topic, namely "a vibrational spectroscopic approach to the human mind". My initial interest in this topic was aroused by none other than Werner Heisenberg. In 1965 when I arrived in Munich as a young postdoctoral Humboldt Fellow, Heisenberg was the long standing President of the Alexander von Humboldt Foundation, a role which he took seriously and not in name only. Like many other great physicists he had become very interested in metaphysics later in life. I admit that at the time his book *Physics and Philosophy: The Revolution in*

Modern Science captivated me greatly, and in particular his statement therein: "We have to remember that what we observe is not nature itself, but nature exposed to our method of questioning". Every so often Heisenberg convened small groups of Humboldt Fellows to debate interdisciplinary topics, a favourite being the *Mind-Body* theme. These round-table discussions, sometimes over pretzels and beer, were well attended by a dynamic mix of physical and social scientists, MDs and even theologians. The deliberations were very stimulating, yet always ended in even more questions ...and of course more uncertainty. Heisenberg was an ardent Platonist, using the German word "Geist" (best translated as spirit or mind) which he regarded as being separate from the physical body. After leaving Germany and plunging into my professional life in Canada, my recollections of these animating discussions lay dormant and resurfaced only now, some 50 years later. Certainly half a century of progress in science, and more specifically in vibrational spectroscopy, should allow us to revisit this topic.

At this point we must review what is known about the human mind. The literature is full of anecdotal and circumstantial testimonies as to its nature however there is disappointingly few hard data or facts. Artists often find it easier to deal with abstract notions and constructs, and thus in the visual arts the mind, spirit or soul is often depicted as a symbolic light that leaves the dying body. Many in the medical profession consider that the brain fully

accounts for the mind and that the mind is simply a matter of brain function. I however prefer to follow Plato, Heisenberg and many others, thinking about the human mind as an immaterial construct or process, involving some form of electromagnetic or hitherto unknown energy (after all, physicists still don't know what dark energy is, although they readily admit it exists).

We certainly know more about the physical brain. As a corporeal object the brain generates measurable output via EEG, the electroencephalographic potentials emitted by the brain, the so called "*brain waves*". These electromagnetic waves, which occur in the frequency range below 100 Hz, are associated with specific mental arousal levels and a set of distinctive behavioural activities. It is not my intent to go into details here, as I am not a neuroscientist and certainly am not qualified to interpret EEGs or brain waves. However as a vibrational spectroscopist dealing regularly with electromagnetic waves, I cannot ignore the fact that brain waves have been shown to cause physiological effects. For instance, neuroscience experiments have shown that exposure to 12 Hz radiation stimulates the production of serotonin, a well-known mood elevation agent. With so many people taking antidepressant drugs today, would it be too far-fetched to contemplate the possibility of using molecular vibrations to diagnose and/or treat psychosomatic disorders or emotional brain diseases?

I suppose we have all experienced the feeling casually known as "*having good vibrations*" when encountering another person. Is this only a figure of speech or could it suggest a relationship between our brain and the molecular vibrations so familiar to those practising vibrational spectroscopy? It might not be unreasonable to assume that there exists a connection between the physical brain and what we

perceive as the non-physical mind, with the brain being the receiver and emitter, much like a radio or TV set. If we were to continue this analogy, then the mind could be thought of as representing the content of these audio or video messages. Certainly the air around us is filled with music and images which we cannot perceive unless they are detected and amplified by appropriate external devices. Another thought-provoking analogy is that of the brain as a computer and the mind as the programmer. Yet others think of the human brain as a kind of universal "transformer station" that converts the energy of the mind to frequencies suitable for us to use. Perhaps such analogies are oversimplified, but they provide a good basis for pondering the brain-mind issue.

So let us return to the matter at hand, namely brain waves. From a pragmatic point of view the challenge lies in finding a link between brain waves, which occur in the range of 1-100 Hz and the molecular vibrations, which occur in the frequency range around 10^{12} Hz. Such a link is not unimaginable since both the brain waves and the molecular vibrations are part of the same electromagnetic spectrum, being separated only by about 40 octaves. Thus, if we were to take the brain wave at 12 Hz that is involved in the release of serotonin, we will find its 40th octave at 13.2 THz or 440 cm^{-1} which falls in the mid-IR/Raman range. What is needed at this point is a modality to convert brain waves into molecular vibrations and vice versa. To accomplish such a conversion, the waves or frequencies would have to be transduced 40 octaves up or down the continuum of the electromagnetic spectrum, something conceivable in theory, but not yet achieved in practice. By exploiting such bio-harmonic resonances we should then be able to detect brain waves in the vibrational spectrum (which is of diagnostic value) and/or use

discrete vibrational frequencies to affect and manipulate brain waves for therapeutic purposes.

The vision of harnessing vibrational resonances in clinical neurophysiology might seem a dream today, but we must not let present day limitations pose an insurmountable challenge to reaching this frontier. Over the years vibrational biospectroscopy has been enriched by numerous novel developments such as Resonance Raman-, Tip Enhanced Raman-, Stimulated Raman Spectroscopy or Surface Enhanced Raman/IR Spectroscopy, to name only a few, all providing *tricks* to overcome various limitations of conventional

vibrational spectroscopy. There are abundant examples of former dreams becoming reality, from those of Jules Verne to that of overcoming the diffraction limit of light as recognized by the latest Nobel Prize in Chemistry.

Reflecting back on half a century of play in the sandbox labelled “*vibrational spectroscopy*” I urge the younger generation to make good use of the spectroscopic toys handed down to them and I challenge them to dare stepping outside the sandbox in order to further advance the applications of vibrational spectroscopy in the life sciences.

Monday

Tuesday

Wednesday

Thursday

Friday

Author Index



Snapshots of ultrafast dynamics in Neuroglobin captured by Femtosecond Stimulated Raman Scattering

Giovanni Batignani^{1,2}, Carino Ferrante², Emanuele Pontecorvo² Tullio Scopigno²

¹Department Chemical and Physical Sciences, University dell'Aquila, I-67100, L'Aquila, Italy

²Department of Physics, University "Sapienza", I-00185, Rome, Italy

*E-mail address: giovannibatignani@gmail.com

Keywords: ultrafast dynamics, Femtosecond Stimulated Raman Scattering, photoexcited Hemeproteins, intermediates states, vibrational relaxation.

Hemeproteins constitute a family present in all living organisms, revealing themselves to be extremely important for life and displaying a wide range of biological functions, related to their capability of binding small gaseous ligands like Oxygen or Amino acids like Histidine to a Ferrous ion.

The photoinduced dynamics of Hemeproteins show different concurring processes like conformational changes, bond breaking, energy redistribution (within the protein and to the solvent) and excited intermediates states. Discerning and characterizing all these processes is a matter of open debate and is of fundamental importance for the studies of these species, especially for understanding the physiological role of the proteins, whose function is as yet unknown.

Neuroglobin is one of the most recently discovered Hemes, so its role for human life is still elusive. Many attempts¹ to study Neuroglobin have been made by Transient Absorption (TA) and Time Resolved Resonance Raman (TR3) but none of these techniques have been capable of providing an unambiguous picture of the dynamics.

Transient absorption studies provide valuable information, but their lack of vibrational sensitivity makes the results subject to contrasting interpretations.

Specifically, the existence of short living intermediates on the way to the ground state has been hypothesized, as opposed to the direct decay from the reactive energy surface down to a cold ground state. On the other hand, TR3 is a vibrational spectroscopy, thus endowed with structural sensitivity, but it suffers from resolution limitations. If a sharp spectral resolution ($<15\text{cm}^{-1}$) is to be maintained, however, no further improvement of the time resolution ($<1\text{ps}$) is obtainable due to the Fourier Transform limit.

Femtosecond Stimulated Raman spectroscopy (FSRS) is a powerful method for studying ultrafast reaction dynamics, in which the simultaneous presence of a narrowband picosecond pulse (the Raman pulse) and a broadband femtosecond continuum (the probe pulse) stimulates vibrational Raman transitions over a wide frequency range². It represents an elegant way of providing an improved spectral and temporal resolution compared to time resolved spontaneous Raman or Transient Absorption. Indeed, using dispersed detection of the probe beam, spectral resolution is fundamentally limited by the vibrational dephasing time only. Nonetheless, the time trigger is only determined by the duration of the pulse initiating the macroscopic polarization in the sample and, of course, by the photochemical

pump. To explore the resonance enhancement in diverse biomolecules and under different conditions, we recently combined the principles of FSRS and TR3, developing a Femtosecond Stimulated Resonance Raman (FSRRS) setup³⁻⁴, with a broadly tunable Raman pulse.

We have applied Femtosecond Stimulated Resonance Raman Scattering (FSRRS) to the study of photoinduced dynamics in oxy and deoxy hexacoordinated Neuroglobin. Taking advantage of combined frequency resolution (10 cm^{-1}) and time precision (40 fs), combined with broad tunability of the Raman excitation, we have been able to unveil the details of the reaction pathway. These include the early stages following ligand dissociation of oxy-Neuroglobin, ascertaining the possible existence of short living intermediates, the

subsequent energy redistribution among different vibrational channels, and the underlying structural rearrangements.

FSRRS data suggest that the photoexcited oxy-Neuroglobin, once the ligand bond breaking is accomplished, evolves to a hot ground state photoproduct. Distinct signatures of anharmonicities are observed with structural sensitivity, evolving during the cooling process. In the specific case of the six coordinated deoxy Neuroglobin, we address the iron-histidine stretching to ascertain the possibility of a bond breaking event on either the proximal or distal side of the iron atom. Taken all together, these observations allow the drawing of a clear scenario for the photoinduced dynamics of Neuroglobin, rationalizing previous transient absorption results.

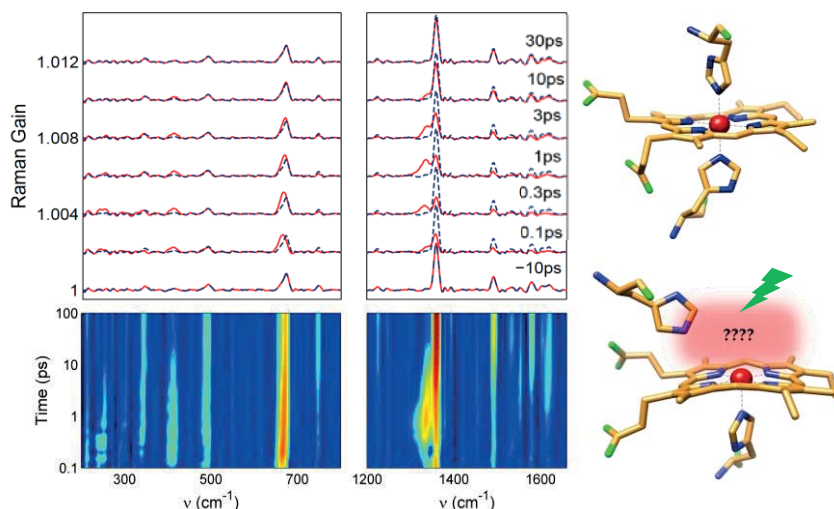


Figure 1. FSRRS data of photoexcited 6-coordinated deoxy Neuroglobin. The high spectral resolution combined with sub picosecond time precision reveals the sub-ps vibrational dynamics following photoexcitation.

¹ M. H. Vos, A. Battistoni, C. Lechaue, M. C. Marden, *et al*, "Ultrafast Heme-Residue Bond Formation in Six-Coordinate Heme Proteins: Implications for Functional Ligand Exchange", *Biochemistry*, 47, 5718 (2008).

Time-resolved Spectroscopy

TH606

- ² D. W. McCamant, P. Kukura, S. Yoon, and R. A. Mathies, “Femtosecond broadband stimulated Raman spectroscopy: apparatus and methods,” *Rev. Sci. Instrum.* 75, 4971-4980 (2004).
- ³ E. Pontecorvo, S.M. Kapetanaki, M. Badioli, D. Brida, M. Marangoni, G. Cerullo and T. Scopigno, “Femtosecond Stimulated Raman Spectrometer in the 320-520nm range”, *Optics Express*, 19, 1107 (2011).
- ⁴ E. Pontecorvo, C. Ferrante, C.G. Elles and T. Scopigno. “Spectrally tailored narrowband pulses for femtosecond stimulated Raman spectroscopy in the range 330nm-750nm”, *Optics Express*, 21, 6866-6872 (2013)

Monday

Tuesday

Wednesday

Thursday

Friday

Author Index



The reinvention of interleaved time-resolved FT-IR spectroscopy

Michael Jörger¹, Arno Simon¹ and Günter Zachmann¹

¹ Bruker Optik GmbH, Rudolf-Plank-Strasse 27, 76275 Ettlingen, Germany

Keywords: FT-IR, FTIR, time, resolved, step-scan.

Time-resolved FT-IR spectroscopy (TRS) is widely used e.g. to track the kinetics of single shot chemical reactions via Rapid-Scan¹⁻² or repeatable kinetics via the step-scan³⁻⁷ technique. Nevertheless both approaches, Rapid-Scan and Step-Scan, also imply limitations.

Depending on spectral resolution the Rapid-Scan technique is limited to a time resolution in the low millisecond range which is not always sufficient for typical applications of interest. For repetitive kinetics the step-scan technique can overcome these limitations and reach a time resolution down to the low nanosecond range. On the other hand step-scan makes less efficient use of the available measurement time since the necessary mirror repositioning requires interrupting data acquisition and increases the fraction of dead time.

Interleaved time-resolved FT-IR spectroscopy is a technique for a certain class of repetitive kinetics, using the measurement time much more efficiently than step-scan. The interferometer mirror is moving continuously and the zero-crossings of the internal HeNe laser are used to trigger the experiment. Data are not only acquired at the HeNe zero crossings (corresponding to $t=0$) but also at mirror positions in between, belonging to certain time delays Δt . Hence the system is continuously acquiring data and in principle a full series of time-resolved interferograms can be collected within one single scan.

It is worth mentioning that interleaved should not be confused with so-called stroboscopic FT-IR spectroscopy⁸ where the interferogram is in general decomposed into several sections, acquired in subsequent scans. Although the interleaved approach is not new⁹⁻¹⁰ it did so far never establish itself as widely accepted technique. A main reason for this might be the technical limitations of last millennium's FT-IR spectrometers: in those days electronics such as analog to digital converters as well as the required stability of scanning speed and software interfaces may not have completely met the requirements of high performance interleaved FT-IR spectroscopy.

In our contribution we will introduce the implementation of interleaved FTIR spectroscopy for modern Vertex series FT-IR spectrometers with state of the art electronics and interferometer technology. By means of time resolved emission spectra of an infrared LED (see fig. 1) we will demonstrate the performance and advantages of this "renewed" interleaved technique and compare it to step-scan as well as rapid-scan data.

Nevertheless this new generation of interleaved FT-IR spectroscopy shall not be understood as general replacement for the step-scan technique. Regarding flexibility due to its huge parameter space and its various powerful modifications such as AC coupled differential spectroscopy or modulation techniques, step-scan remains definitely state of the art. However for a certain class of repeatable experiments

interleaved FT-IR spectroscopy can be a powerful and easy to use alternative with

clear advantages regarding signal to noise ratio and/or measurement duration.

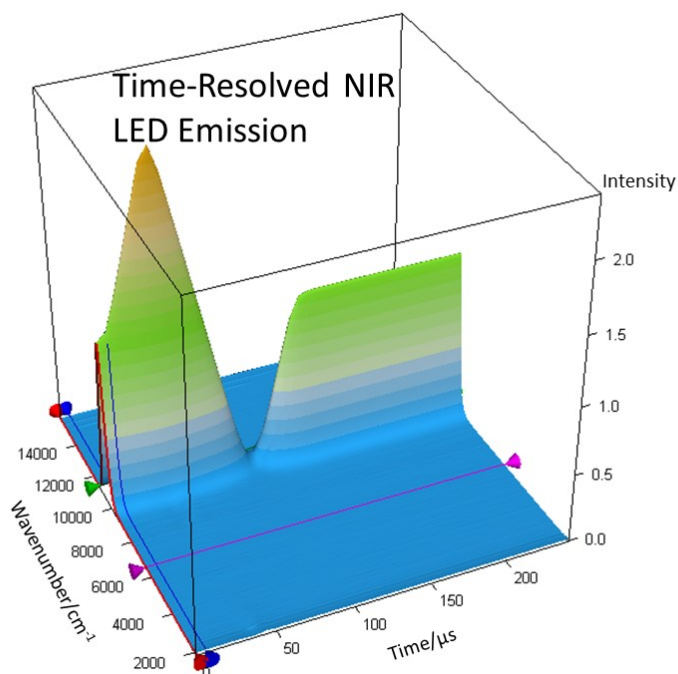


Figure 1. Time-resolved emission of an LED with time profile controlled by a function generator, measured via interleaved FT-IR spectroscopy.

- ¹ Mantz A.W., (1978), *Applied Optics*, 17(9), 1347-1351
- ² Bengali A.A., Fan W.Y., (2008), *Organometallics*, 27(21), 5488-5493
- ³ Palmer R.A., Manning C.J., Rzepiela J.A., Widder J.M., Chou J.L., (1989), *Appl. Spectr.* 43
- ⁴ Uhmman W., Becker A., Taran C., Siebert F., (1991), *Appl. Spectr.* 45, 390-397
- ⁵ Hartland G.V., Xie W., Dai H.L., Simon A., Anderson M.J., (1992), *Rev. Sci. Instr.* 63, 3261-3267
- ⁶ Rammelsberg R., Heßling B., Chorongiewski H., Gerwert K., (1997), *Appl. Spectr.* 51, 558-562
- ⁷ Guttentag, M., Rodenberg, A., Kopelent, R., Probst, B., Buchwalder, C., Brandstätter, M., Hamm, P., Alberto, R., (2012), *Eur. J. Inorg. Chem.*, 59-64
- ⁸ Souvignier G., Gerwert K. (1992), *Biophys J.*, 63(5), 1393-1405
- ⁹ Weidner H., Peale R.E., (1996), *Appl. Opt.* 35, 2849-2855
- ¹⁰ Cheng J., Lin H., Hu S., He S., Zhu Q., Kachanov A., (2000), *Appl. Opt.*, 39(13), 2221-2229

Time-resolved FTIR spectroscopy with sub-microsecond resolution probes
the blue light sensor cryptochrome

Christian Thöing, Sabine Oldemeyer and Tilman Kottke

Physical and Biophysical Chemistry, Bielefeld University, Universitätsstr. 25, 33615,
Bielefeld, Germany

Keywords: step-scan, flavoprotein, proton transfer, unfolding.

Cryptochromes act as blue light sensors in animals, plants, fungi, and bacteria¹. They control diverse responses such as plant development, the biological clock of insects, and magnetoreception. Cryptochromes bind noncovalently the chromophore flavin in the N-terminal 500 amino acids, the photolyase homology region (PHR).

In plant cryptochrome, absorption of blue light leads to formation of the flavin neutral radical from the oxidized state via ultrafast electron transfer and microsecond proton transfer. The neutral radical acts as the putative signaling state. The signal finally activates the C-terminal extension (CCT) of the cryptochrome. Little is known about changes in the secondary and tertiary structure of the PHR.

Here, we investigated the photo-reaction of the PHR by time-resolved step-scan and rapid-scan FTIR spectroscopy complemented by UV/vis spectroscopy². Step-scan FTIR experiments were conducted at a spectral resolution of 4.5 cm⁻¹ and an excitation rate of 0.25 Hz. Single laser pulses were selected from the 10 Hz repetition rate of the Nd:YAG laser with OPO emitting at 450 nm. For the rapid-scan experiments, an electronic synchronization of the laser and interferometer mirror was achieved to obtain a first spectrum at 22.3 ms with an accuracy of ± 1.7 ms at a rate of 0.17 Hz.

The first spectrum at 500 ns shows major contributions from the flavin anion radical. The rise of a band at 1733 cm⁻¹ demonstrates that the radical is protonated by the nearby aspartic acid 393³ with a time constant in the range of 0.4-2 μs, which is much slower than predicted by theory. The global fit of the data set covering the complete time range up to 3.9 s revealed the existence of three spectrally distinct intermediates characterized by changes in secondary structure (Figure 1). A marked loss of β-sheet structure at 1632 cm⁻¹ is observed in the second intermediate I₂ evolving with a time constant of 290 μs (Figure 2). This change is accompanied by a conversion of a tyrosine residue absorbing at 1273 cm⁻¹, which points to a strong hydrogen bond donor. UV/vis spectroscopy identifies this conversion as the formation of a tyrosine radical.

The only β-sheet in the PHR is located within the α/β subdomain, ~25 Å away from the flavin. This subdomain has previously been attributed a role as a putative antenna binding site, but it is now suggested to have evolved to a component in the signaling of plant cryptochrome by activating the CCT. This emerging view of signal progression in plant cryptochrome resembles an activation via a protein quake as it has been coined for the photoactive yellow protein⁴.

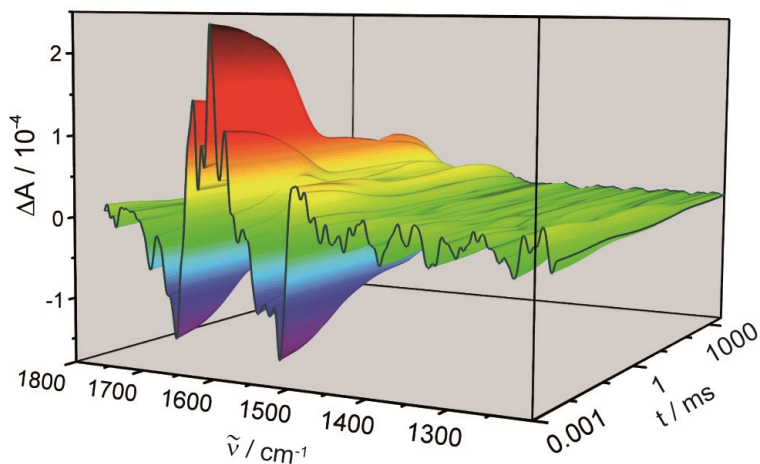


Figure 1. Global fit of the time-resolved data set on plant cryptochrome covering a time range of 3.5 μ s-3.63 s

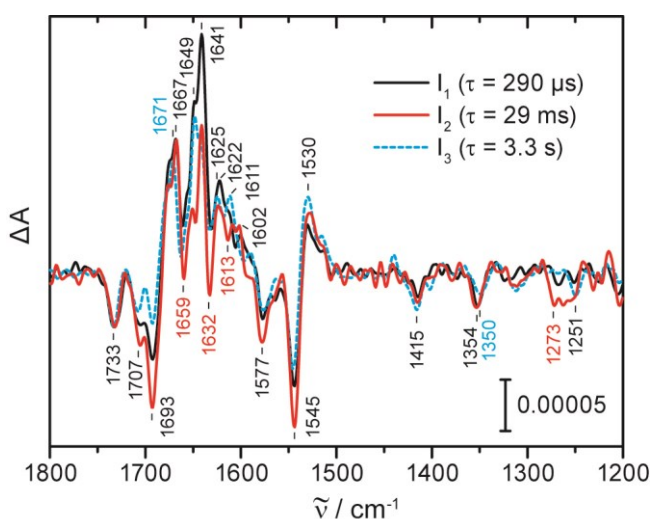


Figure 2. Species-associated difference spectra from the global fit scaled to the band at 1733 cm^{-1} showing a pronounced loss in β -sheet structure in I_2 .

¹ Cashmore A.R., Jarillo J.A., Wu Y.-J., Liu D. (1999), *Science*, 284, 760-765.

² Thöing C., Oldemeyer S., Kottke T., *J. Am. Chem. Soc.*, in revision.

³ Immeln D., Pokorny R., Herman E., Moldt J., Batschauer A., Kottke T. (2010), *J. Phys. Chem. B*, 114, 17155-17161.

⁴ Xie A., Kelemen L., Hendriks J., White B.J., Hellingwerf K.J., Hoff W.D. (2001), *Biochemistry*, 40, 1510-1517.

Two dimensional electronic spectroscopy for analyzing ultrafast vibrational wavepacket dynamics and electron-phonon coupling

Jürgen Hauer¹

¹Photonics Institute, Vienna University of Technology, Gusshausstr. 27, A-1040, Vienna, Austria

Keywords: wavepacket dynamics, ultrafast spectroscopy, two dimensional electronic spectroscopy.

Two-dimensional (2D) ultrafast spectroscopic techniques open an increasingly broad experimental window into the dynamics of molecular systems on femtosecond and picosecond time scales.¹ In the infrared, 2D-methods are already well established for the investigation of solute-solvent dynamics, structural relaxation, or nuclear dynamics in general. The study of electronic phenomena such as exciton migration or coherence transfers in electronically coupled multichromophores requires excitation in the visible spectral range. By performing electronic 2D spectroscopy with ultrabroadband pulses (sub-7 fs at 640 nm central wavelength), we successfully combine the two approaches and extract information from both degrees of freedom, electronic and nuclear.

The scheme of the experimental layout is shown in figure 1. After the incident pulse is split up by a double grating, a diffractive optical element (DOE), a combination of spherical and flat mirrors (SM and M) focuses four phase stable beams onto the sample S. Three of the four beams can be individually delayed by pairs of glass wedges WP 1-3. For electronic 2D spectroscopy, the signal along the $\Upsilon k_1 \pm k_2 + k_3$ phase matching direction is recorded. Interaction with the first pulse (k_1) induces electronic coherence that is converted either into electronic population or vibrational coherence in the electronic

ground or excited state by the second pulse (k_2) at time t_1 . After the second time interval t_2 , the third pulse (k_3) induces electronic coherence that radiates during t_3 . The emitted signal field is detected spectrally dispersed in a spectrometer ($t_3 \rightarrow \omega_3$). A second Fourier transform over $t_1 \rightarrow \omega_1$ is used to construct electronic 2D spectra for a given delay t_2 . Hence, 2D spectroscopy correlates events in excitation frequency ω_1 to those in emission frequency ω_3 .

In the first investigated sample, our excitation pulses cover up to three quanta of vibrational energy in solvated Zinc-Phthalocyanine,² while being on electronic resonance with the molecular Q-band. We interpret our experimental results with the aid of quantum chemistry and third order response function simulations. We show how vibrational modulations in 2D spectroscopy are stronger than in related techniques such as pump-probe.

The second investigated sample is C8O3, a molecular J-aggregate,³ formed by cyanine dyes. In aqueous solution, the monomers assemble to bi-layered tubes of 15 nm outer diameter and micrometers in length with strong excitonic coupling between the dye molecules. Using 2D electronic spectroscopy, we observe strong wavepacket motion on electronic ground and excited states. We discuss the important role of vibrational-electronic coupling in the formation process of J-aggregates.

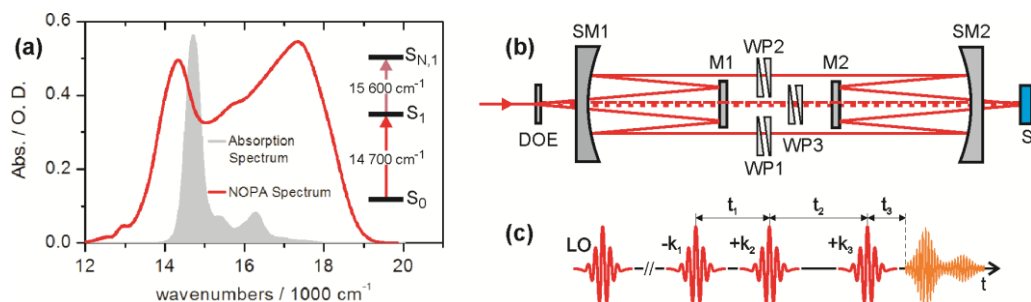


Figure 1. a) Absorption spectrum (grey area) of ZnPc in benzonitrile vs. NOPA-excitation spectrum (red line) and energy level scheme for relevant for short time delays. b) Experimental design as described in text c) Time line of incident pulses in red with LO as local oscillator pulse and the signal as orange wavy line.

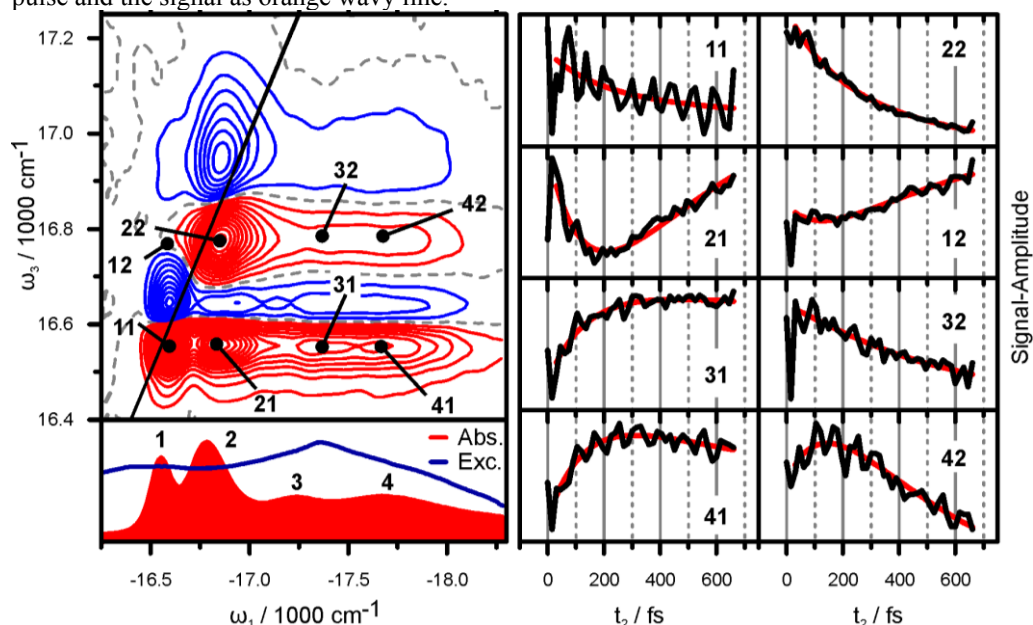


Figure 2. 2D spectrum of C8O3 in comparison to absorption and excitation spectrum on the left. Positive (negative) signals are drawn as red (blue) lines in 5% increments. The right side shows transients at indicated spectral positions. Vibrational wavepacket modulation is observed as periodic modulation on a slowly changing background.

¹ Jonas, D. M., *Ann. Rev. Phys. Chem.* 2003, 54, 425-463.

² Mancal, T.; Christensson, N.; Lukes, V.; Milota, F.; Bixner, O.; Kauffmann, H. F.; Hauer, J. *J. Phys. Chem. Lett.* 2012, 3, 1497-1502.

³ Milota, F.; Prokhorenko, V. I.; Mancal, T.; von Berlepsch, H.; Bixner, O.; Kauffmann, H. F.; Hauer, J., *J. Phys. Chem. A* 2013, 117, 6007-6014.

Energy transfer mechanism in liposome lipid bilayers studied with picosecond time-resolved Raman spectroscopy

Yuki Nojima, Sho Kitamura, Tomohisa Takaya and Koichi Iwata

Department of Chemistry, Faculty of Science, Gakushuin University
1-5-1 Mejiro, Toshima-ku, 171-8588, Tokyo, Japan

Keywords: lipid bilayer, liposome, time-resolved Raman, picosecond.

Lipid bilayer membranes form quasi two-dimensional space, with a thickness of two lipid molecules, in aqueous solution. We expect marked difference between the interior of the lipid bilayers and the outside aqueous phase for their chemical properties, including their polarity, viscosity, and thermal diffusivity. These properties affect the chemical reactions that proceed in or on the lipid bilayer membranes in a crucial way. We have estimated the viscosity inside the lipid bilayer membranes of liposomes formed by six phosphatidylcholines with picosecond time-resolved fluorescence spectroscopy^{1,2}. The experimental results indicate that there are two solvation environments whose viscosity is different by 30 to 290 times in the liposome lipid bilayers.

Conduction of heat in a macroscopic medium is well described by the diffusion equation of heat, with thermal diffusivity as a parameter. We have found that there is a good correlation between the cooling kinetics of *trans*-stilbene in the first excited singlet (S_1) state and the thermal diffusivity of the surrounding solvent, for ordinary organic solvents³. We try to estimate thermal diffusivity inside the lipid bilayer membranes by observing the cooling kinetics of S_1 *trans*-stilbene in the membranes with picosecond time-resolved Raman spectroscopy.

We prepare liposome solutions from six phosphatidylcholines, DOPC

(dioleoylphosphatidylcholine), DSPC (distearoylphosphatidylcholine), DPPC (dipalmitoylphosphatidylcholine), DMPC (dimyristoylphosphatidylcholine), DLPC (dilauroylphosphatidylcholine), and egg-PC (egg-yolk phosphatidylcholine), with *trans*-stilbene molecules enclosed inside the membranes. The lipid bilayers of DOPC, DMPC, DLPC, and egg-PC are in the liquid crystal (LC) phase at the sample temperature of 26°C, while those of DSPC and DPPC are in the gel phase. The diameter of the liposomes is estimated to be 100 nm.

We photoexcite *trans*-stilbene molecules solubilized in the liposome lipid bilayer membranes to the S_1 state with a pump pulse at 300 nm and record the Raman spectra of S_1 *trans*-stilbene with a probe pulse at 590 nm in resonance with the S_n - S_1 transition⁴. The wavenumber width of the probe pulse is limited with a 4-f filter formed by two gratings and a slit.

It has been known that the 1570 cm^{-1} band (central C=C stretch) of S_1 *trans*-stilbene changes its position depending on the temperature³. We deposit the vibrational excess energy of approximately 3000 cm^{-1} by photoexciting the stilbene molecules at 300 nm and follow their cooling process by recording the 1570 cm^{-1} Raman band. The result obtained for S_1 *trans*-stilbene in DOPC lipid bilayer membrane shows the cooling process (Figure 1). A cooling rate constant of 0.13 ps^{-1} is obtained when a single exponential decay function is fitted to

the observed cooling curve. We use the single exponential decay function, which is not the solution of the diffusion equation, because the rate constant thus obtained represents the cooling process as a simple index.

The observed cooling rate constants for the LC phase liposome lipid bilayers from DOPC, DMPC, DLPC, and egg-PC are larger than the rate constants for the gel phase lipid bilayers from DSPC and DPPC. The thermal diffusivity for the LC phase bilayers is larger than that for the gel phase bilayers, if we assume that the correlation between the cooling rate constant and the thermal diffusivity, observed for ordinary solvents, also holds for the lipid bilayer membranes. The thermal diffusivity estimated for the LC phase bilayer membranes and the gel phase bilayer

membranes range from 8.9 to $9.4 \times 10^{-8} \text{ m}^2 \text{ s}^{-1}$ and 8.4 to $8.5 \times 10^{-8} \text{ m}^2 \text{ s}^{-1}$, respectively.

It is not clear at present why the thermal diffusivity is larger for the LC phase lipid bilayers than for the gel phase lipid bilayers. We think, however, that presence of the nearby aqueous phase, with thermal diffusivity of $10.2 \times 10^{-8} \text{ m}^2 \text{ s}^{-1}$, is a reason for the difference. The thickness of the membrane is smaller for the LC phase because the C-C bonds in the acyl groups of the phospholipids take both the *trans*- and *gauche*-conformations while the C-C bonds take the all-*trans* conformation in the gel phase. It is also likely that more water molecules penetrate into the bilayer membranes in the LC phase where the distance between the polar heads is larger than in the gel phase.

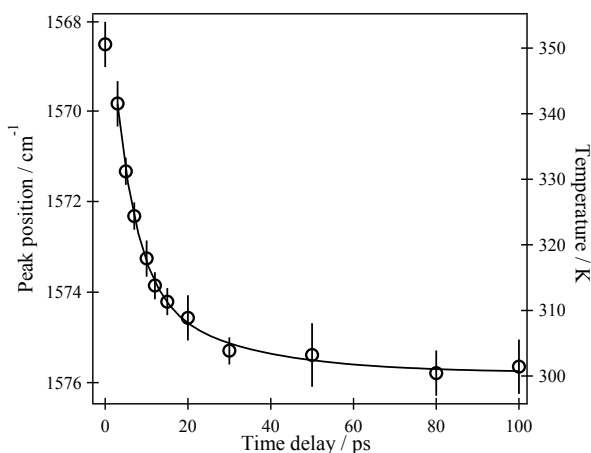


Figure 1. Cooling kinetics of S_1 *trans*-stilbene in DOPC lipid bilayer measured with picosecond time-resolved Raman spectroscopy.

- ¹ Nojima, Y., Iwata, K. (2011), *Chem. Asian J.*, 6, 1817- 1824.
- ² Nojima, Y., Iwata, K. (2014), *J. Phys. Chem.B.*, 118, 8631- 8641.
- ³ Iwata, K., Hamaguchi, H. (1997), *J. Phys. Chem.A.*, 101, 632- 637.
- ⁴ Yoshida, K., Iwata, K., Nishiyama, Y., Kimura, Y., Hamaguchi, H. (2012), *J. Chem. Phys.*, 136, 104504-1-104504-8.

Red blood cell resonators: The hyper-enhanced overtone modes of hemoglobin

Don McNaughton¹, Katarzyna M. Marzec^{1,2}, David Perez-Guaita¹, Marleen de Veij¹, Malgorzata Baranska^{1,3}, Matthew W.A. Dixon⁴, Leann Tilley⁴ and Bayden R. Wood¹

¹Centre for Biospectroscopy, School of Chemistry, Monash University, Clayton, VIC. 3800, Australia.

²Jagiellonian Centre for Experimental Therapeutics, Jagiellonian University, Bobrzynskiego 14, 30–348 Krakow, Poland

³Faculty of Chemistry, Jagiellonian University, Ingardena 3, 30–060 Krakow, Poland.

⁴Department of Biochemistry and Molecular Biology, Bio21 Institute, The University of Melbourne, Victoria 3010, Australia

Keywords: Red blood Cells (RBCs); Hemoglobin (Hb); Resonance Raman (RR) Spectroscopy; Overtone and combination modes; Excitonic coupling.

Resonance Raman (RR) spectroscopy has long been applied to monitor the molecular dynamics of hemoglobin (Hb) in solution. This highly symmetric and chromophoric heme prosthetic group provides strong enhancement when the excitation wavelength is in resonance or pre-resonance with the intense electronic transitions centered at ~400 nm (Soret or B band), 525 nm (Q_v or α band) and 575 nm (Q_0 or β band)¹. More recently it has been found that hemes in the environment of cells or crystals also give rise to enhanced signals through RR mechanisms².

In general the first overtone modes produce very weak bands appearing at approximately twice the wavenumber value of fundamental transitions in vibrational spectra. In this paper we report the existence of a series of hyper-enhanced non-fundamental bands in resonance Raman spectra recorded of Hb inside the highly concentrated heme environment of the red blood cell (RBC) by exciting with a 514.5 nm laser line³. These new bands have been systematically assigned to overtone and

combination bands based on symmetry arguments and polarization measurements. The extraordinary enhancement is explained by excitonic theory invoking a Type C scattering mechanism. Surprisingly these bands are more intense than most of the fundamentals especially when detecting parallel-polarized light. Using malaria diagnosis as an example we demonstrate that combining the non-fundamental and fundamental regions of the resonance Raman spectrum in a Partial Least Square Discriminate Analysis (PLS-DA) model improves the sensitivity and diagnostic capability of the technique compared to analysis using the fundamental region alone. The discovery of an entire new series of intense bands in the overtone/combination region for hemoglobin and other heme derivatives will have considerable implications in the ongoing development of Raman spectroscopy for blood disease diagnoses and monitoring heme perturbation in response to environmental stimuli.

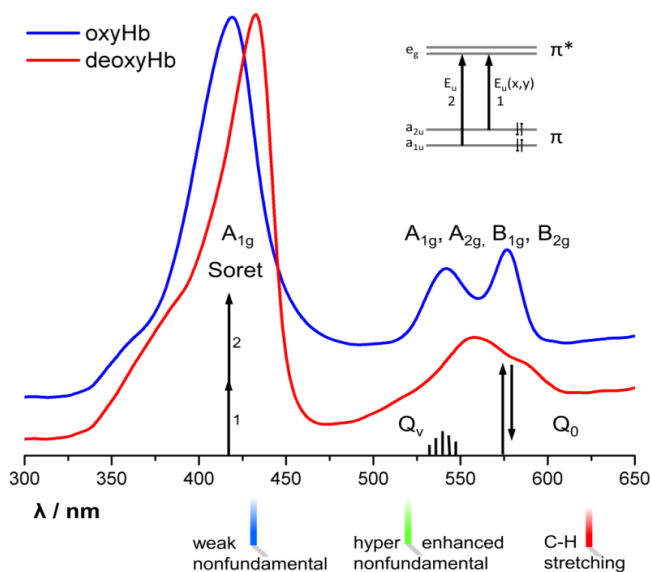


Figure 1. Comparison between average UV-Vis spectra collected from 10 different oxygenated and deoxygenated RBCs .

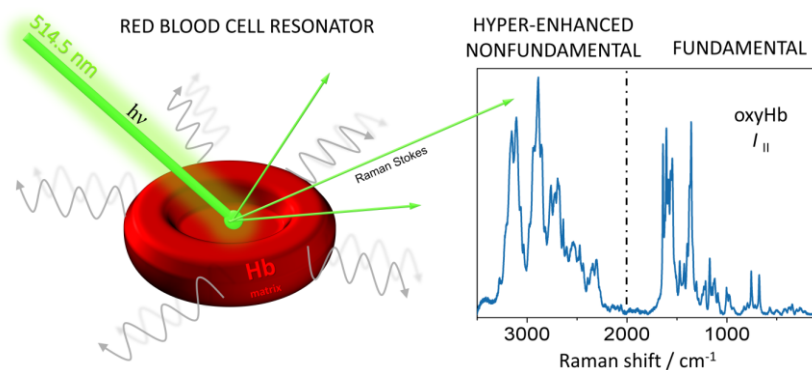


Figure 2. Raman spectrum of oxygenated RBC with , 514.5 nm laser.

1. Kitagawa, T. Heme protein Structure and the iron-histidine stretching mode in Resonance Raman Spectra of Heme and Metalloproteins. In Biological Applications of Raman Spectroscopy, vol. 3, Spiro, G., Ed. Wiley, New York (1988).
2. Wood, B.R. and McNaughton, D, "Resonant Raman scattering of heme molecules in cells and in the solid state", in Biomedical Vibrational Spectroscopy, Eds. J. Kneipp and P. Lasch, p. 181-208, John Wiley and sons ISBN: 978-0-470-22945-3 (2008).
3. Marzec, K; Perez-Guaita, D; de Veij, M; McNaughton, D; Baranska, M; Wood, B. , Phys Chem Phys DOI: 10.1002/cphc.201402598 (2014).

Reliable blood glucose monitoring for intensive care patients using micro-dialysis and infrared spectrometry with on-line recovery rate determination

Thorsten Vahlsing, Sven Delbeck, Janpeter Budde, Dieter Ihrig and H. Michael Heise

Interdisziplinäres Zentrum für Lebenswissenschaften, Fachhochschule Südwestfalen,
Frauenstuhweg 31, D-58644 Iserlohn, Germany

Keywords: infrared spectrometry, glucose monitoring, micro-dialysis, recovery determination, multi-analyte quantification

Nowadays, point-of-care diagnostics are frequently demanding for continuous sensing systems, especially for blood glucose monitoring, although intermittent testing is still practiced even for critically ill patients.¹ In this context, micro-dialysis has often been used in the clinical environment for continuously harvesting body fluids in a minimal invasive manner, but a drawback of this process are variable recovery rates. By using multivariate infrared spectroscopy and its inherent multi-analyte capability for whole blood, interstitial fluid or dialysate measurements, the application of acetate or mannitol containing perfusates has been investigated as recovery marker substances.

Mannitol has been suggested especially for application with single external cavity tunable quantum cascade lasers, which render only a limited wavenumber interval compared with FTIR-spectrometers, but can be much smaller in device size.² However, as severe spectral overlap exists for mannitol and glucose, studies for the simultaneous quantification of both monosaccharides were carried out with impressive selectivity.

In-vitro recovery rate experiments were carried out on interstitial fluid simulating aqueous samples and serum. By investigating simultaneously the depletion of the concentration of the marker substances from the perfusate using different micro-dialysis catheters for subcutaneous skin

implantation or vascular insertion for whole blood application, micro-dialysis recovery rates under push-pull operation with peristaltic pumps for perfusate flow-rates between 1 and 20 $\mu\text{L}/\text{min}$ were determined by infrared spectrometry. Results confirmed the theoretically expected nonlinear and linear relationship between the recovery rates of glucose and the relative dialysate marker concentration of acetate and mannitol, respectively. This can be predicted from the diffusion constants of the analytes of interest.

A limiting factor for the lifetime of the inserted microdialysis catheter and hence the amount of collected substances, i.e. relative recoveries, is the adsorption of proteins onto the surface of the microdialysis probe, but this can now be monitored. Protein adsorption may also lead to inflammatory responses, which in turn can limit the duration of in-vivo sampling.

Again the versatility of infrared spectroscopy for reagent-free multi-analyte assays has been illustrated with spectra of aqueous samples of high quality with regard to signal-to-noise ratio and baseline stability after application of an optical lowpass filter with access of the fingerprint interval up to 1900 cm^{-1} . Also interferences from atmospheric water vapour were successfully avoided, with the consequence of a straightforward spectral evaluation by

multivariate classical least-squares based on a small number of component reference spectra.

The advantages of the internal standard for reliable recovery assessment allow also a safe extension of catheter lifetimes. Substantial progress has been achieved for infrared spectrometry in combination with micro-dialysis, and in-

vivo applications for intensive care patients can be envisaged, especially as further analytes and parameters are accessible, which are of interest for intensive medicine such as lactate, urea, pCO₂ and pH. Further progress may come from the use of miniaturised quantum cascade laser systems,³ by which wearable devices could be possible in the not too distant future.

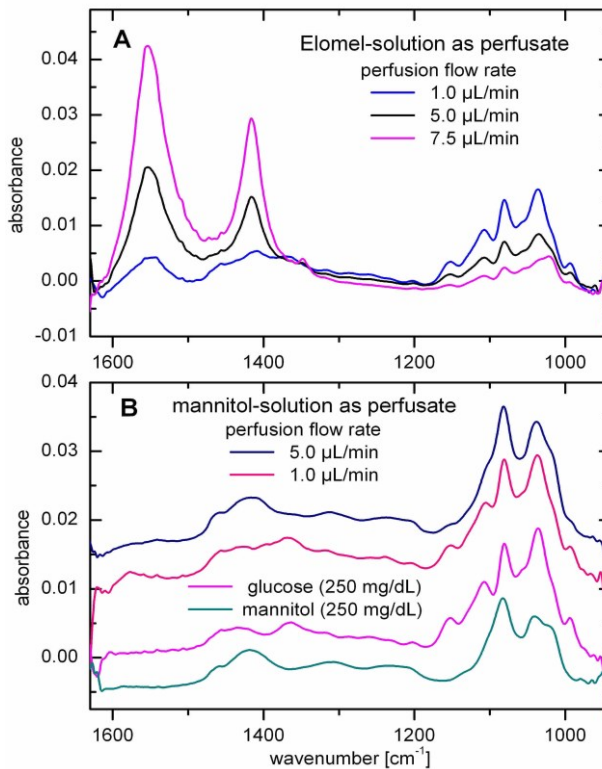


Figure 1. Absorbance spectra obtained with a 30 μm pathlength cell from dialysates under different flow-rates with acetate containing ELO-MEL solution (A) and an isotonic mannitol solution as perfusate including the pure sugar solution spectra (B).

- ¹ Amrein K., Kachel N., Fries H., Hovorka R., Pieber T.R., Plank J., Wenger U., Lienhardt B., Magorini M. (2014) *BMC Endocrine Disorders* 14, 62.
- ² Heise H.M. and Vahlsing T. (2014) *Proc. SPIE* 8951, 895108.
- ³ Heise H.M., Kondepoti V.R., Damm U., Licht M., Feichtner F., Mader J.K. and Ellmerer M. (2008) *Proc. SPIE* 6863, 686308.

Sensing molecular changes due to protein translation inside cells using surface-enhanced Raman spectroscopy

Anna Huefner^{1,2,3}, Wei-Li Kuan², Roger Barker², Sumeet Mahajan³

¹University of Cambridge, Sector for Biological and Soft Systems, Cavendish Laboratory, 19 JJ Thompson Avenue, CB3 0HE, Cambridge, UK, ²University of Cambridge, Centre for Brain Repair, Forvie Site, Robinson Way, CB2 0PY, Cambridge, UK, ³University of Southampton, Institute of Life Sciences and Department of Chemistry, Highfield, SO17 1BJ, Southampton, UK

Keywords: SERS, gold nanoparticles, cell, protein detection, alpha synuclein.

As the life-expectancy increases worldwide, neurodegenerative disorders such as Parkinson's, Alzheimer's disease or Huntington disease have become a growing challenge for our healthcare systems. Increasingly, biomedical research focuses on the misfolding, aggregation and intracellular interactions of involved proteins with other biomolecules. Various techniques have been employed to study the protein dynamics and interactions *in vitro* and in living cells with relevance to different stages of protein misfolding and aggregation in these neurological disorders¹.

Alpha synuclein is the protein involved in the formation of intracellular protein inclusions in neurons of Parkinson's patients. Previously, alpha synuclein and its oligomerisation have been studied with Raman spectroscopy, a (bio)chemical fingerprinting method. While it has been shown that Raman spectroscopy is a suitable tool to characterise its morphology as well as its conformational changes while interacting with other molecules², cellular *in vitro* studies have not yet been done although they are required to gain an understanding of the intracellular interaction of alpha synuclein with other biomolecules, particularly in the context of aggregation processes.

Our approach employs non-invasive, label-free surface-enhanced Raman spectroscopy (SERS) for biosensing inside cells to address this issue. Nanoparticle-based SERS has widely been employed for intracellular measurements and imaging^{3,4}. We use gold nanoparticles delivered to the cytoplasm of cells to act as SERS sensors allowing the study of the molecular make-up of human neuroblastoma cells under the influence of the induced expression of alpha synuclein. This approach is successfully combined with chemometric analysis methods in order to visualise the intracellular distribution of various biomolecules as well as to explore specific molecular alterations due to the expression of alpha synuclein. Beside the detection of intracellular alpha synuclein, we report a decrease of the cellular protein-to-lipid ratio suggesting the interaction of alpha synuclein with phospholipids and lipid membranes. Furthermore, molecule groups and residues were identified which interact with alpha synuclein such as cysteine residues and/or disulfide bonds.

The gained insights into intracellular molecular modifications due to the expression of alpha synuclein in cells not only revealed the changes in the

biomolecular make-up of the cell, they also open up directions for further, more specific research in the context of protein aggregation by the identification of molecules that interact with alpha synuclein. Moreover, this approach is generic and

suitable for the intracellular investigation of molecular interactions and modifications relevant to not only neurodegeneration but all intracellular disease mechanisms.

- 1 Gregoire, S., Irwin, J. & Kwon, I. Techniques for Monitoring Protein Misfolding and Aggregation in Vitro and in Living Cells. *Korean J Chem Eng* **29**, 693-702, doi:10.1007/s11814-012-0060-x (2012).
- 2 Maiti, N. C., Apetri, M. M., Zagorski, M. G., Carey, P. R. & Anderson, V. E. Raman Spectroscopic Characterization of Secondary Structure in Natively Unfolded Proteins: α -Synuclein. *J Am Chem Soc* **126**, 2399-2408, doi:10.1021/ja0356176 (2004).
- 3 Kneipp, J. & Drescher, D. in *Frontiers of Surface-Enhanced Raman Scattering* 285-308 (John Wiley & Sons, Ltd, 2014).
- 4 Huefner, A., Kuan, W.-L., Barker, R. A. & Mahajan, S. Intracellular SERS Nanoprobes For Distinction Of Different Neuronal Cell Types. *Nano Lett* **13**, 2463-2470, doi:10.1021/nl400448n (2013).

MicroRaman Spectroscopic Signature of Drug Action Pd-based Anticancer Agents Towards Human Breast Cancer

Ana L. M. Batista de Carvalho¹, Luís A. E. Batista de Carvalho¹, Gianfelice Cinque³, Chris Kelley³, Peter Gardner⁴, James Doherty⁴, Mike Pilling⁴ and Maria P. M. Marques^{1,2}

¹Molecular Physical-Chemistry R&D Unit; ²Department of Life Sciences
Faculty of Sciences and Technology, University of Coimbra, Portugal

³Diamond Light Source, STFC Harwell Science and Innovation Campus, Chilton, UK

⁴Manchester Interdisciplinary Biocentre, University of Manchester, Manchester, UK

Keywords: microRaman, Breast cancer, Pd(II) Anticancer drugs, Cellular response

Vibrational spectroscopy has emerged as a suitable analytical tool for the accurate chemical characterisation of heterogeneous biological systems such as cells and tissues, since it provides information, at the molecular level, with very high spectral and spectral resolution. In particular, Raman confocal microspectroscopy of cell cultures allows a non-invasive probing of living cells, constituting an invaluable method for monitoring the effect of drugs on the intracellular biochemical profile.¹ Indeed, the high sub-cellular spatial resolution of this technique enables to observe the distinct cell components without the use of dyes or molecular probes. Furthermore, it requires minimal sample preparation and is very sensitive to structural and conformational changes, providing a complete fingerprint of the molecular composition of the cell.²

Goals – Following the success of cisplatin (*cis*-Pt(NH₃)₂Cl₂) as an anticancer agent, numerous cisplatin-like compounds have been studied in the last decades aiming at an optimised therapeutic profile coupled to decreased deleterious side effects and minimal acquired resistance. The present study focuses on a dinuclear Pd(II) complex with the polyamine spermine (Spm, H₂N(CH₂)₃NH(CH₂)₄NH(CH₂)₃NH₂), that has been extensively studied by the authors as to its conformational behaviour and

cytotoxicity on several human cancer cell lines³⁻⁵, with promising results against an estrogen-independent breast cancer⁶. The goal of the reported experiment was to determine the biodistribution and metabolic impact of this prospective anticancer agent in this human breast adenocarcinoma cell line (MDA-MB-231), through Raman microspectroscopy, for distinct drug concentrations, at a definite exposure time (using cisplatin as a reference). This data will help to understand the *in vitro* pharmacokinetic and pharmacodynamic profiles of Pd₂Spm, which is pivotal for a rational design of improved cisplatin-like antineoplastic drugs.

Methods – MicroRaman spectra were recorded (in the 600 to 4000 cm⁻¹ range) at two confocal configurations: (i) in a Jobin-Yvon T64000 Raman microspectrometer coupled to a liquid nitrogen-cooled non-intensified CCD detector (1024x256 pixels), using an Olympus 60x water immersion objective, with a 514 nm exciting radiation (30-50 spectra *per* sample, 2 co-added scans *per* chosen point); (ii) in a Bruker Senterra Raman microspectrometer with CCD detection, using a 100x objective and a 532 nm laser line (150-200 spectra *per* sample, 6 co-added scans *per* chosen point). Spectra of formalin-fixed MDA-MB-231 cells in exponential phase growth (3x10⁴ cells/cm²)

were obtained, in MgF_2 windows, in both the absence and presence of $\text{Pd}_2\text{-Spm}$. 4 and 8 μM drug dosages were tested, for a 48 h incubation period. Individual cells were selected using the microscope and the aperture adjusted to the cell size ($10 \times 10 \mu\text{m}$).

Main Results – The results thus gathered clearly evidenced a spectral differentiation between the control and the drug-treated cells (Figure 1), as well as between the two administered Pd_2Spm concentrations (4 μM being close to the drug's IC_{50} value at 48 h). Interpretation of the data was carried out through unsupervised PCA analysis of the

spectra (upon baseline correction and vector normalization). The major metabolic impact observed for this Pd(II) drug was verified to be: (i) on DNA – $\nu_{\text{as}}(\text{O-P-O})$ at ca. 1235 cm^{-1} ; (ii) on the lipids – $\nu(\text{CH}_2)$, $\delta(\text{CH}_2)$ and $\nu(\text{CH}_2)$ bands, respectively at ca. 1300 , 1450 and $2850\text{-}2900 \text{ cm}^{-1}$. This is in accordance with the expected mode of action for these cisplatin-like compounds (which covalently bind to DNA), as well as with HRMAS-NMR metabolomic experiments previously carried out for the same systems⁷.

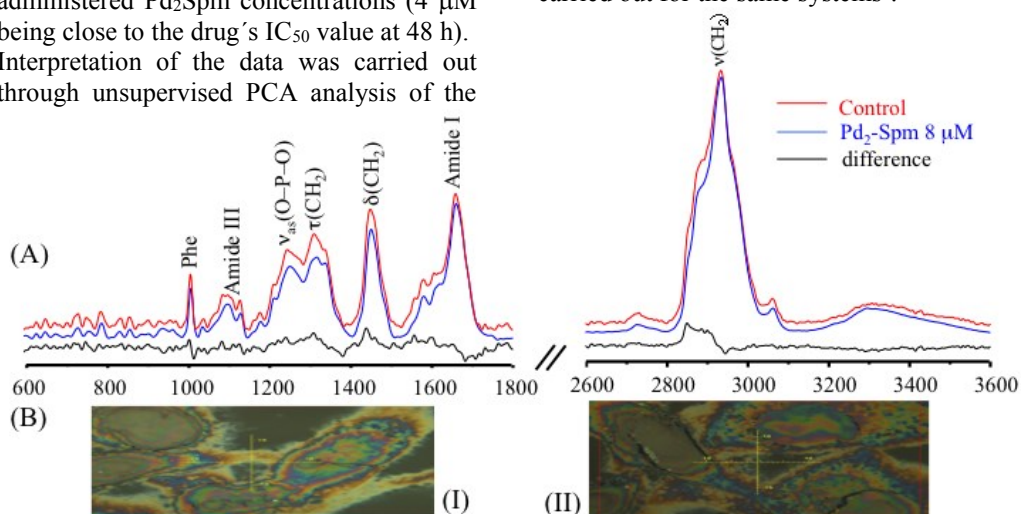


Figure 1. (A) Average Raman spectra for Pd_2Spm treated cells vs control.

(B) Cell images (100x magnification) upon exposure to 8 μM - Pd_2Spm (I) versus control (II).

- Draux F., Gobinet C., Sulé-Suso J., Manfait M., Jeannesson P., Sockalingum G.D. (2011), *The Analyst*, 136 (13), 2718-2725.
- Dorney J., Bonnier F., Garcia A., Casey A., Chambers G., Byrne H.J. (2012), *The Analyst*, 137 (5), 1111-1119.
- Tummala R., Diegelman P., Fiuza S. M., Batista de Carvalho L.A.E., Marques M.P.M., Kramer D.L., Clark K., Vujcic S., Porter C.W., Pendyala L. (2010), *Oncology Report*, 24(1) 15-24.
- Corduneanu O., Chiorcea-Paquim A.M., Diculescu V., Fiuza S.M., Marques M.P.M., Oliveira-Brett A.M. (2010), *Analytical Chemistry*, 82(4) 1245-1252.
- Silva T.M., Fiuza S.M., Marques M.P.M., Persson L., Oredsson S. (2014), *Amino Acids* 46 (2) 339-352, and refs therein.
- Fiuza S.M., Holy J., Batista de Carvalho L.A., Marques M.P., (2011), *Chemical Biology & Drug Design*, 77 (6), 477-488.
- Lamego I., Duarte I.F., Marques M.P., Gil A.M. (2014), *Journal of Proteome Research*, 13(12) 6033-6045.

Real-time Physiological Characterization of Bioprocesses using In-situ Spectroscopy and Soft-sensors

Aydin Golabgir¹, Christoph Herwig^{1,2}

1 Research Area Biochemical Engineering, Institute of Chemical Engineering, Vienna University of Technology, Gumpendorferstrasse 1a - 166/4, A-1060 Vienna, Austria

2 CD Laboratory on Mechanistic and Physiological Methods for Improved Bioprocesses, Vienna University of Technology, Gumpendorferstrasse 1a - 166/4, A-1060 Vienna, Austria

Keywords: bioprocess analysis, chemometrics, soft-sensors

Bioprocesses are used for the production of a wide range of value-added products, including therapeutics and renewable energy sources. Monitoring and control of physiological and morphological variables, such as specific growth, substrate uptake, and production rates, can lead to higher process efficiency and improved stability¹. However, implementation of advanced monitoring and control strategies is hindered by the lack of availability of analytical methods that are capable of measuring physiological and morphological characteristics directly and in a timely manner. In this contribution, the utility of first-principle soft-sensors for estimating inaccessible bioprocess variables (such as biomass) using more accessible measurements provided by in-situ spectroscopic devices is demonstrated.

Since optical in-situ spectroscopic devices are able to provide accurate and timely measurements of metabolite, biomass, and product concentrations², they are suitable for incorporation in real-time soft-sensing strategies. For real-time estimation of physiological and morphological characteristics of the penicillin-production process by *P. chrysogenum*, measurements provided by Raman and NIR spectroscopy of various

process-related concentrations have been exploited using a soft-sensor.

For successful utilization of spectroscopic measurements in soft-sensing approaches, it must be decided which components are required to be measured directly. Also, the effects of measurement frequency and accuracy on soft-sensor estimations have to be considered. Therefore, using an innovative method for analysis of the observability of the underlying bioprocess model, we demonstrate an approach for selection of target substances that are needed to be measured in order to arrive at accurate measurements. Also, using this method, the required measurement accuracy of the spectroscopic measurements can be determined. This method is able to deliver an important decision-making criterion for selection of control strategies.

In addition, by combining real-time spectroscopic measurements and other information sources, such as measurements of the respiratory rates, the developed soft-sensor is demonstrated to be superior to traditional chemometric approaches that utilize fewer measurement sources. A computational framework for real-time implementation of mechanistic soft-sensors using observer algorithms for improved

monitoring and control of upstream cultivation processes is presented.

Acknowledgements: Financial support was provided by the Austrian research funding association (FFG) under the scope of the COMET program (contract # 843546).

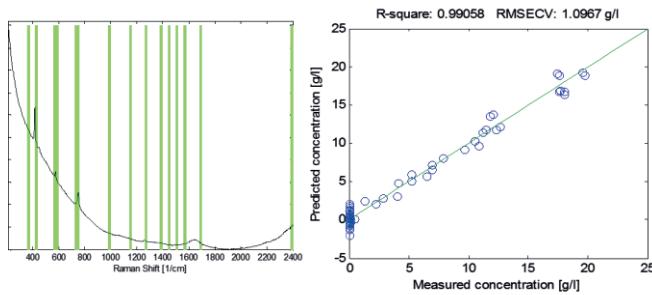


Figure 1. Gluconate concentration measurement via Raman spectroscopy used as input for soft-sensor assisted estimation of physiological variables.

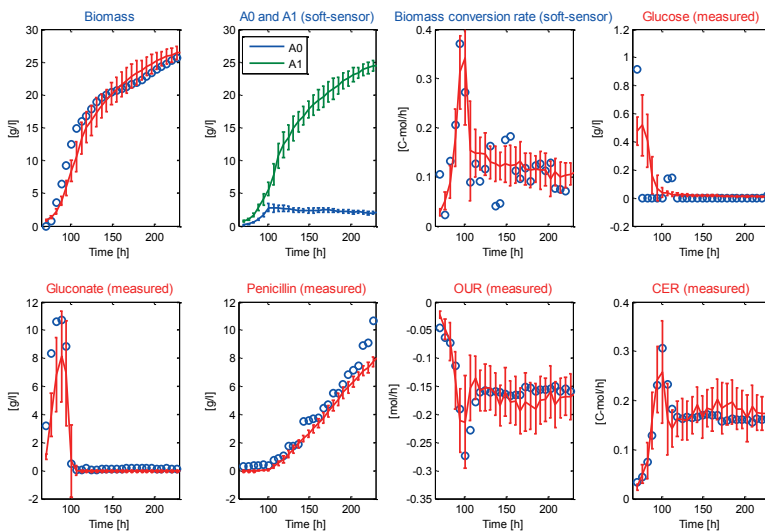


Figure 2. Estimation of biomass concentration, morphological characteristics (growing A0, non-growing A1 biomass), and growth rate using a first-principle soft-sensor that is guided by spectroscopic measurements of glucose, gluconate, and penicillin concentrations. Blue symbols: offline measurements, red lines: soft-sensor estimations.

¹ Posch, A. E., Herwig, C. & Spadiut, O. Science-based bioprocess design for filamentous fungi. *Trends in Biotechnology* **31**, 37–44 (2013).

² Koch, C., Posch, A. E., Goicoechea, H. C., Herwig, C. & Lendl, B. Multi-analyte quantification in bioprocesses by FTIR spectroscopy by Partial Least Squares Regression and Multivariate Curve Resolution. *Analytica Chimica Acta*

Characterisation of viscose fibre spin bath by FTNIR-spectroscopy and its implementation for process control

Georg Mayr¹, Peter Hintenaus², Wolfgang Märzinger² and Thomas Röder³

¹Kompetenzzentrum Holz, Altenbergerstraße 69, 4040, Linz, Austria

²i-RED Infrarot Systeme GmbH, Hafenstraße 47-51, 4020, Linz, Austria

³Lenzing AG, Werksstraße 2, 4860, Lenzing, Austria

Keywords: NIR-spectroscopy, viscose fibre, spin bath, process analysis.

FTNIR spectroscopy is a proven analytical method for process analysis. Due to its technological preferences¹ it can be easily implemented in production environment. The application of a FTNIR analytical method for the characterisation of viscose fibre spin bath and its implementation for process control is presented.

The viscose fibre is an important industrial product with global relevance, which is expected to increase in future years and decades. Viscose fibre serves as a suitable alternative to cotton. The cultivation of cotton requires environmentally problematic, intensive soil irrigation. This will become a significant issue with increasing global population.

In viscose fibre production one parameter, which governs the quality of the viscose fibre, is the composition of the spin bath. The spin bath is a strongly concentrated aqueous solution of sulphuric acid, sodium sulphate and zinc sulphate, in which the fibre is precipitated out of the viscose dope. The concentrations of the acid and the salts in the spin bath have to be well defined, accurately determined and controlled, in order to achieve a steadily high product quality. Due to short recycle times of the spin bath in the continuous process, there is a demand for a fast analytical method. Those requirements

suggest NIR-spectroscopy as a process analytical technique for application.

We report the development of the FTNIR-spectroscopic method for the determination of sulphuric acid, sodium sulphate and zinc sulphate simultaneously in the viscose fibre spin bath, its performance and its restrictions. The problems and its solutions concerning the implementation in process environment are topic of this contribution.

NIR-spectroscopic methods demand proper calibration. The selection and composition of the calibration set is a relevant issue², especially in the case of application for process control. Calibration samples can be specifically prepared in laboratory conditions or drawn from the ongoing production with subsequent reference analysis. Both approaches to calibration have benefits, which will be elucidated.

The application of spectroscopic methods implicates the utilization of reference measurements, in order to subtract the spectral background and compensate for hardware fluctuations, for instance varying illumination intensity. Under process conditions the selection of reference materials and samples, respectively, is a critical issue. We discuss the advantages and disadvantages of reference measurements in the current application. The corresponding

performances of the argued points are judged on the basis of RMSEP values.

Calibration and validation of chemometric models, which are regularly applied in NIR-spectroscopy, naturally are based on a limited number of samples, collected in a limited time span. During the calibration procedure it is not possible to take into account future changes in sample composition, like matrix changes or varying secondary components. Possible actions to

ensure a constant and satisfying long time performance³ are reported based on the current application spin bath characterisation as example.

Figure 1 shows the comparison of the NIR-measurement result for sulphuric acid compared to the wet chemical reference analysis. The results, acquired with the NIR-measurement system operated online in process environment, are depicted for a time period of approximately two and a half day.

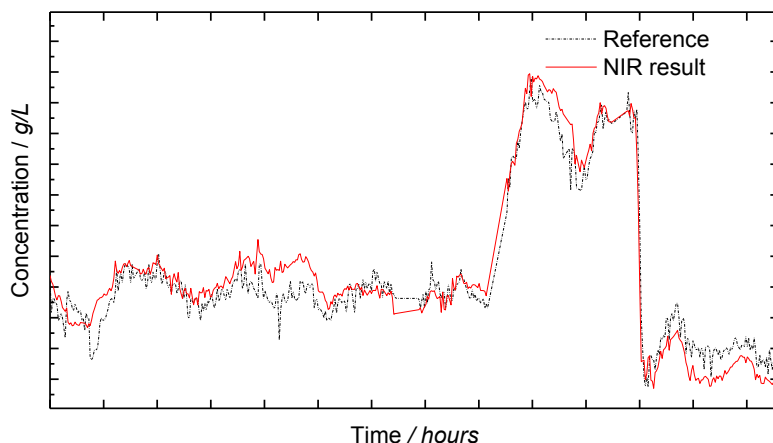


Figure 1. NIR measurement results for sulphuric acid. The NIR measurement results are compared to the results of regular wet chemical reference analysis. The data are acquired online in process environment

¹ Beaten V., Dardenne P., (2002), *Grasas y Aceites*, 53 (1), 45-63.

² Naes T., Issakson T., (1989), *Applied Spectroscopy*, 43 (2), 328-335.

³ De Noord O.E., (1994), *Chemometrics and Intelligent Laboratory Systems*, 25, 85-97.

Quantum cascade laser based photoacoustic spectroscopy with remote optical detection

Markus Brandstetter,¹ Armin Hochreiner,¹ Elisabeth Leiss-Holzinger,¹ Gregor Langer,^{1,2} Peter Burgholzer,^{1,2} Christian Kristament,³ Bernhard Lendl³ and Thomas Berer^{1,2}

¹RECENDT GmbH – Research Center for Non-Destructive Testing, 4040 Linz, Austria

²Christian Doppler Laboratory for Photoacoustic Imaging and Laser Ultrasonics, 4040 Linz, Austria

³Vienna University of Technology, Institute of Chemical Technologies and Analytics, 1060 Vienna, Austria

Keywords: Quantum Cascade Laser, Photoacoustic Spectroscopy, Remote-detection, Ultrasound, Interferometry

We demonstrate remote absorption spectroscopy based on the photoacoustic effect with a tunable mid-infrared (mid-IR) Quantum Cascade Laser (QCL) as excitation source and near-infrared (near-IR) contactless optical detection.

Recently, the field of mid-IR spectroscopy has seen a number of highly-relevant technological developments. Most notably the QCL technology has brought a large number of new measurement concepts or rediscoveries of concepts known from other research fields. QCLs offer excellent spectral properties. Especially their high optical power density compared to standard thermal emitters has to be noted in this context. In contrast to classical direct absorption spectroscopy where light attenuation has to be detected, the signal in photothermal spectroscopy is proportional to the excitation laser intensity. Thus, signal generation through photothermal effects in combination with high-power QCLs is an attractive route. Among the photothermal effects that have been utilized in combination with QCLs are blackbody radiation, refractive index change and, most commonly used, the photoacoustic effect¹. However, the acoustic impedance mismatch between sample and air (and the strong

ultrasonic attenuation in air) makes direct acoustic detection, e.g. with microphones or ultrasound transducers, impossible. In order to achieve remote detection of the photoacoustic effect we measure the sample surface's deformation with a laser vibrometer² (Fig. 1).

In this work we employed a pulsed external cavity (EC) QCL, tunable between 1030 cm⁻¹ and 1230cm⁻¹ as excitation source. The laser vibrometer for the detection of the ultrasonic waves consisted of a fiber-optic Mach-Zehnder interferometer with balanced detection. We present the theoretical background of the technique and demonstrate measurements of various samples. For comparison, absorption spectra of a 250µm thick polystyrene film obtained by the remote photoacoustic spectroscopy technique and by a FTIR Attenuated Total Reflection (ATR) measurement are shown in Fig. 2.

The proposed measurement concept can be applied to a wide range of analytical problems, e.g. for surface contamination monitoring in a bioreactor. In general the method represents an attractive approach for measurements in reflection geometry, since it provides direct absorption information and

takes full benefit of the high spectral power density of QCLs.

This work was funded by the Austrian research funding association (FFG) under the scope of the COMET programme within the research project imPACTs (contract # 843546), by the Austrian Science Fund (FWF), project number P25584-N20, by the Christian Doppler Research Association

(Christian Doppler Laboratory for Photoacoustic Imaging and Laser Ultrasonics), and the Federal Ministry of Economy, Family and Youth. Additionally we acknowledge support from the European Regional Development Fund (EFRE) in the framework of the EU-program REGIO 13, and the Federal State of Upper Austria.

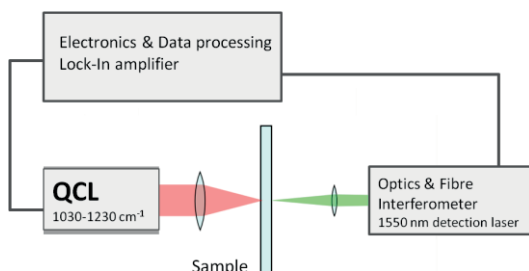


Figure 1. Schematic illustration of the measurement concept for remote detection of photoacoustic signals.

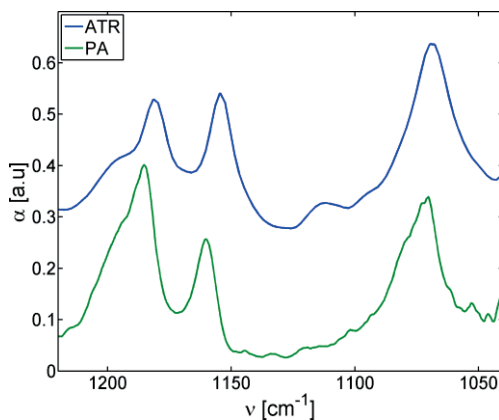


Figure 2. Absorption spectra of a 250 μm polystyrene film; PA (bottom) - Excitation with a mid-IR tunable EC-QCL and remote optical detection; ATR (top) - Reference spectrum obtained by a FTIR ATR measurement

¹ Waclawek J.P., Moser H., Brandstetter M., Tittel F.K., Lendl B. (2014), *Appl. Phys. B* 117(1), 113-120.

² Hochreiner A., Bauer-Marschallinger, J., Burgholzer P., Jakoby B. and Berer T. (2013), *Biomed. Opt. Express* 4, 2322-2331.

IN-LINE RAMAN ANALYSIS OF ETHYLENE VINYL ACETATE CURING FOR AND IN INDUSTRIAL PV MODULE MANUFACTURING

Ch. Hirschl¹, M. DeBiasio¹, L. Neumaier¹, R. Leitner¹, G. Eder², S. Seufzer³ and M. Kraft¹

¹ CTR Carinthian Tech Research AG, 9524 Villach, A

² OFI Österreichisches Forschungsinstitut für Chemie und Technik, 1030 Wien, A

³ KIOTO Photovoltaics GmbH, 9300 St. Veit/Glan, A

Keywords: industrial process analysis, material analysis, Raman spectroscopy, photovoltaics

Modern photovoltaic (PV) modules come with operation warranties of 25+ years, which puts tremendous pressure on the modules' long-time reliability and hence on manufacturing quality control. Of particular interest is the polymeric encapsulant, in most cases a radically crosslinked PV-grade ethyl/vinyl acetate copolymer (E/VA). The curing of the encapsulant is vital for quality and performance of the PV module. However, once cured, the E/VA inside the laminated module stack is virtually inaccessible to any analytical method without destroying the module and extracting a sample. Raman spectroscopy could be a viable alternative here, as it would enable a direct, contact-free and non-destructive *in-situ* measurement through the front glass.

In a first step, Raman spectra of differently crosslinked E/VA were acquired using a high-end Raman lab system (Renishaw InVia). Following a full spectroscopic evaluation, a ratiometric model was developed that evaluates the relative intensities of the CH₂- and CH₃-bands (Fig. 1) as measurand for the degree of E/VA crosslinking. This Raman approach was then validated both in the lab and within a pan-European Round Robin study on chemical extraction analysis procedures for measuring the degree of crosslinking of E/VA. The comparison of the Raman predictions of 25 separate E/VA samples to the degrees of crosslinking reported by different qualified laboratories (Fig. 2) clearly validates this new approach.

In a second step, the laboratory method was adapted to production line requirements, which include identical spectral quality at ≤ 1 s analysis time per point. Incorporating an industrial Raman Real Time Monitoring system from Tornado Spectral Systems, an in-line Raman analysis demonstrator was designed, built and installed in a productive PV production line (Fig. 3). With this in-line system, the total analysis time could be reduced from typically 5 x 5 s per point to down to 100 ms. In practice, a measurement time of 0.5 s proved the best compromise between rapid in-line measurement and the spectral quality (Fig. 4) required for analytical reliability.

The in-line device prototype was finally operated in routine production for an extended period of time. Analytical results recorded during these tests were repeatedly compared to analysis of the same samples using the validated Raman laboratory method. The results of one such validation experiment are shown in Fig. 5, showing a nearly perfect agreement

Summarising, Raman spectrometry enables reliably and quantitatively measuring the degree of crosslinking of E/VA inside assembled PV modules, both off-line in the lab and in-line in an industrial manufacturing line. Still, since the method is inherently relative, it requires either a reliably constant composition of the EVA raw material, or regular testing of the uncured material as reference for the data evaluation.

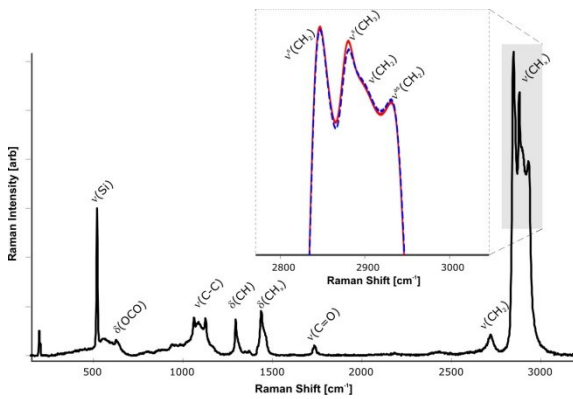


Fig. 1: Raman spectra of pre- (red) and post-crosslinking (blue) EVA in an assembled, full-scale PV module

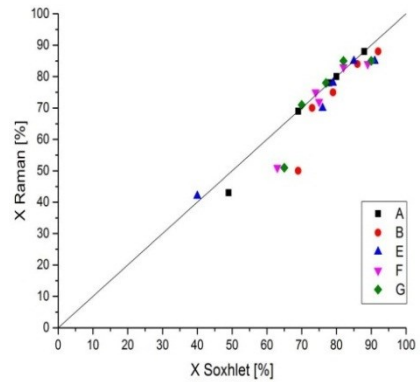


Fig. 2: Validation of the Raman-based determination of the degree of EVA crosslinking against validated analytical standard procedures



Fig. 3: Industrial functional demonstrator of an in-line Raman analyser for PV applications; left: overall system design; centre: sensor head design; right: system in in-line use

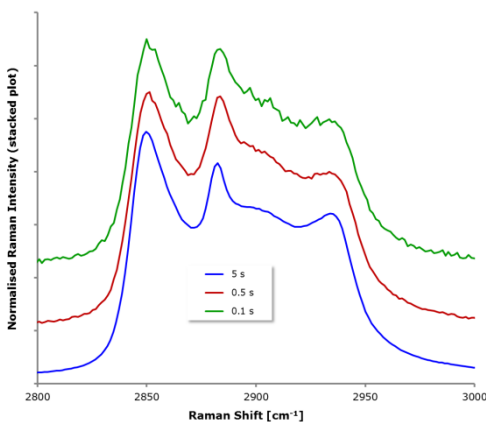


Fig. 4: Comparison of the spectral quality of the evaluated spectral range; blue: lab system; red & green: in-line system

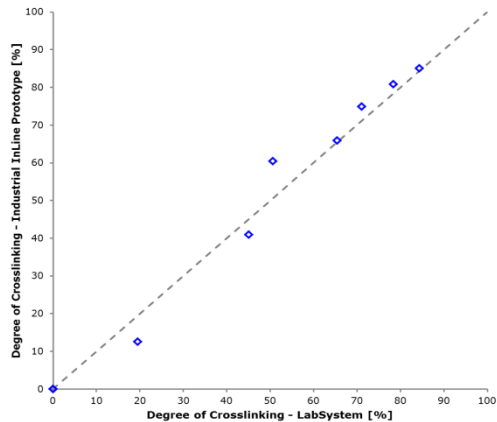


Fig. 5: Validation of the results of the in-line device against the – validated – lab method



Development and Implementation of a QCL based gas sensor for sub-ppm H₂S measurements in petrochemical process gas streams

Harald Moser¹, Johannes Ofner¹ and Bernhard Lendl¹

¹Institute of Chemical Technologies and Analytics, Vienna University of Technology, Getreidemarkt 9 / 164 UPA, 1060, Vienna

Keywords: Quantum Cascade Laser, Optical Sensor, Hydrogen Sulfide, Wavelength Modulation Spectroscopy, Petrochemical

Sensitive detection of hydrogen sulfide (H₂S) is essential for production control and environmental monitoring purposes in the field of petrochemical, paper and pulp or biotechnological processes. Despite a variety of online monitoring options for gaseous hydrogen sulfide, its quantitative reliable determination still remains a challenge in the field of chemical sensors.

A sensitive, selective and industrial fit gas sensor based on second harmonic wavelength modulation spectroscopy (2f-WMS) employing a 8 μm cw-DFB-QCL was developed for detecting H₂S at sub-ppm levels in petrochemical process gas streams.

The H₂S sensor was tested at a petrochemical research hydrogenation platform. In order to meet with the on-site safety regulations the H₂S sensor platform was installed in an industry rack and equipped with the required safety infrastructure meeting the ATEX directive for hazardous and explosive environments. The H₂S sensor rack combines a purge and pressurization system with intrinsic safety electronic devices achieving a versatile

explosion prevention and malfunction protection.

Figure 1 shows the sensor platform layout with the safety implementations and the detailed view of the optical setup. The laser radiation was passed through an optical isolator, overlaid with a visible 532 nm DPSS trace laser beam, collimated with a plano-convex lens and coupled into an astigmatic Herriott gas cell with a total path length of 100 m (AMAC100, Aerodyne Inc.). The laser radiation exiting the multipass sample cell containing the spectral information of the target analytes was focused onto an optically immersed TE cooled MCT detector (PCI-2TE-12, Vigo Systems).

The sensitivity and linear response of the H₂S sensor was investigated at different H₂S concentrations. A recorded calibration curve yielded a limit of detection (LOD) of H₂S better than 150 ppbV. An exemplary online purge gas process spectrum downstream the hydration reaction plant containing ~300ppmV H₂S is shown in Figure 2.

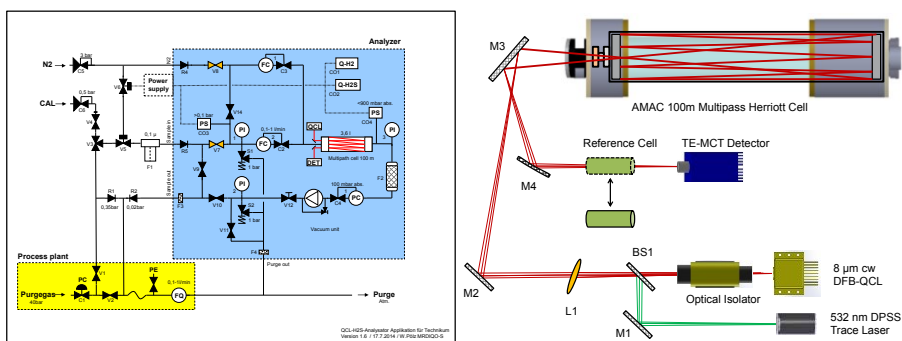


Figure 1. Piping, instrumentation and safety flow diagram (left) and the optical layout of the H₂S sensor (right)

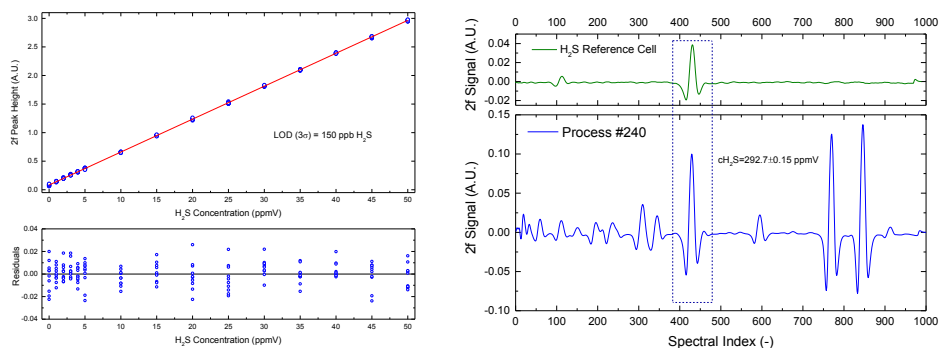


Figure 2. Calibration curve of the H₂S sensor in the range of 0-50ppmV H₂S in N₂ (left) and an online purge gas process spectrum downstream the hydration reaction plant containing ~300ppmV H₂S (right).

- ¹ NIOSH Pocket Guide to Chemical Hazards, National Institute for Occupational Safety and Health, 2007.
- ² Pearson, C.D. & Hines, W.J., 1977. Determination of hydrogen sulfide, carbonyl sulfide, carbon disulfide, and sulfur dioxide in gases and hydrocarbon streams by gas chromatography/flame photometric detection. *Analytical Chemistry*, 49(1), pp.123–126.
- ³ Hodgkinson, J. & Tatam, R.P., 2013. Optical Gas Sensing: A Review. *Measurement Science and Technology*, 24(1), p.012004.

Industrial Raman Spectroscopy: Beyond the Analytical Laboratory Setting

Ian R. Lewis¹, Alexander Pitters², Carsten Uerpmann², Herve Lucas², Bruno Lenain², Maryann Cuellar¹, David Strachan¹, Pat Wiegand¹, Sean Gilliam¹, and Joe Slater¹.

¹Kaiser Optical Systems, Inc., 371 Parkland Plaza, 48103, Ann Arbor, USA
²Kaiser Optical Systems, SARL, 5 Allee du moulin Berger, 69130, Ecully, France

Keywords: Raman, process analysis, process monitoring & control, pharmaceutical, PAT.

Introduction

In the last 20 years Raman spectroscopy has emerged as an important *in situ* analytical and process control tool^{1,2}. The early years of this period were dominated by improvements in Raman spectrometer components while recent years have seen a significant increase in the type and quantity of published *in situ* application successes. At the core of this emergence have been developments in sampling (including solid-phase sampling³) and sampling interfaces. The ability to flexibly configure the optical sampling interface allows Raman analyzers to be integrated to reactors and processing equipment. Raman spectroscopy offers a number of attractive features to the process control engineer for on-line characterization including a relatively fast response time, chemical functional specificity, and applicability to a wide variety of chemistries and materials. A secondary benefit when selecting Raman spectroscopy in industry is that a Raman analytical approach can be developed in the laboratory and accompany promising chemistries into manufacturing and throughout their lifecycle. In this work various examples of the application of Raman spectroscopy for characterization of industrial processes will be reported.

Experimental

This example illustrates the use of a Kaiser *RamanRxn Systems*TM analyzer for

monitoring and control of a pharmaceutical tablet coating device (Figure 1). The *RamanRxn Systems*TM analyzer used a 785-nm diode laser for excitation, and an axial transmissive spectrograph with a CCD array for detection. Spectra were collected over the range 175-1825 cm⁻¹, with an approximate laser power of 200 mW at the sample, and a few seconds of acquisition. The analyzer was interfaced to the sample using a Kaiser *P^hAT* probe that avoiding surface sub-sampling by illuminated mm-scale areas³.

Results and Discussion

In this work, the Raman signal from the active drug substance was ratio-ed to a band(s) arising from the coating material (Figure 2). By calculating these ratios and referencing them to a primary standard method process completion information and process end-points could be determined. This completion information can be used on subsequent batches to control the coating operation to a pre-defined completion point; thus ensuring consistent product quality.

Conclusions

In the example provided it was shown that a Raman analyzer can be interfaced to a pharmaceutical unit operation to determine process completion information as well as process end-points. The ability to monitor and control a process ensures a consistent quality outcome, this is aligned with the aims of the US FDA's PAT and Quality by

Design (QbD) initiatives^{4,5}. The Raman measurement generates real-time in-process data and process feedback. This approach minimizes the quantity of off-spec product manufactured as well as disposal / re-work costs associated with traditional off-line testing methods as well as recently developed off-line spectroscopic testing methods including transmission NIR and

Raman. Due to the brevity of this paper the experimental information noted above focuses only on a solid-phase pharmaceutical however other applications in gas-phase Raman measurements, liquid-phase crystallization and polymerization measurements, and polymeric extrusion studies have been shown.



Figure 1. P^h AT Raman Probe interfaced to a spray Tablet Coater.

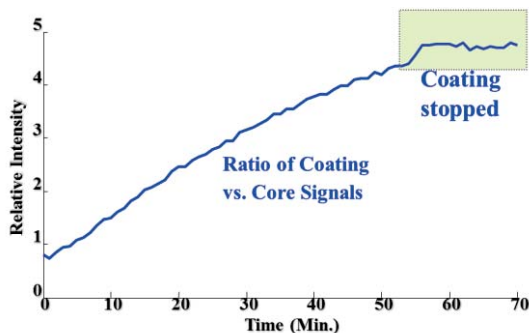


Figure 2. Plot of the ratio of core to coating spectral features for Raman-based Tablet Coater monitoring.

- ¹ Lewis, I.R., (2001) "Process Raman Spectroscopy," in *Handbook of Raman Spectroscopy: From the Research Laboratory to the Process Line*, Lewis I.R. & Edwards, H.G.M., Eds. Marcel Dekker: New York pp. 919-974.
- ² Davis K.L., Kemper M.S., Lewis I.R., (2008) "Raman Spectroscopy for Monitoring Real-Time Processes in the Pharmaceutical Industry," in *Pharmaceutical Applications of Raman Spectroscopy*, Sasic, S. (Ed) Wiley-Interscience: Hoboken pp. 117-162.
- ³ Wikstrom H., Lewis I.R., Taylor L.S., (2005) *Applied Spectroscopy*, **59**, 934-941
- ⁴ US Food and Drug Administration "Guidance for Industry PAT – A framework for innovative pharmaceutical development, manufacturing, and quality assurance", 2004.
- ⁵ US Food and Drug Administration - www.fda.gov

Improved Potential for the Use of Raman Spectroscopy to Enhance Process Understanding

Mark S. Kemper¹ and Yusuf Bismilla¹

¹Tornado Spectral Systems, 555 Richmond West, M5V 3B1, Toronto, ON Canada

Keywords: Raman Spectroscopy, Process Spectroscopy, In Situ Analysis, Process Control

Raman spectroscopy has been applied to process analysis for at least three decades. Raman has been shown to be applicable in a variety of in-line situations where it clearly has added significant value. Examples include the confirmation of titanium dioxide polymorphic constitution¹ and crystal transformation processes².

Unfortunately, Raman has been limited in many cases for three major reasons: 1) debilitating interference due to fluorescence, 2) performance limitations involving detection limits, speed of analysis and repeatability, and 3) cost considerations. In spite of these limitations, the interest in process Raman has risen steadily over the past several years and it is our anecdotal sense that this interest is set for a significant leap. Trends such as the desire of various industries for lower maintenance analysis tools and the movement of the pharmaceutical industry specifically toward continuous processing are two examples that suggest Raman will play a greater role in the future with respect to process analytics.

Ease of sampling and relatively low maintenance (equipment and calibration) are benefits that manifest as major driving forces for the use of Raman in-line. However, the advantage that Raman brings in terms of interpretability on a molecular level is a paramount attraction. Interpretation of the steady state of the process is beneficial but molecular diagnosis

of process excursions is even more crucial. Together, these facilitate process understanding, which in turn allows better process control. Process control, in turn, means smoother production operations and less down time. This all leads ultimately to enhanced profitability.

One of the most recent innovations with Raman is the High Throughput Virtual Slit (HTVS, see Figure 1)³. This has allowed more efficient photon management and this, in turn, means greatly improved throughput. This is significant for a low signal technique such as Raman as it can improve detection limits and/or time resolution substantially. A recent enhancement to HTVS⁴ now has the opportunity to boost signal throughput by an order of magnitude or more. This has the potential to make Raman applicable to situations where it has never been used. It addresses one of the major issues cited above that has limited the technology. The newest iteration of HTVS also has the chance to address the issue of fluorescence as it can, for example, allow better photon management to make measurements possible in the anti-Stokes realm. It can also allow better throughput for the less efficient higher-wavelength lasers where fluorescence is mitigated but signal is low. If this equipment can also be offered at a reasonable cost, that would also address the third issue with Raman cited above and open possibilities that were intractable previously.

In this paper, the design improvements for HTVS will be discussed. The potential for HTVS-based Raman to be used to enhance process understanding will be treated with two specific, unrelated examples as illustrations. The first is the use of Raman in a polymer curing reaction on a

production line where speed of analysis was critical.⁵ The second is the use of Raman to monitor a polymer recycling process where useful molecular information was obtained that was diagnostic of a process excursion.⁶

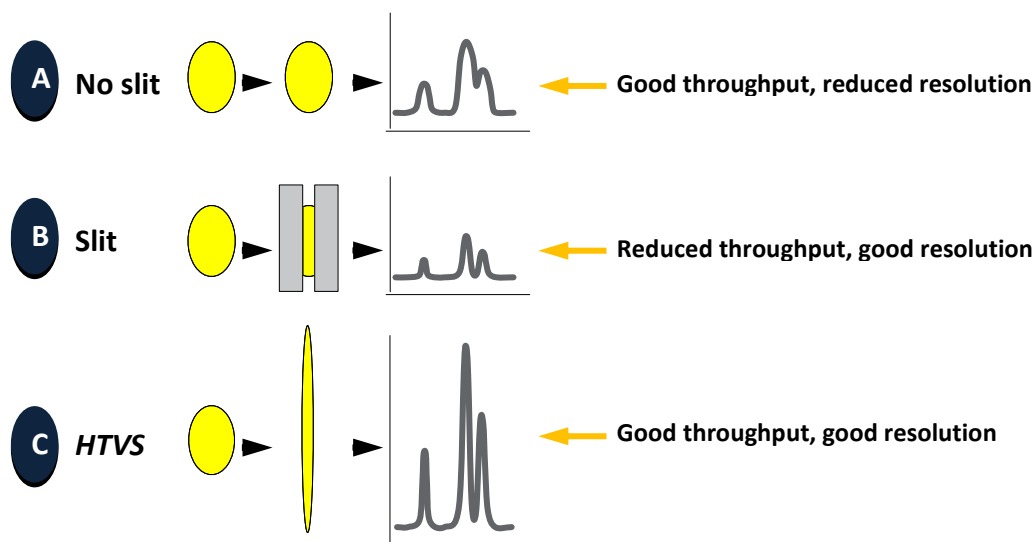


Figure 1. Illustration of the benefit of HTVS

- ¹ Clegg, IM, Everall, NJ, King B, Melvin H Norton C, On-Line Analysis Using Raman Spectroscopy for Process Control During the Manufacture of Titanium Dioxide, (2001) *Applied Spectroscopy*, 55 (9), 1138 -1150.
- ² Fang, W, Wachter JA, Antosz FJ and Berglund KA, An Investigation of solvent-mediated polymorphic transformation of progesterone using in-situ Raman spectroscopy, Lendl B., Ehmoser H., Frank J., Schindler R. (2000), *Organic Process Research and Development*, 4 (5), 391 - 395.
- ³ U.S. Patent number 8,384,896
- ⁴ U.S. Patent number 8,958,065
- ⁵ Kraft M., et. Al., (2015), *Abstract Template for ICAVS 8*.
- ⁶ Silva, E, Discrimination of Recycled PET Using Chemometrics and In-Line Raman Spectroscopy, Submitted to *Journal of Polymers and the Environment* (2015).

REAL TIME MEASUREMENTS OF POLYMER PROPERTIES BY RAMAN SPECTROSCOPY

Patrice Bourson¹, Marie Veitmann¹, Elise Dropsit¹, David Chapron¹, Aurélie Filling¹,
Alain Durand², Sandrine Hoppe³, Jean Guilment⁴ and Nicolas Dupond⁴

¹LMOPS, University of Lorraine – Supelec, 2 rue E. Belin 57070 Metz, France
patrice.bourson@univ-lorraine.fr

²LCPM University of Lorraine- CNRS, ENSIC, 1 rue Grandville 54000 Nancy, France
Alain.durand@univ-lorraine.fr

³LRGP University of Lorraine- CNRS, ENSIC 1 rue Grandville 54000 Nancy, France
Sandrine.hoppe@univ-lorraine.fr

⁴ARKEMA Arkema - Research Center CRDE BP 61005 - 57501 Saint-Avold Cedex,
France jean.guilment@arkema.com, nicolas.dupond@arkema.com

Raman spectroscopy is a technique particularly rapidly evolving in spectral qualities, quality of instruments ... and transportability of the new equipment.

This allows uses in-situ or real time using of these devices and the possibility of their use for monitoring response and industrial flows directly into the plant or reactor

We show, in this presentation, two examples of real-time monitoring by Raman spectroscopy. The first one is the control in real time of industrial flows using Raman spectroscopy combined with chemometrics to monitor very effectively an industrial polymer production. The second example is an original coupling of a Raman spectrometer with a rheometer for monitoring in real time of the polymerization of acrylic acid.

Monday

Tuesday

Wednesday

Thursday

Friday

Author Index



Fiber Optics in Vibrational Spectroscopy for Process Control and Biomedical Diagnostics

V. Artyushenko

art photonics GmbH, Rudower Chaussee 46, 12489 Berlin, Germany

Keywords: fiber probes, spectral sensors, process control, PAT, clinical spectroscopy

Key fiber spectroscopy methods will be compared for an optimal selection of the most appropriate for reaction monitoring or for the synergy of their combinations - starting from media fluorescence up to diffuse reflection in Near IR, Mid IR absorption and Raman scattering spectroscopy used for molecular analysis realized with different types of fiber probes.

Within the last 2 decades the synergy of fiber optics with UV-Vis-NIR-spectroscopy enables fast growth of fiber spectroscopy applications in lab and industry due to the several reasons:

- a) elimination of the need to collect and prepare samples for lab analysis from a running process – as it can be replaced by remote reaction monitoring in real time made with a flexible fiber probes fixed in the critical points of reactor;
- b) high optical transmission of silica fibers in 0,2-2#im range enabling remote process-control at long distance (hundreds meters) from spectral system or sensor;
- c) robust design of various spectral probes to monitor reactions at high pressure, high or low temperature, at vibrations, in toxic or aggressive media, etc.

Silica fibers are the main type used in 0.18-2.4#im range for fabrication of spectral probe required for different methods of vibrational spectroscopy: transmission, attenuated total reflection (absorption), reflection (specular and diffused), linear and non-linear Raman scattering. They can be also used for fluorescence spectroscopy and

some combinations of above listed methods. As silica fibers transmission is limited to 2.4#im by fundamental absorption in silica glass the need in flexible probes for 2-17#im range can be fulfilled by Mid IR-fibers optics. This range is known as “finger-print” for the most of fundamental absorption bands, where Mid IR-fiber probes enable reaction monitoring *in-line* or medical diagnostics *in-vivo*.

Flexible bridge between bioreactor/chemical process and IR-spectral systems or sensor can be realized with fiber probes based on Polycrystalline IR-fibers from Silver Halides, chalcogenide glass IR-fibers or hollow waveguides. Parameters of these probes will be compared to guide for their best selection in use of different methods: ATR-absorption, Transmission and Reflection. Different spectroscopy methods can be combined in single probe to reach synergy effect from complimentary data to enhance sensitivity, specificity and accuracy in diagnostics or in remote process control.

Special focus in review will be done on development of portable spectral fiber sensors of low cost. In difference with broad band spectrometers they can be designed for a customer process by optimal selection of specific spectral bands required for a distinct process control only or for *in-vivo* tumor diagnostics, for example. Key features of fiber sensors based on LED, Fabry-Perot MEMS, interference and other spectral filters will be compared with key parameters of laboratory and industrial spectrometers.

Monday

Tuesday

Wednesday

Thursday

Friday

Author Index



Using Raman Spectroscopy to Show How You ‘Personally Care’ for your Body

Paul.D.A. Pudney¹, Eleanor Y.M. Bonnist¹, Lynette A. Weddell² Fiona L. Baines², Sarah Paterson² Jane R. Matheson² Andrew Jones², Richard Evans² Susan Bates² Tony Dadd¹

¹ Unilever R&D Colworth House, Bedfordshire, MK44 1LQ, UK,

² Unilever R&D, Port Sunlight Laboratory, Bebington, Wirral, CH63 3JW, UK

Keywords: In-vivo Raman, Skin, Stratum corneum, Dandruff, NMF, Glycerol, Climbazole

This paper describes how Raman spectroscopy can be used in the personal care industry. In particular using *in vivo* Raman probe that allows investigation of areas of the body that are otherwise difficult to get access¹ to but are where we apply products we buy in the supermarket every day. These areas include the underarm (axilla) and the scalp. The probe allows the window to be placed against the subject in more curved and recessed areas of subject's body and also for them to be more comfortable whilst the measurements take place. Results from these areas of the body that have been very difficult to study before are described¹. The scalp and axilla stratum corneum (SC) show significant differences from the 'normal' SC of the volar forearm. For instance the scalp is observed to have lower amounts of natural moisturising factors (NMF) compared to the volar forearm within the same subjects. Also for both the axilla and scalp the lipids show a change in order as compared to the lipids in the volar forearm and also differences from each other. This supports the fact that they may be different phenotypes as has been previously suspected.

Dandruff is a disorder of the scalp skin that is thought to affect around half the world's population at some point. The stratum corneum (SC) of dandruff scalp has studied by in-vivo Raman and compared

with the non-dandruff scalp. The dandruff SC has lower NMF than the non-dandruff SC (0.16 compared with 0.39 a.u.), lower hydration, elevated levels of urea and lower levels of lactic acid². It can also be shown what effect these molecules have on the skin. Treatment of dandruff with an anti-dandruff shampoo containing 1% ZnPTO for six weeks substantially restores the levels of each of these components close to the non-dandruff levels.

We show how molecules which can benefit these areas of the body can be measured to see if and when they get delivered to the body. The skin benefit agent retinol, which increases the production of collagen synthesis, is shown to penetrate to a different level depending on which delivery vehicle it is in³⁻⁴. One formulation is a highly effective model delivery system identified from *ex vivo* experiments: trans-retinol in Propylene Glycol (PG)/ethanol, with PG being a well-known and efficient penetration enhancer. The other three formulations are based on 0.3 % trans-retinol in Caprylic/Capric Acid Triglyceride (MYRITOL®318), an oil commonly used in skin creams but in two of them a specific penetration enhancer is added. One contains a lipid extractor, Triton X 100, whereas another formulation contains a lipid fluidiser, Oleic Acid. Remarkable differences in the delivery of trans-retinol

between formulation with or without penetration enhancer can clearly be seen. Without a penetration enhancer virtually no adsorption was seen. With the penetration enhancers Oleic acid was the most effective.

We also show how the moisturising agent glycerol is delivered to the axilla from a full formulation a roll-on antiperspirant containing 8% deuterated glycerol (d₅-glycerol). *In vivo* Raman measurements (1h post application), demonstrated that d₅-glycerol was delivered directly from product to the axillary SC, and was detectable to a depth of 10 - 15 μm. This is the first demonstration that glycerol can be successfully delivered from an antiperspirant product into the axillary SC

Climbazole is widely used in hair care formulations for treating dandruff. It provides improved scalp health through inhibition of the fungi associated with dandruff and it may also improve the scalp skin barrier directly through its ability to increase cornified envelope protein production. To deliver both of these functional benefits climbazole needs to be delivered into the stratum corneum (SC). A solution of 0.5% climbazole in propylene glycol was applied to 10 volunteers and climbazole was detected in the SC.

These studies show there are multiple application of in-vivo Raman which give unique insights into how personal care products work in consumers.

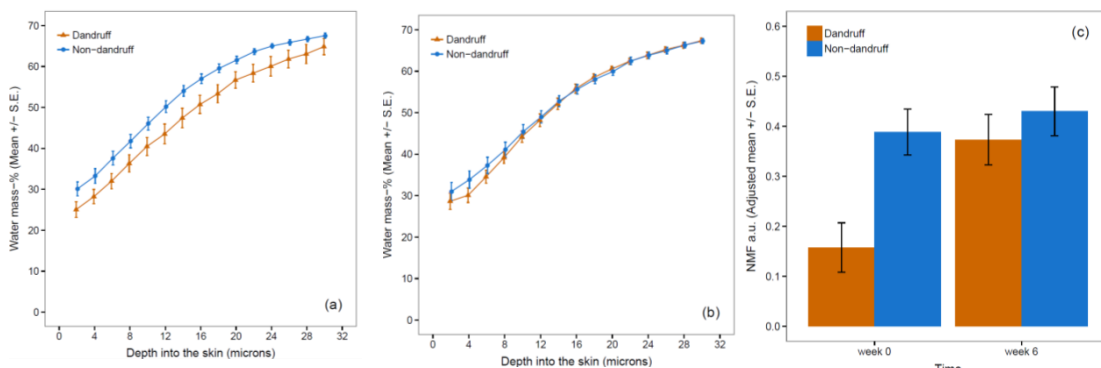


Figure 1. Average water profiles for the dandruff and non-dandruff groups at baseline (a) and after 6 weeks ZnPTO shampoo use (b) Average Natural Moisturising Factor (NMF) across the SC before and after 6 weeks ZnPTO shampoo use (c)

- ¹ Pudney P. D. A., Bonnist E.Y.M., Caspers P.J., Gorce J-P, Marriot C, Puppels G.J. S Singleton S van der Wolf M. J. G. *Applied spectroscopy* 2012, 66, 882-891.
- ² Bonnist E. Y. M., Pudney P. D. A., Weddell L. A., Campbell J, Baines F. L., Paterson S. E. and Matheson J. R. *International Journal of Cosmetic Science*, 2014, 36, 347-354
- ³ Pudney P D.A, Melot M. E, Caspers P. J, Van Der Pol A., Puppels G. J *Applied Spectroscopy* 2007 61, 804-811
- ⁴ Mélot M. E, Pudney P. D.A., Williamson A-M, Caspers P J, Van Der Pol A, Puppels G J, J *Controlled Release*, 2009, 138, 32-39

MWIR Upconversion Detection for Infrared Gas Spectroscopy

Sebastian Wolf¹, Johannes Herbst¹, Frank Kühnemann¹, Armin Lambrecht¹
¹Fraunhofer Institute for Physical Measurement Techniques IPM, Heidenhofstr. 8,
D-79110 Freiburg, Germany

Keywords: infrared spectroscopy, infrared detection, nonlinear optics, upconversion, gas sensing

The importance of the information carried by mid-infrared radiation for applications like thermal imaging, material detection and spectroscopic analysis is undisputed. Considerable effort is hence being made to develop improved detectors (both single-pixel and imaging) especially for MWIR and LWIR wavelength ranges. In contrast to silicon-based sensors for the VIS and NIR, MWIR detectors based on InSb or HgCdTe do, however, require cryogenic cooling for low-noise operation.

Upconversion of infrared photons by a three wave mixing process in nonlinear optical materials, referred to as sum frequency generation (SFG), has long been known as a mechanism to spectrally shift a signal to more easily detectable shorter wavelengths¹. For a long time, however, this approach lacked applicability mainly due to insufficient quantum conversion efficiencies for this process. Recent progress in the fields of diode-pumped solid-state lasers and nonlinear conversion crystals triggered a renaissance of the wavelength conversion approach for MWIR detection and imaging².

In our setup, photons of a 1064 nm Nd:YVO₄ laser interact with the MWIR radiation (2.5 – 5 μm) in a periodically poled LiNbO₃ (PPLN) crystal generating wavelengths between 750 and 900 nm. The crystal is positioned inside the cavity of the diode-pumped Nd:YVO₄ laser. This design

yields strong pump fields (50 W and above) for the SFG process at diode pump powers in the order of 5 W. The upconverted radiation is detected with a silicon single-pixel or array imaging sensor (Fig. 1).

The phase-matching conditions in LiNbO₃ result in a wavelength-selective upconversion process which can be controlled and tuned through the crystal structure (poling period) and crystal temperature. This makes the system a versatile tool, adaptable to a wide range of different MWIR input sources.

The system was first characterized using a 4.53 μm quantum cascade laser (QCL) as a light source. To demonstrate the applicability for remote gas sensing, a tunable mid-IR OPO was used for transmission measurements on a methane (CH₄) sample cell. The transmitted IR laser spot with wavelengths around 3167 nm was imaged on a NIR CMOS camera via the converter system. By pump tuning of the OPO, multiple absorption lines of the CH₄ were resolved as shown in Fig. 2. The results are highly promising for future applications of an upconversion system as a fast, versatile, sensitive and cost-efficient detector for mid-infrared spectroscopy.

Project funding by the Fraunhofer internal programs is gratefully acknowledged.

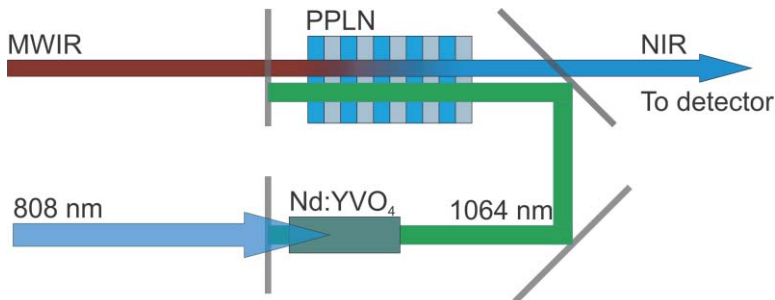


Fig. 1: Schematic setup for MWIR-NIR upconversion process.

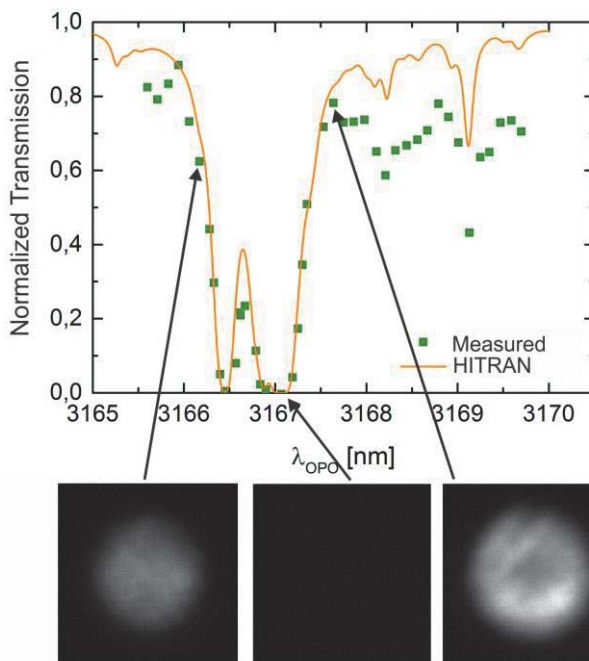


Fig. 2: Methane absorption profile measured with the upconverter imaging system under active illumination by a mid-IR OPO. Measured values are compared to theoretical HITRAN data for a CH₄ volume mixing ratio of 0.4. Shown below are examples of the evaluated spot images.

¹ Midwinter J. E. (1968), *Applied Physics Letters*, 12(3), 68, doi:10.1063/1.1651902

² Dam J.S., Tidemand-Lichtenberg P. & Pedersen C. (2012), *Nature Photonics*, 6, 788–793, doi:10.1038/NPHOTON.2012.231

Quantum Cascade Detectors for Sensing Applications

Andreas Harrer¹, Peter Reininger¹, Benedikt Schwarz¹, Donald MacFarland¹, Hermann Detz¹, Tobias Zederbauer¹, Werner Schrenk¹ and Gottfried Strasser¹

¹Institute for Solid State Electronics, Vienna University of Technology, 1040, Vienna, Austria

Keywords: Detector, Mid-infrared, QCD, Plasmonic

Quantum Cascade Detectors have been extensively investigated and improved in the last years. One major advantage of QCDs is their unbiased operation mode without significant dark current. A key aspect for integrated sensing is room temperature operation of the sources and detectors with sufficient performance. We demonstrate two approaches to enhance the room temperature responsivity and detectivity for mid-infrared QCDs. Standard QCD designs are based on an optic transition between two levels in one active well. The excited electrons are then extracted by resonant tunneling.

We present a diagonal transition design with the active transition between two neighboring active wells. The demonstrated design increases the responsivity and enables for two color detection¹. By the introduced diagonal transition a higher detector resistance and extraction efficiency is achieved. The barrier thickness between the two active wells alters the overlap integral and the dipole matrix element of the transition. We investigated the impact of these parameters on the detector performance and quality factor². The diagonal transition design is robust against small layer thickness variations as it does not rely on precise aligned levels for resonant tunneling. A very low performance drop of 12% within a thickness variation of 10% could be shown by simulation. A by nearly an order of magnitude increased peak responsivity of 16.9mA/W is demonstrated at a design wavelength of $\lambda=8\mu\text{m}$.

Beside heterostructure design and resonant absorption enhancement² in different cavities the coupling efficiency and collection can be enhanced. A common requirement in many applications is surface emission and detection of mid-infrared radiation. As QCDs are intersubband detectors they are only sensitive to electric fields in their growth direction.

We present a method to increase the detector room temperature performance and absorption efficiency utilizing plasmonic structures³. First the normal incident light is coupled to a plasmonic lens and second focused and guided to the detector. A dielectric loaded Au guiding region ensures a high coupling efficiency by end fire coupling to the QCD active region. The presented device exhibits an extended optical area while the electric part of the device stays small. The small electric active area ensures a high device resistance and low detector noise.

We demonstrate three different device designs by simulation and measurement. For a design wavelength of $\lambda=6.5\mu\text{m}$ plasmonic lens detectors in line, star and circular shape (Figure 1) were characterized. The circular lens exhibits the highest photocurrent increase while the line grating offers additional polarization selectivity. With the demonstrated plasmonic lenses the room temperature photocurrent response could be increased up to a factor of 6 compared to the reference devices.

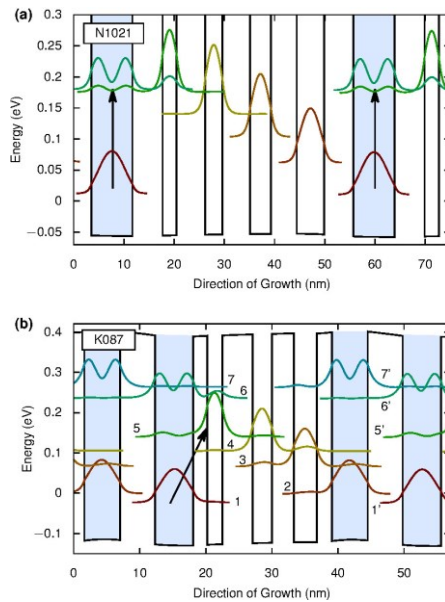


Figure 1. Bandstructure comparison between a standard QCD design (a) and a diagonal transition QCD (b) with arrows illustrating the optical active transition¹.

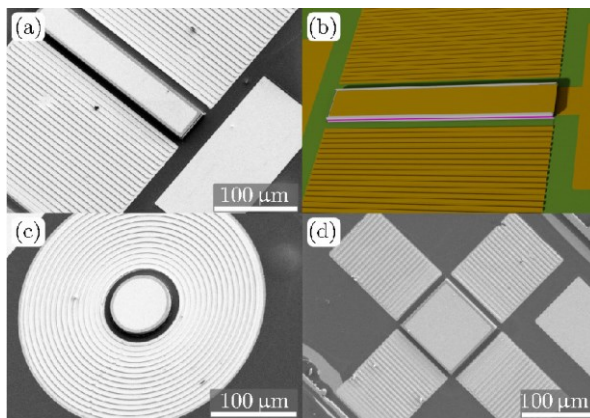


Figure 2. Plasmonic lens enhanced QCDs surrounded by the lenses in line (a), circular (b) and star (d) shape using a dielectrically loaded guiding region³.

- ¹ Reininger P., Schwarz B., Detz H., MacFarland D., Zederbauer T., Andrews A.M., Schrenk W., Baumgartner O., Kosina H. and Strasser G. (2014). *Appl. Phys. Lett.* Vol. 105, 091108
- ² Reininger P., Schwarz B., Detz H., MacFarland D., Zederbauer T., Andrews A.M., Schrenk W., Baumgartner O., Kosina H. and Strasser G. (2015). *Opt. Express*, Vol. 23, Issue 5, pp. 6283-6291,
- ³ Harrer A., Schwarz B., Gansch R., Reininger P., Detz H., Zederbauer T., Andrews A.M., Schrenk W. and Strasser G., (2014), *Appl. Phys. Lett.* Vol. 105, 171112

Room temperature MCT detectors for FTIR spectroscopy

Karolina Ogrodnik¹, Jaroslaw Pawluczyk¹, Mariusz Romanis¹, Jozef Piotrowski¹

¹VIGO System S.A., Poznanska 129/133 St., 05-850 Ozarow Mazowiecki, POLAND

Keywords: HgCdTe, photodiode, photoconductor, room temperature MCT detector

VIGO System S.A. is the leading manufacturer of standard and customized High Operating Temperature HgCdTe detectors - fast and convenient to use, at any wavelength from 2 to 16 μm , reaching fundamental BLIP limits, without cryocooling¹.

We present detection modules for sensitive and wide bandwidth detection of MWIR and LWIR radiation (Figure 1), that are optimized for operation at frequency bandwidth from DC to GHz range²⁻⁴.

Several types of IR detectors based on advanced HgCdTe heterostructure are presented.

IR detectors with improved performance and high frequency response utilizing optical immersion are reported. Recent efforts concentrated on the extension of useful spectrum range above 13 micrometers for FTIR spectrometer applications is presented⁵. High performance in long wavelength region was achieved with improved design of the active element, monolithic optical immersion technology, enhanced absorption of radiation, applying more efficient Peltier cooler and dedicated electronics. Spectral and frequency response of some modules are reported.

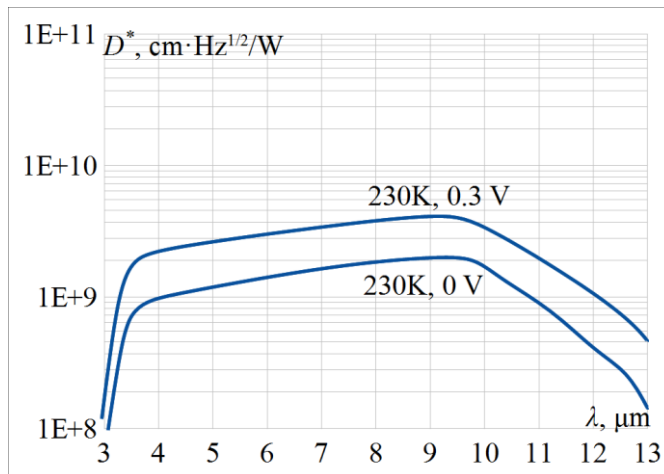


Figure 1. Exemplary spectral characteristic (detectivity D^* vs wavelength λ) of HgCdTe detector optimized for LWIR radiation

- J. Piotrowski and A. Piotrowski "Near room temperature detectors", Mercury Cadmium Telluride, ed. By P. Capper, J. Garland, John Wiley & Sons, To be published,
- D. Stanaszek, J. Piotrowski, A. Piotrowski, W. Gawron, Z. Orman, R. Paliwoda, M. Brudnowski, J. Pawluczyk and M. Pedzińska, „Mid and long infrared detection modules for picosecond range measurements”, *Proc. SPIE*, 7482, pp. 74820M-74820M-11, (2009)
- J. Piotrowski and A. Rogalski, „High-Operating Temperature Infrared Photodetectors”, SPIE, Bellingham (2007),
- A. Piotrowski, J. Piotrowski, W. Gawron, J. Pawluczyk and M. Pedzinska, „Extension of Usable Spectral Range of Peltier Cooled Photodetectors”, *Acta Physica Polonica A*, 116, 52-55, (2009),
- A. Piotrowski, J. Piotrowski, W. Gawron, J. Pawluczyk and M. Pedzinska, „Extension of spectral range of Peltier cooled photodetectors to 16 μm ”, *Proc. SPIE*, 7298, 729824, (2009).



Optimum Drive Conditions for DLaTGS Pyroelectric Detectors in FTIR Applications and its Impact on Performance

Alan Doctor¹ and Johannes Kunsch²

¹Laser Components Pyro Group Inc., 529 SE Central Parkway, 34994 FL, Stuart, USA

²Laser Components GmbH, Werner-von-Siemens-Str. 15, 82140, Olching, Germany

Keywords: Pyroelectric detector, DLaTGS, FTIR, Infrared detector, LWIR

Pyroelectric DLaTGS detectors are the workhorse detectors in FTIR instruments. Detector improvements will directly result in instrument improvements. We are investigating the “ideal pyroelectric FTIR detector”. Typically, these devices require an impedance converting amplifier. There are two basic configurations: The so-called Voltage Mode (VM), which so far dominates the applications, and the Current Mode (CM). Due to basic considerations, current mode operation at appr. 45°C should yield best performance. Furthermore, we developed a unique connection scheme (patent pending) that increases the signal to noise of any pyroelectric detector by a factor of about 1.4. We intend to combine both approaches in order to make the “ideal” DLaTGS detector.

A pyroelectric detector is usually modeled as a current source in parallel with a capacitor. When used in the VM its output is measured as voltage appearing on the plates of the capacitor typically with a JFET as impedance converter. This operation mode is most widely used until today. The reason is that the converter needs to have low power consumption and should also be low cost. Historically, the JFET was the only component that did fulfill these requirements. However, the Voltage Mode does have a drawback at DLaTGS detectors: The output is proportional to the ratio of

pyroelectric constant and dielectric constant. Therefore, there is no sweet spot of ideal performance in VM since both constants increase with increasing temperature (Figure 1 and Figure 2). The situation is completely different in CM since the output in CM is independent of the dielectric constant. Here, it should make sense to use the detector at a temperature around 45°C. Compared to room temperature, nearly a doubling of performance can be expected. We will present experimental data at the conference. In general, CM operation starts to get more popular these days due to availability of affordable opamp chips with low power consumption.

So far, all impedance converters for pyroelectric detectors are “single ended” by nature and thus any electronic perturbation from an external or internal source and other sources of electronic noise can be coupled onto the detector’s output signal. We present a rather unique connection scheme (patent pending) which provides for an increase in the signal to noise of any pyroelectric detector by a factor of the square root of 2 or by about 1.41 times the standard type, thus increasing the D^* of any pyroelectric IR Detector by the same factor. This connection also provides a true differential output. This scheme works in both CM and VM.

Current Response (A/W) vs. Temp. (DLATGS & LTO)

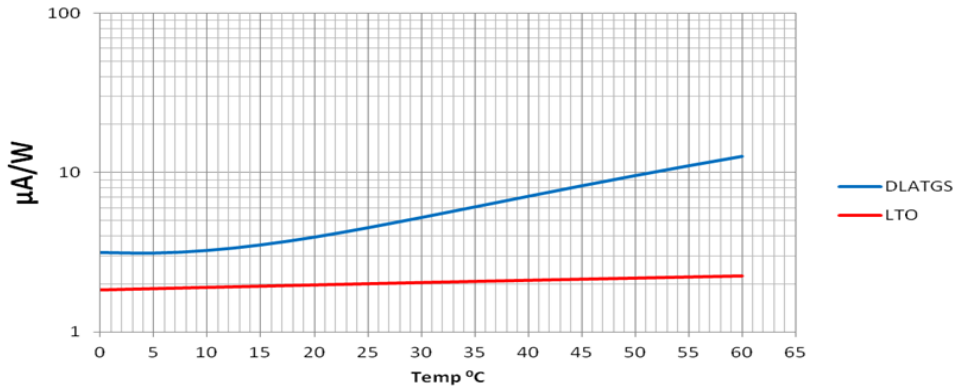


Figure 1. This figure shows the signal versus chip temperature for DLaTGS (blue curve). The signal is directly proportional to the pyroelectric coefficient. The pyroelectric material LiTaO_3 (red curve) is shown for reference purposes. The figure illustrates why DLaTGS is chosen as pyroelectric material in high performance applications like FTIR.

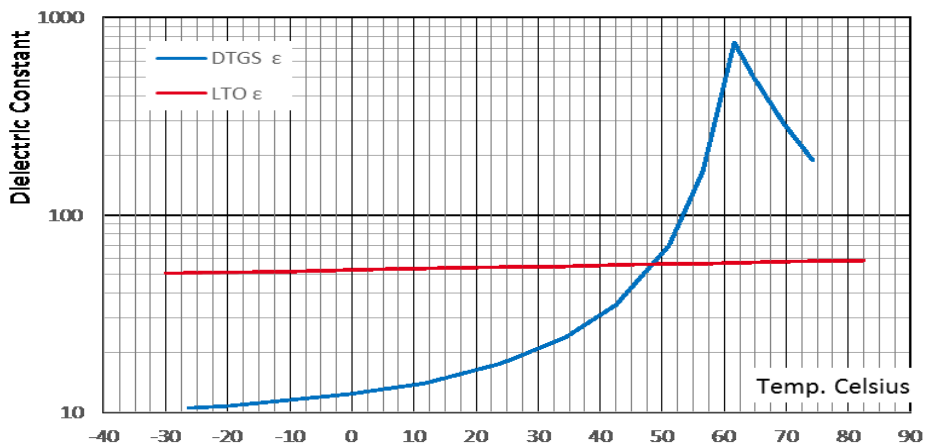


Figure 2. This figure shows the dielectric constant of DLaTGS (blue curve). The characteristic of the pyroelectric material LiTaO_3 (red curve) is shown for reference purposes.

¹ Doctor A., (2014), *Paper at 2nd WORKshop for Infrared Technologies, Olching*

Femtosecond Vibrational Spectroscopy of Simple and Complex Systems

Tahei Tahara^{1,2}

¹Molecular Spectroscopy Laboratory, RIKEN, 2-1 Hirosawa, Wako, Saitama 351-0198, Japan

²Ultrafast Spectroscopy Research Team, RIKEN Center for Advanced Photonics (RAP),
2-1 Hirosawa, Wako, Saitama 351-0198, Japan

Keywords: femtosecond, time-resolved, Raman, photochemistry, photoreceptor protein

Raman spectroscopy is one of the most important optical spectroscopies and has been extensively utilized in a variety of fields of science and technology. In ordinary Raman spectroscopy, we measure energetically-shifted inelastic light scattering, and the energy shift from the excitation light provides information about the vibrational energy of the molecule. On the other hand, by using an ultrashort optical pulse that has a duration shorter than the vibrational period, we can induce coherent nuclear motion of the molecule by the impulsive Raman process and observe Raman-active vibrations directly in the time domain [1]. This way of observing molecular vibrations is called time-domain Raman spectroscopy. In principle, the information obtained by time-domain Raman spectroscopy is equivalent to that obtained by the ordinary frequency-domain Raman spectroscopy. However, because time-domain Raman spectroscopy is performed using only femtosecond pulses, we can trace the temporal change of the Raman spectrum with a femtosecond accuracy by combining it with a femtosecond pump pulse that excites the sample to start chemical reactions.

For investigating ultrafast dynamics by Raman spectroscopy, we developed time-resolved impulsive stimulated Raman spectroscopy (TR-ISRS) and demonstrated its high potential by applying it to simple molecules in solution [2, 3]. In this method,

we use three femtosecond pulses: The first pulse (P1) photoexcites molecules to start chemical reactions. After a certain delay time (ΔT), the second pulse (P2) is irradiated to induce coherent nuclear wavepacket motion in the transient species, and the third pulse (P3) measures the wavepacket motion through the oscillation of the transient absorption and/or stimulated emission. The Fourier transform of the observed oscillation corresponds to the time-resolved Raman spectrum at the time delay at ΔT . Because we use only femtosecond pulses in the TR-ISRS measurements, we can change the delay time with a femtosecond accuracy. Therefore, we can trace the temporal change of the sample through the evolution of femtosecond time-resolved Raman spectra. Using sub-7-fs pulses for the ISRS measurement, we are now able to obtain time-resolved Raman spectra of the transient in the all the fundamental frequency region from terahertz to over 3000 cm^{-1} by this time-domain approach.

In this presentation, we report on our recent TR-ISRS studies for simple and complex molecular systems, in particular, the study on a photoreceptor protein, photoactive yellow protein (PYP). PYP is a water-soluble, phototrophic bacterium, which was discovered in a halophilic purple phototrophic bacterium, *Halorhodospira halophila*. PYP is considered to function as a blue-light photoreceptor for negative phototactic response of this organism. The

function of PYP is realized by a photocycle, which is triggered by the photo-induced trans-to-cis isomerization of the chromophore, p-coumaric acid (pCA). The isomerization reaction has been considered to occur on the femto-to-picosecond time scale, and it gives rise to the formation of the first ground-state intermediate called the I_0 state. We excited PYP with 450 nm (P1), and carried out TR-ISRS measurements with broadband 500-700 nm sub-7-fs pulses (P2 and P3) (Fig. 1). The P2 and P3 pulses are in resonance with the stimulated emission of the first excited pG^* state as well as the transient absorption of the first ground-state intermediate, I_0 . The obtained time-resolved

Raman spectra indicated that the chromophore (p-coumaric acid) retains a trans-configuration in the pG^* state while the surrounding hydrogen-bonding structure changes in a few hundred femtoseconds after photoexcitation. Time-resolved Raman spectra of the I_0 state have also been measured with very high S/N. The comparison between the obtained Raman spectrum and DFT calculation indicates that the chromophore in the I_0 state has a highly distorted cis-form. This study clearly demonstrate that TR-ISRS is highly capable of clarifying the ultrafast structural change of the complex systems such as photoreceptor proteins.

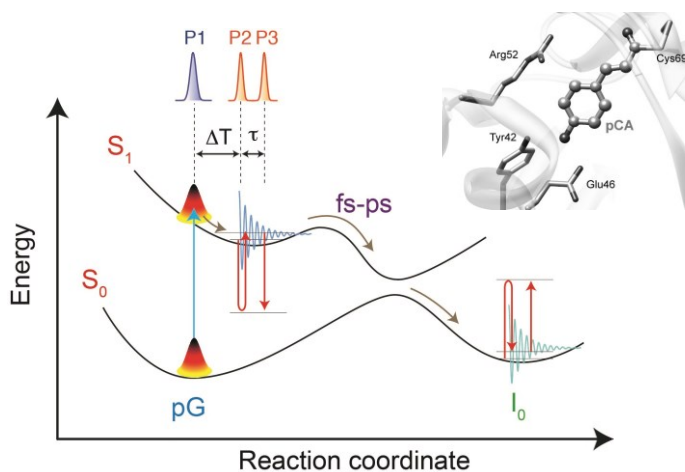


Figure 1. Experimental scheme of TR-ISRS for PYP.

¹ For example, Matsuo S., Tahara, T. (1997), *Chem. Phys. Lett.*, 264, 636-642.

² Fujiyoshi, S., Takeuchi, S., Tahara, T. (2003), *J. Phys. Chem. A*, 107, 494-500.

³ Takeuchi, S., Ruhman, S., Tsuneda, T., Chiba, M., Taketsugu, T., Tahara, T. (2008), *Science*, 322, 1073-1077.

⁴ Kuramochi, H., Takeuchi, S., Yonezawa, K., Kamikubo, H., Kataoka, M. Tahara, (2015), T. in preparation.

From Esoteric to Commonplace: Technological Advances that have Turned 2D IR Spectroscopy into a Robust Research Tool

Martin T. Zanni

Department of Chemistry, University of Wisconsin-Madison, Madison WI 53706 USA

Keywords: femtosecond, 2D infrared, vibrational, spectroscopy

The field of femtosecond 2D IR spectroscopy is at a turning point, both intellectually and technologically. Researchers in the field now understand the nuances behind the technique. We now know how to interpret 2D lineshapes, the intensities of cross peaks, and the polarization dependence of the spectra. From the spectra, we can now reliably obtain dynamical parameters, bond angles, coupling strengths, and many other structural constraints. In parallel to the interpretation have been developments in quantitatively simulating 2D IR spectra. Molecular dynamics simulations of proteins can now be routinely converted to very accurate 2D IR spectra. Technological advances have improved the signal strengths, accuracy, and ease of which 2D IR spectra can now be collected. And the range of applications is now very broad, encompassing chemical reactions, electron transfer, peptide and protein structures, materials research, the energy sciences and more. As a result, the field of 2D IR spectroscopy is pivoting from that of an untested and poorly understood technique to a versatile and widely applied research tool.

This talk will cover recent technological advances that have made 2D IR spectroscopy as easy to implement as common transient absorption spectroscopy.¹ And, having explained this technology, a scientific example will be given in which we have uncovered an explanation for why some species, like humans and cats, develop

type 2 diabetes while other species, like rats and dogs, do not.²

Regarding the technology, I will explain how a pump-probe spectrometer can be converted into a 2D IR spectrometer by adding a mid-infrared pulse shaper. Prior to our work, the most common place design for a 2D IR spectrometer has 4 overlapping laser beams, which made experiments extremely difficult. Our pulse shaper approach enables very accurate spectra to be collected very rapidly. It also enables pulse sequences to be generated that were difficult or impossible to make previously. For example, the phases of the pulses can now be rotated in order to subtract the background without chopping the beam and decreasing the repetition rate. Most importantly, it is now a 2 beam experiment with an easily measured signal.

In a similar manner, sum-frequency generation (SFG) spectrometers can also be converted into 2D SFG spectrometers by the addition of a mid-IR pulse shaper. 2D SFG spectra collected in this manner will be shown briefly.

We have been using our pulse shaping 2D IR spectroscopy to study the aggregation of the human islet amyloid polypeptide (hIAPP or amylin) that is associated with type 2 diabetes. Not all mammals contract type 2 diabetes even though all species contain a very similar peptide. 25 years ago it was postulated that the amino acids in the central region of peptide containing the FGAIL sequence in humans formed the beta-sheets that were the core of the amyloid

fibers. This hypothesis was based on many experiments showing that peptides with mutations in this region to amino acids that could not form beta-sheets did not aggregate. That hypothesis stood the test of time until the fiber structure was solved and the FGAIL region turned out to be a disordered loop instead.

Using 2D IR spectroscopy, we have monitored the formation of amyloid fibers made from hIAPP. We have used isotope labels to monitor individual residues during aggregation. The vibrational coupling between isotope labeled residues that form parallel beta-sheets is very strong and so have a characteristic frequency shift and cross peaks. From our experiments, we discovered that the FGAIL sequence adopts a parallel beta-sheet prior to rearranging into the structure of the fiber. This intermediate appears to explain many of the prior experiments and resolves the contradiction of the 25 year old hypothesis with the structure of the fibers.

This example is very apt for describing the technology of pulse shaping 2D IR spectroscopy, because the measurements are done at low protein concentrations, utilize phase cycling to remove background scatter, and must be acquired very quickly to monitor kinetics on-the-fly. Because it deals with aggregates and kinetics, it is unlikely that this information could be obtained by any other technique. It exemplifies the transition that 2D IR spectroscopy has undergone to become a sophisticated research tool for probing cutting-edge topics in the life sciences.

Acknowledgements: This work was funded in part by the NIH NIDDK 79895 and the NSF CHEM-1266422. Zanni is co-founder of PhaseTech Spectroscopy, Inc., which manufactures commercial 2D IR spectrometers.

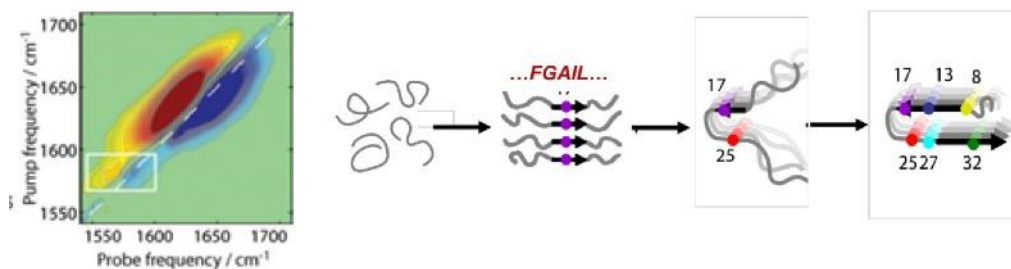


Figure 1. (left) 2D IR spectrum of the human islet amyloid polypeptide (hIAPP or amylin) showing an isotope labeled peak created by a beta-sheet secondary structure. (right) Schematic for the structural changes that hIAPP undergoes as it aggregates into amyloid fibers.

- Middleton, C.T., Woys, A.M., Mukherjee, S. S., Zanni, M. T., “Residue-Specific Structural Kinetics of Proteins through the Union of Isotope Labeling, Mid-IR Pulse Shaping, and Coherent 2D IR Spectroscopy,” *Methods*, 52, 12 (2010).
- Lauren E. Buchanan, Emily B. Dunkelberger, Huang Q. Tran, Pin-Nan Cheng, Chi-Cheng Chiu, Ping Cao, Daniel P. Raleigh, Juan J. de Pablo, James S. Nowick, Martin T. Zanni, “Mechanism of IAPP amyloid fibril formation involves an intermediate with a transient β -sheet,” *PNAS*, 110, 19285 (2013).

Investigating the binding of metal ions to peptides and inhibitors to proteins using two-dimensional infrared spectroscopy

Julia Davies, Hugh Sowley, Keith Willison and David Klug

Department of Chemistry, Imperial College London, SW7 2AZ, London, UK

Keywords: infrared spectroscopy, 2DIR, Alzheimer's disease, cancer.

An unusual variant of two-dimensional infrared (2DIR) spectroscopy has been used to investigate several biological systems of interest. The first is the chelation of zinc ions to histidine residues in the amyloid beta peptide, which is of relevance to the formation of senile plaques in Alzheimer's Disease¹. The second system is the binding of an inhibitor to the tyrosine kinase domain of a fibroblast growth factor receptor, FGFR1, which is of therapeutic significance for a number of growth disorders and cancers².

Electron-vibration-vibration (EVV) 2DIR spectroscopy is a frequency-resolved technique in which three laser beams are spatially overlapped in a biological sample and the emitted photons are detected whilst the frequencies of the two mid-IR beams are systematically varied³. The resulting spectra are less congested than those obtained using one-dimensional IR techniques, allowing for easy identification of cross-peaks from protein/peptide residues and backbone modes, as well as small molecule inhibitors.

EVV 2DIR spectra have been measured for the amyloid beta peptide fragment, A β (11-17), with sequence H-Glu-Val-His-His-Gln-Lys-Leu-OH, because the two adjacent His residues are implicated in zinc chelation¹. Spectra recorded as a function of pH have resulted in the successful assignment of His cross-peaks for both the protonated state (pH<6) and deprotonated state (pH>6). The addition of

ZnCl₂ to A β (11-17) at pH7 leads to significant changes in the 2DIR spectra, including a reduction in the His cross-peak intensity due to zinc ion binding. Structural changes in the peptide are also indicated by the amide I cross-peak.

EVV 2DIR spectra for the tyrosine kinase domain of FGFR1 have been measured, both with and without the addition of a known inhibitor SU5402; this enables the cross-peaks to be assigned to either the drug or the protein. Figure 1 shows a 2DIR spectrum for a 1:1 molar ratio of SU5402 and FGFR1, with the drug cross-peaks labelled D* and the protein cross-peaks labelled P*. The cross-peak intensities for all drug peaks have been measured at six different molar ratios of drug to protein, ranging from no drug to an excess of drug. Some of the cross-peaks exhibit different behaviors from others. For example, certain cross-peaks show an increase in intensity up to 1:1 stoichiometry, after which no further increase in intensity is observed. This indicates that the signal originates from bound drug only, and has no contribution from the unbound drug or from non-specific binding. In contrast, other cross-peaks show an increase in intensity well above the known stoichiometry. When combined with appropriate calculations^{4,7}, the experimental results have the potential to provide information on both the geometry of the bound inhibitor and the bonds formed between inhibitor and protein.

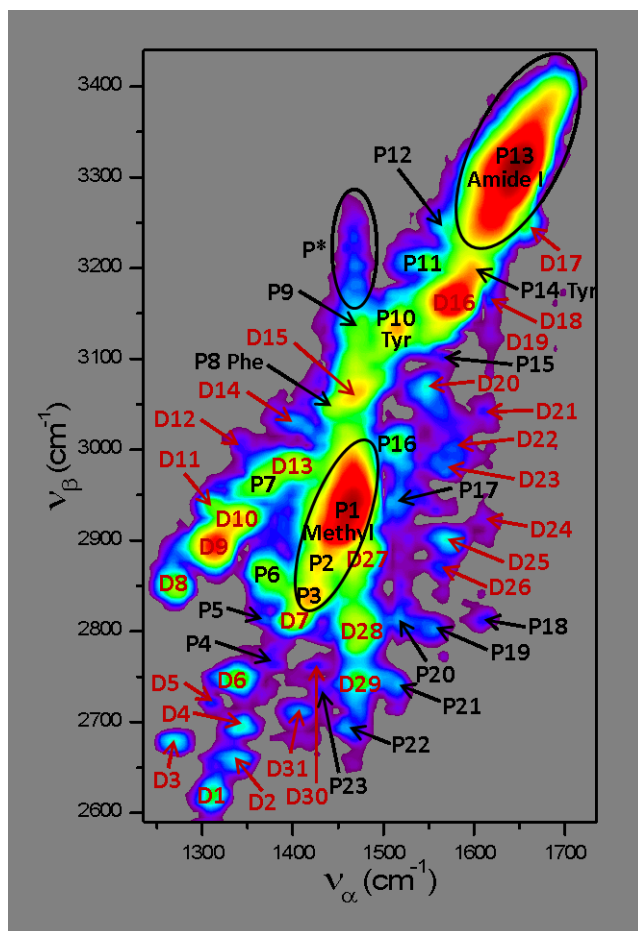


Figure 1. Two-dimensional infrared spectrum of a small molecule inhibitor, SU5402, bound to the kinase domain of FGFR1. The cross-peaks assigned to the drug are labelled D*, whilst the cross-peaks assigned to the protein are labelled P*.

- ¹ Tougu V., Tiiman A., P. Palumaa P. (2011), *Metallomics*, 3, 250-261.
- ² Turner N. & Grose R. (2010), *Nature Reviews Cancer*, 10 (2), 116-129.
- ³ Rezende Valim L., Davies J.A., Tveen Jensen K., Guo R., Willison K.R., Spickett C.M., Pitt A.R., Klug D.R. (2014), *The Journal of Physical Chemistry B*, 118 (45), 12855-12864.
- ⁴ Donaldson P.M., Guo R., Fournier F., Gardner E.M., Barter L.M., Barnett C.J., Gould I.R., Klug D.R., Palmer J., Willison K., (2007), *The Journal of Chemical Physics*, 127, 114513.
- ⁵ Guo R., Fournier F., Donaldson P.M., Gardner E.M., Gould I.R., Klug D.R. (2009), *Physical Chemistry Chemical Physics*, 11 (38), 8417-8421.
- ⁶ Guo R., Miele, M., Gardner E.M., Fournier F., Kornau K.M., Gould I.R., Klug D.R. (2011), *Faraday Discussions*, 150, 161-174.
- ⁷ Guo R., Mukamel S., Klug D.R. (2012), *Physical Chemistry Chemical Physics*, 14 (40), 14023-14033.

High resolution FTIR tomographic imaging of single cells

Kathleen M. Gough¹ and Catherine R. Findlay¹

¹Department of Chemistry, University of Manitoba, R3T 2N2, Winnipeg, Canada

Keywords: 3D FTIR imaging, microspectroscopy, tomography, human cells

The generation of 3D FTIR images is feasible if one takes advantage of the speed and resolution of FTIR instrumentation and the established principles of computed tomography (CT). FTIR tomography was first demonstrated¹ at the InfraRed ENvironmental Imaging beamline (IRENI) at the Synchrotron Radiation Center (SRC), Univ. of Wisconsin-Madison in 2013. At the time, only IRENI had sufficiently high spatial resolution, area of illumination, Focal Plane Array (FPA), acquisition speed and brilliance to make FTIR tomography feasible.

Here, we present tomographic imaging achieved with a thermal source FTIR microscope, using our Agilent Cary 620 FTIR microscope (64×64 FPA) and Agilent Cary 670 spectrometer. The optics in the microscope can be operated at normal magnification (5.5×5.5 μm² pixels), or higher magnification (1.1×1.1 μm² pixels)². Key features to success are rapid collection of individual 2D images, at sufficient non-redundant angles to comprise a tomographic data set. For this dimension of array, at least 64 non-redundant angles should be acquired, to ensure that the data set is not under sampled. While crude images can be created with normal magnification, evaluation of the 3D composition of individual cells requires the higher magnification optics and preferably 4 cm⁻¹ spectral resolution for sub-cellular analysis, although 8 cm⁻¹ can be chosen if the spectral features warrant.

The individual spectrum corresponding to a single voxel in the 3D FTIR image is

reconstructed from the 2D images using MatLab™ batch data import, computed tomography (CT) and voxelated display algorithms adapted for back-projection of infrared images. Our 3D FTIR data processing employs the inverse Radon transform, used with linear interpolation and without convolution or filtering. Once a data set is processed and displayed, micron-scale 3D FTIR images show the relative concentrations of compounds in a cell, voxel by voxel, based on their FTIR spectroscopic signatures.

Factors intrinsic to the reconstruction method and sampling of viewing angles can generate spatial aliasing error and further reduce the resolution of a 3D FTIR image. This aliasing is not an optical effect, but rather an image processing artefact that can impact spatial resolution. It is possible to have negligible aliasing error in FTIR 3D reconstructions provided that sufficient non-redundant projection angles are sampled. Discretization error can be improved by increasing sampling of viewing angles, with a trade-off for speed of data set acquisition. The final discretization will depend on the chosen sampling parameters.

Here, we show the biochemical composition of diatoms and of different mammalian cells as imaged using FTIR tomography. Individual cells, selected from suspension, were mounted onto our in-house designed tomography accessory (US provisional patent application 62/131,655). The latter has advantages over the design employed previously¹, including precise

alignment and rotation of the sample, ease of setup and disassembly, low weight and compatibility with microscope stage translation. With this design, we have also achieved the first mosaic 3D FTIR imaging of samples that extend beyond a single FPA tile. A visible light image of a freshly acquired human buccal cell, mounted on a polyamide protein crystallography loop, is shown in Figure 1A. The size of the sample was such that it was best imaged as a series of three tiles, acquired by lateral translation of the stage-mounted tomography device. The sample was imaged at 64 viewing angles and the data set was processed in

Matlab™. The cell has a strong Amide I band at 1652 cm^{-1} , distinct from that of the loop. The latter is easily identified by integration of a strong band at 1488 cm^{-1} . Still images taken from the tomographic 3D movie display are shown for the cell (Figure 1B) and loop (Figure 1C).

We can now extend the 3D FTIR imaging to other biological systems, while more fully accessing the 3D spatial resolution possible with our thermal source instrument. The portable tomography accessory can be easily accommodated with different instrument configurations and illumination sources.

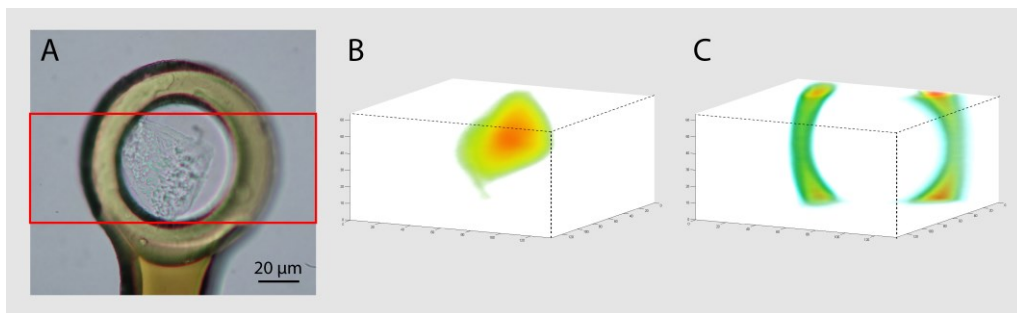


Figure 1. FTIR Tomographic imaging of a human buccal cell, $192 \times 192 \times 64$ voxels, $1.1\ \mu\text{m}$ edge. A) Visible light microscope image of cell mounted on polyamide loop. Red box delineates the 3×1 tile area acquired at each viewing angle. Still images of 3D rendered tomographic movie show: (B) cell body imaged on Amide I band at 1652 cm^{-1} and (C) loop imaged at 1488 cm^{-1} .

- ¹ Martin M. C., Dabat-Blondeau C., Unger M., Sedlmair J., Parkinson D. Y., Bechtel H. A., Illman B., Castro J. M., Keiluweit M., Buschke D., Ogle B., Nasse M. J., Hirschmugl C. J., (2013), *Nature Methods* 10 (9), 861-864.
- ² Findlay C. R., Wiens R., Rak M., Sedlmair J., Hirschmugl C. J., Morrison J., Mundy C. J., Kansiz M., Gough K.M., (2015) *Analyst* 140, 2493 - 2503.

Monday
Tuesday
Wednesday
Thursday
Friday
Author Index

A mid-infrared on-chip sensor array based on bi-functional quantum cascade structures & plasmonics

Gottfried Strasser¹, Daniela Ristanic², Benedikt Schwarz², Peter Reininger¹, Hermann Detz¹, Aaron M. Andrews², Tobias Zederbauer², Donald MacFarland², and Werner Schrenk¹

¹Center for Micro- and Nanostructures, Vienna University of Technology

²Institute for Solid State Electronics, Vienna University of Technology
Floragasse 7, 1040 Vienna, Austria

Keywords: quantum cascade laser, quantum cascade detector, on-chip sensor, plasmonics waveguides, spectroscopy, sensor array

Mid-infrared spectroscopy is a reliable method for the identification of gaseous and liquid mixtures due to their unique and inherent absorption spectra. We used a specially designed intersubband material working as laser for a given bias voltage and as a detector without any bias. By the use of such a bi-functional quantum cascade structure material for the light sources and detectors, operating at the same frequencies in the same material, the realization of mid infrared on-chip sensors is possible [1].

Liquid sensing at room temperature with a monolithic integrated sensor was achieved [2] by a Quantum Cascade Laser (QCL), a dielectric loaded Surface Plasmon Polariton (SPP) waveguide as interaction section of the infrared light with the liquid, and a Quantum Cascade Detector (QCD).

As SPP waveguide structures gold layers with SiN dielectrics, reduce the losses and allow long distance guiding of the mid-infrared light. Without SPP waveguides the light is lost as shown in fig 1.

The monolithic integration allows for miniaturization and is especially suited for portable devices. This talk aims to give a

short introduction in the field of intersubband bi-functional materials with a strong focus on quantum cascade lasers and quantum cascade detectors. The first sensor elements used multimode Fabry-Perot lasers and broadband detector materials [2].

To further improve the sensitivity and selectivity of these monolithically integrated mid-infrared sensors we plan to report about the utilization of distributed feedback quantum cascade lasers. Weakly coupled DFB quantum cascade lasers emit narrow mode mid-infrared light with a FWHM of around 2 cm⁻¹ at 1586 cm⁻¹. The room temperature laser threshold current density of the first demonstrated devices is around 3 kA=cm², a pulsed output power in the range of 200 mW was measured. With the superior laser noise performance, due to narrow mode emission and the compensation of thermal fluctuations, the lower limit of detection was expanded by one order of magnitude into the 10 ppm range [3]. The first proof-of-principle detector array (fig2) working at a frequency range around 1550 cm⁻¹ can be fabricated at all wavelength ranges accessible with quantum cascade lasers.

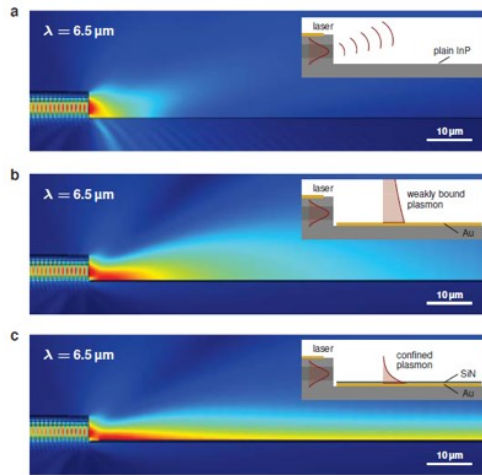


Figure 1. Laser ridge and SPP waveguide concept for our sensors.
(a) Plain InP substrate; (b) thin gold film; (c) gold and SiN layer structure.

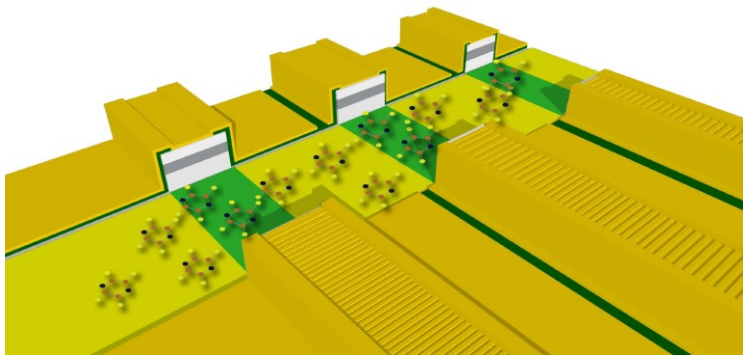


Figure 2. Monolithic integration: array of 3 different DFB QC lasers, each lasing at a different wavelength and 3 broadband detectors. The SPP waveguide is shown in green.

¹ B. Schwarz, P. Reininger, H. Detz, T. Zederbauer, A.M. Andrews, W. Schrenk, and G. Strasser, "Monolithically integrated mid-infrared quantum cascade laser and detector," *Sensors* 13, 2196 (2013).

² B. Schwarz, P. Reininger, D. Ristanic, H. Detz, A. M. Andrews, W. Schrenk, and G. Strasser, "Monolithically integrated mid-infrared lab-on-a-chip using plasmonics and quantum cascade structures," *Nat. Commun.* 5, 4085, (2014)

³ D. Ristanic, B. Schwarz, P. Reininger, H. Detz, T. Zederbauer, A.M. Andrews, W. Schrenk, G. Strasser, "Monolithically integrated mid-infrared sensor using narrow mode operation and temperature feedback", *Appl. Phys. Lett.* 106, 041101 (2015)

Imaging molecular structure of plant cells by Confocal Raman microscopy

Notburga Gierlinger¹

¹Institute of Physics and Material Science, University of Natural Resources and Life Sciences, Peter-Jordan-Straße 82, 1190, Vienna, Austria

Keywords: Raman imaging, cellulose, lignin, cell wall, wood,

During the last years Confocal Raman microscopy evolved as a powerful method to get insights into chemistry and structure of plant cells and cell walls with a spatial resolution of around 300 nm. Two-dimensional spectral maps can be acquired of selected areas and Raman images calculated by integrating the intensity of characteristic spectral bands or by using multivariate data analysis methods. This enables direct visualization of changes in the molecular structure and analyzing the spectra laying behind the chemical images reveal detailed insights into cell wall chemistry and structure¹⁻³.

Plant cell walls are based on cellulose microfibrils embedded in a matrix of hemicelluloses, pectins and lignins. The orientation of the cellulose microfibrils (alignment with respect to the fiber axis) on and its change in different layers is a key parameter as it influences the mechanical properties of the cell wall and fibers as well as swelling behavior. With the help of polarization equipment it was possible to estimate the microfibril angle on the micron-level using Confocal Raman microscopy⁴. The change within different layers was visualized together with the changes in lignin. All these parameters are elucidated at once and in-situ in context with the microstructure and reveal thus import

insights into the design of plant fibers e.g. so called gelatinous fibers⁵⁻⁶. These gelatinous fibers are known for tension wood of hard woods, in which it is built to maintain straight growth on a slop or to uprighten the branches of the tree. On a scan of a microsection of tension wood of poplar we showed by integrating the lignin band that the highest amount of lignin is found in the cell corner for gluing the fibers together (Fig. 1A). No lignin is found in the inner core, which is visualized by integrating the 1370cm⁻¹ band (Fig. 1B). Finally we could show that the orientation changes from the small outer layer to the big inner gelatinous layer as visualized with the help of the orientation sensitive band at 1097 cm⁻¹. So the gelatinous fibers have been identified to consist of an almost pure cellulose core, functionalized by a small outer lignified layer with high microfibril angle. (Figure 1). These two layers together enable plant movement in tension wood, but also in contraction roots of red clover⁵⁻⁶.

Recently the potential of method has also been shown on the algal model system *Micrasterias denticulata*. The changes in the molecular structure within the different cell organelles and structures can be followed as well as the changes in the outer cell wall during growth (Figure2).

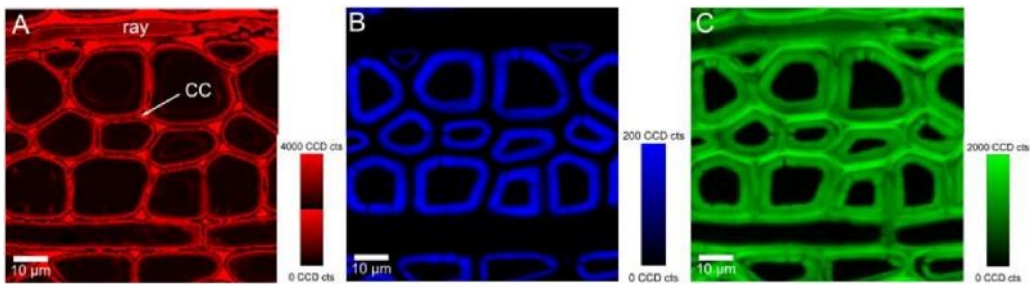


Figure 1. Raman images of poplar tension wood based on the band integration of the lignin marker band around 1602cm^{-1} (A: high amount of lignin is visualised in the cell corner (CC) and middle lamella (2000-4000CCDcts), low in the adjacent layer, and traces towards the lumen (0-2000CCDcts)), the 1370 cm^{-1} cellulose band shows the inner gelatinous layer (pure cellulose) with μ -channels (B) and the cellulose orientation sensitive band at 1097cm^{-1} accentuates a small layer with high MFA in laser polarisation direction (C). (Experimental: 532nm excitation, 100x oil immersion objective, scan area: $80\times 80\mu\text{m}$, Pixels: 240×240 , integration time: 0.4s)

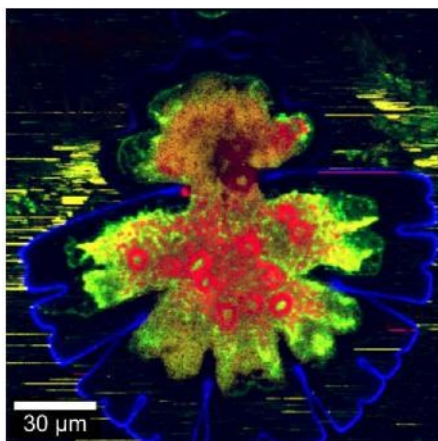


Figure 2. Raman spectroscopic image of *Micrasterias denticulata* ($160 \times 160 \mu\text{m}$, $0.5 \mu\text{m}$ step size, 532nm excitation, WITec300RA). Based on the 102 400 Raman spectra images were calculated with the help of non-negative matrix factorization (NMF), a method to evaluate distribution maps of different components and demixed basis spectra. The different colours represent the different basis spectra (components).

- ¹ Gierlinger, N., Schwanninger, M. (2006), *Plant physiology*, 140: 1246-54
- ² Gierlinger N, Keplinger T, Harrington M (2012), *Nature Protocols* 7(9): 1694-1708
- ³ Gierlinger N (2014) *Frontiers in Plant Science* 5 (306)
- ⁴ Gierlinger, N.; Luss, S.; König, Ch.; Konnerth, J.; Eder, M.; Fratzl, P. (2010), *Journal of Experimental Botany* 62 (2): 587-595
- ⁵ Schreiber, N.; Gierlinger, N.; Pütz, N.; Fratzl, P.; Neinhuis, Ch; Burgert, I. (2010), *Plant Journal* 61: 854-61 L.
- ⁶ Goswami, J. W. C. Dunlop, K. Jungnikl, M. Eder, N. Gierlinger, C. Coutand, G. Jeronimidis, P. Fratzl, and I. Burgert. *Plant J*, 2008, 56, 531-538.

Aamer, Khaled	TH501	Belkin, Mikhail	MOPL2
Agrawal, Megha	TH514	Bell, Gavin	TU603
Ågren, Matilda	MO802	Benko, Aleksandra	TU604
Agresti, Antonio	TU503	Berer, Thomas	TH803
Ahlawat, Anju	TH508	Bernatová, Silva	TU105
Aidam, Rolf	TU812	Bhargava, Rohit	WE101-inv
Akiyama, Kotaro	TU501	Biedermann, P. Ulrich	TU106
Albensi, Benedict	MO110	Bigini, Paolo	MO603
Alstrøm, Tommy	TU512	Bird, Benjamin	MO109
Altug, Hatice	H106	Bird, Benjamin	TU813
Alvarado, Camille	TU613	Bismilla, Yusuf	TH807
Alves, Wagner	TH604	Bismuto, Alfredo	TU804
Amenabar, Iban	MO104	Blanch, Ewan	WE603
Andre, Erwan	TH511	Blaser, Stéphane	TU804
Andre, William	TU613	Błazewicz, Marta	TU604
Andrews, Aaron M.	FR103-inv	Boatwright, Mark	WE802
Andrews, Aaron Maxwell	TU803	Bocklitz, Thomas	MO607
Argov, Shmuel	MO612	Boehmler, Miriam	MO111
Ariese, Freek	MO809	Bögözi, Timea	TU809
Arnone, David	MO109	Bohr, Jakob	MO513
Artyushenko, Viacheslav	TH809	Boisen, Anja	TU512
Ashton, Lorna	MO605	Bonnin, Estelle	TU613
Assi, Sulaf	MO803	Bonnist, Eleanor	TH810
Ataka, Kenichi	TU611-inv	Bornhöfft, Manuel	MO108
Ayora-Cañada, Maria Jose	MO801-inv	Boskovic, Dusan	TU801-inv
Bache, Michael	TU512	Bouchet, Brigitte	TU613
Bachmann, Anne	TU809	Bour, Petr	WE603
Bagnaninchi, Pierre	TH101	Bourotte, Jérémie	TU507
Baillet-Guffroy, Arlette	MO610	Bourson, Patrice	TH808
Baines, Fiona	TH810	Bovi, Daniele	TH602
Baker, Matthew	TU813	Brandl, Christian	TU504
Balbekova, Anna	MO105	Brandstetter, Markus	TH803
Balla, Andre	WE101-inv	Bratoš Cetinić, Ana	MO810
Banno, Motohiro	TH502	Brolo, Alexandre	TH112
Bar-David, Yossi	TU114	Bronner, Wolfgang	TU812
Baranska, Malgorzata	TH611	Brotin, Thierry	TU109
Baranska, Malgorzata	TU104	Brückl, Hubert	TU504
Baranska, Malgorzata	WE102	Brun, Mickael	TU802
Barker, Roger	TH613	Budde, Janpeter	TH612
Barone, Angela	WE804	Buffeteau, Thierry	TU109
Barre, Matt	MO109	Burgholzer, Peter	TH803
Barre, Matt	TU813	Bürgi, Thomas	WE604
Bates, Susan	TH810	Butschek, Lorenz	TU801-inv
Batignani, Giovanni	TH606	Caldwell, Joshua	WE502
Batista de Carvalho, Ana	TH614	Camacho, Felipe	TH604
Batista de Carvalho, Luís	TH614	Camatini, Marina	MO511
Batista, Victor	TH505	Campbell, Colin	TH101
Bazuin, C. Geraldine	TU507	Candeloro, Patrizio	MO613
Beardall, John	MO806-inv	Carneiro, Karina	MO112
Bec, Julien	MO607	Carney, Paul Scott	MO102
Bechtel, Hans	MO103	Carras, Mathieu	TU802
Bechtel, Hans	MO106-inv	Carrier, Stacey	TU112
Belkin, Mikhail	MO113	Carriere, James	MO813

Carron, Keith.....	MO804	Di Bitteto, Arnaud.....	TH511
Carteret, Cedric.....	TH511	Di Carlo, Aldo.....	TU503
Casiraghi, Cinzia.....	WE501-inv	Di Fabrizio, Enzo.....	MO613
Centrone, Andrea.....	MO101-inv	Di Franco, Simone.....	MO613
Cetin, Arif.....	TH106	Dieing, Thomas.....	MO811
Cha, Myeong Geun.....	MO608	Dillon, Eoghan.....	MO113
Champagne, Benoît.....	TU606	Dillon, Eoghan.....	MO505
Chang, Hyejin.....	MO608	Diomede, Luisa.....	MO603
Chapron, David.....	TH808	Dixon, Matthew.....	TH611
Chase, Bruce.....	MO514	Dluhy, Richard.....	TU511
Chen, Hsuen-Li.....	TH103	Dochow, Sebastian.....	MO607
Chernev, Boril.....	TU504	Doctor, Alan.....	TH814
Chernyshev, Vladimir.....	TH509	Doherty, James.....	TH614
Chiadò, Alessandro.....	TH110	Dominguez-Vidal, Ana.....	MO801-inv
Chlopicki, Stefan.....	WE102	Dong, Lei.....	TU814
Cho, Minhaeng.....	TH512	Dong, Zhenchao.....	TUPL1
Choi, Jun-Ho.....	TH512	dos Santos, Diego.....	TH112
Chou, Sin-Yi.....	TH103	Dresselhaus, Mildred.....	TH111
Chung, Hoeil.....	WE803	Dresselhaus, Mildred.....	TU602
Chuvilin, Andrey.....	MO102	Driad, Rachid.....	TU812
Cialla-May, Dana.....	TH102	Dropsit, Elise.....	TH808
Cicerone, Marcus.....	TH501	Dugandžić, Vera.....	TH102
Cinque, Gianfelice.....	TH614	Durand, Alain.....	TH808
Cîntă-Pânzaru, Simona.....	MO810	Durand, Sylvie.....	TU613
Cios, Franciszek.....	TU604	Dybal, Jiří.....	MO503
Clemens, Graeme.....	TU813	Ebert, Martin.....	MO807
Constantino, Vera.....	MO604	Eder, Gabriele.....	TH804
Costa, Sara.....	TU602	Eder, Gabriele.....	TU504
Covert, Paul.....	TU107	Ederth, Thomas.....	TU502
Cozar, Bogdan I.....	MO810	Edlinger, Michael von.....	TU807
Cuellar, Maryann.....	TH806	Ehrenfreund, Eitan.....	MO502
Dadd, Antony.....	TH810	Ek Weis, Johan.....	TU602
Davies, Gareth.....	MO809	El-Mashtoly, Samir.....	MO609
Davies, Julia.....	FR101	EL-Zahry, Marwa R.....	WE105
Davydov, Anton.....	MO512	Elfvig, Anders.....	MO802
Dawson, Simon.....	WE804	Emmenegger, Lukas.....	TU805
De Biasio, Martin.....	TH804	Enengl, Christina.....	MO502
de la Torre-Lopez, Maria Jose.....	MO801-inv	Enengl, Sandra.....	MO502
de Oliveira, Thales V. A. G.....	MO104	Engquist, Isak.....	TU502
de Veij, Marlene.....	TH611	Erbe, Andreas.....	TU106
Deckert-Gaudig, Tanja.....	TU101-inv	Etezadi, Dordaneh.....	TH106
Deckert, Volker.....	TH113	Evans, Richard.....	TH810
Deckert, Volker.....	TU101-inv	Fahel, Jean.....	TH511
Deckert, Volker.....	TU111	Fahlquist, Henrich.....	WE503
Dekhter, Rimma.....	TU114	Faist, Jérôme.....	TU805
Delbeck, Sven.....	TH612	Faria, Dalva.....	MO604
Dendisova, Marcela.....	TH105	Faulds, Karen.....	WE603
Deng, Shubin.....	TH111	Faulques, Eric.....	TU603
Denisova, Anna.....	TU110	Fedorowicz, Andrzej.....	WE102
Detz, Hermann.....	FR103-inv	Ferrante, Carino.....	TH606
Detz, Hermann.....	TH812	Findlay, Catherine.....	FR102-inv
Detz, Hermann.....	TU803	Fischer, Marc.....	TU807
Devaux, Marie-Françoise.....	TU613	Fisher, Kate.....	TH101

Monday

Tuesday

Wednesday

Thursday

Friday

Author Index

Fotheringham, Edeline	MO109	Gupta, P.K.	TH508
Fröhling, Kasper	TU512	Gust, Devens	TH505
Fromm, Felix	MO805	Gygi, Francois	TU106
Frosch, Torsten	TU809	Habelitz, Stefan	MO112
Fuchs, Frank	TU801-inv	Halamkova, Lenka	WE104
Fuchs, Frank	TU812	Hamada, Koji	MO509
Furukawa, Yukio	TU501	Hamra, Patricia	TU114
Gaigeot, Marie-Pierre	TH602	Hanf, Stefan	TU809
Galli, Giulia	TU106	Hangauer, Andreas	TU806-inv
Galvez, Oscar	MO808-inv	Happe, Thomas	TU102
Gardner, Benjamin	MO602	Haroniková, Andrea	TU105
Gardner, Peter	TH614	Harrer, Andreas	TH812
Gaussmann, Fabian	WE502	Harrison, David	TH101
Geiser, Markus	TU805	Hartl, Brad	MO607
Gembus, Armin	MO805	Hasegawa, Takeshi	MO510
Geobaldo, Francesco	TH110	Hasegawa, Takeshi	TU509
Gerwert, Klaus	MO609	Hauer, Benedikt	MO108
Gerwert, Klaus	TH603	Hauer, Juergen	TH610
Gerwert, Klaus	TU612	Häussermann, Ulrich	WE503
Gerwert, Klaus	WEPL2	Havlicek, Marek	MO502
Gierlinger, Notburga	FR104-inv	Heberle, Joachim	TU611-inv
Gil, Otávio	MO604	Heise, H. Michael	TH612
Gilles, Clement	TU802	Helesicova, Tereza	TH105
Gilliam, Sean	TH806	Hellwig, Petra	TU614
Giorgis, Fabrizio	TH110	Heraud, Philip	MO806-inv
Giovannozzi, Andrea Mario	MO603	Heraud, Philip	WE103
Glamuzina, Branko	MO810	Herbst, Johannes	TH811-inv
Glasse, Jarka	WE804	Herwig, Christoph	TH801-inv
Glimtoft, Martin	MO802	Heuzé, Karine	TU109
Golabgir, Aydin	TH801-inv	Heyler, Randy	MO813
Golmar, Federico	MO102	Hidi, Izabella Jolan	TH102
Gong, Liang	MO514	Hikima, Yuta	MO509
Goodacre, Roy	MO605	Hillenbrand, Rainer	MO102
Gordan, Ovidiu	TH506	Hillenbrand, Rainer	MO104
Gordon, Keith	MO506-inv	Hillenbrand, Rainer	MOPL1
Gordon, Keith	WE805	Hingerl, Kurt	MO502
Gorton, Lo	TH109	Hintenaus, Peter	TH802
Goryainov, Sergey	WE504	Hirschl, Christina	TH804
Gough, Kathleen	FR102-inv	Hirschmugl, Carol	MO106-inv
Gough, Kathleen	MO110	Hirschmugl, Carol	MO110
Govyadinov, Alexander	MO102	Ho, Junming	TH505
Govyadinov, Alexander A.	MO104	Hobro, Alison	MO614
Grafova, Michaela	TH105	Hochreiner, Armin	TH803
Graham, Duncan	WE603	Hodoroaba, Vasile-Dan	MO603
Grahmann, Jan	TU801-inv	Höfer, Sonja	TU607
Gresch, Tobias	TU804	Höfling, Sven	TU807
Gualtieri, Maurizio	MO511	Höhl, Martin	TU103
Gudim, Irina	TH507	Hollricher, Olaf	MO811
Guidoni, Leonardo	TH602	Hollywood, Katherine	MO605
Guillon, Fabienne	TU613	Holroyd, Steve	WE805
Guilment, Jean	TH808	Holzbauer, Martin	TU803
Güldenhaupt, Jörn	TU612	Hooijschuur, Jan-Hein	MO809
Gupta, Archana	TH514	Hoppe, Sandrine	TH808

Horch, Marius	TU102	Kazakov, Oleksandr	WE104
Hore, Dennis	TU107	Kazarian, Sergei	TU506-inv
Hrubanová, Kamila	TU105	Keiner, Robert	TU809
Hu, Qichi	MO113	Kelchermans, Mauritz	O505
Huang, Shengxi	TH111	Kelley, Chris	TH614
Huck, Christian	WE801-inv	Kemper, Mark	TH807
Huefner, Anna	TH613	Kerstan, Andreas	MO110
Huefner, Anna	TU513	Kesari, Swayam	TH510
Hugger, Stefan	TU801-inv	Kessler, Rudolf	THPL2
Hugger, Stefan	TU812	Kholkin, Andrei	MO512
Hughes, Caryn	TU813	Kiefer, Johannes	WE605
Hugi, Andreas	TU805	Kielb, Patrycja	TH109
Ibach, Wolfram	MO811	Kim, Gungung	MO608
Ichiro, Tanabe	TU601	Kim, Yong-il	MO608
Idrissi, Abdenacer	WE505	Kish, Elizabeth	TH505
Ihrig, Dieter	TH612	Kish, Elizabeth	TH602
Itoh, Tamitake	TU601	Kitamura, Sho	TH609
Iwata, Koichi	TH609	Kjoller, Kevin	MO113
Jafari, Mohammad Javad	TU502	Kjoller, Kevin	MO505
Jakobsen, Mogens	TU512	Klug, David	FR101
Jalkanen, Karl	MO513	Klyamkina, Alla	MO508
James, Sandy	MO807	Knapp-Mohammady, Michaela	MO513
James, Timothy M.	TU808	Knoll, Christian	TU510
Jamieson, Lauren	TH101	Koeth, Johannes	TU807
Jamme, Frédéric	TU613	Koh, Ivan	MO604
Jarisz, Tasha	TU107	Kokaislova, Alzbeta	TH105
Jarvis, Jan	TU812	Kondo, Takayuki	TH502
Jaworska, Aleksandra	TH101	Kong, Jing	TH111
Jeong, Dae Hong	MO608	Kong, Kenny	MO606-inv
Jeong, Sinyoung	MO608	Kötting, Carsten	MO609
Ježek, Jan	TU105	Kötting, Carsten	TH603
Ji, Wei	TH104	Kötting, Carsten	TU612
Jiang, Jing	TH101	Kottke, Tilman	TH608
Jin, Mingzhou	MO113	Koverga, Volodymyr	WE505
Jin, Mingzhou	MOPL2	Kowallik, Sarah	TU107
Jochum, Tobias	TU809	Kozanecki, Marcin	MO504
Johannessen, Christian	WE601-inv	Kraft, Martin	TH804
Johansson, Niklas	MO802	Kratochvíl, Jaroslav	MO503
Jones, Andrew	TH810	Krawczyk, Aleksandra	WE102
Jonsson, Dan	TU609	Kretinin, Andrey	WE502
Jörger, Michael	TH607	Kriegel, Sébastien	TU614
Jung, Lena	MO108	Kristament, Christian	TH803
Kaczor, Agnieszka	TU104	Krylov, Alexander	MO512
Kalbac, Martin	TU602	Krylov, Alexander	TH507
Kalugin, Oleg	WE505	Krylov, Alexander	WE504
Kamp, Martin	TU807	Krylova, Svetlana	TH507
Kanamori, Toshiyuki	MO510	Krylova, Svetlana	WE504
Kaneko, Tadaaki	TU601	Krzyżanek, Magdalena	TU604
Kang, Homan	MO608	Krzyżanek, Vladislav	TU105
Kansiz, Mustafa	MO110	Kuan, Wei-Li	TH613
Karlsson, Maths	WE503	Kühnemann, Frank	TH811-inv
Kashtiban, Reza	TU603	Kuligowski, Julia	WE105
Katz, Sagie	TU102	Kunsch, Johannes	TH814

Monday

Tuesday

Wednesday

Thursday

Friday

Author Index

Kurki, Lauri.....	MO814	Lucotti, Andrea	MO511
Kurouski, Dmitry	TU101-inv	Ludwig, Roland.....	TH109
Kutsuma, Yasunori	TU601	Ma, Dinglong	MO607
Lamberti, Andrea	TH110	MacFarland, Donald	FR103-inv
Lambrecht, Armin	TH811-inv	MacFarland, Donald	TH812
Landry, Olivier	TU804	MacFarland, Donald	TU803
Langer, Gregor	TH803	Mahajan, Sumeet.....	TH504
Larkin, Peter.....	MO813	Mahajan, Sumeet.....	TH613
Larsen, Jan	TU512	Mahajan, Sumeet.....	TU513
Lasch, Peter.....	TH601-inv	Maisons, Gregory.....	TU802
Latka, Ines.....	MO607	Malek, Kamilla	WE102
Laventure, Audrey.....	TU507	Mandez-Hernandez, Dalvin	TH505
Law, Philippa	MO812	Mandrile, Luisa	MO603
Lebel, Olivier	TU507	Mangold, Markus.....	TU805
Lednev, Igor	TU101-inv	Mänteles, Werner.....	TU811-inv
Lednev, Igor K.	WE104	Mantsch, Henry.....	TH605
Lee, Dong Soo	MO608	Mao, Nannao.....	TH111
Lee, Yoon-Sik.....	MO608	Marcott, Curtis	MO113
Lee, Young Jong.....	TH501	Marcott, Curtis	MO505
Leiss-Holzinger, Elisabeth	TH803	Marcott, Curtis	MO514
Leitner, Raimund	TH804	Marcu, Laura.....	MO607
Lenain, Bruno	TH806	Marekha, Bogdan	WE505
Lenarz, Thomas.....	TU103	Márová, Ivana	TU105
Lendl, Bernhard	MO105	Marques, Maria	TH614
Lendl, Bernhard	TH803	Martin, Michael.....	MO103
Lendl, Bernhard	TH805	Martin, Michael.....	MO106-inv
Lendl, Bernhard	WE105	Martra, Gianmario.....	MO603
Lenferink, Aufried.....	TH114	Marzec, Katarzyna	TH611
Leonidov, Ivan	TH509	Märzinger, Wolfgang	TH802
Leslie, Suzanne	WE101-inv	Maß, Tobias.....	TH107
Lewin, Martin	MO108	Mastel, Stefan	MO102
Lewin, Martin	WE502	Mastel, Stefan	MO104
Lewis, Aaron	TU114	Matejka, Pavel.....	TH105
Lewis, David.....	TU114	Matheson, Jane.....	TH810
Lewis, Ian.....	TH806	Matousek, Pavel.....	MO602
Li, Chunguang.....	TU814	Maulini, Richard	TU804
Li, Peining.....	WE502	Maurino, Valter	MO603
Liao, Catherine.....	MO110	Mavarani, Laven	MO609
Liberale, Carlo	MO613	Mayer, Joachim	MO108
Liegeois, Vincent	TU606	Mayerhöfer, Thomas G.	TU607
Lin, Yuan-Chih.....	WE503	Mayerich, David	WE101-inv
Ling, Xi.....	TH111	Mayr, Georg	TH802
Lipina, Olga	TH509	McBrin, C.J.....	MO514
Liu, Jiang.....	TU502	McDonnell, Liam.....	TU603
Lo, Michael	MO505	McNaughton, Don.....	TH611
Lopez Ramirez, Maria Rosa	TU514	McNaughton, Don.....	WE103
López-Lorente, Ángela I.	TU605	McQuillan, A. James.....	TU108
Lu, Feng	MO113	Medema, Jan Paul	MO613
Lu, Feng	MOPL2	Meinhardt-Wollweber, Merve	TU103
Lu, H. Peter	TU113	Melin, Frédéric.....	TU614
Luber, Sandra	WE604	Mensch, Carl.....	WE601-inv
Luca, Iannareli	MO603	Merten, Andre	TU801-inv
Lucas, Herve	TH806	Meyer, Thomas	TU614

Mezzetti, Alberto.....	TH602	Olejniczak, Magdalena	MO504
Michel, Ann-Katrin U.....	MO108	Ollesch, Julian.....	TH603
Miloudi, Lynda.....	MO610	Olman, Robert.....	MO106-inv
Mink, Janos.....	WE503	Olmon, Rob.....	MO103
Misra, Dileep.....	TU505	Olsen, Kasper.....	MO513
Mittal, Shachi.....	WE101-inv	Osawa, Masatoshi.....	TH108
Mizaikoff, Boris.....	TU605	Osselton, David.....	MO803
Moghe, Prabhas.....	TH501	Ostendorf, Ralf.....	TU801-inv
Möhler, Ottmar.....	MO807	Ostendorf, Ralf.....	TU812
Monfort, Tual.....	TH504	Österberg, Carin.....	WE503
Montague, Gary.....	WE804	Östmark, Henric.....	MO802
Moore, Ana.....	TH505	Ostovar pour, Saeideh.....	WE603
Moore, Thomas.....	TH505	Otto, Cees.....	TH114
Mordechai, Shaul.....	MO612	Oulevey, Patric.....	WE604
Morgner, Uwe.....	TU103	Ozaki, Yukihiro.....	TH104
Morita, Kohei.....	MO510	Ozaki, Yukihiro.....	TU601
Morita, Shigeaki.....	TU508	Pacia, Marta.....	TU104
Moser, Harald.....	TH805	Parchansky, Vaclav.....	WE603
Motobayashi, Kenta.....	TH108	Parkinson, Dilworth.....	MO106-inv
Mueller, Thomas.....	MO112	Parkinson, Dilworth.....	WE103
Müller, Antoine.....	TU804	Pashinin, Pavel.....	MO508
Müller, Csilla.....	MO810	Pastrana-Rios, Belinda.....	MO611-inv
Müller, Danny.....	TU510	Patel, Parth.....	TH501
Muller, Eric.....	MO103	Paterson, Sarah.....	TH810
Muller, Eric.....	MO106-inv	Patimisco, Pietro.....	TU810-inv
Myund, Lubov.....	TU110	Patimisco, Pietro.....	TU814
Nabers, Andreas.....	TH603	Pavillon, Nicolas.....	MO614
Nafie, Laurence.....	WE602	Pawluczyk, Jaroslaw.....	TH813
Nähle, Lars.....	TU807	Pellerin, Christian.....	MO501
Nasse, Michael.....	MO106-inv	Pellerin, Christian.....	MO507
Nayak, Simantini.....	TU106	Pellerin, Christian.....	TU507
Nedorezova, Polina.....	MO508	Pellutiè, Letizia.....	MO603
Neugebauer, Helmut.....	MO502	Pengel, Stefanie.....	TU106
Neumaier, Lukas.....	TH804	Perez-Guaita, David.....	TH611
Niemiec, Wiktor.....	TU604	Pescetelli, Sara.....	TU503
Nikiforov, Anatoliy.....	TH509	Petersen, Dennis.....	MO609
Nikolaeva, Gulnara.....	MO508	Petrou, Katherina.....	MO806-inv
Niu, Fang.....	TU106	Petrov, Vladislav.....	TH509
Noda, Isao.....	MO514	Pham Khac, Duy.....	WE803
Nojima, Yuki.....	TH609	Picqué, Nathalie.....	TUPL2
Norberg, Ola.....	MO802	Pilát, Zdenik.....	TU105
Noth, Jens.....	TU102	Pillai, Smitha.....	TH505
Notingher, Ioan.....	MO606-inv	Pilling, Mike.....	TH614
Novara, Chiara.....	TH110	Piotrowski, Jozef.....	TH813
Novokshonova, Lyudmila.....	MO508	Pitters, Alexander.....	TH806
Novoselov, Kostya.....	WE502	Pontecorvo, Emanuele.....	TH606
Nuraeva, Alla.....	MO512	Popp, Jürgen.....	MO601-inv
Obruèa, Stanislav.....	TU105	Popp, Jürgen.....	MO607
Off, Andreas.....	TU808	Popp, Jürgen.....	TH102
Ofner, Johannes.....	TH805	Popp, Jürgen.....	TU607
Ogrodnik, Karolina.....	TH813	Popp, Jürgen.....	TU809
Ohshima, Masahiro.....	MO509	Prater, Craig.....	MO113
Oldemeyer, Sabine.....	TH608	Prater, Craig.....	MO505

Monday

Tuesday

Wednesday

Thursday

Friday

Author Index



Preston, Stuart.....	MO803	Saramak, Jakob.....	MO504
Prokhorov, Kirill.....	MO508	Sariciftci, Niyazi S.....	MO502
Pudney, Paul.....	TH810	Sarkar, Nirmal.....	TU610
Pukalski, Jan.....	TU104	Satapathy, Srinibas.....	TH508
Quaroni, Luca.....	MO107	Sathe, V.G.....	TU505
Quatela, Alessia.....	MO610	Sathe, Vasant.....	TH508
Quintás, Guillermo.....	WE105	Saulnier, Luc.....	TU613
Rabolt, John.....	MO514	Savela, Jyrki.....	MO814
Rajamanickam, Vijayakumar.....	MO613	Scamarcio, Gaetano.....	TU810-inv
Rakhimbekova, Assima.....	TU110	Scamarcio, Gaetano.....	TU814
Ramer, Georg.....	MO105	Scharber, Markus C.....	MO502
Rao, Rekha.....	TH510	Schartner, Jonas.....	TH603
Raschke, Markus.....	MO103	Schartner, Jonas.....	TU612
Raschke, Markus.....	MO106-inv	Schenk, Harald.....	TU801-inv
Rattunde, Marcel.....	TU812	Scheuermann, Julian.....	TU807
Rawat, R.....	TU505	Schilling, Christian.....	TU812
Reece, David.....	MO812	Schlesinger, Ramona.....	TU611-inv
Reininger, Peter.....	FR103-inv	Schluecker, Sebastian.....	THPL1
Reininger, Peter.....	TH812	Schmid, Rochus.....	TU106
Richard-Lacroix, Marie.....	MO501	Schmidt, Michael.....	TU512
Richard-Lacroix, Marie.....	MO507	Schmidt, Mikkel.....	TU512
Ringholm, Magnus.....	TU609	Schmidt, Ute.....	MO811
Ristanic, Daniela.....	FR103-inv	Schmitt, Heike.....	TU103
Rivolo, Paola.....	TH110	Schmitt, Michael.....	MO607
Robert, Bruno.....	TH505	Schnaiter, Martin.....	MO807
Robert, Bruno.....	TH602	Schrenk, Werner.....	FR103-inv
Robert, Paul.....	TU613	Schrenk, Werner.....	TH812
Rocha, Michele.....	MO604	Schrenk, Werner.....	TU803
Rocks, Louise.....	WE603	Schultz, Zachary.....	TU112
Röder, Thomas.....	TH802	Schwaighofer, Andreas.....	MO105
Romanis, Mariusz.....	TH813	Schwarz, Benedikt.....	FR103-inv
Rossi, Andrea Mario.....	MO603	Schwarz, Benedikt.....	TH812
Roth, Andreas.....	TU811-inv	Scopigno, Tullio.....	TH606
Rowlands, Christopher.....	MO606-inv	Sebbag, Gilbert.....	MO612
Rowlette, Jeremy.....	MO109	Seifried, Marco.....	TU510
Rowlette, Jeremy.....	TU813	Seitz-Moskaliuk, Hendrik.....	TU808
Roy, Anjan.....	MO813	Seufzer, Siegfried.....	TH804
Roy, Sandra.....	TU107	Shimoaka, Takafumi.....	MO510
Rubio-Domene, Ramon.....	MO801-inv	Shimoaka, Takafumi.....	TU509
Rupp, Simone.....	TU808	Shioya, Nobutaka.....	MO510
Ruud, Kenneth.....	TU609	Shoshi, Astrit.....	TU504
Ryan, Kate.....	MO512	Shur, Vladimir.....	MO512
Ryzhikova, Elena.....	WE104	Sieger, Markus.....	TU605
Sackett, Olivia.....	MO806-inv	Sikora, Antonin.....	MO503
Sagitova, Elena.....	MO508	Simon, Arno.....	TH607
Sahu, Ranjit.....	MO612	Singh, Pushkar.....	TU111
Saiz-Lopez, Alfonso.....	MO808-inv	Sinjab, Faris.....	MO606-inv
Salehi, Mohammad.....	THPL1	Siurdyban, Elise.....	TU109
Salke, Nilesh.....	TH510	Slater, Joe.....	TH806
Salman, Ahmad.....	MO612	Sloan, Jeremy.....	TU603
Samek, Ota.....	TU105	Smith, David.....	TU603
Sampaolo, Angelo.....	TU810-inv	Smith, Geoffrey.....	WE805
Sánchez-Illana, Ángel.....	WE105	Smith, Nicholas.....	MO614

Smith, Tim.....	MO812	Tirinato, Luca.....	MO613
Smus, Justyna.....	TH504	Tittel, Frank.....	TU810-inv
Smus, Justyna.....	TU513	Tittel, Frank.....	TU814
Sofronova, Svetlana.....	TH507	Todaro, Matilde.....	MO613
Solonenko, Dmytro.....	TH506	Tomioka, Ryota.....	TH108
Solovyeva, Elena.....	TU110	Tomšić, Sanja.....	MO810
Song, Wei.....	TH104	Towari, Saumya.....	WE101-inv
Sonoyama, Masashi.....	MO510	Trautmann, Steffen.....	TU111
Sowley, Hugh.....	FR101	Tseng, Shao-Chin.....	TH103
Spagnolo, Angelo.....	TU814	Tseng, Yi-Chuan.....	TH103
Spagnolo, Vincenzo.....	TU810-inv	Turnau, Katarzyna.....	TU104
Spagnolo, Vincenzo.....	TU814	Turrell, Sylvia.....	TU604
Spencer, Joe.....	TU603	Tyutyunnik, Alexander.....	TH509
Spezia, Riccardo.....	TH602	Uchida, Taro.....	TH108
Staniszewska-Slezak, Emilia.....	WE102	Uerpmann, Carsten.....	TH806
Starchak, Elena.....	MO508	Ujević, Ivana.....	MO810
Stassi, Giorgio.....	MO613	Ujj, Laszlo.....	TH503
Stavrov, Solomon.....	TH513	Ushakova, Tatiana.....	MO508
Stiufiuc, Rares.....	MO810	Vahlsing, Thorsten.....	TH612
Stodolak-Zych, Ewa.....	TU604	Valcárcel, Miguel.....	TU605
Stone, Nick.....	MO602	Vantasin, Sanpon.....	TU601
Strachan, David.....	TH806	Vapaavuori, Jaana.....	TU507
Strasser, Gottfried.....	FR103-inv	Vardaki, Martha.....	MO602
Strasser, Gottfried.....	TH812	Varnholt, Birte.....	WE604
Strasser, Gottfried.....	TU803	Vasilev, Semen.....	MO512
Šturcová, Adriana.....	MO503	Vega, Sebastián.....	TH501
Suda, Jun.....	TU608	Veitmann, Marie.....	TH808
Surat, Ludmila.....	TH509	Vejpravova, Jana.....	TU602
Suzuki, Toshiaki.....	TU601	Vellutini, Luc.....	TU109
Svanqvist, Mattias.....	MO802	Venter, Monica M.....	MO810
Svecova, Marie.....	TH105	Vento, Máximo.....	WE105
Szedlak, Rolf.....	TU803	Verkaaik, Mattheus.....	MO809
Taha, Hesham.....	TU114	Villares, Gustavo.....	TU805
Tahara, Tahei.....	FRPL1	Virga, Alessandro.....	TH110
Takagi, Toshiyuki.....	MO510	Vitiello, Miriam S.....	TU810-inv
Takaya, Tomohisa.....	TH609	Vogt, Patrick.....	TH506
Tanabe, Ichiro.....	TH104	Voronov, Vladimir.....	WE504
Tanaka, Yoshito.....	TU601	Vovkotrub, Emma.....	TH509
Tanaka, Yuki.....	MO510	Vtyurin, Alexander.....	TH507
Taniguchi, Takashi.....	WE502	Vtyurin, Alexander.....	WE504
Taubner, Thomas.....	MO108	Vuilleumier, Rodolphe.....	TH602
Taubner, Thomas.....	TH107	Wachsmann-Hogiu, Sebastian.....	MO607
Taubner, Thomas.....	WE502	Wagner, Joachim.....	TU801-inv
Tecklenburg, Stefanie.....	TU106	Wagner, Martin.....	MO112
Telle, Helmut H.....	TU808	Wagner, Robert.....	MO807
Temperini, Marcia.....	TH112	Wang, Hao.....	TU112
Tenhunen, Mari.....	MO814	Wang, Yue.....	TH104
Terazzi, Romain.....	TU804	Warring, Suzanne.....	TU108
Tetassi Feugomo, Conrard Giresse.....	TU606	Weber, Karina.....	TH102
Tfayli, Ali.....	MO610	Weddell, Lynette.....	TH810
Thöing, Christian.....	TH608	Weida, Miles.....	MO109
Tilley, Leann.....	TH611	Weidinger, Inez M.....	TH109
Timmermans,.....	Frank TH114	Weigel, Ralf.....	MO807

Monday

Tuesday

Wednesday

Thursday

Friday

Author Index

Weih, Robert	TU807
Weinberger, Peter	TU510
Weselucha-Birczynska, Aleksandra	TU604
Westberg, Jonas	TU806-inv
Wetzel, David	WE802
Whelan, Donna	WE103
Wieda, Mile	TU813
Wiegand, Pat	TH806
Wiercigroch, Ewelina	WE102
Willison, Keith	FR101
Wippermann, Stefan	TU106
Wojtas, Maciej	MO512
Wolf, Sebastian	TH811-inv
Wolferen, Henk van	TH114
Wong Carter, Katherine	TH505
Wood, Bayden	TH611
Wood, Bayden	WE103
Wrobel, Tomasz	WE101-inv
Wysocki, Gerard	TU806-inv
Yamamoto, Jun	TU501
Yamamoto, Shigeki	WEPL1
Yan, Di	TU809
Yang, Honghua	MO113
Yang, Quankui	TU812
Yeh, Kevin	WE101-inv
Yen, Yu-Ting	TH103
Yosef, Hesham	MO609
Yu, Chen-Chieh	TH103
Yu, Yajun	TU814
Yui, Hiroharu	TH502
Zachhuber, Bernhard	MO802
Zachmann, Günter	TH607
Zahn, Dietrich	TH506
Zanni, Martin	FRPL2
Zavgorodnev, Yury	MO508
Zebger, Ingo	TH109
Zebger, Ingo	TU102
Zederbauer, Tobias	TH812
Zederbauer, Tobias	TU803
Zeerbauer, Tobias	FR103-inv
Zelenovskiy, Pavel	MO512
Zemánek, Pavel	TU105
Zerbi, Giuseppe	MO511
Zhang, Eric	TU806-inv
Zhang, Jason	WE103
Zhang, Jin	TH111
Zhang, Yuying	THPL1
Zhang, Zhenglong	TH113
Zhao, Bing	TH104
Zimmerman, Earl A.	WE104
Zubkov, Vladimir	TH509
Zverev, Petr	TU608

Impressum

Vienna, July 2015

Editors: Bernhard Lendl, Cosima Koch, Martin Kraft, Johannes Ofner, Georg Ramer

Layout: Manuel Dauböck

Typeface: Dejavu Sans, Humanist 777, Times New Roman, Calibri

Printer: druck.at

ISBN: 978-3-200-04205-6

